Nonlinear Plate Models for the Numerical Simulation of Thin Elastic Sheets

David G. Robinson
School of Physics and Astronomy

A thesis submitted to the University of Manchester
for the degree of Doctor of Philosophy
in the Faculty of Science and Engineering

2019

Blank page

Contents

Word count 50223

The University of Manchester

David G. Robinson

For the degree of Doctor of Philosophy

Nonlinear Plate Models for the Numerical Simulation of Thin Elastic Sheets

October 21, 2019

Thin elastic sheets are found throughout nature and are also extremely important in industrial applications. Sheets can be described using plate and shell models which, in systems where shear is negligible, are typically fourth-order, two-dimensional, partial differential equations. Many such models exist; however, the circumstances in which a particular model is appropriate to use may not be readily apparent. Therefore a means of comparing different unshearable plate and shell models in a general setting is of interest, and is yet to be systematically addressed in the literature.

The focus of this thesis is the implementation of a generic numerical framework for the discretization of two-dimensional, fourth-order boundary-value problems, using the method of boundary patches. We build upon the literature for curved triangular Hermite elements by outlining the explicit construction formulas for a known class of curved elements, compatible with Bell elements. We implement these elements within the finite element library `oomph-lib`. In this study we consider three plate models: the well-known moderate-rotation Föppl-von Kármán model, the arbitrary-rotation Koiter-Steigmann plate model and a new moderate-to-large rotation model, which we derive herein. We then implement these plate models within the library, so that they can be solved on generic domains.

Finally, we use the implemented plate models, along with analytic and finite difference approaches, to compare the models in three different contexts. The systems we study are the clamped inflation of a circular sheet, the inflation of a circular sheet subject to a rolling clamp, which undergoes a wrinkling instability, and the large cantilever-type displacement of a complicated curved domain, respectively. In all of these systems the choice of plate models is demonstrated to be important: in particular in all cases the predictions of the Föppl-von Kármán model break down for moderate-thickness sheets, yielding inaccurate predictions of the sheet morphology. This serves both to demonstrate the capability of the numerical framework as a comparison tool and highlight why such comparisons are important.

Declaration

No portion of the work referred to in the thesis has been submitted in support of an application for another degree or qualification of this or any other university or other institute of learning.

Copyright Statement

i. The author of this thesis (including any appendices and/or schedules to this thesis) owns certain copyright or related rights in it (the "Copyright") and s/he has given The University of Manchester certain rights to use such Copyright, including for administrative purposes.

ii. Copies of this thesis, either in full or in extracts and whether in hard or electronic copy, may be made **only** in accordance with the Copyright, Designs and Patents Act 1988 (as amended) and regulations issued under it or, where appropriate, in accordance with licensing agreements which the University has from time to time. This page must form part of any such copies made.

iii. The ownership of certain Copyright, patents, designs, trade marks and other intellectual property (the "Intellectual Property") and any reproductions of copyright works in the thesis, for example graphs and tables ("Reproductions"), which may be described in this thesis, may not be owned by the author and may be owned by third parties. Such Intellectual Property and Reproductions cannot and must not be made available for use without the prior written permission of the owner(s) of the relevant Intellectual Property and/or Reproductions.

iv. Further information on the conditions under which disclosure, publication and commercialisation of this thesis, the Copyright and any Intellectual Property and/or Reproductions described in it may take place is available in the University IP Policy (see http://documents.manchester.ac.uk/DocuInfo.aspx?DocID=24420), in any relevant Thesis restriction declarations deposited in the University Library, The University Library's regulations (see http://www.library.manchester.ac.uk/about/regulations/) and in The University's policy on Presentation of Theses.

Acknowledgements

First and foremost I would like to thank my supervisors, Draga Pihler-Puzović and Matthias Heil, whose guidance and support throughout have been unparalleled. Their advice, encouragement and wisdom has been constant and without it this PhD would not have been possible. I would especially like to thank them for their direction and inspiration over the course of my PhD and their extremely valuable feedback on my written work.

A special thank you to Anne Juel, Alice Thompson, Chris Johnson and Andrew Hazel, and the rest of the MCND group and oomph-lunch, who have also provided me with excellent advice and critique over the last four years. I would also like to thank Michael and Simon for the excellent work they produced over the course of their internships, which contributed greatly to the understanding of several physical systems and provided me with excellent feedback on the interface to my code. Further, I would like to thank Emmanuel Siéfert for his excellent idea for a physical realization of the rolling-clamp system considered herein.

I additionally would like to extend my gratitude to Edgar, Andrés, Pallav, Lucie, Callum, Kerstin, João, Ashish, Nico, Finn and Christian for their company, insight and good-humour over lunch and coffee breaks, which provided an excellent working environment. Putting the world to rights every lunchtime is certainly the part I will miss the most of my PhD.

I would like to thank my family and friends, for their patience and understanding, especially when it seemed as if I would never emerge from my write-up. I would especially like to thank my parents, who nurtured my interest in mathematics and science throughout my childhood. Thank you also to Pauline and Phil, for their kindness, generosity and attention to filling my fruit bowl throughout.

Finally I would like to thank my lovely, indefatigable wife, Jess, for her incredible support and incomparable positive attitude during my PhD. This PhD would truly not have been possible without her love, support, humorous repartee and inventive carbohydrate combinations.

Chapter 1

Introduction

1.1 Overview of Elastic Sheets

Thin elastic sheets, or plates and shells, are ubiquitous throughout nature: any elastic material that is much thinner in one dimension than the other two may be regarded as an elastic shell. A plate is simply a shell with zero initial curvature. Theories of thin elastic plates find applications from the nanoscale, in the deformation of graphene flakes [Zhang et al., 2011; Los et al., 2016, 2017] through to the kilometric scale found in continental plates [Mahadevan et al., 2010; Jaupart and Lévy, 2011]. Thin plate and shell models provide a powerful framework for the modelling of physical systems as continua, whereby they reduce full three-dimensional systems to two-dimensional descriptions, by integrating the effect of through-thickness strains.

Thin plate and shell models are utilised for a variety of reasons, but ultimately they are used to provide a model of reality: be that by direct simulation, such as in the simulation of a bio-prosthetic heart valve [Kiendl et al., 2015], or by providing a framework for understanding a particular system, such as in the scarring of human tissue [Cerda, 2005]. Often the model is used to provide a means of measurement when more direct methods are unavailable: such as in the measurement of stiffness for graphene flakes [Los et al., 2016], in which it is not possible to perform a standard uniaxial tension experiment, or in the measurement of skin elasticity [Cerda and Mahadevan, 2003] in which non-invasive procedures are favoured for obvious reasons. These measurements and simulations can inform upon design and manufacturing and allow real engineering problems to be solved: such as in the design of deformable electronics [Kim et al., 2008; Rogers et al., 2010; Kim et al., 2011] or the

deployment and design of space structures, such as reflectors [Wang et al., 2009] and solar sails [Blandino et al., 2002; Fu et al., 2016]. In the latter applications, the accuracy of the model is paramount, as ground testing is difficult due to the presence of gravity [Blandino et al., 2002]. Thus, the understanding of plate models and their ability to accurately capture behaviour is extremely important in many applications.

1.2 Wrinkling as a Ruler

A particularly important phenomenon found in thin sheets is wrinkling: regular undulations of thin sheets that occur due to compression. Wrinkling is a familiar concept to most of us as it is encountered in many aspects of every-day life, from displacement-induced wrinkling of the skin that forms on the top of milk after heating, to the creases found when draping of fabric over an object. In all of these scenarios wrinkles form due to compressive stresses, which are in turn caused by a geometrical incompatibility, i.e having an excess of length or area that needs to be accommodated [Huang et al., 2010; Holmes and Crosby, 2010].

In very thin sheets, bending out-of-plane is 'energetically cheap' as opposed to stretching and compression in-plane, which is relatively speaking 'expensive'. As such, deformation in sheets is characterised by two types of deformation: bending and stretching. The thickness, h^*, of a sheet is extremely important when considering these two types of deformations, as the resistance associated with stretching (in-plane tension) typically scales as $\sim h^*$, as opposed to the resistance associated with bending (out-of-plane) which scales as $\sim (h^*)^3$ [Audoly and Pomeau, 2010]. Thus for thin sheets, large deformations out-of-plane can be made with little resistance from the sheet. It is for this reason that wrinkling occurs readily in extremely thin sheets: under any significant compression thin sheets buckle out-of-plane rather than sustaining compression in-plane.

Wrinkling in thin sheets is often an unfavourable property of a system: for example, with a telescope reflector, wrinkles would effect the quality of the reflected image [Puntel et al., 2010]. In many engineering applications, wrinkling is associated with failure of a material, in which structures lose their rigidity [Genzer and Groenewold, 2006]. However, wrinkling can also be a useful indicator in experiments and in recent years has proved to be a powerful tool for measuring sheet properties, especially in systems where more conventional measurements are difficult or unfeasible [Huang et al., 2007; King et al., 2012].

Studies have focused on using easily measurable properties, such as wrinkle extent, buckling threshold and the number of wrinkles to determine sheet properties such as thickness, h^*, and stiffness (Young's modulus, E) [Cerda and Mahadevan, 2003; Huang et al., 2007; King et al., 2012]. The advantage to such experiments is that measurement can be made directly with a birds-eye view, without reconstruction of the displacement. Predictions for these properties are usually based on either the predictions of the well-known *Föppl-von Kármán equations* or the predictions of *tension field theory*, or a clever combination of the two, both of which we discuss in detail below.

1.2.1 The Föppl-von Kármán Model

The Föppl-von Kármán model is a thin-plate model which is appropriate for moderate rotations and small strains [Audoly and Pomeau, 2010]: it couples small-displacement (linear) bending to the partially linearised (small-strain) *Föppl membrane model*, which neglects higher order in-plane displacement strains. Classically, it is derived by the joint assumptions of moderate rotations and the *Kirchhoff-hypothesis*: an assumption that after deformation the normal to the undeformed middle-surface of a sheet remains normal and unstretched. This latter assumption is tantamount to neglecting shear-strain in the model. Modern derivations have identified the conditions under which the Föppl-von Kármán model emerges as the leading order model from 3D elasticity, instead making assumptions only on the magnitude of applied forces and the small thickness of the sheet [Friesecke et al., 2006]. These corroborate the classical assertions that the Föppl-von Kármán model is appropriate when bending and stretching are of comparable magnitude and strains are small [Audoly and Pomeau, 2010].

The intrinsic assumption of sheet angles and displacements, renders the Föppl-von Kármán model unsuitable when finite displacements need to be considered. Little work has been done comparing higher order plate models that incorporate large displacements and strains to the predictions of Föppl-von Kármán, the former of which become essential in large-deformation systems such as twist-induced wrinkles [Chopin and Kudrolli, 2013; Chopin et al., 2015; Kudrolli and Chopin, 2018].

The Föppl-von Kármán model is a relatively simple model which can predict wrinkling phenomena. Often results are most readily obtained at the wrinkle onset, or near threshold, where *linear stability analysis* is used to deduce information about the sheet near the buckling threshold.

1.2.2 Linear Stability Analysis

Linear stability analysis is a technique whereby the equations are linearised about an unwrinkled base state. First the base-state equations are solved, by making an ansatz using the symmetry of the pre-wrinkling state. This base-state may either be solved analytically, as in Davidovitch et al. [2011], by asymptotic expansion as in Coman et al. [2015], or by numerical simulation [Coman, 2013]. This base-state is then used as a parameter in the solution of the (linearised) perturbation equations, which in turn yield the wrinkling solution near to the threshold. Though this solution is strictly valid only infinitesimally close to the threshold of wrinkling, these solutions may inform upon finite wrinkling patterns close to the threshold, as well as provide valuable information about the buckling onset. An excellent example of linear stability analysis is provided by the studies Coman [2013]; Coman et al. [2015], in which the wrinkling of smoothly-clamped, pressurized, circular sheets, subjected to both weak and strong in-plane tension are studied both numerically and by asymptotic methods. This was ultimately used to derive scaling laws for onset wavenumber variation with in-plane tension [Coman et al., 2015].

1.2.3 Tension-Field Theory and Far-from-Threshold Wrinkling

Tension field theory on the other hand is a formalism that attempts only to identify regions where wrinkling occurs, without resolving the wrinkles individually. Though these ideas originated in the 1960s with the works of Stein and Hedgpeth [1961]; Mansfield [1969], the ideas were later formalized by the work of Pipkin [1986]; Steigmann [1990]. The wrinkled regions are found by neglecting bending stiffness, instead assuming that any would-be regions of compression are slackened by fine-scale wrinkles, which are not resolved. Thus the stress in the sheet is always positive (or zero) and any slack (zero-stress) regions are assumed to be regions in which wrinkling occurs. These ideas saw a renewed interest after a landmark study by Cerda and Mahadevan [2003], in which a form of tension field theory was applied and extended to find scaling laws for both the wavelength, $\lambda \sim (h^{*3}E/T)^{1/4}$, and amplitude, $A \sim \lambda$ of the wrinkles in a rectangular sheet (see figure 1.1a) under tension, T. These scaling laws, in turn, can provide means of measurement of properties such as thickness, h^*, and Young's modulus, E, especially in systems where standard techniques are not possible. The new approach, that included calculation of wrinkle wavenumber was later termed 'far-from-threshold' analysis.

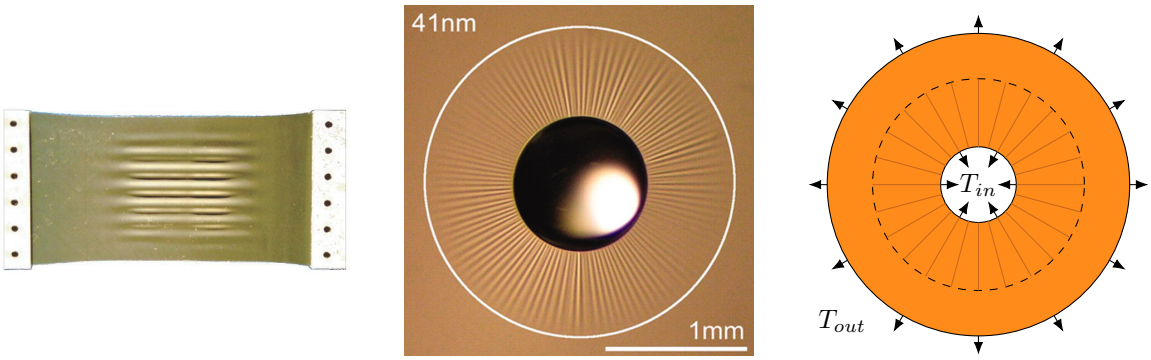

(a) (b) (c)

Figure 1.1: (a) Stretch induced wrinkles in a thin sheet under lateral tension [Cerda et al., 2002], image reproduced with permission from the rights holder, Springer Nature. (b) Thin floating elastic sheet loaded by a liquid drop. From [Huang et al., 2007]. Reprinted with permission from AAAS. (c) The Lamé set-up, involving an annular sheet subject to tension at inner and outer radii. [Davidovitch et al., 2011]. A dashed line indicates the edge of the wrinkled region, in which the minima are shown schematically as radial lines.

Following this, developments were made to apply and extend this framework to various other systems: for example, Huang et al. [2007] performed experiments on a floating film, nanometric in thickness and loaded by a liquid drop of radius, a (figure 1.1b). The sheet was pulled by capillary forces, induced by the drop, which effectively resulted in two tensions applied to an annular sheet: the capillary force of the drop at the contact line and the surface tension, γ, of the liquid bath. A scaling law for number of wrinkles, $m \sim (\gamma/Eh)^{1/4}(R/h^*)^{1/2}$, similar to the one obtained by Cerda and Mahadevan [2003], and an empirically deduced scaling for wrinkling extent, $L \sim (Eh^*/\gamma)^{1/2}\,R$, were used to infer the elastic modulus, E, and thickness, h, of the films. The understanding of this system was then refined by the studies of Vella et al. [2010] and Schroll et al. [2013] where a quantitative understanding of the wrinkle length in the near (i.e. close to the onset) and far-from-threshold regime (i.e when wrinkling has relaxed the compressive stresses) was obtained.

In the closely related Lamé problem [Timoshenko and Goodier, 1969], studied variously by Géminard et al. [2004]; Coman and Bassom [2007]; Davidovitch et al. [2011, 2012], which consists of an annular sheet subjected to tension at inner and outer radii (figure 1.1c), theoretical progress was made in capturing the transition from near to far-from threshold, [Davidovitch et al., 2011, 2012]. This was achieved by solving a linear stability analysis

for the Föppl-von Kármán model at the wrinkling onset and using the tension field theory approach to determine a region of collapsed azimuthal stress. The wrinkle wavenumber can then be reconstructed by force balance arguments in the-out-of-plane direction: the bending induced by wrinkling is assumed to balance the out-of-plane force induced by azimuthal compression and radial tension, which yield scaling arguments on the number of wrinkles and the azimuthal (hoop) stress. These studies resulted in the introduction of two new dimensionless groups to describe wrinkled systems: 'confinement' and 'bendability', which measure the relative strength of the tension and the resistance to bending in relation to the tension, respectively. Thus, in sheets of 'high bendability' the bending stiffness is very small, and the fine-scale wrinkling associated with the far-from-threshold is readily attainable in the physical system. Confinement, on the other hand, describes relative strength of the compressive tension, thus this associated with the onset of wrinkling, and the progression from the near to far-from-threshold state.

These ideas also proved extremely useful in application to related systems, such as sheets draped on drops, in which similar near and far-from-threshold scaling laws were found using force-balance arguments [King et al., 2012]. The theoretical description underlying this study is similar to the pressurized circular sheets of Coman et al. [2015], however the lack of a bending boundary layer in the strong transverse-forcing limit results in a far more tractable system, as noted by Coman and Bassom [2016].

All of these concepts were recently generalized by Paulsen et al. [2016] by considering a local picture of wrinkling, which was then shown to apply to the three systems considered by Cerda and Mahadevan [2003]; Davidovitch et al. [2011]; King et al. [2012], respectively.

1.2.4 Asymptotic Isometries

A more recent approach related to the ideas of far-from-threshold wrinkling is the study of asymptotic isometries, i.e. states in which the sheet remains unstretched: often sheets attain a state of approximate isometry with very little stretching of the midplane in the far-from-threshold wrinkled state. This is exemplified in the experimental and theoretical study of the indentation of ultra-thin floating circular sheets by Vella et al. [2015]. Here it is shown that, for the doubly asymptotic limit of weak applied tension and large bendability, the sheet adopts an approximately isometric shape under large deflections [Vella et al., 2015]. Thus, for large indentations work is mainly done on the fluid, with little being transmitted

into the deformation of the sheet.

Asymptotic isometry provides a novel approach to tackle systems which exhibit 'metric-induced' wrinkling, in which the geometrical incompatibility is intrinsic. These include examples such as in the stamping of elastic sheets into spherical molds [Hure et al., 2012] and the spherical Winkler problem, in which a flat sheet is draped over a spherical shell [King et al., 2012; Bella and Kohn, 2017]. In such systems geometrical incompatibility ultimately results in an induced strain in the system, making the approach of minimizing bending energy subject to zero stretch impossible: thus the ensuing morphology instead approaches an isometric state asymptotically, in the limit of high bendability and confinement [Davidovitch et al., 2019], once again forming an approximately isometric state.

From these studies the connection between wrinkling and isometry is clear: in very thin sheets wrinkles provide a means of slackening sheets undergoing geometrical incompatibility.

1.2.5 Studies of Large Displacement Far-From-Threshold Systems

Several studies have recently focused on analysing the approximately isometric states found in the large deformations of twisted ribbons [Chopin and Kudrolli, 2013; Chopin et al., 2015; Kudrolli and Chopin, 2018]. In particular, the study of Chopin et al. [2015] made progress by considering a set of large-displacement plate equations, which they refer to as the covariant Föppl-von Kármán equations. These particular equations were first derived in the context of elastic growth problems by Dias et al. [2011] and are closely related to the model of Efrati et al. [2009], an extension of the Koiter [1966] model that includes growth terms. The nonlinear Koiter [1966] model, in turn, is an arbitrary-displacement plate model that is derived from 3D elasticity based only on the assumptions of thinness, the assumption that the underlying strains are small and the assumption of approximately plane stress. The resulting model of Koiter [1966] is a large-displacement, geometrically nonlinear plate model. For this model, the Kirchhoff-Love assumption is approximately satisfied, and the model neglects through-thickness shear strains, based on the plane-stress hypothesis.

Chopin et al. [2015] use the Dias et al. [2011] model to study the ribbon system by assuming a helicoid ribbon shape, effectively extending the classical solution of Green [1936, 1937] to finite displacements. Using the small-displacement base-state, near-threshold results are obtained by linear stability analysis. The far-from-threshold regime is also studied, which is achieved by assuming the large-displacement helicoid shape for the strip and searching

for a wrinkling pattern that relaxes the stress in the compressive region: thus the wrinkling pattern is completely determined by the stress-relaxation condition. This analysis allows a complete characterization of the various parameter regimes and is the first study to analyse far-from-threshold wrinkling in a large-displacement setting. It provides a further example of asymptotic isometry, as in the limit of large twist the wrinkles completely relax the compressive stresses, leaving the sheet in an approximately un-stretched configuration [Chopin et al., 2015].

The model of Dias et al. [2011], used by Chopin et al. [2015], is similar to the Koiter [1966] model, but instead of being derived from 3D elasticity, it is based on the kinematical Kirchhoff-Love hypothesis. This model includes additional lower-order strain-curvature terms in the bending energy: however, as their model is based on the two assumptions of the Kirchhoff-hypothesis and plane-stress, rather than the single assumption of approximately plane stress, there is no guarantee that their inclusion provides any additional accuracy from a physical perspective. Indeed given that the recent finite-strain extension to the Koiter plate model of Steigmann [2013], does *not* include these terms, it would suggest that they are not necessary to include. The model of Steigmann [2013], in turn, is a rationally derived finite-strain extension to the Koiter [1966] model, derived from 3D elasticity using minimal assumptions. All of these models will agree in the limit of small strain, however, which is the basic assumption in the studies of Dias et al. [2011] and Chopin et al. [2015].

1.3 Other Metrics for Measurement

Although wrinkling provides a straightforward means of measurement in thin-sheet systems, it is by no means the only observation that can be used to determine material properties. Other observations, such as the out-of-plane displacement (deflection) of deformed sheets naturally provide a means of measurement. In Box et al. [2017] for example, who studied a similar problem to Vella et al. [2015], both the wrinkling threshold and the axisymmetric base state of a circular sheet subject to an indentation (an imposed displacement at the centre) are shown to follow scaling laws, which could be used to measure thickness or stiffness for sheets of varying thickness.

Indeed, in studies of graphene sheets the primary means of measurement is by observing

axisymmetric deformations, and the most common types of experiments are sheet indentations [Zhang et al., 2011]. In a typical set-up, a deformation is imposed by an indenter and the corresponding applied force is measured [Castellanos-Gomez et al., 2012; López-Polín et al., 2015; López-Polín et al., 2017; Los et al., 2016, 2017]. Another common way to deduce sheet properties is instead to consider pressurized sheets [Koenig et al., 2011; Khestanova et al., 2016; Berger et al., 2016], which can also be used to determine adhesion energy in line with classical blister tests [Koenig et al., 2011]. This type of set-up has also been used to create nano-scale pressure sensors, by measuring the capacitance of nano-cavities in the linear-bending regime [Berger et al., 2017a,b].

These studies typically use the predictions of the Föppl-von Kármán model, or the simpler Föppl membrane model, in order to measure quantum mechanical analogues of the stiffness and thickness. Interestingly, the continuum model still gives reasonable estimates for bending modulus even for tri-layer graphene plates, with an error of only 6% [Zhang et al., 2011]. However, for monolayer sheets the measured bending stiffness does not arise from through-thickness stresses, as in classical plate theory, but is instead a consequence quantum mechanical effects [Zhang et al., 2011].

Many of these indentation studies, however, appeal to asymptotic results in order to perform fitting to the experimental data, in an approach recently criticised by Vella and Davidovitch [2017]. Vella and Davidovitch [2017] point out that the formula used for the fitting in the above studies, which is a naive linear combination of two separate asymptotic results at small and large indentation, results in large errors in the intermediate indentation regime. An obvious solution to this is to instead fit to numerical data when in the intermediate regime. One solution proposed by López-Polín et al. [2017], is to fit a complete third-order polynomial in the intermediate regime: however, as shown by Vella and Davidovitch [2017], this may lead to large errors in the determined Young's modulus. Vella and Davidovitch [2017] further critique the use of the full sheet shape to perform fitting for both elastic modulus and pre-stretch, as in Xu et al. [2016], because from the shape of the deflection alone there is no way to distinguish whether the experiment is in the small or large indentation regime [Vella and Davidovitch, 2017].

These studies of graphene build upon a large body of literature for blistering-type problems in classical systems [Dannenberg, 1961; Gent and Lewandowski, 1987; Guo et al., 2005], which have long been used as tools for determining physical properties: in this context the

main focus of experiments was to determine adhesion energy, using known elastic properties. The principal set-ups that have been considered have largely been of clamped circular sheets, under various axisymmetric loading conditions: these include pressure loading, punch loading[1], point indentation and spherical indentation [Wan et al., 2003; Guo et al., 2005]. Pressurized systems have been especially successful for non-porous membranes, but much less successful for sheets with defects, holes or porosity [Begley and Mackin, 2004]: for these systems displacement by indentation is much more practical. Initial conditions have been demonstrated to be extremely important in gaining accurate results, especially control of initial pre-stretch and control of the initial deflection of the film [Small and Nix, 1992].

Linearized models have proven insufficient to describe experimental regimes in many cases, due to the intrinsically minute forcing and displacement associated with such a regime [Voorthuyzen and Bergveld, 1984]. Despite this, most systems are typically considered theoretically either in regimes where the deflections are either very small (bending dominated) or moderate-to-large (membrane-like or stretching dominated). In intermediate regimes the equations are more difficult to solve and standard techniques cannot be applied. Usually in this regime numerical simulations are sought, but some progress has been made analytically using the Föppl-von Kármán equations by Wan et al. [2003], who assumes a constant membrane stress throughout the domain: thus linearising the out-of-plane equation. Typically in such experiments, at moderate displacements, membrane forces dominate and bending can be neglected. If the applied in-plane stress is small compared with self-induced stress, this results in the applied force, F^*, typically scaling as the deflection, v_3^*, cubed: $F^* \sim (v_3^*)^3$ [Wan et al., 2003].

Despite the simplicity of the simple inflation problem, geometrical nonlinearity in these systems can complicate fitting procedures, especially in the intermediate regime. Large displacements and rotations during simple inflation have not been considered and may be expected to lead to a breakdown of the typical membrane scaling predicted by the Föppl-von Kármán model. As such a robust understanding of the underlying physics is necessary. Beyond these intricacies, ultimately we understand an object's properties in the same way as humans have since antiquity, we apply a force to an object to observe how it deforms.

[1]Punch-loading is a load distributed by a cylinder applying a force at the centre of a sheet. It can be clamped to the sheet, in which case the sheet is in contact with the whole face of the cylinder, or resting on the sheet, in which case the load will be applied along a particular radius.

1.4 The Need for Full Numerical Simulations

Whilst a large amount of progress has been made by considering simplified models and analytic scaling laws, the limitations of these laws for the description of more complex systems are readily apparent. Many problems are, to all intents and purposes, insoluble by these means: full numerical simulations are a necessity when fully nonlinear analysis is needed for a system, such as in Pihler-Puzović et al. [2013] where results are needed in the fully nonlinear regime of a bubble displacing a viscous fluid in an elastic-walled Hele-Shaw cell.

Full numerical simulations may also be necessary in systems in which the geometry is complex, such as in the simulation of a bio-prosthetic heart valve [Kiendl et al., 2015]. Full numerical simulations can, of course, also inform on the development of new simplified models, and be used to explore regions in which simplified models break down. Finally, they allow a direct comparison to be made of the predictions of different models, and analytic approaches, thereby providing a powerful tool for assessing the accuracy of different models.

The importance of model selection is exemplified by the study of Healey et al. [2013], who demonstrated that in the strip-pull wrinkling system of Cerda and Mahadevan [2003], nonlinear simulations of the Föppl-von Kármán model predicts an ever increasing amplitude of wrinkles, unlike models which include a geometrically exact membrane term. Healey et al. [2013] introduce an ad hoc model, which supplements the Föppl-von Kármán model with the geometrically exact membrane terms, which does not display this behaviour. This study was performed using a finite element discretization of the rectangular domain. The same predicted decrease in wrinkle-amplitude was later demonstrated to be the behaviour of a real system in experiments performed by Sipos and Fehér [2016].

The Föppl-von Kármán model was implemented in the open-source finite element library `oomph-lib` [Heil and Hazel, 2006], for the special case of fully clamped systems by Pihler-Puzović et al. [2013]. This study uses a particular mixed finite element method (cf. section 1.5.3), which cannot be used to impose general boundary conditions. This was used to study the suppression of the fingering instability in an elastic-walled Hele-Shaw channel: a fully-coupled fluid-structure interaction problem.

Other examples that develop full numerical simulations of plate models include, for instance, the implementation of large-displacement plate models in Taylor et al. [2014] and Taylor et al. [2015], which both obtain numerical solutions to the large-displacement, nonlinear Koiter plate model [Koiter, 1966], which was recently extended to finite strains by

Steigmann [2013]. The Koiter [1966] model is suitable for the study of large displacement systems undergoing small strains, when through-thickness shear can be neglected. These studies develop two-dimensional finite difference schemes for the equations, which are then embedded in a damped pseudo-time-dependent system to minimize the energy, using dynamic relaxation. Dynamical relaxation replaces the physical equations with an artificial, dissipative dynamical system: equilibria to this system, which are obtained once the transience has abated, correspond to solutions to the original physical system [Taylor et al., 2014]. Finite difference methods, however, can only account for simple shapes. This limits their use in generic plate problems.

Many studies in the literature use commercial codes to obtain numerical simulations of thin elastic sheets (e.g. Portela et al. [2008]; Nayyar et al. [2011]; Taylor et al. [2015]), most notably Abaqus [Smith, 2009]. As well as being used to directly simulate systems, such simulations also provide extremely useful data through which to validate analytic predictions and scaling arguments of simplified models: for example in the numerical verification of the predicted far-from-threshold regimes in plates [Taylor et al., 2015], wrinkling in indented shells [Vella et al., 2011] and in the validation of simplified models of orthotropic elastic shells [Vidoli and Maurini, 2008; Seffen and Maurini, 2013; Vidoli, 2013], the latter case of which has proven extremely useful for predicting the phenomena of multi-stability in shell-systems [Coburn et al., 2013; Seffen and Maurini, 2013; Hamouche et al., 2017].

Abaqus simulations have also been used to compare differing numerical approaches for post-buckling analysis by Taylor et al. [2015], in which dynamic relaxation simulations of the Koiter-Steigmann model are compared to Abaqus simulations using S4R shell elements. However, in this study the explicit equations that these elements implement remains obscure, quoting Taylor et al. [2015]:

> "[A]n explicit expression for the strain energy is not given in the Abaqus theory documentation, it is likely to be akin to [the Koiter strain energy] but with the bending strain replaced with the linearised Budiansky-Sanders bending strain."

This study exemplifies two obvious difficulties currently encountered in the literature:

1. Model comparison is complicated by using different discretization methods.

2. Closed source codes often use plate equations for which the explicit equations remain obscure.

The first point is of particular importance in thin-plate models, as the use of sufficiently continuous boundary and bulk discretizations is well known to be important in ensuring solutions converge appropriately under mesh refinement [Ženíšek, 1981a; Ciarlet, 1991]. Further, the second point makes the direct comparison of different continuum models difficult, as the underlying continuum model of the commercial code is not apparent [Taylor et al., 2015].

Thus, a unifying framework in which these kind of models can be discretized, for generic boundaries and boundary conditions, and in which the model used is both configurable and explicit, would be of importance to the literature. As such, the development and implementation of a framework for generic plate models, and generic methods for fourth-order problems is the focus this thesis.

Many methods are used to simulate plate-problems numerically: in the next section we outline the main techniques used and highlight their relative merits and disadvantages for implementation as a generic plate problem.

1.5 Numerical Studies of Thin Plates and Shells

1.5.1 Overview of Numerical Techniques

For the numerical simulation of plates several methods are particularly prevalent, which we outline here. The most straightforward means of simulation is by directly discretizing the governing equations via the finite difference method.

The Finite Difference Method

Typically, in finite difference methods the domain is split into a regular mesh of nodes, which allow derivatives to be determined at discrete points in the domain. At each point a discrete set of equations are constructed and, together with discrete boundary conditions, the equations are converted from a set of differential equations to a set of algebraic equations [Szilard, 2004]. These algebraic equations can then be solved by standard (usually Newton-type) methods. Extensions can be made to use non-uniformly spaced nodes, but ultimately these extensions confound the main advantage of the finite difference method, which lies in its simplicity [Szilard, 2004]. The use of finite difference methods for axisymmetric (1D) systems is straightforward in plate and shell models (see e.g Pihler-Puzović et al. [2013]),

and is a common technique in the literature [Sheploak and Dugundji, 1998; Coman, 2013; Pihler-Puzović et al., 2013].

The main disadvantage in using finite difference methods are that they are difficult to automate for generic problems: the creation of finite difference codes for arbitrary geometry and boundary conditions is difficult. Moreover, each new problem might require new finite difference representation, which can be tedious to construct. Finally, for the standard finite difference method, the geometry is difficult to represent for arbitrary shapes: only simple shapes for which a conformal mapping exists can be readily discretized.

Another disadvantage associated with finite difference methods, especially for plate and shell models, is that the governing equations are often far more complex than the corresponding variational equations. Applying boundary conditions is also often more complicated than in corresponding variational methods.

Collocation Methods

Collocation methods also rely on direct discretization of the governing equations: however, instead of solving approximate equations formed of discrete derivatives, as in the finite difference method, collocation methods rely on approximating unknown functions using an assumed (discrete) set of functions with unknown coefficients. The discrete set of functions are either chosen such that they satisfy the boundary conditions or the boundary conditions are introduced as additional equations. The unknown coefficients are determined by solving the governing equations at a discrete set of points [Szilard, 2004], resulting in a coupled set of (in general nonlinear) algebraic equations. Solutions are sought in a particular finite-dimensional function space [Brunner, 2004]: often functions with local support such as piecewise polynomials or spline functions are selected, due to the sparse nature of the resulting matrices. When used with piecewise polynomial functions with Lagrange-type unknowns, that is unknowns that correspond to the value of the unknown function at a particular point, the collocation method will produce identical discrete equations to a corresponding finite difference scheme on the same mesh.

In axisymmetric problems, collocation methods are frequently used to numerically solve the membrane equations: many studies use the tool `bvp4c` from the numerical computing environment `MATLAB` [Kierzenka and Shampine, 2001], including the studies of Box et al. [2017]; Vella and Davidovitch [2017]. This implements a generic tool for first-order ODES,

using a generic interface to a C^1 (gradient) continuous collocation scheme of third order polynomials. To use `bvp4c`, the equations must first be reduced to a set of first order ODEs, which is straightforward to achieve for second-order problems.

Collocation schemes may be used for two-dimensional boundary-value problems, see for example Reali and Gomez [2015]; Kiendl et al. [2015], but ultimately such schemes rely on similar discretization techniques to the finite-element method which we cover below.

Finite Element Method

A widespread method in use for the numerical solution of partial differential equations is the finite element method. For systems with a variational principle, the finite element method directly discretizes the variational equations. Variational equations minimize a particular functional (say, an energy) over a region of space, by considering the change in the functional due to small, arbitrary variations of the independent variable (say, small, arbitrary displacements): the minimum of the functional occurs when the total variation is zero.

The finite element method discretizes the variational equation, by interpolating the independent variable piecewise, dividing the domain into a finite number of parts, or *elements*. Elements are typically simple geometric shapes, such as triangles and quadrilaterals. Elements represent the solution locally, usually by interpolation which is usually continuous between elements. Variations are also interpolated using the same basis, leading to a discrete set of equations. The ensemble of elements that make up the whole region is known as the *mesh*. Integration within elements is calculated numerically using quadrature[2].

In classical finite element methods elements are made of a set of nodes, each of which represents the corresponding location of an unknown. *Basis functions* are then used to interpolate between these unknowns over a localised region of space. In isoparametric methods, the geometry is also interpolated using the position of the nodes, using the same basis functions, allowing the elements to represent curved domains. For second-order boundary-value problems, the discretization is usually straightforward. As only first derivatives appear in the variational equation, to be integrable the representation of the solution need only be value or C^0-continuous: this is an easy condition to satisfy, which makes it straightforward to construct isoparametric discretization schemes for second-order boundary-value problems.

[2] Numerical integration or numerical quadrature is performed by evaluating a function at a series of integration, or quadrature, points within a region, these contributions are then weighted and summed to approximate the integral over the region.

For fourth-order systems, however, the situation is more complicated. Due to second derivatives appearing in the equations, to be integrable, in general the interpolation scheme must now be C^1 or gradient continuous between elements, which is a far more restrictive constraint.

This is particular relevant for plate models, as plate models in which through-thickness shear-strains are neglected are generally fourth-order in one or more of the displacements.

Direct Energy Minimization

A method that has recently been used for the solution of shell and plate problems is the method of direct minimization [Schroll et al., 2011; Lecieux and Bouzidi, 2012; Arza et al., 2013; Paulsen et al., 2015], using the software `Surface Evolver` [Brakke, 1992]. `Surface Evolver` evolves the energy of a system toward local minima using a first-order gradient descent method [Brakke, 1992]. The energies, in turn, are discretized on a grid of simplicial elements, or facets. This method is favoured because of the flexibility of the underlying software, which can handle many different types of system. Another advantage is that the gradient descent method implemented for this code is inherently more stable near bifurcation points, due to the method being first order [Lecieux and Bouzidi, 2012]. Lecieux and Bouzidi [2012] report that this can make the computation of wrinkled structures more efficient than corresponding finite element simulations.

However, this method relies on discretizations that are identical to the finite element method and as such elements are subject to the same continuity requirements as corresponding finite element methods. Below we therefore proceed by discussing some of the methods for simulating plates and shells, within the context of the finite element method.

1.5.2 Finite Element Methods for Shearable and Solid-Shells

Solid-Shells

The most obvious way of modelling a thin shell or plate is to directly use the three-dimensional equations of elasticity, using very thin elements. However, in large aspect-ratio elements a phenomena known as shear-locking plagues such calculations [Wempner and Talaslidis, 2002]. In 3D elements, unless the thickness and length of the elements is comparable,

spurious shear terms[3] dominate the energy, causing the elastic response to be overly stiff. Many elements are therefore needed to accurately model even simple bending deformations: making this an impractical method of approximation.

Many methods have been introduced to overcome these difficulties. Common methods to alleviate these issues include: the introduction of *discrete Kirchhoff constraints* [Wempner and Talaslidis, 2002], in which the normal at the centre-point of an element is constrained to remain normal; reduced or selective-reduced-integration (RI and SRI) which use numerical integration schemes carefully chosen to eliminate the spurious shear terms [Wempner and Talaslidis, 2002]; the assumed natural strain method (ANS), which uses new quadrature points that are appropriately re-weighted for the integration of the strains [Dvorkin and Bathe, 1984; Sze and Yao, 2000; Caseiro et al., 2014], and the enhanced assumed strain method (EAS) [Simo and Rifai, 1990]. The enhanced-strain-method, in turn, replaces the strain in the three-field (displacement-strain-stress) mixed[4] variational principle with an 'enhanced strain field'. This enhanced strain-field behaves like a Lagrange-multiplier enforcing the relationship between the stress-field and the displacements, but, unusually for a Lagrange-multiplier, vanishes under mesh refinement. A general overview of the topic can be found in Sze [2002].

Whilst being of use for the physical simulation of shells and plates, these methods cannot provide a direct comparison between different thin-plate theories, as they instead model three-dimensional elasticity using thin three-dimensional elements. Therefore any simplifications are not made in the model, but rather are made in the underlying discretization of the equations. Given that the manner in which constraints and simplifications are imposed in plate-models may result in a plethora of distinct plate and shell models, it is not necessarily obvious which thin-plate or shell theory a particular 3D-shell element will correspond to.

Shell and Plate Models with Shear

Shell and plate models can be derived based on the assumptions of thinness and kinematical assumptions about how the displacements vary through the thickness. If shear strains are not neglected in this analysis (i.e. the plate/shell is *not* assumed to be in a state of approximate

[3] These shear terms arise as a consequence of the large aspect ratio of the element: such elements are "legal approximations" and converge under mesh refinement. However, unless they have aspect ratios of order ~ 1 they produce poor results [Wempner and Talaslidis, 2002].

[4] Mixed finite element methods reformulate the governing equations in terms of additional auxiliary fields, and additional equations.

plane-stress) then then the resulting model is of a *shearable* or *thick* plate/shell. Such models include the classical Reissner-Mindlin plates [Ciarlet, 1997], the nonlinear Naghdi [1962, 1973] shell model and shearable versions of the Föppl-von Kármán equations [Kere and Lyly, 2005], all of which introduce new unknown *directors* that are solved for, in addition to the unknown displacements. The directors are the unknown, variable-coefficients associated with thickness-wise expansions of the 3D displacement. The resulting equations are second order in all variables, and thus only require C^0 continuous interpolation.

Unfortunately such models are well known to suffer from the same issues of shear locking as corresponding thick-shell elements; similar techniques are used to alleviate such locking behaviours, such partial-selective-reduced-integration (PSRI) [Chinosi and Lovadina, 1995; Boffi and Lovadina, 1997; Arnold and Brezzi, 1997], assumed natural strains methods (ANS) [Bischoff and Ramm, 1997; Hale et al., 2018], enhanced assumed shear methods (EAS) [Simo and Rifai, 1990; Bischoff and Ramm, 1997] and the mixed interpolated tensorial components approach (MITC) [Bathe and Dvorkin, 1985; Bathe et al., 1989]. The MITC method is based on a mixed method which introduces shear strain fields as an additional variable: these strain-fields are subsequently eliminated from the final linear system, so that no additional unknowns are introduced. For a comprehensive discussion of shearable plates and discretization techniques which are then implemented for several shearable plate models we refer the interested reader to Hale et al. [2018]. The code outlined in this paper forms part of the finite element library `FEniCS` [Alnæs et al., 2015].

The models we intend to compare in this thesis all neglect the effect of through-thickness shear stress: these effects are important in the deformation of thick shells, or shells under strong lateral loading. Such effects can be neglected in the contexts we consider in this thesis; as such, though of interest in general for the characterization of shells, our discussion of shearable models ends here. We proceed instead to discuss the challenges faced in numerically solving unshearable plate and shell models.

1.5.3 Finite Element Methods for Unshearable Shells

Shell and plate models for which shear-strains are neglected, in line with Kirchhoff-Love type approximations, do not exhibit shear locking when discretized directly. Instead such models are described by fourth-order partial differential equations. As discussed, for fourth-order partial differential equations to be integrable in the finite element method it is in general

necessary to discretize the equations using C^1 (gradient) continuous finite elements. In two dimensions, this property is difficult to ensure, especially for elements which attempt to accurately interpolate the geometry. Accurate interpolation of the geometry, in turn, is necessary to ensure correct characterization of the boundary-value problem [Ženíšek, 1981a,b].

Polygonal Domains

For polygonal domains, in which plate boundaries are piecewise linear, constructing and using C^1-continuous interpolation schemes can be achieved using elements with *Hermite* or derivative degrees of freedom. As opposed to standard Lagrange (value-type) interpolation where functions are interpolated by the value of the function at discrete points, Hermite interpolation uses values and derivatives of the unknown function to interpolate. With Hermite interpolation it is possible to represent both the value of a function and its first derivative continuously across the edges of elements. However, most Hermite-type elements are defined only for simplex elements and can therefore only interpolate the geometry linearly.

Commonly used interpolation schemes include the Hermite polynomial triangular elements of Bell [1969] and Argyris et al. [1968], the quadrilateral elements of Bogner-Fox-Schmidt [Bogner, 1965] and the singular Zienkiewicz triangle [Ciarlet, 1991]. Composite or macro-elements, made of several elements, such as the reduced Hsieh-Clough-Tocher triangle can also provide a C^1-continuous interpolation scheme [Ciarlet, 1991].

Isoparametric Methods

Although isoparametric interpolation is often sought for second-order problems, its use in fourth-order problems is not straightforward: the use of C^1-continuous, isoparametric elements often necessitates severe geometric constraints[5] to be imposed on the mesh, which is unfavourable for meshing arbitrary geometries. The only isoparametric Hermite element commonly used in the literature is the Bogner-Fox-Schmidt element, a four-sided element which can be readily adapted to an isoparametric setting [Petera and Pittman, 1994; Fischer et al., 2010; Fischer, 2011]. Unfortunately, for the use of this element, each mesh must be topologically rectangular: that is, each vertex must be at the intersection of exactly four elements. Thus, these elements may only be used on structured meshes, making the meshing of arbitrary domains less flexible than corresponding triangular domains. Isoparametric

[5] This is because the mapping from reference to global coordinates will either need to preserve angles on inter-element boundaries, or be shared between adjacent elements to satisfy C^1-continuity.

Bogner-Fox-Schmidt elements have been used in the context of gradient-elasticity[6] problems by Fischer et al. [2010]; Fischer [2011]. However, the constraints in the meshing procedure make them less suitable for a general-purpose code than other methods considered in this thesis.

Mixed and Hybrid Methods

Instead of solving the original variational problem, one can consider a lower order variational principle that approximates the original system via the introduction of new auxiliary variables. By formulating a system of lower order equations, the unknowns present in such methods are therefore relatively straightforward to interpolate. However, constructing stable[7] approximation schemes is a non-trivial task [Arnold, 1990; Brezzi and Bathe, 1990]:. This, coupled with the fact that such schemes need to be constructed *for a particular equation* [Lovadina, 1996] rather than constructing generic interpolation schemes for *any* fourth order problem makes these methods unattractive for the creation of a general framework for fourth-order boundary-value problems.

Isogeometric Methods

Isogeometric methods are a relatively new method of approaching finite element problems. Originally proposed by Hughes et al. [2005], isogeometric elements aim to combine the elements of design and analysis of physical systems into a single framework through the use of existing techniques from computer-aided-design (CAD). CAD-type basis splines are used to provide representation of both the geometry and the unknowns in physical problems, in a similar manner to traditional isoparametric methods: however the main distinction between isogeometric methods and traditional finite elements is that the reference space in isogeometric methods is localised over so-called patches of elements *not* localised over a particular 'reference element' (cf. figure 1.2). Importantly, bases are not necessarily *interpolatory*: the unknowns, and position of 'nodes' (i.e. control points) do not necessarily represent physical values of the solution or positions in the mesh.

[6] Gradient-elasticity generalizes the notion of continua to incorporate additional types of degrees of freedom at the microscopic level. The result of this is to introduce higher order strain-gradients into the constitutive law of a material [Askes and Aifantis, 2011; Fischer, 2011]. Such models are used for materials in which microstructure is important, such as in concrete or metals in which there is an internal length-scale [Fischer, 2011].

[7] By stability we mean that the solution to the approximate problem converges to the solution at the same rate as the 'best approximation' i.e in a least-squares sense. Unstable mixed schemes will generally not converge at all under mesh refinement [Arnold, 1990].

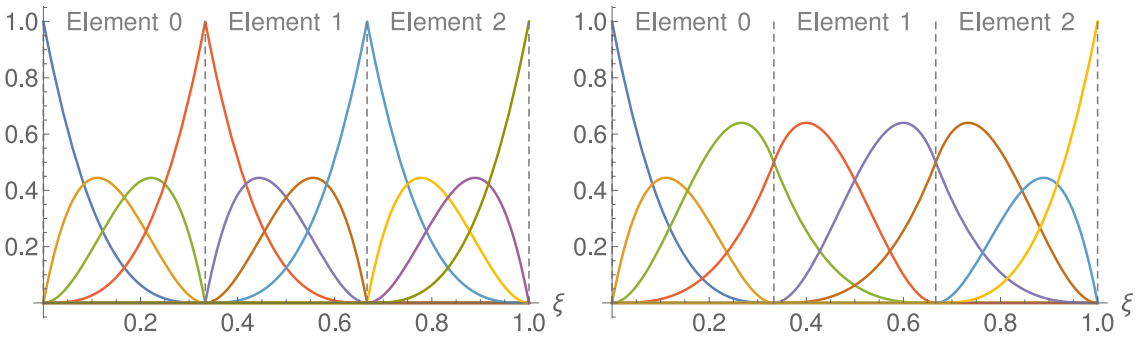

Figure 1.2: Cubic B-spline basis on a single patch with C^0 continuity (left) and C^1 continuity (right). Elements are defined by knot-spans, over which basis functions are smooth. At knots (i.e. element boundaries) the basis is only C^{p-m} continuous: where p is the order if the basis and m is the 'multiplicity' of the knot, which is configurable. The reference space, parametrized by ξ, spans all three elements within the 'patch'.

The most common form of isogeometric analysis uses non-uniform-rational B-splines (NURBS) as basis functions: these functions have the advantage of being able to represent many common geometrical shapes exactly and having configurable smoothness and refinement levels over the domain. Typically, multivariate basis functions are generated by taking tensor products of 1D basis functions: this tensor-product structure forms the basis for a single patch, which results in topologically rectangular meshes over each patch.

In the classical finite element method elements have two representations: one in the reference space, one in the physical space: whereas in a NURBS mesh there is instead a physical mesh and a control mesh. The control mesh is a net of points that controls the shape of the physical mesh. A NURBS mesh consists of a single *patch* (a macro element) subdivided into elements, which are defined by the *knot-spans*: areas in which the basis functions are smooth (C^∞). Similarly to the classical finite element method, basis functions are localised over neighbouring elements, meaning that the resulting matrices are sparse, just as in the finite element method. These *knot spans* define a simple rectangular mesh in the *reference space* which spans the whole patch. Most simple geometries can be represented with a single patch, which is a necessity as inter-patch continuity is only C^0.

Multi-patch geometries are typically joined with 'bending strips', a method introduced by Kiendl et al. [2010]: these are are strips of material that have a configurable bending stiffness and no associated membrane stiffness, which are introduced at patch boundaries to prevent 'kinks' forming. Unfortunately, the 'strips' introduce an additional bending stiffness

into the model, which does not have physical origin and can affect the stability of the method, leading to spurious deformations [Kiendl et al., 2010].

NURBS-based isogeometric methods have been used successfully on a variety of problems within the literature, including the fluid-structure interaction of wind turbines [Hsu and Bazilevs, 2012], the deformation of a bio-prosthetic heart valve [Kiendl et al., 2015] which include the implementation of several large-displacement plate and shell models [Kiendl et al., 2009; Hsu and Bazilevs, 2012; Kiendl et al., 2015; Nguyen et al., 2016], amongst others.

An alternative to this method is the use of T-splines which can mesh any domain as a single patch, meaning that there is no need to introduce 'bending strips' to join patches continuously [Bazilevs et al., 2010]. However, these splines encounter similar gradient discontinuities to NURBS at so-called 'extraordinary vertices', at which the valence (number of meeting elements) is not four [Scott et al., 2013; Kapl et al., 2018].

The creation of non-tensor-product patches was recently achieved by Nguyen et al. [2016], meaning that any number of patches can meet at vertices: this means much more general meshes may be considered using this method. Finally, we mention a very recent contribution to the literature which introduces a multi-patch parameterization that is C^1 continuous between patches, which can be of arbitrary connectivity. This new method combines existing ideas from classical Hermite-type interpolation with the isogeometric method by introducing Hermite-type (derivative) unknowns on patch boundaries [Kapl et al., 2019], which allows a C^1 continuous discretization of an entire domain.

It is worth noting that the isogeometric approach can also be applied to collocation-type methods, which can provide significant benefits over finite element-type simulations [Nguyen et al., 2015]. A brief review of collocation methods in isogeometric analysis is given in Nguyen et al. [2015].

Given that both unstructured C^1-continuous domains and generic shape C^1-domains are still, for the most part, an open problem for the isogeometric method we do not use them for this study.

Subdivision Elements

In a similar vein to NURBS-based isogeometric methods, sub-division elements use patch-type interpolation schemes to provide high continuity representations of unknown fields over a surface. Originally introduced for plate and shell models by Cirak et al. [2000], they have

proven to be an extremely efficient means of solving plate and shell type problems. For example, they have been used simulations of airbag deployment [Cirak and Ortiz, 2001] and growth models for thin structures [Vetter et al., 2014].

These elements, at least in principle, can be used for arbitrary triangular meshes and interpolate both geometry and unknowns. However, at so-called irregular vertices in the mesh: points at which the valence (number of meeting elements) is not equal to six, there exist curvature singularities. These singularities are square-integrable, but affect the accuracy of numerical integration in their vicinity. Another noteworthy point is that basis functions are nonlocal: the basis function associated with a vertex, v, in an element, e, spans all elements surrounding e: this is in contrast to classical finite element basis functions which instead span only elements that contain the vertex, v.

That being said, the basis functions themselves only require a single quadrature point per constituent element, which results in extremely fast construction of residuals and matrices. Most Hermite type elements in contrast require very high order schemes, to maintain their high accuracy.

Unlike NURBS, these basis functions cannot exactly represent common geometrical shapes, but do provide accurate, piecewise (C^2-continuous) boundary interpolation, which is sufficient for use for generic boundary conditions in plate and shell problems.

Boundary-Patch Methods

Classical Hermite elements can only interpolate geometry linearly so cannot represent curved boundaries. However, it is only strictly necessary to have curved elements on the edges of domains, in order to represent curved boundaries. A natural way to account for this is to introduce conforming elements, that are only present at curved edges of the domain (see figure 1.3). By constructing elements with a single curved edge, it is possible to to introduce elements that conform with straight-sided counterparts, whilst being able to account for edge curvature. This turns out to be a flexible method: a major advantage associated with this method is that standard (unstructured) constrained Delaunay triangulation can be used to mesh the domain, for which curved boundaries can be easily introduced as a post-processing step. This means that such a method can flexibly account for generic plate problems, without difficulty for generic domains. Due to the inherent high order of these elements, the geometry and unknowns can be represented using very few elements and results converge very quickly

under mesh refinement.

These elements typically provide high order interpolation of both the unknowns and the geometry, at the cost of introducing additional Lagrange degrees of freedom in the interior of elements.

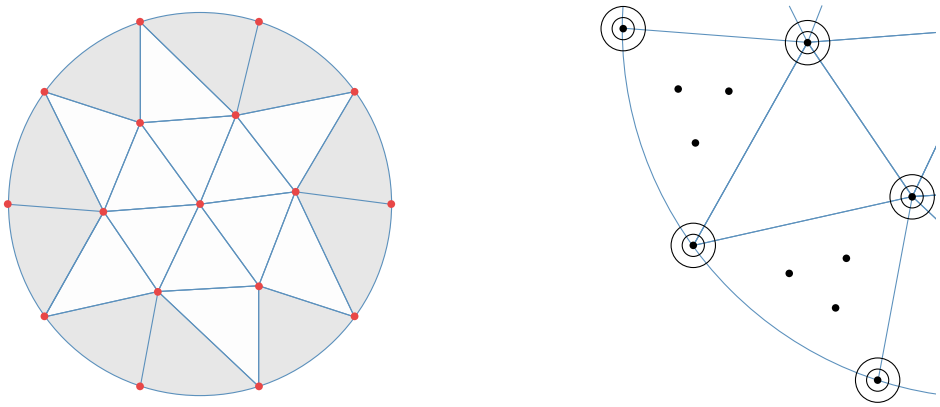

Figure 1.3: A triangular mesh (left) with boundary patches shown as shaded elements. Also shown is a close-up of the same mesh (right) with unknowns indicated schematically. Value-type unknowns are shown as points, first derivative unknowns with a single circle, and second derivative unknowns with a second, concentric circle. Boundary-patch element are C^1-continuous with the interior elements, but introduce additional interior unknowns to allow for a mapping with a single curved edge (cf. right-hand plot).

Several such curved elements have been proposed for both Argyris et al. [1968] and Bell [1969] triangular elements [Ženíšek, 1978; Bernadou, 1992, 1993b], for which explicit construction formulas can be found in Bernadou and Boisserie [1993]. The paper of Bernadou [1992] defines two classes of curved C^1-triangles compatible with Argyris and Bell elements that can be constructed to have any order boundary interpolation: with third and fifth-order interpolating polynomials being the most useful elements in applications [Bernadou, 1993b], resulting in C^1 and C^2 continuous boundary interpolation, respectively. In this method, a mixture of different order boundary interpolation can be used, depending on the needs of the problem, meaning that extra degrees of freedom needed in the vicinity of boundaries are only introduced when necessary.

This latter method is apparently relatively unexplored in the literature: curved Argyris elements have been investigated by Bernadou [1994], in the solution of the linear shell model of Koiter [1970]. These elements were implemented to form part of the finite element library `Modulef`. The curved Bell elements, first outlined by Ženíšek [1978] have been used by

Hřebíček [1982] to solve the general biharmonic equation and by Růžičková and Ženíšek [1984] in the context of linear visco-elastic bending of a plate. The use of curved plate and Bell elements for the solution of arbitrary-displacement, finite-strain plate models, however, appears to be a novel contribution of this thesis.

1.5.4 A Generic Framework for Solving Plate Models

The literature review presented here suggests that a unifying framework in which any plate model can be discretized, for generic boundaries and boundary conditions, would be an important and useful scientific contribution. As such, the development and implementation of a framework for generic fourth-order problems, using a mixture of Hermite triangle elements, is the focus of this thesis.

We specifically set-out to implement selected plate models, the Föppl-von Kármán model and the Koiter-Steigmann model as well as an apparently new moderate-rotation model, which we call the extended Föppl-von Kármán model, to form a part of `oomph-lib`, the open source, object-oriented multi-physics finite element library [Heil and Hazel, 2006]. This is with the aim of

1. Making the solution of generic elastic plate problems possible.
2. Allowing the swift implementation and comparison of different elastic plate models.
3. Facilitating their incorporation into a multi-physics setting.

1.6 Outline of Thesis

We begin in chapter 2 by introducing the basic ideas of three-dimensional elasticity, which provides a framework for ensuing discussion of elastic plates. Following this, in chapter 3, we discuss the general concepts underlying plate models, and then the particular models used in this thesis. This includes the derivation of the recent finite-strain extension to the Koiter model, by Steigmann [2013], and the derivation of the two moderate-rotation plate models from the Koiter-Steigmann plate model, by introduction of more restrictive assumptions: these models are the Föppl-von Kármán model and a new, moderate-to-large rotation plate model, respectively.

In chapter 4 we introduce the finite element method, with a focus on its application to plate theories and outline the theory for two new element types introduced into `oomph-lib`:

curved and straight-sided Bell elements. We then outline the implementation of new plate elements and demonstrate the convergence properties of all of the new element types, in chapter 5.

We illustrate the use of the new plate elements applied to three physical systems in chapters 6, 7 and 8, which investigate the inflation of a fully-clamped, circular sheet, the inflation of a circular sheet subject to a sliding-type clamp and the large displacement of a sheet clamped at one end, respectively. These problems serve to highlight the range of validity of the moderate-rotation Föppl-von Kármán model in several different contexts, which have a direct bearing on inflation-type metrology of thin elastic sheets. The former two problems further provide a useful validation of the new `oomph-lib` capabilities, as they can be cross-checked with a linear stability analysis: the third problem demonstrates the flexibility of the underlying code. Finally, we form conclusions in chapter 9.

Chapter 2

Three-dimensional Elasticity

We begin with a discussion of three-dimensional elasticity, for the purposes of providing a solid framework from which to approach plate models. We start by introducing the notation that is used throughout the thesis then proceed by discussing deformation and measures of deformation. We then discuss the stresses induced by deformation and introduce different measures of the stress. We conclude by discussing constitutive assumptions and their implications, and introduce several material models that are used throughout this work.

2.1 Notation

We begin by defining the notation that we use throughout this work. Throughout, unless otherwise stated, we follow the convention that Roman indices represent all three components and Greek indices label only the first two (in-plane) components of vectors or tensors. Bold script is used for vector and tensor fields, as shown in the example below.

We also use Einstein notation throughout, summing over repeated indices. We denote partial derivatives of a vector field $\boldsymbol{f}$ with respect to a curvilinear coordinate component, θ^j, by a further index separated by a comma:

$$\frac{\partial f_i}{\partial \theta^j} \equiv f_{i,j} \, .$$

In our notation the 3D divergence operator (Div) acting on field, $\boldsymbol{f}$, would be

$$\mathrm{Div}(\boldsymbol{f}) \equiv \frac{\partial f_i}{\partial x_i} \, ,$$

where x_i are a Cartesian basis. We write the two-dimensional divergence (div) instead as

follows:

$$\mathrm{div}(\boldsymbol{f}) \equiv \frac{\partial f_\alpha}{\partial x_\alpha}\,.$$

We further introduce the notation of $\boldsymbol{D}$ for the three-dimensional gradient operator and $\boldsymbol{\nabla}$ for the corresponding two-dimensional gradient. For example, the 3D gradient of a scalar field f would be:

$$\boldsymbol{D}\, f \equiv \frac{\partial f}{\partial x_i}\,\hat{\boldsymbol{e}}_i\,,$$

in which $\hat{\boldsymbol{e}}_i$ are the standard Cartesian unit vectors. By contrast, the two-dimensional gradient vector would be represented as:

$$\boldsymbol{\nabla}\, f \equiv \frac{\partial f}{\partial x_\alpha}\,\hat{\boldsymbol{e}}_\alpha\,.$$

The standard scalar product is denoted using a '$\cdot$'. For the scalar product of two (real-valued) matrices we use the standard Frobenius inner product, denoted $\boldsymbol{A}\cdot\boldsymbol{B} = \mathrm{Tr}(\boldsymbol{A}^T\boldsymbol{B})$.

For the contraction a rank four tensor-valued function, $\mathcal{B} = \mathcal{B}(\cdot)$, with a matrix, $\boldsymbol{C}$, we use the following notation, by analogy to matrix-vector notation:

$$\boldsymbol{A} = \mathcal{B}(\cdot)\,\boldsymbol{C}\,,$$

where $\boldsymbol{A} = \boldsymbol{A}(\cdot)$ is a rank two tensor with the components:

$$A_{ij} = \mathcal{B}_{ijkl}\,C_{kl}\,.$$

We also follow the convention that rank-four tensors are represented by script letters, to distinguish them from matrices. Thus, in line with the above notation for matrix inner products, the double contraction of a tensor $\mathcal{B}(\cdot)$, with two matrices $\boldsymbol{C}$ and $\boldsymbol{D}$ would be written:

$$A = \mathcal{B}(\cdot)\,\boldsymbol{C}\cdot\boldsymbol{D}\,,$$

which in terms of indices would be:

$$A = \mathcal{B}_{ijkl}(\cdot)\,C_{kl}\,D_{ij}\,.$$

We refer to variations in a tensor field by prepending the field with a delta; for example, variations in a tensor field T would be given by δT.

For derivatives with respect to tensorial components we use a subscript of that tensor, for example, the tensor formed from taking the derivative of a scalar field f with respect to the components of the tensor field $\boldsymbol{A}$ would be given by:

$$f_{\boldsymbol{A}} \equiv \left(\frac{\partial f}{\partial A_{ij}}\right)\,,$$

where $f_{\boldsymbol{A}}$ is a tensor of the same rank as $\boldsymbol{A}$.

We write the $n \times n$ identity matrix as $\mathbb{I}_n$, where n is any integer; for example, the three-by-three identity matrix would be $\mathbb{I}_3$. We use the standard $\otimes$ notation for the tensor product of vectors; for example, we can write the three-by-three identity matrix in Cartesian coordinates as:

$$\mathbb{I}_3 = \hat{\boldsymbol{e}}_1 \otimes \hat{\boldsymbol{e}}_1 + \hat{\boldsymbol{e}}_2 \otimes \hat{\boldsymbol{e}}_2 + \boldsymbol{k} \otimes \boldsymbol{k} = \hat{\boldsymbol{e}}_i \otimes \hat{\boldsymbol{e}}_i,$$

in which $\hat{\boldsymbol{e}}_1$, $\hat{\boldsymbol{e}}_2$ and $\boldsymbol{k} \equiv \hat{\boldsymbol{e}}_3$ are the standard Cartesian unit vectors.

We refer to the trace, determinant and cofactor of matrices, $\boldsymbol{A}$, using the standard notation: $\operatorname{Tr} \boldsymbol{A}$, $\det \boldsymbol{A}$ and $\operatorname{cof} \boldsymbol{A}$, respectively.

We observe that dimensional quantities with nondimensional counterparts are denoted with a star and corresponding nondimensional quantities are not starred: for example the dimensional position vector will be $\boldsymbol{Y}^*$ and the corresponding nondimensional position vector will be $\boldsymbol{Y} = \boldsymbol{Y}^*/L$, where L, which has no nondimensional counterpart, is a dimensional length scale. Finally, we denote material quantities that are defined throughout a material using a tilde, which we drop for quantities evaluated at the midplane in shell and plate models.

2.2 Finite-Strain Elasticity

The theory of three-dimensional elasticity is a framework for understanding the deformation of elastic objects under applied loads, modelling them as continua. The displacement of material points are related, purely geometrically, to strains. In large-displacement elasticity this geometrical relationship is exact and is nonlinear. Strains induce internal stresses in materials, which balance externally applied loads and the inertia of the material; the governing equations of three-dimensional elasticity constitute the balance between applied loads and internal stresses at every point within a material. The stress balance and strain-displacement relationship are independent of the material: however, to close the system we need to know the relationship between a deformation, or strain, and the stress that this results in. This relationship is known as the constitutive law and is material dependent. In this work we consider only hyperelastic materials: materials whose behaviour is elastic even at large strains, but whose stress-strain response is in general nonlinear.

Physically speaking, we control either the position of the surface of the body, $\tilde{\boldsymbol{Y}} = \tilde{\mathfrak{Y}}^*$,

or the traction, $\tilde{\boldsymbol{t}}^*$, on the surface, along with any body forces applied to the body, as seen in figure 2.1. The theory of three-dimensional elasticity then provides a prediction of the response of the material under these conditions.

To proceed we begin by defining a framework used to characterise deformation.

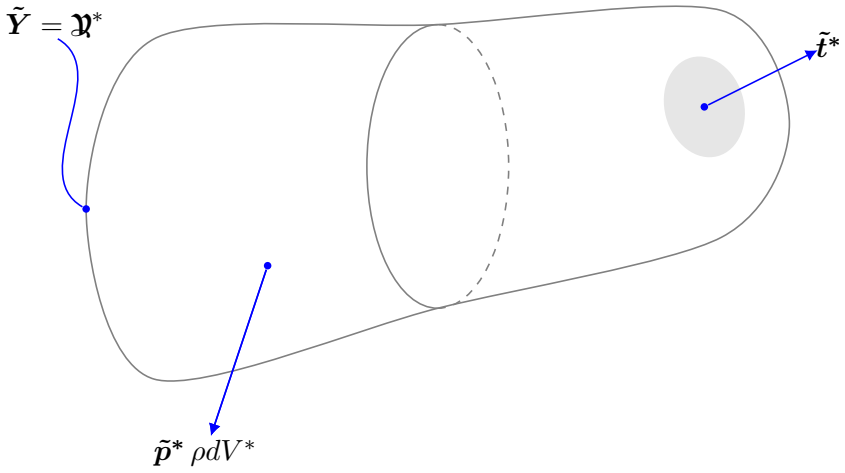

Figure 2.1: Diagram showing an elastic body, subject to a traction $\tilde{\boldsymbol{t}}^*$, a body force, $\tilde{\boldsymbol{p}}^*\rho dV^*$, and an imposed position vector $\tilde{\boldsymbol{Y}}^* = \tilde{\mathfrak{Y}}^*$. Here $\tilde{\boldsymbol{p}}^*$ is the body force per unit mass, ρ is the mass density and dV^* is a deformed volume element.

2.2.1 Deformation

We start by defining a reference, or undeformed, configuration. We denote the position of a point within the continuum by $\tilde{\boldsymbol{y}}^*$ as shown in figure 2.2. After the body undergoes some arbitrary deformation, the material point moves to $\tilde{\boldsymbol{Y}}^*$, by a displacement $\tilde{\boldsymbol{v}}^*$ such that $\tilde{\boldsymbol{Y}}^* = \tilde{\boldsymbol{y}}^* + \tilde{\boldsymbol{v}}^*$, as shown in figure 2.3.

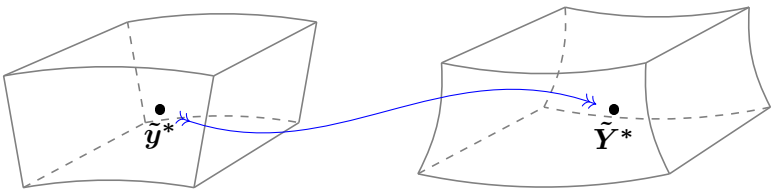

Figure 2.2: A solid undergoing a deformation: the point $\tilde{\boldsymbol{y}}^*$ in the initial configuration, is displaced to $\tilde{\boldsymbol{Y}}^*$.

We now define a material basis, using vectors tangent to the, in general, curvilinear coordinate lines at each point. We assume that the position of material points in space is parameterised in terms of a generic set of curvilinear coordinates, $\tilde{\theta^*}^i$, such that $\tilde{\boldsymbol{y}}^* = \tilde{\boldsymbol{y}}^*(\theta^{*i})$.

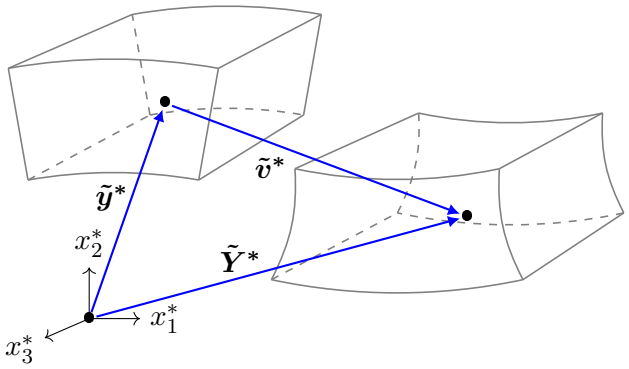

Figure 2.3: The relationship between the deformed and undeformed positions, now displayed as vectors relative to a fixed Cartesian reference frame, with coordinates x_i.

We can express a set of tangent vectors (to the coordinate lines) in this coordinate system, given by

$$\tilde{\boldsymbol{g}}_i \equiv \tilde{\boldsymbol{y}}^*{}_{,i} \,. \tag{2.2.1}$$

Using these vectors we can define a dual space $\tilde{\boldsymbol{g}}^i$ such that

$$\tilde{\boldsymbol{g}}^i \cdot \tilde{\boldsymbol{g}}_j = \delta_{ij} \,, \tag{2.2.2}$$

and a metric tensor

$$\tilde{g}_{ij} = \tilde{\boldsymbol{g}}_i \cdot \tilde{\boldsymbol{g}}_j \,. \tag{2.2.3}$$

The inverse metric tensor is given by

$$\tilde{g}^{ij} = \tilde{\boldsymbol{g}}^i \cdot \tilde{\boldsymbol{g}}^j \,. \tag{2.2.4}$$

The metric tensor describes the 'length', $(d\tilde{\boldsymbol{t}}^*)^2 = \tilde{g}_{ij}\, d\theta^{*i}\, d\theta^{*j}$, of an infinitesimal line vector, $d\tilde{\boldsymbol{t}}^*$. The infinitesimal undeformed volume element, dv^*, can be expressed in terms of the curvilinear coordinates as $dv^* = \sqrt{\tilde{g}}\, d\theta^{*1}\, d\theta^{*2}\, d\theta^{*3}$ where $\tilde{g}$ is the determinant of the metric tensor of the undeformed surface.

After deformation in the solid we can define a new 'deformed' basis, now using upper case letters,

$$\tilde{\boldsymbol{G}}_i \equiv \tilde{\boldsymbol{Y}}^*{}_{,i} \,, \tag{2.2.5}$$

and a dual space $\tilde{\boldsymbol{G}}^i$ such that

$$\tilde{\boldsymbol{G}}^i \cdot \tilde{\boldsymbol{G}}_j = \delta_{ij} \,. \tag{2.2.6}$$

We can also define a metric tensor in the deformed solid,

$$\tilde{G}_{ij} = \tilde{\boldsymbol{G}}_i \cdot \tilde{\boldsymbol{G}}_j \tag{2.2.7}$$

with inverse

$$\tilde{G}^{ij} = \tilde{\boldsymbol{G}}^i \cdot \tilde{\boldsymbol{G}}^j \,. \tag{2.2.8}$$

Throughout we will use the deformation gradient, $\tilde{\boldsymbol{F}}$, defined as the rate of change of the deformed position, with respect to the undeformed position

$$\tilde{\boldsymbol{F}} \equiv \boldsymbol{D}^* \, \tilde{\boldsymbol{Y}}^* \tag{2.2.9}$$

where we recall that $\boldsymbol{D}^*$ is the three-dimensional (dimensional) gradient operator. Not all deformations are admissible: the deformation gradient must have the property $\det\tilde{\boldsymbol{F}} > 0$, which corresponds to the deformation gradient preserving orientation [Ciarlet, 1988]: material points cannot pass through one another.

Having defined the metric tensor, a 'ruler' for measuring length in both deformed and undeformed configurations, we can define an objective measure of the change in length of the material: the Green-Lagrange strain tensor

$$\tilde{E}_{ij} \equiv \frac{1}{2}(\tilde{G}_{ij} - \tilde{g}_{ij}) \,. \tag{2.2.10}$$

Alternatively we can define this tensor in terms of the deformation gradient as follows

$$\tilde{\boldsymbol{E}} = \frac{1}{2}(\tilde{\boldsymbol{F}}^T \tilde{\boldsymbol{F}} - \tilde{\boldsymbol{g}}) \,, \tag{2.2.11}$$

in which $\tilde{\boldsymbol{g}} = \tilde{g}_{ij} \, \tilde{\boldsymbol{g}}_i \otimes \tilde{\boldsymbol{g}}_j$ is the three-by-three metric tensor of the undeformed surface.

Finally, we introduce the right Cauchy-Green deformation tensor, which is a symmetric tensor given by

$$\tilde{\boldsymbol{C}} = \tilde{\boldsymbol{F}}^T \tilde{\boldsymbol{F}} = 2\tilde{\boldsymbol{E}} + \tilde{\boldsymbol{g}} \,. \tag{2.2.12}$$

2.2.2 Stress

We now discuss the effect of deformation: stress. Stresses are distributed internal forces that occur in response to deformations of the material. The stresses act to restore the material to its initial, unstressed state. To understand stress we first consider the force transmitted through an infinitesimal area element, dA^*, within the deformed body, with unit normal $\tilde{\boldsymbol{N}}$ as shown in figure 2.4. The total force acting on the area element will be

$$d\tilde{\boldsymbol{\mathcal{S}}}^* = \tilde{\boldsymbol{\tau}}^* \, dA^* \,, \tag{2.2.13}$$

in which $\tilde{\boldsymbol{\tau}}^*$ is the Cauchy stress vector normal to the surface, defined as

$$\tilde{\boldsymbol{\tau}}^* \equiv \lim_{\Delta A^* \to 0} \frac{\Delta \tilde{\boldsymbol{\mathcal{S}}}^*}{\Delta A^*} \,. \tag{2.2.14}$$

Following this, we introduce the Cauchy stress tensor, $\tilde{\boldsymbol{\sigma}}^*$ such that

$$\tilde{\boldsymbol{\tau}}^* \equiv \tilde{\boldsymbol{\sigma}}^* \, \tilde{\boldsymbol{N}} \, . \tag{2.2.15}$$

The Cauchy stress is, by definition, the force per unit *deformed* area, which is the physical stress that would be applied to an elastic body.

For the infinitesimal force, $d\tilde{\boldsymbol{\mathfrak{F}}}^*$, we can also define a force per unit *reference* area, or Piola stress vector, $\tilde{\boldsymbol{\mathfrak{T}}}^*$, as

$$d\tilde{\boldsymbol{\mathfrak{F}}}^* = \tilde{\boldsymbol{\mathfrak{T}}}^* \, da^* \, . \tag{2.2.16}$$

Here da^* is an infinitesimal area element on the reference surface (i.e. the surface that will be deformed to form the area element dA^*). To obtain the relationship between the two stress vectors we use Nanson's formula [Ciarlet, 1988]

$$\tilde{\boldsymbol{N}} \, dA^* = (\det \tilde{\boldsymbol{F}}) \, \tilde{\boldsymbol{F}}^{-T} \tilde{\boldsymbol{n}} \, da^* \, , \tag{2.2.17}$$

in which $\tilde{\boldsymbol{N}}$ is the normal to the deformed surface element, dA^*, and $\tilde{\boldsymbol{n}}$ is the normal to the undeformed surface element, da^*. This formula is then used to rewrite the expression for $d\tilde{\boldsymbol{\mathfrak{F}}}^*$:

$$d\tilde{\boldsymbol{\mathfrak{F}}}^* = \tilde{\boldsymbol{\sigma}}^* \, \tilde{\boldsymbol{N}} \, dA^* = (\det \tilde{\boldsymbol{F}}) \, \tilde{\boldsymbol{\sigma}}^* \, \tilde{\boldsymbol{F}}^{-T} \, \tilde{\boldsymbol{n}} \, da^* \, . \tag{2.2.18}$$

Therefore, the Piola stress vector, $\tilde{\boldsymbol{\mathfrak{T}}}^*$, across the surface is given by

$$\tilde{\boldsymbol{\mathfrak{T}}}^* = (\det \tilde{\boldsymbol{F}}) \, \tilde{\boldsymbol{\sigma}}^* \, \tilde{\boldsymbol{F}}^{-T} \, \tilde{\boldsymbol{n}} \, , \tag{2.2.19}$$

and we can introduce a new stress tensor, known as the first Piola-Kirchhoff stress tensor $\tilde{\boldsymbol{P}}^*$, and write

$$d\tilde{\boldsymbol{\mathfrak{F}}}^* = \tilde{\boldsymbol{P}}^* \, \tilde{\boldsymbol{n}} \, da^* \, . \tag{2.2.20}$$

This is related to the Cauchy stress tensor in the following manner [Ciarlet, 1988]

$$\tilde{\boldsymbol{P}}^* = (\det \tilde{\boldsymbol{F}}) \, \tilde{\boldsymbol{\sigma}}^* \, \tilde{\boldsymbol{F}}^{-T} \, . \tag{2.2.21}$$

This stress tensor is associated with the force per unit *undeformed* area of the sheet. It is worth noting that the transpose of this tensor is often known as the nominal stress tensor.

The first Piola-Kirchhoff stress tensor is, in general, asymmetric, owing to the fact that it has one index pertaining to the deformed material frame and the other index pertaining to the reference material frame [Ciarlet, 1988]. To define a symmetric quantity, we express

the first Piola stress tensor, $\tilde{\boldsymbol{P}}^*$, in terms of a new force per unit undeformed area with both indices attached to the reference configuration. We define the following stress tensor

$$\tilde{\boldsymbol{S}}^* = \tilde{\boldsymbol{F}}^{-1}\,\tilde{\boldsymbol{P}}^*\,, \tag{2.2.22}$$

which is known as the (symmetric) second Piola-Kirchhoff stress. This tensor can be expressed in terms of the Cauchy stress tensor as follows

$$\tilde{\boldsymbol{S}}^* = (\det\tilde{\boldsymbol{F}})\,\tilde{\boldsymbol{F}}^{-1}\,\tilde{\boldsymbol{\sigma}}^*\,\tilde{\boldsymbol{F}}^{-T}\,. \tag{2.2.23}$$

The interpretation of this stress may not be immediately obvious, so for clarity we exposit the concept below. By equation (2.2.23) we see that the second Piola-Kirchhoff stress tensor is merely the Cauchy stress tensor rotated and stretched to the axes of the reference configuration: it is merely the force per unit deformed area element acting as considered from the reference configuration.

The second Piola-Kirchhoff stress has properties that make it an attractive measure to use: it is symmetric [Ciarlet, 1988], which makes manipulations involving it comparatively simpler. Additionally, the constitutive equation in the reference configuration often takes a simpler form than when expressed in terms of a Cauchy stress [Ciarlet, 1988].

2.2.3 Strain Energy

To determine the change in internal energy caused by a deformation, we consider the internal forces acting on an infinitesimal volume of elastic material, as shown in figure 2.4, adapting the arguments of Wempner and Talaslidis [2002]. In this diagram we only show the forces acting on the faces perpendicular to $\tilde{\boldsymbol{G}}_1$, but there are forces associated with each face, perpendicular to all three coordinate directions. In general, we also consider the effect of body forces, such as gravity, which are denoted $\tilde{\boldsymbol{p}}^*\rho\,dV^*$ in figure 2.4. Here, dV^*, is the infinitesimal volume element in the deformed material and $\tilde{\boldsymbol{p}}^*$ is a force per unit mass and ρ is the mass density of the deformed medium.

We consider a small increment of the deformed position on the far face, $\delta\tilde{\boldsymbol{Y}}^*$, and at the near face $\delta\tilde{\boldsymbol{Y}}^* + \delta\tilde{\boldsymbol{Y}}^*{}_{,1}d\theta^{*1}$, where forces $-\tilde{\boldsymbol{\tau}}^{*1}dA_1^*$ and $\tilde{\boldsymbol{\tau}}^{*1}\,dA_1^* + (\tilde{\boldsymbol{\tau}}^{*1}dA_1^*)_{,1}\,d\theta^{*1}$ act respectively (as shown in figure 2.4). Using this and adding the contribution from each face, labelled by area element dA_i^*, we can write the work done by the forces acting on the volume

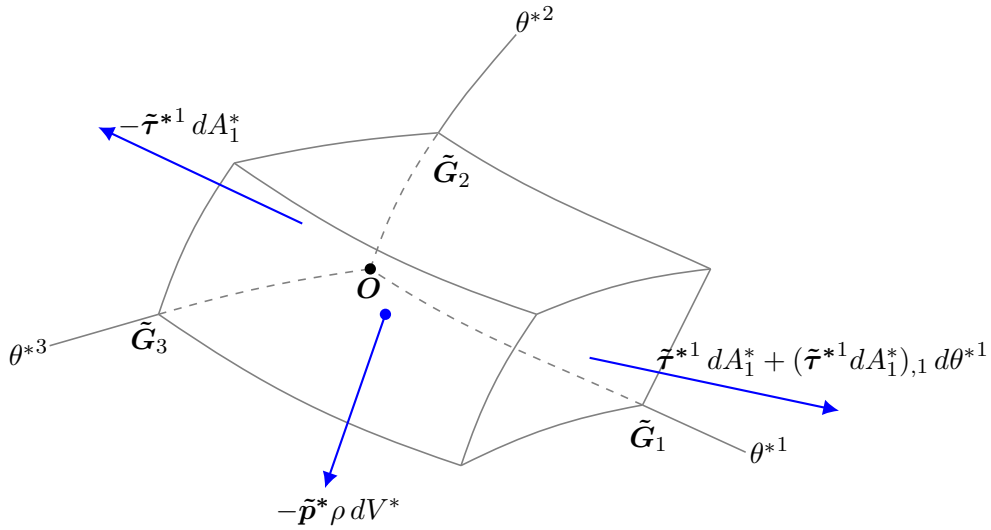

Figure 2.4: Forces acting upon faces of an infinitesimal element.

element:

$$\delta \mathbb{W}^* = \tilde{\boldsymbol{p}}^* \rho\, dV^*\, \delta \tilde{\boldsymbol{Y}}^* + \sum_{i=1}^{3} (\tilde{\boldsymbol{\tau}}^{*i}\, dA_i^* + (\tilde{\boldsymbol{\tau}}^{*i} dA_i^*)_{,i}\, d\theta^{*i}) \cdot (\delta \tilde{\boldsymbol{Y}}^* + \delta \tilde{\boldsymbol{Y}}^*{}_{,i} d\theta^{*i}) - \tilde{\boldsymbol{\tau}}^{*i} \cdot \delta \tilde{\boldsymbol{Y}}^*\, dA_i^* \,, \tag{2.2.24}$$

in which we use an explicit summation for clarity. Expanding this, and neglecting terms of smaller order, we find

$$\delta \mathbb{W}^* = \tilde{\boldsymbol{p}}^* \rho\, dV^*\, \delta \tilde{\boldsymbol{Y}}^* + \sum_{i=1}^{3} \tilde{\boldsymbol{\tau}}^{*i} \cdot \delta \tilde{\boldsymbol{Y}}^*{}_{,i} d\theta^{*i}\, dA_i^* + (\tilde{\boldsymbol{\tau}}^{*i} dA_i^*)_{,i} \cdot \delta \tilde{\boldsymbol{Y}}^*\, d\theta^{*i} \,. \tag{2.2.25}$$

Now, the work done, $\delta \mathbb{W}^*$, must be equal to the sum of the change in translational energy, $\delta \mathbb{T}^*$, and the change in internal energy, $\delta \mathbb{U}^*$:

$$\delta \mathbb{W}^* = \delta \mathbb{T}^* + \delta \mathbb{U}^* \,. \tag{2.2.26}$$

However, work done by rigid translations and rotations, $\delta \tilde{\boldsymbol{Y}}^*$, cannot be stored in the system as elastic potential energy or dissipated by inelasticity. Thus, terms involving $\delta \tilde{\boldsymbol{Y}}^*$, only contribute to the energy, $\delta \mathbb{T}^*$, which is associated with translational changes [Wempner and Talaslidis, 2002].

Thus we can re-write the expression above as

$$\delta \mathbb{U}^* = \sum_{i=1}^{3} \tilde{\boldsymbol{\tau}}^{*i} \cdot \delta \tilde{\boldsymbol{Y}}^*{}_{,i}\, d\theta^{*i}\, dA_i^* \,, \tag{2.2.27}$$

which is the internal energy stored elastically or dissipated inelastically. In this study we consider only purely elastic deformations, such that no energy is dissipated in the system.

Thus, the change in internal energy, $\delta\mathbb{U}^*$, is equal to the strain energy, δW^*. We can rewrite the above expression using the undeformed area, in the same manner as described previously, resulting in

$$\delta W^* = \sum_{i=1}^{3} \tilde{\mathfrak{T}}^{*i} \cdot \delta \tilde{\boldsymbol{Y}}^*{}_{,i}\, d\theta^{*i}\, da_i^* \,, \tag{2.2.28}$$

or in terms of the first Piola-Kirchhoff stress

$$\delta W^* = \sum_{i=1}^{3} \tilde{\boldsymbol{P}}^* \tilde{\boldsymbol{g}}^i \cdot \delta \tilde{\boldsymbol{Y}}^*{}_{,i}\, d\theta^{*i}\, da_i^* \,. \tag{2.2.29}$$

This expression is in turn equivalent to

$$\delta W^* = \tilde{\boldsymbol{P}}^* \cdot \delta \tilde{\boldsymbol{F}}\, dv^* \,, \tag{2.2.30}$$

where dv^* is the unit undeformed volume. Thus, it follows that the change in energy per unit undeformed volume, $\delta\mathcal{W}^*$, due to a deformation gradient, $\delta\tilde{\boldsymbol{F}}$, is

$$\delta\mathcal{W}^* = \tilde{\boldsymbol{P}}^* \cdot \delta \tilde{\boldsymbol{F}} \,, \tag{2.2.31}$$

which demonstrates that the Piola-Kirchhoff stress can be directly computed by the tensor derivative

$$\tilde{\boldsymbol{P}}^* = \mathcal{W}^*_{\tilde{\boldsymbol{F}}} \equiv \left(\frac{\partial \mathcal{W}^*}{\partial F_{ij}} \right) . \tag{2.2.32}$$

Henceforth, we consider hyperelastic bodies with a strain-energy function $\mathcal{W}^*(\tilde{\boldsymbol{F}})$ such that the total internal energy of a configuration can be written as

$$W^* = \int_V \mathcal{W}^*(\tilde{\boldsymbol{F}})\, dv^* \tag{2.2.33}$$

for an elastic body with undeformed volume v^* and with volume element dv^*. This energy is a function of the deformation gradient $\tilde{\boldsymbol{F}}$. Thus, $\mathcal{W}^*(\tilde{\boldsymbol{F}})$ is a tensor valued function of the deformation gradient, $\tilde{\boldsymbol{F}}$, but we can equivalently express the energy as a tensor-valued function of the Green-Lagrange strain, $\tilde{\boldsymbol{E}}$:

$$\mathcal{U}^*(\tilde{\boldsymbol{E}}) = \mathcal{U}^* \left(\frac{1}{2}(\tilde{\boldsymbol{F}}^T \tilde{\boldsymbol{F}} - \tilde{\boldsymbol{g}}) \right) = \mathcal{W}^*(\tilde{\boldsymbol{F}}) \,. \tag{2.2.34}$$

This is possible as a direct consequence of material objectivity, which we discuss further in the next section: a reasonable material model should be frame-indifferent, meaning it must be expressible in terms of an objective strain measure such as the Green-Lagrange strain [Ciarlet, 1988].

We reiterate here that we treat each tensor-valued function of the strain as a particular function with a three-by-three matrix argument: as such, a particular strain-energy may be expressed by two distinct functions of different strain measures, as illustrated in equation (2.2.34). This formalism becomes important later in chapter 3, in order to keep the derivation of the finite-strain extension to the Koiter model reasonably succinct.

The deformation of the body induces internal stresses which balance the externally applied loads. This culminates in a balance of stresses in the three coordinate directions. As we have seen, by equation (2.2.32), in hyperelastic media the first Piola stress is given by [Ciarlet, 1988]

$$\tilde{\boldsymbol{P}}^{*} = \mathcal{W}^{*}_{\tilde{\boldsymbol{F}}} \tag{2.2.35}$$

which arises in response to deformations of the body. By the definition of the symmetric Green-Lagrange strain, $\boldsymbol{E}$, and the chain rule we may deduce that

$$\mathcal{W}^{*}_{\tilde{\boldsymbol{F}}} = \boldsymbol{F}\,\mathcal{U}^{*}_{\tilde{\boldsymbol{E}}}\,, \tag{2.2.36}$$

which by definition of the Piola-Kirchhoff and the second Piola-Kirchhoff stress tensor implies that

$$\tilde{\boldsymbol{S}}^{*} = \mathcal{U}^{*}_{\tilde{\boldsymbol{E}}}\,. \tag{2.2.37}$$

The stress balance results in the following governing equations and boundary conditions [Ciarlet, 1988], which can be derived by taking the variational (Gateaux) derivative of the strain-energy function

$$\mathrm{Div}\,\tilde{\boldsymbol{P}}^{*} = \tilde{\boldsymbol{p}}^{*}\rho \tag{2.2.38}$$

subject to the boundary conditions

$$\tilde{\boldsymbol{Y}}^{*} = \tilde{\mathfrak{Y}}^{*} \quad \text{or} \quad \tilde{\boldsymbol{P}}^{*}\,\tilde{\boldsymbol{n}} = \tilde{\boldsymbol{t}}^{*}\,. \tag{2.2.39}$$

We can either apply a stress, $\tilde{\boldsymbol{t}}^{*}$, at the boundary or alternatively impose a particular deformed position, $\tilde{\mathfrak{Y}}^{*}$, of the boundary, as seen in figure 2.1. In the terminology of boundary-value problems a displacement-type boundary condition (i.e a constraint on the unknown) is known more generally as a Dirichlet or essential boundary condition. The stress-type boundary condition is referred to as a Neumann or 'flux-type' boundary condition.

The vector $\tilde{\boldsymbol{p}}^{*}$ is a body force field (per unit mass) acting on the (deformed) continuum and $\tilde{\boldsymbol{t}}^{*}$ is a traction per unit undeformed area applied on surfaces of the body, with the

normal to the undeformed faces of the body $\tilde{\boldsymbol{n}}$. Choosing a particular strain-energy function, $\mathcal{W}^* = \mathcal{W}^*(\tilde{\boldsymbol{F}})$, tantamount to selecting a constitutive relation, closes the system.

It is useful to have a measure of the 'stiffness' of the material at a given strain. In small-strain elasticity is is possibly to define a constant rank-four tensor which relates stress to strain, independent of the stress tensor. The components of this tensor are known as the small-strain elastic moduli, which describe the response of a material to deformation. Heuristically, this tensor can be thought of as the 'slope' of the stress-strain curve. In large-strain elasticity it is also possible to define elastic moduli, which are in general strain dependent and depend on which stress-strain 'slope' we use [Ciarlet, 1980]. These are useful in characterising the response of a material to a deformation.

The deformation-gradient-dependent elastic moduli, are defined as follows

$$\mathcal{M}^*(\tilde{\boldsymbol{F}}) = \mathcal{W}^*_{\tilde{\boldsymbol{F}}\tilde{\boldsymbol{F}}}\,. \tag{2.2.40}$$

We may instead define strain-dependent elastic moduli

$$\mathcal{C}^*(\tilde{\boldsymbol{E}}) = \mathcal{U}^*_{\tilde{\boldsymbol{E}}\tilde{\boldsymbol{E}}}\,, \tag{2.2.41}$$

where we recall that $\mathcal{U}^*(\tilde{\boldsymbol{E}}) = \mathcal{W}^*(\tilde{\boldsymbol{F}})$ is the strain-energy as a function of the *Green-Lagrange strain*.

By considering the contraction of $\mathcal{M}^*$ with a generic matrix $\boldsymbol{A}$ and the chain rule, it can be shown that the deformation-gradient dependent moduli can be related to the strain-dependent elastic moduli by the following expression:

$$\mathcal{M}^*(\tilde{\boldsymbol{F}})\,\boldsymbol{A} = \boldsymbol{A}\,\tilde{\boldsymbol{S}}^* + \frac{1}{2}\tilde{\boldsymbol{F}}\,\mathcal{C}^*(\tilde{\boldsymbol{E}})\left(\boldsymbol{A}^T\,\tilde{\boldsymbol{F}} + \tilde{\boldsymbol{F}}^T\,\boldsymbol{A}\right)\,. \tag{2.2.42}$$

These two moduli will agree in the limit of infinitesimal strain, which can be seen by considering the above expression for small strain, when $\tilde{\boldsymbol{F}} \approx \mathbb{I}_3$.

2.2.4 Physical Considerations for Constitutive Relations

For a strain-energy function to be physically reasonable it must satisfy certain criteria. Previously, in introducing the physical basis for elasticity, we have made a number of assumptions about the underlying constitutive behaviour, which we now elucidate here. We also introduce some additional assumptions, that are used in the later derived models.

An extremely important physical condition is material objectivity, which is defined by Ciarlet [1988] as follows:

Criterion 1. *Observables such as traction and mass density must be frame independent to constitute a reasonable physical model.*

Further to this, we make certain assumptions regarding the constitutive models that are to be used, based on the types of materials we aim to model. The first assumption we make is that the materials we consider are hyperelastic: the material only ever behaves elastically, even at large strains, storing any energy transferred to the material through applied forces as elastic potential energy. Thus, all energy transferred to the system through applied forces is stored as elastic potential energy. This can be summarised as follows [Ciarlet, 1988]

Assumption 1. *There exists a stored energy function, $\mathcal{W}^*(\tilde{\boldsymbol{y}}^*, \tilde{\boldsymbol{F}})$, such that the first Piola-Kirchhoff stress is $\tilde{\boldsymbol{P}}^* = \mathcal{W}^*_{\tilde{\boldsymbol{F}}}$, with $\tilde{\boldsymbol{y}}^* \in V$ and with $\tilde{\boldsymbol{F}}$ a 3×3 matrix with a positive determinant, such that*

$$\tilde{\boldsymbol{P}}^* = \mathcal{W}^*_{\tilde{\boldsymbol{F}}}\,. \tag{2.2.43}$$

If this is the case, then the applied forces are conservative and thus all of the work energy done is stored as elastic potential energy. This is a simplifying assumption that is appropriate for rubber-like materials which exhibit little visco-elastic and plastic behaviour even at large strains.

We also take the material to be isotropic with respect to material properties everywhere within the reference state. A material is said to be isotropic at a given point the response of the material does not depend on the direction of the applied force. We can express this as [Ciarlet, 1988]

Assumption 2. *A material is isotropic at point $\tilde{\boldsymbol{y}}^*$ if the Cauchy stress satisfies*

$$\tilde{\boldsymbol{\sigma}}^*(\tilde{\boldsymbol{y}}^*, \tilde{\boldsymbol{F}}\boldsymbol{Q}) = \tilde{\boldsymbol{\sigma}}^*(\tilde{\boldsymbol{y}}^*, \tilde{\boldsymbol{F}}) \tag{2.2.44}$$

for all 3×3 matrices with positive determinant, $\tilde{\boldsymbol{F}}$, and all 3×3 rotation matrices $\boldsymbol{Q}$.

Said differently, if we rotate the reference configuration about point $\tilde{\boldsymbol{y}}^*$ by an arbitrary amount, then the Cauchy stress will be unaltered if the material is isotropic at that point [Ciarlet, 1988]. Isotropy is a property of a material in a particular configuration, if a material is deformed it may not remain isotropic [Ciarlet, 1988].

The last physical restriction we make is that the material has a stress-free ('natural') reference state.

Assumption 3. *There exists a stress-free reference state, such that* $\tilde{\boldsymbol{\sigma}}^*(\tilde{\boldsymbol{F}}) = \tilde{\boldsymbol{\sigma}}^*(\mathbb{I}_3) = \tilde{\boldsymbol{\sigma}}^*(\boldsymbol{Q}) = \boldsymbol{0}$*, for all three-by-three rotation matrices* $\boldsymbol{Q}$*.*

This asserts that the reference configuration and rigid rotations of the reference configuration are stress free. A corollary of this is that for small strain the second Piola-Kirchhoff stress, $\tilde{\boldsymbol{S}}^*$, has the following form [Ciarlet, 1988]

$$\tilde{\boldsymbol{S}}^*(\tilde{\boldsymbol{E}}) = \mathcal{C}^*(\boldsymbol{0})\,\tilde{\boldsymbol{E}} + o(|\tilde{\boldsymbol{E}}|) \tag{2.2.45}$$

in which $\mathcal{C}^*(\boldsymbol{0})$ are the strain dependent elastic moduli, evaluated at zero strain. For isotropic materials we can express this in terms of Lamé constants as follows [Ciarlet, 1988]:

$$\tilde{\boldsymbol{S}}^*(\tilde{\boldsymbol{E}}) = \lambda^* \operatorname{Tr}(\tilde{\boldsymbol{E}})\,\tilde{\boldsymbol{g}} \,+\, 2\mu^*\tilde{\boldsymbol{E}} \,+ o(|\tilde{\boldsymbol{E}}|) \tag{2.2.46}$$

in which λ^* and μ^* are the Lamé constants, which experimentally are found to be positive.

Now we have made physical assumptions, we make a final mathematical assumption that is necessary for the existence of solutions to the equations. We adopt strongly elliptic strain-energy functions, which by definition satisfy the strong Legendre-Hadamard condition.

Assumption 4. *We assume that the deformation-gradient-dependent elastic moduli,* $\mathcal{M}^*(\tilde{\boldsymbol{F}})$*, of the chosen strain-energy function,* $\mathcal{W}^*(\tilde{\boldsymbol{F}})$*, satisfies:* $\mathcal{M}^*_{ijkl}(\tilde{\boldsymbol{F}})a_i\,a_j\,b_k\,b_l > 0$ *for all real vectors* $\boldsymbol{a}, \boldsymbol{b} \neq \boldsymbol{0}$*.*

The Legendre Hadamard condition plays an important role in the calculus of variations [Ciarlet, 1988], where it is used to study the regularity of solutions. The above inequality is satisfied if the deformation, $\tilde{\boldsymbol{Y}}^*$, is a minimizer of the energy (i.e. a solution) [Ciarlet, 1988; Hilgers and Pipkin, 1996]: if it is not satisfied for all $\tilde{\boldsymbol{Y}}^*$ then there may be certain classes of deformation for which no solutions exist [Hilgers and Pipkin, 1996; Steigmann, 2010][1]. Hilgers and Pipkin [1996] provide an example of a model for which this condition is *not* generally satisfied: they found that their derived plate model did not satisfy the Legendre-Hadamard condition for any deformations involving a compressive stress. This means that no compressive stress solutions exist for that model, despite these types of deformation presumably being solutions to the full, 3D system for certain loadings.

[1] This is because the Legendre-Hadamard condition is a necessary (but not sufficient) condition for the existence of a particular weak minimizer (i.e. a weak, stable solution). Weak solutions are merely solutions that satisfy the governing equations in a *distributional* sense, that is over a region of space not necessarily point-wise.

A special class of strain-energy functions are polyconvex strain-energy functions: polyconvex strain-energy functions satisfy: $\mathcal{W}^*(\tilde{\boldsymbol{F}}) = \underline{\mathcal{W}^*}(\tilde{\boldsymbol{F}}, \text{cof}\tilde{\boldsymbol{F}}, \det\tilde{\boldsymbol{F}})$ for a function $\underline{\mathcal{W}^*}(\cdot)$ that is convex[2] for all admissible deformations $\tilde{\boldsymbol{F}}$ in each of its arguments. In the above expression we used $\text{cof}\tilde{\boldsymbol{F}}$ to denote the cofactor matrix of the matrix $\tilde{\boldsymbol{F}}$. It can be shown that polyconvex strain-energy functions, that are twice continuously differentiable, are also strongly elliptic (that is they satisfy the Legendre-Hadamard condition) [Ball, 1976; Steigmann, 2013]. Polyconvexity is a property common to many strain-energy models including the well known Neo-Hookean, Mooney-Rivlin and Ogden material models [Zeidler, 1986; Ciarlet, 1988]. We will discuss some of these models in the next section.

2.2.5 Material Models

We now briefly discuss the material models that we use in this study. We do not derive any of the following models from statistical thermodynamics, as this is beyond the scope of the present work. We instead direct the interested reader to relevant texts such as Rubinstein and Colby [2003], which covers this topic in great detail.

Saint-Venant Kirchhoff Materials

The Saint-Venant Kirchhoff material model assumes that linear stress-strain behaviour holds even at large strains. The strain-energy for this type of material is given by [Ciarlet, 1988]

$$\mathcal{W}^*(\tilde{\boldsymbol{F}}) = \mathcal{U}^*(\tilde{\boldsymbol{E}}) = \frac{1}{2}\,\lambda^*\,(\text{Tr}\,\tilde{\boldsymbol{E}})^2 \;+\; \mu^*\,\text{Tr}\,\tilde{\boldsymbol{E}}^2\,. \tag{2.2.47}$$

The two Lamé parameters, λ^* and μ^*, can also be written in terms of the Young's modulus E and the Poisson ratio, ν: which are more physically intuitive measures of material properties. Their relationship to the Lamé parameters is as follows $\mu^* = E\,/(2+2\nu)$ and $\lambda^* = E\,\nu/\left((1+\nu)(1-2\nu)\right)$ [Landau and Lifshitz, 1986].

The Poisson ratio is a measure of the compressibility: the tendency of materials to expand transversely in response to lateral compression. A perfectly incompressible material would have a Poisson ratio $\nu \to 1/2$ and a perfectly compressible material has a Poisson ratio $\nu = 0$: almost all conventional materials lie between these two parameter values[3] [Landau

[2]Convexity of $f(x)$ on an interval $[a,b]$ is defined as $f(\lambda a + (1-\lambda)b) \leq f(a)\lambda + f(b)(1-\lambda)$ for all $\lambda \in [0,1]$. This can be extended to tensor-valued functions, $f(\boldsymbol{a})$ with $\boldsymbol{a} \in U$, where the 'interval' instead becomes a subset of the space U.

[3]Some materials, known as auxetic materials, exhibit a *negative* Poisson ratio and can expand laterally when stretched. Naturally occurring auxetic materials are anisotropic and this effect only occurs in specific directions: however, isotropic auxetic materials can exist and have been synthesized [Audoly and Pomeau, 2010].

and Lifshitz, 1986; Audoly and Pomeau, 2010]. Rubber-like materials are usually close to being incompressible, so we frequently take the Poisson ratio to be $\nu \to 1/2$. Young's modulus is simply defined as the stress per unit strain under uniaxial tension in the linearly elastic regime.

Given that $\mathcal{W}^*(\tilde{\boldsymbol{F}}) = \mathcal{U}^*(\tilde{\boldsymbol{E}})$ is quadratic in $\tilde{\boldsymbol{E}}$, for the Saint-Venant Kirchhoff model we can write

$$\mathcal{C}^*(\tilde{\boldsymbol{E}}) = \mathcal{C}^*(\boldsymbol{0}) = \mathcal{C}^* \,, \tag{2.2.48}$$

with components of $\mathcal{C}^*$ given by

$$\mathcal{C}^*_{ijkl} = \lambda^* \, \tilde{g}_{ij} \, \tilde{g}_{kl} \, + \, \mu^* \, (\tilde{g}_{ik} \, \tilde{g}_{jl} \, + \, \tilde{g}_{il} \, \tilde{g}_{jk}) \,. \tag{2.2.49}$$

We can use this tensor to relate the Green-Lagrange strain tensor, $\tilde{\boldsymbol{E}}$ to the second Piola-Kirchhoff stress, $\tilde{\boldsymbol{S}}^*$ as follows

$$\tilde{\boldsymbol{S}}^* = \mathcal{C}^* \, \tilde{\boldsymbol{E}} \,. \tag{2.2.50}$$

The Saint-Venant Kirchhoff material model can easily be shown to satisfy the Legendre-Hadamard condition for $\lambda^*, \mu^* > 0$. The model itself, however, is not physically realistic at large strains [Ciarlet, 1988]. Nevertheless, as the models we consider coincide with this model in the small deformation limit, and it is comparatively simple, it is useful to study this model in its own right.

For the condition of in-plane plane-stress ($\sigma_{3i} = 0$) we may eliminate some components of the Green-Lagrange strain tensor. The Second Piola-Kirchhoff stress tensor can be immediately deduced from the strain energy to be

$$\tilde{\boldsymbol{S}}^*(\tilde{\boldsymbol{E}}) = \lambda^* \, \mathrm{Tr} \, (\tilde{\boldsymbol{E}}) \, \tilde{\boldsymbol{g}} + \, 2\mu^* \tilde{\boldsymbol{E}} \,. \tag{2.2.51}$$

Clearly, $\tilde{E}_{3\alpha} = 0$, and $\tilde{S}^*_{33} = (\lambda^* + 2\mu^*)\tilde{E}_{33} + \lambda^* \tilde{E}_{\gamma\gamma} = 0$. Using this to determine E_{33}, we can now write the Saint-Venant Kirchhoff plane strain energy as

$$\mathcal{W}^*(\tilde{\boldsymbol{F}}) = \frac{\lambda^* \mu^*}{\lambda^* + 2\mu^*} \, (\mathrm{Tr} \, \tilde{\boldsymbol{\epsilon}})^2 \, + \, \mu^* \, \mathrm{Tr} \, \tilde{\boldsymbol{\epsilon}}^2 \,. \tag{2.2.52}$$

where $\tilde{\boldsymbol{\epsilon}} = \tilde{E}_{\alpha\beta} \hat{\boldsymbol{e}}_\alpha \otimes \hat{\boldsymbol{e}}_\beta$ is the $x - y$ strain tensor. We can also write this in terms of ν and E to obtain

$$\mathcal{W}^*(\tilde{\boldsymbol{F}}) = \frac{E}{2(1-\nu^2)} \, \left(\nu (\mathrm{Tr} \, \tilde{\boldsymbol{\epsilon}})^2 \, + \, (1-\nu) \, \mathrm{Tr} \, \tilde{\boldsymbol{\epsilon}}^2 \right) \,. \tag{2.2.53}$$

Finally, we compute the plane-stress elastic moduli (stiffness tensor), $\mathcal{G}^* \equiv \mathcal{U}^*_{\tilde{\boldsymbol{\epsilon}}\tilde{\boldsymbol{\epsilon}}}$, for this model

$$\mathcal{G}^*_{\alpha\beta\gamma\delta} = \frac{E}{(1-\nu^2)} [(1-\nu) \, (\tilde{g}_{\alpha\delta} \tilde{g}_{\beta\gamma} + \tilde{g}_{\alpha\gamma} \tilde{g}_{\beta\delta}) \, /2 + \nu \, \tilde{g}_{\delta\gamma} \tilde{g}_{\alpha\beta}] \,. \tag{2.2.54}$$

Incompressible Neo-Hookean Materials

The Neo-Hookean material model is a simple nonlinear model based on the statistical thermodynamics of cross linked polymers [Müller and Strehlow, 2004; Rubinstein and Colby, 2003]. This model is attractive due to its physical basis in the molecular chain statistics of polymers, which links the macroscopic material behaviour to microscopic polymer networks [Rubinstein and Colby, 2003; Marckmann and Verron, 2006]. We consider only the incompressible Neo-Hookean model, which has only a single free parameter: the Young's modulus. The strain-energy function for this model is given by [Müller and Strehlow, 2004]

$$\mathcal{W}^*(\tilde{\boldsymbol{F}}) = \dot{\mathcal{W}}^*(\tilde{I}_1, \tilde{I}_2, \tilde{I}_3) = C_1^* \left(\tilde{I}_1 - 3 \right) , \tag{2.2.55}$$

in which $\tilde{I}_1 = \mathrm{Tr}\, \tilde{\boldsymbol{C}}$ is the first invariant of the right Cauchy-Green deformation tensor and C_1^* is a material constant. By considering the small-strain (linear) behaviour, we see that the constant C_1^* can be related to the Young's modulus by $E = 6C_1^*$ [Li and Healey, 2016]. The Neo-Hookean strain energy is polyconvex [Ciarlet, 1988], so satisfies the Legendre-Hadamard condition for $C_1^* > 0$ [Ciarlet, 1988].

It is necessary to add an additional Lagrange multiplier to impose incompressibility, as incompressibility is a constraint on the admissible deformations: $\det \tilde{F} = 1$ [Ciarlet, 1988]. Adding a Lagrange multplier to impose the constraint amounts to adding an unknown hydrostatic pressure to the stress, to maintain a constant volume of material [Wempner and Talaslidis, 2002]. This subtlety is avoided in plate models, however, as in plate models the plane stress assumption allows one of the stress components to be eliminated from the constitutive model.

Incompressible Mooney-Rivlin Materials

A well-advocated phenomenological model for rubber elasticity is the Mooney-Rivlin model which, whilst not finding origin in the theory of polymer chain statistics, is known to be an appropriate model for use in rubber elasticity for up to 200% strain [Marckmann and Verron, 2006]. This model introduces a new material parameter: C_2^*. We draw a distinction here from the generalised Rivlin model (or polynomial hyperelastic model) which is sometimes referred to as Mooney-Rivlin, despite the classical Mooney-Rivlin model being only a special case of the former model. The strain-energy function for an incompressible Mooney-Rivlin

material is given by [Müller and Strehlow, 2004]

$$\mathcal{W}^*(\tilde{\boldsymbol{F}}) = C_1^* \left(\tilde{I}_1 - 3\right) + C_2^* \left(\tilde{I}_2 - 3\right) , \tag{2.2.56}$$

where $\tilde{I}_1 = \mathrm{Tr}\,\tilde{\boldsymbol{C}}$ and $\tilde{I}_2 = [(\mathrm{Tr}\,\tilde{\boldsymbol{C}})^2 - \mathrm{Tr}\,(\tilde{\boldsymbol{C}}^2)]/2$ are the first two invariants of the right Cauchy-Green deformation tensor, $\tilde{\boldsymbol{C}}$. The final invariant, $\tilde{I}_3 = \det\tilde{\boldsymbol{C}}$ is unity, due to the assumption of incompressibility. We can see that the Neo-Hookean model forms the special case when $C_2^* = 0$. By considering the limit of small-strain (linear) behaviour we can see that the Young's modulus is related to the two material constants by the relation: $E = 6(C_1^* + C_2^*)$ [Li and Healey, 2016]. The Mooney-Rivlin model is polyconvex for $C_1^*, C_2^* > 0$ and therefore satisfies the Legendre-Hadamard condition [Ciarlet, 1988]. Again it is generally necessary to impose incompressibility via a Lagrange multiplier, however, in plate models the plane stress assumption is used to eliminate one of the stress components, which avoids this subtlety.

For the conditions of plane-stress in-plane and incompressibility, we may eliminate some of the components of the strain tensor to obtain the useful form [Müller and Strehlow, 2004; Li and Healey, 2016]

$$\mathcal{W}^*(\tilde{\boldsymbol{F}}) = C_1^* \left(\mathrm{Tr}\,(\tilde{\boldsymbol{c}}) + \det\tilde{\boldsymbol{c}}^{-1} - 3\right) + C_2^* \left(\mathrm{Tr}\,(\tilde{\boldsymbol{c}})\,(\det\tilde{\boldsymbol{c}})^{-1} + \det\tilde{\boldsymbol{c}} - 3\right) , \tag{2.2.57}$$

in which $\tilde{\boldsymbol{c}} = \tilde{Y}^*_{i,\alpha}\tilde{Y}^*_{i,\beta}\hat{\boldsymbol{e}}_\alpha \otimes \hat{\boldsymbol{e}}_\beta$, is the plane Cauchy-Green strain. Again, setting $C_2^* = 0$ we obtain the plane-stress Neo-Hookean model. As we have eliminated one of the stretches using the condition of plane stress in this expression, here we do not need a Lagrange multiplier to impose incompressibility.

We now proceed to discuss plate and shell theories, which are relevant to situations in which one dimension of an elastic body is much smaller than the other two.

Chapter 3

Plate Models with a Bending Stiffness

In this section we discuss several plate models in both variational form and as Euler-Lagrange equations. We first detail the motivation behind shell theories in generality, with the aim of later specialising to flat plates. We then discuss some important aspects of the differential geometry of surfaces, for use in the proceeding plate theory: the recent finite-strain extension to the Koiter model, as derived by Steigmann [2013]. We then show, heuristically, how to obtain the Föppl-von Kármán model using the Koiter-Steigmann model as an intermediate step in its derivation from 3D elasticity. Finally, we derive an extension to the Föppl-von Kármán model, which appears to be novel.

This section ultimately aims to highlight the differences between several different plate models and illustrate when the use of each model is appropriate.

3.1 Classical Shell Theories

The basic concept guiding the derivation of shell models is the concept of 'thinness': bodies are assumed to be much smaller in one dimension than the other two-dimensions. This allows a 3D solid mechanics problem to be reduced to a 2D problem, embedded in the 3D space.

Consider an elastic body of uniform thickness h^* in the θ^{*3} direction, and much larger lateral lengths, $L \sim R_c$, where R_c is the radius of curvature, such that $h \ll 1$, where $h = h^*/L$ is the relative thickness. This 'shell'-like body is illustrated in figure 3.1. Typically we characterise the position of the whole elastic body by considering its position relative to

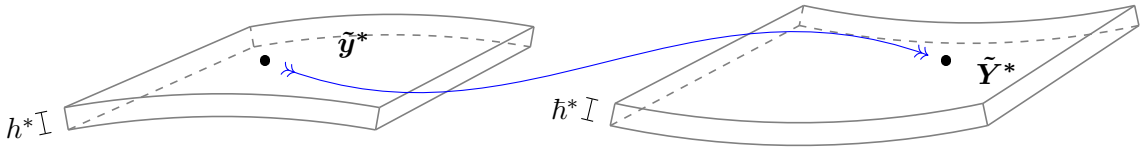

Figure 3.1: A shell undergoing a deformation: the point $\tilde{\boldsymbol{y}}^*$ in the initial configuration, is transformed onto the new material point $\tilde{\boldsymbol{Y}}^*$. This, in general, will be accompanied by some change in thickness, h^*, to a thickness $\hbar^* = \hbar^*(\tilde{\boldsymbol{y}}^*)$.

a particular surface: often the midplane. The displacement, strain and stress are then integrated through the thickness to eliminate the dependence on θ^{*3}. Throughout this work we always take the reference surface to be the midsurface at $\theta^{*3} = 0$ where we parameterize the through-thickness direction $\theta^{*3} \in (-h^*/2, h^*/2)$ (as shown in figure 3.2).

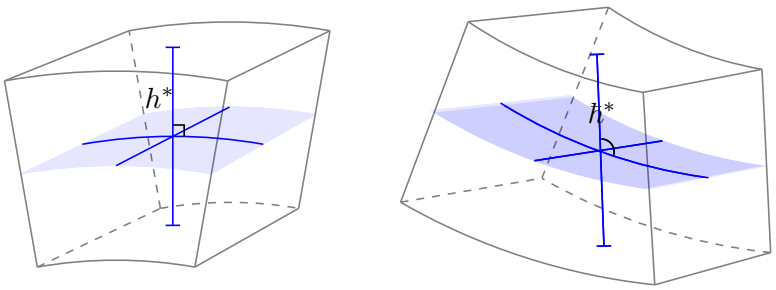

Figure 3.2: Deformation of a small element of material for which the shell hypothesis has been made. The displacements have a linear dependence on the through-thickness coordinate after deformation, but the material line parallel to the reference normal does not necessarily remain normal to the (shaded) midsurface.

Recall that we use characters with a tilde to indicate 3D quantities and no tilde to denote quantities evaluated on the midsurface. For example, the deformed position on the midplane will be

$$\boldsymbol{Y}^*(\theta^{*1}, \theta^{*2}) \equiv \tilde{\boldsymbol{Y}}^*(\theta^{*1}, \theta^{*2}, 0)\,. \tag{3.1.1}$$

The objective of shell theories is to characterise the deformation of the full 3D body in terms of deformations of the midplane only.

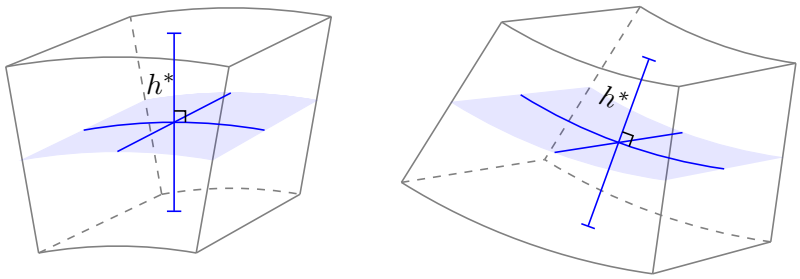

Figure 3.3: Deformation of a small element of material assuming that the Kirchhoff–Love hypothesis holds. The normal line to the (shaded) midsurface remains normal and unstretched after deformation.

Classically, to derive shell models from 3D elasticity, we first make the 'linear shell hypothesis' by assuming that the displacements vary linearly through the thickness [Wempner and Talaslidis, 2002]. We parameterise the undeformed position, $\tilde{\boldsymbol{y}}^*$, in terms of the through-thickness coordinate θ^{*3}:

$$\tilde{\boldsymbol{y}}^*(\theta^{*1},\theta^{*2},\theta^{*3}) = \boldsymbol{y}^*(\theta^{*1},\theta^{*2}) + \theta^{*3}\,\hat{\boldsymbol{n}}(\theta^{*1},\theta^{*2})\,, \tag{3.1.2}$$

where $\theta^{*3} \in (-h/2, h/2)$ and $\hat{\boldsymbol{n}}$ is the unit normal to the undeformed midsurface[1]. Using this parametrisation the linear shell hypothesis can be equivalently be expressed as

$$\tilde{\boldsymbol{Y}}^*(\theta^{*1},\theta^{*2},\theta^{*3}) = \boldsymbol{Y}^*(\theta^{*1},\theta^{*2}) + \theta^{*3}\,\boldsymbol{G}_3(\theta^{*1},\theta^{*2})\,, \tag{3.1.3}$$

where $\boldsymbol{G}_3$ is the tangent to the deformed θ^{*3} line. Here we have assumed that the deformed θ^{*3} line remains straight, but in general neither parallel to the deformed normal, $\hat{\boldsymbol{N}}$ nor unstretched.

It may be more intuitive to view this assumption in terms of displacements, whereby the linear shell hypothesis becomes [Wempner and Talaslidis, 2002]

$$\tilde{\boldsymbol{v}}^*(\theta^{*1},\theta^{*2},\theta^{*3}) = \boldsymbol{v}^*(\theta^{*1},\theta^{*2}) \;+\; \theta^{*3}\,\boldsymbol{\xi}(\theta^{*1},\theta^{*2}) \tag{3.1.4}$$

where the change in unit normal vector, $\boldsymbol{\xi}$, is given by

$$\boldsymbol{\xi}(\theta^{*1},\theta^{*2}) = \boldsymbol{G}_3(\theta^{*1},\theta^{*2}) - \hat{\boldsymbol{n}}(\theta^{*1},\theta^{*2})\,, \tag{3.1.5}$$

[1]The unit normal to the undeformed surface is equivalently the unit tangent to the θ^{*3} line, $\hat{\boldsymbol{n}} \equiv \hat{\boldsymbol{g}}_3$, by definition of the θ^{*3} line as the normal line to the undeformed surface.

in which $\theta^{*3}\boldsymbol{\xi}$ is the displacement of the midplane line. This is illustrated in figure 3.2. In general, the thickness of the deformed shell will not be h^*.

From here on, we shall use $\zeta^* \equiv \theta^{*3}$, to make clear the distinction between the through-thickness coordinate and the two in-plane coordinate directions and to avoid cumbersome constructs such as $(\theta^{*3})^m$ in the later expansions of the deformed position. Therefore, the linear shell hypothesis becomes

$$\tilde{\boldsymbol{v}}^*(\theta^{*1}, \theta^{*2}, \zeta^*) = \boldsymbol{v}^*(\theta^{*1}, \theta^{*2}) \, + \, \zeta^* \, \boldsymbol{\xi}(\theta^{*1}, \theta^{*2}) \, . \tag{3.1.6}$$

Further simplifications to the underlying shell model can be achieved if the Kirchhoff-Love hypothesis is made: it assumes that the material line that was orthogonal to the undeformed midplane remains normal to the midplane and unstretched such that the deformed material vector $\boldsymbol{G}_3$ is equal to the unit normal to the deformed midsurface $\hat{\boldsymbol{N}}$, as shown in figure 3.3. By the Kirchhoff-Love hypothesis

$$\tilde{\boldsymbol{v}}^*(\theta^{*1}, \theta^{*2}, \zeta^*) = \boldsymbol{v}^*(\theta^{*1}, \theta^{*2}) + \zeta^* \, \hat{\boldsymbol{N}}(\theta^{*1}, \theta^{*2}) \quad , \quad \boldsymbol{G}_3 \equiv \hat{\boldsymbol{N}} \, , \tag{3.1.7}$$

and the thickness of the deformed sheet, $\hbar^*$, is given by $\hbar^* = h^*$. This hypothesis holds when shells are thin enough to allow the transverse shear to be neglected. As pointed out by Koiter [1966], this assumption is usually used in conjunction with the mutually contradictory[2] assumption of plane stress: $\tilde{\boldsymbol{S}}^* \, \boldsymbol{n}_3 = \boldsymbol{0}$. The latter is then used to eliminate $\boldsymbol{n}_3 \cdot \tilde{\boldsymbol{E}} \, \boldsymbol{n}_3$ (cf. section 2.2.5), whose value is, in general, non-zero and determined entirely in terms of the in-plane (membrane) strain. As such, the assumption of plane-stress violates the Kirchhoff-Love hypothesis when non-zero strains are considered.

Upon making the Kirchhoff-Love hypothesis, it can be shown that the internal elastic energy separates into a bending energy and a stretching (membrane) energy [Wempner and Talaslidis, 2002]:

$$W^{*\,KL} = h \, W^{*\,M} \, + \, h^3 \, W^{*\,B} \, , \tag{3.1.8}$$

in which the first term pertains only to membrane-type deformations such as stretching and shearing of the midplane and the second term, the bending energy, is related only to changes of curvature. Here $W^{*\,M}$ and $W^{*\,B}$ are scaled energies that are order $\mathcal{O}(1)$ in relative thickness, and have units of energy.

[2] Using these two assumptions one arrives at identical equations as when using the single assumption of approximately plane stress: only the reconstruction of the full 3D displacement field differs [Koiter, 1966].

One can imagine the deformation of a surface with no change in curvature, such as the shearing of a flat, rectangular plate, to be purely associated with the first term. By contrast the inextensional deformation of a flat plane rolled to a cylinder could be considered as a deformation of pure bending, associated with only the second term. Due to these two modes, it is natural to refer to the relative difficulty of bending as the 'bending modulus' which scales as h^3.

3.2 Modern Perspective on Shell Theories

As many shell theories exist, all purported to approximate the full 3D parent theory, the question of choosing an accurate shell model becomes an important one. This status is worsened by the kinematical assumptions used as the starting point for classical shell theories, which sever the link to the 3D theory. It is for this reason that, in contrast to classical derivations, modern derivations of shell theories attempt to make assumptions only on the thickness and the magnitude of applied forces - which provides a more instructive way of selecting a theory. This is in contrast to classical theories that can only verify a posteriori, for example, that both the Kirchhoff-Love hypothesis and plane stress assumptions approximately hold. Modern derivations instead provide a concrete means of relating the models to the parent 3D theory.

Formal asymptotic methods have been used to provide justification for classical shell models and relate them to their parent three-dimensional theory, for example by Ciarlet [1980] and Fox et al. [1993]. However, these studies did not provide rigorous estimates of the errors nor show that the solutions to the expanded equations converge to the solutions of the three-dimensional equations in the limit of $h \to 0$ [Ciarlet, 1980; Trabelsi, 2006]. By contrast, gamma convergence [Le Dret and Raoult, 1996; Friesecke et al., 2006] provides a rigorous means of obtaining shell and plate models from three-dimensional elasticity, complete with error bounds and proof that solutions to the derived theory are also solutions to the parent theory [Trabelsi, 2006]. The method of gamma convergence can be viewed as an asymptotic method but, unlike formal asymptotic methods that only expand the equations, the method of gamma convergence demonstrates the convergence of the parent, three-dimensional minimization problem to the derived minimization problem [Braides, 2002]. The advantage to

this method is that it provides a direct, rigorous link between the parent and derived theories, with the convergence of minimum points and minimum values directly implied by the proof [Acerbi et al., 1988]. A review of the recent advances in gamma convergence has been compiled by Focardi [2012].

However, as discussed by Steigmann [2008], a downside to both asymptotic and gamma convergence methods is that both require the limit of $h \to 0$ in their derivation, and thus can only generate a leading order model in which successive terms are negligibly small in comparison to preceding ones, effectively decoupling smaller terms [Friesecke et al., 2006; Steigmann, 2008]. Methods of gamma expansion, as opposed to convergence, which involve more than a single order have been proposed in the literature, for example by Braides and Truskinovsky [2008] who also demonstrated the method to be successful in justifying several existing empirical theories within solid mechanics. The implications of this framework for shell and plate theories appears to be an open question.

To date, a number of shell and plate models have been derived using gamma convergence: most notably nonlinear membrane theory [Le Dret and Raoult, 1996], nonlinear bending [Friesecke et al., 2006], the Föppl-von Kármán model and linear bending [Friesecke et al., 2006]. A summary of the various conditions under which we expect models to emerge, based on the scaling of the energy and boundary conditions, is provided in appendix C. We will discuss the details of some of these models in later sections.

An alternative to these approaches, as advocated by Steigmann [2013], is to avoid the rigour of gamma convergence whilst still using the overriding concept that for a shell theory to accurately represent the three-dimensional theory, the energies must agree in the small thickness limit. This approach whilst informal, provides a route to expansion of the three-dimensional energy and allows the derivation of an energy in which bending and stretching are comparable with minimal assumptions [Steigmann, 2013]. This model extends the classical nonlinear plate model of Koiter [1966], which is widely advocated as the 'best all-round model' [Ciarlet, 2005], to finite strains, coinciding with it in the small-strain limit.

Given the status of the small-strain nonlinear Koiter model within the literature [Ciarlet, 2005] and the recent extension to finite strains [Steigmann, 2013], the Koiter-Steigmann model is the most appropriate theory for the objectives of this study. As such, we will discuss this model in more detail in section 3.4.

We proceed to discuss the deformation of surfaces, which we will use in the derivation of

forthcoming plate theories.

3.3 Differential Geometry on a Surface

We now present some important relations pertaining to the differential geometry of a surface. In this section we will present results generic to surfaces, but using the terminology associated with the deformed surface in order to characterise plate models in which only the deformed surface is curved.

3.3.1 The Surface Vectors

The tangent vectors, $\boldsymbol{G}_\alpha$, of a surface $\boldsymbol{Y}^*$ embedded in 3D space are given by

$$\boldsymbol{G}_\alpha \equiv \boldsymbol{Y}_{,\alpha}\,. \tag{3.3.1}$$

We also introduce the tangent vectors, $\boldsymbol{G}^\alpha$, in the dual space, such that [Wempner and Talaslidis, 2002]

$$\boldsymbol{G}^\alpha \cdot \boldsymbol{G}_\alpha = 1. \tag{3.3.2}$$

We use these vectors to express the surface metric tensor, $G_{\alpha\beta}$ and inverse metric tensor $G^{\alpha\beta}$, defined as [Wempner and Talaslidis, 2002]

$$G_{\alpha\beta} \equiv \boldsymbol{G}_\alpha \cdot \boldsymbol{G}_\beta \quad \text{and} \quad G^{\alpha\beta} \equiv \boldsymbol{G}^\alpha \cdot \boldsymbol{G}^\beta\,. \tag{3.3.3}$$

Thus, we can express the vectors in the dual space as linear combinations of the tangent space and vice-versa:

$$\boldsymbol{G}^\alpha = G^{\alpha\beta}\,\boldsymbol{G}_\beta \quad \text{and} \quad \boldsymbol{G}_\alpha = G_{\alpha\beta}\,\boldsymbol{G}^\beta\,. \tag{3.3.4}$$

We use the two in-plane unit vectors and the metric tensor to define the unit normal to the deformed surface, $\hat{\boldsymbol{N}}$, as [Wempner and Talaslidis, 2002]

$$\hat{\boldsymbol{N}} = \frac{\boldsymbol{G}_1 \times \boldsymbol{G}_2}{|\boldsymbol{G}_1 \times \boldsymbol{G}_2|} \quad \text{or} \quad \hat{\boldsymbol{N}} = \frac{1}{2\sqrt{G}}\epsilon^{\alpha\beta 3}\boldsymbol{G}_\alpha \times \boldsymbol{G}_\beta\,. \tag{3.3.5}$$

Here $\epsilon^{\alpha\beta 3}$ is the unit alternator, defined from components of the Levi-Civita tensor: ϵ^{ijk} and G is the determinant of the surface metric tensor $G_{\alpha\beta}\,\boldsymbol{g}_\alpha \otimes \boldsymbol{g}_\beta$. We can demonstrate the equivalence of the two expressions by using the quadruple product identity and noting the anti-commutative property of the cross product.

3.3.2 Derivatives of Surface Vectors

We now consider the derivatives of surface vectors. First we consider the derivatives of tangents, which can be written in the form of the Gauss formulae

$$\boldsymbol{G}^*_{\alpha,\beta} = \Gamma^*{}_{\alpha\beta\gamma}\,\boldsymbol{G}^\gamma \,+\, B^*_{\alpha\beta}\hat{\boldsymbol{N}} \,=\, \Gamma^{*\gamma}_{\alpha\beta}\,\boldsymbol{G}_\gamma \,+\, B^*_{\alpha\beta}\hat{\boldsymbol{N}}\,, \tag{3.3.6}$$

where we define the 2D Christoffel symbols of the first and second kind respectively as

$$\Gamma^*{}_{\alpha\beta\gamma} \equiv \boldsymbol{G^*}_{\alpha,\beta}\cdot\boldsymbol{G}_\gamma \quad \text{and} \quad \Gamma^{*\gamma}_{\alpha\beta} \quad \equiv \boldsymbol{G^*}_{\alpha,\beta}\cdot\boldsymbol{G}^\gamma\,, \tag{3.3.7}$$

and the curvature components on the deformed surface, $B^*_{\alpha\beta}$, by

$$B^*_{\alpha\beta} \,=\, \Gamma^{*3}_{\alpha\beta} \,=\, \hat{\boldsymbol{N}}\cdot\boldsymbol{G^*}_{\alpha,\beta}\,. \tag{3.3.8}$$

It can be shown [Wempner and Talaslidis, 2002], using the product rule and the relation $\boldsymbol{G}^*_{\alpha,\beta} = \boldsymbol{G}^*_{\beta,\alpha}$, that the first Christoffel symbol is related to the metric tensor as follows

$$\Gamma^*{}_{\alpha\beta\gamma} \,=\, \frac{1}{2}\left(G^*_{\gamma\alpha,\beta} \,+\, G^*_{\beta\gamma,\alpha} \,-\, G^*_{\alpha\beta,\gamma}\right)\,. \tag{3.3.9}$$

Using the product rule it can be shown that

$$B^*_{\alpha\beta} \,=\, -\boldsymbol{G}_\alpha\cdot\hat{\boldsymbol{N}}^*_{,\beta}\,. \tag{3.3.10}$$

Thus we see that the derivatives of the normal can be written as follows

$$\hat{\boldsymbol{N}}_{,\alpha} = -B^*_{\alpha\beta}\,\boldsymbol{G}^\beta\,, \tag{3.3.11}$$

which is known as the Weingarten formula.

The curvature tensor on the deformed surface is therefore

$$\boldsymbol{B^*} = B^*_{\alpha\beta}\boldsymbol{G}^\alpha\otimes\boldsymbol{G}^\beta\,, \tag{3.3.12}$$

in the spatial frame. We can define instead a curvature tensor in the reference material frame: the relative curvature, $\boldsymbol{\kappa^*}$, which is given by

$$\boldsymbol{\kappa^*} = \kappa^*_{\alpha\beta}\boldsymbol{g}^\alpha\otimes\boldsymbol{g}^\beta \tag{3.3.13}$$

which has components $\kappa^*_{\alpha\beta} = -B^*_{\alpha\beta}$. This curvature tensor is related to the derivative of the deformed normal by

$$\boldsymbol{\kappa^*} = (\boldsymbol{\nabla}^*\boldsymbol{Y^*})^T(\boldsymbol{\nabla}^*\boldsymbol{N})\,, \tag{3.3.14}$$

Thus we can relate the two curvature tensors by the following formula

$$\boldsymbol{\kappa}^* \;=\; -(\boldsymbol{\nabla}^*\boldsymbol{Y}^*)^T\,\boldsymbol{B}^*\,(\boldsymbol{\nabla}^*\boldsymbol{Y}^*)\,. \tag{3.3.15}$$

Finally, for completeness, we define the well-known Gaussian curvature, k_G, and mean curvature, k_M, which are given by

$$k_G^* \;=\; B^{*1}{}_1\,B^{*2}{}_2 - B^{*1}{}_2\,B^{*2}{}_1 \quad \text{and} \quad k_M^* \;=\; \frac{1}{2}\,B^{*\alpha}{}_{\alpha}\,, \tag{3.3.16}$$

where the curvature tensor $B^{*\alpha}{}_{\beta}$ is obtained by raising the index: $B^{*\alpha}{}_{\beta} = G^{\alpha\gamma}B^*_{\gamma\beta}$.

3.4 The Koiter-Steigmann Model

In this section we present Koiter's nonlinear plate model [Koiter, 1966], which was recently extended by Steigmann [2013] to incorporate finite strains. Plate models are a special type of shell model, for which there is no initial curvature [Audoly and Pomeau, 2010]. In the limit of small strains, or under assumption of a linear constitutive relation, the Koiter-Steigmann model and Koiter's original model coincide [Steigmann, 2013]. The Koiter-Steigmann model has not been derived by means of gamma convergence (as a rigorous variational limit of three-dimensional elasticity), but still has a rational descent from three-dimensional elasticity, using minimal assumptions, as opposed to classical theories which begin with kinematical assumptions, like the Kirchhoff-Love hypothesis.

The first study that attempted to relate 2D and 3D theories in the case of finite strain was made by Hilgers and Pipkin [1992a,b, 1996]. They found that their plate model, whilst being optimal in terms of accuracy compared to the three-dimensional theory, was generally ill-posed as a minimization problem [Hilgers and Pipkin, 1996]: so traditional methods that rely on minimizing the total energy would fail. This ill-posedness arises for any deformations with compressive stress, similar to membrane theory; however, unlike in the case of membrane theory the model is not suitable for relaxation (cf. tension field theory), due to the presence of a bending stiffness [Steigmann, 2013]. The process of relaxation, which is suitable for plate models without a bending stiffness, is the process of assuming that all compressive stress is automatically relieved by fine-scale wrinkles (which are not resolved) as outlined by the tenets of tension field theory [Steigmann, 1990]. To regularize the model Hilgers and Pipkin [1996] instead supplemented the equations with an ad hoc term.

The study of Steigmann [2013] derives an energy which is free of the ad hoc term of Hilgers and Pipkin [1996] that can still constitute a meaningful minimization problem. Steigmann

[2013] instead shows that if the stress is smaller than $o(1)$ in h^*/L, such that a linear constitutive model is assumed in the bending term, then the destabilising term can be neglected, regularizing the model with no additional penalty to accuracy.

The model itself contains both the nonlinear bending energy derived by means of gamma convergence by Friesecke et al. [2006] and a nonlinear membrane energy that, upon relaxation of compressive stresses, also yields the gamma convergent limit [Friesecke et al., 2006]. We reiterate, however, that Steigmann's model is not suitable for relaxation as the model contains a bending stiffness.

More details of these relations can be found in Steigmann [2013]. Despite its close relation to several gamma-convergent models, the Steigmann model is not a gamma-convergent limit. In fact, the Koiter-Steigmann model *cannot* be derived by conventional methods of gamma convergence, because it assumes a small but nonzero plate thickness [Friesecke et al., 2006; Braides and Truskinovsky, 2008].

The original derivation of the small-strain version of the model is presented by Koiter [1966], who assumes an approximate state of plane stress and then uses this to derive the model. As noted by Koiter [1966], by assuming the contradictory Kirchhoff-Love hypothesis and the plane-stress constitutive relations one can arrive at an identical energy and an equivalent model: only the construction of the true, 3D deformation from the identical midplane deformation would differ.

In the next section we will present the Koiter-Steigmann model, starting with the derivation of the energy principle and proceeding by deriving the variational equations and the corresponding Euler-Lagrange equations.

3.4.1 Outline of the Derivation

We will now derive the Koiter-Steigmann plate energy, following closely the derivation of Steigmann [2013]. As a rough guide to the process, we outline here, in words, the direction the derivation takes. The basic assumption is that the plate has small thickness, h^*, in comparison with the horizontal length scale, L. The derivation begins by performing a Taylor expansion in $\zeta^* \sim h^* \ll L$, the through–thickness coordinate, of the displacements, using this to express the deformation gradient, and the ζ^* derivatives of the deformation gradient, at the midsurface as a power series in ζ^*. By expanding the energy in terms of these quantities and then integrating through the thickness, an $o(h^3)$ energy is computed,

where we recall that $h = h^*/L \ll 1$ is relative thickness. This energy is then simplified further by using physical restrictions on the magnitude of the pressure load, permitting a relatively simple representation of the energy.

To achieve this, we must show that the energy is entirely determined in terms of the midplane deformation, and that the higher order 'directors' in the expansion can be reconstructed entirely using the position of the deformed midplane position vector. This is achieved by assuming that the forces applied to the lateral faces of the sheet are of order $\mathcal{O}(h^3)$ in magnitude. It transpires that this latter assumption is equivalent to the assumption of approximately plane stress, leading to a model in which through-thickness shear is neglected.

The assumptions above lead to a model that is known to be generally ill-posed as a minimization problem: with the requirement of tensile stress everywhere in the sheet necessary for the existence of minimizers [Steigmann, 2013]. This restriction can be removed by neglecting the problematic terms in the strain gradients, which formally would result in an ad hoc model. However, following the arguments of Steigmann [2013], it will be shown that a weak assumption on the magnitude of stress allows these terms to be neglected with no cost to accuracy, thereby restoring the rationality of the model.

The energy is then simplified for the cases of reflection symmetry of material properties about the midplane and the special case of isotropic material properties, in pursuit of our objective of characterising hyperelastic plates with uniform properties.

3.4.2 The 3D Energy

As before, we use tildes to indicate quantities defined throughout the material and remove tildes for their counterparts evaluated on the midplane. We proceed to derive the Koiter-Steigmann plate energy in the manner outlined in Steigmann [2013].

Dimensionless Quantities

We start by introducing nondimensional quantities, to make our assumptions on the magnitude of quantities explicit. We introduce nondimensional stress tensors as follows

$$[\boldsymbol{\sigma}\,,\,\boldsymbol{S}\,,\,\boldsymbol{P}] = \frac{1}{E}\,[\boldsymbol{\sigma}^*\,,\,\boldsymbol{S}^*\,,\,\boldsymbol{P}^*]\,, \tag{3.4.1}$$

in which E is the Young's modulus.

We rescale the position vectors on the horizontal length scale L, where $L \sim \sqrt{A^*}$ and A^* is the area of undeformed midplane. Thus, we obtain the following nondimensional position vectors:

$$\left[\boldsymbol{Y}\,,\,\boldsymbol{v}\,,\,\boldsymbol{y}\,,\,\theta^i\right] = \frac{1}{L}\left[\boldsymbol{Y}^*\,,\,\boldsymbol{v}^*\,,\,\boldsymbol{y}^*\,,\,\theta^{i*}\right]\,. \tag{3.4.2}$$

Nondimensionalizing on inverse-length for the curvature, we define

$$\left[\boldsymbol{B}\,,\,\boldsymbol{\kappa}\right] = \frac{1}{L^{-1}}\left[\boldsymbol{B}^*\,,\,\boldsymbol{\kappa}^*\right]\,. \tag{3.4.3}$$

We further introduce the energy scale EL^3, and define the nondimensional energy

$$W = \frac{1}{EL^3}W^*\,, \tag{3.4.4}$$

and nondimensional energy density functions

$$\left[\mathcal{W}(\tilde{\boldsymbol{F}})\,,\,\mathcal{W}(\tilde{\boldsymbol{E}})\right] = \frac{1}{E}\left[\mathcal{W}^*(\tilde{\boldsymbol{F}})\,,\,\mathcal{W}^*(\tilde{\boldsymbol{E}})\right]\,. \tag{3.4.5}$$

Finally we introduce the nondimensional elastic moduli

$$\left[\mathcal{M}(\tilde{\boldsymbol{F}})\,,\,\mathcal{C}(\tilde{\boldsymbol{E}})\right] = \frac{1}{E}\left[\mathcal{M}^*(\tilde{\boldsymbol{F}})\,,\,\mathcal{C}^*(\tilde{\boldsymbol{E}})\right]\,. \tag{3.4.6}$$

All of these nondimensional quantities are initially assumed to be $\mathcal{O}(1)$ in relative thickness, except for θ^3 which will be $\mathcal{O}(h)$.

Problem Set-up

To set-up the problem, we first define the geometry of a plate, which is a special case of shell with zero initial curvature. We use Ω to represent the midsurface of the undeformed plate, which occupies a volume $v = \Omega \times (-h/2, h/2)$ in 3D space. We introduce the undeformed midplane material coordinate for a plate, given by: $\boldsymbol{y} \equiv x_1\hat{\boldsymbol{e}}_1 + x_2\hat{\boldsymbol{e}}_2$, where x_1 and x_2 are the standard Cartesian coordinates in the $\hat{\boldsymbol{e}}_1$, $\hat{\boldsymbol{e}}_2$ directions, respectively. Henceforth, we will always use Cartesian coordinates, unless otherwise noted.

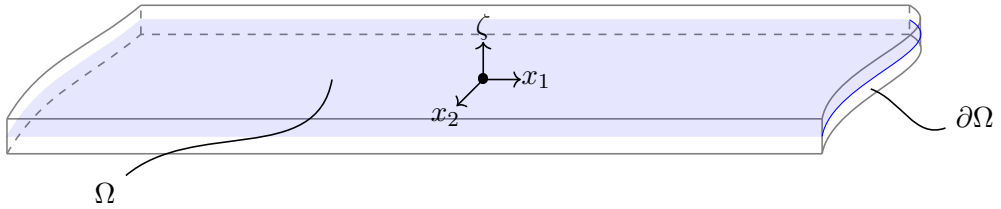

Figure 3.4: Diagram showing the plate geometry. The midsurface, Ω, is located at $\zeta = 0$.

Our main assumption is that the thickness $h \ll 1$, where we recall that $h = h^*/L$ is the relative thickness of the plate. The edge (boundary) of the midplane, at which lateral loading conditions are applied, is represented by $\partial\Omega$. We show this plate in figure 3.4. In this section we follow closely the derivation of Steigmann [2010, 2013] with the aim of deriving an order $\mathcal{O}(h^3)$ accurate plate model[3], with minimal assumptions.

We recall from section 2.2.3, that the (nondimensional) energy for an elastic body is

$$W = \int_v \mathcal{W}(\tilde{\boldsymbol{F}})\, dv\,, \tag{3.4.7}$$

and the (nondimensional) Piola stress is

$$\boldsymbol{P} \equiv \mathcal{W}_{\tilde{\boldsymbol{F}}}\,. \tag{3.4.8}$$

The (nondimensional) deformation-gradient-dependent elastic moduli are related to the strain energy density by:

$$\mathcal{M}(\tilde{\boldsymbol{F}}) = \mathcal{W}_{\tilde{\boldsymbol{F}}\tilde{\boldsymbol{F}}}\,. \tag{3.4.9}$$

We again use the Green-Lagrange strain

$$\tilde{\boldsymbol{E}} = \frac{1}{2}\left(\tilde{\boldsymbol{F}}^T\tilde{\boldsymbol{F}} - \mathbb{I}_3\right) \tag{3.4.10}$$

and the (nondimensional) strain-dependent energy

$$\mathcal{U}(\tilde{\boldsymbol{E}}) = \mathcal{W}(\tilde{\boldsymbol{F}})\,, \tag{3.4.11}$$

to define (nondimensional) strain-dependent elastic moduli

$$\mathcal{C}(\tilde{\boldsymbol{E}}) = \mathcal{U}_{\tilde{\boldsymbol{E}}\tilde{\boldsymbol{E}}}\,, \tag{3.4.12}$$

and the (nondimensional) second Piola-Kirchhoff stress

$$\tilde{\boldsymbol{S}}(\tilde{\boldsymbol{E}}) = \mathcal{U}_{\tilde{\boldsymbol{E}}}\,. \tag{3.4.13}$$

For clarity of exposition, in the remainder of this section we refer to quantities such as stress and energy on the understanding that we are describing their nondimensional counterparts, unless explicitly stated otherwise. We continue to use starred and unstarred notation for dimensional and nondimensional quantities respectively, however.

[3]That is, an energy that is accurate to $\mathcal{O}(h^3)$, with smaller terms of order $o(h^3)$ neglected.

We can use the chain rule to connect the deformation-gradient-dependent moduli, $\mathcal{M}(\tilde{\boldsymbol{F}})$, acting on a matrix $\boldsymbol{A}$, to the strain-dependent moduli, $\mathcal{C}(\tilde{\boldsymbol{E}})$ resulting in the following formula [Steigmann, 2013]

$$\mathcal{M}(\tilde{\boldsymbol{F}})\,\boldsymbol{A} = \boldsymbol{A}\,\tilde{\boldsymbol{S}} + \frac{1}{2}\tilde{\boldsymbol{F}}\,\mathcal{C}(\tilde{\boldsymbol{E}})\left(\boldsymbol{A}^T\,\tilde{\boldsymbol{F}} + \tilde{\boldsymbol{F}}^T\,\boldsymbol{A}\right). \tag{3.4.14}$$

We also assume that we can expand about a stress-free reference state, such that the stress vanishes at zero strain, $\tilde{\boldsymbol{E}} = \boldsymbol{0}$, and that $\mathcal{C}(\boldsymbol{0})$ is positive definite such that $\boldsymbol{A}\cdot\mathcal{C}(\boldsymbol{0})\,\boldsymbol{A} > 0$ for all nonzero matrices $\boldsymbol{A}$. Then,

$$\tilde{\boldsymbol{S}}(\tilde{\boldsymbol{E}}) = \mathcal{C}(\boldsymbol{0})\,\tilde{\boldsymbol{E}} + o(|\tilde{\boldsymbol{E}}|)\,. \tag{3.4.15}$$

We emphasize that, though we assume that the stress adopts this form when expanding about the reference state, we have *not* assumed a linear constitutive hypothesis for all strain, as we retain several orders in the thickness-wise expansion.

We also note that, using equation (3.4.14), at zero strain the relationship between the two sets of elastic moduli acting on a matrix $\boldsymbol{A}$, will be

$$\mathcal{M}(\mathbb{I}_3)\,\boldsymbol{A} = \mathcal{C}(\boldsymbol{0})\,\boldsymbol{A} \tag{3.4.16}$$

where at zero strain $\tilde{\boldsymbol{F}} = \mathbb{I}_3$ and $\tilde{\boldsymbol{E}} = \boldsymbol{0}$. Thus, we can see our constitutive hypothesis, equation (3.4.15), satisfies strong ellipticity, defined in section 2.2.4, at zero strain.

Below we break convention slightly and use

$$\boldsymbol{S}^0 \equiv \tilde{\boldsymbol{S}}(\theta^1, \theta^2, 0)\,, \tag{3.4.17}$$

in order to make clear the distinction between the stress at the centre, $\boldsymbol{S}^0$, and the membrane stress

$$\boldsymbol{S} \equiv \mathcal{U}^M_{\boldsymbol{\epsilon}}\,, \tag{3.4.18}$$

where $\boldsymbol{\epsilon} \equiv E_{\alpha\beta}\hat{\boldsymbol{e}}_\alpha \otimes \hat{\boldsymbol{e}}_\beta$ is the 2D plane-strain and $\mathcal{U}^M(\boldsymbol{\epsilon})$ is the membrane strain-energy, in which the condition of plane stress has been used to eliminate out-of-plane strain components.

3.4.3 Expanding the Basic Quantities

We express the undeformed material coordinate as

$$\tilde{\boldsymbol{y}} = \boldsymbol{y} + \zeta\,\boldsymbol{k}\,, \tag{3.4.19}$$

in the same manner as in section 3.1, but this time asserting the planar reference configuration by using the Cartesian unit vector $\boldsymbol{k}$ as the undeformed normal. Here, as in section 3.1, $\zeta \in (-h/2, h/2)$, is the nondimensional through-thickness coordinate.

We start by expressing the 3D position $\tilde{\boldsymbol{Y}}$ as an expansion in the through-thickness coordinate $\zeta \ll L$:

$$\tilde{\boldsymbol{Y}} = \boldsymbol{Y}(\boldsymbol{y}) + \zeta\, \boldsymbol{d}(\boldsymbol{y}) + \frac{1}{2}\zeta^2\, \boldsymbol{e}(\boldsymbol{y}) + \frac{1}{6}\zeta^3\, \boldsymbol{f}(\boldsymbol{y}) + \dots\,, \tag{3.4.20}$$

in which $\boldsymbol{Y}(\boldsymbol{y})$ is a material position on the deformed midplane and the functions $\boldsymbol{d}(\boldsymbol{y})$, $\boldsymbol{e}(\boldsymbol{y})$ and $\boldsymbol{f}(\boldsymbol{y})$ are known as the *directors*.

We can then express the deformation gradient, $\tilde{\boldsymbol{F}} = \boldsymbol{D}\tilde{\boldsymbol{Y}}$, as

$$\tilde{\boldsymbol{F}} = \boldsymbol{\nabla}\tilde{\boldsymbol{Y}} + \left(\boldsymbol{d}(\boldsymbol{y}) + \zeta\, \boldsymbol{e}(\boldsymbol{y}) + \frac{1}{2}\zeta^2\, \boldsymbol{f}(\boldsymbol{y}) + \dots\right) \otimes \boldsymbol{k}\,, \tag{3.4.21}$$

recalling that in our notation $\boldsymbol{DV} = \boldsymbol{\nabla V} + \boldsymbol{V}_{,3} \otimes \boldsymbol{k}$, for some vector field $\boldsymbol{V}$. It is useful to define the deformation gradient and ζ derivatives at the midplane, which we denote with successive primes, as follows

$$\boldsymbol{F} = \boldsymbol{\nabla}\, \boldsymbol{Y} + \boldsymbol{d} \otimes \boldsymbol{k} \quad , \quad \boldsymbol{F}' = \boldsymbol{\nabla}\, \boldsymbol{d} + \boldsymbol{e} \otimes \boldsymbol{k} \quad \text{and} \quad \boldsymbol{F}'' = \boldsymbol{\nabla}\, \boldsymbol{e} + \boldsymbol{f} \otimes \boldsymbol{k}\,, \tag{3.4.22}$$

where we have used the notation

$$(\cdot)' \equiv \frac{\partial}{\partial \zeta}(\tilde{\cdot})|_{\zeta=0}\,, \quad (\cdot)'' \equiv \frac{\partial^2}{\partial \zeta^2}(\tilde{\cdot})|_{\zeta=0} \quad \text{etc.} \quad . \tag{3.4.23}$$

This allows us to easily express quantities as power series in ζ, for example the 3D deformation gradient would be

$$\tilde{\boldsymbol{F}} = \boldsymbol{F} + \zeta\, \boldsymbol{F}' + \frac{1}{2}\zeta^2 \boldsymbol{F}'' + \dots\,. \tag{3.4.24}$$

3.4.4 The Expanded Energy

Now Taylor expanding the energy in $\zeta \ll 1$ about the midplane and using the chain rule we get

$$W = \int_\Omega \int_{-h/2}^{h/2} \left(\mathcal{W}(\boldsymbol{F}) + \zeta \boldsymbol{P}(\boldsymbol{F}) \cdot \boldsymbol{F}' + \frac{1}{2}\,\zeta^2 (\mathcal{M}(\boldsymbol{F})\, \boldsymbol{F}' \cdot \boldsymbol{F}' + \boldsymbol{P}(\boldsymbol{F}) \cdot \boldsymbol{F}'') + \dots\right) d\zeta\, d\Omega \tag{3.4.25}$$

in which $\cdot$ is a Frobenius inner product and refers to the contraction of both indices in the case of matrices. For example the inner product of matrices A and B would be

$$\boldsymbol{A} \cdot \boldsymbol{B} \equiv \mathrm{Tr}\,(\boldsymbol{A}\boldsymbol{B}^T) = A_{ij} B_{ij}\,. \tag{3.4.26}$$

We can integrate the energy through the thickness, ζ, to obtain the approximate energy:

$$W = \int_\Omega \left(h\,\mathcal{W}(\boldsymbol{F}) + \frac{h^3}{24}\left(\mathcal{M}(\boldsymbol{F})\,\boldsymbol{F}'\cdot\boldsymbol{F}' \,+\, \boldsymbol{P}(\boldsymbol{F})\cdot\boldsymbol{F}''\right)\right) d\Omega \,+\, \mathcal{O}(h^5)\,. \tag{3.4.27}$$

which is a function of $\boldsymbol{y}$ via the independent (unknown) functions $\boldsymbol{Y}$, $\boldsymbol{d}$, $\boldsymbol{e}$ and $\boldsymbol{f}$ that describe the deformation.

Thus we have reduced the three-dimensional functional, in 3 fields, to a two-dimensional functional evaluated at the midplane, with 12, as yet unknown, director fields. We can now make further simplifications to this energy on the grounds of the applied forces, in order to eliminate the directors.

3.4.5 Simplifying the Energy

In this section we use arguments on the scale of the forces applied to the lateral faces of the sheet to further simplify the model. Following Steigmann [2013] the force balance normal to the reference surface, Ω, is given by

$$\boldsymbol{t}^{\pm} = \pm\boldsymbol{P}(\tilde{\boldsymbol{F}})|_{\xi=\pm h/2}\,\hat{\boldsymbol{n}}\,, \tag{3.4.28}$$

where $\hat{\boldsymbol{n}} = \boldsymbol{k}$ is the normal to the undeformed midplane and $\boldsymbol{t}^{\pm}$ is the (nondimensional) applied traction. If we Taylor expand the through thickness strain, in powers of $h \ll 1$, about the reference surface, and evaluate it on the top and bottom surfaces we get

$$\boldsymbol{t}^{\pm} = \pm\boldsymbol{P}(\boldsymbol{F})\boldsymbol{k} \,+\, \frac{1}{2}h(\mathcal{M}(\boldsymbol{F})\,\boldsymbol{F}')\boldsymbol{k} \,\pm\, \mathcal{O}(h^2) \tag{3.4.29}$$

for the top and bottom plates respectively, where $\boldsymbol{t}^{\pm}$ are the (nondimensional) applied tractions at the top and bottom surfaces respectively. This implies that

$$\boldsymbol{t}^{+} + \boldsymbol{t}^{-} = h\,\boldsymbol{P'}\boldsymbol{k} \,+\, \mathcal{O}(h^3) \quad \text{and} \quad \boldsymbol{t}^{+} - \boldsymbol{t}^{-} = 2\,\boldsymbol{P}(\boldsymbol{F})\boldsymbol{k} + \mathcal{O}(h^2)\,, \tag{3.4.30}$$

where $\boldsymbol{P'} \equiv (\mathcal{M}(\boldsymbol{F})\,\boldsymbol{F}')$.

We now make the simplifying assumption that forces applied on the top and bottom faces are $\boldsymbol{t}^{\pm} = \mathcal{O}(h^3)$ then this implies

$$\boldsymbol{P}\boldsymbol{k} = \mathcal{O}(h^2) \quad \text{and} \quad \boldsymbol{P'}\boldsymbol{k} = \mathcal{O}(h^2)\,, \tag{3.4.31}$$

so that we can assume $\boldsymbol{P}\boldsymbol{k} = \boldsymbol{0}$ and $\boldsymbol{P'}\boldsymbol{k} = \boldsymbol{0}$ in the coefficients of h^3, with no loss in accuracy.

These assumptions can be physically interpreted as restriction to forces which do not result in large transverse shear strains. To incorporate these strains would necessitate solving

for the director $\boldsymbol{d}$ as a coupled equation - leading to a shearable, Naghdi-type model with additional unknowns. Thus, we are assuming that the transverse forces are "small enough" that significant shearing of the plate does not occur. Instead, we may relate $\boldsymbol{d}$ directly in terms of the displacements, which we do below.

We now apply these to the derived energy in equation (3.4.27). By imposing the condition $\boldsymbol{Pk} = \boldsymbol{0}$ in the bending energy we can neglect the term involving the director, $\boldsymbol{f}$. The resulting energy becomes

$$W = \int_\Omega \left(h\,\mathcal{W}(\boldsymbol{F}) + \frac{h^3}{24}\left(\mathcal{M}(\boldsymbol{F})\,\boldsymbol{F}'\cdot\boldsymbol{F}' \,+\, \boldsymbol{P}(\boldsymbol{F})\cdot\boldsymbol{\nabla e}\right)\right) d\Omega \,+\, \mathcal{O}(h^5)\,. \tag{3.4.32}$$

We now perform an integration by parts of the final term:

$$\begin{aligned} W = \int_\Omega \left(h\,\mathcal{W}(\boldsymbol{F}) + \frac{h^3}{24}\left(\mathcal{M}(\boldsymbol{F})\,\boldsymbol{F}'\cdot\boldsymbol{F}' \,-\, div(\boldsymbol{P}(\boldsymbol{F})\,\mathbb{1})\cdot\boldsymbol{e}\right)\right) d\Omega \\ + \frac{h^3}{24}\int_{\partial\Omega} (\boldsymbol{P}(\boldsymbol{F})\,\mathbb{1}\,\boldsymbol{\nu}\cdot\boldsymbol{e})\; dt + \mathcal{O}(h^5)\,, \end{aligned} \tag{3.4.33}$$

where dt is an element along the boundary $\partial\Omega$ and $\boldsymbol{\nu}$ is the outward unit normal to the boundary $\partial\Omega$. Here we also introduced the following tensor

$$\mathbb{1} \equiv \mathbb{I}_3 - \boldsymbol{k}\otimes\boldsymbol{k}\,, \tag{3.4.34}$$

which acts as a two-dimensional identity matrix embedded in the 3D space.

We then note that the equations of 3D elasticity predict, by equation (2.2.38), that

$$Div\tilde{\boldsymbol{P}} = div(\tilde{\boldsymbol{P}}\mathbb{1}) + \tilde{\boldsymbol{P}}'\cdot\boldsymbol{k} = \boldsymbol{0}\,, \tag{3.4.35}$$

allowing us to replace the last bulk term as follows

$$\begin{aligned} W = \int_\Omega \left(h\,\mathcal{W}(\boldsymbol{F}) + \frac{h^3}{24}\left(\mathcal{M}(\boldsymbol{F})\,\boldsymbol{F}'\cdot\boldsymbol{F}' \,+\, \boldsymbol{P}'(\boldsymbol{F})\boldsymbol{k}\cdot\boldsymbol{e}\right)\right) d\Omega \\ + \frac{h^3}{24}\int_{\partial\Omega} (\boldsymbol{P}(\boldsymbol{F})\,\mathbb{1}\,\boldsymbol{\nu}.\boldsymbol{e})\; dt + \mathcal{O}(h^5)\,, \end{aligned} \tag{3.4.36}$$

and then immediately eliminate it, as it is of order $\mathcal{O}(h^6)$, by the condition on $\boldsymbol{t}^+ - \boldsymbol{t}^-$ in equation (3.4.30). This gives the following expression for energy for a plate subject to transverse forcing of order $\mathcal{O}(h^3)$, accurate to order $\mathcal{O}(h^5)$

$$W = \int_\Omega \left(h\,\mathcal{W}(\boldsymbol{F}) + \frac{h^3}{24}\left(\mathcal{M}(\boldsymbol{F})\,\boldsymbol{F}'\cdot\boldsymbol{F}'\right)\right) d\Omega + \frac{h^3}{24}\int_{\partial\Omega} (\boldsymbol{P}(\boldsymbol{F})\,\mathbb{1}\,\boldsymbol{\nu}.\boldsymbol{e})\; dt + \mathcal{O}(h^5) \tag{3.4.37}$$

However, though we have eliminated the term $\boldsymbol{f}$ entirely, we still need to solve this set of equations for the as yet unknown directors $\boldsymbol{d}$ and $\boldsymbol{e}$, that enter via $\boldsymbol{F}'$. With this in mind,

we proceed to simplify the energy using the results of Steigmann [2010]. By definition of $\boldsymbol{P}' \equiv \mathcal{M}(\boldsymbol{F})\,\boldsymbol{F}'$ and $\boldsymbol{F}' = \boldsymbol{\nabla d} + \boldsymbol{e} \otimes \boldsymbol{k}$, the condition $\boldsymbol{P}'\boldsymbol{k} = \mathcal{O}(h^2)$ is equivalent to the following expression

$$\{\mathcal{M}(\boldsymbol{F})\,(\boldsymbol{e} \otimes \boldsymbol{k})\}\boldsymbol{k} = -\{\mathcal{M}(\boldsymbol{F})\,(\boldsymbol{\nabla d})\}\boldsymbol{k} + \mathcal{O}(h^2)\,. \tag{3.4.38}$$

We can also write the approximate plane stress condition, $\boldsymbol{P}\boldsymbol{k} = \mathcal{O}(h^2)$, as

$$\left\{\mathcal{W}_{\tilde{\boldsymbol{F}}}(\boldsymbol{\nabla Y} + \boldsymbol{d} \otimes \boldsymbol{k})\right\}\boldsymbol{k} = \mathcal{O}(h^2)\,. \tag{3.4.39}$$

Steigmann [2010] shows that these two equations form a complete system to uniquely determine the directors $\boldsymbol{d}$ and $\boldsymbol{e}$ to order $\mathcal{O}(h^2)$. Thus, we can replace the directors in some parts of equation (3.4.37) with the solutions $\bar{\boldsymbol{d}}$ and $\bar{\boldsymbol{e}}$ to equations (3.4.38) and (3.4.39) with no loss of accuracy. We substitute

$$\boldsymbol{d} = \bar{\boldsymbol{d}}(\boldsymbol{\nabla Y}) + \mathcal{O}(h^2) \quad \text{and} \quad \boldsymbol{e} = \bar{\boldsymbol{e}}(\boldsymbol{\nabla Y}) + \mathcal{O}(h^2)\,,$$

in the order h^3 term *only*. This results in the new expression for the energy

$$W = \int_\Omega \mathring{W}\, d\Omega \; + \frac{h^3}{24} \int_{\partial\Omega} (\boldsymbol{P}(\boldsymbol{F})\,\mathbb{1}\,\boldsymbol{\nu}.\boldsymbol{e})\; dt \; + \; \mathcal{O}(h^5)\,, \tag{3.4.40}$$

with $\mathring{W}$ given by

$$\mathring{W} = h\,\mathcal{W}(\boldsymbol{\nabla Y} + \boldsymbol{d} \otimes \boldsymbol{k}) + \frac{h^3}{24}\left(\mathcal{M}(\boldsymbol{\nabla Y} + \bar{\boldsymbol{d}} \otimes \boldsymbol{k})\left(\boldsymbol{\nabla}\bar{\boldsymbol{d}} + \bar{\boldsymbol{e}} \otimes \boldsymbol{k}\right) \cdot \left(\boldsymbol{\nabla}\bar{\boldsymbol{d}} + \bar{\boldsymbol{e}} \otimes \boldsymbol{k}\right)\right)\,, \tag{3.4.41}$$

where we emphasise that we *cannot* yet replace $\boldsymbol{d}$ with the solution $\bar{\boldsymbol{d}}$ in the first term, as it, at first inspection, contributes order $\mathcal{O}(h^3)$ terms to the energy. Taking variations in $\boldsymbol{d}$, Steigmann [2010] finds that the Euler-Lagrange equation for $\boldsymbol{d}$, is given by

$$\mathring{W}_{\boldsymbol{d}} = h\mathcal{W}_{\boldsymbol{d}}\,,$$

which can be seen by taking the Gateaux derivative of equation (3.4.41). These are then used to further simplify the energy. By the chain rule the above relation yields the equation

$$\mathcal{W}_{\boldsymbol{d}} = \mathcal{W}_{\tilde{\boldsymbol{F}}}\,\boldsymbol{k} = 0\,,$$

which has the unique solution $\bar{\boldsymbol{d}}$ [Steigmann, 2010]. Thus no accuracy is lost by imposing $\boldsymbol{d} = \bar{\boldsymbol{d}}$ everywhere in the energy. This, in turn, gives the final, $\mathcal{O}(h^5)$ energy as

$$W^{KS} = \int_\Omega \left(h\,\mathcal{W}(\boldsymbol{F}) + \frac{h^3}{24}\left(\mathcal{M}(\boldsymbol{F})\,\boldsymbol{F}' \cdot \boldsymbol{F}'\right)\right)\, d\Omega \; + \frac{h^3}{24} \int_{\partial\Omega} (\boldsymbol{P}(\boldsymbol{F})\,\mathbb{1}\,\boldsymbol{\nu}.\boldsymbol{e})\; dt\;, \tag{3.4.42}$$

in which $\bar{\boldsymbol{d}}$ is uniquely determined by solving equation (3.4.39), which we demonstrate in the proceeding section for the special case of isotropy. This condition on $\bar{\boldsymbol{d}}$ is equivalent to the statement of approximate plane stress, or that

$$\boldsymbol{S}\boldsymbol{k} = \boldsymbol{0}\,, \tag{3.4.43}$$

as in Koiter's original derivation [Koiter, 1966; Steigmann, 2013]. To reduce the notational burden we henceforth drop the bar notation on the solutions $\bar{\boldsymbol{d}}$ and $\bar{\boldsymbol{e}}$, remembering that the plane-stress equations can be solved separately to reconstruct the 3D deformation.

On the boundary, the value of $\boldsymbol{d}$ cannot be arbitrarily chosen: on boundaries where essential conditions are assigned, the position, $\tilde{\boldsymbol{Y}}$, is specified. This effectively means that on the boundary we assign combinations $\boldsymbol{Y}$ and the normal derivative $\boldsymbol{Y}_{,\alpha}\,\nu_\alpha$ which in turn control the value of $\boldsymbol{d}$ through the equations (3.4.38) and (3.4.39).

Along each boundary we have four independent degrees of freedom: three displacements, $\boldsymbol{Y}$, and an angle, Θ, formed between the tangent to the deformed sheet and the plane of the undeformed sheet. We cannot arbitrarily set the value of $\boldsymbol{Y}_{,\nu}$ as well as the displacements, $\boldsymbol{Y}$, as this would also impose an in-plane strain, which is a priori unknown. Instead we impose the boundary condition $\boldsymbol{N}\cdot\boldsymbol{\nu}_d = 0$ where $\boldsymbol{\nu}_d$ is the imposed outward normal to the edge of the deformed sheet. Alternatively, we may set $\boldsymbol{N}_I\cdot\boldsymbol{Y}_{,\alpha}\,\nu_\alpha = 0$ where instead we specify an imposed normal $\boldsymbol{N}_I$. This latter form is more accessible for the case of smoothly clamped boundary conditions, for which $\boldsymbol{Y} = \boldsymbol{0}$ and $\boldsymbol{N} = \boldsymbol{k}$, such that we may simply set $Y_{3,\alpha}\nu_\alpha = 0$ and $Y_i = 0$.

If the values of $\boldsymbol{d}$ or $\boldsymbol{e}$ determined from the boundary data of the original three-dimensional problem disagree with the values determined by equations (3.4.38)and (3.4.39), then it is in principle necessary to introduce a small 3D 'matching region' adjoining the boundary. Alternatively, conflicting elements of the boundary data may be relaxed and the approximate problem may solved as substitute for the original problem. This situation is not new, and is also the case in theories that use the Kirchhoff-Love hypothesis as a basis in their derivation.

3.4.6 The Steigmann Energy

Unfortunately, the energy derived in the section above fails to satisfy the Legendre-Hadamard condition (see section 2.2.4) necessary for the existence of energy minimizers unless the stress is point-wise non-compressive [Hilgers and Pipkin, 1996; Steigmann, 2013]. This is much like

the similar restriction on membrane theory, which needs to be 'relaxed' by fine scale wrinkling in the manner outlined by tension field theory. However, in this instance the energy functional is not suitable for relaxation as the current model contains a bending stiffness [Steigmann, 2013].

This unexpected restriction on the stress is not a failing of the model from the point of view of accuracy: the energy accurately describes 3D elasticity in thin sheets. However, from the point of view of the analysis of the 2D energy, it fails to form a well-posed minimization problem within its own right, which means conventional means of solving the equations will fail [Steigmann, 2010].

This restriction arises from a single problematic term. In the h^3 (bending) term of equation (3.4.42) the term $(\boldsymbol{\nabla d}\, \boldsymbol{S}^0) \cdot \boldsymbol{\nabla d}$ appears: this term involves gradients of the through-thickness stretch, so Hilgers and Pipkin [1996] refer to it as a strain-gradient term. If this term is omitted, as in Koiter's original formulation [Koiter, 1966], then the Legendre-Hadamard condition is satisfied automatically - provided strong ellipticity is satisfied at equilibrium, as the weak constitutive hypothesis we made in equation (3.4.15) implies [Steigmann, 2010]. The problematic parts of this term will automatically vanish in theories for which the classical Kirchhoff-Love hypothesis has been made, as through-thickness stretch is neglected.

Steigmann [2013] instead makes a further restriction by assuming the stresses are $|\boldsymbol{S}^0| = o(1)$. This culminates in the use of a linear constitutive law in the *bending term only*. This can be viewed as a restriction to small bending strains, whilst still allowing arbitrary rotations. This is in contrast to membrane theory which assumes $|\boldsymbol{S}^0| = \mathcal{O}(1)$. Due to the constitutive hypothesis outlined in equation (3.4.15), the assumption $|\boldsymbol{S}^0| = o(1)$ implies that the strain is also $|\boldsymbol{E}| = o(1)$.

We now simplify the energy, based on the above stress assumption, $|\boldsymbol{S}^0| = o(1)$. Considering the coefficient of the h^3 term the leading order energy, defined in equation (3.4.42), we have the construct $\mathcal{M}(\boldsymbol{F})\, \boldsymbol{F}'$. Using the connection between the two sets of elastic moduli defined in equation (3.4.14) evaluated on the midplane we write

$$\mathcal{M}(\boldsymbol{F})\, \boldsymbol{F}' = \boldsymbol{F}' \boldsymbol{S}^0 + \frac{1}{2} \boldsymbol{F}\, \mathcal{C}(\boldsymbol{E}) \left(\boldsymbol{F}'^T \boldsymbol{F} + \boldsymbol{F}^T \boldsymbol{F}' \right) . \tag{3.4.44}$$

The deformation gradient, $\boldsymbol{F}$, can be decomposed into a rotation, $\boldsymbol{R}$, and a stretch, $\boldsymbol{U}$, such that $\boldsymbol{F} = \boldsymbol{R}\boldsymbol{U}$. These matrices have the following properties [Ciarlet, 1988]

$$\boldsymbol{U}^T = \boldsymbol{U} \quad \text{and} \quad \boldsymbol{R}^T = \boldsymbol{R}^{-1} . \tag{3.4.45}$$

Accordingly, the Green-Lagrange strain tensor at the midplane can be written as

$$\boldsymbol{E} = \frac{1}{2}(\boldsymbol{F}^T\boldsymbol{F} - \mathbb{I}_3) = \frac{1}{2}(\boldsymbol{U}^2 - \mathbb{I}_3)\,. \tag{3.4.46}$$

By Taylor expansion of $\sqrt{\boldsymbol{C}} = \boldsymbol{U}$ about $\boldsymbol{E} = \boldsymbol{0}$, it can be shown that

$$\boldsymbol{U} = \mathbb{I}_3 + \boldsymbol{E} + \mathcal{O}(|\boldsymbol{E}|^2)\,, \tag{3.4.47}$$

which can be easily verified by substitution into equation (3.4.46). Using the above relation, we can conclude that $\boldsymbol{F} = \boldsymbol{R} + o(1)$, i.e that the deformation gradient is equal to the rotation matrix in the polar decomposition, to leading order.

Thus, using the relation $\boldsymbol{F} = \boldsymbol{R} + o(1)$, and our assumption on the stress, equation (3.4.47), we can write the final term in the energy, equation (3.4.44), as

$$\mathcal{M}(\boldsymbol{F})\,\boldsymbol{F}' = \frac{1}{2}\boldsymbol{R}\mathcal{C}(\boldsymbol{0})\left(\boldsymbol{F}'^T\boldsymbol{R} + \boldsymbol{R}^T\boldsymbol{F}'\right) + o(1)\,. \tag{3.4.48}$$

Here, we found the first term $\boldsymbol{F}'\,\boldsymbol{S}\cdot\boldsymbol{F}'$ to be of order $o(1)$, and therefore neglected it. This term contained the problematic strain gradients, which enter via $\boldsymbol{\nabla d}$: thus, by neglecting this term we have regularised the model.

In the above equation, equation (3.4.48), we have demonstrated that we can replace the nonlinear constitutive relation used in the h^3 terms with a linear constitutive hypothesis whilst still maintaining $\mathcal{O}(h^3)$ accuracy. Heuristically, we can view this as a statement that bending strains are small, so a linear constitutive relationship is appropriate, in this term. The energy now becomes

$$W = \int_\Omega \left(h\,\mathcal{W}(\boldsymbol{F}) + \frac{h^3}{24}\left(\mathcal{M}(\boldsymbol{R})\,\boldsymbol{F}'\cdot\boldsymbol{F}'\right)\right)\,d\Omega + o(h^3)\,, \tag{3.4.49}$$

where we have also neglected the boundary term, that enters at order $o(h^3)$.

Using the generic relationship between the two elastic moduli (equation (3.4.14)) for $\boldsymbol{F} = \boldsymbol{R}$, we can write

$$\mathcal{M}(\boldsymbol{R})\,\boldsymbol{A} = \boldsymbol{R}\,\mathcal{M}(\mathbb{I}_3)\left(\boldsymbol{R}^T\boldsymbol{A}\right)\,, \tag{3.4.50}$$

for a generic three-by-three matrix $\boldsymbol{A}$. Using this expression to simplify the term appearing in the energy, we have

$$\mathcal{M}(\boldsymbol{R})\,\boldsymbol{F}'\cdot\boldsymbol{F}' = \mathcal{M}(\mathbb{I}_3)\left(\boldsymbol{R}^T\boldsymbol{F}'\right)\cdot\boldsymbol{R}^T\boldsymbol{F}'\,, \tag{3.4.51}$$

which using equation (3.4.16) gives the final expression for the energy

$$W^{KS} = \int_\Omega \left(h\,\mathcal{W}(\boldsymbol{F}) + \frac{h^3}{24}\left(\mathcal{C}(\boldsymbol{0})\left(\boldsymbol{R}^T\boldsymbol{F}'\right)\cdot\boldsymbol{R}^T\boldsymbol{F}'\right)\right)d\Omega\,. \tag{3.4.52}$$

The tensor $\boldsymbol{F}'$ is determined by equation (3.4.22) with the director $\boldsymbol{d}$ determined by solving equation (3.4.38).

To sum up, the assumption on the stress, $|\boldsymbol{S}^0| = o(1)$, allows us to replace the constitutive law in the h^3 (bending) term with a linear one, as well as eliminating certain strain gradient terms. This model is therefore appropriate for finite strains and finite rotations, provided that the energy scales as $o(h)$ with thickness [Steigmann, 2013]. For cases in which the energy scales as $\mathcal{O}(h)$, tension field theory would instead be appropriate [Steigmann, 2013].

Though this model is now complete, we proceed to make simplifications based on the commonly encountered conditions of reflection symmetry of material properties with respect to the midplane and the case of isotropy of material properties.

3.4.7 Reflection Symmetry and Isotropy

Reflection symmetry about the midplane implies that the energy will be an even function of the shear strain, $E_{\alpha 3}$. Mathematically this means: $\mathcal{U}(\boldsymbol{E}) = \mathcal{U}(\boldsymbol{Q}^T \boldsymbol{E} \boldsymbol{Q})$ with $\boldsymbol{Q} = \mathbb{I}_3 - 2\boldsymbol{k}\otimes\boldsymbol{k}$.

The shear stress at the midplane will be

$$\frac{\partial \mathcal{U}(\boldsymbol{E})}{\partial E_{\alpha 3}} = \hat{\boldsymbol{e}}_\alpha \cdot \mathcal{U}_{\boldsymbol{E}} \boldsymbol{k}\,, \tag{3.4.53}$$

which is an *odd* function of $E_{3\alpha}$. However, the shear stress vanishes by equation (3.4.43) and the definition of the second Piola-Kirchhoff stress (equation (3.4.13)) , thereby vanishing in the order h^3 energy term. Due to the *odd* nature of the ($\mathcal{O}(h^2)$) stress with respect to $E_{3\alpha}$, we conclude that $E_{3\alpha} = 0$ to leading order. Therefore, we have the following expression for the strain

$$\boldsymbol{E} = \boldsymbol{\epsilon} + \frac{1}{2}(\phi^2 - 1)\boldsymbol{k}\otimes\boldsymbol{k}\,, \tag{3.4.54}$$

in which $\boldsymbol{\epsilon} = \mathbb{1}\,\boldsymbol{E}\,\mathbb{1}$ is the two-dimensional membrane strain and ϕ is the transverse (ζ-line) stretch, determined by solving

$$\boldsymbol{k}\cdot\boldsymbol{S}^0\boldsymbol{k} = 0\,. \tag{3.4.55}$$

Given that

$$\boldsymbol{E} = \frac{1}{2}\left((\boldsymbol{\nabla Y})^T(\boldsymbol{\nabla Y}) + (\boldsymbol{d}\otimes\boldsymbol{k})^T(\boldsymbol{d}\otimes\boldsymbol{k}) - \mathbb{I}_3\right)\,, \tag{3.4.56}$$

we conclude that

$$\boldsymbol{d} = \phi\,\boldsymbol{N}\,, \tag{3.4.57}$$

in which $\boldsymbol{N}$ is the unit normal to the deformed sheet.

We can make further simplifications to the bending energy in the case of isotropy, for which we have the linear Saint-Venant constitutive behaviour at small strain, as introduced in section 2.2.5

$$\mathcal{C}(\mathbf{0})\,\boldsymbol{A} = \lambda Tr(\boldsymbol{A})\mathbb{I}_3 + 2\mu sym(\boldsymbol{A})\,. \tag{3.4.58}$$

in which $\mu = \mu^*/E$ and $\lambda = \lambda^*/E$ are nondimensional Lamé coefficients and $\boldsymbol{A}$ is a rank two tensor. We have also used the notation $sym(\boldsymbol{A})$ to refer to the symmetric part of the matrix $\boldsymbol{A}$ such that

$$\boldsymbol{A} = sym(\boldsymbol{A}) + skew(\boldsymbol{A})\,, \tag{3.4.59}$$

where $skew(\boldsymbol{A})$ is the skew symmetric part. We can use this to write

$$\{\mathcal{C}(\mathbf{0})\,\boldsymbol{a}\otimes\boldsymbol{k}\}\boldsymbol{k} = (\lambda+2\mu)\,(\boldsymbol{a}\cdot\boldsymbol{k})\,\boldsymbol{k} + \mu\mathbb{1}\boldsymbol{a}\,, \tag{3.4.60}$$

for a tensor composed of the outer product of any vector $\boldsymbol{a}$ and the unit normal to the undeformed sheet, $\boldsymbol{k}$. Focusing on the terms $\boldsymbol{R}^T\boldsymbol{F}'$, we then use the above relation, equation (3.4.60), in conjunction with equation (3.4.38), modified using the assumption on stress,

$$\{\mathcal{C}(\mathbf{0})\,\big(\boldsymbol{R}^T\boldsymbol{e}\otimes\boldsymbol{k} + \boldsymbol{k}\otimes\boldsymbol{e}\,\boldsymbol{R}\big)\}\boldsymbol{k} = -\{\mathcal{C}(\mathbf{0})\,\big(\boldsymbol{R}^T\boldsymbol{\nabla}\boldsymbol{d} + (\boldsymbol{\nabla}\boldsymbol{d})^T\boldsymbol{R}\big)\}\boldsymbol{k}\,, \tag{3.4.61}$$

to write

$$\boldsymbol{k}\cdot\boldsymbol{R}^T\boldsymbol{e} = -\frac{\lambda}{\lambda+2\mu}\,\mathrm{Tr}(\boldsymbol{R}^T\boldsymbol{\nabla}\boldsymbol{d}) - \frac{2\mu}{\lambda+2\mu}\,\boldsymbol{k}\cdot\,sym(\boldsymbol{R}^T\boldsymbol{\nabla}\boldsymbol{d})\boldsymbol{k} \tag{3.4.62}$$

and

$$\mathbb{1}\,\boldsymbol{R}^T\boldsymbol{e} = -2\,\mathbb{1}\,\{sym(\boldsymbol{R}^T\boldsymbol{\nabla}\boldsymbol{d})\}\boldsymbol{k}\,. \tag{3.4.63}$$

We have the following expression for $\boldsymbol{\nabla}\boldsymbol{d} = \boldsymbol{\nabla}\boldsymbol{N} + \boldsymbol{N}\otimes\boldsymbol{\nabla}\phi$. Here we have used the fact that the transverse stretch is given by $\phi = 1 + o(1)$ in the normal term. This is to remain consistent with the truncation of any terms smaller than order $\mathcal{O}(h^3)$ in the energy, as any $o(1)$ terms in the coefficient of h^3 will enter at lower order. Therefore, using the definition of $\boldsymbol{R}^T$ as the rotation matrix from deformed to undeformed surface, and additionally recalling the definition of the relative curvature, $\boldsymbol{\kappa}$, from section 3.3, we can write

$$\boldsymbol{R}^T\boldsymbol{N} = \boldsymbol{k} \quad \text{and} \quad \boldsymbol{R}^T\,\boldsymbol{\nabla}\boldsymbol{N} = \boldsymbol{\kappa} \tag{3.4.64}$$

where $\boldsymbol{\kappa} = -(\boldsymbol{\nabla}\boldsymbol{Y})^T\boldsymbol{B}(\boldsymbol{\nabla}\boldsymbol{Y})$ and $\boldsymbol{B}$ is the curvature on the deformed surface, as defined in section 3.3. In Cartesian coordinates

$$\boldsymbol{\kappa} = -B_{\alpha\beta}\,\hat{\boldsymbol{e}}_\alpha\otimes\hat{\boldsymbol{e}}_\beta \quad \text{and} \quad B_{\alpha\beta} = N_i\,Y_{i,\alpha\beta}\,. \tag{3.4.65}$$

Using this, and equation (3.4.64) we can write

$$\boldsymbol{R}^T\boldsymbol{\nabla d} = \boldsymbol{\kappa} + \boldsymbol{k}\otimes\boldsymbol{\nabla\phi} \quad \text{and} \quad \boldsymbol{R}^T\boldsymbol{e} = -\frac{\lambda}{\lambda+2\mu}\,\mathrm{Tr}(\boldsymbol{\kappa})\,\boldsymbol{k} - \boldsymbol{\nabla}\phi\,, \tag{3.4.66}$$

which combined with the definition of $\boldsymbol{F'}$ yields

$$\boldsymbol{R}^T\boldsymbol{F'} = \kappa - \frac{\lambda}{\lambda+2\mu}\mathrm{Tr}(\boldsymbol{\kappa})\boldsymbol{k}\otimes\boldsymbol{k} + \boldsymbol{k}\otimes\boldsymbol{\nabla}\phi - \boldsymbol{\nabla}\phi\otimes\boldsymbol{k}\,, \tag{3.4.67}$$

and thus the bending energy

$$\mathcal{C}(\boldsymbol{0})\left(\boldsymbol{R}^T\boldsymbol{F}\right)\cdot\boldsymbol{R}^T\boldsymbol{F} = \frac{2\lambda\mu}{\lambda+2\mu}\left(\mathrm{Tr}(\boldsymbol{\kappa})\right)^2 + 2\mu\left(\boldsymbol{\kappa}\cdot\boldsymbol{\kappa}\right). \tag{3.4.68}$$

Therefore our final expression for the Koiter-Steigmann plate energy is

$$W^{KS} = \int_\Omega \left(h\mathcal{W}(\boldsymbol{F}) + \frac{h^3}{24}\left(\frac{2\lambda\mu}{\lambda+2\mu}\left(\mathrm{Tr}(\boldsymbol{\kappa})\right)^2 + 2\mu\left(\boldsymbol{\kappa}\cdot\boldsymbol{\kappa}\right)\right)\right) d\Omega\,. \tag{3.4.69}$$

To complete the model we must choose a particular strain-energy function, $\mathcal{W}(\boldsymbol{F})$ for the membrane part of the strain-energy function. As a consequence of the derived plane-stress condition, the constitutive law must be modified using the plane stress condition to eliminate components of the strain (cf. section 2.2.5). This, in turn, leads to an expression for the in-plane strain-energy purely in terms of the gradient of the midplane, $\boldsymbol{\nabla Y}$, so that $h\mathcal{W}(\boldsymbol{F}) = \mathcal{W}^M(\boldsymbol{\nabla Y})$, which is the *membrane* strain-energy. Once this has expression has been determined, we can write the above energy as

$$W^{KS} = \int_\Omega \mathcal{W}^{KS}(\boldsymbol{G}_\alpha, \boldsymbol{G}_{\alpha,\beta})\, d\Omega\,. \tag{3.4.70}$$

where the model is a function of only the first and second derivatives of the midplane tangent vectors, defined in section 3.3. Finally, it should be noted that the material constants in the constitutive law must be chosen so that they linearise appropriately to agree with the Lamé parameters for the infinitesimal strain limit.

3.4.8 Summary of the Koiter-Steigmann Model

In this section we summarize the derived energy and other relevant equations from the previous section for a uniform thickness plate with zero initial deformation and isotropic material properties. As seen in the previous section, the total strain-energy density for this case is given by [Steigmann, 2013]:

$$W^{KS} = \int_\Omega \mathcal{W}^{KS}(\boldsymbol{G}_\alpha, \boldsymbol{G}_{\alpha,\beta})\, d\Omega\,. \tag{3.4.71}$$

where

$$\mathcal{W}^{KS}(\boldsymbol{G}_\alpha, \boldsymbol{G}_{\alpha,\beta}) = \mathcal{W}^{M}(\boldsymbol{G}_\alpha) + \mathcal{W}^{B}(\boldsymbol{G}_\alpha, \boldsymbol{G}_{\alpha,\beta})\,. \tag{3.4.72}$$

Here $\mathcal{W}^{M}(\boldsymbol{G}_\alpha)$ is the membrane (plane stress) part of the energy, which arises when eliminating the through-thickness stress from the strain-energy function $\mathcal{W}(\boldsymbol{F})$ (cf. section 2.2.5). The bending energy, $\mathcal{W}^{B}(\boldsymbol{G}_\alpha, \boldsymbol{G}_{\alpha,\beta})$ is given by:

$$\mathcal{W}^{B}(\boldsymbol{G}_\alpha, \boldsymbol{G}_{\alpha,\beta}) = \frac{1}{24}h^3\left(\frac{2\lambda\mu}{\lambda+2\mu}(\mathrm{Tr}\boldsymbol{\kappa})^2 + 2\mu(\boldsymbol{\kappa}\cdot\boldsymbol{\kappa})\right)\,. \tag{3.4.73}$$

The relative curvature tensor, $\boldsymbol{\kappa}$ is given by

$$\boldsymbol{\kappa} = -B_{\alpha\beta}\hat{\boldsymbol{e}}_\alpha \otimes \hat{\boldsymbol{e}}_\beta\,, \tag{3.4.74}$$

with the components:

$$B_{\alpha\beta} = \hat{N}_i Y_{i,\alpha\beta}\,. \tag{3.4.75}$$

We can also write equation (3.4.73) as:

$$\mathcal{W}^{B}(\boldsymbol{G}_\alpha, \boldsymbol{G}_{\alpha,\beta}) = M_{i\alpha\beta}Y_{i,\alpha\beta}\,, \tag{3.4.76}$$

where $M_{i\alpha\beta}$ is the bending moment. Due to the small, through-thickness strains involved in bending, the bending moment is linearly related to the curvature tensor, $B_{\alpha\beta} = Y_{i,\alpha\beta}\hat{N}_i = v_{i,\alpha\beta}\hat{N}_i$:

$$M_{i\alpha\beta} = \frac{1}{12}h^3\hat{N}_i\left(\frac{2\lambda\mu}{\lambda+2\mu}B_{\gamma\gamma}\delta_{\alpha\beta} + 2\mu B_{\alpha\beta}\right), \tag{3.4.77}$$

in which $\mu = 1/(2+2\nu)$ and $\lambda = \nu/(1+\nu)(1-2\nu)$ are the nondimensional Lamé coefficients. Reintroducing dimensions, such that $\boldsymbol{M^*} = (EL^2)\,\boldsymbol{M}$, the (resultant) bending moment may be more revealingly expressed in terms of E and ν:

$$M^*_{i\alpha\beta} = \frac{E\,(h^*)^3}{12(1-\nu^2)}\hat{N}_i\left(\nu\,B^*_{\gamma\gamma}\delta_{\alpha\beta} + (1-\nu)B^*_{\alpha\beta}\right). \tag{3.4.78}$$

In this form we clearly see that the resistance to bending, the bending modulus, will be $D = E\,h^{*3}/12(1-\nu^2)$. The small strains inherent in the bending energy can be considered as a restriction to deformations with a radius of curvature that is not comparable to the thickness: as such they would not be suitable for 'crumpling'-type problems in which there is significant stress concentration.

Taking the variational (Gateaux) derivative of this energy [Steigmann and Ogden, 1999; Steigmann, 2013] we can write the variations in energy (the energy functional) as

$$\delta\mathcal{W}^{KS} = \mathfrak{N}_{i\alpha}\delta v_{i,\alpha} + M_{i\alpha\beta}\delta v_{i,\alpha\beta}\,, \tag{3.4.79}$$

with the total stress tensor $\mathfrak{N}_{i\alpha}$ given by:

$$\mathfrak{N}_{i\alpha} = hS_{\gamma\alpha}Y_{i,\gamma} - M_{i\beta\gamma}\Gamma_{\alpha\beta\gamma}\,, \tag{3.4.80}$$

where S is the plane stress tensor and M_i are the bending moments and quantities prepended with a δ refer to variations (a Gateaux derivative) of that quantity. The complete derivation of this result can be found in Appendix A. Here we note that, in accordance with our assumption $|\tilde{\boldsymbol{S}}| = o(1)$, we replaced the Christoffel symbol of the first kind $\Gamma^{\alpha}_{\beta\gamma}$ with a Christoffel symbol of the second kind $\Gamma_{\alpha\beta\gamma}$, at no penalty to overall accuracy.

The variation of a particular functional can be viewed as a small change in the functional due to a small change in its input. For example the variation of $U(Y_i)$ is the small change in energy, $\delta\mathcal{W}^{KS}$ induced by a small deformation, δY_i [Becker et al., 1981].

The tensor $\Gamma_{\alpha\beta\gamma}$ is the Christoffel symbol of the second kind, defined as:

$$\Gamma_{\alpha\beta\gamma} = G_{\alpha\delta}\Gamma^{\delta}_{\beta\gamma}\,, \tag{3.4.81}$$

where $\Gamma^{\delta}_{\beta\gamma} \equiv \boldsymbol{G}^{\delta}\cdot\boldsymbol{G}_{\beta,\gamma}$ is the Christoffel symbol of the first kind.

We can also express the Christoffel symbol of the second kind in terms of gradients of the midplane Green-Lagrange strain tensor $\boldsymbol{\epsilon}$ [Steigmann, 2013]:

$$\Gamma_{\alpha\beta\gamma} = E_{\alpha\beta,\gamma} + E_{\gamma\alpha,\beta} - E_{\beta\gamma,\alpha}\,. \tag{3.4.82}$$

We can express the Green-Lagrange strain tensor in terms of the metric tensors:

$$E_{\alpha\beta} = \frac{1}{2}(G_{\alpha\beta} - \delta_{\alpha\beta})\,, \tag{3.4.83}$$

or the undeformed position vector:

$$E_{\alpha\beta} = \frac{1}{2}(Y_{i,\alpha}Y_{i,\beta} - \delta_{\alpha\beta})\,, \tag{3.4.84}$$

or the displacements:

$$E_{\alpha\beta} = \frac{1}{2}(v_{\alpha,\beta} + v_{\beta,\alpha} + v_{i,\alpha}v_{i,\beta})\,. \tag{3.4.85}$$

As we only need the in-plane components of the strain tensor, we could replace all components of the 3D strain tensor evaluated at the midplane $E_{\alpha\beta}$ with components $\epsilon_{\alpha\beta}$ of the two-dimensional, membrane strain tensor $\boldsymbol{\epsilon} = E_{\alpha\beta}\hat{\boldsymbol{e}}_{\alpha}\times\hat{\boldsymbol{e}}_{\beta}$. However, to reduce the notational burden, we continue to use the identical, 3D components, and favour index notation.

The model is then closed by assuming a particular strain-energy function (a constitutive model) $\mathcal{W}^{M}(\boldsymbol{G}_{\alpha})$ that is specialised to plane stress. This then defines the second Piola-Kirchhoff stress in terms of the deformed position vector. The adopted constitutive model is

required to coincide with the linear Saint Venant-Kirchhoff model (equation (3.4.58)) in the limit of vanishing strain by the constitutive hypothesis (equation (3.4.15)). The plane stress specialisations outlined in section 2.2.5 are therefore appropriate for this purpose.

Certain restrictions exist on the constitutive model that can be chosen: the constants should be chosen such that the linearisation of the model agrees with the model assumed in the bending moment. Additionally, the strain-energy function should be strongly elliptic for a large range of strain, which is guaranteed for polyconvex strain-energy functions [Steigmann, 2013]. Included in this class of functions are the Neo-Hookean and two-dimensional Mooney-Rivlin energy provided that the coefficients are non-negative [Ciarlet, 1988].

3.4.9 The Euler-Lagrange Equations

We will now derive the Euler-Lagrange equations. In simple terms, these are achieved by repeated integration by parts. We start with the above variational principle

$$\int_\Omega \delta\mathcal{W}^{KS} d\Omega = \int_\Omega \left(\mathfrak{N}_{i\alpha}\delta v_{i,\alpha} + M_{i\alpha\beta}\delta v_{i,\alpha\beta}\right) d\Omega = 0\,, \tag{3.4.86}$$

where Ω is the area of the midplane of the undeformed sheet and $d\Omega$ is an area element on the undeformed sheet.

Integrating by parts, we obtain

$$\int_\Omega \delta\mathcal{W}^{KS} d\Omega = \int_{\partial\Omega} \left(\mathfrak{N}_{i\alpha}\nu_\alpha\delta v_i \,+\, M_{i\alpha\beta}\nu_\beta\delta v_{i,\alpha}\right) dt - \int_\Omega \left(\mathfrak{N}_{i\alpha,\alpha}\delta v_i + M_{i\alpha\beta,\beta}\delta v_{i,\alpha}\right) d\Omega = 0\,, \tag{3.4.87}$$

where $\boldsymbol{\nu}$ is the normal vector to the edge $\delta\Omega$.

We can further integrate the boundary-integral by parts, if we decompose the bending moment into normal and tangential, with tangent $\boldsymbol{\tau}$, components as follows

$$\begin{aligned}\int_\Omega \delta\mathcal{W}^{KS} d\Omega = \int_{\partial\Omega} \left(\mathfrak{N}_{i\alpha}\nu_\alpha\delta v_i \,+\, \left(M_{i\alpha\beta}\nu_\alpha\nu_\beta\,\delta v_{i,\gamma}\nu_\gamma \,+ M_{i\alpha\beta}\nu_\alpha\tau_\beta\delta\frac{\partial v_i}{\partial t}\right)\right) dt \\ - \int_\Omega \left(\mathfrak{N}_{i\alpha,\alpha}\delta v_i + M_{i\alpha\beta,\beta}\delta v_{i,\alpha}\right) d\Omega = 0\,,\end{aligned} \tag{3.4.88}$$

to obtain

$$\begin{aligned}\int_{\partial\Omega} \left(\mathfrak{N}_{i\alpha}\nu_\alpha\delta v_i \,+\, M_{i\alpha\beta}\nu_\alpha\nu_\beta\delta v_{i,\gamma}\nu_\gamma \,-\, \frac{\partial}{\partial t}\left(M_{i\alpha\beta}\nu_\alpha\tau_\beta\right)\,\delta v_i\right) dt \\ + \lim_{\iota\to 0}\sum_{\boldsymbol{\xi}_l} [M_{i\alpha\beta}\nu_\alpha\tau_\beta\delta v_i]_{\boldsymbol{\xi}_l-\boldsymbol{\iota}}^{\boldsymbol{\xi}_l+\boldsymbol{\iota}} - \int_\Omega \left(\mathfrak{N}_{i\alpha\alpha}\delta v_i + M_{i\alpha\beta,\beta}\delta v_{i,\alpha}\right) d\Omega = 0\,,\end{aligned} \tag{3.4.89}$$

where $\boldsymbol{\xi}_l$ labels the l^{th} discontinuity and in this case l labels a finite number of corners on the boundary $\delta\Omega$, rather than the three components of a vector field. A diagram showing discontinuities in the boundary of a plate is shown in figure 3.5

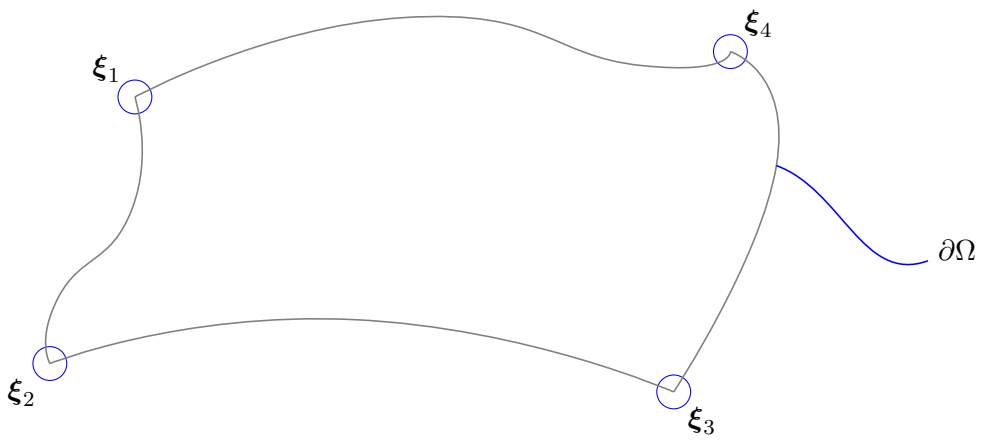

Figure 3.5: Birds eye view of an (undeformed) plate with four discontinuities (corners) in the otherwise smooth boundary, $\partial\Omega$.

As can be seen, the tangential angle variation along the boundary $\delta\left(\partial v_i/\partial t\right)$ is completely determined by the variation of the displacement along the boundary δv_i. By integration of this term by parts, we see that a twisting moment that varies along the boundary will result in an additional contribution to the shear force on the boundary.

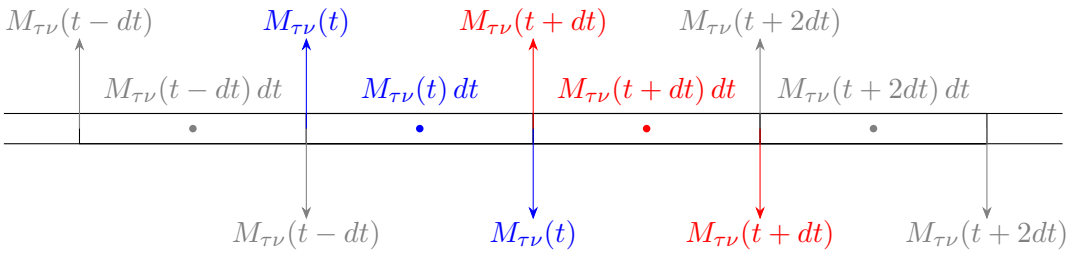

Figure 3.6: Twisting moments applied to the edge of a flat plate. One can replace each force couple generated by a twisting moment $M_{\tau\nu}$ along the edge by opposing forces acting a distance dt apart - the only difference will be the local stress distribution [Timoshenko and Woinowsky-Krieger, 1959a]. From here it can be seen that variations in the twisting moment along the edge give rise to a net upward (or downward) force, as at the edge of each segment the forces are slightly unbalanced.

The origin of this additional shear force may be interpreted by considering a series of twisting moments applied along the edge of a body, as displayed in figure 3.6. We can imagine the edge split into a number of parts of length dt; upon each part a twisting moment is applied which acts to twist the element out-of-plane. If we consider a single segment, the applied moment exerts a force at either end of the segment. However, the next segment is also twisting *in the same sense*, which prevents it from moving out-of-plane with an opposing

force. If the (continuous) twisting moment varies along the boundary, each segment will have a slightly unbalanced twisting force at the segment edge, resulting a net upward shear force.

We finally integrate the bulk bending moment term for the second time to obtain:

$$\int_{\partial\Omega}\left(\left(\mathfrak{N}_{i\alpha}\nu_\alpha-\frac{\partial}{\partial t}\left(M_{i\alpha\beta}\nu_\alpha\tau_\beta\right)-M_{i\alpha\beta,\beta}\nu_\alpha\right)\delta v_i\,+\,M_{i\alpha\beta}\nu_\alpha\nu_\beta\delta v_{i,\gamma}\nu_\gamma\right)dt \\ +\lim_{\epsilon\to 0}\sum_{\boldsymbol{\xi}_l}[M_{i\alpha\beta}\nu_\alpha\tau_\beta\delta v_i]_{\boldsymbol{\xi}_l-\boldsymbol{\epsilon}}^{\boldsymbol{\xi}_l+\boldsymbol{\epsilon}}-\int_\Omega\left(\mathfrak{N}_{i\alpha\alpha}\delta v_i-M_{i\alpha\beta,\beta\alpha}\delta v_i\right)d\Omega=0\,. \tag{3.4.90}$$

Thus by inspection, the full equations and boundary conditions (as stated in [Taylor et al., 2014]) are:

$$\mathrm{div}\boldsymbol{T}=\boldsymbol{0}\quad\text{or}\quad T_{i\beta,\beta}=0\,, \tag{3.4.91}$$

with components of $\boldsymbol{T}$ given by:

$$T_{i\alpha}=\mathfrak{N}_{i\alpha}-M_{i\alpha\beta,\beta}\,, \tag{3.4.92}$$

subject to the boundary conditions [Steigmann, 2013]:

$$q_i=Q_i\quad\text{or}\quad\delta v_i=0\,, \tag{3.4.93}$$

$$M_{i\alpha\beta}\nu_\alpha\nu_\beta=\Psi N_i\quad\text{or}\quad\delta v_{i,\alpha}\nu_\alpha=0\,, \tag{3.4.94}$$

with the generalised, internal 'Kirchhoff shear' $q_i=\mathfrak{N}_{i\alpha}\nu_\alpha-(M_{i\alpha\beta}\nu_\alpha\tau_\beta)_{,\gamma}\tau_\gamma-M_{i\alpha\beta,\alpha}\nu_\beta$, applied shear force $\boldsymbol{Q}$ and applied normal moment Ψ where $\boldsymbol{\nu}$ and $\boldsymbol{\tau}$ are the normal and tangent to the edge $\partial\Omega$, respectively.

So on an edge, we may set the deformed position $\boldsymbol{Y}$ and the normal to the plate edge $\boldsymbol{N}_I\cdot\boldsymbol{r}_{,\alpha}\,\nu_\alpha=0$ where we specify an imposed normal $\boldsymbol{N}_I$. Alternatively we may apply a bending moment Ψ, and a traction to the edge of the plate, $\boldsymbol{Q}$, as displayed in figure 3.7.

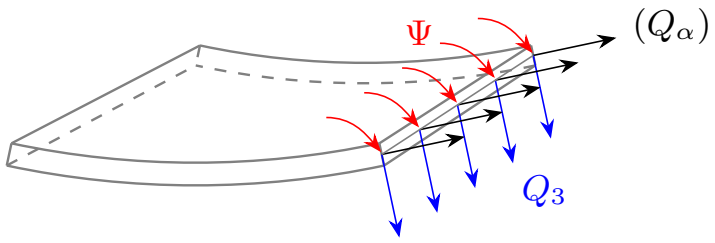

Figure 3.7: Diagram showing the forces that can be applied to the edge of a sheet. Q_3, the shear force, is shown separately to the in-plane traction Q_α in this diagram.

There are also the following conditions:

$$\lim_{\boldsymbol{\iota}\to 0} [M_{i\alpha\beta}\,\nu_\alpha\,\tau_\beta]_{\boldsymbol{\xi}_l-\boldsymbol{\iota}}^{\boldsymbol{\xi}_l+\boldsymbol{\iota}} = \Upsilon_i \quad \text{or} \quad \delta v_i = 0\,, \tag{3.4.95}$$

on a corner $\boldsymbol{\xi_l}$, on which we can apply a twisting moment, $\boldsymbol{\Upsilon}$. The twisting moments at the discontinuities (corners) are concentrated reaction forces that arise in response to lateral loads.

3.4.10 Applied Forces

The work done, δW^-, by a pressure, P^-, displacing a surface, ω^-, quasistatically by a small amount $\delta\boldsymbol{Y}$, is given by [Steigmann, 2004]:

$$\delta W^- = \int_{\omega^-} P^- \boldsymbol{N}^- \cdot \delta\boldsymbol{Y}\, d\omega\,, \tag{3.4.96}$$

where $d\omega$ is an area element of the surface and $\boldsymbol{N}^-$ is the unit normal to the surface.

In the case of a shell-like structure we have two pressures, P^+ and P^- acting on the top, ω^+ and bottom, ω^-, faces of the deformed sheet respectively:

$$\delta W = \int_{\omega^+} P^- \boldsymbol{N}^- \cdot \delta\boldsymbol{Y}\, d\omega \,+\, \int_{\omega^+} P^+ \boldsymbol{N}^+ \cdot \delta\boldsymbol{Y}\, d\omega\,, \tag{3.4.97}$$

in which $\boldsymbol{N}^+$ and $\boldsymbol{N}^-$ are the normals the top and bottom surface of the shell respectively. Due to the inherent assumption of small thickness, we may write

$$\delta W = \int_{\omega} P^- (-\hat{\boldsymbol{N}}) \cdot \delta\boldsymbol{Y}\, d\omega \,+\, \int_{\omega} P^+ \hat{\boldsymbol{N}} \cdot \delta\boldsymbol{Y}\, d\omega \,+ \mathcal{O}(h)\,, \tag{3.4.98}$$

as $\boldsymbol{N}^\pm d\omega^\pm = \hat{\boldsymbol{N}} d\omega + \mathcal{O}(h)$, which can be shown by considering Nanson's formula and performing a Taylor expansion. Here ω is the *deformed* midsurface of the shell. This expression can be further simplified to

$$\delta W = \int_{\omega} \Delta P \hat{\boldsymbol{N}} \cdot \delta\boldsymbol{Y}\, d\omega \,+ \mathcal{O}(h)\,, \tag{3.4.99}$$

where $\Delta P = P^+ - P^-$ is the pressure difference across the plate. If, as previously supposed in section 3.4.5, $P^\pm = \mathcal{O}(h^3)$, then we can write this as:

$$\delta W = \int_{\omega} \Delta P \hat{\boldsymbol{N}} \cdot \delta\boldsymbol{Y}\, d\omega \,+ \mathcal{O}(h^4)\,, \tag{3.4.100}$$

meaning that only the leading order pressure difference enters into the model in the forcing. Finally, we write this in terms of an integral over the reference midsurface as: [Steigmann, 2013]:

$$\delta W = \int_{\Omega} \Delta P \sqrt{G}\, \hat{\boldsymbol{N}} \cdot \delta\boldsymbol{Y}\, d\Omega \,+ \mathcal{O}(h^4)\,. \tag{3.4.101}$$

Therefore, we obtain the result from Steigmann [2013], for the Euler-Lagrange equations subject to a uniform pressure load:

$$\mathrm{div}\boldsymbol{T} + \alpha\Delta P\hat{\boldsymbol{N}} = 0 \quad \text{or} \quad T_{i\beta,\beta} + \alpha\Delta P\hat{N}_i = 0\,, \tag{3.4.102}$$

in which $\alpha = \sqrt{G}$ is the ratio of deformed to undeformed area elements on the sheet, specialised to a Cartesian reference material frame.

3.4.11 Comments on the Koiter-Steigmann Model

The Koiter-Steigmann equations are extremely complicated ($\sim 370\times$ more terms[4] than the Föppl-von Kármán model) when written out explicitly in terms of displacements, which restricts analytical progress to the most simple of cases. We acknowledge that the counting of terms is an imprecise measure, but provide this characterization to give some insight into the complexity of the underlying equations.

In the present model, inverse square-roots of the surface metric tensor enter via the unit normal, which results in non-polynomial nonlinearity in the equations. This makes analytical progress with the equations comparatively more difficult than the other plate models we consider in this work. However, given that there are no geometric restrictions in the derivation, this model can accommodate arbitrarily large displacements and rotations [Koiter, 1966] and finite strains [Steigmann, 2013], with a wide range of available constitutive laws justified [Steigmann, 2013].

The equations are fourth order in all three displacements, which means that for the finite element method the solution space will be $H^2(\Omega)$ for all three displacements, which will have a bearing on the ensuing speed of numerical solutions of the model.

Due to the weak assumption on the stress, all bar one of the models in the hierarchy outlined in Friesecke et al. [2006] can be obtained with stronger assumptions on the stress (see appendix C), the exception being membrane theory which is not suitable when any compressive stress is present [Steigmann, 2013], as the model needs to be relaxed in the manner described by Steigmann [1990]. This freedom makes the model attractive from a numerical standpoint: it has a flexibility that makes it applicable to almost any thin plate problem and allows for an assessment of whether simpler models provide an accurate

[4]By this we mean that, upon expanding all derivatives of products in the equations, written only in terms of displacements, we have $\sim 370N$ where $N = 22$ is the number of unique terms in the Föppl-von Kármán model. For example, in $a(v_{i,\alpha}, v_{i,\alpha\beta}) + b(v_{i,\alpha}, v_{i,\alpha\beta})$ where a, and b are distinct monomials, we would say there are two terms.

picture, without having to resort to 3D elasticity which, as discussed in the previous section, is frequently far too expensive to be useful in studying thin-plate problems.

Finally, we relate the obtained expression for the three-dimensional displacement, expressed in equation 3.4.20, to classical kinematic assumptions. Recalling our original expansion in ζ, the 3D displacements are given by the following equations for isotropic materials:

$$\tilde{\boldsymbol{v}} = \boldsymbol{v} + (\phi\hat{\boldsymbol{N}} - \boldsymbol{k})\,\zeta \,+\, \boldsymbol{e}\,\zeta^2 \,+\, \boldsymbol{f}\,\zeta^3 \,+ \cdots . \tag{3.4.103}$$

Now, recalling that $\phi = 1 + o(1)$, so that the normal-line remains unstretched, and noting that $\zeta \sim h$, we see that to leading order the expression becomes:

$$\tilde{\boldsymbol{v}} = \boldsymbol{v} + (\hat{\boldsymbol{N}} - \boldsymbol{k})\,\zeta \,+\, o(h)\,. \tag{3.4.104}$$

Thus, the Kirchhoff-Love hypothesis, equation (3.1.7), approximately holds. This has emerged naturally from derivation and has not been assumed. We reiterate here that, given that the model is accurate up to order $o(h^3)$, the three-dimensional displacement can be reconstructed with far more accuracy than the leading-order Kirchhoff-Love approximation.

The full reconstructed position vector will instead be given by;

$$\tilde{\boldsymbol{Y}} = \boldsymbol{Y} \,+\, (\phi\hat{\boldsymbol{N}})\,\zeta \,-\, \left(\frac{\lambda}{\lambda+2\mu}\mathrm{Tr}(\boldsymbol{\kappa})\hat{\boldsymbol{N}} + \boldsymbol{R}\,(\boldsymbol{\nabla}\phi)\right)\,\zeta^2 + \mathcal{O}(h^3)\,. \tag{3.4.105}$$

where the midplane-stretch, ϕ, and the rotation matrix, $\boldsymbol{R}$, can be readily computed from the plane-strain tensor and unit-normal respectively. Here we note that the Lamé constants enter via the assumptions of reflection symmetry and isotropy, along with the assumptions on stress $|\boldsymbol{S}| = o(1)$.

We will now investigate the Föppl-von Kármán model and its derivation from the Koiter model.

3.5 The Föppl-von Kármán Model

The Föppl-von Kármán model is a popular model throughout the literature as it is the simplest plate model to incorporate both a bending and a stretching energy. It can be derived heuristically from 3D elasticity by making assumptions on the relative magnitude of the displacements,

$$v_\alpha \sim h^2 \quad \text{and} \quad v_3 \sim h\,. \tag{3.5.1}$$

It is not necessary to assume a linear constitutive relation, as the above assumption implies that the strain scales as $E \sim \mathcal{O}(h^2)$, and therefore that material nonlinearity enters at lower order. These assumptions are then consistent with the assumptions of the Koiter-Steigmann model: thus we can derive the Föppl-von Kármán model from the Koiter-Steigmann model by incorporating these stronger assumptions. Rather than deriving the model directly from 3D elasticity, we will instead derive the same equations from the Koiter-Steigmann model, using these heuristic displacement scaling assumptions.

As has been shown in the previous section, the Kirchhoff-Love hypothesis is approximately satisfied by the Koiter-Steigmann model. Introducing these assumptions into equation (3.4.105), we see that in fact the Kirchhoff-Love hypothesis now holds to $\mathcal{O}(h^3)$, as a consequence of the stronger scaling assumptions.

Though we derive the equations in this manner, we stress that these assumptions are *not* necessary to obtain the Föppl-von Kármán model: the model can instead be derived directly by the method of gamma convergence purely based on a scaling assumption on the applied forces, as shown by Friesecke et al. [2006]. The linear constitutive hypothesis, Kirchhoff-Love hypothesis and the scaling of the displacements emerge naturally in the derivation. Assuming a different scaling behaviour for the applied forces results in a different model in the limit of vanishing thickness [Friesecke et al., 2006]. We will not repeat the derivation via gamma convergence here, as for our purposes the heuristic arguments on the scaling of the displacements will suffice. The assumed scaling of the applied forces in the Föppl-von Kármán model constitute a model in which bending and stretching are of comparable importance, allowing for moderate rotations and small in-plane displacements. We display the relationship between the various models graphically in figure 3.8.

We will now proceed by deriving the Föppl-von Kármán model from the Koiter-Steigmann model.

3.5.1 Rescaling of the Basic Quantities

The basic kinematic hypothesis we use to derive these equations can be expressed as follows:

$$v_\alpha = h^2 \, \bar{v} \,, \tag{3.5.2}$$

$$v_3 = h \, \bar{v} \,, \tag{3.5.3}$$

where we introduce the rescaled nondimensional displacements $\bar{v}_\alpha = \mathcal{O}(1)$ and $\bar{v}_3 = \mathcal{O}(1)$.

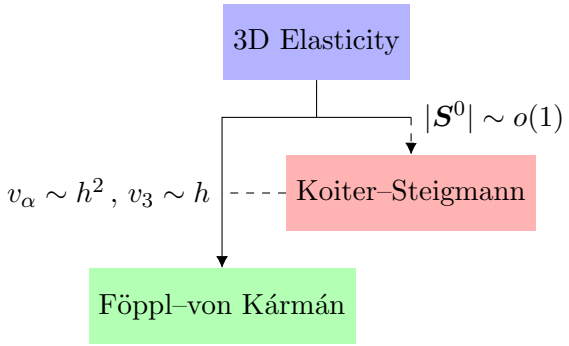

Figure 3.8: Relationship between 3D elasticity, the Koiter-Steigmann model and the Föppl-von Kármán model, including the main assumptions used in their derivation. Solid-line connections indicate a gamma convergent limit whilst dashed lines indicate connections via heuristic scaling arguments.

3.5.2 Leading Order Bending Variations

We now apply the assumptions on the displacements to the Koiter-Steigmann equations, in variational form, as expressed in equation (3.4.79). The first term we inspect is the bending term, $\delta\mathcal{W}^B = M_{i\alpha\beta}\delta v_{i,\alpha\beta}$, which can be expressed as follows:

$$\delta\mathcal{W}^B = \frac{h^3}{12}\mathcal{G}_{\alpha\beta\gamma\delta}\left(\hat{N}_i\, v_{i,\gamma\delta}\right)\hat{N}_j\,\delta v_{i,\alpha\beta}\,, \tag{3.5.4}$$

in which $\mathcal{G}_{\alpha\beta\gamma\delta} = \mathcal{G}^*_{\alpha\beta\gamma\delta}/E$ is the nondimensional Saint Venant-Kirchhoff membrane stiffness tensor (c.f section 2.2.5), with coefficients

$$\mathcal{G}_{\alpha\beta\gamma\delta} = \frac{1}{(1-\nu^2)}[(1-\nu)\left(\delta_{\alpha\delta}\delta_{\beta\gamma} + \delta_{\alpha\gamma}\delta_{\beta\delta}\right)/2 + \nu\,\delta_{\delta\gamma}\delta_{\alpha\beta}]\,. \tag{3.5.5}$$

Here we used the standard notation $\delta_{\alpha\beta}$ for the Kronecker delta.

We substitute the scaled quantities into this expression, splitting up the in-plane and out-of-plane terms:

$$\begin{aligned}\delta\mathcal{W}^B = &\frac{h^5}{12}\mathcal{G}_{\alpha\beta\gamma\delta}\left(h^2\,\hat{N}_\mu\,\bar{v}_{\mu,\gamma\delta} + h\,\hat{N}_3\,\bar{v}_{3,\gamma\delta}\right)\hat{N}_\mu\,\delta\bar{v}_{\mu,\alpha\beta}\\ &+\frac{h^4}{12}\mathcal{G}_{\alpha\beta\gamma\delta}\left(h^2\,\hat{N}_\mu\,\bar{v}_{\mu,\gamma\delta} + h\,\hat{N}_3\,\bar{v}_{3,\gamma\delta}\right)\hat{N}_3\,\delta\bar{v}_{3,\alpha\beta}\,.\end{aligned} \tag{3.5.6}$$

To truncate this, we must first expand the normal using the kinematical assumptions expressed in equations (3.5.2) and (3.5.3). By considering the case of zero displacement, it is clear that the leading order for the deformed normal to the sheet will be perpendicular to the undeformed sheet: $\hat{\boldsymbol{N}} \approx \boldsymbol{k}$. In fact, a detailed calculation (see Appendix B) reveals that

$$\hat{\boldsymbol{N}} \approx -h\bar{v}_{3,\alpha}\,\hat{\boldsymbol{e}}_\alpha + (1 + \frac{1}{2}h^2\bar{v}_{3,\gamma}\bar{v}_{3,\gamma})\,\boldsymbol{k}\,, \tag{3.5.7}$$

or, as we only need the expression at leading order

$$\hat{\boldsymbol{N}} = (1 + \mathcal{O}(h^2))\boldsymbol{k} + \mathcal{O}(h)\hat{\boldsymbol{e}}_\alpha \,. \tag{3.5.8}$$

Substituting this into the equations we can see that the resulting bending energy variation is

$$\delta\mathcal{W}^B = \frac{h^5}{12}\mathcal{G}_{\alpha\beta\gamma\delta}\left(h\,\hat{n}_3\,\bar{v}_{3,\gamma\delta}\right)\hat{n}_3\,\delta\bar{v}_{3,\alpha\beta} + \mathcal{O}(h^7)\,, \tag{3.5.9}$$

with $\hat{\boldsymbol{n}} = \boldsymbol{k}$.

Thus, we see that under the displacement scaling assumptions the bending moment, $M_{i\alpha\beta}$, is of order $\mathcal{O}(h^4)$ and linear in the displacements:

$$\boldsymbol{M}_{\alpha\beta} = \frac{h^4}{12}\,\mathcal{G}_{\alpha\beta\gamma\delta}\,\bar{v}_{3,\gamma\delta}\,\boldsymbol{k} \,+\, o(h^4)\,. \tag{3.5.10}$$

We define a linear bending moment, $M^L_{\alpha\beta}$, as follows

$$\boldsymbol{M}_{\alpha\beta} = M^L_{\alpha\beta}\,\boldsymbol{k} \,+\, o(h^4)\,, \tag{3.5.11}$$

where the components are given by

$$M^L_{\alpha\beta} = \frac{h^4}{12}\,\mathcal{G}_{\alpha\beta\gamma\delta}\,\bar{v}_{3,\gamma\delta}\,. \tag{3.5.12}$$

Thus, the linear bending energy emerges as the leading order bending term under the assumptions of the Föppl-von Kármán model. We also note that in the treatment of the bending moment we effectively evaluate the moment and curvature using the normal to the *undeformed* sheet: all corrections to the normal of the sheet enter at higher order. This confirms that the Föppl-von Kármán model is appropriate for sheets which undergo 'moderate' rotations.

3.5.3 Leading Order Membrane Variations

We now consider the truncation of the total stress term, from equation (3.4.79). This is made up of the membrane term, $\mathcal{W}^M$, and a Christoffel term, $\delta\mathcal{W}^\Gamma$:

$$\delta\mathcal{W}^T = \delta\mathcal{W}^W + \delta\mathcal{W}^\Gamma \tag{3.5.13}$$

with

$$\delta\mathcal{W}^M = hS_{\alpha\gamma}Y_{i,\alpha}\delta v_{i,\gamma}\,, \tag{3.5.14}$$

$$\delta\mathcal{W}^\Gamma = -M_{i\alpha\beta}\Gamma_{\gamma\alpha\beta}\delta v_{i,\gamma}\,. \tag{3.5.15}$$

Using the assumption of a stress-free reference state, expressed in equation (3.4.15), in conjunction with our assumptions on the displacement leads to

$$\delta\mathcal{W}^M = h\mathcal{G}_{\alpha\gamma\delta\mu}E_{\delta\mu}Y_{i,\alpha}\delta v_{i,\gamma} + o(h^5)\,. \tag{3.5.16}$$

Thus, linear constitutive behaviour emerges at leading order as a consequence of the scaling assumptions on the magnitude of the displacements and the assumption of a stress-free reference state.

We may therefore write the variations as follows

$$\delta\mathcal{W}^T = (h\mathcal{G}_{\alpha\beta\gamma\delta}\,E_{\gamma\delta}\,Y_{i,\alpha} - M_{i\alpha\beta}\Gamma_{\gamma\alpha\beta})\delta v_{i,\gamma} + o(h^5)\,. \tag{3.5.17}$$

To tackle the first term we expand the strain, $E_{\alpha\beta}$, which is given in terms of the scaled displacements by

$$E_{\alpha\beta} = \frac{h^2}{2}(\bar{v}_{\alpha,\beta} + \bar{v}_{\beta,\alpha} + \bar{v}_{3,\alpha}\bar{v}_{3,\beta} + h^2\,\bar{v}_{\gamma,\alpha}\bar{v}_{\gamma,\beta})\,. \tag{3.5.18}$$

Therefore, we see the in-plane nonlinearity enters at higher order. We now define the (rescaled) Föppl-von Kármán strain tensor

$$\bar{E}^{vK}_{\alpha\beta} \equiv \frac{1}{2}(\bar{v}_{\alpha,\beta} + \bar{v}_{\beta,\alpha} + \bar{v}_{3,\alpha}\bar{v}_{3,\beta})\,. \tag{3.5.19}$$

Re-writing the first term of the stretching energy in terms of the scaled displacement, we get the final expression for the membrane term

$$\delta\mathcal{W}^M = h^5\mathcal{G}_{\alpha\beta\gamma\delta}\,\left(\bar{E}^{vK}_{\gamma\delta}\,\delta\bar{v}_{\alpha,\beta} + \bar{E}^{vK}_{\gamma\delta}\,\bar{v}_{3,\alpha}\,\delta\bar{v}_{3,\beta}\right) + o(h^5)\,. \tag{3.5.20}$$

We now examine the term that contains the Christoffel symbol:

$$\delta\mathcal{W}^\Gamma = -M_{i\alpha\beta}\Gamma_{\gamma\alpha\beta}\delta v_{i,\gamma}\,. \tag{3.5.21}$$

First we consider the out-of-plane (3^{rd}) component of this term: the order of the linear bending moment is $\mathcal{O}(h^4)$ and the strain, $E_{\alpha\beta}$, is $\mathcal{O}(h^2)$. This implies that $\Gamma_{\alpha\beta\gamma}$, which is a linear combination of the strain gradients, will also be order $\mathcal{O}(h^2)$. Thus, this whole term will be of order $\mathcal{O}(h^7)$ and will not appear in the Föppl-von Kármán equations.

The in-plane components of this tensor contain the in-plane component of the nonlinear bending moment, $M_{\gamma\alpha\beta}$ which is of order $\mathcal{O}(h^6)$. When combined with the Christoffel symbol and the variations $\delta v_{\gamma,\alpha\beta}$, it becomes of order $\mathcal{O}(h^9)$ and can safely be neglected in equation (3.5.15). Thus no terms containing the Christoffel symbol enter the leading order energy.

3.5.4 The Loading Term

Before continuing, we examine the load term: as the Föppl-von Kármán model is the leading order model under the scaling assumptions (equations (3.5.2-3.5.3)), we include only the leading order loading terms. As we found in section 3.4.10, the load term is given by

$$\hat{N}_i \Delta p \sqrt{G} \delta v_i \tag{3.5.22}$$

Based on the kinematical assumptions on the size of displacements, $\sqrt{G} = 1 + \mathcal{O}(h^2)$. Using this, and the expression for the unit normal (equation 3.5.7), which is given by $\boldsymbol{N} \approx \boldsymbol{k} + \mathcal{O}(h)$, to leading order the loading term will be given by

$$\hat{N}_i \Delta p \sqrt{G} \delta v_i = \Delta p \, \delta v_3 + \mathcal{O}(h^7) \, . \tag{3.5.23}$$

Thus, the Föppl-von Kármán model does not distinguish between the *deformed* and *undeformed* sheet in then load term, due to the underlying assumption of small displacements.

3.5.5 Föppl-von Kármán as the Leading Order Model

We can now combine the bending and stretching variations to find the leading order energy variations under the assumptions of the Föppl-von Kármán model. The total variation is given by

$$\delta \mathcal{W}^{FvK} = \frac{h^5}{12} \mathcal{G}_{\alpha\beta\gamma\delta} \, \bar{v}_{3,\gamma\delta} \, \delta \bar{v}_{3,\alpha\beta} \; + \; h^5 \mathcal{G}_{\alpha\beta\gamma\delta} \bar{E}^{vK}_{\gamma\delta} \delta \bar{v}_{\alpha,\beta} + h^5 \mathcal{G}_{\alpha\beta\gamma\delta} \bar{E}^{vK}_{\gamma\delta} \bar{v}_{3,\alpha} \delta \bar{v}_{3,\beta} + \mathcal{O}(h^7) \, , \tag{3.5.24}$$

which can be written in terms of dimensional quantities in the familiar form:

$$\delta \mathcal{W}^{* \, FvK} = \frac{E \, h^{*3}}{12(1-\nu^2)} ((1-\nu) v^*_{3,\alpha\beta} \, \delta v^*_{3,\alpha\beta} + \nu v^*_{3,\alpha\alpha} \, \delta v^*_{3,\beta\beta}) + h^* \, S^{* \, vK}_{\alpha\beta} (\delta v^*_{\alpha,\beta} + v^*_{3,\alpha} \delta v^*_{3,\beta}) + \mathcal{O}(h^7) \, , \tag{3.5.25}$$

where we have defined the Föppl-von Kármán stress as $\boldsymbol{S}^{* \, vK} = \boldsymbol{\mathcal{G}}^* \, \boldsymbol{\epsilon}^{vK}$ where

$$\boldsymbol{\epsilon}^{vK} = h^2 \bar{E}^{vK}_{\alpha\beta} \; \hat{\boldsymbol{e}}_\alpha \otimes \hat{\boldsymbol{e}}_\beta \, , \tag{3.5.26}$$

is the unscaled, Föppl-von Kármán strain tensor. Thus, the equations comprise the famous coupling of linear bending to the Föppl membrane model.

The Föppl-von Kármán Equations

From this variational principle, we can derive the Euler-Lagrange equations, in the same way as for the Koiter-Steigmann model in section 3.4.9, to get the Föppl-von Kármán equations:

$$D\nabla^{*4}v_3^* - h^*\left(S_{\alpha\beta}^{*vK}v_{3,\alpha}^*\right)_{,\beta} = \Delta P^*\,, \tag{3.5.27}$$

$$S_{\alpha\beta,\beta}^{*\,vK} = 0\,, \tag{3.5.28}$$

with the bending modulus $D = E\,h^{*3}/12(1-\nu^2)$.

These equations are subject to two boundary conditions on v_3:

$$\delta v_3^* = 0 \quad \text{or} \quad q_3^{*\,vK} = Q_3^*\,, \tag{3.5.29}$$

$$\delta v_{3,\alpha}^*\nu_\alpha = 0 \quad \text{or} \quad M_{3\alpha\beta}^{*L}\nu_\alpha\nu_\beta = \Psi_3^*\,, \tag{3.5.30}$$

where $q_3^{*\,vK}$, the generalised shear force for the Föppl-von Kármán model, is given by:

$$q_3^{*\,vK} = -D(\nabla^{*2}v_3^*)_{,\beta}\nu_\beta - (M_{3\alpha\beta}^{*L}\nu_\alpha\tau_\beta)_{,\gamma}\tau_\gamma + h^*\,v_{3,\alpha}^*\,S_{\alpha\,\beta}^{*\,vK}\nu_\beta\,. \tag{3.5.31}$$

We also have the two in-plane boundary conditions:

$$\delta v_\alpha^* = 0 \quad \text{or} \quad S_{\alpha\beta}^{*\,vK}\,\nu_\beta = Q_\alpha^*\,. \tag{3.5.32}$$

Here, once again, $\boldsymbol{\nu}$ denotes the normal to the edge of the sheet and $\boldsymbol{\tau}$ the unit tangent. Q_3^* is an applied shear force (normal to the undeformed sheet), Ψ_3^* is an applied moment and Q_α^* is an applied stress (tangent to the undeformed sheet). At the l^{th} discontinuity, $\boldsymbol{\xi}_l$, along the edge (corners) we also have the following conditions:

$$\delta v_3^* = 0 \quad \text{or} \quad \lim_{\boldsymbol{\iota}^*\to 0}[M_{3\alpha\beta}^{*L}\nu_\alpha\nu_\beta]_{\boldsymbol{\xi}_l-\boldsymbol{\iota}^*}^{\boldsymbol{\xi}_l+\boldsymbol{\iota}^*} = \Upsilon_3^*\,, \tag{3.5.33}$$

where Υ_3^* is an applied twisting moment.

3.5.6 Comments on the Föppl-von Kármán Model

The Föppl-von Kármán model is the leading order model when bending and stretching energies are of comparable magnitude [Friesecke et al., 2006]. For planar problems, the equations reduce to those of linear plane-stress elasticity, with identical solutions to 3D infinitesimal elasticity, under conditions of plane-stress. Additionally, the nonlinearity only enters the equations though the Föppl-von Kármán strain tensor via the term involving $\boldsymbol{\nabla}^* v_3^* \cdot \boldsymbol{\nabla}^* v_3^*$. It is the combination of these properties that make the solution of the equations

in planar wrinkling problems particularly tractable: as they have a linear base state, for which a linear stability analysis can readily be performed to calculate the onset of wrinkling.

We also saw that, in terms of displacements scaled on nondimensional thickness, the Föppl-von Kármán equations represent the leading order in a (nondimensional) thickness-wise expansion: this means that when considering scaled displacements, no explicit thickness parameter can enter the equation. This is in contrast to the Koiter-Steigmann model which retains multiple thickness orders and therefore must incorporate an explicit (nondimensional) thickness parameter.

The equations are semi-linear [Ciarlet, 1980], as the coefficients of the highest derivative do not depend on derivatives of the unknown functions. The Föppl-von Kármán equations are fourth order in the out-of-plane displacement, v_3, and second order in the in-plane displacements, meaning they require special interpolation schemes for the out-of-plane displacements, as we will see in the following chapter.

Examining the variational equation, we note that the Föppl-von Kármán model is the superposition of the nonlinear membrane model of Föppl, suitable for small displacements and moderate rotations, and the linear (small displacement) Kirchhoff-Love bending model [Friesecke et al., 2006].

As we have discussed in previous sections with other membrane-like models, the Föppl membrane energy is not suitable for use when the stress becomes compressive. Instead the energy needs to be 'relaxed' in the manner outlined by [Steigmann, 1990]. Alternatively, as in Föppl-von Kármán, the superposition of a bending energy regularizes the model.

3.6 The Extended Föppl-von Kármán Model

Using the same assumptions of Föppl-von Kármán it is possible to derive an extension to the Föppl-von Kármán model: which we call the extended Föppl-von Kármán model. The model derived here appears to be novel, although its relation to 3D elasticity will only be established by heuristic scaling arguments. We proceed with the heuristic derivation used to justify Föppl-von Kármán, but now incorporate higher order terms into the model. We maintain terms up to $\mathcal{O}(h^7)$ in our variational equation, suppressing terms of higher order.

In this section we proceed by using a bar to denote quantities scaled on the leading order in thickness, as in the previous section.

3.6.1 Correction to the Normal

The first step in this derivation is the expansion of the unit normal, which leads to nonlinearity in the bending moment. This nonlinear bending term appears to be novel and represents a trade off between accuracy and simplicity.

We Taylor expand the normal using thickness as the small parameter, replacing the displacements with explicitly scaled counterparts, to yield the unit normal to order $\mathcal{O}(h^2)$. A detailed calculation can be found in Appendix B.

This yields the following expression for the unit normal in terms of the scaled displacements, $\bar{v}_i$:

$$\hat{\boldsymbol{N}} = (-h\bar{v}_{3,\alpha} + \mathcal{O}(h^3))\,\hat{\boldsymbol{e}}_\alpha + (1 + \frac{1}{2}h^2\bar{v}_{3,\gamma}\bar{v}_{3,\gamma} + \mathcal{O}(h^4))\,\boldsymbol{k}\,, \tag{3.6.1}$$

so maintaining terms up to order h^2 we have:

$$\hat{\boldsymbol{N}} \approx -h\bar{v}_{3,\alpha}\,\hat{\boldsymbol{e}}_\alpha + (1 + \frac{1}{2}h^2\bar{v}_{3,\gamma}\bar{v}_{3,\gamma})\,\boldsymbol{k}\,, \tag{3.6.2}$$

which constitutes the first correction to the unit normal of the Föppl-von Kármán model. We define the correction to the unit normal as follows:

$$\hat{\boldsymbol{N}}^C \equiv -h\bar{v}_{3,\alpha}\,\hat{\boldsymbol{e}}_\alpha + \frac{1}{2}h^2\bar{v}_{3,\gamma}\bar{v}_{3,\gamma}\,\boldsymbol{k}\,. \tag{3.6.3}$$

We compare this approximation to the exact unit-normal and the approximation underlying the Föppl-von Kármán equations for a plate undergoing large rotations in figure 3.9. As can be seen this approximation is appropriate for moderate-to-large rotations, but will break down once angles approach 90°.

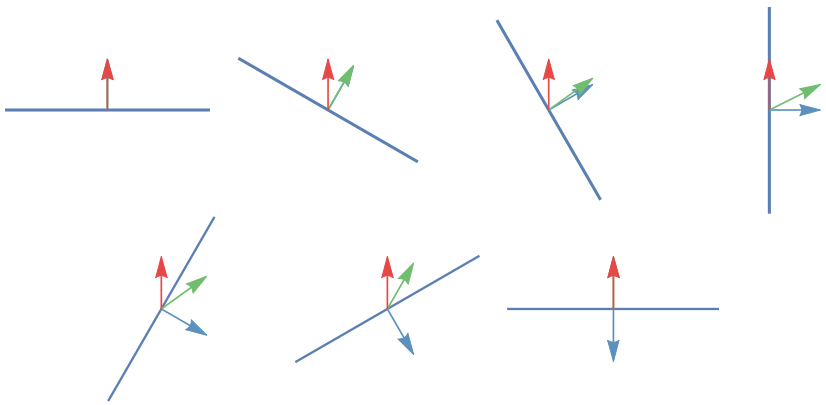

Figure 3.9: Illustration of the approximations to the unit normal used in the Föppl-von Kármán model (red), which remains constant, and the extended Föppl-von Kármán model (green), as compared to the true normal (blue), under basic rotation of a plate (blue).

3.6.2 Moment and Curvature Correction

We start by considering the bending term, $\delta\mathcal{W}^B$ of the Koiter-Steigmann model

$$\delta\mathcal{W}^B = M_{i\alpha\beta}\delta v_{i,\alpha\beta}\,. \tag{3.6.4}$$

Introducing the approximate expression for the unit normal into the expression for the curvature, to order $\mathcal{O}(h^4)$ the scaled, nondimensional curvature, $\bar{B}_{\alpha\beta} = \hat{\boldsymbol{N}}.\boldsymbol{Y}_{,\alpha\beta}/h$, is

$$\bar{B}_{\alpha\beta} = -h^2\bar{v}_{3,\gamma}\bar{v}_{\gamma,\alpha\beta} + (1+\frac{1}{2}h^2\bar{v}_{3,\gamma}\bar{v}_{3,\gamma})\bar{v}_{3,\alpha\beta} + \mathcal{O}(h^4)\,. \tag{3.6.5}$$

We see that the correction to the unit normal introduces an in-plane component to the bending moment, resulting in the fourth derivatives of in-plane displacements in the Euler-Lagrange equations.

We re-write this as:

$$\bar{B}_{\alpha\beta} = \bar{B}^L_{\alpha\beta} + h^2\bar{B}^C_{\alpha\beta} + \mathcal{O}(h^4)\,, \tag{3.6.6}$$

where $\bar{B}^L_{\alpha\beta} \equiv \bar{v}_{3,\alpha\beta}$ are components of the linear bending moment and

$$\bar{B}^C_{\alpha\beta} \equiv \frac{1}{2}\bar{v}_{3,\gamma}\bar{v}_{3,\gamma}\bar{v}_{3,\alpha\beta} - \bar{v}_{3,\gamma}\bar{v}_{\gamma,\alpha\beta}\,, \tag{3.6.7}$$

are the components of the nonlinear correction. This results in a nonlinear bending moment:

$$M_{3\alpha\beta} = \frac{h^4}{12}\mathcal{G}_{\alpha\beta\gamma\delta}(\bar{B}^L_{\gamma\delta} + h^2\bar{B}^C_{\gamma\delta})(1+\hat{N}^C_3) + \mathcal{O}(h^8)\,, \tag{3.6.8}$$

and

$$M_{\mu\alpha\beta} = \frac{h^4}{12}\mathcal{G}_{\alpha\beta\gamma\delta}(\bar{B}_{\gamma\delta}\,\hat{N}^C_\mu) + \mathcal{O}(h^7)\,, \tag{3.6.9}$$

Using these results to construct the full bending variation term, we get the expression

$$\delta\mathcal{W}^B = \frac{h^5}{12}\mathcal{G}_{\alpha\beta\gamma\delta}\;\bar{v}_{3,\gamma\delta}\,\delta\bar{v}_{3,\alpha\beta} + \frac{h^7}{12}\mathcal{G}_{\alpha\beta\gamma\delta}(\bar{N}^C_i\,\hat{N}^L_j + \bar{N}^C_j\,\hat{N}^L_i + h^2\bar{N}^C_j\,\bar{N}^C_i)\,\bar{v}_{j,\gamma\delta}\;\delta\bar{v}_{i,\alpha\beta} + \mathcal{O}(h^9)\,, \tag{3.6.10}$$

in which we have introduced the scaled components of the correction to the unit normal

$$\bar{N}^C_\alpha = \frac{1}{h}\hat{N}^C_\alpha \quad \text{and} \quad \bar{N}^C_3 = \frac{1}{h^2}\hat{N}^C_3\,. \tag{3.6.11}$$

and the corrected unit normal $\bar{N}^+_i = \delta_{i3} + h^2\bar{N}^C_i$. Here we have retained some terms of order $\mathcal{O}(h^9)$: according to our assumptions these terms are negligible; however, their truncation only serves to complicate the ensuing expression, so we do not neglect them.

We may alternatively write this in the succinct form

$$\delta\mathcal{W}^B = \frac{h^5}{12}\mathcal{G}_{\alpha\beta\gamma\delta}\,\bar{B}^+_{\alpha\beta}\,\bar{N}^+_i\,\delta\bar{v}_{i,\gamma\delta} + \mathcal{O}(h^9)\,, \tag{3.6.12}$$

where $\bar{B}^+_{\alpha\beta} = \bar{v}_{i,\alpha\beta}\bar{N}^+_i$. Finally, this can be expressed terms of unscaled quantities as

$$\delta\mathcal{W}^B = \frac{h^3}{12}\mathcal{G}_{\alpha\beta\gamma\delta}\,B^+_{\alpha\beta}\,N^+_i\,\delta v_{i,\gamma\delta} + \mathcal{O}(h^9) \tag{3.6.13}$$

where $B^+_{\alpha\beta} = v_{i,\alpha\beta}N^+_i$ and

$$N^+_i = \delta_{i3} + \hat{N}^C_i = -v_{3,\alpha}\,\delta_{i\alpha} + (1 + v_{3,\gamma}v_{3,\gamma})\,\delta_{i3}\,. \tag{3.6.14}$$

3.6.3 Approximation of the Christoffel Term

The next term to consider is the term containing the Christoffel symbol:

$$\delta\mathcal{W}^T = \delta\mathcal{W}^W + \delta\mathcal{W}^\Gamma\,. \tag{3.6.15}$$

The Christoffel symbol itself is formed of derivatives of the strain tensor and therefore is of order $\mathcal{O}(h^2)$, according to our assumptions. Thus, we shall see that order $\mathcal{O}(h^7)$ accuracy is maintained if we consider only the linear bending moment, $M^L_{\alpha\beta} = \mathcal{O}(h^4)$, and the derivatives of the Föppl-von Kármán strain tensor, $E^{vK}_{\alpha\beta}$.

We start by expanding the Christoffel symbol,

$$\Gamma_{\alpha\beta\gamma} = h^2\,(\bar{E}^{vK}_{\alpha\beta,\gamma} + \bar{E}^{vK}_{\gamma\alpha,\beta} - \bar{E}^{vK}_{\beta\gamma,\alpha}) + \mathcal{O}(h^4)\,, \tag{3.6.16}$$

where $\bar{E}^{vK}_{\alpha\beta}$ are components of the scaled, partially-linearised Föppl-von Kármán strain tensor, of section 3.5.5. Thus, we may define the leading order Christoffel symbol, $\Gamma^C_{\alpha\beta\gamma}$, as

$$\Gamma^C_{\alpha\beta\gamma} = h^2\,(\bar{E}^{vK}_{\alpha\beta,\gamma} + \bar{E}^{vK}_{\gamma\alpha,\beta} - \bar{E}^{vK}_{\beta\gamma,\alpha})\,. \tag{3.6.17}$$

The Christoffel term in the equations is then given by

$$\delta\mathcal{W}^+_\Gamma = \Gamma^C_{\alpha\beta\gamma}M^L_{\alpha\beta}\delta v_{3,\gamma} + \mathcal{O}(h^9)\,. \tag{3.6.18}$$

3.6.4 Approximation of the Membrane Term

The final part of the internal-energy variations to consider is the membrane term, $\delta\mathcal{W}^M$, given by

$$\delta\mathcal{W}^M = hS_{\alpha\gamma}Y_{i,\alpha}\delta v_{i,\gamma}\,. \tag{3.6.19}$$

There are new nonlinear stretching terms that enter into the model via the strain tensor, $E_{\alpha\beta}$, and the stress tensor, $\boldsymbol{S} \equiv \mathcal{U}^M_{\boldsymbol{\epsilon}}$, where $\mathcal{U}^M(\boldsymbol{\epsilon}) = \mathcal{W}^M(\boldsymbol{g}_\alpha)$, which can now be a nonlinear function of the strain, if suitably truncated.

The full Green-Lagrange strain tensor (equation (3.4.85)) does not need truncating and is given in terms of scaled displacements by

$$E_{\alpha\beta} = \frac{h^2}{2}(\bar{v}_{\alpha,\beta} + \bar{v}_{\beta,\alpha} + \bar{v}_{3,\beta}\bar{v}_{3,\alpha} + h^2\bar{v}_{\gamma,\alpha}\bar{v}_{\gamma,\beta})\,. \tag{3.6.20}$$

The stress tensor needs to be truncated according to the displacement scaling assumptions to give the following form:

$$\bar{S}_{\alpha\beta} = \bar{S}^{vK}_{\alpha\beta} + h^2\bar{S}^{C}_{\alpha\beta} + o(h^2)\,, \tag{3.6.21}$$

with $\bar{S}^{vk}_{\alpha\beta}$ and $\bar{S}^{C}_{\alpha\beta}$ the (scaled) Föppl-von Kármán stress and stress correction, respectively. This can only be performed once a constitutive equation has been chosen. Alternatively, the full model can be incorporated which will, in general, lead to additional order $\mathcal{O}(h^7)$ terms entering the model.

For example, the linear Saint-Venant-Kirchhoff constitutive law gives the following form for the stress tensor, cf. equation (2.2.50),

$$\bar{S}_{\alpha\beta} = \mathcal{G}_{\alpha\beta\gamma\delta}(\bar{E}^{vK}_{\gamma\delta} + \frac{1}{2}h^2\bar{v}_{\gamma,\alpha}\bar{v}_{\gamma,\beta})\,, \tag{3.6.22}$$

in which we have not needed to truncate any terms, because of the linear constitutive assumption.

Accordingly, the membrane term becomes

$$\delta\mathcal{W}^M = h^5\,\left(\bar{S}^{vK}_{\alpha\beta} + h^2\bar{S}^{C}_{\alpha\beta}\right)\,\bar{G}_{i\alpha}\,\delta\bar{v}_{i,\beta} + o(h^7)\,, \tag{3.6.23}$$

in which $\bar{G}_{i\alpha} = \delta_{i\alpha} + \bar{v}_{3,\alpha}\delta_{i3} + h^2\,\bar{v}_{\beta,\alpha}\delta_{i\beta}$. Or in terms of unscaled variables

$$\delta\mathcal{W}^M = h\,S^{+}_{\alpha\beta}\,Y_{i,\alpha}\,\delta v_{i,\beta} + o(h^7)\,, \tag{3.6.24}$$

with the truncated stress tensor $S^{+}_{\alpha\beta} = h^2\bar{S}^{vK} + h^4\bar{S}^{C}_{\alpha\beta}$. Once again, we retain some $o(h^7)$ membrane terms, as their truncation would only complicate the foregoing model.

3.6.5 Truncation the Load Term

We finally truncate the loading terms in the Koiter-Steigmann model, to further simplify the model. We now consider the form of the truncated follower load, for which the exact expression is:

$$\mathfrak{p} \equiv \Delta P\hat{\boldsymbol{N}}\sqrt{G}\,. \tag{3.6.25}$$

We expand the term $\hat{\boldsymbol{N}}\sqrt{G}$ using an intermediate result from Appendix B, to get the following expression for the forcing:

$$\mathfrak{P} = \Delta P \left[\boldsymbol{k}(1 + h^2 \bar{v}_{\gamma,\gamma} + \mathcal{O}(h^4)) - (h\bar{v}_{3,\gamma} + \mathcal{O}(h^3))\hat{\boldsymbol{e}}_\gamma \right] . \tag{3.6.26}$$

We can, therefore, define a new (non-unit) approximate normal vector:

$$\boldsymbol{\eta} \equiv \boldsymbol{k}(1 + h^2 \bar{v}_{\gamma,\gamma}) - (h\bar{v}_{3,\gamma})\hat{\boldsymbol{e}}_\gamma \, , \tag{3.6.27}$$

which can be split into a constant part, and a correction term:

$$\boldsymbol{\eta} \equiv \boldsymbol{k} + \boldsymbol{\eta}^C \, . \tag{3.6.28}$$

Thus, the forcing term is now *linear* in the unknowns: a significant simplification.

3.6.6 The Variational Principle

Putting everything together we get the full variational form, where we use pluses to denote the quantities of the extended Föppl-von Kármán model

$$\delta\mathcal{W}^+ = h\, S^+_{\alpha\beta}\, Y_{i,\alpha}\, \delta v_{i,\beta} \;+\; \frac{h^3}{12} \mathcal{G}_{\alpha\beta\gamma\delta}\, B^+_{\alpha\beta}\, N^+_i\, \delta v_{i,\gamma\delta} \;+\; \Gamma^C_{\alpha\beta\gamma} M^L_{\alpha\beta} \delta v_{3,\gamma} + o(h^7) \, . \tag{3.6.29}$$

which is order $o(h^7)$ accurate under the assumptions of $v_3 \sim h$ and $v_\alpha \sim h^2$. Here we introduce the truncated bending moment:

$$M^+_{i\alpha\beta} = \mathcal{G}_{\alpha\beta\gamma\delta}\, v_{j,\alpha\beta} N^+_j\, N^+_i \, , \tag{3.6.30}$$

the truncated stress $S^+_{\alpha\beta}$ which must be derived for the chosen material model, and the truncated normal

$$\boldsymbol{N}^+ = -\boldsymbol{\nabla} v_3 + (1 + \frac{1}{2}(\boldsymbol{\nabla} v_3)^2)\boldsymbol{k} \, . \tag{3.6.31}$$

We also take this opportunity to convert the equations back into dimensional form:

$$\delta\mathcal{W}^{*+} = h^*\, S^{*+}_{\alpha\beta}\, Y^*_{i,\alpha}\, \delta v^*_{i,\beta} \;+\; \frac{h^{*3}}{12} \mathcal{G}^*_{\alpha\beta\gamma\delta}\, B^{*+}_{\alpha\beta}\, N^+_i\, v^*_{i,\gamma\delta} \;+\; \Gamma^{*C}_{\alpha\beta\gamma} M^{*L}_{\alpha\beta} \delta v^*_{3,\gamma} + o(h^7) \, . \tag{3.6.32}$$

3.6.7 The Euler-Lagrange Equations

Deriving the Euler-Lagrange equations in the same way as for the Koiter-Steigmann model in section 3.4.9, we now express the governing equations for the correction model

$$D\big(v^*_{i,\alpha\alpha\beta\beta}\,N_i^+N_3^+ \,+\, 2v^*_{i,\alpha\alpha\beta}(N_i^+\,N_3^+)_{,\beta}\big) \,+\, \frac{h^{*3}}{12}\mathcal{G}^*_{\alpha\beta\gamma\delta}\,v^*_{i,\gamma\delta}(N_i^+\,N_3^+)_{,\alpha\beta} \,-\, h^*\big(S^*_{\alpha\beta}Y^*_{j,\alpha}\big)_{,\beta} + \frac{h^3}{12}\big(\mathcal{G}^*_{\beta\gamma\mu\nu}v^*_{3,\mu\nu}\Gamma_{\alpha\beta\gamma}\big)_{,\alpha} \;=\; (1+v_{\gamma,\gamma})\,\Delta p^* \tag{3.6.33}$$

$$D\big(v^*_{i,\alpha\alpha\beta\beta}\,N_\mu^+ \,+\, 2v^*_{i,\alpha\alpha\beta}(N_i^+\,N_\mu^+)_{,\beta}\big) \,+\, \frac{h^{*3}}{12}\mathcal{G}^*_{\alpha\beta\gamma\delta}\,v^*_{i,\gamma\delta}(N_i^+\,N_\mu^+)_{,\alpha\beta} - h^*\big(S^*_{\alpha\beta}Y^*_{\mu,\alpha}\big)_{,\beta} \;=\; -v_{3,\mu}\,\Delta p^* \tag{3.6.34}$$

with

$$\boldsymbol{N}^+ = -\boldsymbol{\nabla}v_3 + (1+\frac{1}{2}\boldsymbol{\nabla}v_3\cdot\boldsymbol{\nabla}v_3)\boldsymbol{k} \tag{3.6.35}$$

subject to the boundary conditions

$$q_i^{*\,+} = Q_i^* \quad \text{or} \quad \delta v_i^* = 0\,, \tag{3.6.36}$$

$$M_{i\alpha\beta}^{*\,+} = \Psi_i^* \quad \text{or} \quad \delta v^*_{i,\alpha}\nu_\alpha = 0\,, \tag{3.6.37}$$

with the truncated, internal shear

$$q_i^{*\,+} = (h^*S^*_{\alpha\beta}Y_{i,\beta} + M_{i\beta\gamma}^{*\,+}\Gamma_{\alpha\beta\gamma})\nu_\alpha - (M_{i\alpha\beta}^{*\,+}\nu_\alpha\tau_\beta)_{,\gamma}\tau_\gamma - M_{i\alpha\beta,\alpha}^{*\,+}\nu_\beta\,, \tag{3.6.38}$$

applied shear force $\boldsymbol{Q^*}$ and applied normal moment $\boldsymbol{\Psi^*}$ where $\boldsymbol{\nu}$ and $\boldsymbol{\tau}$ are the normal and tangent to the edge $\partial\Omega$, respectively.

There are also the following conditions:

$$\lim_{\boldsymbol{\iota}\to 0}[M_{i\alpha\beta}^{+*}\,\nu_\alpha\,\tau_\beta]_{\boldsymbol{\xi^*}_l-\boldsymbol{\iota^*}}^{\boldsymbol{\xi}_l^*+\boldsymbol{\iota}^*} = \Upsilon_i^* \quad \text{or} \quad \delta v_i^* = 0\,, \tag{3.6.39}$$

on a corner $\boldsymbol{\xi_l^*}$, on which we can apply a twisting moment, $\boldsymbol{\Upsilon^*}$.

The Extended Föppl-von Kármán Model

The governing equations for the extended Föppl-von Kármán model can be written far more succinctly in terms of the bending moments, $\boldsymbol{M}^{*\,C}_{\alpha\beta} = \boldsymbol{M}^{*\,+}_{\alpha\beta} - \boldsymbol{M}^{*\,L}_{\alpha\beta}$, and $\boldsymbol{M}^{*\,L}_{\alpha\beta}$ as follows

$$Dv^*_{3,\alpha\alpha\beta\beta} \,+\, M^{*\,C}_{3\,\alpha\beta,\alpha\beta} - \,\big(h^*S^*_{\alpha\beta}Y^*_{j,\alpha} + \,M^{*\,L}_{\mu\gamma}\Gamma_{\beta\mu\gamma}\big)_{,\beta} \;=\; \eta_3\,\Delta p^*\,, \tag{3.6.40}$$

$$M^{*\,C}_{\mu\,\alpha\beta,\alpha\beta} - \,h^*\big(S^*_{\alpha\beta}Y^*_{\mu,\alpha}\big)_{,\beta} \;=\; \eta_\mu\,\Delta p^*\,, \tag{3.6.41}$$

subject to the boundary conditions

$$q_i^{*+} = Q_i^* \quad \text{or} \quad \delta v_i^* = 0\,, \tag{3.6.42}$$

$$M_{i\alpha\beta}^{*+} = \Psi_i^* \quad \text{or} \quad \delta v_{i,\alpha}^* \nu_\alpha = 0\,. \tag{3.6.43}$$

3.6.8 Comments on the Extended Föppl-von Kármán Model

We now comment on several important aspects of this newly derived, extended model. The model now contains nonlinearity in both the bending and the stretching terms and is now nonlinear in both the in-plane and out-of-plane displacements. This contrasts with the Föppl-von Kármán model which contains nonlinearity only in the out-of-plane, stretching terms. It is worth noting that in correcting the equations we have lost the semi-linear property associated with the Föppl-von Kármán equations and the equations instead become quasi-linear (cf. section 3.5.6), i.e. the coefficients of the highest derivative are all lower order derivatives of the unknown. The relationship between the various models is shown in Figure 3.10.

We note that, in the truncation of the model, we have replaced the nonlinear loading term with a linear one. We have also removed the non-polynomial type nonlinearity of the Koiter-Steigmann model, discussed in section 3.4.11, that enters into the model via the exact unit-normal. These simplifications make the expression for the bending energy comparatively simpler.

These equations represent the first two orders of a thickness-wise expansion, when the Föppl-von Kármán scaling holds. Thus, the equations now contain an explicit thickness parameter, even in scaled form. Thus, we see that explicit thickness dependence enters both through the membrane term (as in the model of Healey et al. [2013]) and through the, now nonlinear, bending term.

The variational expression now contains second derivatives (and second variations) in all of the displacements, which means that the solution space is $H^2(\Omega)$ for each displacement, rather than just for the out-of-plane displacement. We will see in later, in chapter 4 that this will require $\mathcal{C}^1$ (gradient) continuous interpolation for all three displacements, not just the out-of-plane displacement, when solving these equations numerically using the finite element method.

This additional continuity requirement will increase the computational burden of the extended model over the Föppl-von Kármán equations. However, the comparative simplicity

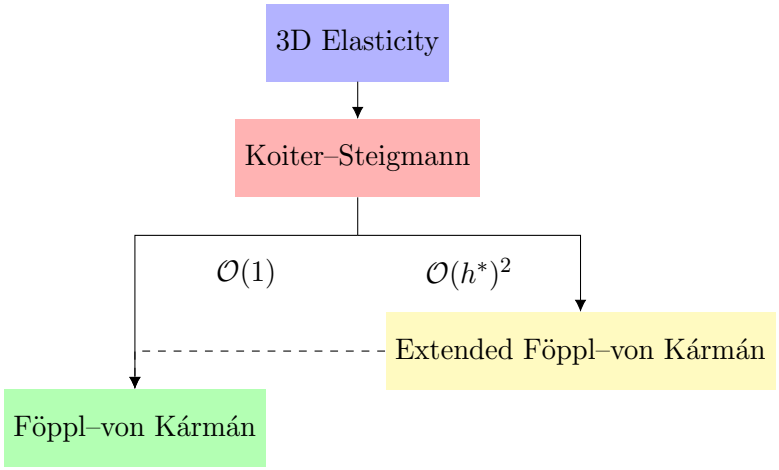

Figure 3.10: Relationship between 3D elasticity, the Föppl-von Kármán model and the extended Föppl-von Kármán model. The dashed line indicates an agreement in the zero thickness limit.

of the present model, as compared to the Koiter-Steigmann model, does introduce some advantage to this theory: it is far more tractable from an analytic perspective and allows certain physical predictions to be made more readily. To give a sense of the complexity[5] of the equations, this model only has $\sim 8\times$ more terms than the Föppl-von Kármán model, when all derivatives have been expanded and explicitly written in terms of displacements, which is a significant simplification as compared to the Koiter-Steigmann model, which contains $\sim 370\times$ more terms.

Finally we relate our newly derived model to the Healey et al. [2013] model: if we replace the new, nonlinear bending moment $M^{*+}_{\alpha\beta}$ for the linearised bending moment $M^{*L}_{\alpha\beta}$ and neglect the term containing the Christoffel symbols, we arrive at the Healey et al. [2013] model. The Healey et al. [2013] model comprises the superposition of the linear bending energy and a nonlinear membrane energy, and is suitable for large-strain systems with moderate-rotations.

[5]See the comments of section 3.4.11 for a discussion regarding this measure.

3.7 Summary

In this chapter we have seen the rational descent of the Koiter-Steigmann model from three-dimensional elasticity. Following this, we used scaling assumptions to connect the Föppl-von Kármán model to the Koiter-Steigmann model, in the limit of small in-plane displacements and moderate rotations. Finally, taking inspiration from this approach, we derived a new model, the extended Föppl-von Kármán model, which represents the next order in the thickness-wise expansion, under the same small-displacement, moderate rotation assumptions of the Föppl-von Kármán model.

Now that we have outlined the derivation of three distinct models, suitable for investigating wrinkling in thin-plate problems, we proceed to explain how these equations can be solved: focusing on their numerical solution using the finite element method - which we see in the next chapter.

Chapter 4

Numerical Methods

4.1 Introduction to the Finite Element Method

The finite element method is a general technique that constructs approximate solutions to boundary-value problems [Becker et al., 1981]. The method consists of dividing the domain of the solution into a finite number of parts, or 'elements', and using localised interpolation over these elements to construct a solution over the whole domain. When a variational principle can be appealed to, this method can be thought of as a direct discretization of the minimization problem. We begin by introducing the guiding principles behind the finite element method for a simple variational problem, proceeding to discuss some extensions that can be made to the outlined framework. In this introduction, we loosely follow the explanation given by Becker et al. [1981], in order to provide an intuitive understanding of the finite element method. Those familiar with the finite element method may proceed directly to the next section.

4.1.1 A Simple 1D Example

To introduce the concepts we begin by considering the one dimensional functional

$$\Pi = \int_{\Omega} \left(\frac{1}{2} \left(\frac{du(x)}{dx} \right)^2 + f(x)u(x) \right) d\Omega = 0\,, \tag{4.1.1}$$

with $\Omega = [0, 1]$ subject to the forcing $f(x)$. Taking variations we obtain the variational equation

$$\delta\Pi = \int_{\Omega} \left(\frac{du(x)}{dx} \frac{d\delta u(x)}{dx} + f(x)\delta u(x) \right) d\Omega = 0\,. \tag{4.1.2}$$

The corresponding Euler-Lagrange equation for this variational principle will be the one-dimensional Poisson equation: $u_{,xx} = f(x)$.

We may consider the expansion in a given, infinite-dimensional, basis set $\{\psi_i(x)\}$, such that we can express any function in the solution space as a linear combination of the new basis functions

$$u(x) = \sum_{i=1}^{\infty} U_i \, \psi_i(x) \,, \tag{4.1.3}$$

where U_i are the set of coefficients. Here, we are deliberately vague about what constitutes an admissible solution space: it suffices to say that the basis functions should be 'sufficiently smooth' so that all operations involved in the variational principle 'make sense mathematically'. For instance, in the example above, solutions must be C^0 (value) continuous everywhere, in order that the zeroth and first derivatives are square integrable over the domain. The relevant space for these will be the C^0 continuous Sobelov space, H^1 [Oden and Reddy, 1976].

We also require that the variations, $\delta u(x)$, vanish on Dirichlet boundaries, i.e. boundaries on which we specify the value of $u(x)$, as on these boundaries there can be *no* variation in the solution: the value is known. These variations are *arbitrary* functions that belong to the solution space and, as such, for $u(x)$ to be a solution to the problem, the above variational principle must be satisfied for all $\delta u(x) \in H_0^1$. Here we have denoted the subset of H^1 that vanishes on Dirichlet boundaries as H_0^1 [Becker et al., 1981]. Thus we are able to represent any arbitrary variation as

$$\delta U(x) = \sum_{i=1}^{\infty} \delta U_i \, \psi_i^0(x) \quad \text{for} \quad \psi_i^0 \in H_0^1 \,, \tag{4.1.4}$$

where δU_i are a set of coefficients and $\psi_i^0(x) \in H_0^1$ are the subset of basis functions that satisfy the Dirichlet boundary conditions.

The above variational problem becomes

$$\delta\Pi = \sum_{i,j=0}^{\infty} \left(\delta U_j \int_\Omega \left(U_i \frac{d\psi_i(x)}{dx} \frac{d\psi_j^0(x)}{dx} + f(x)\psi_j^0(x) \right) d\Omega \right) = 0 \,, \tag{4.1.5}$$

where we have, as yet, made no approximation.

4.1.2 The Galerkin Method

Having set up the exact problem, we now consider the Galerkin method for constructing approximate solutions to the above variational boundary-value problem. Galerkin's method

aims to find approximate solutions in a *finite-dimensional* subset, $\tilde{H}^1$, of the solution space, H^1. Thus, we instead consider the approximate problem,

$$\sum_{i,j=0}^{N} \left(\delta\tilde{U}_j \int_\Omega \left(\tilde{U}_i \frac{d\tilde{\psi}_i(x)}{dx} \frac{d\tilde{\psi}_j^0(x)}{dx} + f(x)\tilde{\psi}_j^0(x) \right) d\Omega \right) = 0\,, \quad \forall\, \delta\tilde{U}_j\,, \tag{4.1.6}$$

where $\tilde{\psi}_i \in \tilde{H}^1$ are the discrete set of basis functions of the subset $\tilde{H}^i$ and $\tilde{\psi}_i^0 \in \tilde{H}_0^1$ are the discrete set of basis functions that satisfy the Dirichlet boundary conditions. The coefficients $\tilde{U}_i$ in the approximation are referred to as the degrees of freedom. Now, as this equation is satisfied for all $\delta\tilde{U}_i$, the coefficients in $\delta\tilde{U}_i$ must be separately equal to zero. Thus, we must have the residuals

$$R_j = \sum_{i=0}^{N} \left(\int_\Omega \left(\tilde{U}_i \frac{d\tilde{\psi}_i(x)}{dx} \frac{d\tilde{\psi}_j^0(x)}{dx} + f(x)\tilde{\psi}_j^0(x) \right) d\Omega \right) = 0\,, \quad j \in \{1, \ldots, N\}\,, \tag{4.1.7}$$

which approximate the continuous equations, for an appropriate choice of basis functions.

We can rewrite this in the more revealing form

$$K_{ij}\tilde{U}_j = F_i(x)\,, \quad i, j \in \{1, \ldots, N\} \tag{4.1.8}$$

with the stiffness matrix components, K_{ij},

$$K_{ij} = \int_\Omega \left(\frac{d\tilde{\psi}_i(x)}{dx} \frac{d\tilde{\psi}_j^0(x)}{dx} \right) d\Omega \tag{4.1.9}$$

and the load term, F_i,

$$F_i = -\int_\Omega \left(f(x)\tilde{\psi}_i^0 \right) d\Omega\,. \tag{4.1.10}$$

To solve the problem, the inverse system must be solved:

$$\tilde{U}_j = (K^{-1})_{ji} F_i(x)\,, \quad i, j \in \{1, \ldots, N\}\,, \tag{4.1.11}$$

where $(K^{-1})_{ij}$ are elements of the inverse of K_{ij}^{-1}.

4.1.3 The Finite Element Method

The Galerkin method provides an elegant tool for determining the approximate solutions to boundary-value problems: however, the analyst is left with a vast array of possible basis functions, on which the quality of approximate solution strongly depends [Becker et al., 1981]. Moreover, in higher dimensions the construction of a set of basis functions which satisfy the boundary conditions of a given problem on an arbitrary boundary is an extremely non trivial problem.

To generalize this method, we need a systematic means of constructing the set of basis functions. As we have described it the Galerkin method has no criteria for the selection of the basis functions $\tilde{\psi}_i^0$ and $\tilde{\psi}_i$: they can be arbitrary, independent members of H_0^1 [Becker et al., 1981]. The quality of the resulting solution will then strongly depend on the choice of these basis functions [Becker et al., 1981]. These difficulties can be alleviated using the finite element method, which provides a general and systematic technique for constructing Galerkin approximations of boundary-value problems.

The overriding concept is that the basis functions can be defined piecewise over subregions of the domain, or 'elements', with simple, interpolating basis functions [Becker et al., 1981]. We begin by discretizing the domain $\Omega = [0, 1]$ as shown in figure 4.1, splitting the domain into N discrete parts, by introducing an equally spaced set of points, or 'nodes' a_i for $i \in \{0, \ldots, N\}$, with $a_i = i/N$. We then consider each of the N parts of the domain $\Omega_i \equiv (a_{i-1}, a_i)$ with $i \in \{1, N\}$ as separate 'pieces' or 'elements' of the discretized domain. The collection of nodes and elements making up the domain is referred to as the finite element mesh.

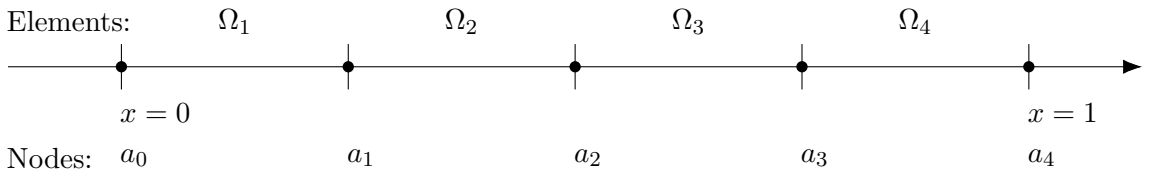

Figure 4.1: A 1D domain, split into finite elements, Ω_i.

One set of basis functions we could use is a piecewise linear basis. To explain this basis, we begin by defining the set of values of the function $u(x)$ evaluated at a_i, as

$$\{U_i\} \equiv \{u(a_i)\}\,, \tag{4.1.12}$$

which we will refer to as the *unknowns*.

We further introduce the set of piecewise linear basis functions

$$\psi_i(x) = \begin{cases} \dfrac{x - a_{i-1}}{a_i - a_{i-1}} & \text{for} \quad a_{i-1} \leq x \leq x_i \\ \dfrac{a_{i+1} - x}{a_{i+1} - a_i} & \text{for} \quad x_i \leq x \leq a_{i+1} \\ 0 & \text{for} \quad x < a_{i-1} \quad \text{and} \quad x > a_{i+1} \end{cases} \tag{4.1.13}$$

These functions provide interpolation of the unknown, which has local support: in other words the basis function ψ_i is only nonzero in the direct vicinity of node a_i. We display

these basis functions in figure 4.2.

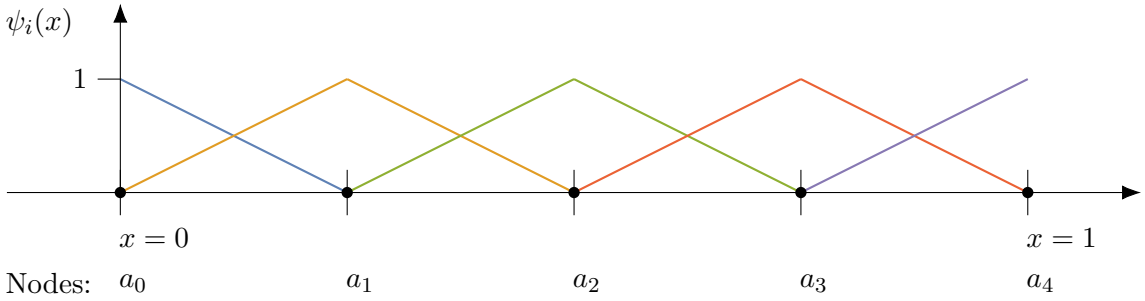

Figure 4.2: The piecewise 1D linear basis functions shown on a 1D mesh of elements. The support of the basis for each unknown is displayed in a different colour.

Using the basis functions and the unknowns, we may define a linear interpolant, $\pi u(x) = u(x)$, of the function $u(x)$ as

$$\pi u(x) = \sum_{i=0}^{N} U_i \, \psi_i(x) \, . \tag{4.1.14}$$

The subset $\tilde{H}_0^1$ of basis functions that satisfy Dirichlet boundary conditions at nodes k can now be easily formed by not including the basis functions at those nodes, such that we have the subset $\{\psi_i\}$, $i \neq k$. We may then interpolate variations, δu, as follows

$$\pi \delta u(x) = \sum_{i=0\,,\, i\neq k}^{N} \delta U_i \, \psi_i(x) \, . \tag{4.1.15}$$

Given that each basis function only has local support, i.e over two neighbouring elements, it is convenient to define a local coordinate on each element such that each element only contains quantities that are intrinsic to it. Thus, we introduce the local coordinate in element e, $\hat{x} \in (0, 1)$ and rewrite the basis functions on a single 'reference' element:

$$\hat{\psi}_0(\hat{x}) = 1 - \hat{x} \quad \text{and} \quad \hat{\psi}_1(\hat{x}) = \hat{x} \, . \tag{4.1.16}$$

Introducing local nodes $\hat{a}_0 = 0$ and $\hat{a}_1 = 1$ we see that basis functions are unity at their own associated node and zero at the other node, or $\hat{\psi}_i(\hat{a}_j) = \delta_{ij}$ for $i\, j \in \{0, 1\}$. This property is known as the Kronecker delta property, and is common to most conventional finite element basis functions. The local coordinate, $\hat{x}$, can be related to the global coordinate in each element, Ω_e, by

$$x(\hat{x}) = a_{i-1} \, \hat{\psi}_0(\hat{x}) + a_i \, \hat{\psi}_1(\hat{x}) \, , \quad x \in \Omega_i \, . \tag{4.1.17}$$

Finally, the Jacobian of this mapping on element i will be given by

$$J_i(\hat{x}) = \frac{dx}{d\hat{x}} \, , \tag{4.1.18}$$

which in general will be dependent on $\hat{x}$, but in the case of linearly interpolated geometry is independent of $\hat{x}$.

In the above scheme both the geometry of the element *and* the solution are interpolated with the same basis functions, so this interpolation scheme is said to be *isoparametric*. If we were to use higher order basis functions to interpolate the solution, as compared to the geometric basis, the scheme would be said to be *subparametric*. Alternatively, with a higher order geometric basis, as compared to the solution we would refer to the scheme as *superparametric*.

We may now construct our approximate variational equation, by splitting up the integral into separate integrals over each element Ω_e:

$$R_j = \sum_{e=1}^{N} \int_{\Omega_e} \Big(\sum_{i=1}^{N} J_i^{-1} \left(U_{i-1}\hat{\psi}_0'(\hat{x}) + U_i(\hat{x})\hat{\psi}_1'(\hat{x}) \right) \tilde{\psi}_j^{0\prime}(x) \quad + f(x)\tilde{\psi}_j^0(x) \Big) dx \,. \tag{4.1.19}$$

for residuals $j \neq k$, where k labels nodes with Dirichlet boundary conditions and we use the notation $g'(x) \equiv dg(x)/dx$. We reiterate here that on boundaries with Dirichlet boundary conditions we know the value of u and therefore the variation coefficient δU_j will be zero.

We can further simplify these equations, by making use of the compact support of basis functions. We know that the representation of $\pi u(x)$ will only depend upon values intrinsic to the element we are integrating over, e, which can be used to greatly simplify the above expression. We rewrite the expression as

$$R_j = \sum_{e=1}^{N} \int_{\Omega_e} \Big(J_e^{-1} \left(U_{e-1}\hat{\psi}_0'(\hat{x}) + U_e(\hat{x})\hat{\psi}_1'(\hat{x}) \right) \tilde{\psi}_j^{0\prime}(x) + f(x)\tilde{\psi}_j^0(x) \Big) dx \,. \tag{4.1.20}$$

Contributions to residual j will arise from elements that contain node j: i.e. $e = j$ and $e = j + 1$, which means we can further rewrite this as

$$R_j = \sum_{e=j}^{j+1\,,\, j\leq N} \int_{\Omega_e} \Big(J_e^{-1} \left(U_{e-1}\hat{\psi}_0'(\hat{x}) + U_e(\hat{x})\hat{\psi}_1'(\hat{x}) \right) \tilde{\psi}_j^{0\prime}(x) + f(x)\tilde{\psi}_j^0(x) \Big) dx \,. \tag{4.1.21}$$

introducing a local node number $l = e - j$ we may write

$$R_j = \begin{cases} \displaystyle\int_{\Omega_1} \Big(J_1^{-1} \left(U_0\hat{\psi}_0'(\hat{x}) + U_1(\hat{x})\hat{\psi}_1'(\hat{x}) \right) J_1^{-1}\hat{\psi}_0'(\hat{x}) + f(x)\hat{\psi}_0(\hat{x}) \Big) dx & j = 1 \\ \displaystyle\sum_{l=0}^{1} \int_{\Omega_{j+l}} \Big(J_{j+l}^{-1} \Big(U_{j+l-1}\hat{\psi}_0'(\hat{x}) + U_{j+l}(\hat{x})\hat{\psi}_1'(\hat{x}) \Big) J_{j+l}^{-1}\hat{\psi}_{\bar{l}}'(\hat{x}) + f(x)\hat{\psi}_{\bar{l}}(\hat{x}) \Big) dx & 1 < j < N \\ \displaystyle\int_{\Omega_N} \Big(J_N^{-1} \left(U_{N-1}\hat{\psi}_0'(\hat{x}) + U_N(\hat{x})\hat{\psi}_1'(\hat{x}) \right) J_N^{-1}\hat{\psi}_1'(\hat{x}) + f(x)\hat{\psi}_1(\hat{x}) \Big) dx & j = N \end{cases} \tag{4.1.22}$$

where $\bar{l}$ is $\bar{l} \in \{0,1\}$, $\bar{l} \neq l$. Finally, we replace the Cartesian integral with an integral over the local coordinate of each node $\hat{x} \in (0,1)$:

$$R_j = \begin{cases} \displaystyle\int_{\Omega_1} \left(J_1^{-1} \left(U_0 \hat{\psi}_0'(\hat{x}) + U_1(\hat{x}) \hat{\psi}_1'(\hat{x}) \right) \hat{\psi}_0'(\hat{x}) + J_1^{-1} f(x) \hat{\psi}_0(\hat{x}) \right) d\hat{x} & j = 1 \\ \displaystyle\sum_{l=0}^{1} \int_{\Omega_{j+l}} \left(J_{j+l}^{-1} \left(U_{j+l-1} \hat{\psi}_0'(\hat{x}) + U_{j+l}(\hat{x}) \hat{\psi}_1'(\hat{x}) \right) \hat{\psi}_{\bar{l}}'(\hat{x}) + J_{j+l}^{-1} f(x) \hat{\psi}_{\bar{l}}(\hat{x}) \right) d\hat{x} & 1 < j < N \\ \displaystyle\int_{\Omega_N} \left(J_N^{-1} \left(U_{N-1} \hat{\psi}_0'(\hat{x}) + U_N(\hat{x}) \hat{\psi}_1'(\hat{x}) \right) \hat{\psi}_1'(\hat{x}) + J_N^{-1} f(x) \hat{\psi}_1(\hat{x}) \right) d\hat{x} & j = N\,. \end{cases} \tag{4.1.23}$$

To impose the boundary conditions we 'pin' nodal values on boundaries with Dirichlet conditions, i.e at nodes k. At these nodes there will be no associated residual, as the discrete variation δU_k will be zero at this point. The value of U_k is then known and enters the equations through the interpolated field $\pi u'(x)$. On boundaries that are not pinned, flux free (Neumann) boundary conditions are imposed automatically as 'do-nothing' boundary conditions.

We may rewrite the above equations in the form

$$K_{ij} \tilde{U}_j = F_i(x)\,, \quad i,j \in \{1,\ldots,N\}\,,\ i,j \neq k \tag{4.1.24}$$

in which k labels the nodes with Dirichlet conditions. The stiffness matrix, K_{ij}, is given by

$$K_{ij} = \begin{cases} \displaystyle\int_{\Omega_1} J_1^{-1} \left(\delta_{i0} \hat{\psi}_0'(\hat{x}) + \delta_{i1}(\hat{x}) \hat{\psi}_1'(\hat{x}) \right) \hat{\psi}_0'(\hat{x}) d\hat{x} & j = 1 \\ \displaystyle\sum_{l=0}^{1} \int_{\Omega_{j+l}} J_{j+l}^{-1} \left(\delta_{i,j+l-1} \hat{\psi}_0'(\hat{x}) + \delta_{i,j+l}(\hat{x}) \hat{\psi}_1'(\hat{x}) \right) \hat{\psi}_{1-l}'(\hat{x})) d\hat{x} & 1 < j < N \\ \displaystyle\int_{\Omega_N} J_N^{-1} \left(\delta_{i,N-1} \hat{\psi}_0'(\hat{x}) + \delta_{i,N}(\hat{x}) \hat{\psi}_1'(\hat{x}) \right) \hat{\psi}_1'(\hat{x}) d\hat{x} & j = N\,. \end{cases} \tag{4.1.25}$$

and the forcing, F_i is

$$F_i = \begin{cases} \displaystyle\int_{\Omega_1} \left(J_1^{-1} f(x) \hat{\psi}_0(\hat{x}) \right) d\hat{x} & j = 1 \\ \displaystyle\sum_{l=0}^{1} \int_{\Omega_{j+l}} \left(J_{j+l}^{-1} f(x) \hat{\psi}_{1-l}(\hat{x}) \right) d\hat{x} & 1 < j < N \\ \displaystyle\int_{\Omega_N} \left(J_N^{-1} f(x) \hat{\psi}_1(\hat{x}) \right) d\hat{x} & j = N\,. \end{cases} \tag{4.1.26}$$

The above equation, once integrated, can be straightforwardly inverted by available linear algebra software. Integration, in turn, can be numerically computed using the well known

Gauss formulae [Becker et al., 1981], where in this case the stiffness matrix is constant and the integral can be computed directly[1].

4.1.4 Extensions

In the above example, we have considered a very basic example of a finite element method for a linear, 1D, variational problem, using linear interpolation. However, this is by no means the only type of problem that the finite element method can be used to tackle: on the contrary, the method can be adapted to wide variety of problems that may otherwise be intractable. We proceed to discuss some basic extensions to the simple finite element method that we have outlined in the section above.

Nonlinear Systems and the Newton Method

The first extension we consider is the solution of nonlinear problems. In general finite element approximations will be of nonlinear systems, in which case the residuals, R_i, will be a nonlinear function of the unknowns, $\boldsymbol{U} = \{U_i\}$. For the case of nonlinear systems the Newton method may be used to determine the solution to the system. If we expand the residuals, $R_i(\boldsymbol{U})$, about an initial guess $\bar{\boldsymbol{U}}$, close to the solution, we may write

$$R_i(\boldsymbol{U}) = R_i(\bar{\boldsymbol{U}}) + \sum_{i=0,\, i\neq k}^{N} \frac{\partial R_i(\boldsymbol{U})}{\partial U_j}(U_j - \bar{U}_j) + \mathcal{O}(U_j - \bar{U}_j)^2 \,, \tag{4.1.27}$$

in which the nodes $i = k$ have Dirichlet boundary conditions. If $\boldsymbol{U}$ is the solution to the system, the left hand side will be zero, and we can rearrange to obtain

$$K_{ij}(\bar{U}_j)(U_j - \bar{U}_j) \approx -R_i(\bar{\boldsymbol{U}}) \,, \tag{4.1.28}$$

with

$$K_{ij} = \frac{\partial R_i(\boldsymbol{U})}{\partial U_j} \,, \tag{4.1.29}$$

provided that $\bar{\boldsymbol{U}}_i \approx \boldsymbol{U}$. If we iteratively solve the above equation, using the previous solution to determine the stiffness matrix in each step [Press et al., 1988], we can find the solution to the nonlinear system. This method needs an initial 'guess' of the solution to begin the iteration: for which convergence is not guaranteed. The method requires an initial guess that

[1] In general, this is not the case and it is in principle necessary to integrate the stiffness term exactly. This can be achieved using quadrature rule such as Gaussian quadrature.

is 'close'[2] to the solution. It is worth noting that, if used with a linear equation, the Newton method will converge in a single step, as the above relation, equation (4.1.28), becomes exact. Here we have described the Newton method in its most basic form: however, many extensions exist to improve the stability and convergence properties of the above algorithm.

Higher Order Basis Functions

Each element need not have only two degrees of freedom: we could introduce a new unknown at the centre of each element, as pictured in figure 4.3, and increase the polynomial order to quadratic. The mesh in this case is shown in figure 4.3. The shape functions, $\psi^Q_{L\,i}$ for $i \in \{1, 2, 3\}$, will then be

$$\psi^Q_{L\,1} = (1 - \hat{x})\,(1 - 2\hat{x})\,, \tag{4.1.30}$$

$$\psi^Q_{L\,2} = 4(1 - \hat{x})\,\hat{x}\,, \tag{4.1.31}$$

$$\psi^Q_{L\,3} = -\hat{x}\,(1 - 2\hat{x})\,. \tag{4.1.32}$$

Once again, the Kronecker delta property applies which can be seen in figure 4.4.

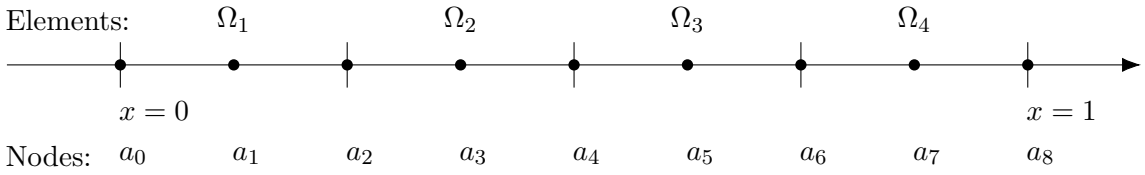

Figure 4.3: A 1D domain, split into finite elements, Ω_i.

The interpolation of the solution will then be piecewise quadratic with three unknowns per element, two of which are shared between adjacent elements. Other than this, the process of constructing the residuals and stiffness matrix remains identical.

Hermite Basis Functions

So far we have only considered geometric elements with 'value' or 'Lagrange-type' degrees of freedom. However, we may also consider elements with 'derivative' or 'Hermite' type degrees of freedom.

[2]By close we require that the guess is inside the Newton method's basin of attraction, which may be arbitrarily complicated [Press et al., 1988]. It usually suffices to use an initial guess that is 'close' in a physical sense: for example the solution at a slightly smaller value of forcing, or the solution to the linearised problem.

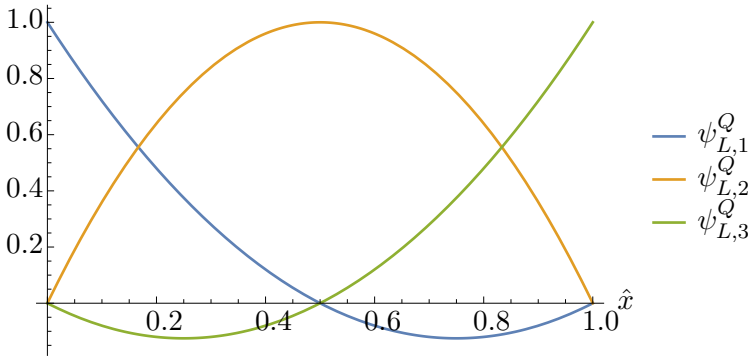

Figure 4.4: The 1D Quadratic Lagrange basis functions.

Consider a one dimensional geometric element with two nodes, each with two degrees of freedom: a value degree of freedom, $U_i(\hat{x})$ and a first derivative[3] degree of freedom, $(-1)^i U_i'(\hat{x})$ for $i \in \{0, 1\}$. The corresponding (cubic) basis functions, $\psi^{C\,m}_{H\,i}$, will be

$$\begin{aligned} \psi^{C\,0}_{H\,0} &= (1-\hat{x})^2\,(1+2\hat{x})\,, & \psi^{C\,1}_{H\,0} &= (1-\hat{x})^2\,\hat{x}\,, \\ \psi^{C\,0}_{H\,1} &= (3-2\hat{x})\,\hat{x}^2\,, & \psi^{C\,1}_{H\,1} &= (1-\hat{x})\,\hat{x}^2\,, \end{aligned} \tag{4.1.33}$$

Here i labels the node and m labels the order of the derivative of the degree of freedom. These basis functions will satisfy a version of the Kronecker delta property: the m^{th} derivative at the l^{th} node will be nonzero only only for the basis function $\psi^{C\,m}_{H\,i}$:

$$a_{nj}\frac{d^n}{d\hat{x}^n}\,\psi^{C\,m}_{H\,i}(\hat{a}_j) = \delta_{mn}\delta_{ij}\,, \tag{4.1.34}$$

with

$$a_{nj} = \begin{cases} -1 & \text{for} \quad j=1\,,\, n=1 \\ +1 & \text{otherwise} \end{cases} \tag{4.1.35}$$

This property can clearly be seen in figures 4.5 and 4.6.

These basis functions are naturally C^1 or gradient continuous across inter-element boundaries; in 1D an inter-element boundary is simply a shared node between two elements. At each node we have two values, the zeroth and first derivative degrees of freedom: as such the first derivative is continuous between elements. Thus, the second derivative will be well defined everywhere and the basis functions are therefore suitable for the approximation of fourth-order boundary-value problems.

[3]Here we use a symmetric definition for the 1D Hermite elements, which becomes useful later in the definition of curved C^1-Bell Elements

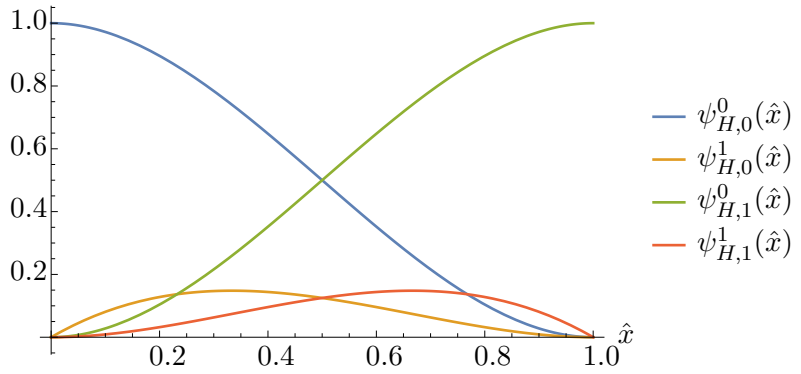

Figure 4.5: The 1D Hermite basis functions.

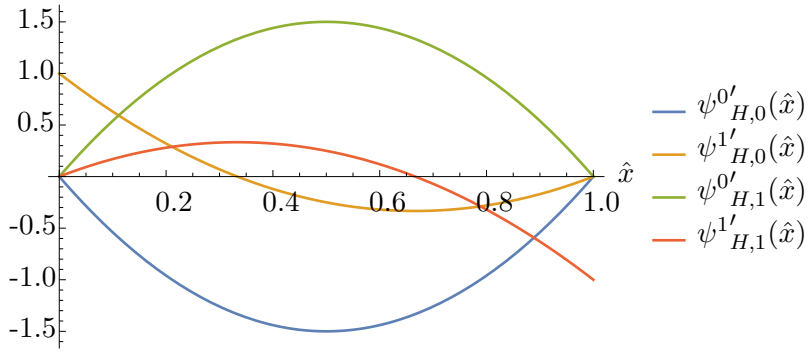

Figure 4.6: The first derivative of the 1D Hermite basis functions.

Two-Dimensional Variational Problems

For two-dimensional variational problems, we instead split the domain into elements that are two-dimensional subdomains of the original region: typically quadrilateral or triangular regions. For example, for a two-dimensional triangle a linear interpolation scheme over the element is be given by

$$\psi^L_{L\,1} = \hat{x}_1 \tag{4.1.36}$$

$$\psi^L_{L\,2} = \hat{x}_2 \tag{4.1.37}$$

$$\psi^L_{L\,3} = (1 - \hat{x}_1 - \hat{x}_2)\,, \tag{4.1.38}$$

in which $\hat{x}_\alpha$, for $\alpha \in \{1, 2\}$, are the two local coordinates of the element. In an isoparametric element, these are related to the Cartesian coordinate by the following expression

$$\boldsymbol{x} = \sum_{i=1}^{3} \boldsymbol{a}_i \psi^L_{L\,i}(\hat{\boldsymbol{x}})\,, \tag{4.1.39}$$

and $\boldsymbol{a}_i$ are the positions of the vertices in the physical domain, as shown in figure 4.7.

As we have seen, it is convenient to express the basis functions in terms of the local coordinate system on the reference triangle, that is shared between all elements: however, to

express the equations, derivatives with respect to the global coordinate system are necessary. In the same manner as in the 1D example we considered, we transform between derivatives of local to global coordinates using a Jacobian matrix, as follows

$$\frac{\partial}{\partial x_\beta}\psi^L_{Li}(\hat{\boldsymbol{x}}) = \frac{\partial}{\partial \hat{x}_\alpha}\left(\psi^L_{Li}(\hat{\boldsymbol{x}})\right)\left(J^{-1}\right)_{\alpha\beta} \tag{4.1.40}$$

with the Jacobian matrix

$$\boldsymbol{J} = \frac{\partial \boldsymbol{x}}{\partial \hat{\boldsymbol{x}}}\,. \tag{4.1.41}$$

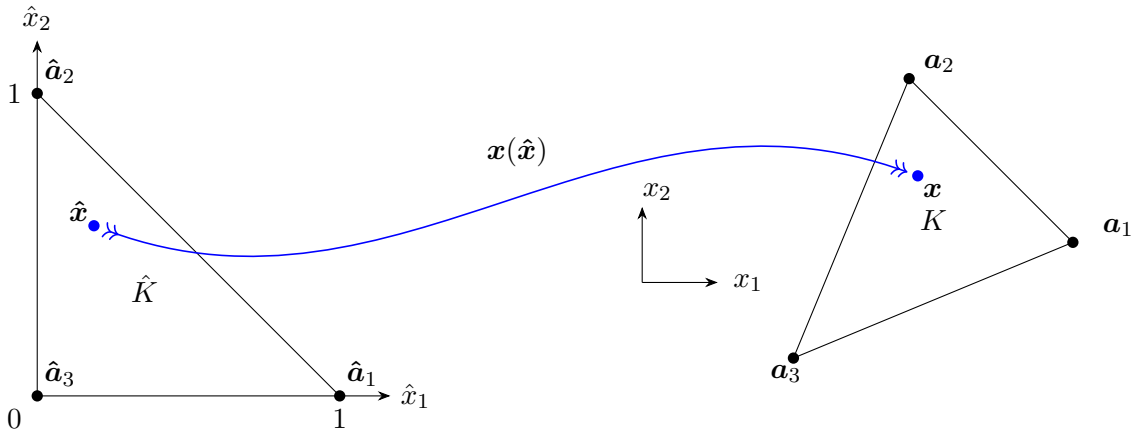

Figure 4.7: Diagram showing the geometry of the reference triangle and a triangle in the physical domain.

The resulting method remains largely the same: we split up the domain into a finite number of triangles and compute the integral of the discretized residual over each one. Each 'node' that is not on a Dirichlet boundary has an associated variation and therefore a corresponding equation. Every node also has corresponding unknown, except on Dirichlet boundaries for which the value is known. We display a typical example mesh, and the basic procedure for interpolation, in figure 4.8.

4.1.5 An Object-Oriented Picture

It can be useful, especially from the perspective of implementation, to summarize ideas in terms of objects, hierarchy and their interaction. We provide this description with the aim of creating a framework through which to understand the structure of a finite element simulation and clarify the ideas we have discussed.

Given that the code discussed during this thesis was developed to form part of `oomph-lib` [Heil and Hazel, 2006], the (open-source) object-oriented multi-physics finite element library, the structures we discuss will naturally reflect the structures found within `oomph-lib`.

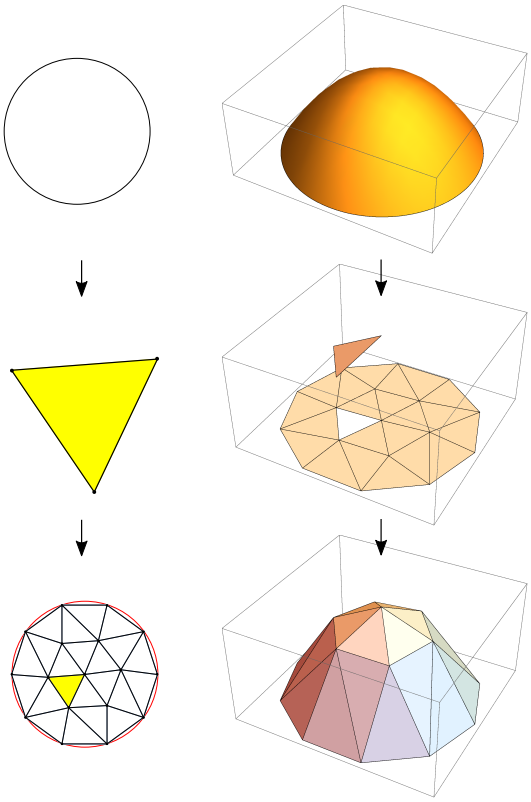

Figure 4.8: A function (top right) interpolated on a 2D domain (top left), split into triangular finite elements (middle), Ω_i and then interpolated on the domain (bottom right).

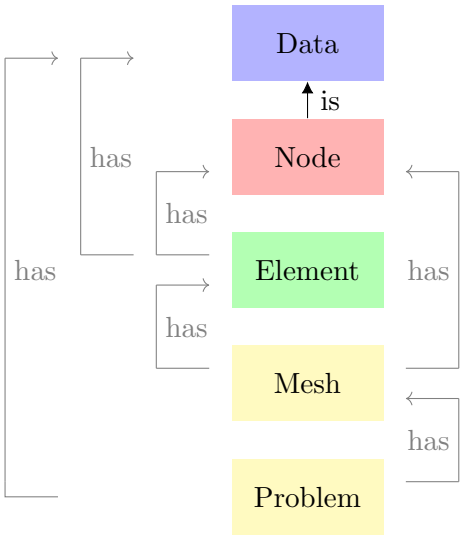

Figure 4.9: The structure of a typical (mathematical) problem within `oomph-lib`.

We start by considering a given (mathematical) problem (`Problem` , in `oomph-lib`), whose structure we summarize in figure 4.9. A `Problem` is a collection of equations, boundary conditions and applied forcing together with a particular discretization. Thus, a problem has a mesh (`Mesh`) of elements (in `oomph-lib` a type of `FiniteElement`), unknown values (which

are `Data`) and nodes (`Node`). Each `FiniteElement` has `Node`(s), which supply geometric information to the elements, and unknown values which supply the information about the unknown fields within the problem; both the `Node`(s) and unknowns are shared with the `Mesh`. A `Node` is a type of `Data` which also has a position. `Data` is the most primitive object we consider, which in turn has a value which is either pinned, i.e. known, or is unpinned i.e. to be solved for.

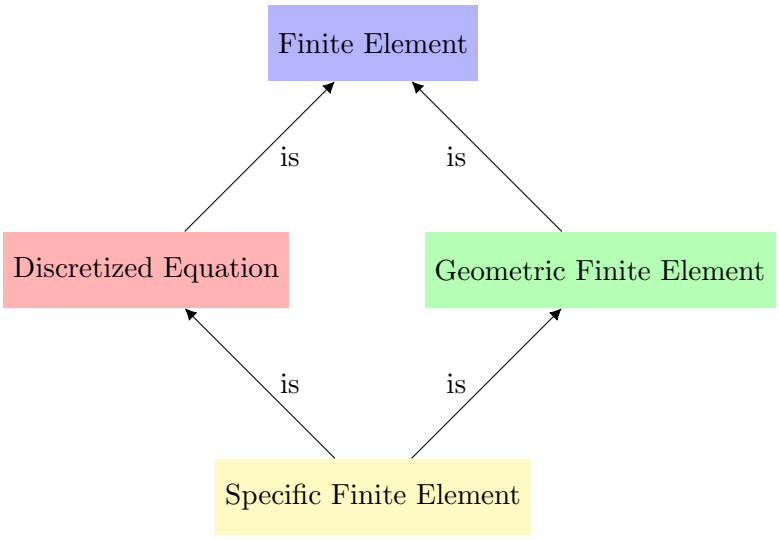

Figure 4.10: The structure of a typical element within `oomph-lib`.

We now describe the structure of the elements, which is summarized in figure 4.10. The elements provide the discretized equations, as well as the basis functions that interpolate the unknowns and the basis functions for the geometry. A `FiniteElement` defines the interface to the geometric basis and has `Data` and `Node`(s): it is a region of space with `Node`(s) and associated functions. A geometric element is a type of `FiniteElement` that implements the basis for the position over the region: the elements `Shape` functions. In an isoparametric element the `Shape` functions are also used to interpolate the unknowns. Each equation is a specific type of `FiniteElement` that provides a discretized set of equations over a region of space. To create a new specific element type we require both a set of equations and a corresponding discretization scheme, which is achieved in `oomph-lib` using multiple inheritance from both a geometric element and a discretized equation.

For example, in the 1D Poisson equation example we would implement several new objects. At the highest level we create a `Problem` which sets up the equation numbering, the

1D `Mesh`, the forcing and the boundary conditions. Boundary conditions are set by specifying which values are 'known' or 'pinned'. The 1D `Mesh` in turn is made of linear, 1D, `FiniteElement` (s) and 1D `Node` (s). Each `Node` has unknown values (`Data`) associated with them and a 1D position. Each 1D, linear Poisson element (`TPoissonElement<1,2>`) consists of two `Node` (s) and two associated unknown values; it also provides the linear `Shape` functions and the equations; it inherits from both the 1D linear geometric element and a 1D Poisson equation class. The basis functions are inherited from the parent 1D linear geometric element class (`TElement<1,2>`), which is in principle parent to many other 1D linear finite element types. The equations will be inherited from the 1D Poisson equation class (`TPoissonEquation<DIM,NNODE_1D>`), which again is in principle parent to many 1D Poisson elements.

4.2 Finite Element for 2D Fourth Order Functionals

Having introduced the basic concepts behind the finite element method and some possible extensions, we now review some of the specific aspects relevant to fourth-order problems, in particular in the context of plate models which are the concern of this thesis.

The focus of this thesis is unshearable plate models which include bending stiffness: as such, all of the studied models are described by two dimensional, fourth-order equations. Fourth order, two-dimensional variational equations represent particularly difficult problems to solve, both analytically and numerically, especially for nonlinear equations. To approximate these problems using the finite element method requires specialised interpolation methods which are required to either support C^1-continuous (H^2) basis functions or alternatively transform the equations to a system of lower order C^0-continuous basis functions, as in mixed and hybrid methods [Brezzi and Fortin, 1991].

Simplex Elements

Direct discretization of these equations is difficult because of the difficulty in providing C^1-continuous basis functions. Whereas constructing C^1-continuous bases in 1D is straightforward, as element boundaries are only at nodes between elements, in 2D the continuity requirement is required to hold along the entire edge between two elements. This requirement proves to be very restrictive, necessitating the use of high-order Hermite-type elements. Such

methods are known as conforming methods, as the elements use a subspace of the solution space.

Most C^1-continuous bases are defined only for simplex elements, that is straight-sided elements, due to the inherent difficulty in providing a basis that remains C^1-continuous when mapped from straight-sided elements to the curved elements. However, this proves restrictive because, unlike in second-order problems, appropriate representation of a curved edge is *necessary* to ensure convergence to the correct solution [Ženíšek, 1981a; Ciarlet, 1991].

The most commonly used C^1 quadrilateral simplex element is the 16 degree of freedom Bogner-Fox-Schmidt element, also known as the Hermite rectangle. However, generating quality rectangular meshes for generic shapes presents a difficult problem: it is far more straightforward to mesh generic shapes using triangulation [Schiffer et al., 2012]. For this reason, triangular elements such as Argyris, Bell and the singular[4] Zienkiewicz triangle [Ciarlet, 1991] or composite triangular elements such as the Hsieh-Clough-Tocher (HCT) element are usually preferred. It should be noted that the Bell triangle is the optimal C^1 element with a polynomial basis: C^1 triangular elements with lower degrees of freedom require the inclusion of non-polynomial functions [Ciarlet, 1991]. However, as mentioned, none of these triangular elements are appropriate for characterising fourth-order problems on curved domains.

Isoparametric Elements

In their basic form, the above C^1 elements only interpolate the geometry linearly, and thus are only suitable for the interpolation of polygonal domains. In second-order finite element methods, isoparametric representation of the domain is usually sought, as it can improve convergence properties on curved domains. However, the use of isoparametric formulations is not straightforward for C^1-continuous bases. For the case of quadrilateral meshes, the Bogner-Fox-Schmidt element can provide an isoparametric representation of the domain and the solution [Fischer, 2011]. These elements, however, have severe geometric constraints: each vertex between elements must comprise of exactly four elements [Fischer, 2011]. Suitable curved meshes, that satisfy this constraint, may be constructed from a generic mesh of straight-sided quadrilaterals, which introduces an extra step in the generation of the mesh for the given problem [Fischer, 2011]. An example of this is shown in figure 4.11. As such,

[4] A singular element uses rational functions in addition to polynomial functions to interpolate the unknowns.

due to the complication in meshing the approach is less flexible than corresponding methods using unstructured triangle meshes.

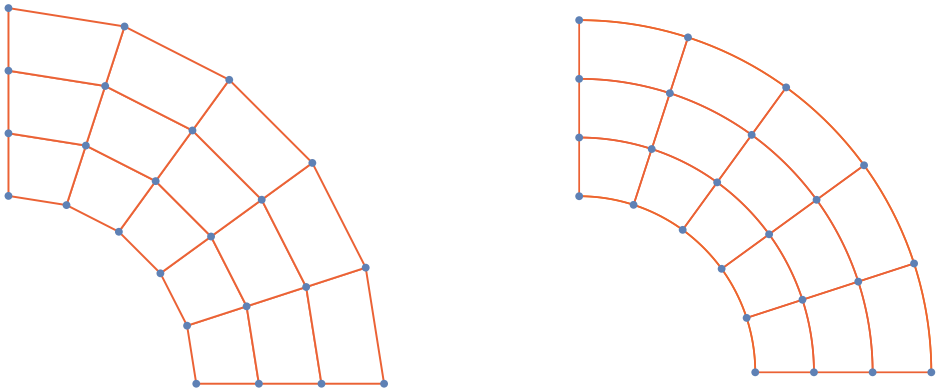

Figure 4.11: Input mesh (left) and interpolated mesh (right) for isoparametric Bogner-Fox-Schmidt elements. To preserve the C^1-continuity of the unknown field, each vertex in the mesh must join exactly four elements.

The formulation of isoparametric Hermite triangle elements presents an even greater challenge: indeed it is not possible to construct an isoparametric mapping for triangles with only a single curved edge [Mansfield, 1978]. However, the construction of an isoparametric mapping for triangular elements with multiple curved edges has apparently been achieved by Fischer [2011] using a transform to an (unknown) intermediate configuration. This transformation entails minimizing a nonlinear system to determine the unknown final mesh shape, to which there may be multiple solutions. Additionally, Fischer [2011] reported that under certain conditions the system of equations for the (initially unknown) local-to-global mapping may become ill-conditioned and produce mesh defects as a consequence.

Mixed and Hybrid Methods

An alternative to the above methods of interpolation, for a particular fourth order problem, is to use a lower order (H^1) system of equations that approximates the original system by introducing additional auxiliary variables. These methods are generally nonconforming and use a space with lower continuity to approximate the equations.

The additional equations and variables augment the system to allow simpler means of interpolation [Brezzi and Fortin, 1991]. Once a scheme is proposed, these methods can be straightforward to implement: however the proposed method is not guaranteed to be numerically stable. Methods that seem reasonable may suffer from numerical instability for

reasons that are not readily apparent. Common drawbacks to these methods include locking effects and unphysical results [Fischer, 2011]. As such, the construction of stable schemes is a non-trivial problem [Arnold, 1990; Brezzi and Bathe, 1990]. Once a stable scheme is obtained, the interpolation scheme is generally easy to construct: however these methods often have a comparable number of degrees of freedom to conforming methods and as such may not confer much advantage in terms of the size of the system required to solve a system to a desired accuracy [Arnold, 1990]. Another downside is that these methods generally need to be constructed *for a particular equation* rather than constructing generic interpolation schemes for *any* fourth order problem. Coming up with consistent, stable approximation schemes is extremely difficult, so it is the opinion of this writer that these methods present an unattractive option for generic fourth-order boundary-value problems.

Isogeometric Analysis

An alternative that can be used for both conforming and nonconforming methods is isogeometric analysis, which has been demonstrated to be effective at producing both accurate representation of the geometry and of the solution, using non-uniform rational B-splines (NURBS). NURBS are weighted rational functions of B-splines, which in turn are piecewise polynomial. In the special case where the weights are all equal, NURBS reduce to normal B-spline functions. This method affords many advantages over the standard finite element method: the inter-element continuity, the size of elements and the order of interpolation can all be easily controlled. A further advantage is that geometrical representation provided by a CAD program can be directly used in the finite element code, without any remeshing necessary.

A NURBS mesh is formed of one or more 'patches' each consisting of 'control points', 'knots' and 'elements'. The physical geometry is mapped onto a set of 'patches' each comprising a regular, rectangular, reference-mesh. This reference mesh is specified by introducing a particular set of 'knots' which assume the place of nodes in standard finite element methods: the patch consists of a regular rectangular mesh of knots. Elements in the patch are defined simply as the rectangular regions created by joining knot points (see e.g figure 4.12): this is a useful description as NURBS curves have only local support over neighbouring elements, just as in classical finite element methods. Control points assume the place of degrees of freedom; in the isogeometric method they are used to interpolate both the geometry and the

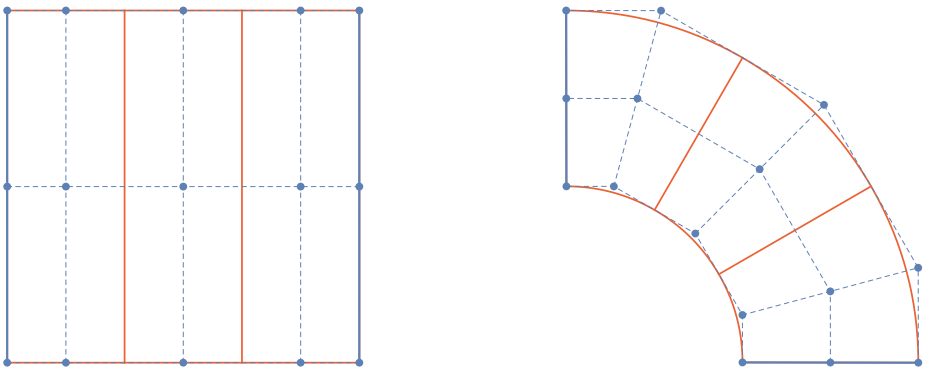

Figure 4.12: Reference mesh (left) and physical mesh (right) for a domain made of a single isogeometric patch, split into 3 elements. Thick blue lines show pinned edges, orange lines show element boundaries and blue dots represent control points.

unknowns.

The control points used to interpolate the geometry will often be specified using separate CAD software, but alternatively the locations of the control points can be determined by solving the linear system that minimizes difference between exact and approximate geometries in a least-squares sense. Sometimes a single patch is not sufficient to describe a whole domain, in these scenarios several 'patches' can be used to create the full mesh. Unfortunately, across patch boundaries the representation is only C^0 continuous [Kiendl et al., 2010], which means that a smooth interpolation over a single, continuous plate of arbitrary shape is not always possible with NURBS.

NURBS have the advantage of being able to exactly represent common geometric shapes such as circles and spheres and additionally have easily modifiable continuity between NURBS 'elements'. However, the aforementioned disadvantage associated with patch continuity, makes them unfavourable for generic problems. Proposed methods to alleviate this include the introduction of 'bending strips' [Kiendl et al., 2010], which effectively introduce a stiff 'strip' over the patch boundary, which have a bending stiffness but no membrane stiffness. This is to prevent kinks forming in the sheet: however, it introduces an additional control parameter (relative stiffness of the strip) at patch boundaries, which does not have a direct physical origin [Kiendl et al., 2010].

Alternatively other, more general, interpolating functions such as T-splines can be used [Bazilevs et al., 2010], of which NURBS form a special case. T-splines can mesh any domains with a single patch: however, at so-called 'extraordinary points', i.e. vertices at which the

number of edges meeting is not four, the T-spline basis forms a gradient discontinuity, similar to the above NURBS elements [Scott et al., 2013; Kapl et al., 2018], again making generic meshing of domains trickier.

A recent contribution to the literature was the introduction of a multi-patch parameterization that is C^1 continuous between patches, which can be of arbitrary connectivity, by utilising ideas from classical Hermite-type interpolation [Kapl et al., 2019]. These multi-patch parameterizations are suitable even for unstructured quadrilateral meshes of patches, therefore providing a powerful and general analysis tool.

For an excellent introduction into the use of the isogeometric analysis for use in plate and shell models we direct the interested reader to the reviews of Kiendl [2011]; Nguyen et al. [2015] and the work of Schillinger [2018], which provide an overview of the subject. For further reading on NURBS see Piegl and Tiller [1997].

Subdivision Surfaces

A closely related method to isogeometric analysis is the method of *subdivision surfaces*: this method once again uses CAD functions to provide interpolation of both geometry and unknowns [Cirak et al., 2000; Cirak and Ortiz, 2001]. These functions can provide extremely efficient numerical simulations, apparently requiring only a single quadrature point per 'element' for quadratic convergence [Cirak et al., 2000; Cirak and Ortiz, 2001; Cirak et al., 2002]; the disadvantage of such methods is that basis functions have support over a ring of neighbouring elements. Additionally, such methods rely on topologically hexagonal tessellations, where on boundaries one can introduce artificial nodes ('control points') to ensure the elements conform to the boundary. Whilst modifications can be made to allow the inclusion of 'extraordinary points', i.e vertices at which more or less than six elements meet, this introduces gradient discontinuities [Cirak et al., 2000]. Thus, meshing arbitrary boundaries becomes a non-trivial affair.

Boundary Patches

Finally, one may augment the Hermite simplex elements by the use boundary patches of 'curved elements' in order to approximate non-polygonal geometries. This is done by introducing a layer of elements which have single curved edge and are C^1-continuous with the chosen bulk elements.

One of the major advantages of this method is that standard triangular mesh generation can be used to generate the mesh. Additionally, because these elements are compatible with their simplex counterparts and as well as other curved element in their class, a mixture can be used to mesh a domain. This means that the curved elements can be confined only to boundaries that require the additional continuity, rather than everywhere in the domain or on all boundaries. This has the added advantage that the increased order integration schemes for higher order elements are only needed for the boundary patches, which results in more efficient evaluation of the residuals and stiffness matrix in the bulk mesh.

We choose this final method of introducing boundary 'patches' of curved elements in this thesis, as this technique remains relatively unexplored in the literature. This is despite the fact that curved boundary patches represent arguably the best solution for solving generic, two-dimensional, fourth-order, boundary-value problems in triangulated domains. Thus the implementation of a generic, conforming method for solving generic fourth-order problems represents an interesting contribution to the literature.

We proceed to first outline the Bell element and then its curved counterpart. Though we discuss the Argyris element and its curved counterpart briefly, we do not discuss it in detail in this thesis as its explicit formulation and implementation has been studied in the context of several (linear) shell problems by Bernadou [1994].

4.3 Notation

In the finite element method it is common, as we have seen in previous sections to refer to basis functions on a *reference* element, which is common to all elements. For this section we use hats to indicate vectors and functions on the reference triangle. For example $\boldsymbol{x}$ would be the Cartesian position on the global triangle, whereas $\hat{\boldsymbol{x}}$ would be the position on the *reference* triangle, as shown in figure 4.13. Similarly the vertices $\boldsymbol{a}_i$ on the physical triangle are denoted $\hat{\boldsymbol{a}}_i$ on the corresponding reference triangle, again shown in figure 4.13.

In this section, once again we denote the standard Cartesian unit vectors as $\hat{\boldsymbol{e}}_\alpha$. We use the two dimensional gradient, $\boldsymbol{\nabla}$, to mean:

$$\boldsymbol{\nabla}(\cdot) = \frac{\partial}{\partial x_\alpha}(\cdot)\hat{\boldsymbol{e}}_\alpha \tag{4.3.1}$$

and the two dimensional gradient operator on the reference triangle:

$$\hat{\boldsymbol{\nabla}}(\cdot) = \frac{\partial}{\partial \hat{x}_\alpha}(\cdot)\hat{\boldsymbol{a}}_\alpha \tag{4.3.2}$$

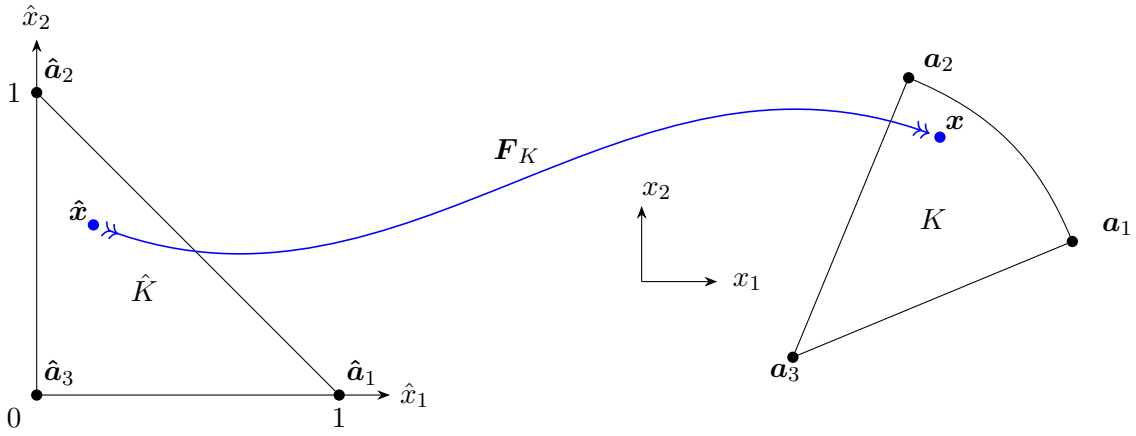

Figure 4.13: Diagram showing the (in general curved) global (right) and reference (left) triangles. The reference triangle is shared between *all* elements.

where we note that the positions of the vertices $\hat{\boldsymbol{a}}_\alpha$ coincide with the Cartesian basis vectors on the reference element, $\hat{\boldsymbol{a}}_\alpha$, and $\hat{\boldsymbol{a}}_3$ is located at the origin as shown in figure 4.13. Finally we use the notation P_n to denote a generic order n polynomial throughout.

4.4 The Bell and Argyris Elements

In this section we discuss the Argyris element and the related Bell element. These elements are both commonly used for C^1-continuous interpolation over triangulated domains: however both elements are subparametric and straight-sided. For this study we use Bell elements, due to the lower number of degrees of freedom as compared to Argyris elements, but as the elements share many properties, we discuss both. The Argyris triangle shares the Bell degrees of freedom: which are the zeroth, first and second derivatives at each vertex, but also has additional normal degrees of freedom along the edges, which allow it to form a complete P_5 polynomial.

4.4.1 Properties

The Bell [1969] triangle provides a C^1 continuous interpolation scheme over a triangulated domain using 18, Hermite-type, degrees of freedom [Okabe, 1994] per element. It is closely related to the Argyris triangle [Masayuki, 1993], and can be obtained from the Argyris triangle by imposing that the normal slope on the edge of the element be a degree 3 polynomial of two variables; this allows the elimination of the mid-side normal-derivative degrees of freedom. The Bell triangle is 4-unisolvent, meaning that any degree 4 polynomial on the

domain can be represented exactly.

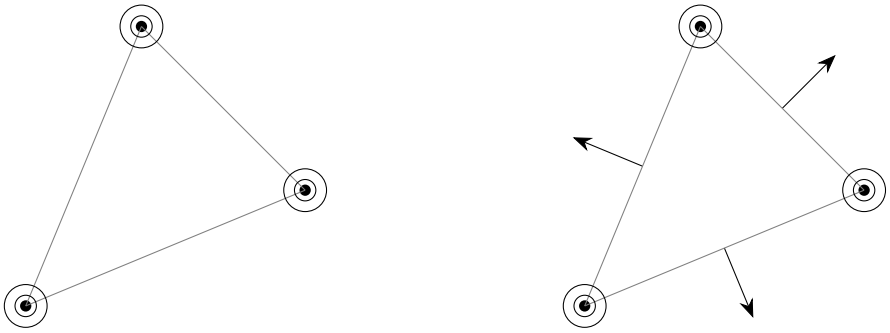

Figure 4.14: The Bell (left) and Argyris (right) elements, showing the degrees of freedom. A dot indicates a normal Lagrange (zeroth derivative) degree of freedom, the (two) first derivative degrees of freedom are indicated by the inner circle and the (three) second derivative degrees of freedom by the outer circle. Normal derivative degrees of freedom are indicated by an arrow.

We proceed to discuss the degrees of freedom and write the explicit interpolation basis. This basis depends on the spatial coordinates, through the linear basis functions defined in section 4.1.4. and the positions of the three vertices in space. The degrees of freedom for the Bell-triangle are the function values at each vertex, $w(\hat{\boldsymbol{a}}_i)$, the first partial derivatives, $\partial w(\hat{\boldsymbol{a}}_i)/\partial x_\alpha$ and the three second partial derivatives, $\partial^2 w(\hat{\boldsymbol{a}}_i)/\partial x_\alpha \partial x_\beta$, with $\alpha \leq \beta$, $\alpha, \beta \in \{1, 2\}$ as displayed in figure 4.14. Also shown is the Argyris triangle, which has three additional normal-derivative degrees of freedom. For the Bell element, this totals 6 degrees of freedom per vertex node - 18 for each element. In this work, we only discuss the explicit formulas for the Bell element.

4.4.2 Defining the Basis

Intuitively, the basis, $\psi_k^{[0]}$, is the unique set of polynomial functions which span the interpolation space and have the Kronecker delta property: that is, if we obtain the k^{th} degree of freedom (or unknowns), $\Sigma_k^{[0]}$, from a function $w(\boldsymbol{x})$ with the transformation $w \underset{U_k}{\rightarrow} \Sigma_k^{[0]}$ by some operator U_k, then the operation of U_k on the basis function yields the Kronecker delta: $\psi_j^{[0]} \underset{U_k}{\rightarrow} \delta_{jk}$.

In the case of Bell elements the operator U_k is a differential operator returning the k^{th} Hermite degree of freedom:

$$\Sigma_i^{[0]\,m,n} = U_k\, w(\boldsymbol{x}) = \frac{\partial^{m+n}}{\partial x_1^m \partial x_2^n} w(\hat{\boldsymbol{a}}_i)\,, \quad m \in \{0, \ldots, 2\}\,,\, n \in \{0, \ldots\, 2 - m\} \tag{4.4.1}$$

where we have labelled the degrees of freedom by the derivative order, m, n, and the node number i. Here the k^{th} degree of freedom is enumerated by a unique combination (i, m, n). Written explicitly, the degrees of freedom are:

$$\boldsymbol{\Sigma}^{[0]} = \left[w(\boldsymbol{a}_i) \; ; \; \frac{\partial w}{\partial x_1}(\boldsymbol{a}_i) \; ; \; \frac{\partial w}{\partial x_2}(\boldsymbol{a}_i) \; ; \; \frac{\partial^2 w}{\partial x_1^2}(\boldsymbol{a}_i) \; ; \; \frac{\partial^2 w}{\partial x_1 \partial x_2}(\boldsymbol{a}_i) \; ; \; \frac{\partial^2 w}{\partial x_2^2}(\boldsymbol{a}_i) \; \middle| \; i \in \{1,2,3\} \right], \tag{4.4.2}$$

In the case of the Bell elements the relevant polynomial space is the trial function space incorporating all P_5 polynomials with P_3 normal derivatives on the edges of the triangle $(\boldsymbol{a}_1, \boldsymbol{a}_2, \boldsymbol{a}_3)$ [Okabe, 1994].

Given this, the interpolated function, $\pi w(\boldsymbol{x})$, on the triangle will be

$$\pi w(\boldsymbol{x}) = \sum_{i=1}^{3} \sum_{m=0}^{2} \sum_{n=0}^{2-m} \Sigma_i^{[0]\,m,n} \, \psi_{H\,i}^{[0]\,m,n}(\boldsymbol{x}). \tag{4.4.3}$$

We now repeat the explicit formulas for the Bell basis polynomials, as outlined by Okabe [1994]. We describe elements in terms of the three linear basis functions for a triangle of section 4.1.4, ω_i, which are given in terms of Cartesian coordinates by

$$\omega_i(\boldsymbol{x}) = \frac{1}{A} \left((\boldsymbol{a}_{i+1} - \boldsymbol{x}) \times (\boldsymbol{a}_{i+2} - \boldsymbol{x}) \right) \cdot \boldsymbol{k} \,. \tag{4.4.4}$$

in which $i \in \{1,2,3\}$ and we have implicitly used modulo 3 for $i+1$, $i+2$ etc.. $\boldsymbol{x}$ labels the Cartesian position $\boldsymbol{x} = x_1 \hat{\boldsymbol{e}}_1 + x_2 \hat{\boldsymbol{e}}_2$, and $\boldsymbol{a}_i$ labels the Cartesian position of the i^{th} vertex, with components $\boldsymbol{a}_i \cdot \hat{\boldsymbol{e}}_1$ and $\boldsymbol{a}_i \cdot \hat{\boldsymbol{e}}_2$ in the two coordinate directions. Here we reiterate that we have *not* used Einstein notation. Finally, A, denotes twice the signed area of the triangle, calculated by

$$A = \left((\boldsymbol{a}_{i+1} - \boldsymbol{a}_i) \times (\boldsymbol{a}_{i+2} - \boldsymbol{a}_i) \right) \cdot \boldsymbol{k} \,. \tag{4.4.5}$$

in which $i \in \{1,2,3\}$ and we implicitly use modulo 3 for $i+1$, $i+2$ etc..

This linear basis is often referred to as a set of area coordinates, as they can be interpreted geometrically as the ratio of signed area of the triangle $(\boldsymbol{x}, \boldsymbol{a}_{i+1}, \boldsymbol{a}_{i+2})$ to the signed area of the triangle $(\boldsymbol{a}_i, \boldsymbol{a}_{i+1}, \boldsymbol{a}_{i+2})$, as shown in figure 4.15.

We now define the constants, α_{ij}, which are used in the expression of the basis functions:

$$\alpha_{ij} = \frac{\omega_{i,n_j}}{\omega_{j,n_j}} \,, \tag{4.4.6}$$

where $f_{,n_j}$ labels the derivative of a function $f(\boldsymbol{x})$ in the direction normal to the j^{th} edge and, once again, there is no implicit summation over j.

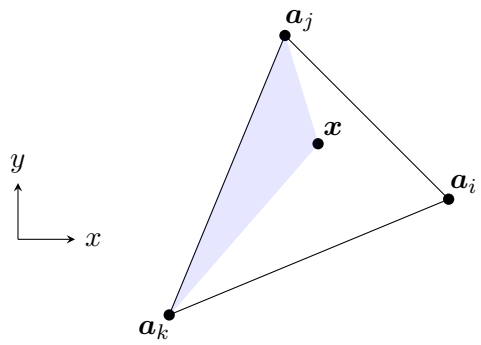

Figure 4.15: Image showing the geometric meaning of area coordinate ω_i. This will be the ratio of the area of the shaded triangle to the total (unshaded) area.

In the constants, α_{ij} we may use either the inward or outward normal: which need not be of unit length. We use the following normal, $\boldsymbol{n}_i$, vector on the side opposite to vertex i

$$\boldsymbol{n}_i \equiv (\boldsymbol{a}_{i+2} - \boldsymbol{a}_{i+1}) \times \boldsymbol{k}\,, \tag{4.4.7}$$

where once again $i \in \{1, 2, 3\}$ and we implicitly use modulo 3 for $i+1$, $i+2$ etc..

The explicit interpolation basis is then given by [Okabe, 1994]

$$\psi^{[0]\,0,0}_{H\,i} = \omega_i^3(10 - 15\omega_i + 6\omega_i^2) - 30(\alpha_{i,(i+1)}\omega_{i+2} + \alpha_{i,(i+2)}\omega_{i+1})\omega_i^2\omega_{i+1}\omega_{i+2}\,, \tag{4.4.8}$$

$$\begin{aligned}\psi^{[0]\,1,0}_{H\,i} = {}& \omega_i^3(4 - 3\omega_i)(x_1 - a_{1\,i}) + \big(15(a_{1\,i} - a_{1\,i+2})\alpha_{i,(i+1)} + 3(a_{1\,i+1} - a_{1\,i+2})\big)\,\omega_i^2\omega_{i+1}\omega_{i+2}^2 \\ & + \big(15(a_{1\,i} - a_{1\,i+1})\alpha_{i,(i+2)} + 3(a_{1\,i+2} - a_{1\,i+1})\big)\,\omega_i^2\omega_{i+1}^2\omega_{i+2}\,,\end{aligned} \tag{4.4.9}$$

$$\begin{aligned}\psi^{[0]\,0,1}_{H\,i} = {}& \omega_i^3(4 - 3\omega_i)(x_2 - a_{2\,i}) + \big(15(a_{2\,i} - a_{2\,i+2})\alpha_{i,(i+1)} + 3(a_{2\,i+1} - a_{2\,i+2})\big)\,\omega_i^2\omega_{i+1}\omega_{i+2}^2 \\ & + \big(15(a_{2\,i} - a_{2\,i+1})\alpha_{i,(i+2)} + 3(a_{2\,i+2} - a_{2\,i+1})\big)\,\omega_i^2\omega_{i+1}^2\omega_{i+2}\,,\end{aligned} \tag{4.4.10}$$

$$\begin{aligned}\psi^{[0]\,2,0}_{H\,i} = {}& \omega_i^3(x_1 - a_{1\,i})^2/2 \\ & - (a_{1\,i} - a_{1\,i+2})\big(5(a_{1\,i} - a_{1\,i+2})\alpha_{i,(i+1)} + 2(a_{1\,i+1} - a_{1\,i+2})\big)\,\omega_i^2\omega_{i+1}\omega_{i+2}^2 \\ & - (a_{1\,i} - a_{1\,i+1})\big(5(a_{1\,i} - a_{1\,i+1})\alpha_{i,(i+2)} + 2(a_{1\,i+2} - a_{1\,i+1})\big)\,\omega_i^2\omega_{i+1}^2\omega_{i+2}\,,\end{aligned} \tag{4.4.11}$$

$$\begin{aligned}\psi^{[0]\,1,1}_{H\,i} = {}& \omega_i^3(x_1 - a_{1\,i})(x_2 - a_{2\,i}) - \big((a_{2\,i} - a_{2\,i+2})\big(5(a_{1\,i} - a_{1\,i+2})\alpha_{i,(i+1)} + 2(a_{1\,i+1} - a_{1\,i+2})\big) \\ & + (a_{1\,i} - a_{1\,i+2})\big(5(a_{2\,i} - a_{2\,i+2})\alpha_{i,(i+1)} + 2(a_{2\,i+1} - a_{2\,i+2})\big)\big)\omega_i^2\omega_{i+1}\omega_{i+2}^2 \\ & - \big((a_{2\,i} - a_{2\,i+1})(5(a_{1\,i} - a_{1\,i+1})\alpha_{i,(i+2)} + 2(a_{1\,i+2} - a_{1\,i+1})) \\ & + (a_{1\,i} - a_{1\,i+1})\big(5(a_{2\,i} - a_{2\,i+1})\alpha_{i,(i+2)} + 2(a_{2\,i+2} - a_{2\,i+1})\big)\big)\omega_i^2\omega_{i+1}^2\omega_{i+2}\end{aligned} \tag{4.4.12}$$

$$\begin{aligned}\psi^{[0]\,0,2}_{H\,i} = {}& \omega_i^3(x_2 - a_{2\,i})^2/2 \\ & - (a_{2\,i} - a_{2\,i+2})\big(5(a_{2\,i} - a_{2\,i+2})\alpha_{i,(i+1)} + 2(a_{2\,i+1} - a_{2\,i+2})\big)\,\omega_i^2\omega_{i+1}\omega_{i+2}^2 \\ & - (a_{2\,i} - a_{2\,i+1})\big(5(a_{2\,i} - a_{2\,i+1})\alpha_{i,(i+2)} + 2(a_{2\,i+2} - a_{2\,i+1})\big)\,\omega_i^2\omega_{i+1}^2\omega_{i+2}\,,\end{aligned} \tag{4.4.13}$$

with $x_\alpha = \sum_{l=0}^{3} a_{\alpha\, l}\, \omega_l$. Once again $i \in \{1, 2, 3\}$ and we implicitly use modulo 3 for $i + 1$, $i + 2$ etc.. Here we note that under permutation, cyclic or otherwise, of the index i the basis functions remain unchanged. These basis functions are plotted in figure 4.16.

4.4.3 Cartesian Derivatives

In the variational principle, derivatives with respect to the physical, Cartesian coordinates appear, $\boldsymbol{x}$, rather than derivatives with respect to the local coordinates, $\hat{\boldsymbol{x}}$. However, it is more convenient to express the derivatives with-respect-to local (reference) coordinates and then transform to the global derivatives, using the Jacobian and Hessian of the mapping.

In the above formulation, derivatives with respect to Cartesian coordinates can be computed in principle, as the basis can be readily expressed in Cartesian coordinates using the definition of the area coordinates. However, in most contexts the derivatives with respect to the local coordinates are more desirable, as the expressions for the basis functions are typically much more straightforward.

We start by considering the first derivatives with respect to Cartesian coordinates. These can be straightforwardly constructed as

$$\frac{\partial \psi_{H\, i}^{[0]\, j,k}}{\partial x_\alpha} = \frac{\partial \psi_{H\, i}^{[0]\, j,k}}{\partial \omega_l} \frac{\partial \omega_l}{\partial x_\alpha} = \frac{\partial \psi_{H\, i}^{[0]\, j,k}}{\partial \omega_l} \frac{\partial \omega_l}{\partial \hat{x}_\beta} \left(\boldsymbol{J}^{-1}\right)_{\beta\alpha} \tag{4.4.14}$$

in which we use the Jacobian of the area to local coordinates:

$$\frac{\partial \omega_\alpha}{\partial \hat{x}_\beta} = \delta_{\alpha\beta}\,, \quad \frac{\partial \omega_3}{\partial \hat{x}_\beta} = -1\,, \tag{4.4.15}$$

and

$$\left(\boldsymbol{J}^{-1}\right)_{\alpha\beta} = \frac{\partial \hat{x}_\beta}{\partial x_\alpha}\,. \tag{4.4.16}$$

are components of the inverse Jacobian of the mapping from local to Cartesian coordinates

Since the mapping from Cartesian to local coordinates is linear, the second derivatives can be expressed in terms of only the area to local and local to Cartesian Jacobian and the second, local derivatives. Thus, Cartesian second derivatives can be constructed in terms of area coordinate derivatives as

$$\frac{\partial^2 \psi_{H\, i}^{[0]\, j,k}}{\partial x_\alpha \partial x_\beta} = \frac{\partial \psi_{H\, i}^{[0]\, j,k}}{\partial \omega_l \partial \omega_m} \frac{\partial \omega_l}{\partial \hat{x}_\gamma} \left(\boldsymbol{J}^{-1}\right)_{\gamma\alpha} \frac{\partial \omega_m}{\partial \hat{x}_\delta} \left(\boldsymbol{J}^{-1}\right)_{\delta\beta}\,. \tag{4.4.17}$$

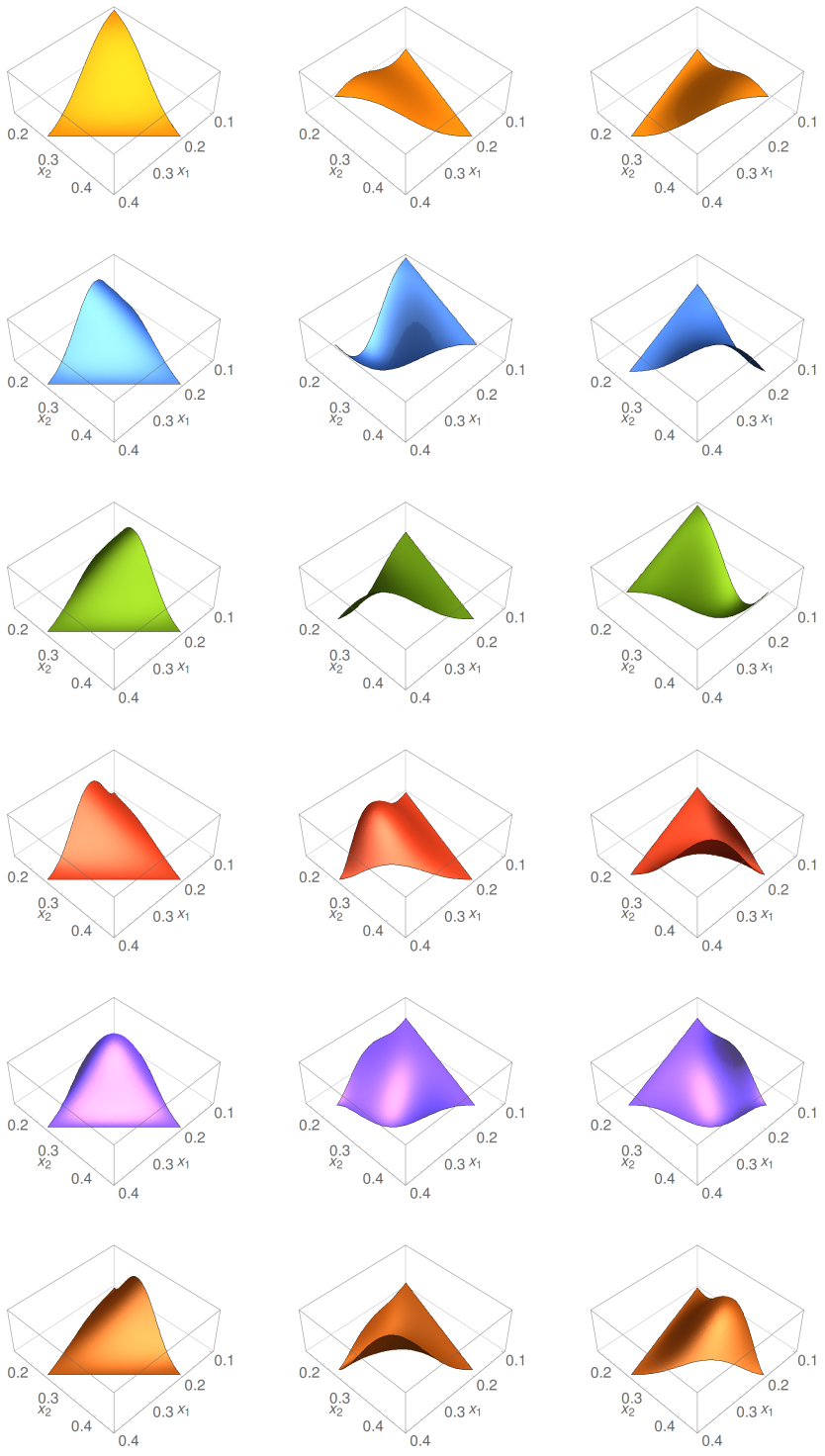

Figure 4.16: Bell basis functions shown for a particular triangle. The different nodal basis functions are shown by column and the different degree of freedom types are shown by row, in various colours. By row the degrees of freedom are ordered as follows: $w(\boldsymbol{a}_i)$, $\partial w(\boldsymbol{a}_i)/\partial x_1$, $\partial w(\boldsymbol{a}_i)/\partial x_2$, $\partial^2 w(\boldsymbol{a}_i)/\partial x_1^2$, $\partial^2 w(\boldsymbol{a}_i)/\partial x_1 \partial x_2$ and $\partial^2 w(\boldsymbol{a}_i)/\partial x_2^2$. The Kronecker-delta property can be readily seen: for example, $\psi_{H,2}^{[0]\,(0,0)}$ is zero at $\boldsymbol{a}_1$ and $\boldsymbol{a}_3$ and unity at $\boldsymbol{a}_2$ with zero slope and curvature at all three nodes.

4.4.4 Subparametric Triangle Elements

To clarify the ideas we now quickly summarize the structure the Bell element will adopt within the library. To begin, we introduce a new object to aid in the description of non-isoparametric elements. We propose a new more generic structure to incorporate such elements, which is shown in figure 4.17. The new object we propose is a non-isoparametric element, which provides both shape functions (to interpolate the geometry) and basis functions (to interpolate the unknowns).

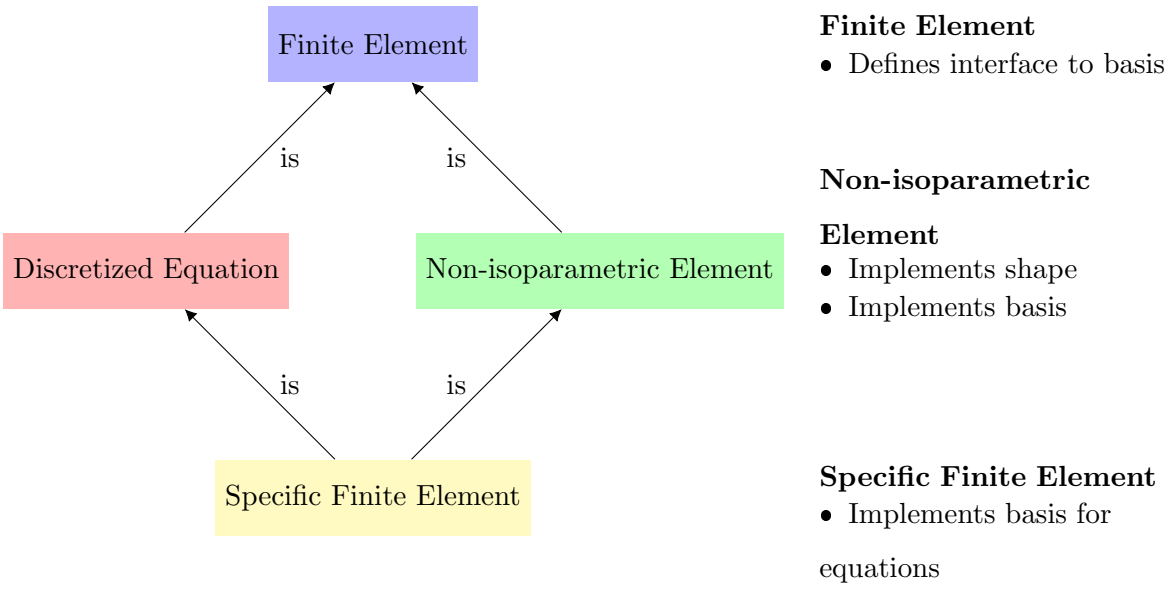

Figure 4.17: The revised structure for non-isoparametric elements within `oomph-lib`. New functionality is required in the sub-parametric triangle element, which replaces the geometric element within the structure, to provide distinct basis and shape functions.

As shown in figure 4.17, a non-isoparametric element assumes the role of a geometric element, but also has basis functions. This is in contrast to isoparametric elements in which the geometric shape functions are reused as basis functions for the unknowns, so this distinction would be unnecessary. We implement a new non-isoparametric element within the library: a subparametric triangle element (`SubparametricTElement`), which provides the base class for the new Bell elements.

A Bell element (`BellElement`) is therefore a kind of geometric element which also has a set of Hermite basis functions (the Bell basis functions) to interpolate the unknowns. It derives directly from a subparametric triangle element, which in turn derives from a two-dimensional triangle element (a geometric element): in `oomph-lib` the parent class is

`TElement<2,NNODE_1D>`. In general subparametric triangle elements may provide any order Lagrange basis (parameterized by the number of nodes per side: `NNODE_1D`). However, Bell triangles must always have straight-sides, so shape must be overridden (i.e. by providing linear shape functions) to account for this. We retain the template parameter `NNODE_1D` however, as the higher order Lagrange bases may be required in derived multi-physics elements. The Bell element must also provide the interface to the number of degree-of-freedom types per node. Subparametic triangle elements fulfil the role of the discussed non-isoparametric element and provide an interface to both a basis and a geometry. This is summarized in figure 4.18.

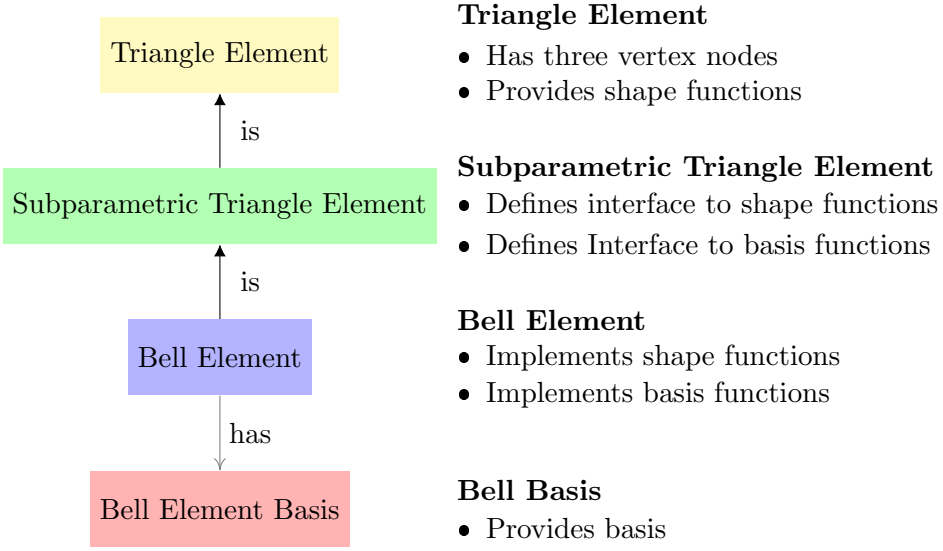

Figure 4.18: The structure of a Bell element within `oomph-lib`. Bell elements are a subparametric triangle element, which assume the role of the outlined non-isoparametric element.

Thus we may outline the new class and its key members, using the following (simplified) code snippets shown in figures 4.19 and 4.20. This is not the final structure: as we add new functionality, this structure will be modified to incorporate new element-types. Now that we have outlined an interpolation scheme suitable for polygonal domains we proceed to discuss the curved counterparts used for boundary patches.

```
// Class for generic subparametric triangle elements
template<unsigned NNODE_1D>
class SubparametricTElement : public TElement<2,NNODE_1D> {
public:
  // Access functions for number of nodal dof types
  virtual unsigned nnodal_basis_types() = 0;
  // Access to basis
  virtual void basis(Vector<double>& local_coord, Shape& basis) = 0;
  // Shape provided by inheritance
```

Figure 4.19: Code snippet illustrating the structure of a subparametric triangle element.

```
// Class for straight-sided Bell elements: a new subparametric element
template<unsigned NNODE_1D>
class BellElement : public SubparametricTElement<NNODE_1D> {
public:
  // Implements functions for number of nodal dof types
  unsigned nnodal_basis_types();
  // Implements basis
  void basis(Vector<double>& local_coord, Shape& basis);
  // Override inherited shape with linear shape.
  void shape(Vector<double>& local_coord, Shape& shape);
private:
 // Pointer to the class that defines the Bell basis functions
 BellElementBasis* Bell_element_basis_pt;
```

Figure 4.20: Code snippet illustrating the implementation of a Bell element. In general we require `NNODE_1D` elements with straight sides, for use in multi-physics problems.

4.5 The Curved Bell Element

As we have previously asserted, (affine) Bell elements are not suitable for the description of curved boundaries as they can only interpolate the geometry linearly. Instead, for the accurate representation of curved domains we use the curved Bell element outlined by Bernadou [1992, 1993a], which was apparently first derived by Ženíšek [1978]: we refer to these elements as curved Bell elements. This element is compatible (C^1-continuous) with the Bell element

but uses an increased polynomial order in the interior to allow a single edge to be curved. An alternative exists for the related Argyris element, which has extra normal degrees of freedom associated with each edge. We frequently refer to curved-Bell elements as 'curved triangles': which we take to mean three–sided shapes in which one of the sides is curved and the other two straight.

This method of interpolation is relatively unexplored in the literature: the curved Argyris elements have been implemented in the finite element library Modulef [Bernadou et al., 1986], which in turn has been used to solve the linear shell model of Koiter [1970] (see [Bernadou, 1994]). Curved Bell elements have been used by Hřebíček [1982] to solve the general biharmonic equation and by Růžičková and Ženíšek [1984] in the approximation of visco-elastic linear bending of a plate. However, the use of curved-Bell elements for the solution of nonlinear, large displacement shell and plate models appears to be untouched in the literature.

The increase in polynomial order is achieved by introducing additional interior, or 'bubble' degrees of freedom, whilst constraining the element to share the same degrees of freedom on the edges. To ensure inter-element C^1 continuity between neighbouring curved and straight-sided Bell elements, the interpolated function, must have the same trace, i.e. the 1D function describing the function on the edge, and normal derivative trace, as any adjacent Bell or curved Bell elements share the same degrees of freedom on that edge. This is achieved, in turn, by constraining the basis to be a polynomial of order 5 on the straight edges, with the normal derivatives on the edges constrained to be order 3 polynomials, as is the case for affine Bell elements. Depending on the order of boundary interpolation required, a higher order polynomial, and thus more bubble degrees of freedom, are required in the interior of the element [Bernadou, 1992, 1993a].

We proceed to construct the basis for the Bell elements in the same manner outlined in Bernadou and Boisserie [1992, 1993] for the Argyris element. The definition of the elements is provided by Bernadou [1992, 1993a] but a detailed account of their construction is a useful addition to the literature, so we provide it in the next section.

4.5.1 Set-up of the Problem

Following Bernadou [1993a], we start by defining a boundary, Γ, which we suppose can be split up into a finite number of arcs, each with described by a sufficiently smooth parametric

function:

$$\boldsymbol{\chi}(s)\,, \quad \underline{s} \leq s \leq \bar{s}\,, \tag{4.5.1}$$

where s is the arc length. We also define an alternative parameterization

$$\boldsymbol{\Psi}(\hat{x}_2) = \boldsymbol{\chi}(\hat{x}_2(\bar{s} - \underline{s}) + \underline{s})\,, \quad 0 \leq \hat{x}_2 \leq 1\,, \tag{4.5.2}$$

where $\hat{x}_2$ is the local coordinate that is 0 at node a_1 and 1 at node a_2. We wish to express the basis on a single 'reference triangle' and with that in mind we define the reference triangle $\hat{K}$, as shown in figure 4.21.

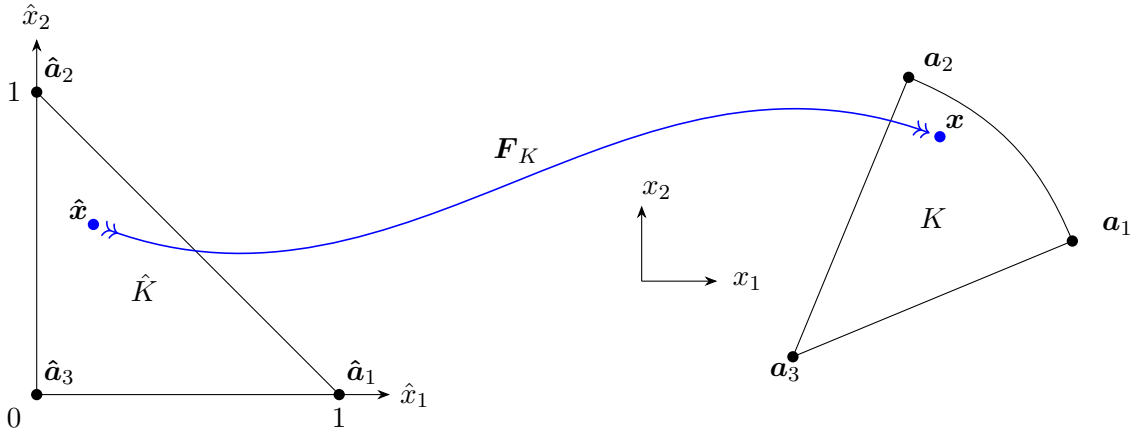

Figure 4.21: Diagram showing the geometry of the reference and curved triangles.

We now define an approximate arc, $\boldsymbol{\Psi}_h(\hat{x}_2)$, that interpolates the exact arc $\boldsymbol{\Psi}(\hat{x}_2)$, by a polynomial of order m:

$$\boldsymbol{\Psi}_h = \boldsymbol{a}_1 + (\boldsymbol{a}_2 - \boldsymbol{a}_1)\hat{x}_2 + \hat{x}_2(1 - \hat{x}_2)\boldsymbol{f}_{m-2}(\hat{x}_2)\,, \tag{4.5.3}$$

where components of $\boldsymbol{f}_{m-2}$ are as-yet undetermined polynomials of degree $m-2$ with respect to $\hat{x}_2$.

In order to define a mapping, $\boldsymbol{F}_K$ that takes us from the unit reference triangle, $\hat{K}$, to the curved triangle on the approximated domain, K, as shown in figure 4.21, we first define the coordinates, $\hat{x}_1$ and $\hat{x}_2$ which parameterize the position on the reference triangle, $\hat{K}$. The mapping is thus given by

$$\boldsymbol{F}_K = \boldsymbol{a}_3 + (\boldsymbol{a}_1 - \boldsymbol{a}_3)\hat{x}_1 + (\boldsymbol{a}_2 - \boldsymbol{a}_3)\hat{x}_2 + \frac{1}{2}\hat{x}_1\hat{x}_2\left(\boldsymbol{f}_{m-2}(1 - \hat{x}_1) + \boldsymbol{f}_{m-2}(\hat{x}_2)\right) \tag{4.5.4}$$

which we have constructed such that $\boldsymbol{F}_K(1 - \hat{x}_2, \hat{x}_2) = \boldsymbol{\Psi}_h(\hat{x}_2)$. We visualize the mapping for the case of an approximated circular arc in figure 4.22.

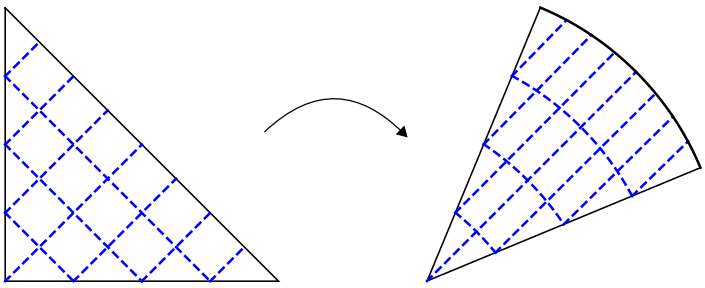

Figure 4.22: An example of a mapping, $\boldsymbol{F}_K$ from reference element $\hat{K}$ to curved element K. K is the approximated domain and the mapping is, in general non-affine. We illustrate the mapping by showing how a set of lines (dashed blue) transform to a set of curves on the curved element. In this instance the curve-section is a polynomial approximation to a circular arc.

With this framework in place, we specialise to two particular cases which are of importance to this study: degree 3 and degree 5 interpolation of the boundary. A well known contribution of Ženíšek [1981a,b] was to demonstrate that in Kirchhoff-Love-type problems it is necessary to use at least third order (C^1-continuous) boundary interpolation to correctly impose homogeneous Dirichlet-type boundary conditions and fifth order (C^2-continuous) interpolation for generic boundary conditions. With these two important cases in mind, we follow Bernadou [1993b] in defining two curved elements of the same class that can use these two boundary interpolations. It is important to note, that the P_5 order elements do not improve upon the convergence rate of the P_3 elements; however, they are necessary for the imposition of generic boundary conditions.

With the aim of characterising both clamped and free systems in mind, we define the mappings for these two cases. For the third order boundary interpolation, we interpolate based on the known values of the tangent at the vertices, $s = \underline{\mathrm{s}}$ and $s = \bar{s}$. These tangents are given by $\boldsymbol{\chi}'(\underline{\mathrm{s}})$ and $\boldsymbol{\chi}'(\bar{s})$. This interpolation provides a C^1-continuous boundary interpolation between curved elements. It can be shown that the approximated boundary is given by [Bernadou, 1993b]

$$\boldsymbol{\Psi}_h = \boldsymbol{a}_1 + (\boldsymbol{a}_2 - \boldsymbol{a}_1)\hat{x}_2 + \hat{x}_2(1 - \hat{x}_2)\boldsymbol{f}_1(\hat{x}_2)\,, \tag{4.5.5}$$

in which $\boldsymbol{f}_1(\hat{x}_2)$ has the following expression:

$$\boldsymbol{f}_1(\hat{x}_2) \equiv \left(2(\boldsymbol{a}_2 - \boldsymbol{a}_1) - (\bar{s} - \underline{\mathrm{s}})(\boldsymbol{\chi}'(\underline{\mathrm{s}}) + \boldsymbol{\chi}'(\bar{s}))\right)\hat{x}_2 + \boldsymbol{a}_1 - \boldsymbol{a}_2 + (\bar{s} - \underline{\mathrm{s}})\boldsymbol{\chi}'(\underline{\mathrm{s}})\,. \tag{4.5.6}$$

Following this, the mapping is given by

$$\boldsymbol{F}_K = \boldsymbol{a}_3 + (\boldsymbol{a}_1 - \boldsymbol{a}_3)\hat{x}_1 + (\boldsymbol{a}_2 - \boldsymbol{a}_3)\hat{x}_2 + \frac{1}{2}\hat{x}_1\hat{x}_2\left(\boldsymbol{f}_1(1-\hat{x}_1) + \boldsymbol{f}_1(\hat{x}_2)\right) . \tag{4.5.7}$$

which can be more straightforwardly expressed, as [Bernadou, 1993b]

$$\begin{aligned}\boldsymbol{F}_K = \boldsymbol{a}_3 + (\boldsymbol{a}_1 - \boldsymbol{a}_3)\hat{x}_1 + (\boldsymbol{a}_2 - \boldsymbol{a}_3)\hat{x}_2 + \frac{1}{2}\hat{x}_1\hat{x}_2\big(\big[2(\boldsymbol{a}_2 - \boldsymbol{a}_1)\\ - (\bar{s} - \underline{s})(\boldsymbol{\chi}'(\underline{s}) + \boldsymbol{\chi}'(\bar{s}))\big](\hat{x}_2 - \hat{x}_1) + (\bar{s} - \underline{s})(\boldsymbol{\chi}'(\underline{s}) - \boldsymbol{\chi}'(\bar{s}))\big) .\end{aligned} \tag{4.5.8}$$

For the fifth order case it can be shown that the interpolation of the boundary has the following expression:

$$\boldsymbol{\Psi}_h = \boldsymbol{a}_1 + (\boldsymbol{a}_2 - \boldsymbol{a}_1)\hat{x}_2 + \hat{x}_2(1-\hat{x}_2)\boldsymbol{f}_3(\hat{x}_2) , \tag{4.5.9}$$

in which $\boldsymbol{f}_3(\cdot) \equiv \{\boldsymbol{f}_{m-2}(\cdot) : m = 5\}$ is given by:

$$\boldsymbol{f}_3 \equiv \boldsymbol{\beta}_3\,\hat{x}_2^3 + \boldsymbol{\beta}_2\,\hat{x}_2^2 + \boldsymbol{\beta}_1\,\hat{x}_2 + \boldsymbol{\beta}_0 , \tag{4.5.10}$$

which is used in the definition of $\boldsymbol{F}_K$ and $\boldsymbol{\Psi}_h$. The polynomial coefficients, β_m, $m \in \{0, \ldots 3\}$, is

$$\boldsymbol{\beta}_0 = \boldsymbol{a}_1 - \boldsymbol{a}_2 + (\bar{s} - \underline{s})\boldsymbol{\chi}'(\underline{s}) , \tag{4.5.11}$$

$$\boldsymbol{\beta}_1 = \boldsymbol{a}_1 - \boldsymbol{a}_2 + (\bar{s} - \underline{s})\boldsymbol{\chi}'(\underline{s}) + \frac{1}{2}(\bar{s} - \underline{s})^2\boldsymbol{\chi}''(\underline{s}) , \tag{4.5.12}$$

$$\boldsymbol{\beta}_2 = 9(\boldsymbol{a}_2 - \boldsymbol{a}_1) - (\bar{s} - \underline{s})\left(5\boldsymbol{\chi}'(\underline{s}) + 4\boldsymbol{\chi}'(\bar{s})\right) - \frac{1}{2}(\bar{s} - \underline{s})^2\left(2\boldsymbol{\chi}''(\underline{s}) - \boldsymbol{\chi}''(\bar{s})\right) , \tag{4.5.13}$$

$$\boldsymbol{\beta}_3 = 6(\boldsymbol{a}_1 - \boldsymbol{a}_2) + 3(\bar{s} - \underline{s})\left(\boldsymbol{\chi}'(\underline{s}) + \boldsymbol{\chi}'(\bar{s})\right) + \frac{1}{2}(\bar{s} - \underline{s})^2\left(\boldsymbol{\chi}''(\underline{s}) - \boldsymbol{\chi}''(\bar{s})\right) . \tag{4.5.14}$$

Thus, the mapping is

$$\boldsymbol{F}_K = \boldsymbol{a}_3 + (\boldsymbol{a}_1 - \boldsymbol{a}_3)\hat{x}_1 + (\boldsymbol{a}_2 - \boldsymbol{a}_3)\hat{x}_1 + \frac{1}{2}\hat{x}_1\hat{x}_2\left(\boldsymbol{f}_3(1-\hat{x}_1) + \boldsymbol{f}_3(\hat{x}_2)\right) , \tag{4.5.15}$$

and again, the expressions in the mapping can be written alternatively as

$$\begin{aligned}\boldsymbol{F}_K = \boldsymbol{a}_3 + (\boldsymbol{a}_1 - \boldsymbol{a}_2)\hat{x}_1 + (\boldsymbol{a}_1 - \boldsymbol{a}_2)\hat{x}_1 - \frac{1}{2}\hat{x}_1\hat{x}_2\Big(\boldsymbol{\beta}_3\,(\hat{x}_2)^3 + \boldsymbol{\beta}_2\,(\hat{x}_2)^2 + \boldsymbol{\beta}_1\,(\hat{x}_2)\\ + \boldsymbol{\beta}_0 + \tilde{\boldsymbol{\beta}}_3\,(\hat{x}_2)^3 + \tilde{\boldsymbol{\beta}}_2\,(\hat{x}_2)^2 + \tilde{\boldsymbol{\beta}}_1\,(\hat{x}_2) + \tilde{\boldsymbol{\beta}}_0\Big) ,\end{aligned} \tag{4.5.16}$$

with the coefficients

$$\tilde{\boldsymbol{\beta}}_0 = \boldsymbol{a}_2 - \boldsymbol{a}_1 - (\bar{s} - \underline{s})\boldsymbol{\chi}'(\bar{s}) , \tag{4.5.17}$$

$$\tilde{\boldsymbol{\beta}}_1 = \boldsymbol{a}_2 - \boldsymbol{a}_1 - (\bar{s} - \underline{s})\boldsymbol{\chi}'(\bar{s}) + \frac{1}{2}(\bar{s} - \underline{s})^2\boldsymbol{\chi}''(\bar{s}) , \tag{4.5.18}$$

$$\tilde{\boldsymbol{\beta}}_2 = 9(\boldsymbol{a}_1 - \boldsymbol{a}_2) + (\bar{s} - \underline{s})\left(5\boldsymbol{\chi}'(\bar{s}) + 4\boldsymbol{\chi}'(\underline{s})\right) - \frac{1}{2}(\bar{s} - \underline{s})^2\left(2\boldsymbol{\chi}''(\bar{s}) - \boldsymbol{\chi}''(\underline{s})\right) , \tag{4.5.19}$$

$$\tilde{\boldsymbol{\beta}}_3 = 6(\boldsymbol{a}_2 - \boldsymbol{a}_1) - 3(\bar{s} - \underline{s})\left(\boldsymbol{\chi}'(\bar{s}) + \boldsymbol{\chi}'(\underline{s})\right) + \frac{1}{2}(\bar{s} - \underline{s})^2\left(\boldsymbol{\chi}''(\bar{s}) - \boldsymbol{\chi}''(\underline{s})\right) . \tag{4.5.20}$$

as shown in Bernadou [1993a].

4.5.2 Requirements

We require the basis to be C^1-continuous with adjacent Bell and curved Bell elements along the straight edges, which we denote by their opposing nodes, such that edge 2 is $[\boldsymbol{a}_1, \boldsymbol{a}_3]$, and edge 1 is $[\boldsymbol{a}_2, \boldsymbol{a}_3]$. The curved edge is then edge 3. Firstly, this entails that all degrees of freedom on edge 1 and 2 are identical to that of the Bell element [Bernadou, 1992]. For C^0-continuity we require that the interpolated function, w, is continuous between adjacent elements. With this in mind we demand the trace of the interpolated function on side $\bar{\alpha}$, $\hat{f}_\alpha \equiv w|_{[\boldsymbol{a}_3, \boldsymbol{a}_\alpha]}$, be a one-variable, degree 5 polynomial, entirely determined by the degrees of freedom at $\boldsymbol{a}_3$ and $\boldsymbol{a}_\alpha$. For C^1-continuity we also require that the normal derivative be continuous across boundaries: i.e that the normal derivative, $\hat{g}_\alpha \equiv \boldsymbol{\nabla} w|_{[\boldsymbol{a}_3, \boldsymbol{a}_\alpha]} \cdot \boldsymbol{n}_{\bar{\alpha}}\,,\ \bar{\alpha} \neq \alpha$, has a trace, which is an order 3 polynomial in a single variable, entirely determined by the first and second derivatives at the nodes $\boldsymbol{a}_3$ and $\boldsymbol{a}_\alpha$ [Bernadou, 1992].

To determine the order that the basis needs to be to satisfy these properties, we consider the derivatives of the interpolated function, $w(x_1, x_2) = \hat{w}(\hat{x}_1, \hat{x}_2)$, with respect to the coordinates $\hat{x}_\alpha$ evaluated at point $\boldsymbol{a} \in [\boldsymbol{a}_3, \boldsymbol{a}_\alpha]$, or $\hat{\boldsymbol{a}} \in [\hat{\boldsymbol{a}}_3, \hat{\boldsymbol{a}}_\alpha]$ on the reference element, which lies on edge $\bar{\alpha} \neq \alpha$, $\alpha \in \{1, 2\}$:

$$\frac{\partial \hat{w}}{\partial \hat{x}_\alpha}(\hat{\boldsymbol{a}}) = \boldsymbol{\nabla} w(\boldsymbol{a}) \cdot \frac{\partial \boldsymbol{F}_K}{\partial \hat{x}_\alpha}(\hat{\boldsymbol{a}}) = \frac{\partial \boldsymbol{F}_K}{\partial \hat{x}_\alpha}(\hat{\boldsymbol{a}}) \cdot (g_\alpha(\hat{x}_\alpha)\boldsymbol{n}_{\bar{\alpha}} + h_\alpha(\hat{x}_\alpha)\boldsymbol{t}_{\bar{\alpha}})\,, \quad \bar{\alpha} \neq \alpha \tag{4.5.21}$$

where we have *not* used summation convention. Here $g_\alpha \equiv \boldsymbol{\nabla} w(\boldsymbol{a}) \cdot \boldsymbol{n}_{\bar{\alpha}}\,,\ \bar{\alpha} \neq \alpha$ and $h_\alpha \equiv \boldsymbol{\nabla} w(\boldsymbol{a}) \cdot \boldsymbol{t}_{\bar{\alpha}}\,,\ \bar{\alpha} \neq \alpha$ are the normal and tangential derivatives on side $\bar{\alpha}$. We first note that, if the element is to conform with the Bell element, g_α and h_α must be a third and fourth order polynomials in $\hat{x}_\alpha$ respectively on the edge $\bar{\alpha}$. Using this in combination with the mapping, $\boldsymbol{F}_K$ which is an m^{th} order polynomial where, by observing the particular form of the mapping defined in equation (4.5.4), we can see that $\partial\hat{w}/\partial\hat{x}_1$ on side 2 and $\partial\hat{w}/\partial\hat{x}_2$ on side 1, must both be order $m+3$ order polynomials. Thus $\hat{w}$ must be at least an $m+4$ order polynomial in the two variables $\hat{x}_1$ and $\hat{x}_2$ [Bernadou, 1993a].

Thus, for the useful cases of $m = 3$ and $m = 5$ that we considered previously we will need a set of 'reference' polynomial basis functions, $\hat{\psi}^{[m]}$, on the reference element, $\hat{K}$, that are of order 7 and 9 respectively. This results in a generic set of 36 polynomials for 3^{rd} order curved element and 55 for the 5^{th} order curved element[5].

[5]The number of degrees of freedom for a generic, 2D, m^{th}-order polynomial is the $(m+1)^{\text{th}}$ triangular number, given by $(m+2)(m+1)/2$.

4.5.3 Outline of Procedure for P_3 Triangles

We now proceed to discuss the construction of the basis for the P_3 triangle. The elements are constructed by relating a generic set of 36 'reference' basis functions, which correspond to 36 degrees of freedom as shown in figure 4.23, to a smaller set of degrees of freedom on the curved triangle. We can visualize this by considering a reference and a curved triangle, as shown in figure 4.24.

We define the 36 reference 'degrees of freedom', $\hat{\boldsymbol{\Sigma}}^{[3]}$, on the reference element to be

$$\hat{\boldsymbol{\Sigma}}^{[3]} = \Big[\hat{w}(\hat{\boldsymbol{a}}_i) \; ; \; \frac{\partial \hat{w}(\hat{\boldsymbol{a}}_i)}{\partial \hat{x}_\alpha} \; ; \; \frac{\partial^2 \hat{w}(\hat{\boldsymbol{a}}_i)}{\partial \hat{x}_\alpha \partial \hat{x}_\beta} \; ; - \frac{\partial \hat{w}(\hat{\boldsymbol{b}}_1)}{\partial \hat{x}_1} \; ; - \frac{\partial \hat{w}(\hat{\boldsymbol{b}}_2)}{\partial \hat{x}_2} \; ; \; \frac{1}{\sqrt{2}} \left(\frac{\partial \hat{w}(\hat{\boldsymbol{b}}_3)}{\partial \hat{x}_1} + \frac{\partial \hat{w}(\hat{\boldsymbol{b}}_3)}{\partial \hat{x}_2} \right) \; ;$$
$$\hat{w}(\hat{\boldsymbol{d}}_j) \; ; - \frac{\partial \hat{w}(\hat{\boldsymbol{d}}_j)}{\partial \hat{x}_1} \; ; \; \hat{w}(\hat{\boldsymbol{d}}_k) \; ; - \frac{\partial \hat{w}(\hat{\boldsymbol{d}}_k)}{\partial \hat{x}_2} \; ; \; \hat{w}(\hat{\boldsymbol{d}}_l) \; ; \; \frac{1}{\sqrt{2}} \left(\frac{\partial \hat{w}(\hat{\boldsymbol{d}}_l)}{\partial \hat{x}_1} + \frac{\partial \hat{w}(\hat{\boldsymbol{d}}_l)}{\partial \hat{x}_2} \right) \; ; \; \hat{w}(\hat{\boldsymbol{e}}_m)$$
$$\mid \; i, m \in \{1,2,3\} \, , \; j \in \{1,2\} \, , \; k \in \{3,4\} \, , \; l \in \{5,6\} \, , \; \alpha \leq \beta \, , \; (\alpha, \beta) \in \{1,2\} \Big] \, . \quad (4.5.22)$$

where we expand Greek indices first *then* Roman indices, as follows

$$\hat{\boldsymbol{\Sigma}}^{[3]} = \Big[\hat{w}(\hat{\boldsymbol{a}}_1) \, ; \; \hat{w}(\hat{\boldsymbol{a}}_2) \, ; \; \hat{w}(\hat{\boldsymbol{a}}_3) \, ; \; \frac{\partial \hat{w}(\hat{\boldsymbol{a}}_1)}{\partial \hat{x}_1} \, ; \; \frac{\partial \hat{w}(\hat{\boldsymbol{a}}_1)}{\partial \hat{x}_2} \, ; \; \frac{\partial \hat{w}(\hat{\boldsymbol{a}}_2)}{\partial \hat{x}_1} \, ; \; \frac{\partial \hat{w}(\hat{\boldsymbol{a}}_2)}{\partial \hat{x}_2} \, ; \; \frac{\partial \hat{w}(\hat{\boldsymbol{a}}_3)}{\partial \hat{x}_1} \, ; \; \frac{\partial \hat{w}(\hat{\boldsymbol{a}}_3)}{\partial \hat{x}_2} \, ;$$
$$\frac{\partial^2 \hat{w}(\hat{\boldsymbol{a}}_1)}{\partial \hat{x}_1 \partial \hat{x}_1} \, ; \; \frac{\partial^2 \hat{w}(\hat{\boldsymbol{a}}_1)}{\partial \hat{x}_1 \partial \hat{x}_2} \, ; \; \frac{\partial^2 \hat{w}(\hat{\boldsymbol{a}}_1)}{\partial \hat{x}_2 \partial \hat{x}_2} \, ; \; \frac{\partial^2 \hat{w}(\hat{\boldsymbol{a}}_2)}{\partial \hat{x}_1 \partial \hat{x}_1} \, ; \; \frac{\partial^2 \hat{w}(\hat{\boldsymbol{a}}_2)}{\partial \hat{x}_2 \partial \hat{x}_2} \, ; \; \frac{\partial^2 \hat{w}(\hat{\boldsymbol{a}}_2)}{\partial \hat{x}_1 \partial \hat{x}_2} \, ; \; \frac{\partial^2 \hat{w}(\hat{\boldsymbol{a}}_3)}{\partial \hat{x}_1 \partial \hat{x}_1} \, ;$$
$$\frac{\partial^2 \hat{w}(\hat{\boldsymbol{a}}_3)}{\partial \hat{x}_1 \partial \hat{x}_2} \, ; \; \frac{\partial^2 \hat{w}(\hat{\boldsymbol{a}}_3)}{\partial \hat{x}_2 \partial \hat{x}_2} \, ; - \frac{\partial \hat{w}(\hat{\boldsymbol{b}}_1)}{\partial \hat{x}_1} \, ; - \frac{\partial \hat{w}(\hat{\boldsymbol{b}}_2)}{\partial \hat{x}_2} \, ; \; \frac{1}{\sqrt{2}} \left(\frac{\partial \hat{w}(\hat{\boldsymbol{b}}_3)}{\partial \hat{x}_1} + \frac{\partial \hat{w}(\hat{\boldsymbol{b}}_3)}{\partial \hat{x}_2} \right) \; ; \hat{w}(\hat{\boldsymbol{d}}_1) \, ; \; \hat{w}(\hat{\boldsymbol{d}}_2) \, ;$$
$$- \frac{\partial \hat{w}(\hat{\boldsymbol{d}}_1)}{\partial \hat{x}_1} \; ; - \frac{\partial \hat{w}(\hat{\boldsymbol{d}}_2)}{\partial \hat{x}_1} \; ; \; \hat{w}(\hat{\boldsymbol{d}}_3) \; ; \; \hat{w}(\hat{\boldsymbol{d}}_4) \; ; - \frac{\partial \hat{w}(\hat{\boldsymbol{d}}_3)}{\partial \hat{x}_2} \; ; - \frac{\partial \hat{w}(\hat{\boldsymbol{d}}_4)}{\partial \hat{x}_2} \; ; \; \hat{w}(\hat{\boldsymbol{d}}_5) \; ; \; \hat{w}(\hat{\boldsymbol{d}}_6) \; ;$$
$$\frac{1}{\sqrt{2}} \left(\frac{\partial \hat{w}(\hat{\boldsymbol{d}}_5)}{\partial \hat{x}_1} + \frac{\partial \hat{w}(\hat{\boldsymbol{d}}_5)}{\partial \hat{x}_2} \right) \; ; \; \frac{1}{\sqrt{2}} \left(\frac{\partial \hat{w}(\hat{\boldsymbol{d}}_6)}{\partial \hat{x}_1} + \frac{\partial \hat{w}(\hat{\boldsymbol{d}}_6)}{\partial \hat{x}_2} \right) \; ; \; \hat{w}(\hat{\boldsymbol{e}}_1) \; ; \; \hat{w}(\hat{\boldsymbol{e}}_2) \; ; \; \hat{w}(\hat{\boldsymbol{e}}_3) \Big] \, . \quad (4.5.23)$$

Here we recall that the coordinates x_α are *global* Cartesian coordinate, whereas the coordinate $\hat{x}_\alpha$ are the *local* coordinates on the reference triangle. Similarly, $\hat{\boldsymbol{a}}_i$ are the vertices of the (unit) *reference* triangle.

We have retained the Bell degrees of freedom on the reference triangle, but increased the polynomial order by introducing additional normal and Lagrange degrees of freedom, spaced uniformly throughout the element. This is then mapped onto degrees of freedom on the curved 'global' triangle. However, the basis now needs to incorporate the constraints on the trace and traces of the normal derivatives on each edge. We note that on each edge there are 5, dependent 'degrees of freedom', which have values entirely determined by the nodal degrees of freedom (see figure 4.24. These dependent 'degrees of freedom' are eliminated in the global basis, as their values are formed of linear combinations of the nodal degrees of

freedom. This the natural consequence of having a high order basis, constrained to be fifth order polynomials and to have third order normal derivatives on the edges.

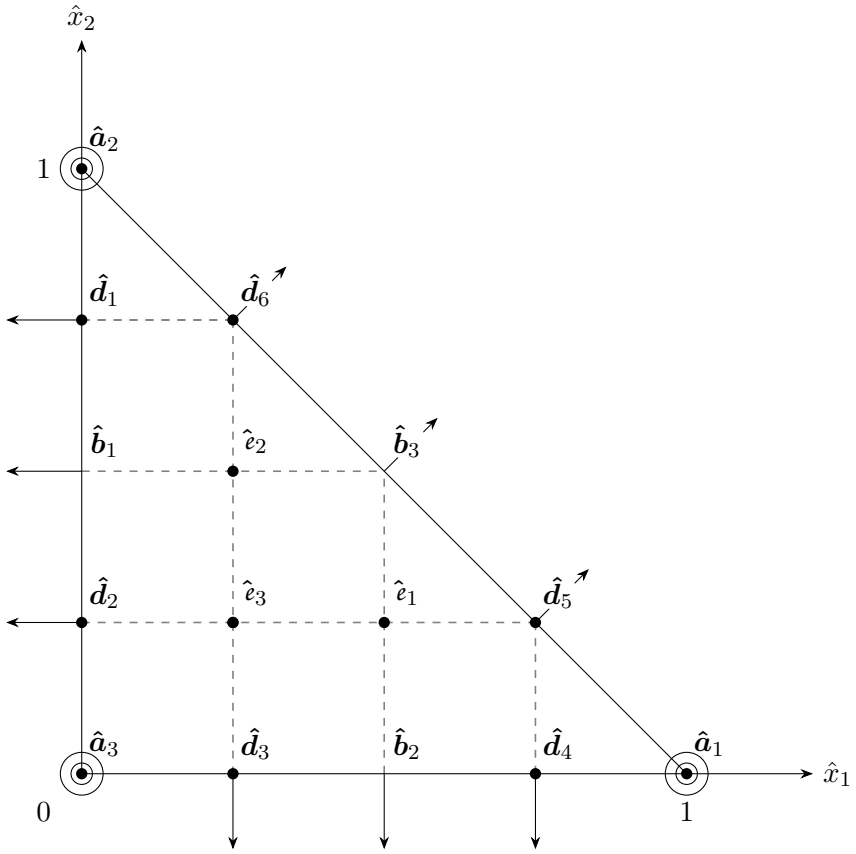

Figure 4.23: Diagram showing the degrees of freedom on the reference triangle.

With this in mind, we define the 21, global degrees of freedom, $\boldsymbol{\Sigma}_G^{[3]}$, on the curved element to be

$$\begin{aligned}\boldsymbol{\Sigma}_G^{[3]} = \big[& w(\boldsymbol{a}_i) \ ; \ (\boldsymbol{\nabla} w(\boldsymbol{a}_i)) \cdot \hat{\boldsymbol{e}}_\alpha \ ; \ (\boldsymbol{\nabla}\boldsymbol{\nabla} w(\boldsymbol{a}_i)) \cdot \hat{\boldsymbol{e}}_\alpha \otimes \hat{\boldsymbol{e}}_\beta \ ; \ w(e_k) \\ & \quad | \ \ i,k \in \{1,2,3\} \, , \, \alpha \leq \beta \, , \, (\alpha,\beta) \in \{1,2\} \big] \, ,\end{aligned} \tag{4.5.24}$$

in which $\hat{\boldsymbol{e}}_\alpha$ are the normal 2D Cartesian unit vectors. These degrees of freedom correspond exactly to the Bell degrees of freedom on the vertices, with three additional 'bubble' degrees of freedom at the points e_i. In index notation, we may write these degrees of freedom as follows

$$\begin{aligned}\boldsymbol{\Sigma}_G^{[3]} = \big[& w(\boldsymbol{a}_i) \ ; \ \frac{\partial w(\boldsymbol{a}_i)}{\partial x_\alpha} \ ; \ \frac{\partial^2 w(\boldsymbol{a}_i)}{\partial x_\alpha \partial x_\beta} \ ; \ w(e_k) \\ & \quad | \ \ i,k \in \{1,2,3\} \, , \, \alpha \leq \beta \, , \, (\alpha,\beta) \in \{1,2\} \big] \, .\end{aligned} \tag{4.5.25}$$

At this stage we iterate that though the zeroth derivative degrees of freedom, $w(\boldsymbol{x})$, are identical to those on the reference element, $\hat{w}(\hat{\boldsymbol{x}}) = w(\boldsymbol{x})$, the Hermite degrees of freedom

will differ:

$$\frac{\partial \hat{w}(\hat{\boldsymbol{a}})}{\partial \hat{x}_\alpha} \neq \frac{\partial w(\boldsymbol{a})}{\partial \hat{x}_\alpha}\,. \tag{4.5.26}$$

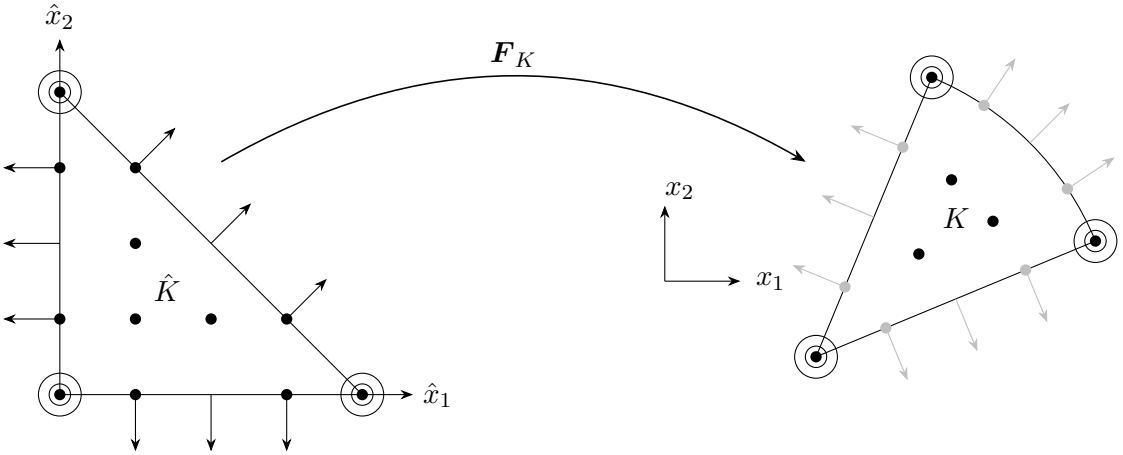

Figure 4.24: Diagram showing the degrees of freedom on the reference and curved triangle. Redundant 'degrees of freedom' on the curved sides are grey, to indicate that they can be eliminated by the constraints on the trace and normal.

We need a means of converting these 36 reference 'degrees of freedom' on the reference triangle, to the 21 global degrees of freedom on the curved triangle. As an intermediate step we convert the global degrees of freedom (that are shared between elements) to *local* degrees of freedom, that are expressed in terms of tangential derivatives on the element. This step makes it more straightforward to compare the degrees of freedom on the reference element to those on the curved element. The usual Lagrange degrees of freedom are unchanged by this transformation, but the Hermite degrees of freedom are re-expressed in terms of tangential derivatives on the triangle. The local degrees of freedom are shown in figure 4.25.

With this aim in mind we define the following tangential vectors

$$\boldsymbol{A}_1 = \boldsymbol{a}_3 - \boldsymbol{a}_1\,, \tag{4.5.27}$$

$$\boldsymbol{A}_2 = (\bar{s} - \underline{s})\boldsymbol{\chi}'(\underline{s})\,, \tag{4.5.28}$$

$$\boldsymbol{B}_1 = -(\bar{s} - \underline{s})\boldsymbol{\chi}'(\bar{s})\,, \tag{4.5.29}$$

$$\boldsymbol{B}_2 = \boldsymbol{a}_3 - \boldsymbol{a}_2\,, \tag{4.5.30}$$

which are the tangents to the curved triangle at vertices 1 and 2 respectively. As the sides 1 and 2 are straight, the two tangents at vertex 3 are $-\boldsymbol{A}_1$ and $-\boldsymbol{B}_2$.

Specifically, we relate the degrees of freedom on the curved element, $\boldsymbol{\Sigma}_G^{[3]}$, to the local

degrees of freedom, $\boldsymbol{\Sigma}_L^{[3]}$, defined by

$$\begin{aligned}\boldsymbol{\Sigma}_L^{[3]} = \Big[&(\boldsymbol{a}_i)\ ;\ (\boldsymbol{\nabla} w(\boldsymbol{a}_1)) \cdot \boldsymbol{A}_\alpha\ ;\ (\boldsymbol{\nabla} w(\boldsymbol{a}_2)) \cdot \boldsymbol{B}_\alpha\ ;\ -(\boldsymbol{\nabla} w(\boldsymbol{a}_3)) \cdot \boldsymbol{A}_1\ ;\ -(\boldsymbol{\nabla} w(\boldsymbol{a}_3)) \cdot \boldsymbol{B}_2\ ; \\ &(\boldsymbol{\nabla}\boldsymbol{\nabla} w(\boldsymbol{a}_1)) \cdot \boldsymbol{A}_1 \otimes \boldsymbol{A}_1\ ;\ (\boldsymbol{\nabla}\boldsymbol{\nabla} w(\boldsymbol{a}_1)) \cdot \boldsymbol{A}_2 \otimes \boldsymbol{A}_2\ ;\quad (\boldsymbol{\nabla}\boldsymbol{\nabla} w(\boldsymbol{a}_2)) \cdot \boldsymbol{B}_1 \otimes \boldsymbol{B}_1\ ; \\ &(\boldsymbol{\nabla}\boldsymbol{\nabla} w(\boldsymbol{a}_2)) \cdot \boldsymbol{B}_2 \otimes \boldsymbol{B}_2\ ;\ (\boldsymbol{\nabla}\boldsymbol{\nabla} w(\boldsymbol{a}_3)) \cdot \boldsymbol{A}_1 \otimes \boldsymbol{A}_1\ ;\quad (\boldsymbol{\nabla}\boldsymbol{\nabla} w(\boldsymbol{a}_3)) \cdot \boldsymbol{B}_2 \otimes \boldsymbol{B}_2\ ; \\ &(\boldsymbol{\nabla}\boldsymbol{\nabla} w(\boldsymbol{a}_1)) \cdot \boldsymbol{B}_2 \otimes \boldsymbol{B}_2\ ;\ (\boldsymbol{\nabla}\boldsymbol{\nabla} w(\boldsymbol{a}_2)) \cdot \boldsymbol{A}_1 \otimes \boldsymbol{A}_1\ ;\ -(\boldsymbol{\nabla}\boldsymbol{\nabla} w(\boldsymbol{a}_3)) \cdot \boldsymbol{A}_2 \otimes \boldsymbol{B}_1\ ; \\ &w(\boldsymbol{e}_k)\ \mid\ i,k \in \{1,2,3\}\,,\ \alpha \in \{1,2\}\Big]\,. \end{aligned} \tag{4.5.31}$$

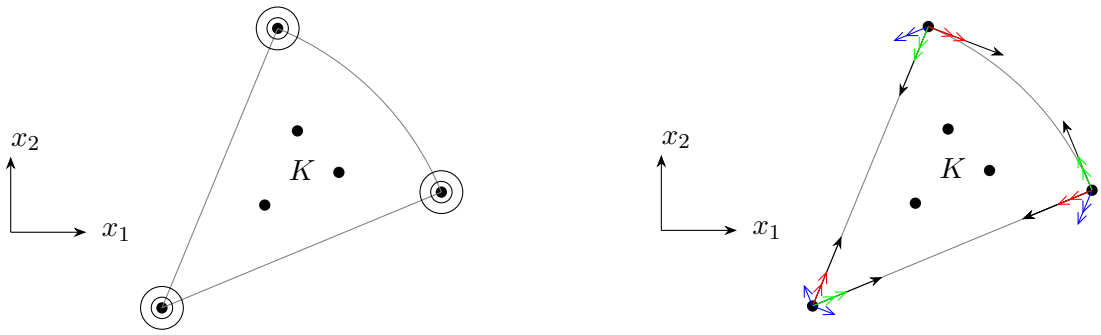

Figure 4.25: Diagram schematically showing the global (left) and local degrees of freedom (right) on the curved triangle. In the right hand image the coloured, double-tipped arrows represent the second, tangent and cross tangent derivative degrees of freedom and black arrows represent the first, tangent derivative degrees of freedom.

This transformation from global, $\boldsymbol{\Sigma}_G^{[3]}$, to local degrees of freedom, $\boldsymbol{\Sigma}_L^{[3]}$, can be performed by multiplication of a 21×21 square matrix, that depends only on the vertices of the triangle and the curved edge. Expressed in terms of matrices we have

$$\underbrace{\boldsymbol{\Sigma}_L^{[3]}}_{1\times 21} = \underbrace{\boldsymbol{\Sigma}_G^{[3]}}_{1\times 21}\ \underbrace{\tilde{\boldsymbol{D}}}_{21\times 21} \tag{4.5.32}$$

in which $\tilde{\boldsymbol{D}}$ is the matrix transform from the global to local degrees of freedom. To construct for Bell elements, rather than Argyris as in Bernadou and Boisserie [1992], we remove the (identity) part which relates the local normal degrees of freedom to global normal degrees of freedom, in a trivial step. Otherwise the construction (which we perform in the next section) follows the arguments of Bernadou and Boisserie [1992] exactly.

Once this intermediate stage is complete we can readily relate the local degrees of freedom to reference 'degrees of freedom', $\hat{\boldsymbol{\Sigma}}^{[3]}$, via another matrix transform, given by

$$\underbrace{\hat{\boldsymbol{\Sigma}}^{[3]}}_{1\times 21} = \underbrace{\boldsymbol{\Sigma}_L^{[3]}}_{1\times 21}\ \underbrace{\tilde{\boldsymbol{B}}}_{21\times 36}\,, \tag{4.5.33}$$

and thus related to the global degrees of freedom by

$$\underbrace{\hat{\boldsymbol{\Sigma}}^{[3]}}_{1\times 36} = \underbrace{\boldsymbol{\Sigma}_G^{[3]}}_{1\times 21}\,\underbrace{\tilde{\boldsymbol{D}}}_{21\times 21}\,\underbrace{\tilde{\boldsymbol{B}}}_{21\times 36}\,. \tag{4.5.34}$$

The matrix is constructed by consideration of the P_5 polynomial trace of the function on the triangle and the P_3 normal derivative trace on each edge: the constraints are incorporated in the same manner as for the Argyris triangle in Bernadou and Boisserie [1992], for the curved Bell elements as outlined in Bernadou [1992], only incorporating the lack of normal degrees of freedom and resulting P_3 (rather than P_4) normal derivatives on the edge. As noted, the explicit construction is not detailed in Bernadou [1992], so we do so here for completeness.

Finally we must express the global basis in terms of the reference basis, $\hat{\Psi}$, the set of 36 basis polynomials associated with the degrees of freedom on the reference element. These can be obtained in terms of the 36 monomials, $x^n\,y^m$ with $m+n \leq 7$ by solving the linear system of equations obtained by expressing the reference degrees of freedom of a generic P_7 polynomial of two variables, as outlined in appendix D.3. Our global basis is then defined such that

$$\boldsymbol{\Sigma}_G^{[3]} \cdot \boldsymbol{\psi}^{[3]} \equiv \hat{\boldsymbol{\Sigma}}^{[3]} \cdot \hat{\boldsymbol{\psi}}^{[3]}\,, \tag{4.5.35}$$

so that finally we get the expression for the global basis as

$$\underbrace{\boldsymbol{\psi}^{[3]}}_{21\times 1} = \underbrace{\tilde{\boldsymbol{D}}}_{21\times 21}\,\underbrace{\tilde{\boldsymbol{B}}}_{21\times 36}\,.\underbrace{\hat{\boldsymbol{\psi}}^{[3]}}_{36\times 1}\,. \tag{4.5.36}$$

To summarize, the procedure for defining the basis for these elements can be split into three steps. We begin with a 'reference' element, defined on the unit right-angled triangle, $\hat{K}$, as pictured in figure 4.23. This reference triangle basis is shared by curved-Bell elements of any geometry with any generically curved edge. We then transform onto an element with local degrees of freedom, as shown in 4.25, using the matrix $\tilde{B}$, which depends only on the geometry of the curved element. This step eliminates the dependent 'degrees of freedom'. Finally the local degrees of freedom are converted to the global, axis-aligned degrees of freedom which are shared between adjacent elements, using the matrix $\tilde{D}$ which again depends only on the geometry of the curved element.

4.5.4 Outline of Procedure for P_5 Triangles

The procedure for the P_5 elements is identical to that of the P_3 element, only now we must account for additional 'bubble' degrees of freedom on the curved element and additional

dependent 'degrees of freedom' on the reference element. Of the 55 degrees of freedom on the reference element, the 27 additional edge degrees of freedom are dependent, leaving a curved element with 28 degrees of freedom: 18 Bell degrees of freedom and 10 bubble degrees of freedom.

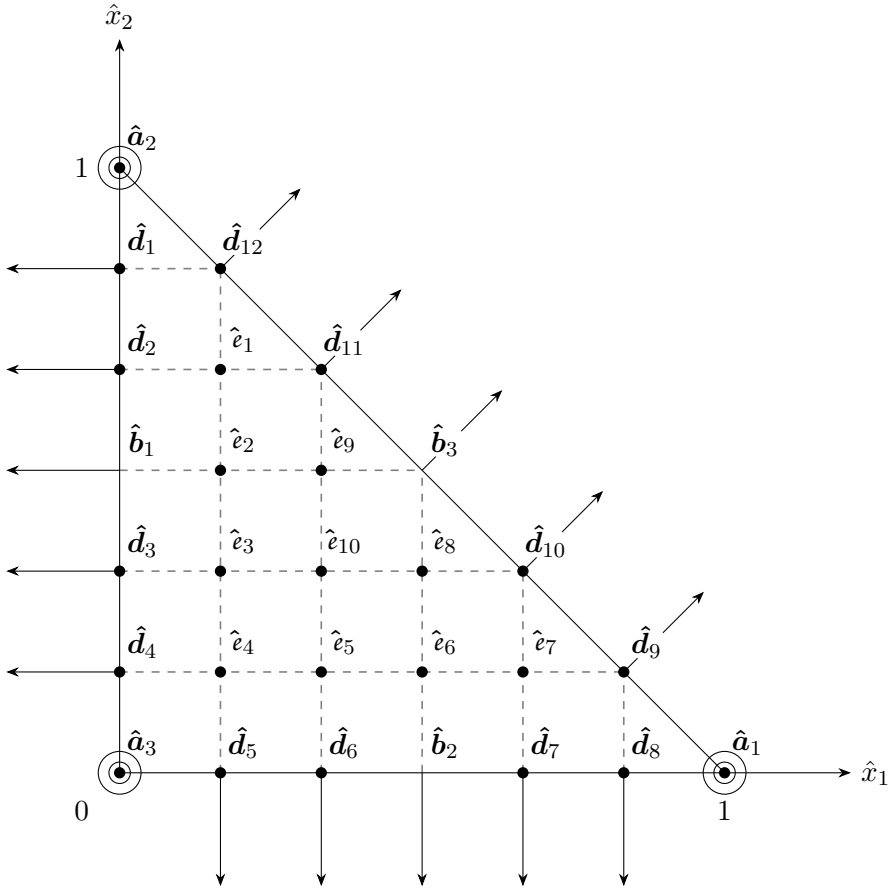

Figure 4.26: Diagram showing the degrees of freedom on the P_5 reference triangle.

We start by expressing the 55 degrees of freedom for the reference triangle, as shown in figure 4.26. The reference degrees of freedom are given by

$$\begin{aligned}\hat{\boldsymbol{\Sigma}}^{[5]} = \Big[& \hat{w}(\hat{\boldsymbol{a}}_i)\ ;\ \frac{\partial \hat{w}(\hat{\boldsymbol{a}}_i)}{\partial \hat{x}_\alpha}\ ;\ \frac{\partial^2 \hat{w}(\hat{\boldsymbol{a}}_i)}{\partial \hat{x}_\alpha \partial \hat{x}_\beta}\ ;\ -\frac{\partial \hat{w}(\hat{\boldsymbol{b}}_1)}{\partial \hat{x}_1}\ ;\ -\frac{\partial \hat{w}(\hat{\boldsymbol{b}}_2)}{\partial \hat{x}_2}\ ;\ \frac{1}{\sqrt{2}}\left(\frac{\partial \hat{w}(\hat{\boldsymbol{b}}_3)}{\partial \hat{x}_1} + \frac{\partial \hat{w}(\hat{\boldsymbol{b}}_3)}{\partial \hat{x}_2}\right)\ ; \\ & \hat{w}(\hat{\boldsymbol{d}}_j)\ ;\ -\frac{\partial \hat{w}(\hat{\boldsymbol{d}}_j)}{\partial \hat{x}_1}\ ;\ \hat{w}(\hat{\boldsymbol{d}}_k)\ ;\ -\frac{\partial \hat{w}(\hat{\boldsymbol{d}}_k)}{\partial \hat{x}_2}\ ;\ \hat{w}(\hat{\boldsymbol{d}}_l)\ ;\ \frac{1}{\sqrt{2}}\left(\frac{\partial \hat{w}(\hat{\boldsymbol{d}}_l)}{\partial \hat{x}_1} + \frac{\partial \hat{w}(\hat{\boldsymbol{d}}_l)}{\partial \hat{x}_2}\right)\ ;\ \hat{w}(\hat{e}_m) \\ & \mid\ i \in \{1,2,3\}\ ,\ j \in \{1,\dots 4\}\ ,\ k \in \{5,\dots,8\}\ ,\ l \in \{9,\dots,12\}\ , \\ & m \in \{1,\dots,10\}\,,\ \alpha \leq \beta\,,\ (\alpha,\beta) \in \{1,2\}\Big]\,. \end{aligned} \tag{4.5.37}$$

Eliminating the dependent 'degrees of freedom' when considering the curved element we have

the following global degrees of freedom, as shown in figure 4.27:

$$\begin{aligned}\boldsymbol{\Sigma}_G^{[5]} = \big[& w(\boldsymbol{a}_i) \; ; \; (\boldsymbol{\nabla} w(\boldsymbol{a}_i)) \cdot \hat{\boldsymbol{e}}_\alpha \; ; \; (\boldsymbol{\nabla}\boldsymbol{\nabla} w(\boldsymbol{a}_i)) \cdot \hat{\boldsymbol{e}}_\alpha \otimes \hat{\boldsymbol{e}}_\beta \; ; \; w(\boldsymbol{e}_j) \\ & \mid \; i \in \{1,2,3\} \, , \, j \in \{1,\ldots,10\} \, , \, \alpha \leq \beta \, , \, (\alpha,\beta) \in \{1,2\} \big] \, ,\end{aligned} \tag{4.5.38}$$

in which $\hat{\boldsymbol{e}}_\alpha$ are the normal 2D Cartesian unit vectors.

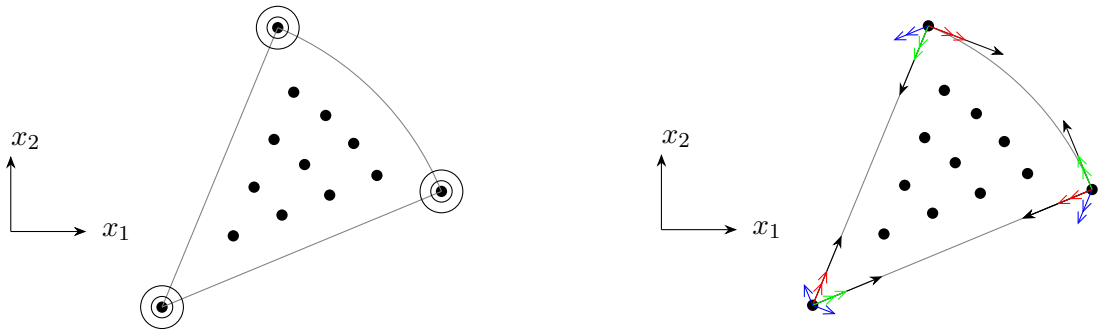

Figure 4.27: Diagram schematically showing the global (left) and local degrees of freedom (right) on the P_5 curved triangle. In the right hand image the double-tipped arrows represent the second, tangent and cross tangent derivative degrees of freedom and black arrows represent the first, tangent derivative degrees of freedom.

To convert between the reference and global degrees of freedom, we again use a matrix $\tilde{\tilde{\boldsymbol{D}}}$ which is essentially the same as $\tilde{\boldsymbol{D}}$ but with additional unit diagonal entries, that correspond to the seven additional degrees of freedom. The matrix $\tilde{\tilde{\boldsymbol{B}}}$ has additional entries corresponding to the additional dependent degrees of freedom, which are calculated in the same manner as for $\tilde{\boldsymbol{B}}$. The P_5 basis is constructed as follows

$$\underbrace{\boldsymbol{\psi}^{[5]}}_{28\times 1} = \underbrace{\tilde{\tilde{\boldsymbol{D}}}}_{28\times 28} \underbrace{\tilde{\tilde{\boldsymbol{B}}}}_{28\times 55} \underbrace{\hat{\boldsymbol{\psi}}^{[5]}}_{55\times 1} \, . \tag{4.5.39}$$

The matrix $\tilde{\tilde{\boldsymbol{D}}}$ relates the global degrees of freedom, $\boldsymbol{\Sigma}_G^{[5]}$ to the local degrees of freedom $\boldsymbol{\Sigma}_L^{[5]}$, defined as

$$\begin{aligned}\boldsymbol{\Sigma}_L^{[5]} = \Big[& (\boldsymbol{a}_i) \; ; \; (\boldsymbol{\nabla} w(\boldsymbol{a}_1)) \cdot \boldsymbol{A}_\alpha \; ; \; (\boldsymbol{\nabla} w(\boldsymbol{a}_2)) \cdot \boldsymbol{B}_\alpha \; ; \; -(\boldsymbol{\nabla} w(\boldsymbol{a}_3)) \cdot \boldsymbol{A}_1 \; ; \; -(\boldsymbol{\nabla} w(\boldsymbol{a}_3)) \cdot \boldsymbol{B}_2 \; ; \\ & (\boldsymbol{\nabla}\boldsymbol{\nabla} w(\boldsymbol{a}_1)) \cdot \boldsymbol{A}_1 \otimes \boldsymbol{A}_1 \; ; \; (\boldsymbol{\nabla}\boldsymbol{\nabla} w(\boldsymbol{a}_1)) \cdot \boldsymbol{A}_2 \otimes \boldsymbol{A}_2 \; ; \quad (\boldsymbol{\nabla}\boldsymbol{\nabla} w(\boldsymbol{a}_2)) \cdot \boldsymbol{B}_1 \otimes \boldsymbol{B}_1 \; ; \\ & (\boldsymbol{\nabla}\boldsymbol{\nabla} w(\boldsymbol{a}_2)) \cdot \boldsymbol{B}_2 \otimes \boldsymbol{B}_2 \; ; \; (\boldsymbol{\nabla}\boldsymbol{\nabla} w(\boldsymbol{a}_3)) \cdot \boldsymbol{A}_1 \otimes \boldsymbol{A}_1 \; ; \quad (\boldsymbol{\nabla}\boldsymbol{\nabla} w(\boldsymbol{a}_3)) \cdot \boldsymbol{B}_2 \otimes \boldsymbol{B}_2 \; ; \\ & (\boldsymbol{\nabla}\boldsymbol{\nabla} w(\boldsymbol{a}_1)) \cdot \boldsymbol{B}_2 \otimes \boldsymbol{B}_2 \; ; \; (\boldsymbol{\nabla}\boldsymbol{\nabla} w(\boldsymbol{a}_2)) \cdot \boldsymbol{A}_1 \otimes \boldsymbol{A}_1 \; ; \; -(\boldsymbol{\nabla}\boldsymbol{\nabla} w(\boldsymbol{a}_3)) \cdot \boldsymbol{A}_2 \otimes \boldsymbol{B}_1 \; ; \\ & w(\boldsymbol{e}_k) \; \mid \; i \in \{1,2,3\} \, k \in \{1,\ldots,10\} \, , \, \alpha \in \{1,2\} \Big] \, .\end{aligned} \tag{4.5.40}$$

We can relate $\tilde{\tilde{\boldsymbol{D}}}$ to $\tilde{\boldsymbol{D}}$ as follows

$$\tilde{\tilde{\boldsymbol{D}}} = \begin{pmatrix} \tilde{\boldsymbol{D}} & \boldsymbol{0} \\ \boldsymbol{0} & \mathbb{I}_7 \end{pmatrix} \, , \tag{4.5.41}$$

where $\mathbb{I}_7$ is the 7×7 identity matrix.

Now we have outlined the procedure, we must deduce of the local-to-global, and local-to-reference matrices to complete the procedure. The calculation of these matrices is long and involved, but will be useful to to readers implementing the relevant elements. However, with the interest of conciseness, we direct readers not interested in the explicit construction to the last subsections of sections 4.5.6 and 4.5.7 which summarize the construction process for P_3 and P_5 elements, respectively.

4.5.5 Construction of the Global-to-Local Matrix

We start by constructing the mapping from the local degrees of freedom, $\boldsymbol{\Sigma}_L^{[3]}$, to the global degrees of freedom $\boldsymbol{\Sigma}_G^{[3]}$: $\tilde{\boldsymbol{D}}$. This step is identical to the construction in Bernadou [1993a], which we follow closely.

We can straightforwardly relate the global Lagrange (zeroth derivative) degrees of freedom element to the local Lagrange degrees of freedom, as they are identical. We then introduce the set of six tangent vectors $\boldsymbol{t}_{i\alpha}$ defined by

$$\boldsymbol{t}_{\alpha 1} = \boldsymbol{A}_\alpha \,, \quad \boldsymbol{t}_{\alpha 2} = \boldsymbol{B}_\alpha \quad \text{and} \quad \boldsymbol{t}_{\alpha 3} = \boldsymbol{C}_\alpha \tag{4.5.42}$$

with $\boldsymbol{C}_1 = -\boldsymbol{B}_2$ and $\boldsymbol{C}_2 = -\boldsymbol{A}_1$. The first derivative degrees of freedom are related by a simple rotation of the coordinate directions:

$$\begin{pmatrix} \boldsymbol{\nabla} w(\boldsymbol{a}_i) \cdot \boldsymbol{t}_{1i} & \boldsymbol{\nabla} w(\boldsymbol{a}_i) \cdot \boldsymbol{t}_{2i} \end{pmatrix} = \begin{pmatrix} \boldsymbol{\nabla} w(\boldsymbol{a}_i) \cdot \hat{\boldsymbol{e}}_1 & \boldsymbol{\nabla} w(\boldsymbol{a}_i) \cdot \hat{\boldsymbol{e}}_2 \end{pmatrix} \tilde{\boldsymbol{d}}_i \tag{4.5.43}$$

where $\tilde{\boldsymbol{d}}_i$ is a rotation matrix, with components

$$\tilde{d}_{i\alpha\beta} = \hat{\boldsymbol{e}}_\alpha \cdot \boldsymbol{t}_{\beta i} \,. \tag{4.5.44}$$

Thus, to relate the full set of first derivative degrees of freedom to local degrees of freedom we have the submatrices

$$\tilde{\boldsymbol{d}}_1 = \begin{pmatrix} \boldsymbol{A}_1 \cdot \hat{\boldsymbol{e}}_1 & \boldsymbol{A}_2 \cdot \hat{\boldsymbol{e}}_1 \\ \boldsymbol{A}_1 \cdot \hat{\boldsymbol{e}}_2 & \boldsymbol{A}_2 \cdot \hat{\boldsymbol{e}}_2 \end{pmatrix} , \quad \tilde{\boldsymbol{d}}_2 = \begin{pmatrix} \boldsymbol{B}_1 \cdot \hat{\boldsymbol{e}}_1 & \boldsymbol{B}_2 \cdot \hat{\boldsymbol{e}}_1 \\ \boldsymbol{B}_1 \cdot \hat{\boldsymbol{e}}_2 & \boldsymbol{B}_2 \cdot \hat{\boldsymbol{e}}_2 \end{pmatrix} , \quad \tilde{\boldsymbol{d}}_3 = - \begin{pmatrix} \boldsymbol{B}_2 \cdot \hat{\boldsymbol{e}}_1 & \boldsymbol{A}_1 \cdot \hat{\boldsymbol{e}}_1 \\ \boldsymbol{B}_2 \cdot \hat{\boldsymbol{e}}_2 & \boldsymbol{A}_1 \cdot \hat{\boldsymbol{e}}_2 \end{pmatrix} . \tag{4.5.45}$$

To express the local-to-global submatrix that relates the second derivative degrees of freedom we need a 9×9 matrix: this is due to the linear nature of the mapping from local-to-global degrees of freedom, whereby the local second derivative degrees of freedom only

depend on global second degrees of freedom. We can relate the degrees of freedom by 3 submatrices, corresponding to each of the three nodes. They are given by

$$\tilde{\boldsymbol{da}} = \begin{pmatrix} (\hat{\boldsymbol{e}}_1 \cdot \boldsymbol{A}_1)^2 & (\hat{\boldsymbol{e}}_1 \cdot \boldsymbol{A}_2)^2 & (\hat{\boldsymbol{e}}_1 \cdot \boldsymbol{B}_2)^2 \\ 2\prod_\gamma \hat{\boldsymbol{e}}_\gamma \cdot \boldsymbol{A}_1 & 2\prod_\gamma \hat{\boldsymbol{e}}_\gamma \cdot \boldsymbol{A}_2 & 2\prod_\gamma \hat{\boldsymbol{e}}_\gamma \cdot \boldsymbol{B}_2 \\ (\hat{\boldsymbol{e}}_2 \cdot \boldsymbol{A}_1)^2 & (\hat{\boldsymbol{e}}_2 \cdot \boldsymbol{A}_2)^2 & (\hat{\boldsymbol{e}}_2 \cdot \boldsymbol{B}_2)^2 \end{pmatrix}, \tag{4.5.46}$$

$$\tilde{\boldsymbol{db}} = \begin{pmatrix} (\hat{\boldsymbol{e}}_1 \cdot \boldsymbol{B}_1)^2 & (\hat{\boldsymbol{e}}_1 \cdot \boldsymbol{B}_2)^2 & (\hat{\boldsymbol{e}}_1 \cdot \boldsymbol{A}_1)^2 \\ 2\prod_\gamma \hat{\boldsymbol{e}}_\gamma \cdot \boldsymbol{B}_1 & 2\prod_\gamma \hat{\boldsymbol{e}}_\gamma \cdot \boldsymbol{B}_2 & 2\prod_\gamma \hat{\boldsymbol{e}}_\gamma \cdot \boldsymbol{A}_1 \\ (\hat{\boldsymbol{e}}_2 \cdot \boldsymbol{B}_1)^2 & (\hat{\boldsymbol{e}}_2 \cdot \boldsymbol{B}_2)^2 & (\hat{\boldsymbol{e}}_2 \cdot \boldsymbol{A}_1)^2 \end{pmatrix}, \tag{4.5.47}$$

and

$$\tilde{\boldsymbol{dc}} = \begin{pmatrix} (\hat{\boldsymbol{e}}_1 \cdot \boldsymbol{A}_1)^2 & (\hat{\boldsymbol{e}}_1 \cdot \boldsymbol{B}_2)^2 & (\hat{\boldsymbol{e}}_1 \cdot \boldsymbol{A}_2)(\hat{\boldsymbol{e}}_1 \cdot \boldsymbol{B}_1) \\ 2\prod_\gamma \hat{\boldsymbol{e}}_\gamma \cdot \boldsymbol{A}_1 & 2\prod_\gamma \hat{\boldsymbol{e}}_\gamma \cdot \boldsymbol{B}_2 & (\hat{\boldsymbol{e}}_2 \cdot \boldsymbol{A}_2)(\hat{\boldsymbol{e}}_1 \cdot \boldsymbol{B}_1) + (\hat{\boldsymbol{e}}_1 \cdot \boldsymbol{A}_2)(\hat{\boldsymbol{e}}_2 \cdot \boldsymbol{B}_1) \\ (\hat{\boldsymbol{e}}_2 \cdot \boldsymbol{A}_1)^2 & (\hat{\boldsymbol{e}}_2 \cdot \boldsymbol{B}_2)^2 & (\hat{\boldsymbol{e}}_2 \cdot \boldsymbol{A}_2)(\hat{\boldsymbol{e}}_2 \cdot \boldsymbol{B}_1) \end{pmatrix}, \tag{4.5.48}$$

in which $\prod_\gamma(\cdot)_\gamma \equiv \prod_{\gamma=1}^{2}(\cdot)_\gamma$ is the usual product operator. Thus, taking into account the ordering of degrees of freedom, we can express the full 9×9 matrix, $\tilde{d}_4$ as

$$\tilde{\boldsymbol{d}}_4 = \begin{pmatrix} \tilde{da}_{11} & \tilde{da}_{12} & 0 & 0 & 0 & 0 & \tilde{da}_{13} & 0 & 0 \\ \tilde{da}_{21} & \tilde{da}_{22} & 0 & 0 & 0 & 0 & \tilde{da}_{23} & 0 & 0 \\ \tilde{da}_{31} & \tilde{da}_{32} & 0 & 0 & 0 & 0 & \tilde{da}_{33} & 0 & 0 \\ 0 & 0 & \tilde{db}_{11} & \tilde{db}_{12} & 0 & 0 & 0 & \tilde{da}_{13} & 0 \\ 0 & 0 & \tilde{db}_{21} & \tilde{db}_{22} & 0 & 0 & 0 & \tilde{da}_{23} & 0 \\ 0 & 0 & \tilde{db}_{31} & \tilde{db}_{32} & 0 & 0 & 0 & \tilde{da}_{33} & 0 \\ 0 & 0 & 0 & 0 & \tilde{da}_{11} & \tilde{da}_{12} & 0 & 0 & \tilde{da}_{13} \\ 0 & 0 & 0 & 0 & \tilde{da}_{21} & \tilde{da}_{22} & 0 & 0 & \tilde{da}_{23} \\ 0 & 0 & 0 & 0 & \tilde{da}_{31} & \tilde{da}_{32} & 0 & 0 & \tilde{da}_{33} \end{pmatrix} \tag{4.5.49}$$

We are then able to write the full (21×21) local-to-global matrix for the P_3 elements as

$$\tilde{\boldsymbol{D}} = \begin{pmatrix} \mathbb{I}_3 & & & & & \\ & \tilde{\boldsymbol{d}}_1 & & & \mathbf{0} & \\ & & \tilde{\boldsymbol{d}}_2 & & & \\ & & & \tilde{\boldsymbol{d}}_3 & & \\ & \mathbf{0} & & & \tilde{\boldsymbol{d}}_4 & \\ & & & & & \mathbb{I}_3 \end{pmatrix}, \tag{4.5.50}$$

and, by extension, for the P_5 elements we have the 28×28 matrix:

$$\tilde{\tilde{\boldsymbol{D}}} = \begin{pmatrix} \mathbb{I}_3 & & & & & \\ & \tilde{\boldsymbol{d}}_1 & & & \mathbf{0} & \\ & & \tilde{\boldsymbol{d}}_2 & & & \\ & & & \tilde{\boldsymbol{d}}_3 & & \\ & \mathbf{0} & & & \tilde{\boldsymbol{d}}_4 & \\ & & & & & \mathbb{I}_{10} \end{pmatrix}. \tag{4.5.51}$$

Now we have constructed the matrices, $\tilde{\boldsymbol{D}}$ and $\tilde{\tilde{\boldsymbol{D}}}$, that map global (axis aligned) degrees of freedom to local degrees of freedom, we proceed to construct the local-to-reference matrices.

4.5.6 Construction of the Local-to-Reference Matrix for the P_3 Triangle

The construction of the local-to-reference matrices is less straightforward, due to the, in general, non-affine mapping between the curved triangle, K, and the reference triangle, $\hat{K}$.

The basic procedure for the vertex degrees of freedom will be familiar to those with a background in vector calculus, as the constructed local-to-reference matrix will effectively be constructed from a set of individual coordinate change Jacobians and Hessians. However, for the dependent 'edge' degrees of freedom the calculation becomes slightly more involved: to achieve this, we construct P_5 and P_3 one-dimensional, Hermite interpolations of the function and normal-derivative on each edge and use these to infer the dependent values from the independent unknowns. This must be done in order to satisfy the constraint that the elements 'conform' with Bell elements: i.e. that their trace and normal derivative trace on straight edges are set entirely by the 'Bell' degrees of freedom at each vertex.

We begin by partitioning the 21×36 matrix, $\tilde{\boldsymbol{B}}$, as follows

$$\tilde{\boldsymbol{B}} = \begin{pmatrix} \tilde{\boldsymbol{B}}_1 & \tilde{\boldsymbol{B}}_2 & \tilde{\boldsymbol{B}}_3 & \tilde{\boldsymbol{B}}_4 & \tilde{\boldsymbol{B}}_5 & \tilde{\boldsymbol{B}}_6 & \tilde{\boldsymbol{B}}_7 \end{pmatrix} \tag{4.5.52}$$

in which the submatrices $\tilde{B}_i$ with $i \in \{1, \ldots, 7\}$ have 21 rows of 3, 6, 9, 3, 6, 6 and 3 columns respectively.

The submatrices $\tilde{B}_i$ with $i \in \{1, 2, 3\}$ relate the (local) Bell degrees of freedom to their counterparts on the reference element and, as such, they are identical to those found by Bernadou and Boisserie [1993]. Similarly, the submatrix $\tilde{B}_5$ which relates the Lagrange degrees of freedom on each reference edge to the (local) Bell degrees of freedom, via a P_5, 1D polynomial, remains unchanged, as the representation of the trace is the same as for Argyris

elements. The submatrix B_7, which (trivially) relates the 'bubble' degrees of freedom from local to reference likewise, remains unchanged. However, the submatrices B_4 and B_6, which relate the normal degrees of freedom on the reference element to their counterparts on the reference element, need to be adapted for use with the Bell element.

Construction of $\tilde{\boldsymbol{B}}_1$

To construct $\tilde{\boldsymbol{B}}_1$ is trivial: the Lagrange degrees of freedom are identical on the reference and curved elements, so the mapping leaves them unchanged. This means that the submatrix $\tilde{\boldsymbol{B}}_1$ is given by

$$\tilde{\boldsymbol{B}}_1 = \begin{pmatrix} \mathbb{I}_3 & \mathbf{0}_{3\times 18} \end{pmatrix}^T . \tag{4.5.53}$$

Construction of $\tilde{\boldsymbol{B}}_2$

We now need to relate the first derivative degrees of freedom at vertices on the reference element to the first derivative degrees of freedom on the reference element, by the submatrix $\tilde{\boldsymbol{B}}_2$. We first consider the tangents on the curved element: by the mapping $\boldsymbol{F}_K$ these transform exactly to the tangents on the reference element. Thus, the tangent degrees of freedom are given in terms of reference degrees of freedom by [Bernadou and Boisserie, 1993]

$$\boldsymbol{\nabla} w(\boldsymbol{a}_1)\cdot\boldsymbol{A}_1 = -\hat{\boldsymbol{\nabla}}\hat{w}(\hat{\boldsymbol{a}}_1)\cdot\hat{\boldsymbol{a}}_1\,, \tag{4.5.54}$$

$$\boldsymbol{\nabla} w(\boldsymbol{a}_1)\cdot\boldsymbol{A}_2 = -\hat{\boldsymbol{\nabla}}\hat{w}(\hat{\boldsymbol{a}}_1)\cdot\hat{\boldsymbol{a}}_1 + \hat{\boldsymbol{\nabla}}\hat{w}(\hat{\boldsymbol{a}}_1)\cdot\hat{\boldsymbol{a}}_2\,, \tag{4.5.55}$$

$$\boldsymbol{\nabla} w(\boldsymbol{a}_2)\cdot\boldsymbol{B}_1 = -\hat{\boldsymbol{\nabla}}\hat{w}(\hat{\boldsymbol{a}}_2)\cdot\hat{\boldsymbol{a}}_2 + \hat{\boldsymbol{\nabla}}\hat{w}(\hat{\boldsymbol{a}}_2)\cdot\hat{\boldsymbol{a}}_1\,, \tag{4.5.56}$$

$$\boldsymbol{\nabla} w(\boldsymbol{a}_2)\cdot\boldsymbol{B}_2 = -\hat{\boldsymbol{\nabla}}\hat{w}(\hat{\boldsymbol{a}}_2)\cdot\hat{\boldsymbol{a}}_2\,, \tag{4.5.57}$$

$$-\boldsymbol{\nabla} w(\boldsymbol{a}_3)\cdot\boldsymbol{B}_2 = \hat{\boldsymbol{\nabla}}\hat{w}(\hat{\boldsymbol{a}}_1)\cdot\hat{\boldsymbol{a}}_2\,, \tag{4.5.58}$$

$$-\boldsymbol{\nabla} w(\boldsymbol{a}_3)\cdot\boldsymbol{A}_1 = \hat{\boldsymbol{\nabla}}\hat{w}(\hat{\boldsymbol{a}}_1)\cdot\hat{\boldsymbol{a}}_1\,, \tag{4.5.59}$$

which can be succinctly expressed in the submatrix, $\tilde{\boldsymbol{b}}_2$,

$$\tilde{\boldsymbol{b}}_2 = \begin{pmatrix} -1 & -1 & 0 & 0 & 0 & 0 \\ 0 & 1 & 0 & 0 & 0 & 0 \\ 0 & 0 & 1 & 0 & 0 & 0 \\ 0 & 0 & -1 & -1 & 0 & 0 \\ 0 & 0 & 0 & 0 & 0 & 1 \\ 0 & 0 & 0 & 0 & 1 & 0 \end{pmatrix}, \tag{4.5.60}$$

such that

$$\begin{aligned}\left[\boldsymbol{\nabla} w(\boldsymbol{a}_1)\cdot\boldsymbol{A}_\alpha\,;\,\boldsymbol{\nabla} w(\boldsymbol{a}_2)\cdot\boldsymbol{B}_\alpha\,;\boldsymbol{\nabla} w(\boldsymbol{a}_3)\cdot\boldsymbol{C}_\alpha\,,\,\alpha\in\{1,2\}\right] = \\ \left[\frac{\partial\hat{w}(\hat{\boldsymbol{a}}_i)}{\partial\hat{x}_\alpha}\,,\,i\in\{1,2,3\}\,,\,\alpha\in\{1,2\}\right]\;\tilde{\boldsymbol{b}}_2\end{aligned} \tag{4.5.61}$$

Thus, the submatrix $\tilde{\boldsymbol{B}}_2$ can be expressed as

$$\tilde{\boldsymbol{B}}_2 = \begin{pmatrix}\boldsymbol{0}_{6\times3} & (\tilde{\boldsymbol{b}}_2)^T_{6\times6} & \boldsymbol{0}_{6\times12}\end{pmatrix}^T. \tag{4.5.62}$$

Construction of $\tilde{\boldsymbol{B}}_3$

The next submatrix to construct is the matrix $\tilde{\boldsymbol{B}}_3$ that relates the 9 second derivative degrees of freedom on the reference element, to the degrees of freedom on the reference element. Again this follows exactly as in Bernadou and Boisserie [1993].

To construct the submatrix, we first express the derivatives on the reference element in terms of the local degrees of freedom. In general the tangent vectors depend on the position, as follows

$$\frac{\partial^2\hat{w}}{\partial\hat{x}_\alpha\partial\hat{x}_\beta} = \frac{\partial}{\partial\hat{x}_\alpha}\left(\frac{\partial w}{\partial x_\gamma}\frac{\partial F_{K\gamma}}{\partial\hat{x}_\beta}\right) = \frac{\partial^2 w}{\partial x_\gamma\partial x_\delta}\frac{\partial F_{K\gamma}}{\partial\hat{x}_\beta}\frac{\partial F_{K\delta}}{\partial\hat{x}_\alpha} + \frac{\partial w}{\partial x_\gamma}\frac{\partial^2 F_{K\gamma}}{\partial\hat{x}_\alpha\partial\hat{x}_\beta}\,, \tag{4.5.63}$$

where $\boldsymbol{F}_k = \boldsymbol{x}$.

After some algebra (see appendix D for details), we obtain

$$\frac{\partial^2\hat{w}}{\partial\hat{x}_1\partial\hat{x}_1}(\hat{\boldsymbol{a}}_1) = \boldsymbol{\nabla}\boldsymbol{\nabla} w(\boldsymbol{a}_1)\cdot(\boldsymbol{A}_1\otimes\boldsymbol{A}_1)\,, \tag{4.5.64}$$

$$\frac{\partial^2\hat{w}}{\partial\hat{x}_1\partial\hat{x}_2}(\hat{\boldsymbol{a}}_1) = \boldsymbol{\nabla}\boldsymbol{\nabla} w(\boldsymbol{a}_1)\cdot(\boldsymbol{A}_1\otimes(\boldsymbol{A}_1-\boldsymbol{A}_2)) + \boldsymbol{\nabla} w(\boldsymbol{a}_1)\cdot\left(2(\boldsymbol{B}_2-\boldsymbol{A}_1)+\frac{1}{2}(3\boldsymbol{A}_2-\boldsymbol{B}_1)\right)\,, \tag{4.5.65}$$

$$\frac{\partial^2\hat{w}}{\partial\hat{x}_2\partial\hat{x}_2}(\hat{\boldsymbol{a}}_1) = \boldsymbol{\nabla}\boldsymbol{\nabla} w(\boldsymbol{a}_1)\cdot((\boldsymbol{A}_1-\boldsymbol{A}_2)\otimes(\boldsymbol{A}_1-\boldsymbol{A}_2)) + \boldsymbol{\nabla} w(\boldsymbol{a}_1)\cdot(2(\boldsymbol{A}_1-\boldsymbol{B}_2)-(\boldsymbol{A}_2-\boldsymbol{B}_1))\,, \tag{4.5.66}$$

$$\frac{\partial^2\hat{w}}{\partial\hat{x}_1\partial\hat{x}_1}(\hat{\boldsymbol{a}}_2) = \boldsymbol{\nabla}\boldsymbol{\nabla} w(\boldsymbol{a}_2)\cdot((\boldsymbol{B}_2-\boldsymbol{B}_1)\otimes(\boldsymbol{B}_2-\boldsymbol{B}_1)) + \boldsymbol{\nabla} w(\boldsymbol{a}_2)\cdot(2(\boldsymbol{B}_2-\boldsymbol{A}_1)+(\boldsymbol{A}_2-\boldsymbol{B}_1))\,, \tag{4.5.67}$$

$$\frac{\partial^2\hat{w}}{\partial\hat{x}_1\partial\hat{x}_2}(\hat{\boldsymbol{a}}_2) = \boldsymbol{\nabla}\boldsymbol{\nabla} w(\boldsymbol{a}_2)\cdot((\boldsymbol{B}_2-\boldsymbol{B}_1)\otimes\boldsymbol{B}_2) + \boldsymbol{\nabla} w(\boldsymbol{a}_2)\cdot\left(2(\boldsymbol{A}_1-\boldsymbol{B}_2)+\frac{1}{2}(3\boldsymbol{B}_1-\boldsymbol{A}_2)\right)\,, \tag{4.5.68}$$

$$\frac{\partial^2\hat{w}}{\partial\hat{x}_2\partial\hat{x}_2}(\hat{\boldsymbol{a}}_2) = \boldsymbol{\nabla}\boldsymbol{\nabla} w(\boldsymbol{a}_2)\cdot(\boldsymbol{B}_2\otimes\boldsymbol{B}_2)\,, \tag{4.5.69}$$

$$\frac{\partial^2 \hat{w}}{\partial \hat{x}_1 \partial \hat{x}_2}(\hat{\boldsymbol{a}}_3) = \boldsymbol{\nabla}\boldsymbol{\nabla} w(\boldsymbol{a}_3) \cdot (\boldsymbol{A}_1 \otimes \boldsymbol{A}_1)\,, \tag{4.5.70}$$

$$\frac{\partial^2 \hat{w}}{\partial \hat{x}_1 \partial \hat{x}_2}(\hat{\boldsymbol{a}}_3) = \boldsymbol{\nabla}\boldsymbol{\nabla} w(\boldsymbol{a}_3) \cdot (\boldsymbol{A}_1 \otimes \boldsymbol{B}_2) + \boldsymbol{\nabla} w(\boldsymbol{a}_3) \cdot \frac{1}{2}(\boldsymbol{B}_1 + \boldsymbol{A}_2)\,, \tag{4.5.71}$$

$$\frac{\partial^2 \hat{w}}{\partial \hat{x}_2 \partial \hat{x}_2}(\hat{\boldsymbol{a}}_3) = \boldsymbol{\nabla}\boldsymbol{\nabla} w(\boldsymbol{a}_3) \cdot (\boldsymbol{B}_2 \otimes \boldsymbol{B}_2)\,. \tag{4.5.72}$$

Now, recalling that $\boldsymbol{C}_1 = -\boldsymbol{B}_2$ and $\boldsymbol{C}_2 = -\boldsymbol{A}_1$, we define the constants, $\tilde{a}^\alpha$, $\tilde{b}^\alpha$, $\tilde{\tilde{a}}^\alpha$, $\tilde{\tilde{b}}^\alpha$, $\tilde{c}^\alpha$ and $\tilde{\tilde{c}}^\alpha$ such that

$$\boldsymbol{B}_2 - \boldsymbol{A}_1 = \tilde{a}^\alpha \boldsymbol{A}_\alpha\,, \qquad \boldsymbol{B}_1 = -\tilde{\tilde{a}}^\alpha \boldsymbol{A}_\alpha\,, \tag{4.5.73}$$

$$\boldsymbol{A}_1 - \boldsymbol{B}_2 = \tilde{b}^\alpha \boldsymbol{B}_\alpha\,, \qquad \boldsymbol{A}_2 = \quad \tilde{\tilde{b}}^\alpha \boldsymbol{B}_\alpha\,, \tag{4.5.74}$$

$$\boldsymbol{A}_2 = \tilde{c}^\alpha \boldsymbol{C}_\alpha\,, \qquad \boldsymbol{B}_1 = \quad \tilde{\tilde{c}}^\alpha \boldsymbol{C}_\alpha\,, \tag{4.5.75}$$

and use these constants to re-express equations (4.5.64–4.5.72) in terms of the local degrees of freedom. After some manipulation, which we detail in appendix D, we obtain the submatrices $\tilde{\boldsymbol{b}}_{3a}$ and $\tilde{\boldsymbol{b}}_{3b}$ which together relate the reference second derivative degrees of freedom to the local second and first derivative degree of freedom. The matrices are given by

$$\tilde{\boldsymbol{b}}_{3a} = \begin{pmatrix}
0 & (2\tilde{a}^1 + \frac{1}{2}\tilde{\tilde{a}}^1) & -(2\tilde{a}^1 + \tilde{\tilde{a}}^1) & 0 & 0 & 0\;0 & 0 & 0 \\
0 & (\frac{3}{2} + 2\tilde{a}^2 + \frac{1}{2}\tilde{\tilde{a}}^2) & -(1 + 2\tilde{a}^2 + \tilde{\tilde{a}}^2) & 0 & 0 & 0\;0 & 0 & 0 \\
0 & 0 & 0 & -(1 + 2\tilde{b}^1 - \tilde{\tilde{b}}^1) & (\frac{3}{2} + 2\tilde{b}^1 - \frac{1}{2}\tilde{\tilde{b}}^1) & 0\;0 & 0 & 0 \\
0 & 0 & 0 & -(2\tilde{b}^2 - \tilde{\tilde{b}}^2) & (2\tilde{b}^2 - \frac{1}{2}\tilde{\tilde{b}}^2) & 0\;0 & 0 & 0 \\
0 & 0 & 0 & 0 & 0 & 0\;0\;\frac{1}{2}(\tilde{c}^1 + \tilde{\tilde{c}}^1) & 0 \\
0 & 0 & 0 & 0 & 0 & 0\;0\;\frac{1}{2}(\tilde{c}^2 + \tilde{\tilde{c}}^2) & 0
\end{pmatrix} \tag{4.5.76}$$

and

$$\tilde{\boldsymbol{b}}_{3b} = \begin{pmatrix}
1 & \left(1 + \frac{1+\tilde{a}^1}{2\tilde{a}^2}\right) & \left(1 + \frac{1+\tilde{a}^1}{\tilde{a}^2}\right) & 0 & 0 & 0 & 0 & 0 & 0 \\
0 & \frac{\tilde{a}^2}{2(1+\tilde{a}^1)} & \left(1 + \frac{\tilde{a}^2}{1+\tilde{a}^1}\right) & 0 & 0 & 0 & 0 & 0 & 0 \\
0 & 0 & 0 & \left(1 + \frac{\tilde{b}^1}{1+\tilde{b}^2}\right) & \frac{\tilde{b}^1}{2(1+\tilde{b}^2)} & 0 & 0 & 0 & 0 \\
0 & 0 & 0 & \left(1 + \frac{1+\tilde{b}^2}{\tilde{b}^1}\right) & \left(1 + \frac{1+\tilde{b}^2}{2\tilde{b}^1}\right) & 1 & 0 & 0 & 0 \\
0 & 0 & 0 & 0 & 0 & 0 & 0 & \frac{-\tilde{c}^1\tilde{\tilde{c}}^1}{\tilde{c}^1\tilde{\tilde{c}}^2 + \tilde{c}^2\tilde{\tilde{c}}^1} & 1 \\
0 & 0 & 0 & 0 & 0 & 0 & 1 & \frac{-\tilde{c}^2\tilde{\tilde{c}}^2}{\tilde{c}^1\tilde{\tilde{c}}^2 + \tilde{c}^2\tilde{\tilde{c}}^1} & 0 \\
0 & \frac{-1}{2\tilde{a}^2(1+\tilde{a}^1)} & \frac{-1}{\tilde{a}^2(1+\tilde{a}^1)} & 0 & 0 & 0 & 0 & 0 & 0 \\
0 & 0 & 0 & \frac{-1}{\tilde{b}^1(1+\tilde{b}^2)} & \frac{-1}{2\tilde{b}^1(1+\tilde{b}^2)} & 0 & 0 & 0 & 0 \\
0 & 0 & 0 & 0 & 0 & 0 & 0 & \frac{-1}{\tilde{c}^2\tilde{\tilde{c}}^2 + \tilde{c}^2\tilde{\tilde{c}}^1} & 0
\end{pmatrix}. \tag{4.5.77}$$

It remains to be discussed how to construct the constants, $\tilde{a}^\alpha$, $\tilde{b}^\alpha$, $\tilde{\tilde{a}}^\alpha$, $\tilde{\tilde{b}}^\alpha$, $\tilde{c}^\alpha$ and $\tilde{\tilde{c}}^\alpha$. By taking cross products of the defining relations it can be shown that the constants are given by the following expressions

$$\tilde{a}^1 = \frac{(\boldsymbol{B}_2 \times \boldsymbol{A}_2)\cdot\boldsymbol{k}}{(\boldsymbol{A}_1 \times \boldsymbol{A}_2)\cdot\boldsymbol{k}} - 1\,, \qquad \tilde{a}^2 = \frac{(\boldsymbol{B}_2 \times \boldsymbol{A}_1)\cdot\boldsymbol{k}}{(\boldsymbol{A}_2 \times \boldsymbol{A}_1)\cdot\boldsymbol{k}} \quad , \tag{4.5.78}$$

$$\tilde{\tilde{a}}^1 = -\frac{(\boldsymbol{B}_1 \times \boldsymbol{A}_2)\cdot\boldsymbol{k}}{(\boldsymbol{A}_1 \times \boldsymbol{A}_2)\cdot\boldsymbol{k}} \quad , \qquad \tilde{\tilde{a}}^2 = -\frac{(\boldsymbol{A}_1 \times \boldsymbol{B}_1)\cdot\boldsymbol{k}}{(\boldsymbol{A}_1 \times \boldsymbol{A}_2)\cdot\boldsymbol{k}} \quad , \tag{4.5.79}$$

$$\tilde{b}^1 = \frac{(\boldsymbol{A}_1 \times \boldsymbol{B}_2)\cdot\boldsymbol{k}}{(\boldsymbol{B}_1 \times \boldsymbol{B}_2)\cdot\boldsymbol{k}} \quad , \qquad \tilde{b}^2 = \frac{(\boldsymbol{B}_1 \times \boldsymbol{A}_1)\cdot\boldsymbol{k}}{(\boldsymbol{B}_1 \times \boldsymbol{B}_2)\cdot\boldsymbol{k}} - 1\,, \tag{4.5.80}$$

$$\tilde{\tilde{b}}^1 = \frac{(\boldsymbol{A}_2 \times \boldsymbol{B}_2)\cdot\boldsymbol{k}}{(\boldsymbol{B}_1 \times \boldsymbol{B}_2)\cdot\boldsymbol{k}} \quad , \qquad \tilde{\tilde{b}}^2 = \frac{(\boldsymbol{B}_1 \times \boldsymbol{A}_2)\cdot\boldsymbol{k}}{(\boldsymbol{B}_1 \times \boldsymbol{B}_2)\cdot\boldsymbol{k}} \quad , \tag{4.5.81}$$

and

$$\tilde{c}^1 = -\frac{(\boldsymbol{A}_1 \times \boldsymbol{A}_2)\cdot\boldsymbol{k}}{(\boldsymbol{A}_1 \times \boldsymbol{B}_2)\cdot\boldsymbol{k}} = -\frac{1}{\tilde{a}^2} \quad , \qquad \tilde{c}^2 = -\frac{(\boldsymbol{A}_2 \times \boldsymbol{B}_2)\cdot\boldsymbol{k}}{(\boldsymbol{A}_1 \times \boldsymbol{B}_2)\cdot\boldsymbol{k}} = -\frac{\tilde{\tilde{b}}^1}{\tilde{b}^1} \quad , \tag{4.5.82}$$

$$\tilde{\tilde{c}}^1 = -\frac{(\boldsymbol{A}_1 \times \boldsymbol{B}_1)\cdot\boldsymbol{k}}{(\boldsymbol{A}_1 \times \boldsymbol{B}_2)\cdot\boldsymbol{k}} = \frac{\tilde{\tilde{a}}^2}{\tilde{a}^2} \quad , \qquad \tilde{\tilde{c}}^2 = -\frac{(\boldsymbol{B}_1 \times \boldsymbol{B}_2)\cdot\boldsymbol{k}}{(\boldsymbol{A}_1 \times \boldsymbol{B}_2)\cdot\boldsymbol{k}} = -\frac{1}{\tilde{b}^1} \quad . \tag{4.5.83}$$

Putting this all together, we can finally express the matrix $\tilde{\boldsymbol{B}}_3$ as

$$\tilde{\boldsymbol{B}}_3 = \begin{pmatrix} \boldsymbol{0}_{9\times 3} & (\tilde{\boldsymbol{b}}_{3a})^T_{9\times 6} & (\tilde{\boldsymbol{b}}_{3a})^T_{9\times 9} & \boldsymbol{0}_{9\times 3} \end{pmatrix}^T \,. \tag{4.5.84}$$

Construction of $\hat{f}_i$ and $\hat{g}_i$

The next submatrices to construct are the matrices that relate the edge degrees of freedom on the reference element, which for the curved Bell element are *all* dependent, to the local (nodal) degrees of freedom. We reiterate that the matrices $\tilde{\boldsymbol{B}}_4$ and $\tilde{\boldsymbol{B}}_6$ differ from their Argyris counterparts and, as such, the explicit construction of these is a new contribution to the literature.

We proceed by constructing 1D polynomials, $\hat{f}_i\,, i \in \{1,2,3\}$ and $\hat{g}_i \in \{1,2,3\}$ that correspond to the interpolant of $\hat{w}(\hat{\boldsymbol{x}})$ on the edges and the interpolant of the normal derivative of $\hat{w}(\hat{\boldsymbol{x}})$ on the edges of the reference element, where we label the trace of the edges $[a_1, a_3]$, $[a_2, a_1]$ and $[a_3, a_2]$ as $\hat{f}_1$, $\hat{f}_2$ and $\hat{f}_3$, respectively.

To do this, we introduce two 1D bases, $\mathfrak{F}_i(s_i)$ and $\mathfrak{G}_i(s_i)$, with $s_1 = \hat{x}_1$ and $s_2 = s_3 = \hat{x}_2$ which, when superposed in conjunction with the degrees of freedom, give the interpolants $\hat{f}_i$ and $\hat{g}_i$. Expressed mathematically we have

$$\hat{f}_i = \boldsymbol{\Sigma}_L^{[3]}\,\mathfrak{F}_i \quad \text{and} \quad \hat{g}_i = \boldsymbol{\Sigma}_L^{[3]}\,\mathfrak{G}_i\,. \tag{4.5.85}$$

Once we have obtained $\mathfrak{F}_i$ and $\mathfrak{G}_i$, we simply have to evaluate these vector-valued functions at the appropriate points along the edge to relate the dependent reference, 'degrees of freedom' to the local degrees of freedom on which they depend.

Since the transformation F_K is affine along the edges 1 and 2,[6] the tangent degrees-of-freedom on the curved triangle map directly to the tangent vectors on the curved element, for example $\boldsymbol{\nabla} w(\boldsymbol{a}_1) \cdot \boldsymbol{A}_1 = -\partial \hat{w}/\partial \hat{x}_1(\hat{a}_1)$. Thus, we can immediately write an expression for the trace $\hat{f}_\alpha$ on both the local and reference element:

$$\hat{f}_\alpha(\hat{x}_\alpha) = \boldsymbol{\Sigma}_L^{[3]}\, \mathfrak{F}_\alpha = \Big[w(\boldsymbol{a}_3)\,;\, \boldsymbol{\nabla} w(\boldsymbol{a}_3)\cdot \boldsymbol{C}_\alpha\,;\, \boldsymbol{\nabla}^2 w(\boldsymbol{a}_3)\cdot(\boldsymbol{C}_{(\alpha)}\otimes \boldsymbol{C}_{(\alpha)})\,;\, w(\boldsymbol{a}_\alpha)\,; \\ - \boldsymbol{\nabla} w(\boldsymbol{a}_{(\alpha)})\cdot \boldsymbol{C}_{(\alpha)}\,;\, \boldsymbol{\nabla}^2 w(\boldsymbol{a}_{(\alpha)})\cdot(\boldsymbol{C}_{(\alpha)}\otimes \boldsymbol{C}_{(\alpha)})\,;\, \Big] \cdot \boldsymbol{\psi}_{\boldsymbol{H}}^{\boldsymbol{Q}}(\hat{x}_\alpha)\,, \quad (4.5.86)$$

where $\hat{x}_\alpha \in [0,1]$ and $\boldsymbol{\psi}_{\boldsymbol{H}}^{\boldsymbol{Q}}$ are the set of six 1D basis polynomials corresponding to the degrees of freedom $\hat{f}_\alpha(0)$, $\hat{f}'_\alpha(0)$, $\hat{f}''_\alpha(0)$, $\hat{f}_\alpha(1)$, $-\hat{f}'_\alpha(1)$ and $\hat{f}''_\alpha(1)$, as detailed in the appendix. Here, we have introduced bracketed indices to indicate that there is no summation.

Thus we can deduce, using the basis polynomials in the appendix, that $\mathfrak{F}^\alpha$ are given by

$$\mathfrak{F}^1 = \Big[\hat{x}_1^3(10-15\hat{x}_1+6\hat{x}_1^2)\,;\, 0\,;\, (1-\hat{x}_1)^3(1+3\hat{x}_1+6\hat{x}_1^2)\,;\, \hat{x}_1^3(4-7\hat{x}_1+3\hat{x}_1^2)\,;\, 0\,0\,0\,0\,; \\ (1-\hat{x}_1)^3\hat{x}_1(1+3\hat{x}_1)\,;\, \frac{1}{2}(1-\hat{x}_1)^2\hat{x}_1^3\,;\, 0\,0\,0\,0\,;\, \frac{1}{2}\hat{x}_1^2(1-\hat{x}_1)^3\,;\, 0\,0\,0\,0\,0\,0 \Big]^T, \quad (4.5.87)$$

$$\mathfrak{F}^2 = \Big[0\,;\, \hat{x}_2^3(10-15\hat{x}_2+6\hat{x}_2^2)\,;\, (1-\hat{x}_2)^3(1+3\hat{x}_2+6\hat{x}_2^2)\,;\, 0\,0\,0\,;\, \hat{x}_2^3(4-7\hat{x}_2+3\hat{x}_2^2)\,; \\ (1-\hat{x}_2)^3\hat{x}_2(1+3\hat{x}_2)\,;\, 0\,0\,0\,0\,;\, \frac{1}{2}(1-\hat{x}_2)^2\hat{x}_2^3\,;\, \frac{1}{2}\hat{x}_2^2(1-\hat{x}_2)^3\,;\, 0\,0\,0\,0\,0\,0\,0 \Big]^T, \quad (4.5.88)$$

which are the expressions obtained by [Bernadou and Boisserie, 1993].

We now construct the trace of the normal on the straight edges 1 and 2. We introduce the altitude (normal) vectors $\boldsymbol{n}_1$ and $\boldsymbol{n}_2$ as

$$\boldsymbol{n}_1 = \boldsymbol{a}_1 - \boldsymbol{c}_1 \quad \text{and} \quad \boldsymbol{n}_2 = \boldsymbol{a}_2 - \boldsymbol{c}_2 \quad (4.5.89)$$

where $\boldsymbol{c}_3$ are the points on side α where the normal vector that passes through vertex $\boldsymbol{a}_\alpha$ intersects, as shown in figure 4.28. We refer to this vector as the altitude vector as its length is the geometric altitude of the triangle.

We may relate the altitude vectors to the tangent vectors as follows

$$\boldsymbol{n}_1 = (\tilde{\boldsymbol{B}}_2 - \tilde{\boldsymbol{A}}_1) - \frac{1}{2}(1+\eta_1)\tilde{\boldsymbol{B}}_{\boldsymbol{2}} \quad \text{and} \quad \boldsymbol{n}_2 = (\tilde{\boldsymbol{A}}_1 - \tilde{\boldsymbol{B}}_2) - \frac{1}{2}(1-\eta_2)\tilde{\boldsymbol{A}}_{\boldsymbol{1}}\,. \quad (4.5.90)$$

[6] By this we mean, the straight edges α on $\hat{K}$ map to straight edges on K.

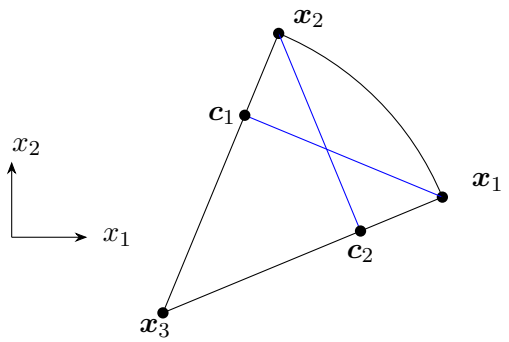

Figure 4.28: The altitudes (blue lines) of a particular triangle. The altitude vectors point from the points $\boldsymbol{c}_\alpha$ to the opposite node $\boldsymbol{x}_\alpha$.

in which η_α are the eccentricity parameters. In the above expression the geometric meaning of, for example, the term $(1+\eta_1)/2$ is the distance of $\boldsymbol{c}_1$ from node $\boldsymbol{a}_2$ relative to the length of the edge. Thus, if $\eta_1 = -1$, $\boldsymbol{c}_1 = \boldsymbol{a}_1$ and the triangle is degenerate. Alternatively, if $\eta_2 = 1$ the triangle will be right-angled at the vertex opposite to the curved edge. These parameters can be determined by the following relations

$$\eta_1 = 1 - 2\left(\frac{\tilde{\boldsymbol{A}}_1 \cdot \tilde{\boldsymbol{B}}_2}{\tilde{\boldsymbol{B}}_{\boldsymbol{2}} \cdot \tilde{\boldsymbol{B}}_2}\right) \quad \text{and} \quad \eta_2 = 2\left(\frac{\tilde{\boldsymbol{B}}_2 \cdot \tilde{\boldsymbol{A}}_1}{\tilde{\boldsymbol{A}}_{\boldsymbol{1}} \cdot \tilde{\boldsymbol{A}}_1}\right) - 1\,. \tag{4.5.91}$$

which can be found by taking the dot product of n_α with the tangent vectors $\boldsymbol{C}_\alpha$.

We wish to express the trace in terms of the normal derivative degrees of freedom on the reference element. Expressed mathematically we have

$$\hat{g}_\alpha(\hat{x}_\alpha) = \boldsymbol{\Sigma}_L^{[3]}\,\boldsymbol{\mathfrak{G}}_\alpha = \Big[\boldsymbol{\nabla} w(\boldsymbol{a}_3)\cdot\boldsymbol{n}_\beta\,;\,\boldsymbol{\nabla}^2 w(\boldsymbol{a}_3)\cdot(\boldsymbol{n}_\beta\otimes\boldsymbol{C}_\beta)\,; \\ \boldsymbol{\nabla} w(\boldsymbol{a}_\alpha)\cdot\boldsymbol{n}_\beta\,;\,\boldsymbol{\nabla}^2 w(\boldsymbol{a}_\alpha)\cdot(\boldsymbol{n}_\beta\otimes\boldsymbol{C}_\beta)\,,\ \beta\neq\alpha\Big]\cdot\boldsymbol{\psi}_{\boldsymbol{H}}^{\boldsymbol{C}}(\hat{x}_\alpha)\,, \tag{4.5.92}$$

where $\hat{x}_\alpha \in [0,1]$ and we are *not* summing over repeated indices. $\boldsymbol{\psi}_{\boldsymbol{H}}^{\boldsymbol{C}}$ are the set of four 1D basis polynomials corresponding to the degrees of freedom $\hat{f}_\alpha(0)$ $\hat{f}'_\alpha(0)$, $\hat{f}_\alpha(1)$, and $-\hat{f}'_\alpha(1)$, which we recall from section 4.1 and can also be found in the appendix. Here, we have introduced bracketed indices to indicate that there is no summation.

Considering g_1 first, we rewrite derivatives in terms of the local degrees of freedom:

$$\hat{g}_1(\hat{x}_1) = \Big[-\frac{1}{2}(1+\eta_2)\boldsymbol{\nabla} w(\boldsymbol{a}_3)\cdot\boldsymbol{C}_2 + \boldsymbol{\nabla} w(\boldsymbol{a}_3)\cdot\boldsymbol{C}_1\,;\,\left(-\frac{1}{2}(1+\eta_2) - \frac{\tilde{c}^2\tilde{\tilde{c}}^2}{\tilde{c}^1\tilde{\tilde{c}}^2+\tilde{c}^2\tilde{\tilde{c}}^1}\right)\boldsymbol{\nabla}^2 w(\boldsymbol{a}_3) \\ \cdot(\boldsymbol{C}_2\otimes\boldsymbol{C}_2) - \frac{\tilde{c}^1\tilde{\tilde{c}}^1}{\tilde{c}^1\tilde{\tilde{c}}^2+\tilde{c}^2\tilde{\tilde{c}}^1}\boldsymbol{\nabla}^2 w(\boldsymbol{a}_3)\cdot(\boldsymbol{C}_1\otimes\boldsymbol{C}_1) + \frac{1}{\tilde{c}^1\tilde{\tilde{c}}^2+\tilde{c}^2\tilde{\tilde{c}}^1}\boldsymbol{\nabla}^2 w(\boldsymbol{a}_3)\cdot(\boldsymbol{A}_2\otimes\boldsymbol{B}_1)\,; \\ -\frac{1}{2}(1+2\tilde{a}^1-\eta_2)\boldsymbol{\nabla} w(\boldsymbol{a}_1)\cdot\boldsymbol{A}_1 - \tilde{a}^2\boldsymbol{\nabla} w\cdot(\boldsymbol{a}_1\cdot\boldsymbol{A}_2)\,;\,\frac{(\tilde{a}^2)^2}{2(1+\tilde{a}^1)}\boldsymbol{\nabla}^2 w(\boldsymbol{a}_1)\cdot(\boldsymbol{A}_2\otimes\boldsymbol{A}_2) \\ -\frac{1}{2}(\tilde{a}^1-\eta_2)\boldsymbol{\nabla}^2 w(\boldsymbol{a}_1)\cdot(\boldsymbol{A}_1\otimes\boldsymbol{A}_1) - \frac{1}{2(1+\tilde{a}^1)}\boldsymbol{\nabla}^2 w(\boldsymbol{a}_1)\cdot(\boldsymbol{B}_2\otimes\boldsymbol{B}_2)\,;\Big]\cdot\boldsymbol{\psi}_{\boldsymbol{H}}^{\boldsymbol{Q}}(\hat{x}_1)\,, \tag{4.5.93}$$

where we have used some results from the appendix in order to express the second derivatives in terms of tangent degrees of freedom. Similarly $\hat{g}_2$ is given by

$$\begin{aligned}\hat{g}_2(\hat{x}_2) = \Big[&-\frac{1}{2}(1-\eta_1)\boldsymbol{\nabla} w(\boldsymbol{a}_3)\cdot\boldsymbol{C}_1 + \boldsymbol{\nabla} w(\boldsymbol{a}_3)\cdot\boldsymbol{C}_2\,;\, \left(-\frac{1}{2}(1-\eta_1) - \frac{\tilde{c}^1\tilde{\tilde{c}}^1}{\tilde{c}^1\tilde{\tilde{c}}^2+\tilde{c}^2\tilde{\tilde{c}}^1}\right)\boldsymbol{\nabla}^2 w(\boldsymbol{a}_3)\\ &\cdot(\boldsymbol{C}_1\otimes\boldsymbol{C}_1) - \frac{\tilde{c}^2\tilde{\tilde{c}}^2}{\tilde{c}^1\tilde{\tilde{c}}^2+\tilde{c}^2\tilde{\tilde{c}}^1}\boldsymbol{\nabla}^2 w(\boldsymbol{a}_3)\cdot(\boldsymbol{C}_2\otimes\boldsymbol{C}_2) + \frac{1}{\tilde{c}^1\tilde{\tilde{c}}^2+\tilde{c}^2\tilde{\tilde{c}}^1}\boldsymbol{\nabla}^2 w(\boldsymbol{a}_3)\cdot(\boldsymbol{A}_2\otimes\boldsymbol{B}_1)\,;\\ &-\frac{1}{2}(1+2\tilde{b}^2+\eta_1)\boldsymbol{\nabla} w(\boldsymbol{a}_2)\cdot\boldsymbol{B}_2 - \tilde{b}^1\boldsymbol{\nabla} w\cdot(\boldsymbol{a}_2\cdot\boldsymbol{B}_1)\,;\, \frac{(\tilde{b}^1)^2}{2(1+\tilde{b}^2)}\boldsymbol{\nabla}^2 w(\boldsymbol{a}_2)\cdot(\boldsymbol{B}_1\otimes\boldsymbol{B}_1)\\ &-\frac{1}{2}(\tilde{b}^2+\eta_1)\boldsymbol{\nabla}^2 w(\boldsymbol{a}_2)\cdot(\boldsymbol{B}_2\otimes\boldsymbol{B}_2) - \frac{1}{2(1+\tilde{b}^2)}\boldsymbol{\nabla}^2 w(\boldsymbol{a}_2)\cdot(\boldsymbol{A}_1\otimes\boldsymbol{A}_1)\,;\,\Big]\cdot\boldsymbol{\psi}^{\boldsymbol{Q}}_{\boldsymbol{H}}(\hat{x}_2)\,.\end{aligned} \tag{4.5.94}$$

We may finally express the matrices $\mathfrak{G}_\alpha$ by using the above expressions for $\hat{g}_\alpha$. The matrices $\mathfrak{G}_\alpha$ are given by

$$\begin{aligned}\mathfrak{G}_1 = \Big[&0\,0\,0\,;\, -\frac{1}{2}(1+2\tilde{a}^1-\eta_2)(3-2\hat{x}_1)\hat{x}_1^2\,;\, -\tilde{a}^2(3-2\hat{x}_1)\hat{x}_1^2\,;\, 0\,0\,;\, (1-\hat{x}_1)^2(1+2\hat{x}_1)\,;\\ &-\frac{1}{2}(1+\eta_2)(1-\hat{x}_1)^2(1+2\hat{x}_1)\,;\, -\frac{1}{2}(\tilde{a}^1-\eta_2)(1-\hat{x}_1)\hat{x}_1^2\,;\, \frac{(\tilde{a}^2)^2}{2(1+\tilde{a}^1)}(1-\hat{x}_1)\hat{x}_1^2\,;\, 0\,0\,;\\ &-\frac{\tilde{c}^1\tilde{\tilde{c}}^1}{\tilde{c}^1\tilde{\tilde{c}}^2+\tilde{c}^2\tilde{\tilde{c}}^1}(1-\hat{x}_1^2)\hat{x}_1\,;\, -\left(\frac{1}{2}(1+\eta_2)+\frac{\tilde{c}^2\tilde{\tilde{c}}^2}{\tilde{c}^1\tilde{\tilde{c}}^2+\tilde{c}^2\tilde{\tilde{c}}^1}\right)(1-\hat{x}_1^2)\hat{x}_1\,;\\ &-\frac{1}{2(1+\tilde{a}^1)}(1-\hat{x}_1)\hat{x}_1^2\,;\, 0\,;\, -\frac{1}{\tilde{c}^1\tilde{\tilde{c}}^2+\tilde{c}^2\tilde{\tilde{c}}^1}(1-\hat{x}_1^2)\hat{x}_1\,;\, 0\,0\,0\,\Big]^T,\end{aligned} \tag{4.5.95}$$

and

$$\begin{aligned}\mathfrak{G}_2 = \Big[&0\,0\,0\,0\,0;\, -\tilde{b}^1(3-2\hat{x}_2)\hat{x}_2^2\,;\, -\frac{1}{2}(1+2\tilde{b}^2+\eta_1)(3-2\hat{x}_2)\hat{x}_2^2\,;\, \frac{1}{2}(\eta_1-1)(1-\hat{x}_2)^2(1+2\hat{x}_2)\,;\\ &(1-\hat{x}_2)^2(1+2\hat{x}_2)\,;\, 0\,0\,;\, \frac{(\tilde{b}^1)^2}{2(1+\tilde{b}^2)}(1-\hat{x}_2)\hat{x}_2^2\,;\, -\frac{1}{2}(\tilde{b}^2+\eta_1)(1-\hat{x}_2)\hat{x}_2^2\,;\\ &-\frac{1}{2}\left((1-\eta_1)+\frac{\tilde{c}^1\tilde{\tilde{c}}^1}{\tilde{c}^1\tilde{\tilde{c}}^2+\tilde{c}^2\tilde{\tilde{c}}^1}\right)(1-\hat{x}_2^2)\hat{x}_2\,;\, -\frac{\tilde{c}^2\tilde{\tilde{c}}^2}{\tilde{c}^1\tilde{\tilde{c}}^2+\tilde{c}^2\tilde{\tilde{c}}^1}(1-\hat{x}_2^2)\hat{x}_2\,;\, 0\,;\\ &-\frac{1}{2(1+\tilde{b}^2)}(1-\hat{x}_2)\hat{x}_2^2\,;\, -\frac{1}{\tilde{c}^1\tilde{\tilde{c}}^2+\tilde{c}^2\tilde{\tilde{c}}^1}(1-\hat{x}_2^2)\hat{x}_2\,;\, 0\,0\,0\,\Big]^T,\end{aligned} \tag{4.5.96}$$

which use a lower order interpolation than the expressions obtained by [Bernadou and Boisserie, 1993], due to the lack of a normal degree of freedom.

We now construct the traces for the curved edges. For these elements the trace $\hat{f}_3$ is determined entirely by the following data of the degrees of freedom

$$\begin{aligned}\big\{&\hat{w}(\hat{\boldsymbol{a}}_2)\,;\, \hat{\boldsymbol{\nabla}}\hat{w}(\hat{\boldsymbol{a}}_2)\cdot(\hat{\boldsymbol{a}}_1-\hat{\boldsymbol{a}}_2)\,;\, \hat{\boldsymbol{\nabla}}\hat{\boldsymbol{\nabla}}\hat{w}(\hat{\boldsymbol{a}}_2)\cdot(\hat{\boldsymbol{a}}_1-\hat{\boldsymbol{a}}_2)\otimes(\hat{\boldsymbol{a}}_1-\hat{\boldsymbol{a}}_2)\,;\\ &\hat{w}(\hat{\boldsymbol{a}}_1)\,;\, \hat{\boldsymbol{\nabla}}\hat{w}(\hat{\boldsymbol{a}}_1)\cdot(\hat{\boldsymbol{a}}_2-\hat{\boldsymbol{a}}_1)\,;\, \hat{\boldsymbol{\nabla}}\hat{\boldsymbol{\nabla}}\hat{w}(\hat{\boldsymbol{a}}_1)\cdot(\hat{\boldsymbol{a}}_2-\hat{\boldsymbol{a}}_1)\otimes(\hat{\boldsymbol{a}}_2-\hat{\boldsymbol{a}}_1)\,\big\}\,,\end{aligned} \tag{4.5.97}$$

which may be expressed in terms of the reference degrees of freedom as

$$\begin{aligned}\big\{ &\hat{w}(\hat{\boldsymbol{a}}_2)\ ;\ \frac{\partial\hat{w}(\hat{\boldsymbol{a}}_2)}{\partial\hat{x}_1}-\frac{\partial\hat{w}(\hat{\boldsymbol{a}}_2)}{\partial\hat{x}_2}\ ;\ \frac{\partial^2\hat{w}(\hat{\boldsymbol{a}}_2)}{\partial\hat{x}_1^2}+\frac{\partial^2\hat{w}(\hat{\boldsymbol{a}}_2)}{\partial\hat{x}_2^2}-2\frac{\partial^2\hat{w}(\hat{\boldsymbol{a}}_2)}{\partial\hat{x}_1\partial\hat{x}_2}\ ;\\ &\hat{w}(\hat{\boldsymbol{a}}_1)\ ;\ \frac{\partial\hat{w}(\hat{\boldsymbol{a}}_1)}{\partial\hat{x}_2}-\frac{\partial\hat{w}(\hat{\boldsymbol{a}}_1)}{\partial\hat{x}_1}\ ;\ \frac{\partial^2\hat{w}(\hat{\boldsymbol{a}}_1)}{\partial\hat{x}_1^2}+\frac{\partial^2\hat{w}(\hat{\boldsymbol{a}}_1)}{\partial\hat{x}_2^2}-2\frac{\partial^2\hat{w}(\hat{\boldsymbol{a}}_1)}{\partial\hat{x}_1\partial\hat{x}_2}\ \big\}\,,\end{aligned} \tag{4.5.98}$$

We can now readily construct the derivatives from the local degrees of freedom by considering relations (4.5.64-4.5.72) and by extension the matrices expressed in equations (4.5.76-4.5.77). We now express $\mathfrak{F}_3$ in the same manner as $\mathfrak{F}_\alpha$:

$$\begin{aligned}\mathfrak{F}_3=\Big[&\hat{x}_1^3\left(6\hat{x}_1^2-15\hat{x}_1+10\right)\ ;\ (1-\hat{x}_1)^{\,3}\left(6\hat{x}_1^2+3\hat{x}_1+1\right)\ ;\ 0\,;\ -(1-\hat{x}_1)^{\,2}\hat{x}_1^3\left(3\tilde{a}^1+\tilde{\tilde{a}}^1\right)\ ;\\ &(1-\hat{x}_1)\,\hat{x}_1^3\left(3\tilde{a}^2\hat{x}_1+\tilde{\tilde{a}}^2\hat{x}_1-\hat{x}_1-3\tilde{a}^2-\tilde{\tilde{a}}^2+2\right)\ ;\ (\hat{x}_1-1)^{\,3}\hat{x}_1\left(3\tilde{b}^1\hat{x}_1-\tilde{\tilde{b}}^1\hat{x}_1-\hat{x}_1-1\right)\ ;\\ &-(1-\hat{x}_1)^{\,3}\hat{x}_1^2\left(3\tilde{b}^2-\tilde{\tilde{b}}^2\right)\ ;\ 0\,0\,0\,;\ \frac{1}{2}(1-\hat{x}_1)^{\,2}\hat{x}_1^3\,;\ \frac{1}{2}(1-\hat{x}_1)^{\,3}\hat{x}_1^2\,;\ 0\,0\,0\,0\,0\,0\,0\,0\,0\Big]^T.\end{aligned} \tag{4.5.99}$$

In general the normal derivative on the curved edge $\hat{\boldsymbol{\nabla}}\hat{w}(1-\hat{x}_2,\hat{x}_2)\cdot(-\hat{\boldsymbol{a}}_1-\hat{\boldsymbol{a}}_2)/2 \neq \boldsymbol{\nabla}w\left(\boldsymbol{\Psi}_h(\hat{x}_2)\right)\cdot\boldsymbol{n}_3$ where $\boldsymbol{n}_3$ is the unit normal to the curved edge, as the mapping is not conformal (i.e. it does not preserve angles). As we have no restriction as to what the trace of the normal need be, we choose a direction which is linearly independent at both nodes on edge 3. Thus we express[7] the normal derivative on the edge

$$\hat{g}_3(\hat{x}_1)=-\hat{\boldsymbol{\nabla}}\hat{w}(\hat{\boldsymbol{x}})\cdot(\hat{\boldsymbol{a}}_1+\hat{\boldsymbol{a}}_{\boldsymbol{2}})/2 \quad \text{for} \quad \hat{x}_2=1-\hat{x}_1\,, \tag{4.5.100}$$

in terms of the independent reference degrees of freedom $\partial\hat{w}(\hat{a}_\alpha)/\partial\hat{x}_\beta$ and $\partial^2\hat{w}(\hat{a}_\alpha)/\partial\hat{x}_\beta\partial\hat{x}_\gamma$. The relevant data of the degrees of freedom are

$$\begin{aligned}\big\{ &\hat{\boldsymbol{\nabla}}\hat{w}(\hat{\boldsymbol{a}}_2)\cdot(-\hat{\boldsymbol{a}}_1-\hat{\boldsymbol{a}}_2)/2\,;\ \hat{\boldsymbol{\nabla}}\hat{\boldsymbol{\nabla}}\hat{w}(\hat{\boldsymbol{a}}_2)\cdot(\hat{\boldsymbol{a}}_1-\hat{\boldsymbol{a}}_2)\otimes(-\hat{\boldsymbol{a}}_1-\hat{\boldsymbol{a}}_2)/2\,;\\ &\hat{\boldsymbol{\nabla}}\hat{w}(\hat{\boldsymbol{a}}_2)\cdot(-\hat{\boldsymbol{a}}_1-\hat{\boldsymbol{a}}_2)/2\,;\ \hat{\boldsymbol{\nabla}}\hat{\boldsymbol{\nabla}}\hat{w}(\hat{\boldsymbol{a}}_1)\cdot(\hat{\boldsymbol{a}}_2-\hat{\boldsymbol{a}}_1)\otimes(-\hat{\boldsymbol{a}}_1-\hat{\boldsymbol{a}}_2)/2\,\big\}\,,\end{aligned} \tag{4.5.101}$$

which must be computed in terms of the local degrees of freedom.

Once again, we can readily calculate the reference normal derivative degrees of freedom by considering relations (4.5.64-4.5.72) and by extension the matrices expressed in equations (4.5.76-4.5.77), to obtain an expression for the matrix $\mathfrak{G}_3$, which differs from that of the

[7] We follow Bernadou and Boisserie [1993] in this convention. However, this means for these elements to be C^1-continuous with other curved elements across the *curved* edge the opposing element must have identical tangents on sides 1 and 2. This complicates their use for internal boundaries.

Argyris element. The matrix, $\mathfrak{G}_3$, is then given by:

$$\mathfrak{G}_3 = \Bigg[0\,0\,0\,;\, \frac{1}{2}\hat{x}_1^2\left(-4\hat{x}_1-(\hat{x}_1-1)\left(2\tilde{a}^1+\tilde{\tilde{a}}^1\right)+6\right)\,;\, \frac{1}{2}\hat{x}_1^2\left(2\hat{x}_1-(\hat{x}_1-1)\left(2\tilde{a}^2+\tilde{\tilde{a}}^2+1\right)-3\right)\,;$$
$$\frac{1}{2}\left(\hat{x}_1-1\right)^2\left(\hat{x}_1\left(2\tilde{b}^1-\tilde{\tilde{b}}^1-1\right)-1\right)\,;\, \frac{1}{2}\left(\hat{x}_1-1\right)^2\left(\hat{x}_1\left(2\tilde{b}^2-\tilde{\tilde{b}}^2+4\right)+2\right)\,;\, 0\,0\,;$$
$$\frac{\left(\hat{x}_1-1\right)\hat{x}_1^2\left(\tilde{a}^1+1\right)}{2\tilde{a}^2}\,;\, \frac{1}{2}\left(\hat{x}_1-1\right)\hat{x}_1^2\left(\frac{\tilde{a}^2}{\tilde{a}^1+1}+1\right)\,;\, \frac{1}{2}\left(\hat{x}_1-1\right)^2\hat{x}_1\left(-\frac{\tilde{b}^1}{\tilde{b}^2+1}-1\right)\,;$$
$$-\frac{\left(\hat{x}_1-1\right)^2\hat{x}_1\left(\tilde{b}^2+1\right)}{2\tilde{b}^1}\,;\, 0\,0\,;\, -\frac{\left(\hat{x}_1-1\right)\hat{x}_1^2}{2\left(\tilde{a}^1+1\right)\tilde{a}^2}\,;\, \frac{\left(\hat{x}_1-1\right)^2\hat{x}_1}{2\tilde{b}^1\left(\tilde{b}^2+1\right)}\,;\, 0\,0\,0\,0\Bigg]. \tag{4.5.102}$$

Construction of $\tilde{\boldsymbol{B}}_4$, $\tilde{\boldsymbol{B}}_5$ and $\tilde{\boldsymbol{B}}_6$

Now we have the expressions $\mathfrak{F}_i$ and $\mathfrak{G}_i$ on each edge, we may construct the final submatrices. First we must express the three normal derivative degrees of freedom at points $\hat{\boldsymbol{b}}_i$ in terms of the local degrees of freedom, which is related by submatrix $\boldsymbol{B}_4$. The reference derivatives are given by

$$-\frac{\partial\hat{w}}{\partial\hat{x}_1}(\hat{\boldsymbol{b}}_1) = -\frac{\partial\boldsymbol{F}_K}{\partial\hat{x}_1}(\hat{\boldsymbol{b}}_1)\cdot\left(\frac{\boldsymbol{B}_2}{|\boldsymbol{B}_2|^2}\,\hat{f}_2'\left(\frac{1}{2}\right)+\frac{\boldsymbol{n}_1}{|\boldsymbol{n}_1|^2}\,\hat{g}_2\left(\frac{1}{2}\right)\right), \tag{4.5.103}$$
$$-\frac{\partial\hat{w}}{\partial\hat{x}_2}(\hat{\boldsymbol{b}}_2) = -\frac{\partial\boldsymbol{F}_K}{\partial\hat{x}_2}(\hat{\boldsymbol{b}}_2)\cdot\left(\frac{\boldsymbol{A}_1}{|\boldsymbol{A}_1|^2}\,\hat{f}_1'\left(\frac{1}{2}\right)+\frac{\boldsymbol{n}_2}{|\boldsymbol{n}_2|^2}\,\hat{g}_1\left(\frac{1}{2}\right)\right), \tag{4.5.104}$$

and

$$\frac{1}{\sqrt{2}}\left(\frac{\partial\hat{w}}{\partial\hat{x}_1}(\hat{\boldsymbol{b}}_3)+\frac{\partial\hat{w}}{\partial\hat{x}_2}(\hat{\boldsymbol{b}}_3)\right) = -\sqrt{2}\hat{g}_3\left(\frac{1}{2}\right), \tag{4.5.105}$$

where we note that $\hat{g}_3$ is by definition the derivative $-\hat{\boldsymbol{\nabla}}\hat{w}(\hat{\boldsymbol{x}})\cdot\hat{\boldsymbol{b}}_3$ evaluated on the edge, such that $\hat{x}_1 = 1-\hat{x}_2$ and that in general, because the mapping is not conformal, derivatives in the direction $\boldsymbol{n}_\alpha$ on the curved element are not equal to derivatives in the direction $\partial\boldsymbol{F}_K/\partial\hat{x}_\alpha$ on the reference element.

Using the above relations, we define the following constants

$$E^1 = -\frac{\partial\boldsymbol{F}_K}{\partial\hat{x}_1}(\hat{\boldsymbol{b}}_1)\cdot\left(\frac{\boldsymbol{B}_2}{|\boldsymbol{B}_2|^2}\right), \quad E^2 = -\frac{\partial\boldsymbol{F}_K}{\partial\hat{x}_1}(\hat{\boldsymbol{b}}_1)\cdot\left(\frac{\boldsymbol{n}_1}{|\boldsymbol{n}_1|^2}\right), \tag{4.5.106}$$
$$F^1 = -\frac{\partial\boldsymbol{F}_K}{\partial\hat{x}_2}(\hat{\boldsymbol{b}}_2)\cdot\left(\frac{\boldsymbol{A}_1}{|\boldsymbol{A}_1|^2}\right), \quad F^2 = -\frac{\partial\boldsymbol{F}_K}{\partial\hat{x}_2}(\hat{\boldsymbol{b}}_2)\cdot\left(\frac{\boldsymbol{n}_2}{|\boldsymbol{n}_2|^2}\right), \tag{4.5.107}$$

in order to finally construct submatrix $\tilde{\boldsymbol{B}}_4$, as follows

$$\tilde{\boldsymbol{B}}_4 = \left[E^1\mathfrak{F}_2\left(\frac{1}{2}\right)+E^2\mathfrak{G}_2\left(\frac{1}{2}\right)\,;\, F^1\mathfrak{F}_1\left(\frac{1}{2}\right)+F^2\mathfrak{G}_1\left(\frac{1}{2}\right)\,;\, \sqrt{2}\mathfrak{G}_3\left(\frac{1}{2}\right)\right]. \tag{4.5.108}$$

Next we must express the submatrix $\boldsymbol{B}_5$ which, using the results of the previous section,

is straightforward. The six dependent Lagrange degrees of freedom can be expressed as

$$\hat{w}(\hat{\boldsymbol{d}}_{\mathbf{1}}) = \hat{f}_2\left(\frac{3}{4}\right), \quad \hat{w}(\hat{\boldsymbol{d}}_{\mathbf{2}}) = \hat{f}_2\left(\frac{1}{4}\right), \tag{4.5.109}$$

$$\hat{w}(\hat{\boldsymbol{d}}_{\mathbf{3}}) = \hat{f}_1\left(\frac{1}{4}\right), \quad \hat{w}(\hat{\boldsymbol{d}}_{\mathbf{4}}) = \hat{f}_1\left(\frac{3}{4}\right), \tag{4.5.110}$$

$$\hat{w}(\hat{\boldsymbol{d}}_{\mathbf{5}}) = \hat{f}_3\left(\frac{3}{4}\right), \quad \hat{w}(\hat{\boldsymbol{d}}_{\mathbf{6}}) = \hat{f}_3\left(\frac{1}{4}\right), \tag{4.5.111}$$

leading directly to the definition of submatrix $\tilde{\boldsymbol{B}}_5$

$$\tilde{\boldsymbol{B}}_5 = \left[\mathfrak{F}_2\left(\frac{3}{4}\right) \;;\; \mathfrak{F}_2\left(\frac{1}{4}\right) \;;\; \mathfrak{F}_1\left(\frac{1}{4}\right) \;;\; \mathfrak{F}_1\left(\frac{3}{4}\right) \;;\; \mathfrak{F}_3\left(\frac{3}{4}\right) \;;\; \mathfrak{F}_3\left(\frac{1}{4}\right)\right] \tag{4.5.112}$$

Finally, in the same manner as for submatrix $\tilde{\boldsymbol{B}}_4$ we relate the remaining dependent normal degrees of freedom on the reference element to the local degrees of freedom. We first introduce the following constants

$$G^1 = -\frac{\partial \boldsymbol{F}_K}{\partial \hat{x}_1}(\hat{\boldsymbol{d}}_{\mathbf{1}}) \cdot \left(\frac{\boldsymbol{B}_2}{|\boldsymbol{B}_2|^2}\right), \quad G^2 = -\frac{\partial \boldsymbol{F}_K}{\partial \hat{x}_1}(\hat{\boldsymbol{d}}_{\mathbf{1}}) \cdot \left(\frac{\boldsymbol{n}_1}{|\boldsymbol{n}_1|^2}\right), \tag{4.5.113}$$

$$H^1 = -\frac{\partial \boldsymbol{F}_K}{\partial \hat{x}_1}(\hat{\boldsymbol{d}}_{\mathbf{2}}) \cdot \left(\frac{\boldsymbol{B}_2}{|\boldsymbol{B}_2|^2}\right), \quad H^2 = -\frac{\partial \boldsymbol{F}_K}{\partial \hat{x}_1}(\hat{\boldsymbol{d}}_{\mathbf{2}}) \cdot \left(\frac{\boldsymbol{n}_1}{|\boldsymbol{n}_1|^2}\right), \tag{4.5.114}$$

$$J^1 = -\frac{\partial \boldsymbol{F}_K}{\partial \hat{x}_2}(\hat{\boldsymbol{d}}_{\mathbf{3}}) \cdot \left(\frac{\boldsymbol{A}_1}{|\boldsymbol{A}_1|^2}\right), \quad J^2 = -\frac{\partial \boldsymbol{F}_K}{\partial \hat{x}_2}(\hat{\boldsymbol{d}}_{\mathbf{3}}) \cdot \left(\frac{\boldsymbol{n}_2}{|\boldsymbol{n}_2|^2}\right), \tag{4.5.115}$$

$$K^1 = -\frac{\partial \boldsymbol{F}_K}{\partial \hat{x}_2}(\hat{\boldsymbol{d}}_{\mathbf{4}}) \cdot \left(\frac{\boldsymbol{A}_1}{|\boldsymbol{A}_1|^2}\right), \quad K^2 = -\frac{\partial \boldsymbol{F}_K}{\partial \hat{x}_2}(\hat{\boldsymbol{d}}_{\mathbf{4}}) \cdot \left(\frac{\boldsymbol{n}_2}{|\boldsymbol{n}_2|^2}\right), \tag{4.5.116}$$

which we then use to define the submatrix $\tilde{\boldsymbol{b}}_6$, as follows

$$\begin{aligned}\tilde{\boldsymbol{B}}_6 = \Bigg[&G^1\mathfrak{F}_2\left(\frac{3}{4}\right) + G^2\mathfrak{G}_2\left(\frac{3}{4}\right) \;;\; H^1\mathfrak{F}_2\left(\frac{1}{4}\right) + H^2\mathfrak{G}_2\left(\frac{1}{4}\right) \;;\; J^1\mathfrak{F}_1\left(\frac{1}{4}\right) + J^2\mathfrak{G}_1\left(\frac{1}{4}\right) \;;\\ &K^1\mathfrak{F}_1\left(\frac{3}{4}\right) + K^2\mathfrak{G}_1\left(\frac{3}{4}\right) \;;\; \sqrt{2}\mathfrak{G}_3\left(\frac{1}{4}\right) \;;\; \sqrt{2}\mathfrak{G}_3\left(\frac{3}{4}\right)\Bigg].\end{aligned} \tag{4.5.117}$$

Construction of $\tilde{\boldsymbol{B}}_7$

As the bubble degrees of freedom, $w(e_i), i \in \{1, 2, 3\}$, are Lagrange-type degrees of freedom, they remain unchanged on the reference element. Therefore the final, local-to-reference submatrix, $\tilde{\boldsymbol{B}}$, can be immediately deduced to be

$$\tilde{\boldsymbol{B}}_7 = \begin{pmatrix}\mathbf{0}_{3\times 18} & \mathbb{I}_3\end{pmatrix}^T. \tag{4.5.118}$$

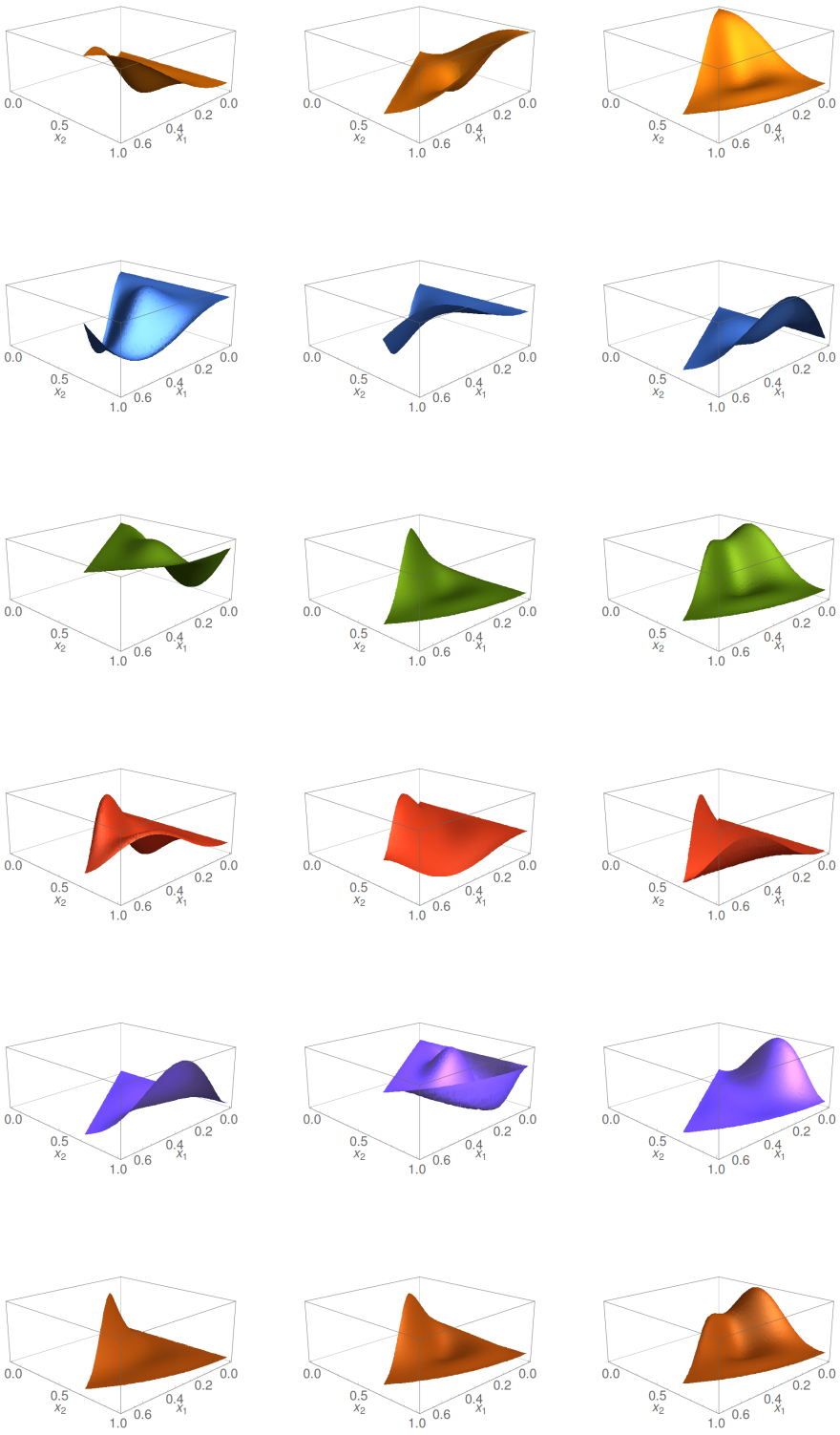

Figure 4.29: P_3 Curved Bell nodal basis functions shown for a particular curved triangle. The different nodal basis functions are shown by column and the different degree of freedom types are shown by row, in various colours. By row the degrees of freedom are ordered as follows: $w(\boldsymbol{a}_i)$, $\partial w(\boldsymbol{a}_i)/\partial x_1$, $\partial w(\boldsymbol{a}_i)/\partial x_2$, $\partial^2 w(\boldsymbol{a}_i)/\partial x_1^2$, $\partial^2 w(\boldsymbol{a}_i)/\partial x_1 \partial x_2$ and $\partial^2 w(\boldsymbol{a}_i)/\partial x_2^2$.

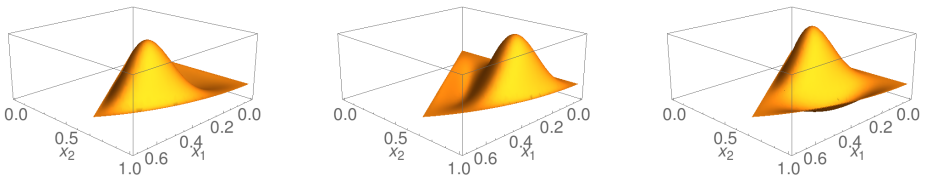

Figure 4.30: P_3 Curved Bell bubble basis functions shown for a particular curved triangle.

Construction of the Reference Basis functions

Now that we have deduced the matrices that transform the reference degrees of freedom to global degrees of freedom, we must construct a set of basis functions on the reference element. This set of 36 basis functions are the set of degree 7, two dimensional polynomials that satisfy the delta property. They can be readily deduced in the manner outlined in appendix D.3: such that we have a 36×36 association matrix, $\tilde{\boldsymbol{A}}$, and the set of 36, 2D monomials of degree less than or equal to seven, $\tilde{\boldsymbol{m}}_7$, which are detailed in the appendix. Thus the basis $\hat{\boldsymbol{\psi}}^{[3]}$ is given by

$$\underbrace{\hat{\boldsymbol{\psi}}^{[3]}}_{36\times 1} = \underbrace{\tilde{\boldsymbol{A}}}_{36\times 36}\ \underbrace{\tilde{\boldsymbol{m}}_7}_{36\times 1} \tag{4.5.119}$$

The association matrix, in turn, can be deduced in the manner outlined in the appendix, and has been computed and expressed therein for the reader's convenience.

Constructing the Global Basis Functions

Finally, we may compute the full basis functions for the P_3 curved triangle element by the following equation

$$\underbrace{\boldsymbol{\psi}^{[3]}}_{21\times 1} = \underbrace{\tilde{\boldsymbol{D}}}_{21\times 21}\ \underbrace{\tilde{\boldsymbol{B}}}_{21\times 36}\ \underbrace{\tilde{\boldsymbol{A}}}_{36\times 36}\ \underbrace{\tilde{\boldsymbol{m}}_7}_{36\times 1} \tag{4.5.120}$$

where the matrices $\tilde{\boldsymbol{D}}$ and $\tilde{\boldsymbol{B}}$ were defined in the preceding sections and $\tilde{\boldsymbol{A}}$ may be found in the appendix. We display the basis functions for the P_3 triangle in figures 4.29 and 4.30.

4.5.7 Construction of the Local-to-Reference Matrix for the P_5 Triangle

Having outlined the method for the P_3-triangle, we now, by the same method, construct the matrix for the P_5-triangle. Once again, we direct the reader not interested in the detailed calculation of the matrices to the summary of these elements in at the end of section 4.5.7.

The methods in the construction remain largely the same, but the details differ due to the form of the mapping, $\boldsymbol{F}_K$.

We begin by partitioning the 21×55 matrix, $\tilde{\tilde{\boldsymbol{B}}}$, as follows

$$\tilde{\tilde{\boldsymbol{B}}} = \begin{pmatrix} \tilde{\tilde{\boldsymbol{B}}}_1 & \tilde{\tilde{\boldsymbol{B}}}_2 & \tilde{\tilde{\boldsymbol{B}}}_3 & \tilde{\tilde{\boldsymbol{B}}}_4 & \tilde{\tilde{\boldsymbol{B}}}_5 & \tilde{\tilde{\boldsymbol{B}}}_6 & \tilde{\tilde{\boldsymbol{B}}}_7 & \tilde{\tilde{\boldsymbol{B}}}_8 & \tilde{\tilde{\boldsymbol{B}}}_9 \end{pmatrix} \tag{4.5.121}$$

in which the submatrices $\tilde{B}_i$ with $i \in \{1, \ldots, 9\}$ have 28 rows of 3, 6, 9, 3, 12, 4, 4, 4 and 10 columns respectively. This corresponds the following partition of the reference degrees of freedom:

$$\begin{aligned} \hat{\boldsymbol{\Sigma}}^{[5]} = \Big[& \big\{ \hat{w}(\hat{\boldsymbol{a}}_i), i \in \{1,2,3\} \big\} \; ; \; \big\{ \frac{\partial \hat{w}(\hat{\boldsymbol{a}}_i)}{\partial \hat{x}_\alpha} \, , \, i \in \{1,2,3\} \big\} \; ; \; \big\{ \frac{\partial^2 \hat{w}(\hat{\boldsymbol{a}}_i)}{\partial \hat{x}_\alpha \partial \hat{x}_\beta} \, , \, \alpha \geq \beta \, , \, i \in \{1,2,3\} \big\} \; ; \\ & \big\{ \hat{\boldsymbol{\nabla}} \hat{w}(\hat{\boldsymbol{b}}_i) \cdot \hat{\boldsymbol{n}}_i \, , \, i \in \{1,2,3\} \big\} \; ; \big\{ \hat{w}(\hat{\boldsymbol{d}}_i) \, , \, i \in \{1 \ldots 12\} \big\} \; ; \big\{ \hat{\boldsymbol{\nabla}} \hat{w}(\hat{\boldsymbol{d}}_i) \cdot \hat{\boldsymbol{n}}_1 \, , \, i \in \{1 \ldots 4\} \big\} \; ; \\ & \big\{ \hat{\boldsymbol{\nabla}} \hat{w}(\hat{\boldsymbol{d}}_i) \cdot \hat{\boldsymbol{n}}_2 \, , \, i \in \{5 \ldots 8\} \big\} \; ; \big\{ \hat{\boldsymbol{\nabla}} \hat{w}(\hat{\boldsymbol{d}}_i) \cdot \hat{\boldsymbol{n}}_3 \, , \, i \in \{9 \ldots 12\} \big\} \; ; \big\{ \hat{w}(\hat{\boldsymbol{e}}_i) \, , \, i \in \{1, \ldots, 10\} \big\} \Big], \end{aligned} \tag{4.5.122}$$

in which as usual we use $\alpha, \beta \in \{1, 2\}$ and we recall that $\hat{\boldsymbol{n}}_\alpha = -\hat{\boldsymbol{a}}_\alpha$ and $\hat{\boldsymbol{n}}_3 = \hat{\boldsymbol{b}}_3 / \sqrt{2}$.

Construction of the Submatrices $\tilde{\boldsymbol{B}}_1$, $\tilde{\boldsymbol{B}}_2$ and $\tilde{\boldsymbol{B}}_3$

The matrix $\tilde{\tilde{B}}_1$ can be immediately deduced to be

$$\tilde{\tilde{\boldsymbol{B}}}_1 = \begin{pmatrix} \mathbb{I}_3 & \boldsymbol{0}_{3\times 25} \end{pmatrix}^T , \tag{4.5.123}$$

as the Lagrange degrees of freedom on the reference element are identical to those on the curved element.

Similarly, as the P_3 and P_5 triangle tangent vectors coincide at vertices, the matrix $\tilde{\boldsymbol{b}}_2$, which relates the first tangent derivatives to reference first derivatives at vertices on the P_3 triangle, also relates the first tangent derivatives to the reference first derivatives. Therefore we can express $\tilde{\tilde{B}}_2$ as

$$\tilde{\tilde{\boldsymbol{B}}}_2 = \begin{pmatrix} \boldsymbol{0}_{6\times 3} & (\tilde{\boldsymbol{b}}_2)^T_{6\times 6} & \boldsymbol{0}_{6\times 19} \end{pmatrix}^T . \tag{4.5.124}$$

We now construct the submatrix $\tilde{\tilde{\boldsymbol{B}}}_3$. Following the same procedure as before, we first construct two matrices $\tilde{\tilde{\boldsymbol{b}}}_{3a}$ and $\tilde{\tilde{\boldsymbol{b}}}_{3b}$. After some algebra, involving second derivatives of the

mapping, we may express the degrees of freedom as

$$\frac{\partial^2\hat{w}}{\partial\hat{x}_1\partial\hat{x}_1}(\hat{\boldsymbol{a}}_1) = \boldsymbol{\nabla}\boldsymbol{\nabla}w(\boldsymbol{a}_1)\cdot(\boldsymbol{A}_1\otimes\boldsymbol{A}_1)\,, \tag{4.5.125}$$

$$\frac{\partial^2\hat{w}}{\partial\hat{x}_1\partial\hat{x}_2}(\hat{\boldsymbol{a}}_1) = \boldsymbol{\nabla}\boldsymbol{\nabla}w(\boldsymbol{a}_1)\cdot(\boldsymbol{A}_1\otimes(\boldsymbol{A}_1-\boldsymbol{A}_2))+\frac{1}{2}\boldsymbol{\nabla}w(\boldsymbol{a}_1)\cdot(\boldsymbol{B}_2-\boldsymbol{A}_1+\boldsymbol{A}_2-\frac{1}{2}\boldsymbol{D}_1)\,, \tag{4.5.126}$$

$$\frac{\partial^2\hat{w}}{\partial\hat{x}_2\partial\hat{x}_2}(\hat{\boldsymbol{a}}_1) = \boldsymbol{\nabla}\boldsymbol{\nabla}w(\boldsymbol{a}_1)\cdot((\boldsymbol{A}_1-\boldsymbol{A}_2)\otimes(\boldsymbol{A}_1-\boldsymbol{A}_2))+\boldsymbol{\nabla}w(\boldsymbol{a}_1)\cdot(\boldsymbol{B}_2-\boldsymbol{A}_1+\boldsymbol{A}_2+\frac{1}{2}\boldsymbol{D}_1)\,, \tag{4.5.127}$$

$$\frac{\partial^2\hat{w}}{\partial\hat{x}_1\partial\hat{x}_1}(\hat{\boldsymbol{a}}_2) = \boldsymbol{\nabla}\boldsymbol{\nabla}w(\boldsymbol{a}_2)\cdot((\boldsymbol{B}_2-\boldsymbol{B}_1)\otimes(\boldsymbol{B}_2-\boldsymbol{B}_1))+\boldsymbol{\nabla}w(\boldsymbol{a}_2)\cdot(\boldsymbol{A}_1-\boldsymbol{B}_2+\boldsymbol{B}_1+\frac{1}{2}\boldsymbol{D}_2)\,, \tag{4.5.128}$$

$$\frac{\partial^2\hat{w}}{\partial\hat{x}_1\partial\hat{x}_2}(\hat{\boldsymbol{a}}_2) = \boldsymbol{\nabla}\boldsymbol{\nabla}w(\boldsymbol{a}_2)\cdot((\boldsymbol{B}_2-\boldsymbol{B}_1)\otimes\boldsymbol{B}_2)+\frac{1}{2}\boldsymbol{\nabla}w(\boldsymbol{a}_2)\cdot(\boldsymbol{A}_1-\boldsymbol{B}_2+\boldsymbol{B}_1-\frac{1}{2}\boldsymbol{D}_2), \tag{4.5.129}$$

$$\frac{\partial^2\hat{w}}{\partial\hat{x}_2\partial\hat{x}_2}(\hat{\boldsymbol{a}}_2) = \boldsymbol{\nabla}\boldsymbol{\nabla}w(\boldsymbol{a}_2)\cdot(\boldsymbol{B}_2\otimes\boldsymbol{B}_2)\,, \tag{4.5.130}$$

$$\frac{\partial^2\hat{w}}{\partial\hat{x}_1\partial\hat{x}_2}(\hat{\boldsymbol{a}}_3) = \boldsymbol{\nabla}\boldsymbol{\nabla}w(\boldsymbol{a}_3)\cdot(\boldsymbol{A}_1\otimes\boldsymbol{A}_1)\,, \tag{4.5.131}$$

$$\frac{\partial^2\hat{w}}{\partial\hat{x}_1\partial\hat{x}_2}(\hat{\boldsymbol{a}}_3) = \boldsymbol{\nabla}\boldsymbol{\nabla}w(\boldsymbol{a}_3)\cdot\frac{1}{2}(\boldsymbol{A}_1\otimes\boldsymbol{B}_2)+\boldsymbol{\nabla}w(\boldsymbol{a}_3)\cdot\frac{1}{2}(\boldsymbol{B}_1+\boldsymbol{A}_2)\,, \tag{4.5.132}$$

$$\frac{\partial^2\hat{w}}{\partial\hat{x}_2\partial\hat{x}_2}(\hat{\boldsymbol{a}}_3) = \boldsymbol{\nabla}\boldsymbol{\nabla}w(\boldsymbol{a}_3)\cdot(\boldsymbol{B}_2\otimes\boldsymbol{B}_2)\,, \tag{4.5.133}$$

in which we introduced the new vectors

$$\boldsymbol{D}_1 = (\bar{s}-\underset{\sim}{s})^2\chi''(\underset{\sim}{s})\,,\quad \boldsymbol{D}_2 = (\bar{s}-\underset{\sim}{s})^2\chi''(\bar{s})\,, \tag{4.5.134}$$

which enter via second derivatives of the mapping, equation (4.5.15).

After some manipulation we obtain the submatrices $\tilde{\tilde{\boldsymbol{b}}}_{3a}$ and $\tilde{\tilde{\boldsymbol{b}}}_{3b}$ which together relate the reference second derivative degrees of freedom to the local second and first derivative degree of freedom. Once again we note that, as the tangents on the P_3 and P_5 elements coincide, only the terms involving second derivatives of the mapping on the vertices change. As a consequence of this, $\tilde{\tilde{\boldsymbol{b}}}_{3b} = \tilde{\boldsymbol{b}}_{3b}$. The matrix $\tilde{\tilde{\boldsymbol{b}}}_{3a}$ is then be given by

$$\tilde{\tilde{\boldsymbol{b}}}_{3a} = \begin{pmatrix}
0 & \frac{1}{4}(2\tilde{a}^1-\underset{\sim}{a}^1) & (\tilde{a}^1+\frac{1}{2}\underset{\sim}{a}^1) & 0 & 0 & 0\;0 & 0 & 0\\
0 & \frac{1}{4}(2+2\tilde{a}^2-\underset{\sim}{a}^2) & (1+\tilde{a}^2+\frac{1}{2}\underset{\sim}{a}^2) & 0 & 0 & 0\;0 & 0 & 0\\
0 & 0 & 0 & (1+\tilde{b}^1+\frac{1}{2}\underset{\sim}{b}^1) & \frac{1}{4}(2+2\tilde{b}^1-\underset{\sim}{b}^1) & 0\;0 & 0 & 0\\
0 & 0 & 0 & -(\tilde{b}^2+\frac{1}{2}\underset{\sim}{b}^2) & \frac{1}{4}(2\tilde{b}^2-\underset{\sim}{b}^2) & 0\;0 & 0 & 0\\
0 & 0 & 0 & 0 & 0 & 0\;0 & \frac{1}{2}(\tilde{c}^1+\tilde{\tilde{c}}^1) & 0\\
0 & 0 & 0 & 0 & 0 & 0\;0 & \frac{1}{2}(\tilde{c}^2+\tilde{\tilde{c}}^2) & 0
\end{pmatrix} \tag{4.5.135}$$

in which we have introduced the constants, $\underset{\sim}{a}^{\alpha}$, $\underset{\sim}{b}^{\alpha}$ such that

$$\boldsymbol{D}_1 = (\bar{s}-\underline{s})^2\chi''(\underline{s}) = \underset{\sim}{a}^{\alpha}\boldsymbol{A}_{\alpha}\,, \quad \boldsymbol{D}_2 = (\bar{s}-\underline{s})^2\chi''(\bar{s}) = \underset{\sim}{b}^{\alpha}\boldsymbol{B}_{\alpha}\,. \tag{4.5.136}$$

Construction of $\hat{f}_i^*$ and $\hat{g}_i^*$

Due to the affine nature of the mapping on sides 1 and 2, $\hat{f}_{\alpha}^*$ and $\hat{g}_{\alpha}^*$ $\alpha \in \{1,2\}$ are identical to $\hat{f}_{\alpha}$ and $\hat{g}_{\alpha}$ respectively. The traces $\hat{f}_3^*$ and $\hat{g}_3^*$, and therefore the corresponding matrices $\mathfrak{F}_3^*$ and $\mathfrak{G}_3^*$, however, differ.

We first construct the derivatives from the local degrees of freedom by considering relations (4.5.125-4.5.133) and by extension the matrix expressed in equation (4.5.135). We now express $\mathfrak{F}_3^*$ in the same manner as $\mathfrak{F}_3$, using the corresponding relations for the P_5 element:

$$\begin{aligned}\mathfrak{F}_3^* = \Bigg[& \hat{x}_1^3\left(6\hat{x}_1^2-15\hat{x}_1+10\right)\,;\, -\left(\hat{x}_1-1\right)^3\left(6\hat{x}_1^2+3\hat{x}_1+1\right)\,;\, 0\,;\, \frac{1}{2}\underset{\sim}{a}^1\left(\hat{x}_1-1\right)^2\hat{x}_1^3\,; \\ & \frac{1}{2}\left(\hat{x}_1-1\right)\hat{x}_1^3\left(\hat{x}_1\underset{\sim}{a}^2-\underset{\sim}{a}^2+6\hat{x}_1-8\right)\,;\, -\frac{1}{2}\left(\hat{x}_1-1\right)^3\hat{x}_1\left(\underset{\sim}{b}^1\hat{x}_1+6\hat{x}_1+2\right)\,; \\ & -\frac{1}{2}\underset{\sim}{b}^2\left(\hat{x}_1-1\right)^3\hat{x}_1^2\,;\, 0\,0\,0\,;\, \frac{1}{2}\left(\hat{x}_1-1\right)^2\hat{x}_1^3\,;\, -\frac{1}{2}\left(\hat{x}_1-1\right)^3\hat{x}_1^2\,;\, 0\,0\,0\,0\,0\,0\,0\,0 \\ & 0\,0\,0\,0\,0\,0\,0\Bigg]^T\,. \end{aligned} \tag{4.5.137}$$

Similarly by considering the normal derivative trace $\hat{g}_3^*$ we may express the matrix $\mathfrak{G}_3^*$ as

$$\begin{aligned}\mathfrak{G}_3^* = \Bigg[& 0\,0\,0\,;\, \frac{1}{2}\left(6-4\hat{x}_1+(\frac{1}{2}\underset{\sim}{a}^1+\tilde{a}^1)(\hat{x}_1-1)\right)\hat{x}_1^2\,;\, \frac{1}{4}\left((\underset{\sim}{a}^2+2\tilde{a}^2)(\hat{x}_1-1)+(6\hat{x}_1-8)\right)\hat{x}_1^2\,; \\ & -\frac{1}{4}\left((\underset{\sim}{b}^1+2\tilde{b}^1)\hat{x}_1+(6\hat{x}_1+2)\right)\left(1-\hat{x}_1\right)^2\,;\, \frac{1}{4}\left((8\hat{x}_1+4)-(\underset{\sim}{b}^2+2\tilde{b}^2)\hat{x}_1\right)\left(1-\hat{x}_1\right)^2\,; \\ & 0\,0\;\frac{\tilde{a}^1+1}{2\tilde{a}^2}\left(\hat{x}_1-1\right)\hat{x}_1^2\,;\, \frac{1}{2}\left(\frac{\tilde{a}^2}{\tilde{a}^1+1}+1\right)\left(\hat{x}_1-1\right)\hat{x}_1^2\,;\, -\frac{1}{2}\left(\frac{\tilde{b}^1}{\tilde{b}^2+1}+1\right)\left(\hat{x}_1-1\right)^2\hat{x}_1\,; \\ & -\left(\frac{\tilde{b}^2+1}{2\tilde{b}^1}\right)\left(\hat{x}_1-1\right)^2\hat{x}_1\,;\, 0\,0\,-\frac{\left(\hat{x}_1-1\right)\hat{x}_1^2}{2\tilde{a}^2\left(\tilde{a}^1+1\right)}\,;\, \frac{\left(\hat{x}_1-1\right)^2\hat{x}_1}{2\tilde{b}^1\left(\tilde{b}^2+1\right)}\,;\, 0\,0\,0\,0\,0\,0\,0\,0\,0\,0\,0\Bigg]^T\,. \end{aligned} \tag{4.5.138}$$

Construction of the submatrices $\tilde{\boldsymbol{B}}_4$ through $\tilde{\boldsymbol{B}}_8$

We now proceed to construct the submatrices that refer to the dependent, reference degrees of freedom. This is carried out in the same manner is for the P_3-element, but this time using the higher order mapping.

We first relate the eliminated Argyris degrees of freedom to the local degrees of freedom, by the matrix $\tilde{\tilde{\boldsymbol{B}}}_4$. We have

$$\tilde{\tilde{\boldsymbol{B}}}_4 = \left[\tilde{\tilde{E}}^1\mathfrak{F}_2\left(\frac{1}{2}\right)+\tilde{\tilde{E}}^2\mathfrak{G}_2\left(\frac{1}{2}\right)\;;\;\tilde{\tilde{F}}^1\mathfrak{F}_1\left(\frac{1}{2}\right)+\tilde{\tilde{F}}^2\mathfrak{G}_1\left(\frac{1}{2}\right)\;;\;\sqrt{2}\mathfrak{G}_3^*\left(\frac{1}{2}\right)\right]\,, \tag{4.5.139}$$

where we have introduced the constants

$$\tilde{\tilde{E}}^1 = -\frac{\partial \boldsymbol{F}_K^*}{\partial \hat{x}_1}(\hat{\boldsymbol{b}}_1) \cdot \left(\frac{\boldsymbol{B}_2}{|\boldsymbol{B}_2|^2} \right), \quad \tilde{\tilde{E}}^2 = -\frac{\partial \boldsymbol{F}_K^*}{\partial \hat{x}_1}(\hat{\boldsymbol{b}}_1) \cdot \left(\frac{\boldsymbol{n}_1}{|\boldsymbol{n}_1|^2} \right), \tag{4.5.140}$$

$$\tilde{\tilde{F}}^1 = -\frac{\partial \boldsymbol{F}_K^*}{\partial \hat{x}_2}(\hat{\boldsymbol{b}}_2) \cdot \left(\frac{\boldsymbol{A}_1}{|\boldsymbol{A}_1|^2} \right), \quad \tilde{\tilde{F}}^2 = -\frac{\partial \boldsymbol{F}_K^*}{\partial \hat{x}_2}(\hat{\boldsymbol{b}}_2) \cdot \left(\frac{\boldsymbol{n}_2}{|\boldsymbol{n}_2|^2} \right). \tag{4.5.141}$$

We now relate the dependent Lagrange degrees of freedom to the local degrees of freedom, freedom, by the matrix $\tilde{\tilde{\boldsymbol{B}}}_5$. The submatrix $\tilde{\tilde{\boldsymbol{b}}}_5$ is given by

$$\begin{aligned}\tilde{\tilde{\boldsymbol{B}}}_5 = \Big[&\mathfrak{F}_2\left(\frac{5}{6}\right) \; ; \; \mathfrak{F}_2\left(\frac{2}{3}\right) \; ; \; \mathfrak{F}_2\left(\frac{1}{3}\right) \; ; \; \mathfrak{F}_2\left(\frac{1}{6}\right) \; ; \; \mathfrak{F}_1\left(\frac{1}{6}\right) \; ; \; \mathfrak{F}_1\left(\frac{1}{3}\right) \; ; \; \mathfrak{F}_1\left(\frac{2}{3}\right) \; ; \; \mathfrak{F}_1\left(\frac{5}{6}\right) \; ; \\ &\mathfrak{F}_3^*\left(\frac{5}{6}\right) \; ; \; \mathfrak{F}_3^*\left(\frac{2}{3}\right) \; ; \; \mathfrak{F}_3^*\left(\frac{1}{3}\right) \; ; \; \mathfrak{F}_3^*\left(\frac{1}{6}\right) \Big]. \end{aligned} \tag{4.5.142}$$

We now define submatrices $\tilde{\tilde{\boldsymbol{B}}}_6$, $\tilde{\tilde{\boldsymbol{B}}}_7$ and $\tilde{\tilde{\boldsymbol{B}}}_8$, which correspond to the additional dependent normal degrees of freedom on sides 1, 2 and 3 respectively. We first express the matrix $\tilde{\tilde{\boldsymbol{B}}}_6$:

$$\begin{aligned}\tilde{\tilde{\boldsymbol{B}}}_6 = \Big[&\tilde{\tilde{G}}^1 \mathfrak{F}_2\left(\frac{5}{6}\right) + \tilde{\tilde{G}}^2 \mathfrak{G}_2\left(\frac{5}{6}\right) \; ; \; \tilde{\tilde{H}}^1 \mathfrak{F}_2\left(\frac{2}{3}\right) + \tilde{\tilde{H}}^2 \mathfrak{G}_2\left(\frac{2}{3}\right) \; ; \; \tilde{\tilde{J}}^1 \mathfrak{F}_2\left(\frac{1}{3}\right) + \tilde{\tilde{J}}^2 \mathfrak{G}_2\left(\frac{1}{3}\right) \; ; \\ &\tilde{\tilde{K}}^1 \mathfrak{F}_2\left(\frac{1}{6}\right) + \tilde{\tilde{K}}^2 \mathfrak{G}_2\left(\frac{1}{6}\right) \Big], \end{aligned} \tag{4.5.143}$$

where we have introduced the constants

$$\tilde{\tilde{G}}^1 = -\frac{\partial \boldsymbol{F}_K^*}{\partial \hat{x}_1}(\hat{\boldsymbol{d}}_1) \cdot \left(\frac{\boldsymbol{B}_2}{|\boldsymbol{B}_2|^2} \right), \quad \tilde{\tilde{G}}^2 = -\frac{\partial \boldsymbol{F}_K^*}{\partial \hat{x}_1}(\hat{\boldsymbol{d}}_1) \cdot \left(\frac{\boldsymbol{n}_1}{|\boldsymbol{n}_1|^2} \right), \tag{4.5.144}$$

$$\tilde{\tilde{H}}^1 = -\frac{\partial \boldsymbol{F}_K^*}{\partial \hat{x}_1}(\hat{\boldsymbol{d}}_2) \cdot \left(\frac{\boldsymbol{B}_2}{|\boldsymbol{B}_2|^2} \right), \quad \tilde{\tilde{H}}^2 = -\frac{\partial \boldsymbol{F}_K^*}{\partial \hat{x}_1}(\hat{\boldsymbol{d}}_2) \cdot \left(\frac{\boldsymbol{n}_1}{|\boldsymbol{n}_1|^2} \right), \tag{4.5.145}$$

$$\tilde{\tilde{J}}^1 = -\frac{\partial \boldsymbol{F}_K^*}{\partial \hat{x}_1}(\hat{\boldsymbol{d}}_3) \cdot \left(\frac{\boldsymbol{B}_2}{|\boldsymbol{B}_2|^2} \right), \quad \tilde{\tilde{J}}^2 = -\frac{\partial \boldsymbol{F}_K^*}{\partial \hat{x}_1}(\hat{\boldsymbol{d}}_3) \cdot \left(\frac{\boldsymbol{n}_1}{|\boldsymbol{n}_1|^2} \right), \tag{4.5.146}$$

$$\tilde{\tilde{K}}^1 = -\frac{\partial \boldsymbol{F}_K^*}{\partial \hat{x}_1}(\hat{\boldsymbol{d}}_4) \cdot \left(\frac{\boldsymbol{B}_2}{|\boldsymbol{B}_2|^2} \right), \quad \tilde{\tilde{K}}^2 = -\frac{\partial \boldsymbol{F}_K^*}{\partial \hat{x}_1}(\hat{\boldsymbol{d}}_4) \cdot \left(\frac{\boldsymbol{n}_1}{|\boldsymbol{n}_1|^2} \right). \tag{4.5.147}$$

The matrix $\tilde{\tilde{\boldsymbol{B}}}_7$ is given by

$$\begin{aligned}\tilde{\tilde{\boldsymbol{B}}}_7 = \Big[&\tilde{\tilde{L}}^1 \mathfrak{F}_1\left(\frac{1}{6}\right) + \tilde{\tilde{L}}^2 \mathfrak{G}_1\left(\frac{1}{6}\right) \; ; \; \tilde{\tilde{M}}^1 \mathfrak{F}_1\left(\frac{1}{3}\right) + \tilde{\tilde{M}}^2 \mathfrak{G}_1\left(\frac{1}{3}\right) \; ; \; \tilde{\tilde{N}}^1 \mathfrak{F}_1\left(\frac{2}{3}\right) + \tilde{\tilde{N}}^2 \mathfrak{G}_1\left(\frac{2}{3}\right) \; ; \\ &\tilde{\tilde{P}}^1 \mathfrak{F}_1\left(\frac{5}{6}\right) + \tilde{\tilde{P}}^2 \mathfrak{G}_1\left(\frac{5}{6}\right) \Big], \end{aligned} \tag{4.5.148}$$

in which we have introduced the constants

$$\tilde{\tilde{L}}^1 = -\frac{\partial \boldsymbol{F}_K^*}{\partial \hat{x}_2}(\hat{\boldsymbol{d}}_5) \cdot \left(\frac{\boldsymbol{A}_2}{|\boldsymbol{A}_2|^2} \right), \quad \tilde{\tilde{L}}^2 = -\frac{\partial \boldsymbol{F}_K^*}{\partial \hat{x}_2}(\hat{\boldsymbol{d}}_5) \cdot \left(\frac{\boldsymbol{n}_2}{|\boldsymbol{n}_2|^2} \right), \tag{4.5.149}$$

$$\tilde{\tilde{M}}^1 = -\frac{\partial \boldsymbol{F}_K^*}{\partial \hat{x}_2}(\hat{\boldsymbol{d}}_6) \cdot \left(\frac{\boldsymbol{A}_2}{|\boldsymbol{A}_2|^2} \right), \quad \tilde{\tilde{M}}^2 = -\frac{\partial \boldsymbol{F}_K^*}{\partial \hat{x}_2}(\hat{\boldsymbol{d}}_6) \cdot \left(\frac{\boldsymbol{n}_2}{|\boldsymbol{n}_2|^2} \right), \tag{4.5.150}$$

$$\tilde{\tilde{N}}^1 = -\frac{\partial \boldsymbol{F}_K^*}{\partial \hat{x}_2}(\hat{\boldsymbol{d}}_7) \cdot \left(\frac{\boldsymbol{A}_2}{|\boldsymbol{A}_2|^2} \right), \quad \tilde{\tilde{N}}^2 = -\frac{\partial \boldsymbol{F}_K^*}{\partial \hat{x}_2}(\hat{\boldsymbol{d}}_7) \cdot \left(\frac{\boldsymbol{n}_2}{|\boldsymbol{n}_2|^2} \right), \tag{4.5.151}$$

$$\tilde{\tilde{P}}^1 = -\frac{\partial \boldsymbol{F}_K^*}{\partial \hat{x}_2}(\hat{\boldsymbol{d}}_8) \cdot \left(\frac{\boldsymbol{A}_2}{|\boldsymbol{A}_2|^2} \right), \quad \tilde{\tilde{P}}^2 = -\frac{\partial \boldsymbol{F}_K^*}{\partial \hat{x}_2}(\hat{\boldsymbol{d}}_8) \cdot \left(\frac{\boldsymbol{n}_2}{|\boldsymbol{n}_2|^2} \right). \tag{4.5.152}$$

We finally express the matrix $\tilde{\tilde{\boldsymbol{B}}}_8$, that relates the local degrees of freedom to the additional reference normal degrees of freedom on side 3:

$$\tilde{\tilde{\boldsymbol{B}}}_7 = \Big[-\sqrt{2}\mathfrak{G}_3^*\left(\frac{5}{6}\right) \;;\; -\sqrt{2}\mathfrak{G}_3^*\left(\frac{2}{3}\right) \;;\; -\sqrt{2}\mathfrak{G}_3^*\left(\frac{1}{3}\right) \;;\; -\sqrt{2}\mathfrak{G}_3^*\left(\frac{1}{6}\right) \Big]. \tag{4.5.153}$$

Construction of the Submatrix $\tilde{\boldsymbol{B}}_9$

The interior, Lagrange (or bubble) degrees of freedom are identical on the reference element as on the curved element. Therefore the final submatrix $\tilde{\tilde{\boldsymbol{B}}}_9$ is given by

$$\tilde{\tilde{\boldsymbol{B}}}_9 = \Big(\mathbf{0}_{10\times 18} \quad \mathbb{I}_{10} \Big)^T. \tag{4.5.154}$$

Finally, we may construct the full local-to-reference matrix using the above definitions. The only remaining task is to define the 55, reference basis functions. This set of 55 basis functions is the set of degree 9, bivariate polynomials that satisfy the delta property for the defined degrees of freedom. They can be readily deduced in the manner outlined in the appendix such that we have a 55×55 association matrix, $\tilde{\boldsymbol{A}}$, and the set of 55, 2D monomials of degree less than or equal to nine, $\tilde{\boldsymbol{m}}_9$. Thus the basis $\hat{\boldsymbol{\psi}}^{[5]}$ is given by

$$\underbrace{\hat{\boldsymbol{\psi}}^{[5]}}_{55\times 1} = \underbrace{\tilde{\tilde{\boldsymbol{A}}}}_{55\times 55}\,\underbrace{\tilde{\boldsymbol{m}}_9}_{55\times 1} \tag{4.5.155}$$

The association matrix, in turn, can be deduced in the manner outlined in appendix D.3.

Constructing the Global Basis Functions for the P_5 Triangle

Finally, we may compute the full basis functions for the P_5 curved triangle element by the following equation

$$\underbrace{\boldsymbol{\psi}^{[3]}}_{28\times 1} = \underbrace{\tilde{\tilde{\boldsymbol{D}}}}_{28\times 28}\,\underbrace{\tilde{\tilde{\boldsymbol{B}}}}_{28\times 55}\,\underbrace{\tilde{\tilde{\boldsymbol{A}}}}_{55\times 55}\,\underbrace{\tilde{\tilde{\boldsymbol{m}}}_9}_{55\times 1} \tag{4.5.156}$$

where the matrices $\tilde{\tilde{\boldsymbol{D}}}$ and $\tilde{\tilde{\boldsymbol{B}}}$ were defined in the preceding sections and $\tilde{\tilde{\boldsymbol{A}}}$ may be derived by the method outlined in appendix D.3. We plot the basis functions in figure 4.31-4.32.

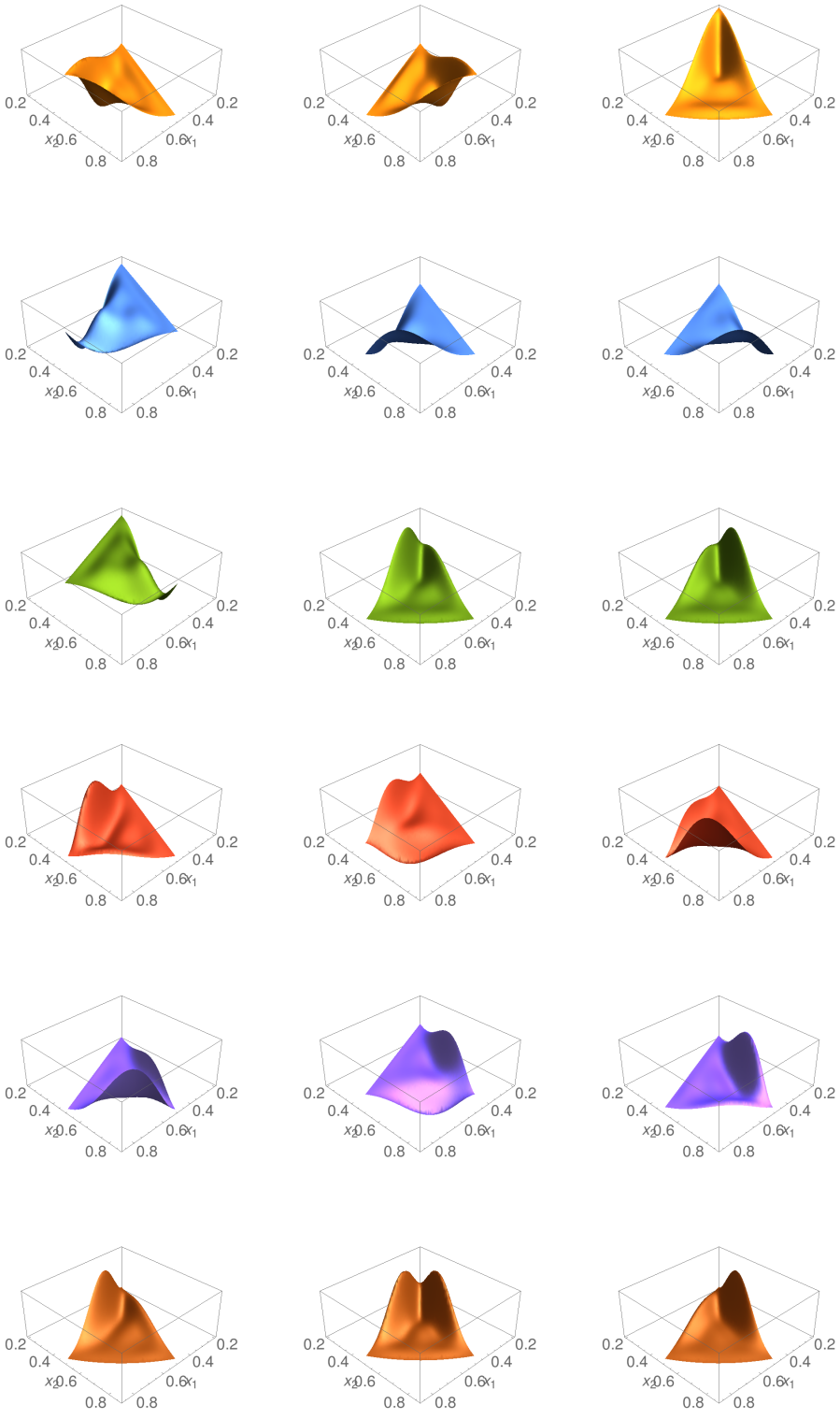

Figure 4.31: Curved Bell P_5 nodal basis functions shown for a particular curved triangle. The different nodal basis functions are shown by column and the different degree of freedom types are shown by row, in various colours. By row the degrees of freedom are ordered as follows: $w(\boldsymbol{a}_i)$, $\partial w(\boldsymbol{a}_i)/\partial x_1$, $\partial w(\boldsymbol{a}_i)/\partial x_2$, $\partial^2 w(\boldsymbol{a}_i)/\partial x_1^2$, $\partial^2 w(\boldsymbol{a}_i)/\partial x_1 \partial x_2$ and $\partial^2 w(\boldsymbol{a}_i)/\partial x_2^2$.

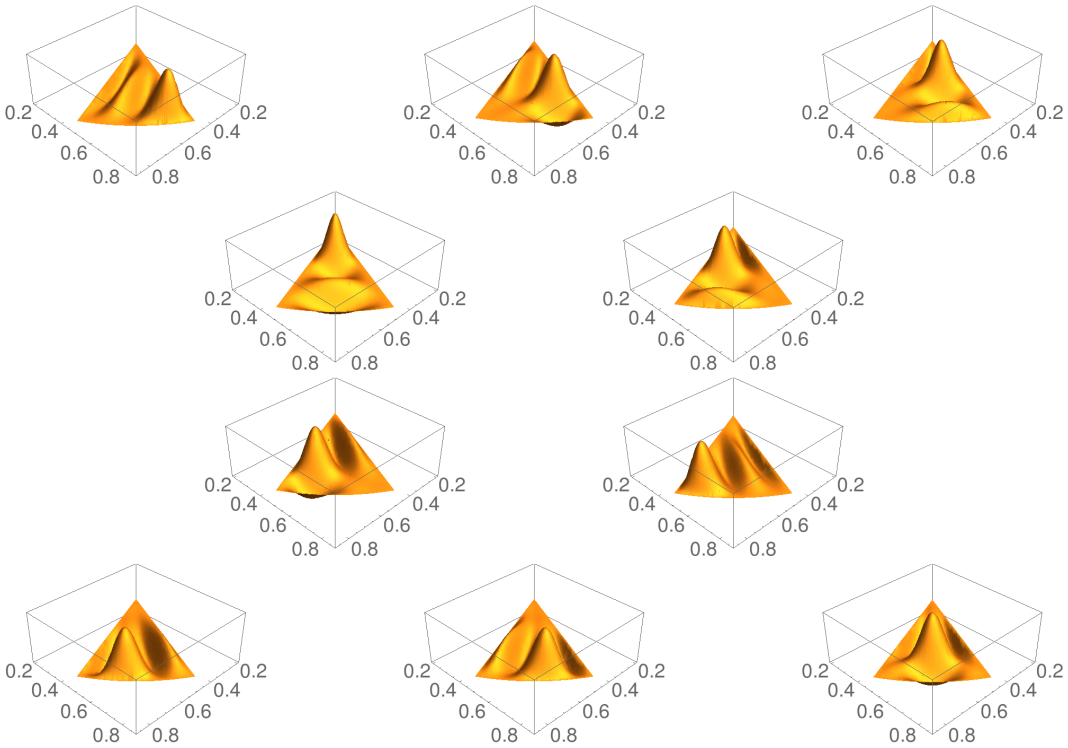

Figure 4.32: Curved Bell P_5 bubble basis functions shown for a particular curved triangle. The basis functions are associated with the unknowns at points $\hat{\boldsymbol{e}}_i$ with $i \in \{1, \ldots, 10\}$, which are shown ascending from left-to-right, top-to-bottom.

4.5.8 Cartesian Derivatives of Basis Functions

We now discuss the relationship between the local and global (Cartesian) derivatives of the basis vectors, which are computed by taking derivatives of the mapping defined in equation (4.5.4).

Firstly, we define the Jacobian of the mapping, $\boldsymbol{J}$, as

$$\boldsymbol{J} = \frac{\partial \boldsymbol{x}}{\partial \hat{\boldsymbol{x}}}\,, \tag{4.5.157}$$

and the Hessian of the mapping, $\boldsymbol{H}$, as:

$$\boldsymbol{H} = \frac{\partial^2 \boldsymbol{x}}{\partial \hat{\boldsymbol{x}} \partial \hat{\boldsymbol{x}}}\,, \tag{4.5.158}$$

which are accessible by taking derivatives of the mapping defined in equation 4.5.4.

To express first derivatives we use the chain rule as follows

$$\frac{\partial \psi_l^{[m]}}{\partial x_\alpha} = \frac{\partial \psi_l^{[m]}}{\partial \hat{x}_\beta} \frac{\partial \hat{x}_\beta}{\partial x_\alpha} = \frac{\partial \psi_l^{[m]}}{\partial \hat{x}_\beta} \left(\boldsymbol{J}^{-1}\right)_{\beta\alpha}\,. \tag{4.5.159}$$

Second derivatives can then be computed as follows

$$\frac{\partial^2 \psi_l^{[m]}}{\partial x_\alpha \partial x_\beta} = \frac{\partial \psi_l^{[m]}}{\partial \hat{x}_\gamma \partial \hat{x}_\delta} \left(\boldsymbol{J}^{-1}\right)_{\delta\alpha} \left(\boldsymbol{J}^{-1}\right)_{\gamma\beta} + \frac{\partial \psi_l^{[m]}}{\partial \hat{x}_\gamma} \frac{\partial^2 \hat{x}_\gamma}{\partial x_\alpha \partial x_\beta} . \tag{4.5.160}$$

Since an explicit expression for the final term is not readily available, we make some manipulations, detailed in appendix D.5, to express this as

$$\frac{\partial^2 \psi_l^{[m]}}{\partial x_\alpha \partial x_\beta} = \frac{\partial \psi_l^{[m]}}{\partial \hat{x}_\gamma \partial \hat{x}_\delta} \left(\boldsymbol{J}^{-1}\right)_{\delta\alpha} \left(\boldsymbol{J}^{-1}\right)_{\gamma\beta} - \frac{\partial \psi_l^{[m]}}{\partial \hat{x}_\gamma} (\boldsymbol{J}^{-1})_{\alpha\delta} \left(\boldsymbol{H}\right)_{\delta\mu\nu} \left(\boldsymbol{J}^{-1}\right)_{\mu\beta} \left(\boldsymbol{J}^{-1}\right)_{\nu\gamma} . \tag{4.5.161}$$

This allows for the calculation of the second Cartesian derivatives, whilst only using the known expressions for the Hessian and the inverse Jacobian. The expressions for the basis functions are now complete. The implementation is described in the next section.

4.5.9 New Subparametric Elements

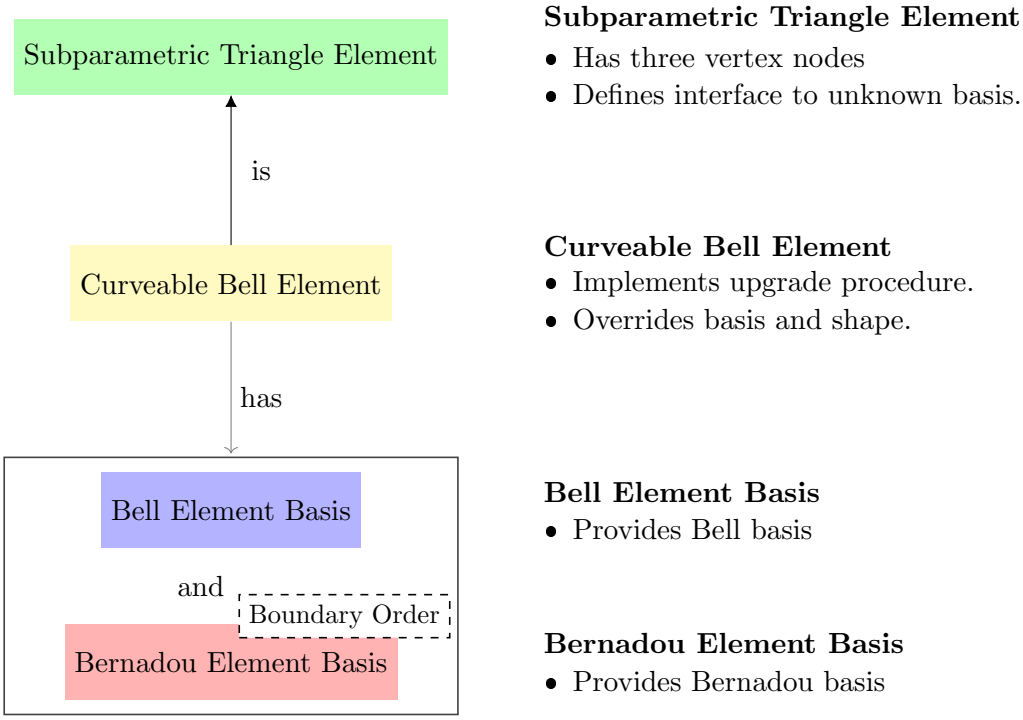

Figure 4.33: The revised structure of the Bell and curved Bell elements within `oomph-lib`. Template parameters are indicated by dashed boxes.

We incorporate the new basis functions into the hierarchy containing the Bell elements, for which the revised structure is shown in figure 4.33. The new curved basis provides a representation of the geometry and basis functions for the elements. The interface to this class is illustrated in figure 4.34. A new subparametric element type takes the place of the

Bell element of section 4.4: the curveable subparametric element. This element type behaves as a straight-sided Bell element until it is 'upgraded' to have a single curved side.

```
// Pure virtual base class for curveable Bell elements
template<unsigned NNODE_1D>
class CurveableBellElement : public SubparametricTElement<NNODE_1D> {
public:
  // Access functions for basis
  unsigned nbubble_basis();
  unsigned nnodal_basis_types();
  // Upgrade element
  virtual void upgrade_to_curved_element(const double& s_at0, const double& s_at1,
    const GeomObject1Variable2D& parametric_curve, const Edge& edge,
    const unsigned& boundary_order);
  // Defines the basis (nodal basis functions and bubble basis functions)
  // Provides the Bell basis before the upgrade and the Bernadou basis after
  void basis(Vector<double>& local_coord, Shape& nodal_basis, Shape& bubble_basis);
  // Override inherited shape with linear shape.
  void shape(Vector<double>& local_coord, Shape& shape);
private:
 // Pointer to the class that provides the Bell basis functions
 BellElementBasis* Bell_element_basis_pt;
 // Pointer to the class that provides the Bernadou-Bell basis functions
 BernadouElementBasisBase* Bernadou_element_basis_pt;
 // Bool to indicate whether element has been upgraded to curved
 bool Element_is_curved;
```

Figure 4.34: Simplified code snippet illustrating the curveable Bell element class.

The new curved element has a Bell element basis and a curved Bell element basis, which can either be a P_3 curved Bell element or a P_5 curved Bell element: this allows a mixture of element types to be used in any given domain. The two curved bases share much of the functionality, but contain different methods and data used to construct the final basis. They are therefore templated by the boundary order to maximise code reuse.

To use these elements for a curved edge, the function

```
void upgrade_to_curved_element(const double& s_at0, const double& s_at1,
  const GeomObject1Variable2D& parametric_curve, const Edge& e, const unsigned&
      boundary_order)
```

must be called. This function requires a specialized geometric object (a new `oomph-lib` class) to be provided as an argument: a `GeometricObject1Variable2D`. This object defines a parametric curve (an arc in 2D) as a function of a single variable (the arc length). The other arguments needed are the `Edge` (an enumerated type) to be upgraded, and the start and end points on the arc. Finally the order of the boundary must be specified. Given that, in principle, other curved Bell elements with different boundary orders (such as quadratic or heptic) may be required in the future, we keep this interface generic.

The upgrade procedure has a general-purpose interface defined in `CurveableBellement`, which can be overridden as required in derived classes. The procedure is illustrated in figure 4.35. This function sets up the Bernadou basis and henceforth when

```
void basis(const Vector<double>& s, Shape& nodal basis, Shape& bubble_basis)
```

is called it will return the (curved) Bernadou basis, as shown in figure 4.36. This permits a mixture of different Bell-type elements to exist within a single mesh. The curved-Bell elements define the geometry of the element through $\boldsymbol{F}_K$, *not* a set of shape functions. As such, once the elements are upgraded we 'break' the shape functions, by introducing a thrown error with an informative error message.

```
virtual void upgrade_to_curved_element(const double& su, const double& so,
 const GeomObject1Variable2D& parametric_curve, const Edge& e, const unsigned&
     boundary_order){
  // Get the element vertices for the set-up
  Vector<Vector<double> > vertices = get_vertices();
  // Set bool to indicate that the element has been upgraded to be curved
  Element_is_curved = true;
  // New Basis
  if(boundary_order == 3)
   { Bernadou_element_basis_pt =
    new BernadouElementBasis<3>(vertices,su,so,parametric_curve,e); }
  else if (boundary_order = 5)
   { Bernadou_element_basis_pt =
    new BernadouElementBasis<5>(vertices,su,so,parametric_curve,e); }
  else  { /* throw */ }}
```

Figure 4.35: Simplified code snippet illustrating the upgrade procedure.

```
// Interface to basis
void basis(const Vector<double>& local_coord, Shape& basis){
  if(Element_is_curved)
   { Bernadou_element_basis_pt->basis(local_coord, basis);}
  else
   { Bell_element_basis_pt->basis(local_coord, basis);}
  }
// Interface to interpolated position
void interpolated_x(const Vector<double>& local_coord, Vector<double>& coord){
  if(Element_is_curved)
   { Bernadou_element_basis_pt->::coordinate_x(local_coord, coord);}
  else
   { TElement<2,2>::interpolated_x(local_coord, coord);}
  }
```

Figure 4.36: Simplified code snippet illustrating the functionality of the basis and interpolated position members.

4.6 Summary

In this section we discussed two element types: straight-sided Bell-elements, and curved Bell-elements, which are mutually C^1 continuous. The combination of these two element types is sufficient to provide a C^1-continuous basis over any domain. We further provided explicit construction formulas for the curved-Bell elements, which was previously missing in the literature. Finally we discussed an object-oriented structure for these elements, in order to translate the mathematical descriptions into a form that can be used within the finite element library, `oomph-lib`.

Now we have the relevant basis functions for generic fourth-order problems we proceed to discuss the implementation of the various plate models.

Chapter 5

Numerical Implementation and Validation

5.1 Implementation of the Plate Models

We now proceed to discuss how the Bell and their curved counterparts are used, in conjunction with regular Lagrange elements when required, to discretize the plate models of the proceeding section. For pedagogical purposes, we start by detailing the implementation of linearised bending elements. The Bell and curved Bell basis functions and proceeding equations have been implemented to form part of the open-source object-oriented multi-physics finite element library `oomph-lib` [Heil and Hazel, 2006].

5.1.1 Linear Bending Elements

We recall from the section 3.5.6 that the relevant nondimensional variational equation for linear bending will be

$$\int_{\Omega} \delta U_B d\Omega = \int_{\Omega} \left(\frac{h^3}{12} \mathcal{G}_{\alpha\beta\gamma\delta}\, \bar{v}_{3,\gamma\delta}\, \delta v_{3,\alpha\beta} - \Delta p \delta v_3 \right) d\Omega \,, \tag{5.1.1}$$

with relative thickness h and

$$\mathcal{G}_{\alpha\beta\gamma\delta} = \frac{1}{(1-\nu^2)} [(1-\nu)\delta_{\alpha\delta}\delta_{\beta\gamma} + \nu\delta_{\delta\gamma}\delta_{\alpha\beta}] \,. \tag{5.1.2}$$

In order to keep the formulation consistent with previously implemented plate models within `oomph-lib`, we divide through by $h^3/12(1-\nu^2)$. Thus the equations become

$$\int_{\Omega} \left(\tilde{\tilde{\mathcal{G}}}_{\alpha\beta\gamma\delta}\, \bar{v}_{3,\gamma\delta}\, \delta v_{3,\alpha\beta} - \Delta \tilde{\tilde{p}} \delta v_3 \right) d\Omega \,. \tag{5.1.3}$$

with $\Delta\tilde{\tilde{p}} = 12(1-\nu^2)\Delta p/h^3$ and $\tilde{\tilde{\mathcal{G}}} = (1-\nu^2)\mathcal{G}$.

Now, to discretize this we use, in general, a mixture of Bell and curved Bell elements, since the variational equation is fourth order and requires C^1-continuous interpolation.

Discretizing the Equations

In a domain with a piecewise m^{th} order boundary discretization we can express the interpolated transverse displacement, $v_3^{(e)}(\boldsymbol{y})$, on a particular element, e, in terms of discrete nodal unknowns $N_3^{(e,i,m)}$ and bubble unknowns, $B_3^{(e,i)}$, as follows

$$v_3^{(e)}(\hat{\boldsymbol{x}}) = \sum_{i=1}^{3}\sum_{j=1}^{6} N_3^{(e,i,j)}\ \psi^{[N]}_{(i,j,e)}(\hat{\boldsymbol{x}}) + \sum_{i=1}^{N_b} B_3^{(e,i)}\ \psi^{[B]}_{(i,e)}(\hat{\boldsymbol{x}})\,. \tag{5.1.4}$$

Here, we have split the basis function to pertain to nodal degrees of freedom and bubble degrees of freedom separately. The basis will differ depending on whether the element in question is a straight sided Bell element, a P_3 curved-Bell element, or a P_5 curved-Bell element: in principle a mesh may consist of all three. In the bulk, there are no bubble degrees of freedom and thus $N_b = 0$. On curved edges the elements will have $N_b = 3$ and $N_b = 10$ for P_3 and P_5 elements respectively. For Bell elements the second summation will be the empty sum, as there are no bubble degrees of freedom.

Similarly we may express the discrete variations as

$$\delta v_3^{(e)}(\hat{\boldsymbol{x}}) = \sum_{i=1}^{3}\sum_{j=1}^{6} \delta N_3^{(e,i,j)}\ \psi^{[N]}_{(i,j,e)}(\hat{\boldsymbol{x}}) + \sum_{i=1}^{N_b} \delta B_3^{(e,i)}\ \psi^{[B]}_{(i,e)}(\hat{\boldsymbol{x}})\,. \tag{5.1.5}$$

Thus introducing these approximations into our variational form, we have

$$\begin{aligned}\int_\Omega \delta U_B d\Omega \approx \sum_{e,e',e''=1}^{N_e} \int_{\Omega_e} \Bigg[&\tilde{\tilde{\mathcal{G}}}_{\alpha\beta\gamma\delta} \left(\sum_{i=1}^{3}\sum_{j=1}^{6} N_{e'}^{(i,j)}\ \psi^{[N]}_{(i,j,e'),\gamma\delta}(\hat{\boldsymbol{x}}) + \sum_{i=1}^{N_b} B_{e'}^{(i)}\ \psi^{[B]}_{(i,e'),\gamma\delta}(\hat{\boldsymbol{x}}) \right) \\ &\cdot \left(\sum_{i=1}^{3}\sum_{j=1}^{6} \delta N_{e''}^{(i,j)}\ \psi^{[N]}_{(i,j,e''),\alpha\beta}(\hat{\boldsymbol{x}}) + \sum_{i=1}^{N_b} \delta B_{e''}^{(i)}\ \psi^{[B]}_{(i,e''),\alpha\beta}(\hat{\boldsymbol{x}}) \right) \\ &+ \Delta\tilde{\tilde{p}} \left(\sum_{i=1}^{3}\sum_{j=1}^{6} \delta N_{e''}^{(i,j)}\ \psi^{[N]}_{(i,j,e'')}(\hat{\boldsymbol{x}}) + \sum_{i=1}^{N_b} \delta B_{e''}^{(i)}\ \psi^{[B]}_{(i,e'')}(\hat{\boldsymbol{x}}) \right) \Bigg] d\Omega\,. \end{aligned} \tag{5.1.6}$$

in which N_e is the number of elements. These equations must hold for *arbitrary* discrete

variations, thus we are lead to the following discrete residuals

$$R^N_{(i,j,e)} = \sum_{e=1}^{N_n} \int_{\Omega_e} \left[\tilde{\tilde{\mathcal{G}}}_{\alpha\beta\gamma\delta} \left(\sum_{i=1}^{3} \sum_{j=1}^{6} N_3^{(e,i,j)} \, \psi^{[N]}_{(i,j,e),\gamma\delta} + \sum_{i=1}^{N_b} B_3^{(e,i)} \, \psi^{[B]}_{(i,e),\gamma\delta} \right) \psi^{[N]}_{(i,j,e),\alpha\beta} + \Delta\tilde{\tilde{p}} \psi^{[N]}_{(i,j,e)} \right] d\Omega \tag{5.1.7}$$

$$R^B_{(i,e)} = \int_{\Omega_e} \left[\tilde{\tilde{\mathcal{G}}}_{\alpha\beta\gamma\delta} \left(\sum_{i=1}^{3} \sum_{j=1}^{6} N_3^{(e,i,j)} \, \psi^{[N]}_{(i,j,e),\gamma\delta} + \sum_{i=1}^{N_b} B_3^{(e,i)} \, \psi^{[B]}_{(i,e),\gamma\delta} \right) \psi^{[B]}_{(i,e),\alpha\beta} + \Delta\tilde{\tilde{p}} \psi^{[B]}_{(i,e)} \right] d\Omega \tag{5.1.8}$$

in which we have used the fact that each element's support is compact, and thus involves a sum over the N_n elements which contain the node i. In the case of the bubble degrees of freedom which are not shared between elements, the support is confined to a single element. Here, the second set of residuals will only be present in curved elements, not straight-sided Bell elements.

The basis functions are enumerated by the degree of freedom type and by the degree of freedom number which correspond to points within the element. The number of degrees of freedom types for the nodal degrees of freedom are provided by the function:

```
unsigned nnodal_basis_type()
```

For bubble degrees of freedoms the number of degrees of freedom is given by

```
unsigned nbubble_basis()
```

This interface is defined in the `SubparametricTElement`, as discussed in section 4.5.9. The basis functions are accessed using the `SubparametricTElement` member function:

```
void basis(const Vector<double>& s, Shape& nodal_basis, Shape& bubble_basis)
```

which is overridden in the derived `CurveableBellElement` class.

We can write these equations more compactly as

$$R^N_{(i,j,e)} = \sum_{e=1}^{N_n} \int_{\Omega_e} \left[\tilde{\tilde{M}}^L_{e\alpha\beta} \, \psi^{[N]}_{(i,j,e),\alpha\beta} - \Delta\tilde{\tilde{p}} \, \psi^{[N]}_{(i,j,e)} \right] d\Omega \tag{5.1.9}$$

$$R^B_{(i,e)} = \int_{\Omega_e} \left[\tilde{\tilde{M}}^L_{e\alpha\beta} \, \psi^{[B]}_{(i,e),\alpha\beta} - \Delta\tilde{\tilde{p}} \, \psi^{[B]}_{(i,e)} \right] d\Omega \, . \tag{5.1.10}$$

where we define the (interpolated) bending moment on the element as

$$\tilde{\tilde{M}}^L_{e\alpha\beta} = \tilde{\tilde{\mathcal{G}}}_{\alpha\beta\gamma\delta} \left(\sum_{i=1}^{3} \sum_{j=1}^{6} N_3^{(e,i,j)} \, \psi^{[N]}_{(i,j,e),\gamma\delta} + \sum_{i=1}^{N_b} B_3^{(e,i)} \, \psi^{[B]}_{(i,e),\gamma\delta} \right) . \tag{5.1.11}$$

The structure of this equation will form the basis of more complicated variational problems in the proceeding sections.

In practise the integration is done discretely, using a suitable Gauss scheme such that that the stiffness matrix can be integrated exactly. Therefore for Bell elements, we require full integration up to at least sixth order, for P_3 curved bell elements we require full integration up to at least tenth order and finally for P_5 curved bell elements we require full integration up to at least fourteenth order. We utilise existing schemes within `oomph-lib`, using the 13 point, sixth order Gauss rule, the order 11 quadrature rules of de Doncker and Robinson [1984], and the 64 point, fifteenth order Gauss rule respectively.

Imposing Boundary Conditions

Imposing physical boundary conditions with Hermite degrees of freedom is not as straightforward as for Lagrange degrees of freedom: this is due to the fact that physically admissible boundary conditions are not necessarily possible to impose with axis aligned degrees of freedom. This difficulty can be overcome by making local rotations of the Hermite degrees of freedom on the boundary.

For example, if we wish to introduce a new set of coordinates ξ_α, such that $\boldsymbol{x}(\boldsymbol{\xi})$, where $\boldsymbol{x}$ is the position vector of a point in the domain and $\boldsymbol{\xi}$ is the new coordinate, we may introduce the new first derivative Hermite degrees of freedom of a function $w(\boldsymbol{x})$

$$\frac{\partial w}{\partial x_\alpha} = \frac{\partial w}{\partial \xi_\beta}\frac{\partial \xi_\beta}{\partial x_\alpha} = \frac{\partial w}{\partial \xi_\beta}\ \left(\boldsymbol{J_R}^{-1}\right)_{\beta\alpha}. \tag{5.1.12}$$

In general, for the mapping, we also need to specify the Hessian, in order to express second derivatives with respect to the new coordinate:

$$\frac{\partial^2 w}{\partial x_\alpha \partial x_\beta} = \frac{\partial \xi_\nu}{\partial x_\beta}\frac{\partial^2 w}{\partial \xi_\mu \partial \xi_\nu}\frac{\partial \xi_\mu}{\partial x_\alpha} + \frac{\partial w}{\partial \xi_\mu}\frac{\partial^2 \xi_\mu}{\partial x_\alpha \partial x_\beta}. \tag{5.1.13}$$

Or, in terms of the inverse Jacobian and inverse Hessian, we may write

$$\frac{\partial^2 w}{\partial x_\alpha \partial x_\beta} = \left(\boldsymbol{J_R}^{-1}\right)_{\mu\alpha}\frac{\partial^2 w}{\partial \xi_\mu \partial \xi_\nu}\left(\boldsymbol{J_R}^{-1}\right)_{\nu\beta} + \frac{\partial w}{\partial \xi_\mu}\left(\boldsymbol{H_R}^{-1}\right)_{\mu\alpha\beta} \tag{5.1.14}$$

where the inverse Hessian may be calculated from the Hessian and inverse Jacobian of the mapping (cf. appendix D.5).

Our interpolation of the function $v_3(\boldsymbol{x})$ is provided by the superposition of unknowns and the Hermite basis

$$v_3^{(e)}(\hat{\boldsymbol{x}}) = \sum_{i=1}^{3}\sum_{j=1}^{6} N_3^{(e,i,j)}\ \psi^{[N]}_{(i,j,e)}(\hat{\boldsymbol{x}}) + \sum_{i=1}^{N_b} B_3^{(e,i)}\ \psi^{[B]}_{(i,e)}(\hat{\boldsymbol{x}}). \tag{5.1.15}$$

Thus, we introduce new rotated unknowns, keeping this sum constant. Using the results from equation 5.1.14, we may introduce a set of 'rotated' Hermite degrees of freedom, $\tilde{N}_3^{(e,i,j)}$, at node i:

$$\tilde{N}_3^{(e,i,j)} = \left[v_3(\boldsymbol{a}_{e\,i})\,;\, \frac{\partial v_3}{\partial \xi_1}(\boldsymbol{a}_{e\,i})\,;\, \frac{\partial v_3}{\partial \xi_2}(\boldsymbol{a}_{e\,i})\,;\, \frac{\partial v_3}{\partial \xi_1 \partial \xi_1}(\boldsymbol{a}_{e\,i})\,;\, \frac{\partial v_3}{\partial \xi_1 \partial \xi_2}(\boldsymbol{a}_{e\,i})\,;\, \frac{\partial v_3}{\partial \xi_2 \partial \xi_2}(\boldsymbol{a}_{e\,i}) \right]_j \tag{5.1.16}$$

and associated 'rotated' basis functions, $\tilde{\psi}^{[N]}_{(i,j,e)}$,

$$\tilde{\psi}^{[N]}_{(1,j,e)}(\hat{\boldsymbol{x}}) \qquad = \psi^{[N]}_{(1,j,e)}(\hat{\boldsymbol{x}})\,, \tag{5.1.17}$$

$$\tilde{\psi}^{[N]}_{(1+\mu,j,e)}(\hat{\boldsymbol{x}}) \quad = \left(\boldsymbol{J_R}^{-1}\right)_{\mu\alpha} \psi^{[N]}_{(1+\alpha,j,e)}(\hat{\boldsymbol{x}}) + \left(\boldsymbol{H_R}^{-1}\right)_{\mu\alpha\beta} \psi^{[N]}_{(2+\alpha+\beta,j,e)}(\hat{\boldsymbol{x}})\,, \tag{5.1.18}$$

$$\tilde{\psi}^{[N]}_{(2+\mu+\nu,j,e)}(\hat{\boldsymbol{x}}) = \left(\boldsymbol{J_R}^{-1}\right)_{\mu\alpha} \psi^{[N]}_{(2+\alpha+\beta,j,e)}(\hat{\boldsymbol{x}}) \left(\boldsymbol{J_R}^{-1}\right)_{\nu\beta}. \tag{5.1.19}$$

such that the product of the degrees of freedom and basis functions (i.e. the interpolant) remains unchanged:

$$v_3^{(e)}(\hat{\boldsymbol{x}}) = \sum_{i=1}^{3}\sum_{j=1}^{6} N_3^{(e,i,j)}\ \psi^{[N]}_{(i,j,e)}(\hat{\boldsymbol{x}}) + \sum_{i=1}^{N_b} B_3^{(e,i)}\ \psi^{[B]}_{(i,e)}(\hat{\boldsymbol{x}}) \tag{5.1.20}$$

$$= \sum_{i=1}^{3}\sum_{j=1}^{6} \tilde{N}_3^{(e,i,j)}\ \tilde{\psi}^{[N]}_{(i,j,e)}(\hat{\boldsymbol{x}}) + \sum_{i=1}^{N_b} B_3^{(e,i)}\ \psi^{[B]}_{(i,e)}(\hat{\boldsymbol{x}})\,. \tag{5.1.21}$$

Thus, by providing a Jacobian and a Hessian, we may transform the degrees of freedom into a different basis.

Finally we consider the case where only a *boundary* parametrization is specified, i.e. we have a mapping of a single coordinate $\boldsymbol{x}(\xi_1)$. In this case the tangent is given by $\boldsymbol{x}'(\xi_1)$ and the normal by $\boldsymbol{x}'(\xi_1) \times \boldsymbol{k}$, where $\boldsymbol{k}$ is the direction perpendicular to the domain. To construct a two-dimensional parametrization, we may introduce a new coordinate ξ_2 extruded in the normal direction

$$\boldsymbol{x}(\xi_1, \xi_2) = \boldsymbol{x}(\xi) + \xi_2 \left(\boldsymbol{x}'(s) \times \boldsymbol{k}\right)\,, \tag{5.1.22}$$

where the curved boundary occupies the $\xi_2 = 0$ line. This allows us to use the general formulation expressed in equation (5.1.14) for boundaries expressed in terms of a single parameter.

With rotated degrees of freedom it is now possible to specify a function along an entire edge: to set the values of the deflection along the edge we adjust the values of the single Lagrange degree of freedom and the first and second tangential derivatives, allowing us to

approximate the deflection on the boundary as a piecewise fifth order polynomial, for a sufficiently continuous boundary discretization. The normal derivative of the deflection, in turn may be imposed up to a piecewise third order polynomial. Leaving these degrees of freedom unpinned results in the 'natural' physical stress and moment free boundary conditions. Here, we reiterate that the P_3 curved elements are appropriate only for the imposition homogeneous Dirichlet boundary conditions, sometimes known as a 'built-in' clamp.

The rotation of the degrees of freedom is performed by helper function

```
void set_up_rotated_dofs_on_edge(const Vector<std::pair<unsigned, BasisFctPt> >
 nodal_basis_lookup);
```

which takes a single argument that associates new bases with nodes in the element. The type `BasisFctPt` is an alias for the existing type:

```
typedef void (*BasisVectorsFctPt) (const Vector<double>& x, DenseMatrix<double>&
 jacobian,  RankThreeTensor<double>& hessian);
```

where, in general, the mapping is a function of $\boldsymbol{x}$. A `BasisVectorFctPt` is a function pointer to a function that provides the Hessian and Jacobian of the transform, which may be a function of position. In general each node may also have a distinct basis, to allow the possibility of specifying physical boundary conditions at corner points. This helper function forms a new member of the `KirchhoffPlateBendingCurveableBellElement` class which we discuss in the next section.

Summary: Linear Bending Elements

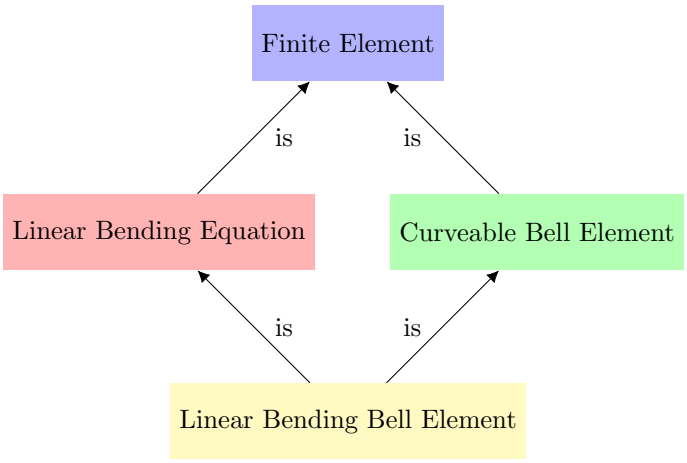

Finite Element
- Defines interface to basis

Linear Bending Equations
- Implements generic equations

Curveable Bell Element
- Implements geometric basis
- Implements unknown basis

Linear Bending Bell Element
- Implements basis for equations

Figure 5.1: The structure of the new linear plate bending elements within `oomph-lib`.

We incorporate these equations into a new set of discrete equations: the linear plate

bending equations, as shown in figure 5.1. These inherit directly from the existing finite element class within `oomph-lib` (`FiniteElement`). The complete linear bending element combines the linear bending equations and the curveable Bell elements via multiple inheritance to form a usable plate element. Two new interfaces are needed to set up linear bending problems:

```
virtual void upgrade_to_curved_element(const double& s_at0, const double& s_at1,
 const GeomObject1Variable2D& parametric_curve, const Edge& e, const unsigned&
     boundary_order);
```

and the previously mentioned

```
void set_up_rotated_dofs_on_edge(const Vector<std::pair<unsigned, BasisFctPt> >
 nodal_basis_lookup);
```

The former function cannot be called automatically, as it is not known a priori which edges will be curved or what order boundary interpolation will be specified. The latter function must be called separately as the rotation of degrees of freedom may be necessary on straight-sided boundaries as well as curved edges. Simplified code showing the new functionality and structure of the class is shown in figure 5.2.

```
// KirchhoffPlateBendingEquations using CurveableBellElements
class KirchhoffPlateBendingCurveableBellElement :
  public virtual CurveableBellElement<2>,
  public virtual KirchhoffPlateBendingEquations
{
public:
  // Helper function to upgrade straight-sided Bell elements to be curved
  // (provided by inheritance)
  // virtual void upgrade_to_curved_element( ... );
  // Helper function to set-up rotated Hermite degrees of freedom
  void set_up_rotated_dofs_on_edge(const Vector<std::pair<unsigned, BasisFctPt> >
    nodal_basis_lookup);
```

Figure 5.2: Simplified code snippet illustrating the new helper functions for a linear bending Bell element.

5.1.2 Föppl-von Kármán Elements

We now introduce the interpolation scheme for the Föppl-von Kármán elements. The structure of Föppl-von Kármán elements differs from the linear bending elements, because we also require C^0 interpolation for the in-plane displacements. This results in using standard Lagrange basis functions to interpolate the in-plane degrees of freedom.

We use standard, cubic, Lagrange interpolation for the in-plane degrees of freedom, to provide a convergence rate comparable to that of the out-of-plane displacement. Quadratic and linear versions of these elements have also been implemented, but we do not use them in this study, so we will not discuss them further. The interpolation schemes for the three main types Föppl-von Kármán element are displayed in figure 5.3.

We introduce the in-plane displacements, interpolated on a particular element, as follows

$$v_\alpha^{(e)} = \sum_{l=1}^{10} L_\alpha^{(e,l)} \psi_{Ll}^C \,, \tag{5.1.23}$$

and variations

$$\delta v_\alpha^{(e)} = \sum_{l=1}^{10} \delta L_\alpha^{(e,l)} \psi_{Ll}^C \,, \tag{5.1.24}$$

in which ψ_{Ll}^C for $l \in \{1, \ldots, 10\}$ are the cubic, Lagrange basis functions, as outlined in appendix E.

These elements are not necessarily isoparametric: the mapping is supplied by the relevant C^1-element which will supply either linear, cubic or quintic interpolation of the boundary. Due to this, the straight-sided Föppl-von Kármán elements can be thought of as subparametric in both in-plane and out-of-plane displacements whereas the P_3 Föppl-von Kármán element will be isoparametric in-plane and subparametric out-of-plane. Finally, the P_5 Föppl-von Kármán elements will be subparametric in the out-of-plane displacements and superparametric in the in-plane displacements. Due to the mapping being provided by the C^1-elements, the derivatives of the in-plane displacement will be given by

$$v_{\alpha,\beta}^{(e)} = \sum_{l=1}^{10} L_\alpha^{(e,l)} \, \psi_{Ll,\gamma}^C(\boldsymbol{s}) \, (\boldsymbol{J}_{(e)}^{-1}(\boldsymbol{s}))_{\gamma\beta}, \tag{5.1.25}$$

in which $\boldsymbol{J}_{(e)}$ will be the Jacobian of the mapping, provided by the relevant C^1 basis (see sections 4.4.3 and 4.5.8). Here we note in passing that the Lagrange basis functions *do not* depend on element geometry and thus we have dropped the subscript e.

We reiterate, that unlike in standard isoparametric settings the position vector is *not* in general interpolated by the same basis as the unknowns, except in the P_3-elements in

Straight-Sided Föppl-von Kármán Elements

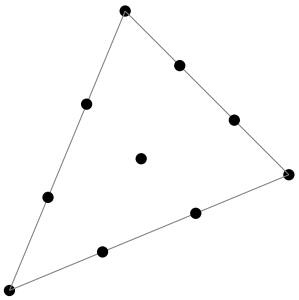

(a) v_α for straight-sided elements.

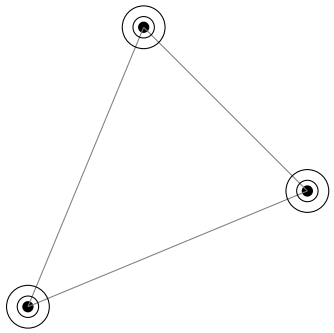

(b) v_3 for straight-sided elements.

P_3 Föppl-von Kármán Elements

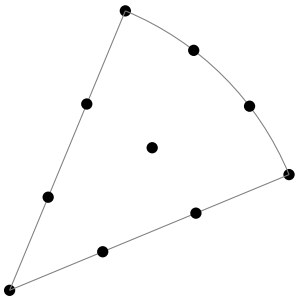

(c) v_α for P_3 elements.

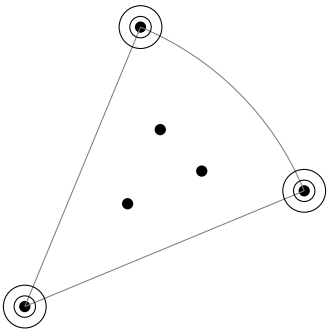

(d) v_3 for P_3 elements.

P_5 Föppl-von Kármán Elements

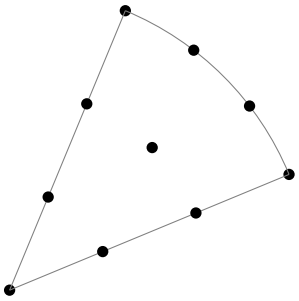

(e) v_α for P_5 elements.

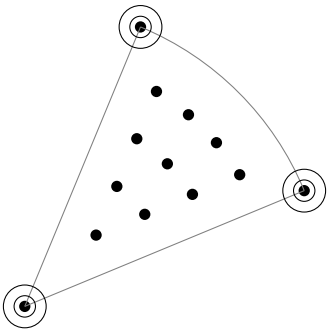

(f) v_3 for P_5 elements.

Figure 5.3: The interpolation schemes for the three Föppl-von Kármán elements.

which the two mappings coincide. However, in this case although the Lagrange interpolated mapping and the curved Bell element mapping are identical, we observe the convention that the mapping is likewise supplied by the curved Bell elements in order to avoid confusion.

We reiterate that the `TElement` implementation of `interpolated_x`, is instead overridden in the `CurveableBellElement` class, as described in section 4.5.9.

Using the above interpolation, in the same way as before we may discretize the Föppl-von Kármán equations (cf. section 3.5.6). Using identical steps to previously we arrive at the following discrete set of equations

$$R^N_{(i,j,e)} = \sum_{e=1}^{N_n} \int_{\Omega_e} \left[\tilde{\tilde{M}}^L_{e\alpha\beta}\, \psi^{[N]}_{(i,j,e),\alpha\beta} + \eta\, S^{vK}_{\alpha\beta} v^{(e)}_{3,\alpha} \psi^{[N]}_{(i,j,e),\beta} - \Delta\tilde{\tilde{p}}\, \psi^{[N]}_{(i,j,e)} \right] d\Omega\,, \tag{5.1.26}$$

$$R^B_{(i,e)} = \int_{\Omega_e} \left[\tilde{\tilde{M}}^L_{e\alpha\beta}\, \psi^{[B]}_{(i,e),\alpha\beta} + \eta\, S^{vK}_{\alpha\beta} v^{(e)}_{3,\alpha} \psi^{[B]}_{(i,e),\beta} - \Delta\tilde{\tilde{p}}\, \psi^{[B]}_{(i,e)} \right] d\Omega\,, \tag{5.1.27}$$

$$R^S_{(i,e)} = \sum_{e=1}^{N_n} \int_{\Omega_e} \left[S^{vK}_{\alpha\beta} \psi^C_{L\ i,\beta} \right] d\Omega\,, \tag{5.1.28}$$

in which we replace v_α and v_3 with their element-wise interpolated counterparts $v^{(e)}_\alpha$ and $v^{(e)}_3$ in the calculation of the matrix $\boldsymbol{S}^{vK}$. Once again, we have divided through by $h^3/(12(1-\nu^2))$ to remain consistent with other models within `oomph-lib`. Thus, η here is $12(1-\nu^2)/h^2$.

Summary: Föppl-von Kármán Elements

We incorporate these equations into a new discrete equation class: the Föppl-von Kármán equations, as shown in figure 5.5. These inherit directly from an existing finite element class within `oomph-lib` (`FiniteElement`). The complete Föppl-von Kármán element combines the Föppl-von Kármán equations, and the curveable Bell elements to form a usable plate element. The Föppl-von Kármán plate elements are templated by the C^0 basis used, which forms a set of new plate elements with various Lagrange interpolation schemes used for the in-plane displacements; in this thesis we only consider elements that use cubic Lagrange basis functions.

The interface will be largely the same as for the linear bending equations; however, we introduce some new functionality which is necessary to use two sets of basis functions per element. Additionally, these elements *must* now derive from `CurveableBellElement<NNODE_1D>`, in order to

1. Access the higher order Lagrange basis for the in-plane degrees of freedom

2. Set-up the correct equation numbering for the in-plane degrees of freedom

As such, in order to set-up the equations and stiffness matrix correctly, the basic element is required to be of type `TElement<2,NNODE_1D>`, despite the elements being assumed to be straight-sided by default. This is easily ensured by overriding the shape functions as described in section 4.5.9.

A new member function `basis_inplane` is needed to access the in-plane basis:

```
void basis_inplane(const Vector<double>& s, Shape& psi_u, Shape& test_u)
 {
  // Access TElement<2,NNODE_1D> implementation of shape
  TElement<2,NNODE_1D>::shape(s,psi_u,test_u);
  // Copy over to Test
  for(unsigned l=0; l<nnode();++l)
   { test_u[lm = psi_u[l]; }
 }
```

Additionally, the number of unknowns now *varies* between nodes: at vertex nodes there are 6 out-of-plane degrees of freedom and 2 in-plane degrees of freedom, whereas at all other nodes there are only the 2 in-plane degrees of freedom. We observe the convention that the in-plane degrees of freedom are always the first two degrees of freedom, and that on vertex nodes the out-of-plane degrees of freedom begin after the in-plane degrees of freedom. This complicates the prescription of boundary conditions, however.

To aid in the prescription of boundary conditions we provide the helper functions `fix_in_plane_displacements` and `fix_out_of_plane_displacements`. Both functions pin a nodal displacement degree of freedom that lies on a specified boundary: the value on the boundary is specified by passing a function pointer as an argument, as follows

```
void fix_out_of_plane_displacement(const unsigned& boundary, const unsigned& dof_number,
  const void (*deflection_on_edge)(const Vector<double>&, const double&)&);
```

The function pointer provides the displacement degrees of freedom as a function of the global (Cartesian) position - which is known when Dirichlet boundary conditions are specified. An overloaded version of these functions exists which takes a `double` instead of a function pointer: this is useful for the commonly encountered case of setting homogeneous boundary conditions.

A simplified code snippet illustrating this class and the new functionality is shown in

figure 5.4.

```
// GeneralizedFoepplVonKarmanElement using CurveableBellElements for the deflection
template <unsigned NNODE_1D>
class FoepplVonKarmanCurveableBellElement :
  public virtual CurveableBellElement<NNODE_1D>,
  public virtual FoepplVonKarmanEquations,
{
public:
 // Helper function for fixing the out-of-plane displacement dofs to a constant
     value
 void fix_out_of_plane_displacement(const unsigned& boundary, const unsigned&
   dof_number, const double& w);

 // Helper function for fixing the out-of-plane displacement dofs
 void fix_out_of_plane_displacement(const unsigned& boundary, const unsigned&
   dof_number, const void (*w_on_edge)(const Vector<double>&, const double&)&);

 // Get the Lagrange interpolated basis
 void basis_inplane(const Vector<double>& s, Shape& psi_u, Shape& test_u);

 // Get the curveable Bell basis
 void basis_and_test_fvk(const Vector<double>& s, Shape& psi_w, Shape& psib_w,
  Shape& test_w, Shape& testb_w);
```

Figure 5.4: Simplified code snippet illustrating the new helper functions for the new Föppl-von Kármán element.

We now proceed to detail the implementation of the Koiter Steigmann and extended Föppl-von Kármán-model elements.

5.1.3 Large-Rotation Plate Elements

We finally describe the implementation of the Koiter Steigmann and extended-Föppl-von Kármán-model elements. Because of the nature of the equations, both of these elements must use C^1-continuous interpolation for all three displacements components and share much of the underlying code. As such, we refer to both models as large-rotation plate models, as

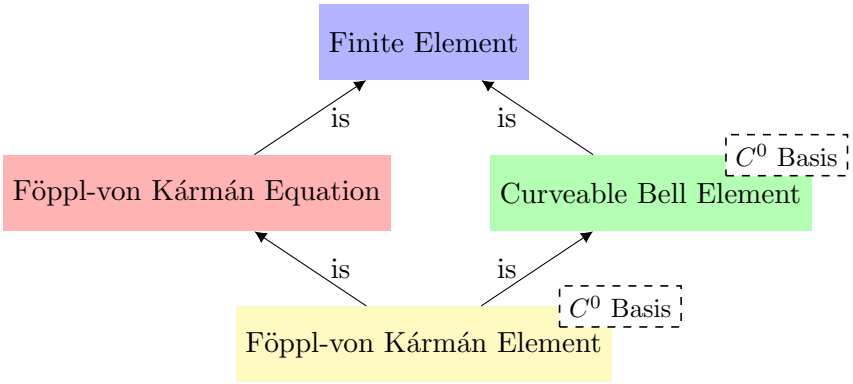

Figure 5.5: The structure of the new Föppl-von Kármán elements within `oomph-lib`. Dashed boxes are used to represent template parameters.

both will be treated in the same manner. We display the various interpolation schemes used for both models in figure 5.6.

We discretize all three displacements using the relevant C^1-basis, resulting in the following interpolated displacements on an element e

$$v_i^{(e)}(\hat{\boldsymbol{x}}) = \sum_{j=1}^{3}\sum_{k=1}^{6} N_i^{(e,j,k)}\ \psi^{[N]}_{(j,k,e)}(\hat{\boldsymbol{x}}) + \sum_{j=1}^{N_b} B_i^{(e,j)}\ \psi^{[B]}_{(j,e)}(\hat{\boldsymbol{x}}) \quad , i \in 1\ldots 3\,. \tag{5.1.29}$$

where we have three of each of the 18 nodal unknowns $N_i^{(j,k,e)}$ of the basis and three of each of N_b bubble unknowns of the basis $B_i^{(e,j)}$. We also now have the three arbitrary variations that also need to be interpolated with a C^1-basis

$$\delta v_i^{(e)}(\hat{\boldsymbol{x}}) = \sum_{j=1}^{3}\sum_{k=1}^{6} \delta N_i^{(e,j,k)}\ \psi^{[N]}_{(j,k,e)}(\hat{\boldsymbol{x}}) + \sum_{j=1}^{N_b} \delta B_i^{(e,j)}\ \psi^{[B]}_{(j,e)}(\hat{\boldsymbol{x}}) \quad , i \in 1\ldots 3\,. \tag{5.1.30}$$

where we have three of each of the 18 arbitrary, discrete, nodal variations, $\delta N_i^{(j,k,e)}$ and three of each of N_b arbitrary, discrete, bubble unknowns, $\delta B_i^{(e,j)}$.

Discretizing the equations in the same manner as previously we arrive at

$$R^N_{(i,j,k,e)} = \sum_{e=1}^{N_n}\int_{\Omega_e}\left[\tilde{\tilde{M}}_{ei\alpha\beta}\,\psi^{[N]}_{(j,k,e),\alpha\beta} + \tilde{\tilde{\mathfrak{N}}}_{ei\alpha}\psi^{[N]}_{(j,k,e),\alpha} - (\Delta\tilde{\tilde{p}})\alpha_e\hat{N}_{e\,i}\,\psi^{[N]}_{(j,k,e)}\right]d\Omega\,, \tag{5.1.31}$$

$$R^B_{(i,j,e)} = \int_{\Omega_e}\left[\tilde{\tilde{M}}_{ei\alpha\beta}\,\psi^{[B]}_{(j,e),\alpha\beta} + \tilde{\tilde{\mathfrak{N}}}_{ei\alpha\beta}\psi^{[B]}_{(j,e),\alpha} - (\Delta\tilde{\tilde{p}})\alpha_e\hat{N}_{e\,i}\,\psi^{[B]}_{(j,e)}\right]d\Omega\,, \tag{5.1.32}$$

with the discrete moment components $\tilde{\tilde{M}}_{ei\alpha\beta}$ and tension components $\tilde{\tilde{\mathfrak{N}}}_{ei\alpha}$. Here $\tilde{\tilde{M}}_{ei\alpha\beta}$ is the rescaled bending moment, given by:

$$\tilde{\tilde{M}}_{ei\alpha\beta} = \tilde{\tilde{\mathcal{G}}}_{\alpha\beta\gamma\delta}\hat{N}_i\hat{N}_k\,v^{(e)}_{i,\gamma\delta}(\hat{\boldsymbol{x}})\,, \tag{5.1.33}$$

Straight-Sided large-rotation plate Elements

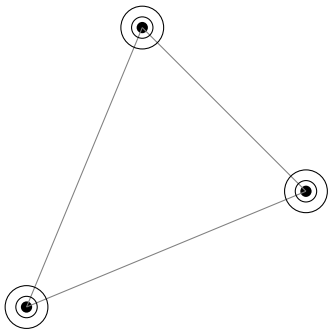

(a) v_α for straight-sided elements.

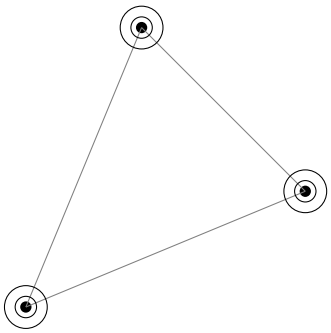

(b) v_3 for straight-sided elements.

P_3 Koiter Steigmann Elements

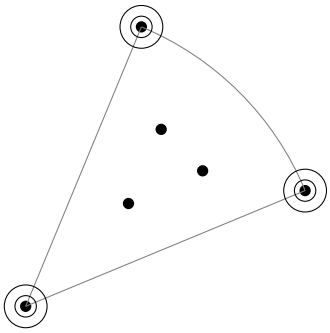

(c) v_α for P_3 elements.

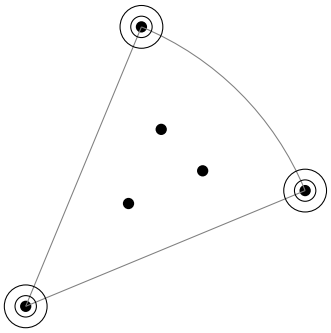

(d) v_3 for P_3 elements.

P_5 large-rotation plate Elements

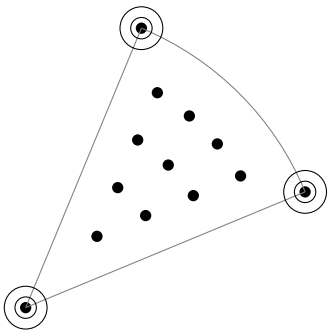

(e) v_α for P_5 elements.

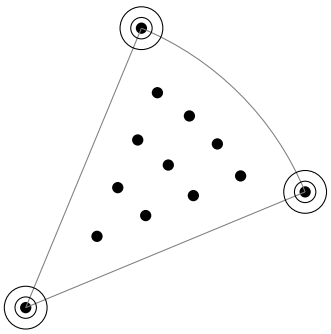

(f) v_3 for P_5 elements.

Figure 5.6: The interpolation schemes for the three large-rotation plate elements.

and $\hat{N}_i$ will be either the exact unit normal (for Koiter-Steigmann) or the approximate unit normal (for the extended Föppl-von Kármán model). Finally, the total stress tensor components $\mathfrak{N}_{i\alpha}$ is given by

$$\tilde{\tilde{\mathfrak{N}}}_{ei\alpha} = \eta \; S_{\gamma\alpha} Y_{i,\gamma} - \tilde{\tilde{M}}_{i\beta\gamma} \Gamma_{\alpha\beta\gamma} \,, \tag{5.1.34}$$

where again $\eta = 12(1-\nu^2)/h^2$.

Boundary Conditions

We now discuss the imposition of boundary conditions for the large-rotation plate models. In this case generic boundary conditions for these equations are a little more tricky to impose.

For the case of a free edge, the imposition of boundary conditions is trivial: the free boundary conditions are simply imposed as a 'do-nothing' condition. No rotation of the degrees of freedom need take place.

For the case of a pinned edge, or a resting clamp, 'rotation' of the Hermite degrees of freedom is necessary to impose physical boundary conditions. This allows the normal derivative and the displacement to be specified along the entire edge of an element. Under resting-clamp conditions, the moment free condition will be imposed naturally as a 'do nothing' condition.

The situation is complicated when we wish to impose a particular angle on the boundary. The direction of the unit normal to the deformed boundary (i.e normal to the edge of the plate in the lateral plane) can be set in this case, but importantly the 'stretch' of the deformed lateral normal *cannot* be set as this would overconstrain the problem. Thus, in general to impose a particular angle on the boundary we cannot simply impose the derivatives of the displacement, as this will also impose a particular stretch.

Instead we impose the boundary condition via a Lagrange multiplier, by augmenting the variational equation as follows

$$\delta \int_{\partial\Omega} \left(\Lambda \, \hat{\boldsymbol{N}} \cdot \boldsymbol{\nu}_d \right) ds \tag{5.1.35}$$

in which $\boldsymbol{\nu}_d$ is the (imposed) deformed (in–plane) normal to the edge of the sheet and Λ is an unknown Lagrange multiplier: a new field introduced on the edge of the sheet. ds is an infinitesimal line element along the edge of the sheet.

Computing the variations we obtain

$$\int_{\partial\Omega} \left(\hat{\boldsymbol{N}} \cdot \boldsymbol{\nu}_d \right) \delta\Lambda ds + \int_{\partial\Omega} \Lambda \; \boldsymbol{\nu}_d \cdot \delta\hat{\boldsymbol{N}} ds \tag{5.1.36}$$

which introduces a new equation to be solved on the edge and a new unknown Lagrange multiplier, Λ, applied to the edge. Following the arguments of Steigmann [2013], we can directly interpret the Lagrange multiplier as a pure bending moment applied to the edge of the plate.

The above process is in principle necessary for all clamped or sliding conditions: however, for the particular, commonly-encountered, case of homogeneous, clamped boundary conditions on the out-of-plane displacement, an easier solution is available. For homogeneous Dirichlet conditions on $v_{3,\alpha}$, the transverse normal is in the $\boldsymbol{k}$ direction. Thus we may impose the conditions more easily by simply pinning $v_{3,\nu} = 0$ and pinning $v_3 = 0$ along the whole edge, which by the definition of $\hat{\boldsymbol{N}}$ results in the unit normal on the edge being $\boldsymbol{k}$. This can be done in the same manner as for the linear bending elements and the Föppl-von Kármán elements.

Summary: Large-Rotation Elements

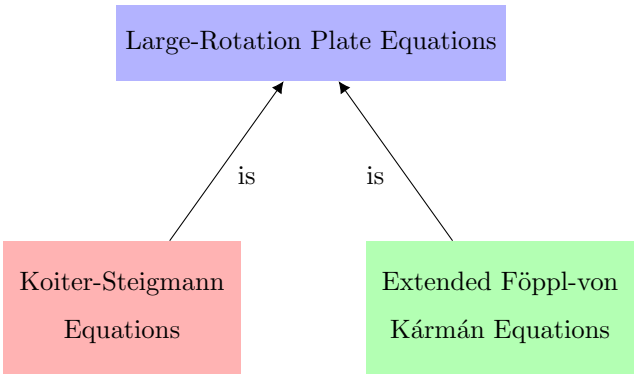

Large Rotation Plate Equations

- Defines interface to normal, bending moment, membrane tension etc.

Koiter-Steigmann Equations

- Implements normal, bending moment, membrane tension etc.

Extended Föppl-von Kármán Equations

- Implements normal, bending moment, membrane tension etc.

Figure 5.7: The structure of the new large-rotation plate equation classes within `oomph-lib`.

We incorporate the interface to both the Koiter-Steigmann plate and the extended-Föppl-von Kármán equations into a new set of discrete equations: large displacement plate equations, as shown in figure 5.7. The interface remains the same, but the definitions for moment and total tension will differ in the derived classes. The equations themselves inherit directly from the existing finite element class within `oomph-lib`.

Using the new equations, we introduce a new class of plate elements: large-rotation plate

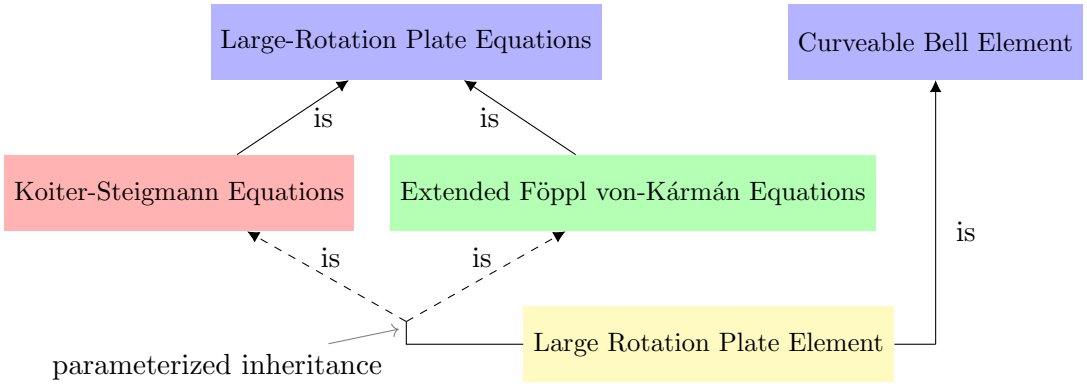

Figure 5.8: The structure of the new large-rotation plate element classes within `oomph-lib`.

elements, which are summarized in figure 5.8. The large-rotation element uses parameterised inheritance (i.e. inheritance from a template argument) to create complete finite elements using a set of large-rotation plate equations and the basis provided by the curveable Bell elements. This provides a large amount of code reuse and promotes the rapid integration of future large-rotation plate equations. The code structure that this parameterized inheritance introduces is summarized in figure 5.9.

```
// LargeRotationPlateEquations using CurveableBellElements
// Parametrized inheritance
template <class LARGE_ROTATION_PLATE_EQUATIONS>
class LargeRotationCurveableBellElement :
  public virtual CurveableBellElement<2>,
  public virtual LARGE_ROTATION_PLATE_EQUATIONS
```

Figure 5.9: Simplified code snippet illustrating the inheritance structure for the large-rotation curveable bell elements.

This concludes the details of the implementation. We proceed by validating the new functionality, to ensure correctness of the implemented methods and equations.

5.2 Validation of the Plate Models

To ensure the methodology that we developed in chapter 4 is functioning correctly, we implement several stages of numerical tests. We begin in section 5.2.1 by verifying the

functionality of a single curved element, by investigating the convergence behaviour of the interpolation error. Once the implementation is verified for a single geometric element with no associated equations, we proceed to validate the implementation of the various plate models individually in sections 5.2.2–5.2.5.

The first set of discrete elements we validate are the linear bending equations in section 5.2.2. Since these equations are linear and only contain a single variable, we can easily verify that the implemented geometric elements, defined in chapter 4, work in practise in a finite element simulation. We demonstrate that the equations attain excellent convergence rates in all tested cases.

In section 5.2.3 we proceed by demonstrating that the Föppl-von Kármán elements, which introduce new methodology for solving mixed-type displacement problems, can be used to solve plate problems, attaining high convergence rates.

Following this we test the Koiter-Steigmann elements in section 5.2.4 and then the extended Föppl-von Kármán model elements in section 5.2.5. Though these two sets of equations introduce no new methodology, it is necessary to verify that the governing equations have been implemented correctly. Therefore several convergence tests are carried out, for which high rates of convergence are obtained.

5.2.1 Interpolation Error on a Single Element

We start by examining the convergence behaviour of the error in interpolation on a single element. We examine the convergence of the interpolant of a known function on a series of triangles with decreasing diameter, keeping the angles of the triangle constant. We consider the interpolation of a particular function, $w(\boldsymbol{y})$, on a series of triangles that form a section of the curved edge, with decreasing arc-length, to investigate the interpolation error over a small 'element' of a particular function. This hierarchy is displayed graphically in figure 5.10.

To examine the convergence of the function we require a metric for measuring how accurate our approximation is. We choose the L^2-norm, denoted by $||\cdot||_2$, which is defined for a region Ω as the square root of the integrated, squared errors. Expressed mathematically we have

$$||w - w_e||_2 = \left[\int_\Omega \left(w(\boldsymbol{y}) - w_e(\boldsymbol{y})\right)^2 d\Omega\right]^{\frac{1}{2}}, \tag{5.2.1}$$

in which $w(\boldsymbol{y})$ is the approximated function and $w_e(\boldsymbol{y})$ is the exact function. We frequently

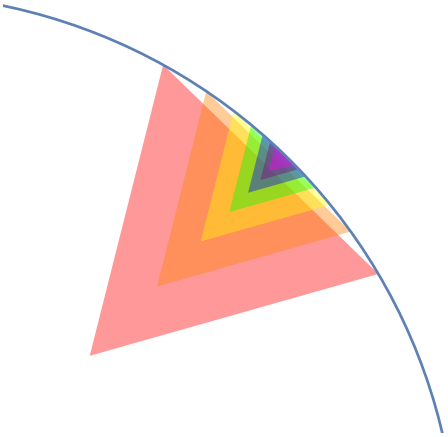

Figure 5.10: The hierarchy of equilateral triangles used to generate the convergence results for the validation of the interpolation on a single element.

quote the ratio of this measure relative to the L^2 norm of the exact solution $||w_e||_2$, which we call the relative L^2 norm.

We first examine the behaviour of this norm for a P_3 curved Bell element, introduced in section 4.5.3, used to approximate a circular boundary. The boundary, in this case, will not be approximated exactly but instead will be locally interpolated as a P_3 polynomial. The exact parametric representation of the boundary is

$$\boldsymbol{\chi}(s) = (\cos(s), \sin(s)) \ . \tag{5.2.2}$$

We define the hierarchy of equilateral triangles with vertices

$$\boldsymbol{a}_1 = \left(\cos(s_n^-), \sin(s_n^-)\right) \ , \tag{5.2.3}$$

$$\boldsymbol{a}_2 = \left(\cos(s_n^+), \sin(s_n^+)\right) \ , \tag{5.2.4}$$

$$\boldsymbol{a}_3 = \frac{1}{2}(\boldsymbol{a}_2 + \boldsymbol{a}_1) - \frac{\sqrt{3}}{2}(\boldsymbol{a}_2 - \boldsymbol{a}_1) \times \boldsymbol{k} \, , \tag{5.2.5}$$

where for the hierarchy displayed in figure 5.10, we choose $s_n^{\pm} = (4/5) \pm (2/5)(3/2)^{-n}$. Here n labels the n^{th} triangle with side length:

$$h_n = \sqrt{(\boldsymbol{a}_2 - \boldsymbol{a}_1) \cdot (\boldsymbol{a}_2 - \boldsymbol{a}_1)} \, . \tag{5.2.6}$$

For the set of triangles defined by the above relation, displayed in figure 5.10, we examine the behaviour of the L^2 norm in figure 5.11.

In the case of curved Bell elements it can be shown [Bernadou, 1992] that the L^2 error estimate for the interpolation over an element is $\mathcal{O}(h_n^5)$ when used to interpolate functions

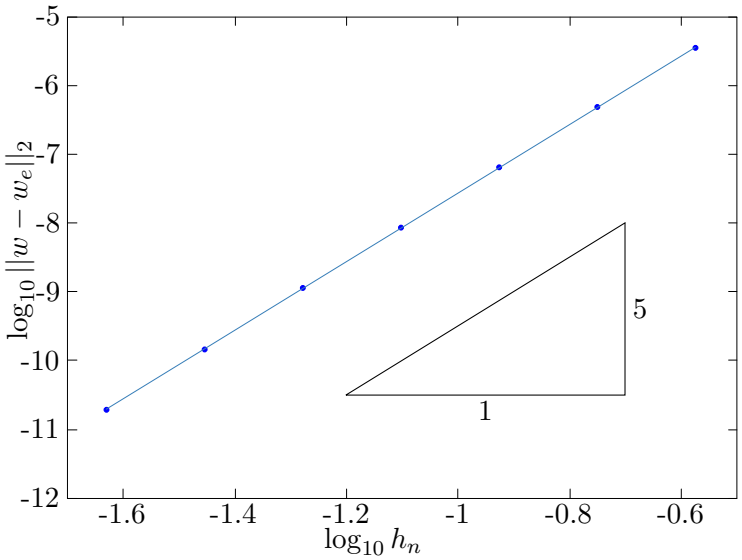

Figure 5.11: Convergence results for the hierarchy of triangles as a log-log plot of side-length, h_n, versus L^2 norm for the P_3 curved Bell element. The gradient is found to be 5.0, in agreement with the expected convergence rate.

$w \in \mathcal{H}^4$, which is verified numerically in the above test (see figure 5.11). We do this by taking a log-log plot of the errors versus side length and measuring the gradient. We proceed to perform the same test for the P_5 element, which has identical error estimates [Bernadou, 1992]. As can be seen in figure 5.12, the expected rate of convergence is obtained. We reiterate that, though these elements do not improve upon the convergence rate of the P_3 elements, the boundary interpolation is of higher continuity. This higher continuity is necessary for free boundary conditions, as discussed in section 4.5.1.

Having obtained the expected convergence rates for the basis, we have thus verified the correctness of the implementation of the basis functions. We proceed by verifying that the relevant plate equations have been correctly implemented.

5.2.2 Validation of Linear Bending

Validation for Polygonal Domains

To validate the implementation of the linear bending equations, defined in section 5.1.1, we check the convergence rates on both polygonal and curved domains. Although there are no convergence results for the L^2 norm for this set of discretized equations, it is reasonable to expect that the convergence will be dominated by the largest errors in the interpolation scheme which, as we saw in the previous section, scale as h^5. Additionally, for low-order

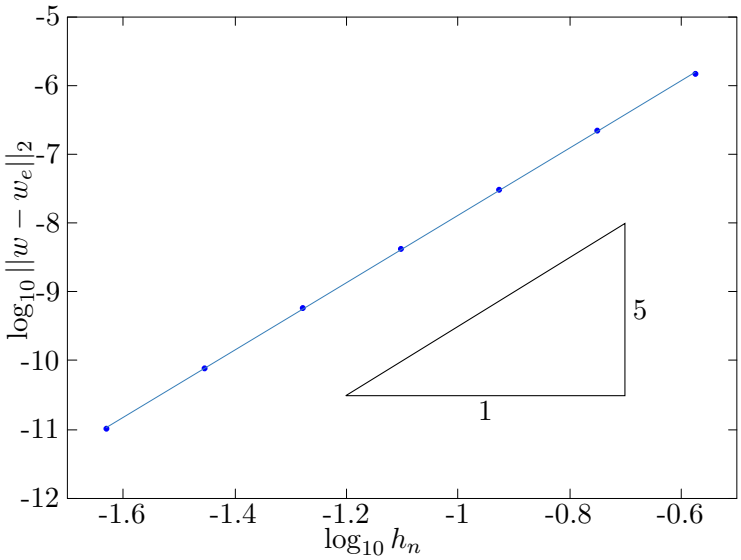

Figure 5.12: Convergence results for the hierarchy of triangles as a log-log plot of side-length, h_n, versus L^2 norm for the P_5 curved Bell element. The gradient is found to be 4.9.

polynomial solutions that are exactly representable on the mesh, we expect that the equations can be solved exactly with the minimum number of elements necessary to correctly impose the boundary conditions. In cases for which the rate of convergence is faster than expected it is common to describe the rate as superconvergent.

We first test the two, simple, polynomial solutions for a rectangular sheet, corresponding to sliding-type boundary conditions on two opposing edges and resting or clamped-type boundary conditions on the other opposing edges. These conditions result in a deflection field that is only a function of a single variable, which coincides with the solutions for the bending of a beam. The two cases, resting and clamped, with sliding edges at $x_1 = \pm\frac{1}{2}$, have the following deflections [Timoshenko and Woinowsky-Krieger, 1959b]

$$v_3(x_2) = \frac{\Delta\tilde{\tilde{p}}}{24}(a^2 - x_2^2)(5a^2 - x_2^2) \quad \text{and} \quad v_3(x_2) = \frac{\Delta\tilde{\tilde{p}}}{24}(a^2 - x_2^2)^2 \tag{5.2.7}$$

where the sheet has been clamped at $x_2 = \pm a$. These solutions are fourth-order polynomials and therefore are exactly representable by the Bell basis functions [Okabe, 1994]. As such, we expect that the solutions in these cases will be fully converged even on the coarsest possible mesh.

We solve the linear bending equations on the smallest possible square mesh, setting the in-plane aspect ratio to $2a = 1$, which consists of two elements as shown in figure 5.13. As expected, even with the minimum number of elements the exact solution is smoothly

represented, with the machine precision L^2-norms of 3.6×10^{-14} and 1.8×10^{-13} for resting and clamped respectively. The smooth solutions are shown in figure 5.13.

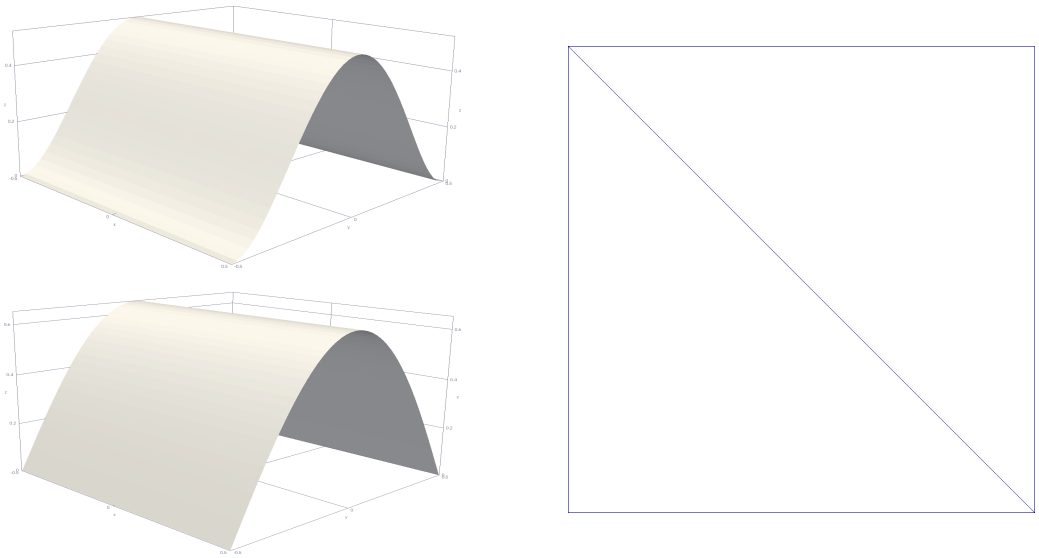

Figure 5.13: The computed solution for a square sheet subjected to a uniform pressure load, with opposing clamped (top left) or resting (bottom left) and sliding edges (left). Shown also is the mesh on which the solution was computed (right).

We proceed to test the sheet for the less trivial example of opposing resting and free boundary conditions. In this case, due to the Poisson effect, the sheet adopts a saddle shape, which can be described by a series solution. This additional test is necessary as the previous test cannot validate the cross derivative terms in either the discrete equations or the underlying Bell basis. The series solution to the resting-free case may be found in Timoshenko and Woinowsky-Krieger [1959b] and is given by

$$v_3(x_1, x_2) = \Delta\tilde{\tilde{p}}\, a^4 \sum_{m=1,3,\cdots}^{\infty} \Big(\frac{4}{\pi^5 m^5} + A_m \cosh(2\alpha_m x_2) + 2B_m\, \alpha_m x_2 \sinh(2\alpha_m x_2) \Big) \sin(2\alpha_m x_1) \ , \tag{5.2.8}$$

where the constant $\alpha_m = m\pi/2a$, and the constants A_m and B_m are given by:

$$\begin{aligned} A_m &= \frac{4}{m^5\pi^5} \frac{\nu(1+\nu)\sinh\alpha_m - \nu(1-\nu)\alpha_m \cosh\alpha_m}{(3+\nu)(1-\nu)\sinh\alpha_m \cosh\alpha_m - (1-\nu)^2\alpha_m} \ , \\ B_m &= \frac{4}{m^5\pi^5} \frac{\nu(1-\nu)\sinh\alpha_m}{(3+\nu)(1-\nu)\sinh\alpha_m \cosh\alpha_m - (1-\nu)^2\alpha_m} \ . \end{aligned} \tag{5.2.9}$$

The solution is shown computed on a particular mesh in figure 5.14. We test the simulation on a series of meshes with decreasing maximum element area, A_E, and record how the L^2 norm decreases with the decreasing diameter of the elements $h \sim \sqrt{A_E}$. This is plotted in figure 5.15. As can be seen the gradient of the line is 5.2, which is in line with the predicted

interpolation errors.

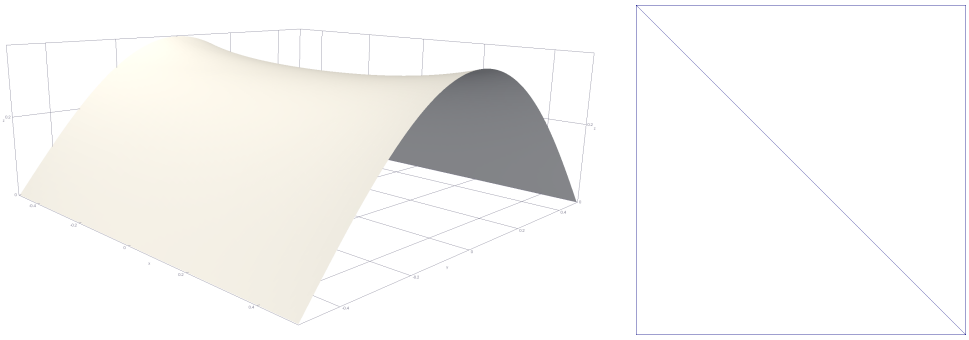

Figure 5.14: The computed solution for a square sheet subjected to a uniform pressure load, with opposing resting and free edges (left). The L^2 norm of this solution is 7.8×10^{-3}. Shown also is the mesh on which the solution was computed (right).

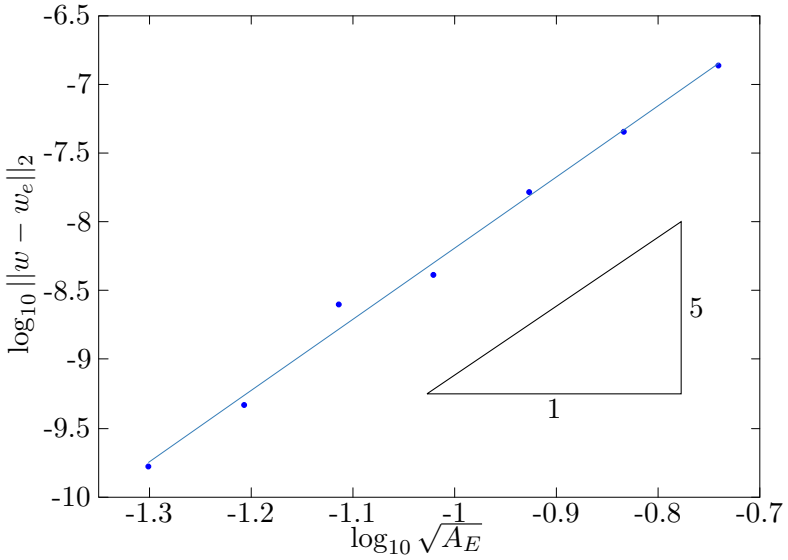

Figure 5.15: Convergence results for a series of unstructured meshes with decreasing maximum element area as a log-log plot of typical element size, $\sqrt{A_E}$, versus L^2 norm. The gradient is found to be 5.2.

Having tested the implementation of the simple linear bending equations for a rectangular domain, which tests the implementation of Bell elements in a plate model, we proceed to examine the convergence behaviour on curved domains, which necessitates the use of curved-Bell elements.

Validation for Curved Domains

To test the use of curved element patches in a physical problem, we begin by testing resting and clamped conditions on a circular domain subject to a uniform pressure loading. The linear bending solutions for these cases are axisymmetric and described by low order polynomials. For the clamped case, the solution is [Timoshenko and Woinowsky-Krieger, 1959b]

$$v_3(\rho) = \frac{\Delta\tilde{\tilde{p}}}{64}(1-\rho^2)^2 \tag{5.2.10}$$

in which $\rho = \sqrt{x_1^2 + x_2^2}$ is the standard radial coordinate. For the resting case, the solution is [Timoshenko and Woinowsky-Krieger, 1959b]

$$v_3(\rho) = \frac{\Delta\tilde{\tilde{p}}(1-\rho^2)}{64}\left(\frac{5+\nu}{1+\nu} - \rho^2\right) \tag{5.2.11}$$

in which the Poisson ratio enters via the moment free condition on the outer edge. We display the computed solutions to these cases, at low resolution, in figure 5.16. For the clamped case only, we may use the P_3 elements with impunity. For free and resting cases, we expect the use of P_5 elements to be necessary.

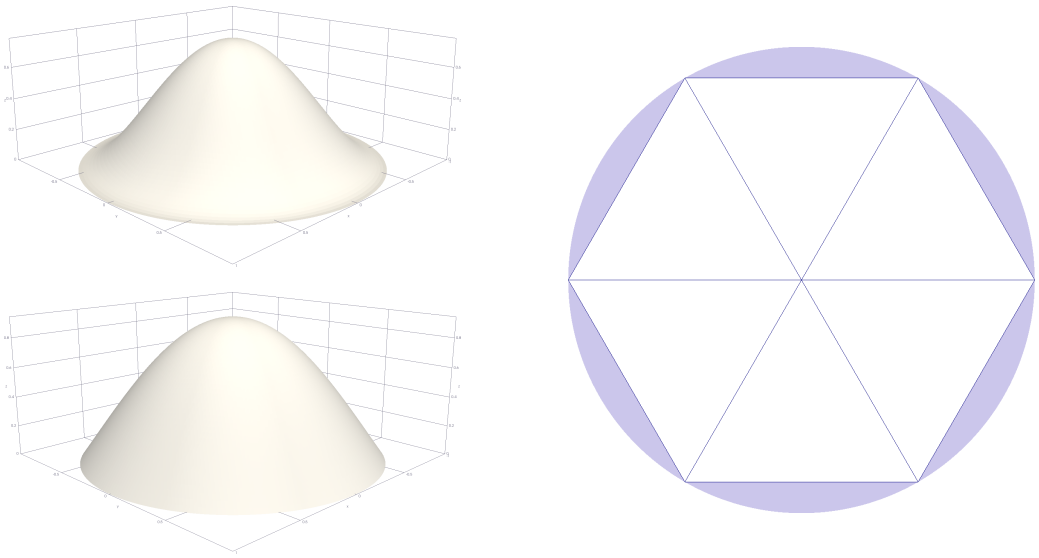

Figure 5.16: The computed solutions for a circular sheet subjected to a uniform pressure load, with clamped (top, left) and resting (top, right) boundary conditions respectively. The relative L^2 norms for these plots are 1.2×10^{-4} and 6.6×10^{-5} respectively. We also display the mesh on which the solution was computed (right) for which the shaded region is the approximated circular domain and the white triangles show the input mesh and vertices.

Although both of these cases are fourth-order polynomials, the curved elements are not unisolvent to degree 4 for general curved plates. We instead examine the convergence rates

as shown in figure 5.17. The observed convergence rate for the clamped and resting cases are 6.2 and 5.1 respectively. The resting case is in agreement with the expected rate of 5, but we have obtained a superconvergent rate of 6 for the fully clamped case.

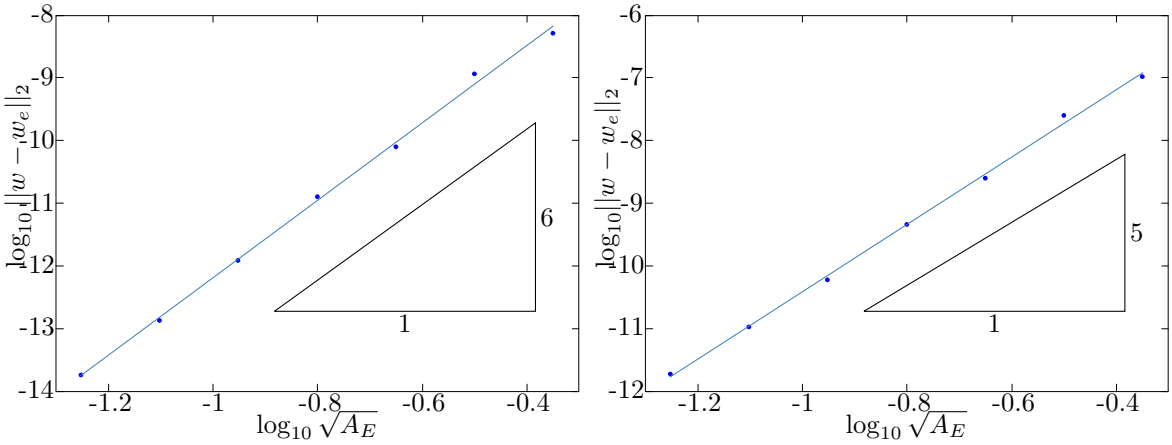

Figure 5.17: Mesh convergence results for the clamped circular sheet using P_3 elements (left) and resting circular sheet using P_5 elements (right). We show L^2 errors versus the typical element sizes $\sqrt{A_E}$ for a series of unstructured meshes as log-log plots. The gradients of the log-log plots are 6.2 and 5.1 respectively.

The final test case we examine for linear bending is a free boundary case subject to quadratic loading. The pressure loading we consider is

$$\Delta\tilde{\tilde{p}} = (\rho^2 - \frac{1}{2}) \tag{5.2.12}$$

which we apply to a plate with free boundary conditions on the outer edge. It can can be shown that this system has the analytic solution

$$v_3(\rho) = \frac{\rho^2\left((1+\nu)(2\rho^4 - 9\rho^2) + 12(2+\nu)\right)}{1152(1+\nu)} \tag{5.2.13}$$

where the solution v_3 is chosen such that the centre point has zero deflection. We display the simulation result for this system at low resolution in figure 5.18 and the convergence test in figure 5.19. The measured convergence rate is 5.1, in concordance with the expected value.

5.2.3 Validation of the Föppl-von Kármán Elements

Having implemented the Föppl-von Kármán elements which make use of both the C^1 basis functions discussed in sections 4.4-4.5 and cubic Lagrange shape functions discussed in section 5.1.2, we must validate the efficacy of such an implementation. We expect the largest errors to dominate, and therefore the interpolation error of the in–plane displacements to set the

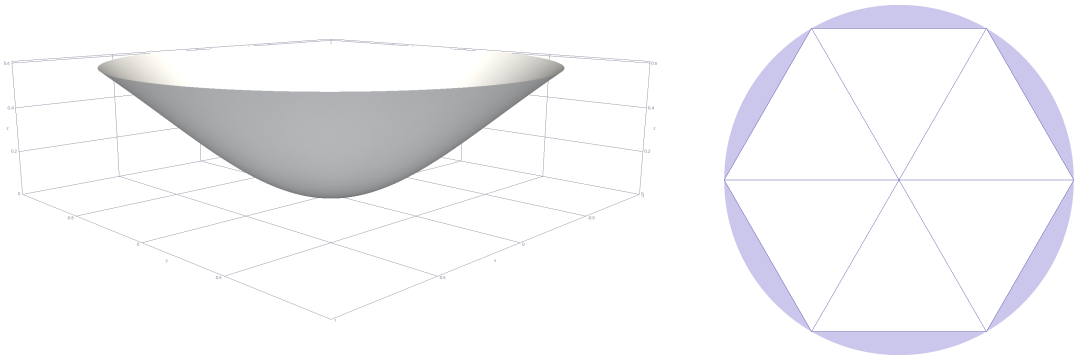

Figure 5.18: The computed solutions for a circular sheet subjected to a quadratic pressure load, free boundary conditions. The relative L^2 norm in this case is 5.7×10^{-4}. We also display the mesh on which the solution was computed (right) for which the shaded region is the approximated circular domain and the white triangles show the input mesh and vertices.

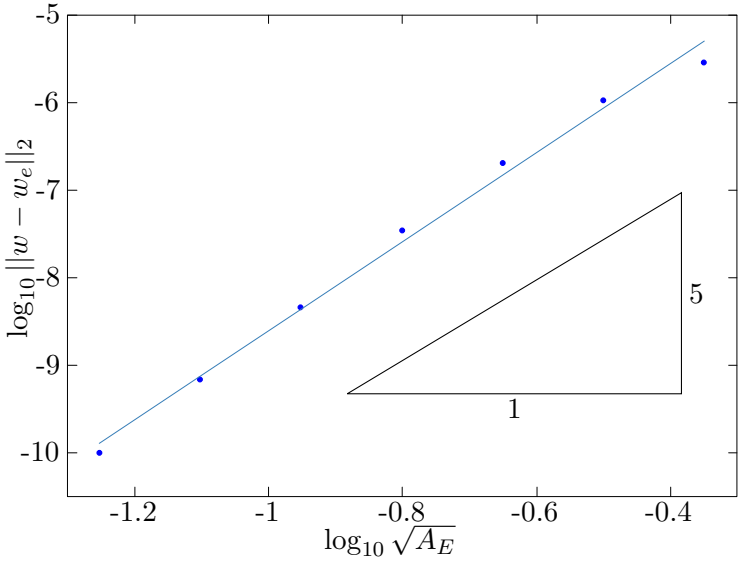

Figure 5.19: Mesh convergence results for a free sheet subject to a quadratic loading, for the linear bending equations. Shown is a log-log plot are the measured L^2 errors against typical element size $\sqrt{A_E}$ for a series of free circular sheets. The gradient for this plot is 5.1 in agreement with the expected rate of 5.

rate of convergence. Cubic Lagrange elements are unisolvent to degree 3, so a convergence rate of 4 is expected.

The first test case we examine is the small pressure solution for a free sliding sheet, $v_3(\rho = 1) = 0$, $dv_3(\rho = 1)/d\rho = 0$, with stress free conditions on the outer edge, $\boldsymbol{S}(\rho = 1) \cdot \hat{\boldsymbol{e}}_\rho = \boldsymbol{0}$ in which $\hat{\boldsymbol{e}}_\rho$ is the radial unit vector. We consider the small pressure limit in which linear bending applies. At subleading order, the Föppl membrane model is forced via a one-way coupling. The solution to this (linearised) case is:

$$v_3 = \frac{A(1-\rho^2)^2}{64} \tag{5.2.14}$$

with the (lower order) in-plane displacements:

$$v_\alpha = x_\alpha \frac{A^2}{24576}\left(3(1-\nu) + (\nu - 18\rho^2) + 4(5-\nu)\rho^4 + (\nu-7)\rho^6\right) , \tag{5.2.15}$$

with $x_1 = \rho\cos(\phi)$, $x_2 = \rho\sin(\phi)$ with ϕ as the azimuthal polar coordinate. A here is the magnitude of the forcing.

The above solution holds in the small pressure limit of a clamped Föppl-von Kármán plate subject to uniform pressure loading, however, by applying an appropriate (non-uniform) forcing (i.e. by the method of manufactured solutions [Oberkampf et al., 2004]), we can extend this solution to the entire range of pressures. We can enforce this by application of the following forcing

$$\Delta p = A + \frac{\left(5\rho^8 - 20\rho^6 + 30\rho^4 - 18\rho^2 + 3\right)}{196608} . \tag{5.2.16}$$

Using this 'manufactured' solution as our test case, we examine the convergence of the L^2 norm under mesh refinement. The results for this test are displayed in figure 5.20.

The second test we consider is the convergence of the azimuthal derivative of an axisymmetric solution under mesh refinement. As the domain we consider only approximates a circle, and the solutions are solved in a Cartesian coordinate system, the computed solutions in a circular system will only be approximately axisymmetric.

We examine the convergence under mesh refinement of the L^2 norm of the ϕ derivative of the deflection:

$$||\rho^{-1}\partial_\phi v_3||_2 = \left[\int_\Omega \left(\frac{1}{\rho}\frac{\partial v_3(\boldsymbol{y})}{\partial \phi})\right)^2 d\Omega\right]^{\frac{1}{2}} , \tag{5.2.17}$$

which for a perfectly axisymmetric solution is zero. In the case of the quadratic forcing on a free sheet, as seen in the section 5.2.2, we expect an axisymmetric solution to apply at small

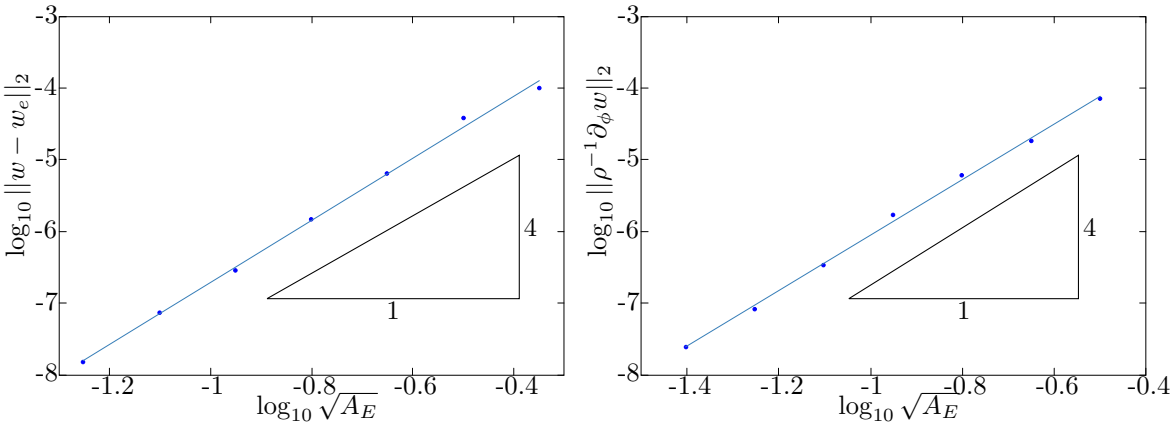

Figure 5.20: Convergence plots for the clamped manufactured solution (left) and the non-axisymmetry measure in the free plate case (right). The convergence rates are measured to be 4.3 and 3.9 respectively.

pressures. We therefore examine in this case how the non-axisymmetry measure decreases with mesh refinement. The rate of convergence is measured to be 3.9, which agrees with the expected rate of 4. These convergence results are displayed in figure 5.20.

5.2.4 Validation of the Koiter-Steigmann Elements

Having tested the Föppl-von Kármán equations, we proceed by testing the Koiter-Steigmann equations. We discuss this validation before testing the extended Föppl-von Kármán model in the following section, as large parts of the functionality is shared between the two elements. Given that all three displacements are now interpolated by the Bell and curved Bell elements, it is once again reasonable to expect a convergence rate of 5, in line with the interpolation error.

To validate that the implementation of the Koiter-Steigmann equations is correct by considering a simple physical example. To test the bending terms, we deform a flat, circular sheet to the shape of a cylinder with no stretching, thus allowing the testing of the bending terms in isolation.

The solution we wish to impose will be

$$v_2 = \frac{1}{A}\sin(A\,x_1) - x_1 \tag{5.2.18}$$

$$v_1 = 0 \tag{5.2.19}$$

$$v_3 = \frac{1}{A}\left(\cos(A\,x_1) - 1\right) \tag{5.2.20}$$

which is the equation for a cylinder of radius $1/A$ centred at $(0, 0, -1/A)$. The solution will

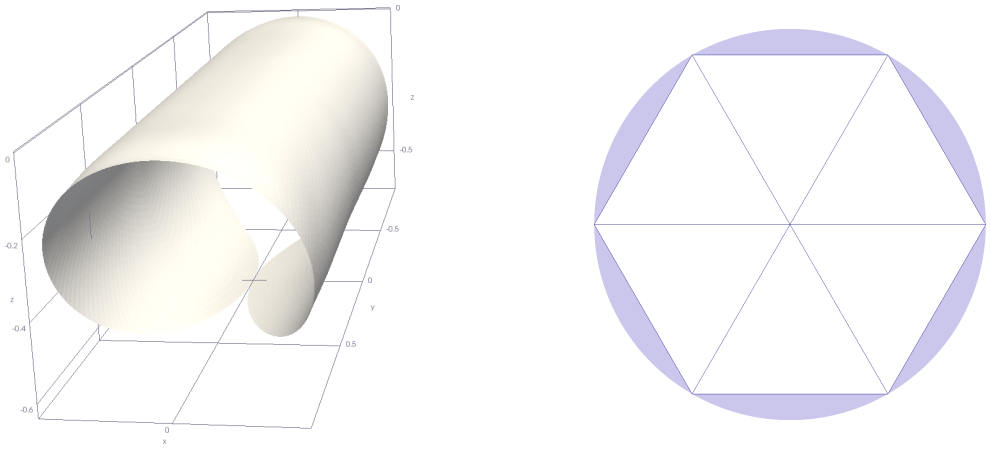

Figure 5.21: The computed solution for a circular sheet bent to a cylinder of radius $1/\pi$ and the mesh on which it was computed. The relative L^2 norm is 6.2×10^{-3}.

have constant curvature (cf. figure 5.21), $b_{11} = A$, which for a finite thickness sheet will need to be supported by a constant normal pressure load:

$$\Delta\tilde{p} = A^3\,, \tag{5.2.21}$$

acting in the direction of the unit normal. Here we recall that for a constant pressure $\boldsymbol{F} = \Delta p \hat{\boldsymbol{N}}\sqrt{G}$ where for isometric deformations $\sqrt{G} = \sqrt{g} = 1$. For this solution, when $h \ll A$ the pressure load needed to support the sheet becomes negligible, and the pure membrane solution corresponding to isometric deformation holds, which provides an additional physical check. Computing the L^2 norm for a series of meshes of decreasing maximum element area, we find the rate of convergence to be 5.5, which is better than the expected rate of 5. The convergence graph is plotted in figure 5.22.

The next test case we consider is the case of a circle deformed to a sphere. This deformation must involve both bending and stretching and will allow the final test of the validity of the discretized Koiter-Steigmann equations.

The solution we wish to impose will be

$$v_1 = A\sin\left(\frac{x_2}{A}\right) - x_1 \tag{5.2.22}$$

$$v_2 = A\cos\left(\frac{x_2}{A}\right)\sin\left(\frac{2x_1}{A}\right) - x_2 \tag{5.2.23}$$

$$v_3 = A\cos\left(\frac{x_2}{A}\right)\cos\left(\frac{2x_1}{A}\right) - 1 \tag{5.2.24}$$

which is the equation for a sphere of radius A centred at $(0, 0, -A)$. The forcing, $\boldsymbol{F}$, required

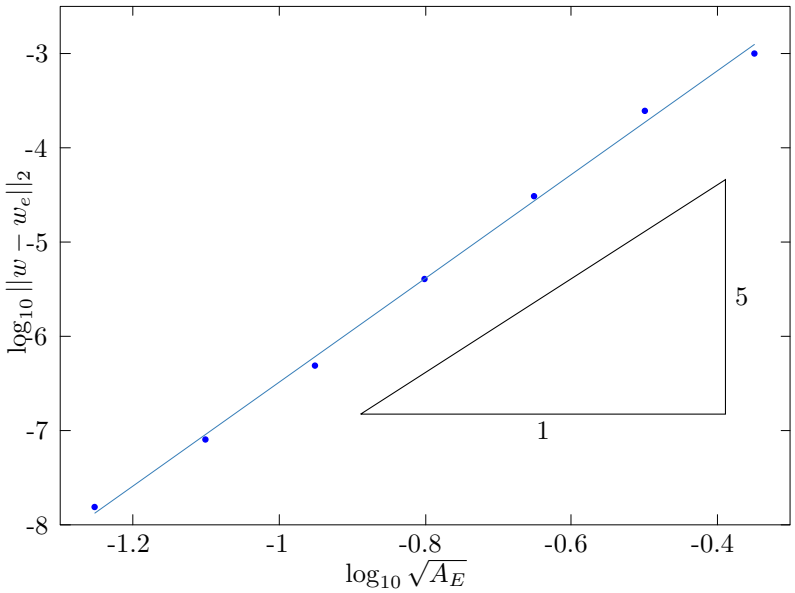

Figure 5.22: Maximum element area versus L^2 norm for a series of unstructured meshes, solving the Koiter-Steigmann equations for bending to a cylinder. The test was run for a plate of thickness $h = 1/50$ and bent to a cylinder with curvature $A = \pi$. The observed convergence rate is 5.5.

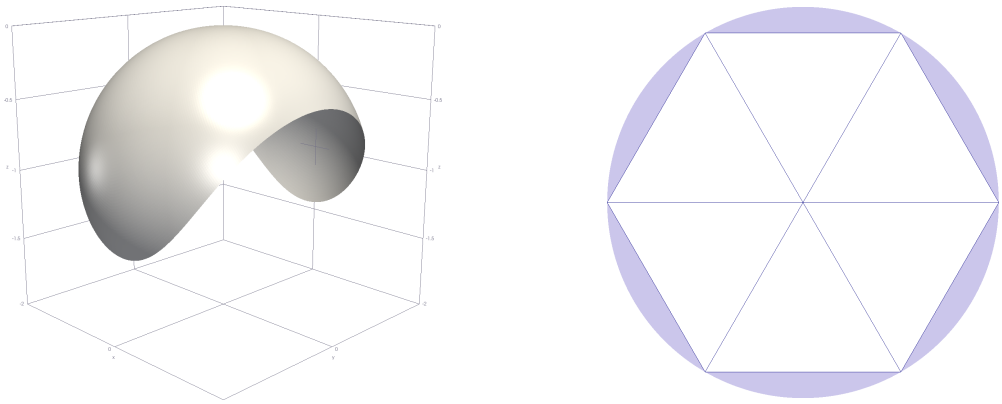

Figure 5.23: The computed solution for a circular sheet deformed to a sphere of unit radius and the mesh on which it was computed. The relative L^2 norm is 1.2×10^{-3}.

to impose this solution will be:

$$F_1 = \frac{\left(12A^2\nu + h^2(2\nu+3)\right)\sin(\xi) + 3\left(6A^2\nu + h^2(2\nu-1)\right)\sin(3\xi) - 5h^2\sin(5\xi)}{-h^2A^3} \tag{5.2.25}$$

$$F_2 = \frac{\sin(2\chi)\cos(\xi)\left(12\left(A^2(3\nu+4) + h^2\nu\right)\cos(2\xi) + 6A^2(4-3\nu) - 10h^2\cos(4\xi) + 11h^2\right)}{-h^2A^3} \tag{5.2.26}$$

$$F_3 = \frac{\cos(2\chi)\cos(\xi)\left(12\left(A^2(3\nu+4) + h^2\nu\right)\cos(2\xi) + 6A^2(4-3\nu) - 10h^2\cos(4\xi) + 11h^2\right)}{-h^2A^3} \tag{5.2.27}$$

with $\chi = x_1/A$ and $\xi = x_2/A$. We display the computed solution in figure 5.23.

Computing the L^2 norm for a series of meshes of decreasing maximum element area, we find the rate of convergence to be 5.0: exactly the expected rate. This is shown in figure 5.24.

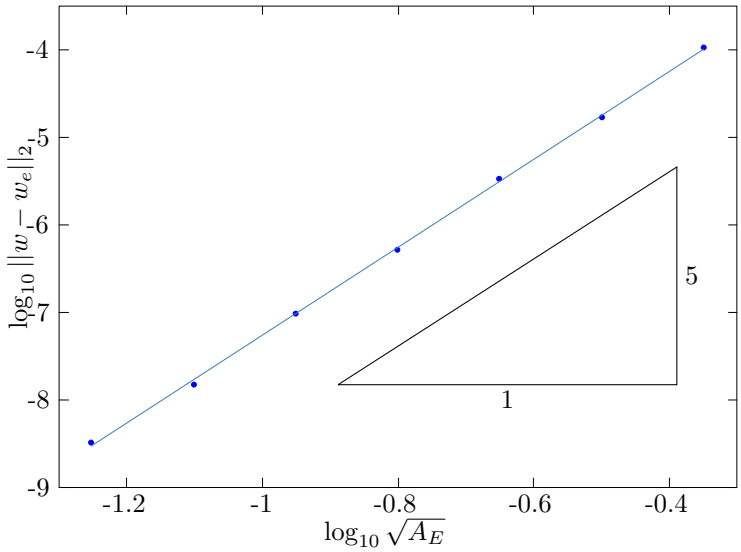

Figure 5.24: Maximum element area versus L^2 norm for a series of unstructured meshes, solving the Koiter-Steigmann equations for deformation to a sphere. The test was performed for a plate of thickness $h = 1/5$, deformed to a sphere of unit radius. The measured convergence rate 5.0.

5.2.5 Validation of the Extended Föppl-von Kármán Elements

To test the extended Föppl-von Kármán model, we only require testing of the bending terms and truncated Christoffel terms, as the membrane terms are identical to the Koiter-Steigmann membrane terms. We therefore choose a deformation which is strain free[1] to simplify the resulting manufactured solution. We choose the following strain-free deformation, chosen such that it scales appropriately with thickness as per the underlying kinematical assumption:

$$v_1 = E(x_1\,;\,5h) - x_1 \tag{5.2.28}$$

$$v_2 = 0 \tag{5.2.29}$$

$$v_3 = 5h\,(\cos(x_1) - 1) \tag{5.2.30}$$

[1] This will be exactly isometric, so the (truncated) Föppl-von Kármán strain tensor will *not* be zero. This is therefore sufficient to test the Christoffel term.

in which $E(\phi\,;\,k)$ is the incomplete elliptic integral of the second kind, defined as

$$E(\phi\,;\,k) = \int_0^{\phi} \left(\sqrt{1 - k^2 \sin^2(\theta)}\right) d\theta\,. \tag{5.2.31}$$

This describes the bending of a plane to an approximately elliptical shell, with no stretching.

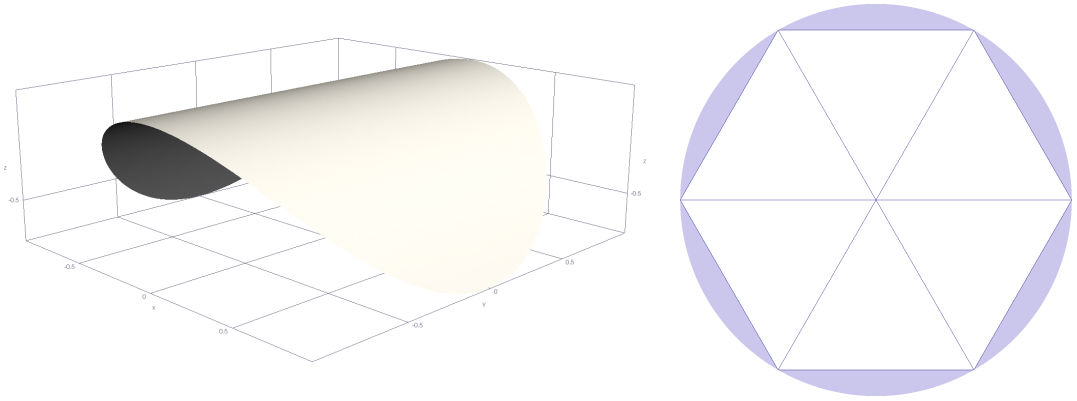

Figure 5.25: The computed solution for a circular sheet deformed to a strain-free approximately elliptical shape and the mesh on which it was computed. The relative L^2 norm for this solution is 1.0×10^{-3}.

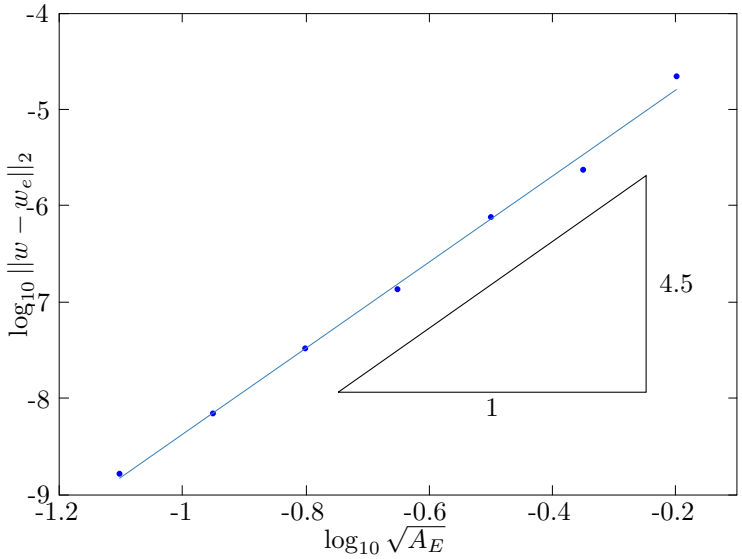

Figure 5.26: Maximum element area versus L^2 norm for a series of unstructured meshes, solving the extended Föppl-von Kármán equations for the strain-free test case. The test was run for a plate of thickness $h = 0.075$ and the measured convergence rate is 4.5.

Introducing the function, $\chi = 1 - h^2 \sin^2(x_1)$, we may then express the forcing required

to impose the above solution as:

$$F_1 = 50h^2 \sin(x_1)\cos(x_1) \tag{5.2.32}$$

$$F_2 = 0 \tag{5.2.33}$$

$$F_3 = \frac{10h\cos(x_1)\left(5\chi^{7/2} - 2\chi^3 - 4\chi^{5/2} - \chi^2 + 3\chi\right)}{2\chi^{5/2}} - \frac{6250(h)^5\left(\chi^{3/2} + \chi\right)\sin^2(2x_1)}{2\chi^{5/2}} + \frac{20(5h)^3\left(\chi^{3/2}((\chi-2)\chi+2) - 1\right)\cos^2(x_1)}{12\chi^{5/2}} \tag{5.2.34}$$

We show the computed displacement field in figure 5.25 and the corresponding mesh on which it was computed. Computing the error for a series of unstructured meshes we find that the rate of convergence is 4.5, as shown in figure 5.26.

Plate Model	**Test Case**	**Curved Edge**	**Rate**	**Expected**
Linear Bending	Rectangle, Resting/Sliding	N	Exact	Exact
	Rectangle, Clamped/Sliding	N	Exact	Exact
	Rectangle, Resting/Free	N	5.2	5
	Circle, Clamped	Y	6.2	5
	Circle, Resting	Y	5.1	5
	Circle, Free	Y	5.1	5
Föppl-von Kármán	Circle, Manufactured	Y	4.3	4
	Circle, Free, Axi-asymmetry	Y	3.9	4
Koiter Steigmann	Circle, Conform to Cylinder	Y	5.5	5
	Circle, Conform to Sphere	Y	5.0	5
Extended Föppl von Kármán	Circle, Manufactured	Y	4.5	5

Table 5.1: Table showing the measured and expected convergence rates of the validation cases.

5.2.6 Summary

This concludes the validation of the plate models. We have found that all of the discretized equations are correctly implemented and attain high rates of convergence, summarized in table 5.1. This makes them both suitable and attractive for use in generic plate problems. We now proceed to compare the various plate model predictions for several physical systems.

Chapter 6

Inflation of a Fully Clamped Circular Sheet

The first system we consider is the inflation of a clamped circular elastic sheet, which is displayed schematically in figure 6.1. In this system a thin, circular, elastic plate is smoothly clamped, such that the deflection gradient is zero at the clamp and that no sliding past the clamp is possible. This system can be viewed as a version of the blister test, which has been the subject of many studies, including Dannenberg [1961]; Gent and Lewandowski [1987]; Williams [1997]; Guo et al. [2005], to name a few.

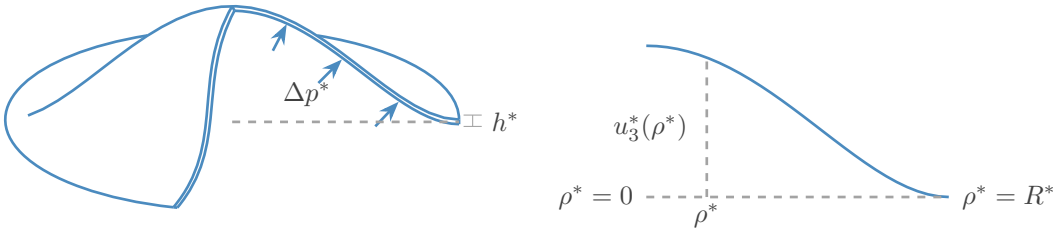

(a) (b)

Figure 6.1: Diagram showing the set-up of the clamped inflation problem from an oblique perspective (a) and a side view (b).

Under application of a pressure load, this system forms an axisymmetric bulge, which grows in size. Though the deflection, u_3^*, initially grows linearly in pressure, this behaviour quickly gives way to a relatively stiffer response due to nonlinear membrane effects. In related systems (see chapter 7) wrinkling instabilities may occur: however under this combination of loading and boundary conditions conditions the sheet will always be under tensile stress, so

no wrinkling is expected [Audoly and Pomeau, 2010]. Typically, in an experiment a pressure is applied to the sheet and the corresponding deflection at the centre is measured. The measured pressure-deflection curve can then be compared to predictions from the relevant plate theory, and this can be used to determine a value for Young's modulus.

Methods such as these have been the subject of renewed interest for the determination of macroscopic properties of nanoscale sheets, including in monolayer crystals such as graphene and graphene-oxides [Los et al., 2016, 2017; Delfani, 2018; Drozdov and deClaville Christiansen, 2017]. This is because conventional methods, such as uniaxial extension experiments, *cannot* be performed on such sheets. In many of these systems, however, experimental properties such as the effective Young's modulus and the pre-stretch[1] involved are a priori unknown. In nano-scale systems the effective values of these properties arise from inherently quantum-mechanical effects and can depend on temperature and system-size [Zhang et al., 2011; Los et al., 2016, 2017]. As such, they are difficult to control and measurement of effective stiffness cannot be done by conventional tension tests.

Although most studies have used indentation-type experiments, for which a detailed overview of the metrology can be found in Vella et al. [2015], there has been a renewed interest in classical pressurized blister tests for nanoscale materials [Koenig et al., 2011; Khestanova et al., 2016; Berger et al., 2016]. However, in these studies a quantitative understanding of how pre-stretch, as well as large-displacement and finite-strain-effects, are missing.

We aim to give a thorough analysis of the clamped, circular-sheet-system and compare predictions at large strains and displacements to the predictions of the Föppl-von Kármán model. Ultimately we use this information to outline a fitting strategy, in order to develop a robust means of determining Young's modulus for axisymmetric systems when pre-stretch is unknown, which provides an interesting contribution to the literature.

In macroscopic systems, pre-stretch is found to greatly affect the response of the material, especially in thin sheets, as can be seen the experimental measurements displayed in figures 6.5. In systems in which it is difficult to quantify pre-stretch, this introduces a large (unknown) error into to the fitting procedure, leading to erroneous measured values for Young's modulus.

Typically, for very thin sheets the Föppl-von Kármán model is appropriate, especially when the deflections are small. In cases when the tensile stress dominates it is possible

[1] By pre-stretch, we mean a non-zero, horizontal displacement imposed at the boundary.

to use the Föppl membrane model instead, which coincides with Föppl-von Kármán when bending can be neglected. In regimes where bending cannot be neglected these equations are difficult to solve analytically [Landau and Lifshitz, 1986]: the Föppl-von Kármán equations constitute a singular perturbation of the Föppl membrane model, and as such a bending layer needs to be accounted for in asymptotic analysis. However, given that the discretization of this system is straightforward, it is of little extra difficulty accounting for bending terms numerically, which affords the model extra flexibility to account for low pressure behaviour in the system.

In this chapter we outline two experimental procedures that are typically used for determining material properties: an axisymmetric inflation experiment and a uniaxial tension experiment. Following this, in section 6.2, we then investigate the predictions for the clamped inflation system, using a finite difference simulation of the Föppl-von Kármán equations. In section 6.3, we then address when and how this model breaks down at larger pressures, considering the effects of pre-stretch, nonlinear material behaviour and additional geometrical nonlinearity. Finally, in section 6.4, having identified the regime in which the Föppl-von Kármán model is appropriate, we use a nonlinear least-squares fit to the experimental data in the inflation experiment and compare the obtained values for Young's modulus to that found in a uniaxial tension experiment.

6.1 Outline of Experimental Procedures

Two experiments were performed in order to determine Young's modulus: a uniaxial extension experiment, in which samples of a material were cut into long strips and extended subject to a uniaxial force, and an inflation experiment. Schematic diagrams of the two experiments are shown in figure 6.2. The first experiment we describe is the uniaxial tension experiment.

6.1.1 Experimental Procedure for the Uniaxial Tension Experiment

We first measure the Young's modulus using a conventional uniaxial extension experiment: long strips of latex sheet, from a commercial latex supplier (Supatex), are subjected to a

known relative extension, e_U, and the resulting force is measured, using an Instron single-arm model 3345 machine. Large aspect ratio strips (length $\gtrsim 4.5\times$ width)[2] were used, so that the strip was approximately in a state of simple tension with $\sigma_{22} = \sigma_{33} = 0$, with σ_{11} corresponding to the Cauchy stress in the direction of the extension.

Two separate latex samples were considered: one of thickness (0.365 ± 0.006)mm and another of thickness (0.887 ± 0.018)mm: throughout this chapter we will use the parenthesis shorthand for uncertainty where, for example, these values would be written 0.887(18)mm and 0.365(6)mm. Each sheet was cut into strips of varying widths and lengths: the data was then aggregated by combining the force displacement curves and taking an average of the measured values at regular (interpolated) intervals of the engineering strain. This is made possible because the behaviour under uniaxial extension is independent of aspect-ratio. The error on each data point is then the standard deviation of the mean at that point: thus, the error bars are representative of the variation between individual strip-pull experiments. This experimental data is shown in figures 6.3 and 6.4.

Using the combined data, the known result for uniaxial tension of a strip made of a Mooney-Rivlin material can be used to perform a nonlinear least-squares fit in order to deduce the material parameters.

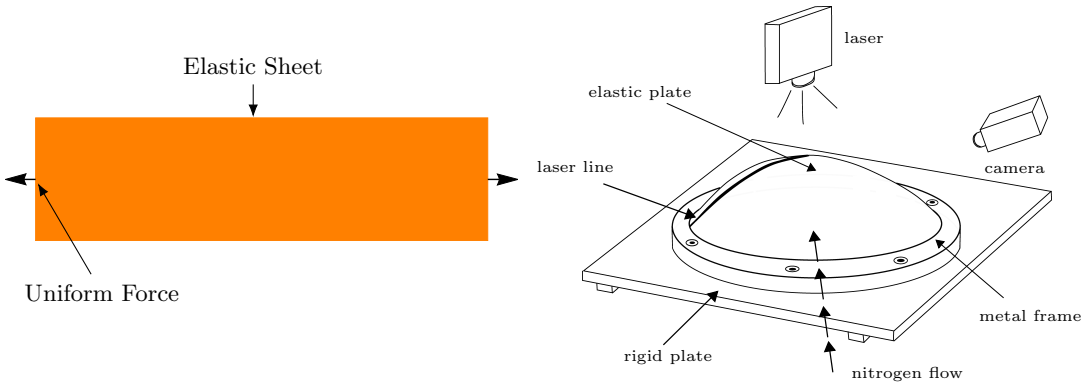

Figure 6.2: Schematics of the strip pull experiment (a) and the inflation experiment (b).

[2]For the thinner (0.365mm) sheet, the strip dimensions were (14.7×133.82)mm, (30.01×133.82)mm, (15.21×133.80)mm, (30.08×133.80)mm. For the thicker (0.887mm) sheet, the strip dimensions were (15.76×133.35)mm, (30.04×133.55)mm, (15.14×133.35)mm, (29.92×133.35)mm.

6.1.2 Fitting to Strip-Pull Experiments

For uniaxial extension[3], the Mooney-Rivlin prediction for stress in the direction of the stretch is [Mooney, 1940]

$$\sigma^*_{11} = \left(2C_1^* + \frac{2C_2^*}{1+e_U}\right)\left((1+e_U)^2 - \frac{1}{1+e_U}\right), \tag{6.1.1}$$

where we recall that $\boldsymbol{\sigma}$ is the Cauchy stress. It is more convenient to measure the engineering stress in experiments, which will instead be given by:

$$\sigma^{*E}{}_{11} = \left(2C_1^* + \frac{2C_2^*}{1+e_U}\right)\left((1+e_U) - \frac{1}{(1+e_U)^2}\right). \tag{6.1.2}$$

As discussed in section 2.2.5, the Young's modulus, E, is given by $E = 6(C_1^* + C_2^*)$. With this in mind, we introduce nondimensional material constants $C_1 = C_1^*/E$ and C_2^*/E, related by the formula $C^1 + C^2 = 1/6$. As both constants C_1^* and C_2^* must be non-negative, this implies that $0 \leq C_2 \leq 1/6$ with $C_1 = 1/6 - C_2$. For the special case of $C_2 = 0$ the model is Neo-Hookean, otherwise the material model is Mooney-Rivlin.

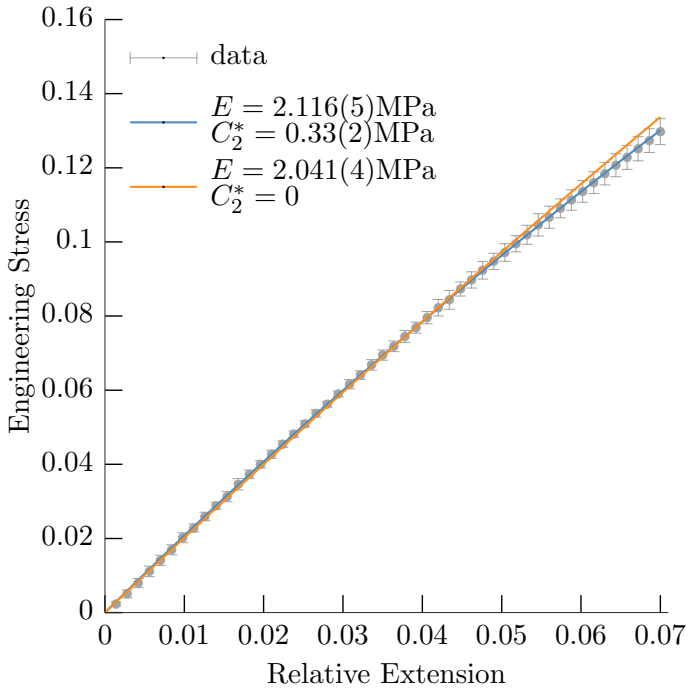

Figure 6.3: Engineering stress, σ^E_{11}, versus relative extension, e_U, for sheets of thickness $h^* = 0.365$mm under simple tension. Young's modulus is obtained by fitting to the experimental data (markers) using the Mooney-Rivlin and neo-Hookean models, with corresponding reduced χ^2 values 0.071 and 0.41, respectively.

[3]Assuming a state of simple tension: i.e. $\sigma^*_{3i} = \sigma^*_{22} = 0$.

The above formula can be obtained from the Cauchy stress by multiplying it by the deformed cross-sectional areal stretch of the sample. This areal stretch is equal to $(1 + e_U)^{-1}$ for the case of uniaxial extension. The above functional form can then be used to fit for Young's modulus using a nonlinear least squares method: we will use the Levenberg-Marquardt algorithm to determine the best fit [Bard, 1974; Eaton et al., 2014].

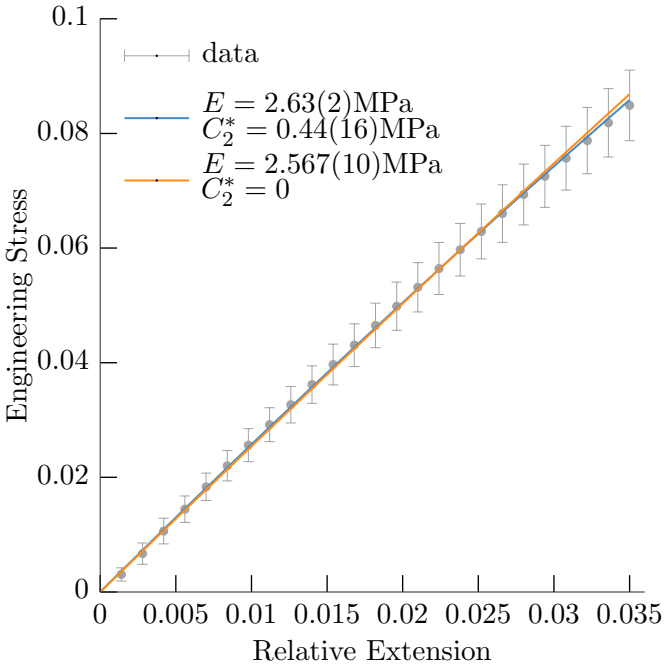

Figure 6.4: Engineering stress, σ_{11}^E, versus relative extension, e_U, for sheets of thickness $h^* = 0.887$mm under simple tension. Young's modulus is obtained by fitting to the experimental data (markers) using the Mooney-Rivlin and neo-Hookean models, with corresponding reduced χ^2 values 0.027 and 0.045, respectively.

We show the experimental data for strips of two Mooney-Rivlin sheets, of different thickness, and corresponding fits in figures 6.3 and 6.4. We find that for both sheets a neo-Hookean fit well describes the data, without the need to introduce the additional material parameter associated with the Mooney-Rivlin model. The Young's modulus for the sheets of thickness $h^* = 0.365$mm and $h^* = 0.887$ are found to be 2.041(4)MPa and 2.57(1)MPa respectively. The reduced χ^2 of both fits are lower than would be expected, 0.071 and 0.045 for the thinner and thicker sheets, respectively, indicating that the estimated errors over-state the variability of the data. This can be seen clearly in the graphs, as the fitted line never lies outside of the errorbars. A possible explanation of this is that the errors associated with the fit arise systematically, not randomly, as is assumed by the χ^2 measure of goodness of fit. This may

be due to the difficulty determining when the sheet is first tensile, which could introduce an offset in measured values of extension.

6.1.3 Experimental Procedure for Inflation

The same material was then used in an inflation experiment: the sheet was clamped, using a circular frame of radius 80mm, to a plate that was accurately levelled and contained a small nozzle in the centre, as shown in the schematic of this set-up (figure 6.2). Air was then injected into the cavity between the plate and sheet, through the nozzle. The pressure difference between atmospheric pressure and the pressure inside the cavity was measured using an ultra-low (Honeywell) pressure sensor (pressure range ±625Pa, with resolution ±5Pa). The deflection was measured by using a high-resolution camera (Nikon D7000100, 6000 × 4000 pixels) oriented at an oblique (31°) angle and projecting a laser line onto the sheet, such that it passed through the centre. Sub-pixel resolution was achieved by locally fitting a Gaussian profile to the line intensity, in the same manner as in Pihler-Puzović et al. [2015]. The sheet's deflection could then be determined by measuring the movement of the laser line from its undeflected position to the new position, within the frame of the camera, allowing the determination of deflection to within ∼ 10µm.

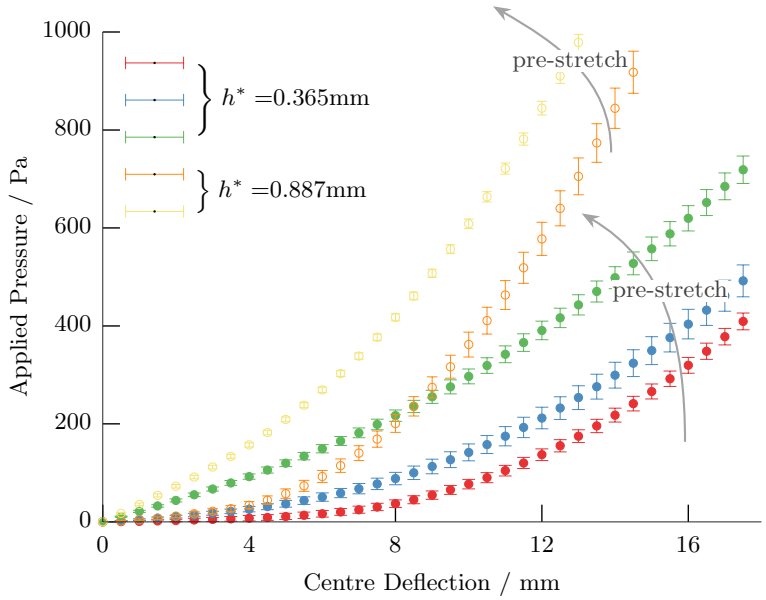

Figure 6.5: The combined data from each inflation experiment. The thicker sheets ($h^* = 0.887$) are shown as hollow circles and the thinner sheets ($h^* = 0.365$) are shown as solid circles. It can be seen that pre-stretch, which increases in the direction of the arrows, has a significant stiffening effect, when considering the inflation of otherwise identical sheets.

Each experiment was set up by clamping a sheet sample to the rig with a deliberately imposed pre-stretch - which was not measured. In practise, some amount of imposed pre-stretch is unavoidable when applying the clamp. Once the sheet was fixed in place several inflation experiments were performed on the sheet, which could then be aggregated to form a single pressure-deflection curve. This also provided errors for each point, which are the standard deviation on the mean of the measured values.

Using this combined data, separate nonlinear fits can be carried out using the predictions of a particular plate model and a standard-deviation-weighted average of the measured values of the of Young's modulus at different pre-stretch can be made.

6.2 The Föppl-von Kármán Model

The model we first consider to simulate the inflation system is the Föppl-von Kármán model, suitably specialised to an axisymmetric domain. This model is appropriate for thin sheets undergoing moderate rotations and small strains.

The axisymmetric Föppl-von Kármán equations are given by [Coman et al., 2015]:

$$D\Delta^{*2}u_3^* - h^*\left(S_{\rho\rho}^* u_3^{*\prime\prime} + \frac{1}{\rho^*}S_{\phi\phi}^* u_3^{*\prime}\right) = \Delta p^*\,, \tag{6.2.1}$$

$$S_{\rho\rho}^{*\,\prime} + \frac{1}{\rho^*}\left(S_{\rho\rho}^* - S_{\phi\phi}^*\right) = 0\,, \tag{6.2.2}$$

using (ρ^*, ϕ) as dimensional plane polar coordinates and $D = Eh^{*3}/12(1-\nu^2)$ as the bending moment. Here Δp^* is the pressure difference between the top and bottom plates, as discussed in section 3.4.10. The second Piola-Kirchhoff stress components, the radial and hoop stress, are given by

$$S_{\rho\rho}^* = \frac{E}{1-\nu^2}\left(\epsilon_{\rho\rho} + \nu\epsilon_{\phi\phi}\right)\,, \quad S_{\phi\phi}^* = \frac{E}{1-\nu^2}\left(\epsilon_{\phi\phi} + \nu\epsilon_{\rho\rho}\right)\,, \tag{6.2.3}$$

with Young's modulus, E, and Poisson ratio ν. In turn, the Green-Lagrange strain components, $\epsilon_{\rho\rho}$ and $\epsilon_{\phi\phi}$, are given by

$$\epsilon_{\rho\rho} = u_\rho^{*\prime} + \frac{1}{2}\left(u_3^{*\prime}\right)^2 \quad \text{and} \quad \epsilon_{\phi\phi} = \frac{1}{\rho^*}u_\rho^*\,. \tag{6.2.4}$$

Here u_ρ^* is the radial displacement. For this system, the equations are subject to the boundary conditions:

$$u_\rho^*(\rho^* = R) = e_\rho R\,, \quad u_3^*(\rho^* = R) = 0 \quad u_3^{*\prime}(\rho^* = R) = 0\,. \tag{6.2.5}$$

in which e_ρ is the applied pre-stretch. At the centre, we have the regularity conditions

$$u_\rho^*(\rho=0)=0\,,\quad u_3^{*\prime}(\rho=0)=0\quad u_3^{*\prime\prime\prime}(\rho=0)=0\,. \tag{6.2.6}$$

In the above equations R is the outer radius as displayed in figure 6.1.

We can nondimensionalize these equations by introducing the following nondimensional quantities:

$$w=\frac{\sqrt{12(1-\nu^2)}}{h^*}\,w^*\,,\quad u_\rho=\frac{12(1-\nu^2)R}{h^{*2}}\,u_\rho^*\,,\quad \Delta p=\frac{R^4\left(12(1-\nu^2)\right)^{\frac{3}{2}}}{h^{*4}E}\,\Delta p^*\,, \tag{6.2.7}$$

with $\rho=\rho^*/R$. This yields the following nondimensional equations:

$$\Delta^2 u_3-\left(S_{\rho\rho}u_\rho''+\frac{1}{\rho}S_{\phi\phi}u_\rho'\right)=\Delta p\,, \tag{6.2.8}$$

$$S_{\rho\rho}'+\frac{1}{\rho}\left(S_{\rho\rho}-S_{\phi\phi}\right)=0\,. \tag{6.2.9}$$

subject to the boundary conditions

$$u_\rho(\rho=1)=e_\rho\,\frac{12(1-\nu^2)}{h^2}\,,\quad u_3(\rho=1)=0\,,\quad u_3'(\rho=1)=0\,, \tag{6.2.10}$$

in which $e_\rho>0$ is the pre-stretch parameter. At the centre, we have the regularity conditions

$$u_\rho(\rho=0)=0\,,\quad u_3^{*\prime}(\rho=0)=0\quad u_3^{*\prime\prime\prime}(\rho=0)=0\,, \tag{6.2.11}$$

which ensure that the stress and displacements are continuous. Here we have introduced the nondimensional stress, $\boldsymbol{S}$, and the scaled Green-Lagrange strain, $\bar{\boldsymbol{\epsilon}}$,

$$\boldsymbol{S}=\frac{12(1-\nu^2)R^2}{E\,h^{*2}}\,\boldsymbol{S}^*\quad\text{and}\quad\bar{\boldsymbol{\epsilon}}=\frac{12(1-\nu^2)R^2}{h^{*2}}\,\boldsymbol{\epsilon}^* \tag{6.2.12}$$

such that the nondimensional stress is related to the scaled strain by

$$S_{\rho\rho}=\frac{1}{1-\nu^2}\left(\bar{\epsilon}_{\rho\rho}+\nu\bar{\epsilon}_{\phi\phi}\right)\quad\text{and}\quad S_{\phi\phi}=\frac{1}{1-\nu^2}\left(\bar{\epsilon}_{\phi\phi}+\nu\bar{\epsilon}_{\rho\rho}\right)\,. \tag{6.2.13}$$

We can rescale the experimental data, shown in figure 6.5, according to the predictions of this model, which in principle should remove any explicit thickness dependence in the data. An implicit thickness dependence instead enters via the ratio of pre-stretch to pressure-load, which are scaled differently on h^*. We plot rescaled data in figure 6.6, where we instead consider the rescaled, dimensional pressure, $\Delta p^*_{Rescaled}$, defined as

$$\Delta p^*_{Rescaled}=\left(12(1-\nu^2)\right)^{\frac{3}{2}}\left(R/h^*\right)^4\Delta p^*/10^{13}, \tag{6.2.14}$$

which is more convenient to fit to, as it removes any explicit thickness dependence.

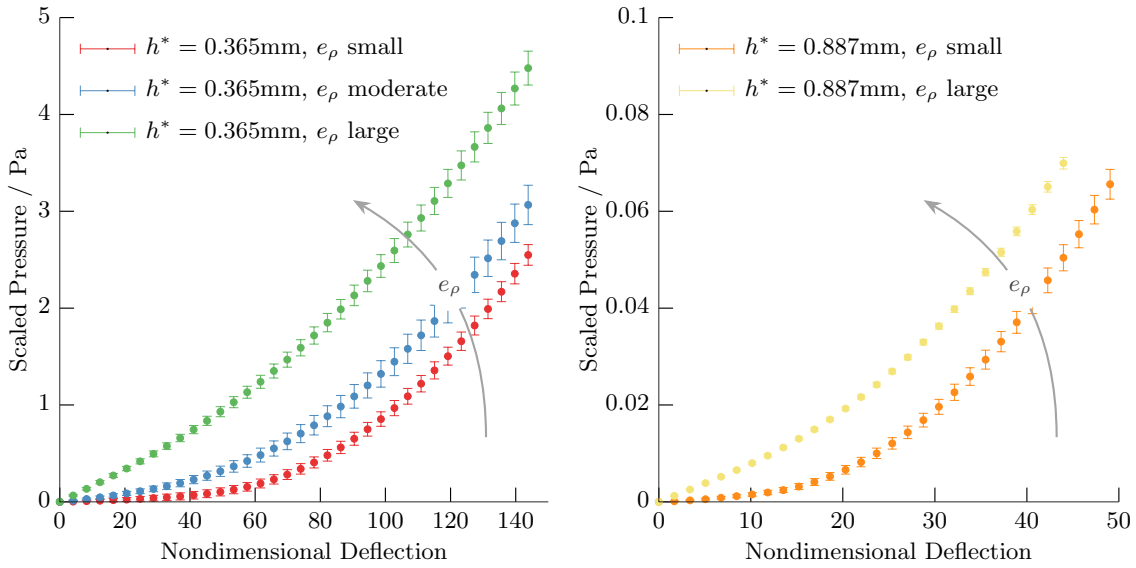

Figure 6.6: Experimental data re-plotted in terms of the nondimensional deflection, and a rescaled dimensional pressure for the thinner sheet (left) and the thicker sheet (right) defined as $\Delta p^*_{Rescaled} = \left(12(1-\nu^2)\right)^{\frac{3}{2}} (R/h^*)^4 \, \Delta p^*/10^{13}$.

As can be seen in equations 6.2.9 and 6.2.10, if the nondimensional displacement $u_\rho(\rho = 1)$, can be neglected, i.e. $e_\rho/h^2 \ll 1$, then this system contains only a single free parameter: the pressure. This results in a h^*-independent pressure-deflection curve that provides a powerful tool for determining Young's modulus. However, the nondimensional applied pre-stretch scales as $u_\rho(\rho = 1) \sim e_\rho \, (R/h^*)^2$. This means that in extremely thin sheets even a minute, but nonzero, applied strain can result in a large pre-stretch parameter entering the equations. This extreme sensitivity to boundary conditions makes it necessary to consider the pressure-deflection-pre-stretch surface, which remains independent of an explicit relative-thickness parameter, h. Thus, there are only two fitting parameters: $u(\rho = 1)$ and E.

We solve equations (6.2.9-6.2.11) using a 1D, finite difference scheme as detailed in appendix G.3. This results in the displacement curves shown in figure 6.7. We also plot the rescaled hoop stress in figure 6.9, where we can see that the sheet will be under tensile hoop so that no wrinkling is expected. Given that that the sheet is expected to remain axisymmetric, we can quantify the size of the deflection using only the centre value, $u_3(\rho = 0)$. We then combine the results and plot them as a series of curves in pressure-deflection space, as shown in figure 6.10.

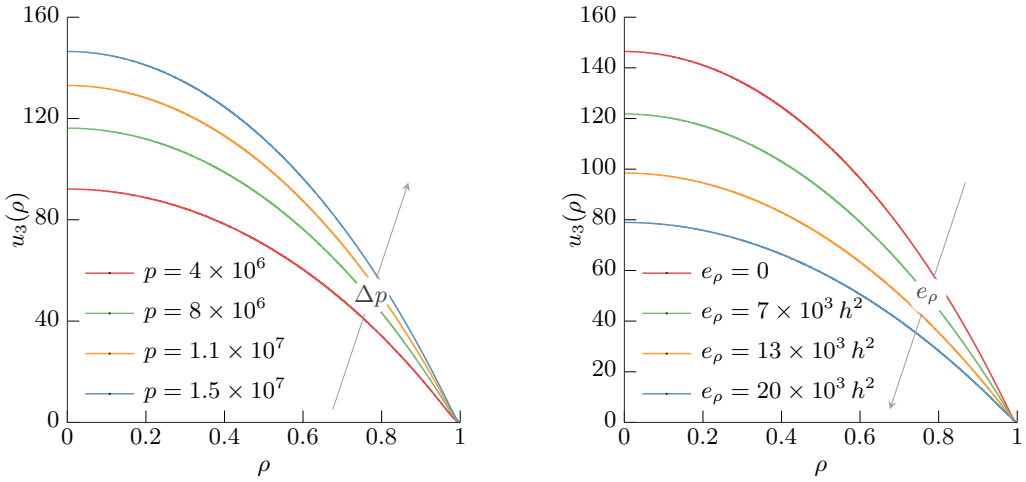

Figure 6.7: Nondimensional deflection over the domain plotted at several values of nondimensional pressure, subject to zero pre-stretch (left) and at several values of pre-stretch (right) with fixed nondimensional pressure of 1.5×10^7.

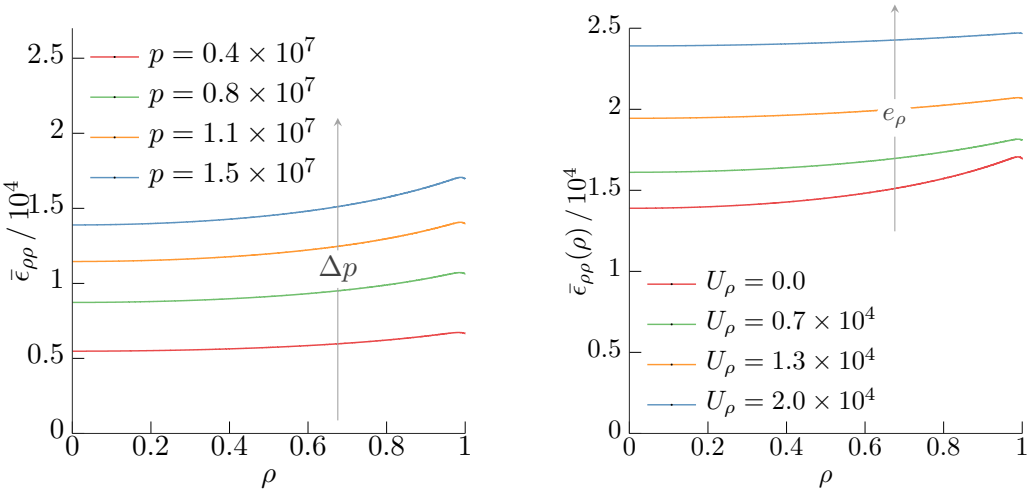

Figure 6.8: Rescaled radial strain over the domain plotted for several values of nondimensional pressure, subject to zero pre-stretch (left) and at several values of pre-stretch, $e_\rho = U_\rho\, h^2/(12(1-\nu^2))$, (right) at a fixed nondimensional pressure of 1.5×10^7.

A special consideration can be made when the imposed pre-stretch dominates[4]: in the tension dominated regime, when pre-stretch is large the bending terms can be neglected. If the pre-stretch is large enough, the stress will be approximately constant and determined purely by the in-plane deformation. The solution to the above equation for equi-biaxial

[4]For the case of dominant bending the pressure will scale as $\Delta p = 64\, u_3(\rho = 0)$. However, this regime was not observed experimentally.

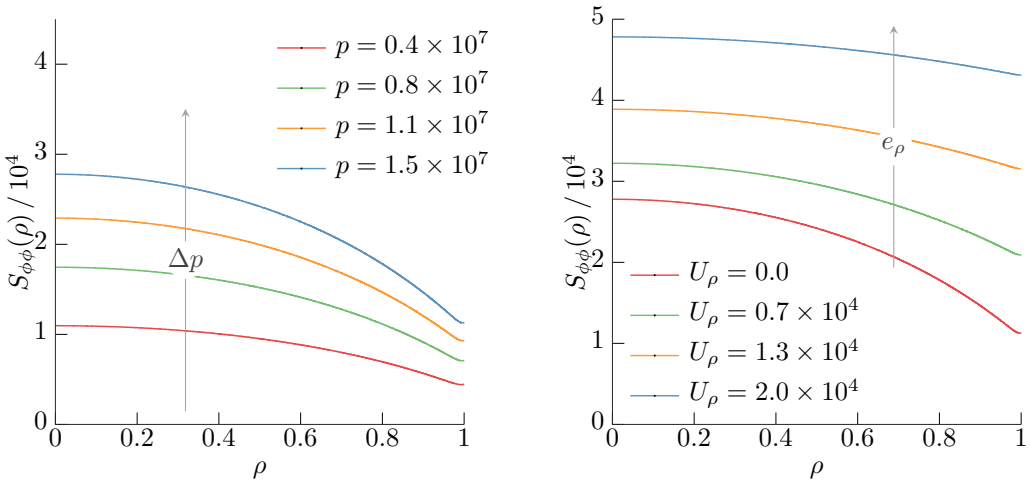

Figure 6.9: Nondimensional hoop stress over the domain plotted for several values of nondimensional pressure, subject to zero pre-stretch (left) and at several values of pre-stretch, $e_\rho = U_\rho\, h^2/(12(1-\nu^2))$, (right) at a fixed nondimensional pressure of 1.5×10^7. As can be seen the hoop stress is always tensile, so no wrinkling is expected.

stress ($S_{\rho\rho} = S_{\phi\phi} = \sigma$) is (see appendix F for details)

$$u_\rho(\rho) = \frac{\Delta p}{4\sigma}(1-\rho^2)\,, \tag{6.2.15}$$

In this case we expect the central deflection to be given by :

$$u_3(\rho = 0) = \frac{\Delta p(1-\nu)}{4U_\rho}\,. \tag{6.2.16}$$

with $U_\rho = 12(1-\nu^2)e_\rho/h^2$. If either pre-stretch or Young's modulus are known, this makes fitting for the other straightforward. However, if both remain unknown it becomes impossible to determine either in this regime, as the two values in the fit will be perfectly correlated. Thus it is necessary in experiments to ensure that the *nonlinear* behaviour is explored, if both pre-stretch and Young's modulus are unknown.

Alternatively, we may assume that the stress is approximately constant but dominated by out-of-plane deformations: $\sigma \sim {U_3}^2$, where U_3 is the typical size of the deflection. For this case, from the out-of-plane force balance, we would expect the pressure to scale instead as $p \sim {U_3}^3$, assuming that bending is negligible. Thus, naively combining these two predictions, one might expect that the pressure-deflection curve behaves as

$$\Delta p \sim a\, U_{\rho 0}\, U_3 + b\, {U_3}^3\,, \tag{6.2.17}$$

with prefactors a and b. In fact, a more detailed approximation of the membrane solution

(see appendix F) gives the following prediction for the pressure-deflection relation

$$\Delta p \approx \frac{1}{1-\nu}\left(4U_\rho U_3 + {U_3}^3(3-\nu)\right) , \tag{6.2.18}$$

with $U_3 = u_3(\rho = 0)$. From this we see that for large U_3, the initially linear behaviour gives way to a cubic scaling: it is this regime that is important for fitting to Young's modulus. We show this result, along with the linear, pre-stretch dominated solution, in figure 6.10.

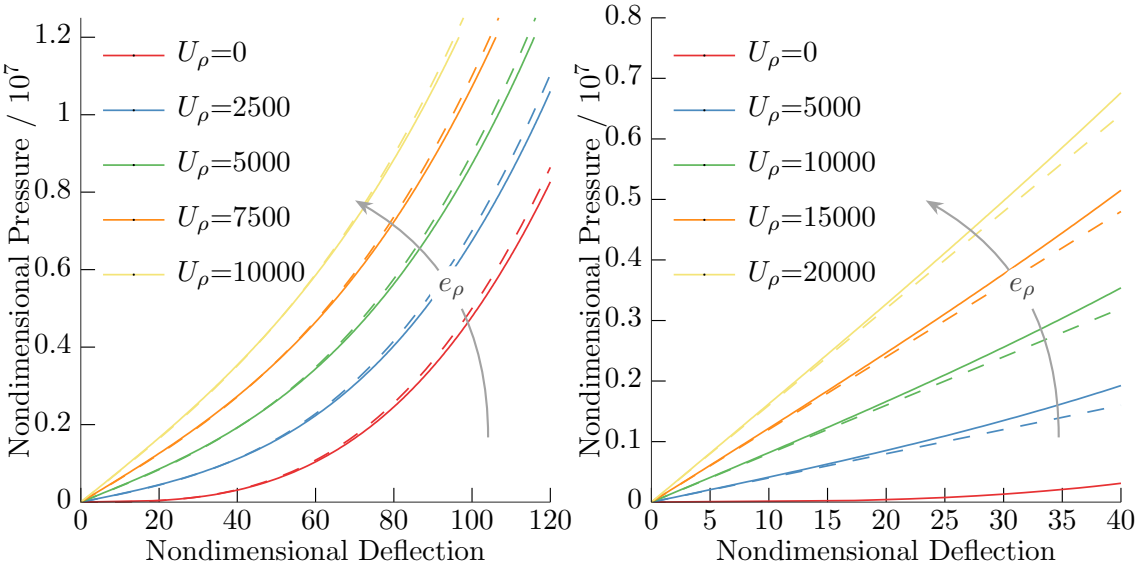

Figure 6.10: Nondimensional pressure versus centre-deflection plotted for various nondimensional pre-stretch, $e_\rho = U_\rho\, h^2/(12(1-\nu^2))$, (left), with the approximate solution (equation (6.2.18)) shown as dashed lines. In the right hand figure, we show the same solid curves at low values of deflection where the imposed stretch dominates. For comparison in this latter plot we show the linear, pre-stretch dominated solution (equation (6.2.16)) as dashed lines.

Estimates of Neglected Effects

To provide insight into the importance of material nonlinearity, we consider a simple scaling argument to predict the size of the maximum radial strain. By equation (6.2.4), the typical size of the strain will be $\epsilon_{\rho\rho} \sim e_\rho + (u_3^*/R)^2$. We expect the second term to dominate, as all pressure-deflection curves exhibit nonlinear dependence over large portions of the range. Thus, for the strain[5] to remain below $\epsilon_{\rho\rho} \lesssim 0.05$, which by figures 6.3 and 6.4 is within the linear regime, we have $u_3^*/R \lesssim \sqrt{\epsilon_{\rho\rho}} = 0.22$. In all experiments $u_3^*(\rho^* = 0)/R^* < 0.22$, therefore we expect that the linear constitutive hypothesis will hold over the experimental

[5]The Green-Lagrange strain for simple tension is $\epsilon_{11} = e_U + e_U^2/2$, which for $e_U^2 \ll 1$ becomes $\epsilon_{11} \approx e_U$.

range. Comparing the radial-strain as a function of both deflection and pre-stretch in figure 6.8 we see that for the typical pre-stretch values considered, the value of pre-stretch only alters the magnitude of the strains up to an order 1 factor, so even with relatively large stretch we expect that the above argument will hold.

Additionally, given that in experiments deflections are relatively small (less than 25% of the radius), we expect that the moderate-rotation assumption of the Föppl-von Kármán model will be satisfied for the majority of the experimental range. To assess this, in the next section we investigate the regimes in which the axisymmetric Föppl-von Kármán model, as we have described it, does not apply. We instead consider the Koiter-Steigmann model, as outlined in section 3.4, which has a geometrically accurate bending term and can include nonlinear material behaviour. We also consider non-axisymmetric applied pre-stretch and determine what effect this has on the resulting pressure-deflection curves. We expect that this will corroborate with the assumption that the axisymmetric Föppl-von Kármán model is appropriate for the fitting of the performed experiments, based on the above arguments.

6.3 Exploring Additional Nonlinear Effects in Plate Models During Inflation

To begin, we consider the effect of the additional geometrical nonlinearity introduced by accurate treatment of the (varying) unit normal. As discussed in sections 3.5.6 and 3.6, explicit thickness dependence is introduced into the rescaled Föppl-von Kármán model when the geometry of sheet is treated accurately. In practise, this means that we no longer assume that rotations are small, such that $\hat{\boldsymbol{N}} \approx \boldsymbol{k}$ during inflation. We therefore consider the case with no pre-stretch, $u_\rho(\rho = 1, \phi) = 0$, and examine what effect the additional geometrical nonlinearity introduced by the Koiter-Steigmann model has on the pressure-deflection curve.

As demonstrated in section 6.2, the Föppl-von Kármán model can be nondimensionalized such that it is independent of the explicit thickness parameter, $h = h^*/R$. However, for large enough deformations this 'thickness independent' behaviour is expected to break down. Thus, by comparing the predictions of the Koiter-Steigmann model, using the finite element simulation developed in chapter 5.1, to the Föppl-von Kármán model at varying nondimensional thickness, h, we can assess when the Föppl-von Kármán ceases to become an appropriate model. We investigate this in the next section.

6.3.1 Thickness Variation

The Föppl-von Kármán model predicts a strain-hardening pressure-deflection curve that monotonically increases: it is expected that at large strains and large deflections the Föppl-von Kármán model will break down due to the assumptions of moderate rotations and small strains. We first compare the predictions of the Föppl-von Kármán model to the Koiter-Steigmann model for a range of relative thickness, first using a linear constitutive assumption. For example in figure 6.11, for thickness parameter, $h = h^*/R = 0.008$, only a 5% difference in applied pressure is seen, as compared to Föppl-von Kármán, by deflection $u_3(\rho = 0) \gtrsim 122$. This difference only reaches 10% by $u_3(\rho = 0) \gtrsim 175$, for relative thickness $h = 0.008$.

At the greater relative thickness value of $h = 0.016$ a much larger disparity can be seen, which reaches 18%, as compared to Föppl-von Kármán, by relative deflection $u_3 \gtrsim 120$. The Koiter-Steigmann model consistently predicts a relatively softer response from the material as compared to the Föppl-von Kármán model. In the experiment we considered relative thickness of 0.0045625 and 0.0110875, which indicates that at large enough deflections these effects become relevant: however in the range of the experiments, for which $u_3 \lesssim 150$ and $u_3 \lesssim 50$ for thinner and thicker sheets, respectively) these effects are demonstrably small if the linear constitutive law is appropriate.

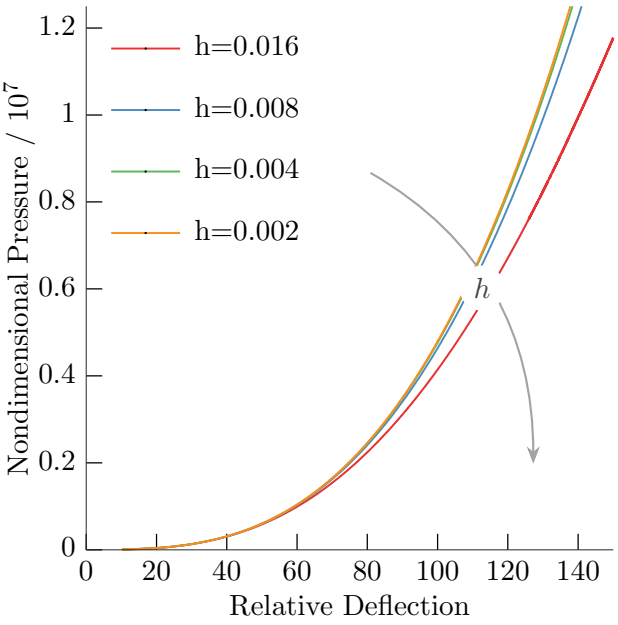

Figure 6.11: Nondimensional pressure, Δp, plotted versus maximum nondimensional deflection, $u_3(\rho = 0)$, for various relative thickness values, h, as predicted by the Koiter-Steigmann model. Here we have assumed a linear (Saint-Venant Kirchhoff) constitutive relation.

The difference between the two models is exacerbated when nonlinear constitutive relations are considered, however, as shown in figure 6.12. We study the Mooney-Rivlin material model (see section 2.2.5) , with nondimensional material parameter C_2 and focus on the case of the minimum value of $C_2 = 0$ (neo-Hookean) and the maximum value of $C_2 = 0.166$, by comparing the results for different thickness (see figure 6.12). It can be seen that the difference between the Föppl-von Kármán model and Koiter-Steigmann prediction is most pronounced for the neo-Hookean model, but is comparable for both values of C_2.

At relative thickness of $h = 0.004$, only a 5% difference in the applied pressure, as compared to the Föppl-von Kármán prediction, is expected by $u_3(\rho = 0) \gtrsim 102$, which grows to 10% by $u_3(\rho = 0) \gtrsim 150$. For the maximum C_2 value of $C_2 = 0.166$, the effect is lessened, reaching only a 5% difference by $u_3(\rho = 0) \gtrsim 108$. This effect is minor, in thinner sheets, in comparison to the difference between linear and nonlinear constitutive relations.

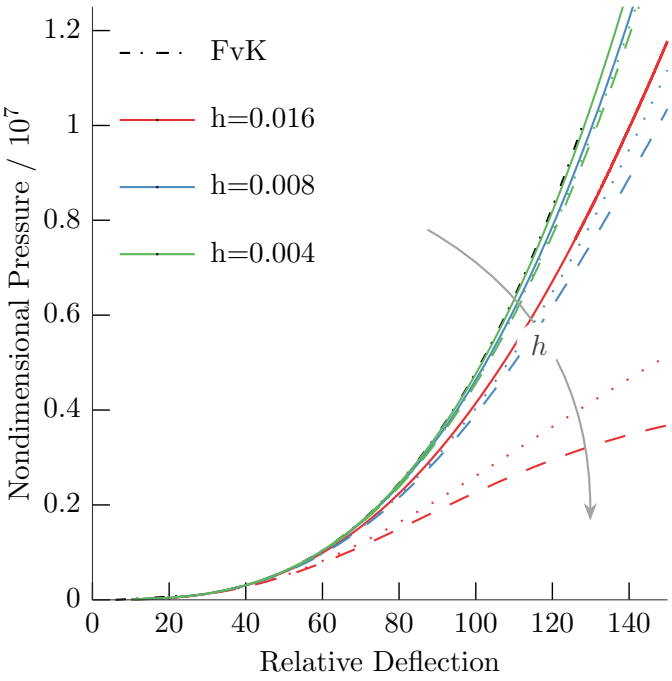

Figure 6.12: Nondimensional pressure, Δp, plotted versus maximum nondimensional deflection, $u_3(\rho = 0)$, for various relative thickness values, h, as predicted by the Koiter-Steigmann model. We show curves for a neo-Hookean material ($C_2 = 0$, dashed), a Mooney-Rivlin material ($C_2 = 0.166$) and a linear material (solid). For comparison the curve for the Föppl-von Kármán plate model is also shown (dash-dot).

For thicker sheets, the effects are far more pronounced: considering the relative thickness

$h = 0.008$, we find a 10% difference by relative deflection $u_3(\rho = 0) \gtrsim 80$ and $u_3(\rho = 0) \gtrsim 74$ for $C_2 = 0.166$ and $C_2 = 0$, respectively. By $u_3(\rho = 0) \gtrsim 150$ the differences are 36% and 11% respectively: clearly, for large deflections of thicker sheets both constitutive nonlinearity, and the additional geometrically nonlinear effects become important.

Thus, for a nonlinear constitutive model, explicit thickness dependence becomes significant even at small values of relative thickness and is pertinent even for thickness of $h = 0.004$. It is clear that thickness dependence is important when considering large deformations of hyperelastic sheets, as rubber-like constitutive models predict a significant softening effect. However, for thinner sheets ($h \lesssim 0.004$) or at smaller nondimensional pressure values these effects are less significant and the Föppl-von Kármán model is sufficient, for the case of negligible pre-stretch.

Interestingly, at high values of deflection, this system seems significantly *more* sensitive to the choice of material parameter, C_2, than the uniaxial tension experiment, at least for thicker sheets. Assuming that both pre-stretch and thickness are known this could therefore be a useful experiment for measuring material properties. We proceed by considering in detail the effects of the material parameter, at two values of relative thickness of $h = 0.0045625$ and $h = 0.0110875$, which correspond to our experimental parameters.

6.3.2 Material Model Parameter Variation

Given that the effect of using a nonlinear material model is significant at higher thickness values, it is useful to assess how important the Mooney-Rivlin parameter, C_2, is in determining the overall shape. To this end, we compare the pressure-deflection curves for a range of C_2 parameters at two pertinent thickness values: $h = 0.0045625$ and $h = 0.0110875$, which correspond to relative sheet thicknesses that inflation experiments have been performed for (see section 6.1). Once again, in this section we only consider the case of zero pre-stretch $u_\rho(\rho = 1, \phi) = 0$.

As can be seen in figure 6.13, in which the C_2 parameter is varied between the physical limits of 0 and 1/6 for the thinner sheet, the value of the C_2 parameter does not have a large effect on the pressure-deflection curve at this thickness: even at a nondimensional deflection of $u_3(\rho = 0) \approx 175$ the difference in applied pressure is only 5%. However, for any value of C_2 the curves differ to a greater extent from the linear constitutive model, and also with Föppl-von Kármán, with differences of $\gtrsim 10\%$ and $\gtrsim 9\%$ respectively for $u_3(\rho = 0) = 150$.

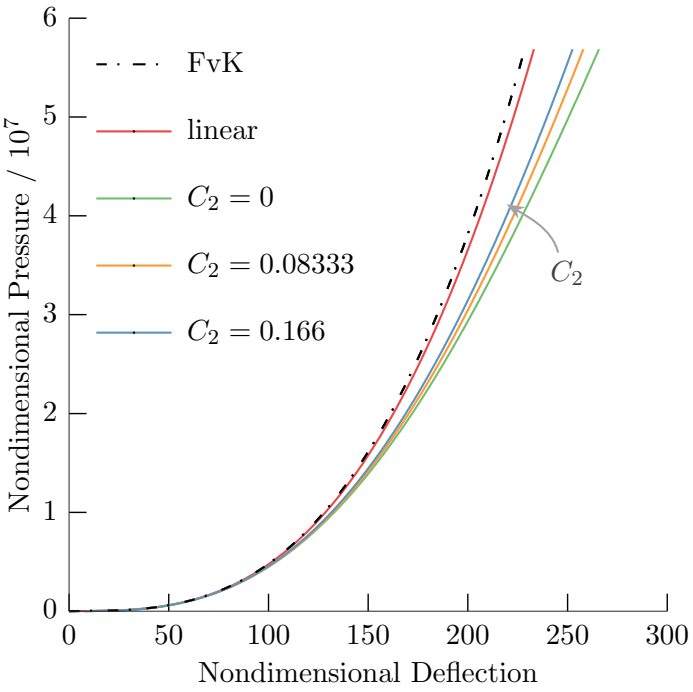

Figure 6.13: Nondimensional pressure, Δp, plotted versus maximum nondimensional deflection, $u_3(\rho = 0)$, for relative thickness value $h = 0.0045625$, plotted for a series of C_2 parameters between the physical limits. Again, the Föppl-von Kármán model is shown (dashed) for comparison, as well as the linear constitutive model prediction.

For relative thickness 0.0045625, using an incorrect value of C_2 for the constitutive model would result in errors smaller than 4% over the experimental range ($u_3(\rho = 0) \leq 150$) Using the Föppl-von Kármán model for $u_3(\rho = 0) \sim 150$ could lead to up to 13% errors, at which point the error in the model would start to overtake the experimental uncertainty. The linear constitutive model is thus only appropriate at smaller deflections, as is to be expected.

The picture is a little more complicated for thicker sheets (figure 6.14): at this thickness we see a significant softening of the deflection curve, which happens at lower deflections for lower values of C_2. Clearly, at greater nondimensional deflections, $u_3(\rho = 0)$, the value of C_2 becomes important. Restricting to the case when the nondimensional deflection, $u_3(\rho = 0) \lesssim 75$, we can see that once again, though a nonlinear model is appropriate, the value of the C_2 parameter has only a small effect ($\lesssim 5\%$) and it is thus appropriate to use the neo-Hookean model which introduces no new constitutive parameters. At lower values still, $u_3(\rho = 0) \lesssim 50$, the Föppl-von Kármán model gives relatively good agreement with the Koiter-Steigmann model, to 7.5%, indicating that for the experimental range the Föppl-von Kármán is appropriate at small strain.

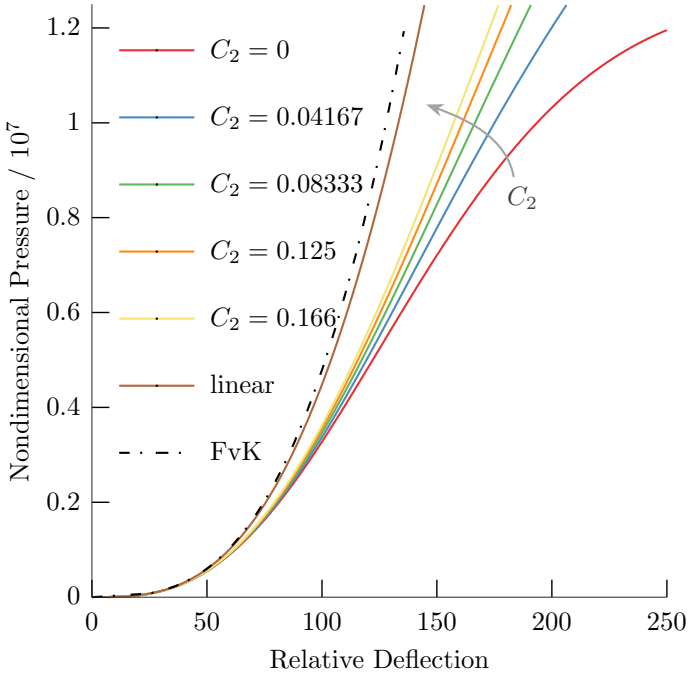

Figure 6.14: Nondimensional pressure, Δp, plotted versus maximum nondimensional deflection, $u_3(\rho = 0)$, for relative thickness value $h = 0.0010875$, plotted for a series of C_2 parameters between the physical limits. Again, the Föppl-von Kármán model is shown (dashed) for comparison, as well as the linear constitutive model prediction.

6.3.3 Pre-stretch Variation

Next we consider the effect of non-uniform applied pre-stretch on the ensuing pressure-deflection curve. By investigating several different distributions of pre-stretch along the outer edge, we can assess how important the form of the pre-stretch is to the measured curve. We display the results in figure 6.15 for a range of pre-stretch, $e(\phi)$, from 0-1% average extension[6], $\langle e_\rho \rangle$, for radial pre-stretch, uniaxial pre-stretch and a pre-stretch consisting of the superposition of several Fourier modes, in all cases using the neo-Hookean constitutive relation. As can be seen by comparison of the three plots, the distribution of pre-stretch is relatively unimportant: only the magnitude is important.

The out-of-plane deflection of the sheet is virtually unaffected by the distribution of pre-stretch, as can be seen in figure 6.16. Although this distribution imposes non-axisymmetric in-plane deformations, the shape of the deflection is virtually indistinguishable by eye. Thus, the distribution of the pre-stretch is not important: only its magnitude.

[6]Here we define the average radial extension to be $\langle e_\rho \rangle = 1/(2\pi) \int_{-\pi}^{\pi} u_\rho^*(\rho = 1, \phi)/R \, d\phi$.

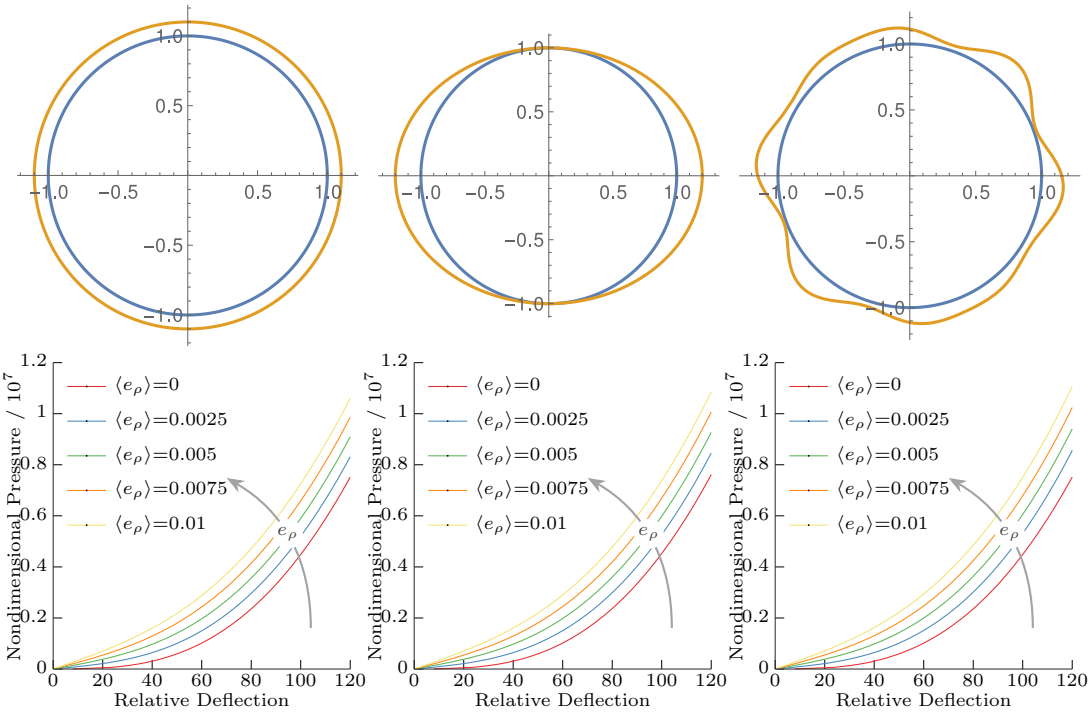

Figure 6.15: Comparison of pressure-deflection curves at varying pre-stretch for radial (left), uniaxial (centre) and modal (right) stretches for a sheet of relative thickness $h = 0.0045625$ using the neo-Hookean model. Shown above are corresponding displacements for $e_\rho = 0.1\%$.

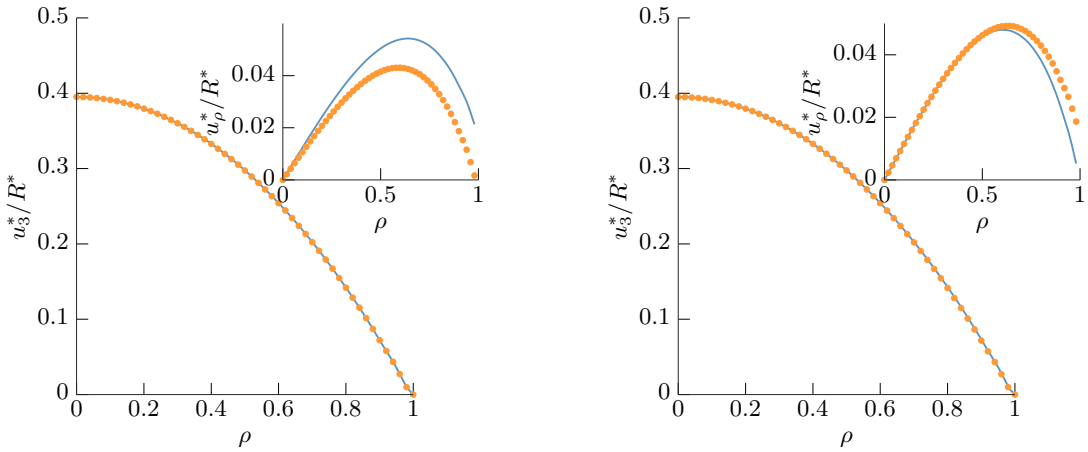

(a) Uniaxial displacement at $\phi = 0$ (blue line) and $\phi = 90^\circ$ (orange points)

(b) Modal displacement at $\phi = 45^\circ$ (orange points) and $\phi = 204.5^\circ$ (blue line)

Figure 6.16: The deflection and radial displacements (inset) for uniaxial and modal imposed pre-stretch of $\langle e_\rho \rangle = 0.1$ with nondimensional forcing $\Delta p = 5.45 \times 10^7$, each shown at two distinct values of the azimuthal coordinate, ϕ.

Having demonstrated that there is little effect from non-axisymmetric pre-stretch, we now compare the predictions of the Föppl-von Kármán model to that of the Koiter Steigmann model at various values of radial pre-stretch, e_ρ. This is shown in figures 6.17 and 6.18 for the smaller and larger thickness values respectively.

We observe that for the thinner sheet even a pre-stretch smaller than 0.002% has a significant effect on the pressure-deflection curve, which is apparent from zero pressure. This is to be expected, as the modified, pre-stretch boundary condition enters even in the linearised limit. We see a disparity between the Föppl-von Kármán model and the Koiter-Steigmann model for larger values of the pressure which is exacerbated by the pre-stretch: at zero pre-stretch the relative difference between the two models reaches 5% by nondimensional deflection $u_\rho(\rho = 1) = 105$. For the highest value of pre-stretch (0.02) the difference is 15% by this value of nondimensional deflection. Thus, one might expect that using the Föppl-von Kármán model to fit to the experimental data in this case would only be appropriate up to nondimensional deflections of $u_\rho(\rho = 1) \lesssim 105$, especially for large pre-stretch. As the experimental range exceeds this, when fitting to the Föppl-von Kármán model we will instead truncate the range, excluding points where we expect the error to exceed 15% for the largest values of pre-stretch, as this will begin to exceed the experimental error.

For the thicker sheet (figure 6.18) the pre-stretch parameter is similarly important in determining the pressure-deflection curve as at lower thickness. However, the discrepancy between the two models now occurs at lower values of the nondimensional deflection, $u_\rho(\rho = 1)$. For this case the relative difference between the two models at a pre-stretch of $e_\rho = 0.02$ reaches 15% by relative deflection of $u_3(\rho = 0) \sim 50$. For zero pre-stretch a relative difference of 7.5% is reached by this value of nondimensional deflection. Thus, for fitting over the whole range of pre-stretch, it is appropriate to use the predictions of Föppl-von Kármán up to nondimensional deflection up to $u_3(\rho = 0) \sim 50$, for the thicker sheet. This includes the complete range of experimental data taken for the thicker sheet, as seen in section 6.1.

From these graphs it is clear to see that once the relative deflection gets sufficiently large, $u_3(\rho = 0) \sim 105$ and $u_3(\rho = 0) \sim 50$ for the thin and thick sheet, respectively, the assumptions of the Föppl-von Kármán model break down and both geometrical and constitutive nonlinearity begin to play an important role. Up to these points, use of the Föppl-von Kármán model is justified. However, for data that exceeds these deflection values, we instead fit to the pressure-deflection curve the Koiter-Steigmann model.

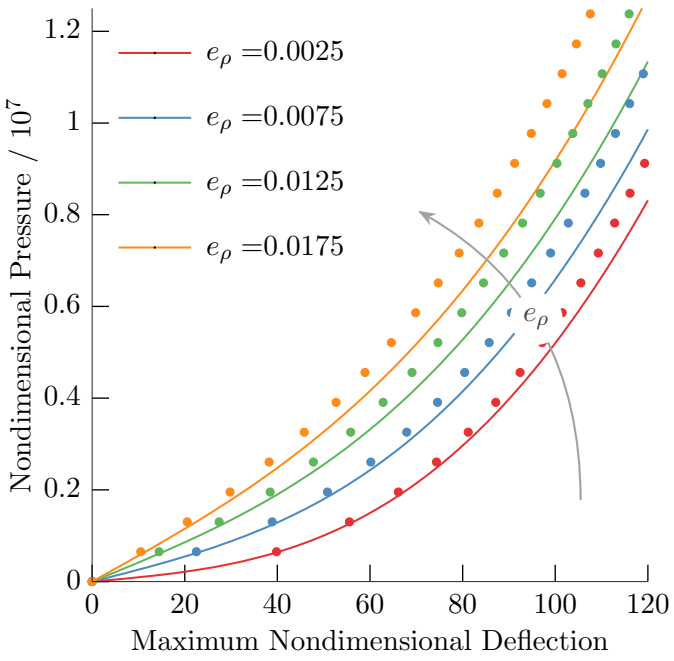

Figure 6.17: Comparison of pressure-deflection curves between Föppl-von Kármán (dotted) and Koiter-Steigmann for varying radial pre-stretch, e_ρ. This is computed for a neo-Hookean sheet of thickness $h = 0.0045625$.

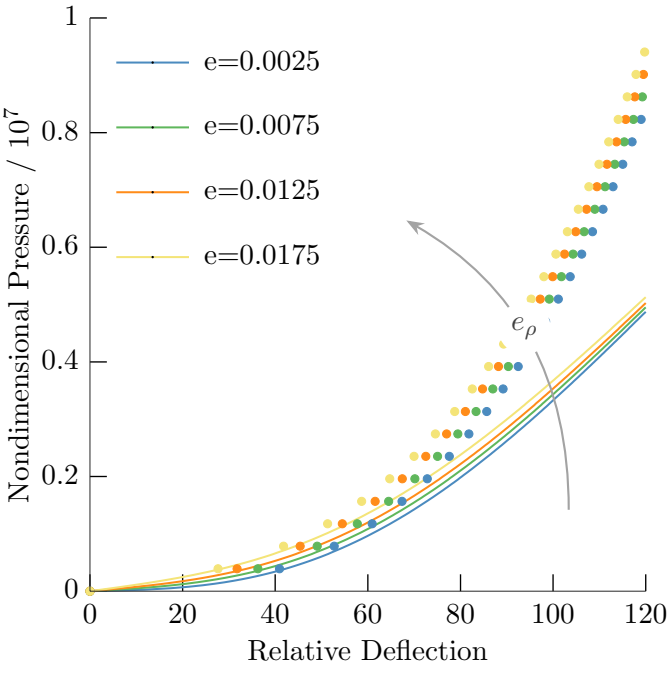

Figure 6.18: Comparison of pressure-deflection curves between Föppl-von Kármán (dotted) and Koiter-Steigmann for varying radial pre-stretch. This is computed for a sheet of thickness $h = 0.0110875$ and using the neo-Hookean material model.

We now proceed to fit results from the Föppl-von Kármán model to experimental data in the regimes described and, where necessary, compare them to Koiter -Steigmann fits over the whole range.

6.4 Fitting Procedure for Inflation Experiments

Using everything that we have learned, we can predict that a Föppl-von Kármán fit is appropriate for nondimensional deflection up to approximately $u_3(\rho = 0) \sim 105$ for the thinner sheet and up to about $u_3(\rho = 0) \sim 50$ for the thicker sheet: within this range we expect the largest error introduced by the model to be $\sim 15\%$. For smaller values of pre-stretch, the error introduced by the model will be smaller than this, never exceeding 7.5%. In these regimes it is not necessary to consider any of the parameters other than the radial pre-stretch and Young's modulus. A two parameter fit for pre-stretch and Young's modulus is therefore appropriate.

It is tempting to truncate the data further to further reduce errors introduced by the Föppl-von Kármán prediction: however, for this system further truncation means that fitting will be performed over the pre-stretch dominated regime which, as discussed in section 6.2, results in highly correlated parameters in the two parameter fit. Thus, limiting the fitting region to the regime in which the Föppl-von Kármán model performs better may paradoxically result in worse results.

We perform the fit by taking axisymmetric Föppl-von Kármán data for a range of values of pre-stretch and constructing an piecewise linear mesh over which the solution can be interpolated using rectangular elements, as shown in figure 6.19. A two-parameter, nonlinear least squares fit can then be performed for the data, to deduce values for Young's modulus, E, and pre-stretch, e_ρ. The values can then be compared to the results obtained for the strip pull experiment described in section 6.1.

A similar strategy was used for the thinner sheets using the Koiter-Steigmann predictions, with a neo-Hookean model: this time, however, the data had to be acquired for a particular value of thickness, as the curves exhibit thickness dependence. This was to allow a comparative fit using the entire range of data for the thinner sheet in which a large proportion (18%) of the experimental data points lie outside the range of the Föppl-von Kármán model. For the thicker sheet, all of the data lay within the established bounds of

the Föppl-von Kármán model.

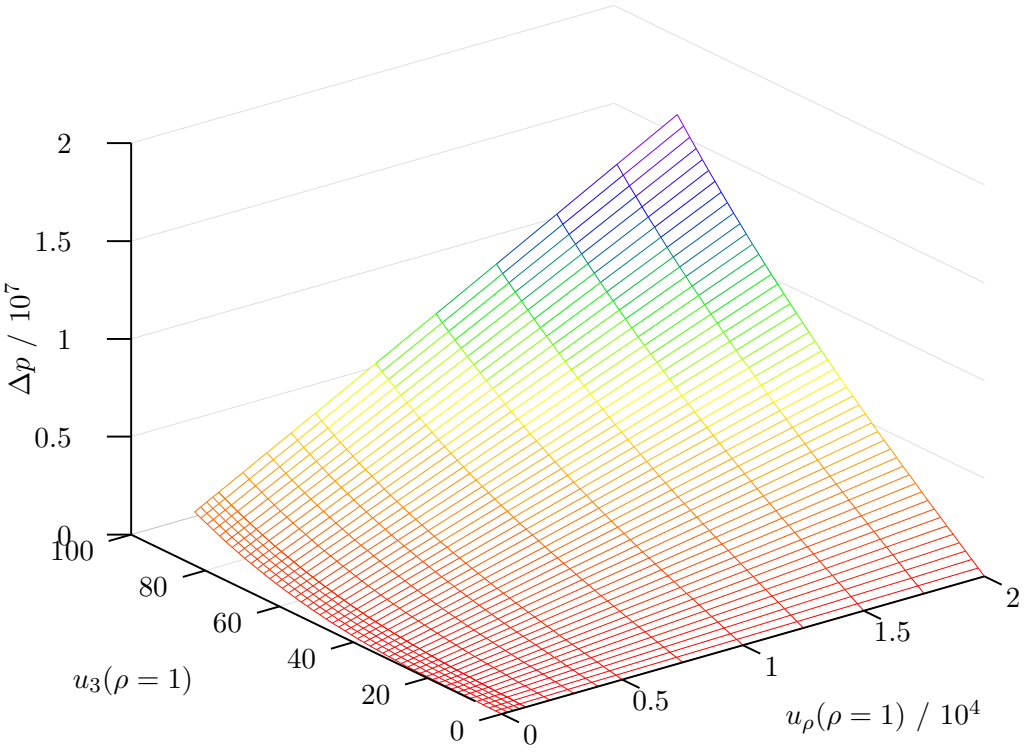

Figure 6.19: The nondimensional pressure-deflection-pre-stretch surface. Here pre-stretch is plotted in terms of the h scaled quantity that enters the nondimensional boundary-value problem: $u_\rho(\rho = 1) = e_\rho(h/L)^2/(12(1-\nu^2))$.

An obvious downside to this using the Koiter-Steigmann model is that it introduces an explicit thickness parameter, so new data needs to be taken for each experimental value of thickness considered.

We recall that for the sheet of relative thickness $h = 0.0045625$, three experiments were performed: one in which pre-stretch was kept to a minimum, one in which a moderate (unknown) pre-stretch was imposed deliberately and one with a large (unknown) imposed pre-stretch.

We display the weighted least-squares fits to the data in figures 6.20, 6.21 and 6.22, respectively, and tabulate the fitted values of Young's modulus and pre-stretch in table 6.1, for the readers convenience. All fits were weighted by the relative error of each data point.

h^* (mm)	E (MPa)	e_ρ
	Föppl-von Kármán thinner	
0.365(10)	1.67(19)	0.0007(12)
0.365(10)	2.09(34)	0.0054(25)
0.365(10)	1.76(30)	0.027(6)
	Koiter-Steigmann thinner	
0.365(10)	1.95(8)	0.0003(9)
0.365(10)	2.19(15)	0.0057(18)
0.365(10)	2.24(13)	0.028(4)
	Föppl-von Kármán thicker	
0.887(10)	2.84(15)	0.0014(7)
0.887(10)	2.36(9)	0.013(9)

Table 6.1: A summary of the fitted values from the various inflation experiments. The uncertainty quoted on the fitted values (columns two and three) are the standard deviation, σ, of the weighted nonlinear least-squares fit.

Fitting to the Föppl-von Kármán predictions, we find the weighted mean of the measured values to be 1.76(14)MPa, where the bracketed value is the estimated error on the least-squares fit of 0.14MPa, which is within 2σ of the value of 2.041(4)MPa determined by the uniaxial tension experiment. The fitted values exhibited a large variability between successive experiments, which was well described by estimated errors on the fit: this provides further motivation for measuring Young's modulus at various values of pre-stretch, and then averaging the results. The estimated values of pre-stretch concord with the predicted order (i.e small, moderate and large), though the estimated errors on the pre-stretch are large especially for the smaller values of pre-stretch (see the last column of table 6.1). The graphs used to generate this weighted mean are shown in figures 6.20-6.22.

Fitting to the whole range, using the Koiter-Steigmann model we find the weighted mean of the values for the thinner sheet to be 2.06(6)MPa, which is in excellent agreement with the value of 2.041(4)MPa measured in the uniaxial strip pull experiment. It also agrees with the Föppl-von Kármán fit, but has a smaller associated error due to the additional data points used in each fit. All of the pre-stretch predictions agree, within the quoted errors, with the

values obtained Föppl-von Kármán fits as well, which provides support of the robustness of this fitting procedure.

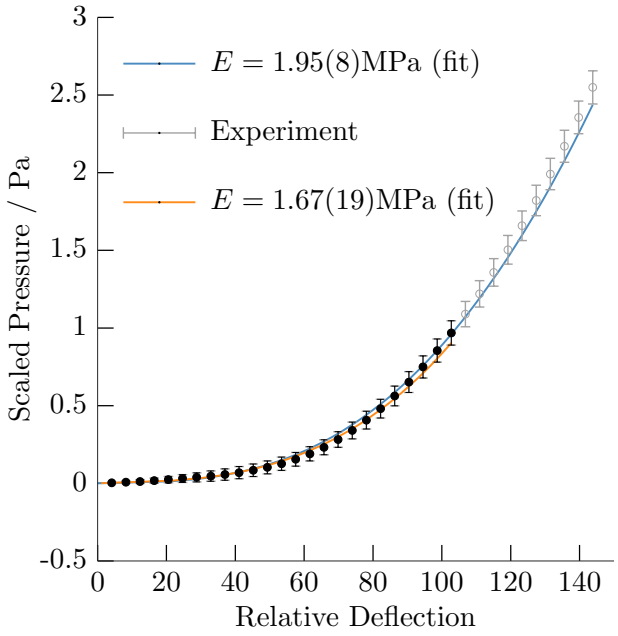

Figure 6.20: Experimental pressure versus deflection data, with fitted curves for the thin sheet ($h = 0.0045625$), small pre-stretch dataset. The Föppl-von Kármán model (orange) is fitted only to solid data points, whereas the fit to the Koiter-Steigmann model (blue) uses the full range of (hollow) data points. The fitted pre-stretches are $e_\rho = 0.0007(12)$ and $e_\rho = 0.0003(9)$ for Föppl-von Kármán and Koiter-Steigmann respectively, with corresponding reduced χ^2 values of 0.13 and 0.30.

Similar measurements were made at small and large pre-stretch for the thicker latex sheet. Least-squares fitting was performed and the results are displayed in figures 6.23 and 6.24 for small and large pre-stretch respectively. For the thicker sheets, all data was within the established bounds for the Föppl-von Kármán model, as it was not necessary to fit using the Koiter-Steigmann model. Once again, the fitted values of Young's modulus and pre-stretch are summarized in table 6.1. We find the weighted sum of the Young's modulus to be 2.49(8)MPa, which is in good agreement with the measured value from the strip-pull of 2.57(1)MPa. However, we find that the two values of Young's modulus for the thick sheet, 2.84(15)MPa and 2.36(9), are not in good agreement with one another, implying that the errors on the fit do not describe the variability between experiments. This could instead be representative of the error introduced by using the Föppl-von Kármán model, which could account for up to 15% error, corresponding to ~ 0.4MPa.

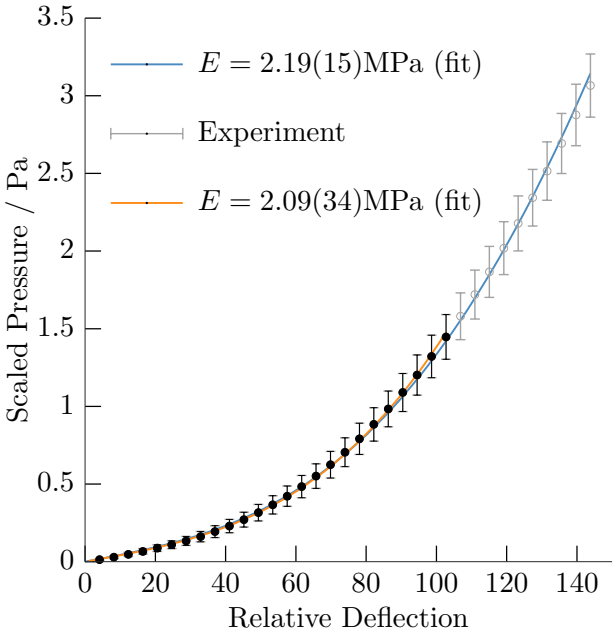

Figure 6.21: Experimental pressure versus deflection data, with fitted curves for the thin sheet ($h = 0.0045625$), moderate pre-stretch dataset. The Föppl-von Kármán model (orange) is fitted only to solid data points, whereas the fit to the Koiter-Steigmann model (blue) uses the full range of (hollow) data points. The fitted pre-stretches are $e_\rho = 0.0054(25)$ and $e_\rho = 0.0057(19)$ for Föppl-von Kármán and Koiter-Steigmann respectively, with corresponding reduced χ^2 values of 0.06 and 0.10.

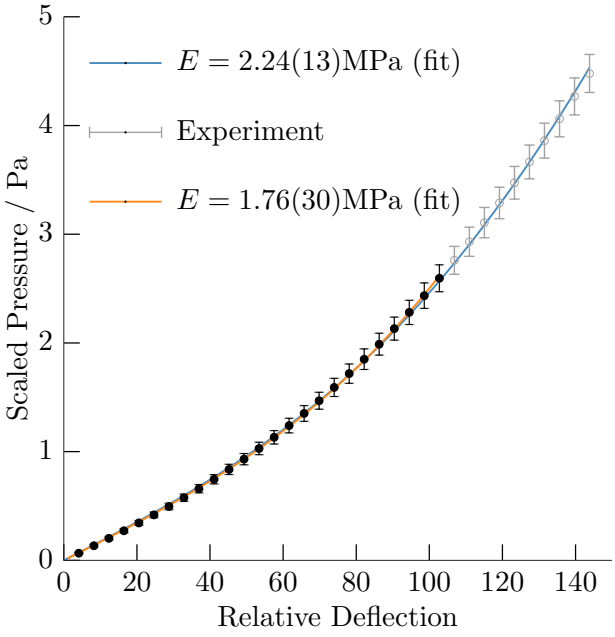

Figure 6.22: Experimental pressure versus deflection data, with fitted curves for the thin sheet ($h = 0.0045625$), large pre-stretch dataset. The Föppl-von Kármán model (orange) is fitted only to solid data points, whereas the fit to the Koiter-Steigmann model (blue) uses the full range of (hollow) data points. The fitted pre-stretches are $e_\rho = 0.027(6)$ and $e_\rho = 0.028(4)$ for Föppl-von Kármán and Koiter-Steigmann respectively, with corresponding reduced χ^2 values for the fits of 0.07 and 0.17.

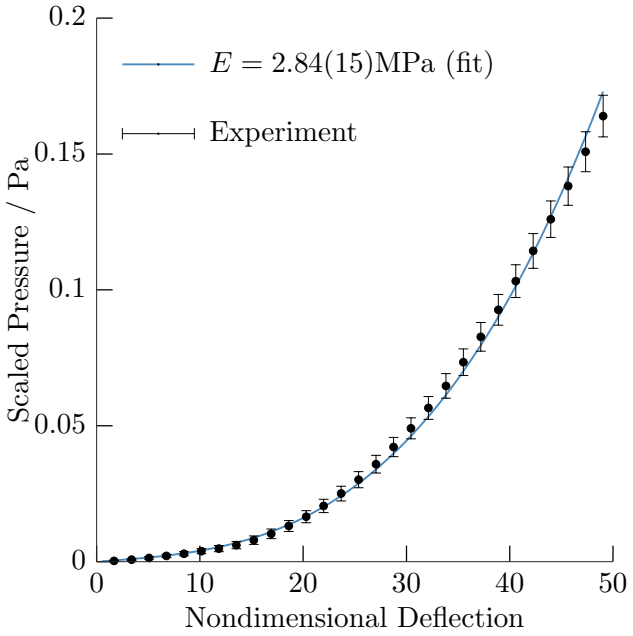

Figure 6.23: Experimental pressure versus deflection data with fitted curves for a sheet of relative thickness $h = 0.011088$ undergoing a small pre-stretch. The data is fitted to the Föppl-von Kármán prediction which yields an estimated pre-stretch value of $e_\rho = 0.0014(8)$. The χ^2 value for the fit is 0.33

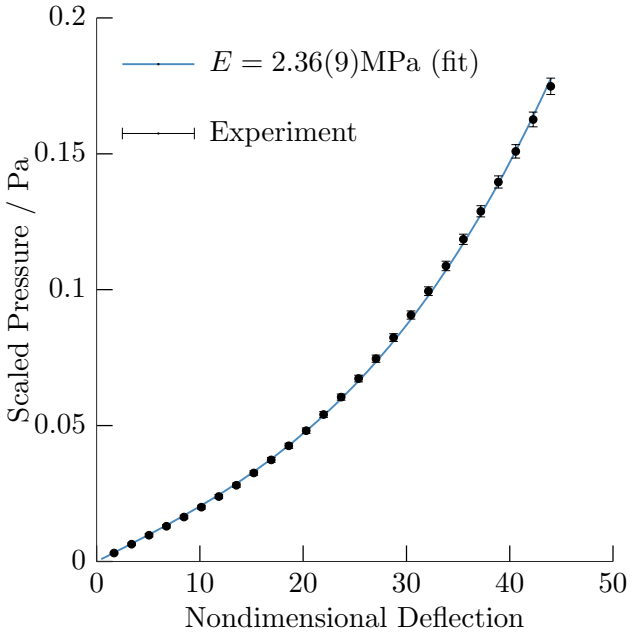

Figure 6.24: Experimental pressure versus deflection data with fitted curves for a sheet of relative thickness $h = 0.011088$ undergoing a large pre-stretch. The data is fitted to the Föppl-von Kármán prediction which yields an estimated pre-stretch value of $e_\rho = 0.0133(9)$. The χ^2 value for the fit is 0.50.

Another possible explanation for this variability is large scale heterogeneity in the thickness of the sheets, created by the manufacture process. This would likely result in a similar variability in the uniaxial tension experiment, however, as in membrane-dominated inflation, energy is stored mainly in stretching modes, just as in the strip-pull experiment. Alternatively it could be that during the experimental procedure damage is occurring in the process, which degrades the sheet when stretched. This would manifest in very different strain curves between re-runs, as the sheet degrades upon the first inflation.

Finally, another possible explanation could lie in the nature of the two-material parameter fit performed for the parameters. As the shape of the curve does not vary much between differing values of pre-stretch, this could result in shallow and/or multiple minima in the resulting fitting which could confound the fitting procedure. This is evident in the large errors on the strain parameters, which are strongly correlated with the error on Young's modulus. This observation further supports the procedure of acquiring data at several pre-stretch values and combining the results, which will reduce the errors on the final measurement by averaging any errors incurred by the degeneracy in strain parameter: weighting by error will additionally penalize fitted values in regimes in which the minima is broader, with increased associated errors on the fitted values.

One extension that could be considered would be to leave the thickness a priori unknown in the fitting procedure: this would be made easier using the Föppl-von Kármán model, whereby only a rescaling of the curves is necessary to obtain the fit. However, based on the apparent difficulties in finding minima with a two-parameter fit, it is unlikely that a global minima for thickness, pre-stretch and Young's modulus could be obtained, so reasonably tight bounds on the estimates would need to be established in order to use this method. Additionally, to gain a reliable fit, the regime over which bending gives way to membrane-like response would have to be considered, otherwise the thickness parameter will be strongly correlated with the pressure, in the same manner as observed with the pre-stretch in the strongly stretched (linear) regime: thus, a three-parameter fit is unsuitable for the experimental data of this study.

Finally, we note that though we included a bending stiffness in the model, bending was demonstrated to be unimportant in this regime, meaning that it would be appropriate to consider the large-strain, nonlinear membrane model instead. If instead a regime in which bending was comparable to stretching needed to be considered, the recent model of Healey

et al. [2013] would possibly make a better choice of model than Koiter-Steigmann - due to its comparative simplicity. A linear bending model would likely be appropriate, as the bending would only occur in a small boundary layer, in which angles would be small. This model could then be extended to finite strains, as in Li and Healey [2016], and supplemented with a large-displacement follower-load to capture the ensuing behaviour.

6.5 Summary of Results

In conclusion, in this section we have seen that the pre-stretch, thickness and choice of material model greatly affect the ensuing pressure-deflection curve. Thus, careful selection of the experimental region, or use of an appropriate model, is of tantamount importance to determining correct parameter values in the fit. Interestingly the distribution of pre-stretch seemed unimportant in determining the value maximum vertical deflection, only the average magnitude affects the shape of the curves. A two-parameter fit for the radial pre-stretch and Young's modulus of inflation experiments was performed and was found to be an accurate means of determining the Young's modulus. It was found that in regimes in which the Föppl-von Kármán becomes inaccurate the Koiter-Steigmann model provides a realistic alternative. The downside to this method is that the equations now depend explicitly on thickness. An attractive alternative to both is the nonlinear membrane model, which in the regimes considered would likely provide the optimal trade-off between accuracy and simplicity, provided that bending may be neglected.

This bears considerable importance for future measurements made using this method, as many scenarios in which a strip-pull experiment is unfeasible still require accurate determination of Young's modulus. Given that in these scenarios it may be difficult or impossible to control the pre-stretch, the method outlined provides a robust fitting strategy which avoids this issue.

Chapter 7

Inflation of a Circular Sheet with a Rolling Clamp

7.1 Outline of the Problem

The next problem we consider is the inflation of a circular, membrane, subject to approximately stress-free in-plane boundary conditions with zero vertical displacement and angle at the boundary. These conditions are sometimes known as a 'sliding' or 'rolling' clamp and have been studied for Föppl-von Kármán plates by Coman [2013]; Coman et al. [2015]; Coman and Bassom [2016].

In this problem the deflection of the sheet is smoothly constrained to zero at a certain radius on the undeformed sheet, but this material line is free to deform in-plane. One possible physical realization of this would be two circular sheets glued on the rim, with a cavity in between, which could then be inflated.

In a related system considered by Box et al. [2017], a circular sheet is indented in the low tension regime: this system has similar boundary conditions applied at the outer edge but is forced by an indenter rather than a constant pressure. Other similar problems include the studies of sheets draped on liquid drops by King et al. [2012], which use the same equations but with a slightly modified boundary condition. In their system, however, the lack of a bending boundary layer results in qualitatively different wrinkling dynamics and ensuing morphology: the system considered in their study is tension dominated. Here on the other hand, we discuss a system in which the bending boundary layer cannot be neglected and we focus on the low tension regime.

(a) $\Delta p = 0$ (b) $\Delta p < p_c$ (c) $\Delta p > p_c$

Figure 7.1: Illustration of the evolution of the sheet shape as nondimensional pressure, Δp, is increased: at a critical nondimensional pressure, p_c, a symmetry breaking bifurcation occurs and the sheet wrinkles.

In the present system, application of pressure to the sheet initially results in an axisymmetric bulge forming as displayed in figure 7.1. As the pressure increases the sheet deforms inward, which results in the build up of a compressive hoop stress as excess material is accommodated. Once the compressive stress passes a certain threshold, it becomes energetically favourable to wrinkle, rather than continuing to compress. At this value of pressure, p_c, a supercritical pitchfork (symmetry-breaking) bifurcation occurs, with an azimuthal wrinkling pattern. The bifurcation can occur with any phase - resulting in a pitchfork of revolution. However this would not be observed experimentally or in full numerical simulation, as imperfections due to meshing are present that break the degeneracy. The resulting wrinkling pattern is shown in figure 7.1.

We begin by considering the Föppl-von Kármán prediction for the system, in section 7.2, first considering the pre-wrinkling axisymmetric base state. We then discuss results of a linear stability analysis and briefly investigate the effects of pre-tension. Following this, in section 7.2.1, we use the predictions of the linear stability analysis to estimate when the Föppl-von Kármán predictions will break down. We then proceed to consider a 2D simulation of the Föppl-von Kármán equations in section 7.2.2, which we finally compare to the predictions of the two nonlinear-bending models outlined in chapter 3 in section 7.3.

Ultimately we show that in this simple system the wrinkling behaviour of the Föppl-von Kármán model can be described by a universal curve with a single nondimensional onset pressure and a universal wavenumber, independent of relative thickness, $h = h^*/R^*$: this prediction also remains true in extremely thin sheets for the nonlinear bending models. However, the nonlinear bending models predict that for sheets of greater relative thickness,

h, this universal behaviour quickly gives way to a h-dependent onset behaviour, for which the wavenumber and nondimensional onset-pressure becomes functions of the relative thickness.

7.2 The Föppl-von Kármán Prediction

For extremely thin sheets the governing equations will be the Föppl-von Kármán equations, which can be found expressed in terms of polar coordinates (ρ, ϕ) in [Coman et al., 2015]. Using the nondimensionalization of chapter 6, the equations are:

$$\Delta^2 u_3 - S_{\rho\rho}\frac{\partial^2 u_3}{\partial \rho^2} - \frac{2}{\rho}S_{\rho\phi}\left(\frac{1}{\rho}\frac{\partial^2 u_3}{\partial \rho \partial \phi} - \frac{\partial u_3}{\partial \phi}\right) - \frac{1}{\rho}S_{\phi\phi}\left(\frac{1}{\rho}\frac{\partial^2 u_3}{\partial \phi^2} + \frac{\partial u_3}{\partial \rho}\right) = \Delta p\,, \tag{7.2.1}$$

$$\frac{\partial S_{\rho\rho}}{\partial \rho} + \frac{1}{\rho}\frac{\partial S_{\rho\phi}}{\partial \phi} + \frac{1}{\rho}\left(S_{\rho\rho} - S_{\phi\phi}\right) = 0\,, \tag{7.2.2}$$

$$\frac{\partial S_{\rho\phi}}{\partial \rho} + \frac{1}{\rho}\frac{\partial S_{\phi\phi}}{\partial \phi} + \frac{2}{\rho}S_{\rho\phi} = 0\,, \tag{7.2.3}$$

subject to the boundary conditions

$$u_3(\rho = 1, \phi) = 0\,, \quad \frac{\partial u_3}{\partial \rho}(\rho = 1, \phi) = 0 \quad \text{and} \quad S_{\rho\rho}(\rho = 1, \phi) = 12\mu^2\,. \tag{7.2.4}$$

Assuming low radial forcing, we may neglect the $12\mu^2$ term and use a stress-free boundary condition, instead. At the centre, we have the following regularity conditions

$$u_\rho(\rho = 0, \phi) = 0\,, \quad \frac{\partial u_3}{\partial \rho}(\rho = 0, \phi) = 0 \quad \frac{\partial^3 u_3}{\partial \rho^3}(\rho = 0, \phi) = 0\,, \tag{7.2.5}$$

which ensure that the stress and displacements are continuous. The nondimensional stress components are given by:

$$S_{\rho\rho} = \frac{1}{1-\nu^2}\left(\bar{\epsilon}_{\rho\rho} + \nu\bar{\epsilon}_{\phi\phi}\right) \quad \text{and} \quad S_{\phi\phi} = \frac{1}{1-\nu^2}\left(\bar{\epsilon}_{\phi\phi} + \nu\bar{\epsilon}_{\rho\rho}\right)\,. \tag{7.2.6}$$

in terms of the corresponding scaled strain components. The scaled strains, in turn, can be written in terms of displacements as [Davidovitch et al., 2012]:

$$\bar{\epsilon}_{\rho\rho} = \frac{\partial u_\rho}{\partial \rho} + \frac{1}{2}\left(\frac{\partial u_3}{\partial \rho}\right)^2\,, \tag{7.2.7}$$

$$\bar{\epsilon}_{\rho\phi} = -\frac{1}{2\rho}u_\phi + \frac{1}{2\rho}\frac{\partial u_\phi}{\partial \rho} + \frac{1}{2\rho}\frac{\partial u_\rho}{\partial \phi} + \frac{1}{2\rho}\frac{\partial u_3}{\partial \rho}\frac{\partial u_3}{\partial \phi}\,, \tag{7.2.8}$$

$$\bar{\epsilon}_{\rho\rho} = \frac{1}{\rho}u_\rho + \frac{1}{\rho}\frac{\partial u_\phi}{\partial \phi} + \frac{1}{2\rho^2}\left(\frac{\partial u_3}{\partial \phi}\right)^2\,, \tag{7.2.9}$$

in which u_ρ is the nondimensional radial displacement and u_ϕ is the nondimensional azimuthal displacement. For the axisymmetric base state, these equations reduce to the equations of chapter 6, except for the in-plane boundary condition, which is stress free for the present system.

As can be seen in equations (7.2.1–7.2.5), for low radial forcing $\mu \ll 1$, this system has only a single control parameter: the nondimensional pressure. This implies that the onset of wrinkling, and ensuing morphology, will be described by a 'universal onset curve'. A system of any relative thickness will have a single value of critical pressure, p_c, and a universal onset wavenumber, k. Experimentally, one would observe the collapse of a range of dimensional onset pressures, Δp^*, onto a single value of nondimensional pressure.

Knowing the nondimensional onset pressure, and designing a suitable experiment to measure the wrinkling onset, gives a means of deducing the Young's modulus of any sheet. In principle, if the corresponding thickness of the sheet is unknown, it could be measured by comparing the magnitude of the deflection of the sheet to the maximum deflection at the bifurcation point, which it is linearly related to. Thus, this approach can be used for measuring the properties of thin elastic sheets. However, the universal onset curve only applies when the assumptions of the Föppl-von Kármán model are satisfied: small displacements and moderate rotations. Otherwise, explicit relative-thickness dependence will be introduced for thicker sheets, or correspondingly larger displacements, and the Föppl-von Kármán prediction will cease to apply (see section 3.5.6).

By solving the axisymmetric Föppl-von Kármán equations, as outlined in appendix G, we can investigate the pre-buckling, axisymmetric base state.

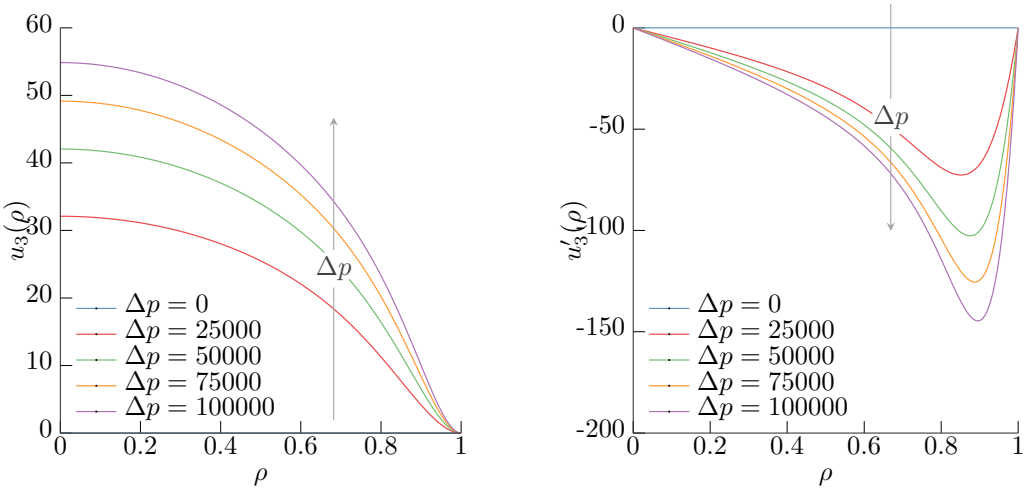

Figure 7.2: Deflection, $u_3(\rho)$, (a) and gradient of deflection, $u_3'(\rho)$, (b) for axisymmetric deformations, predicted by the Föppl-von Kármán model. The arrow indicates the direction of increasing nondimensional pressure.

We see in figure 7.2a, that as the nondimensional pressure increases, the deflection also increases, forming a membrane-like solution in the bulk of the sheet, with a bending boundary layer at the outer clamp. This is more obvious in the plot of the gradient of the deflection (figure 7.2b), where we can be seen that as the nondimensional pressure increases, the boundary layer forms at the edge. Prior to wrinkling a build-up of compressive hoop stress, seen in figure 7.3b, occurs in a localised region near to the edge of the sheet as might be expected for a wrinkling solution. This negative hoop stress is present even in the linear regime, and can be accommodated without wrinkling due to the presence of a bending stiffness.

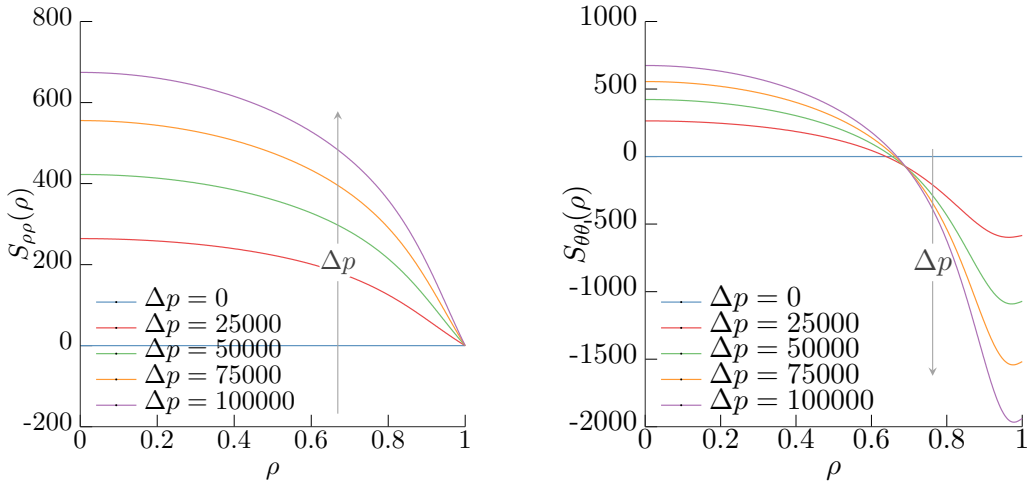

Figure 7.3: Nondimensional radial stress, $S_{\rho\rho}$, (a) and nondimensional hoop stress, $S_{\phi\phi}$, (b) as a function of the radial position. These results were obtained using the axisymmetric Föppl-von Kármán model and are shown with increasing nondimensional pressure, with the direction of increasing nondimensional pressure indicated by an arrow.

The radial strain in the sheet remains positive and increases with increasing nondimensional pressure, as seen in figure 7.4a, indicating that the solution is tensile in the radial direction. These observations fit with physical intuition: as the sheet deforms due to the pressure load it generates a tensile stress which pulls material inward. This additional material must be accommodated at a decreased circumference, causing the sheet to buckle out-of-plane.

A linear stability analysis, as outlined in appendix G, reveals that the sheet first wrinkles at a nondimensional pressure of $\Delta p_c = 65130$ with onset wavenumber $k = 14$. As stated, under low radial forcing, this onset wavenumber and nondimensional onset pressure will be

independent of the relative thickness of the sheet and the material properties.

We note that at the onset value of the nondimensional pressure the scaled radial strain within the sheet (cf. figure 7.4a) is $\bar{\epsilon}_{\rho\rho} \sim 10^3$, which corresponds to a physical strain of $\epsilon_{\rho\rho} \sim 0.01$ for a sheet of relative thickness $h = h^*/R^* = 0.01$, which is within the limits usually considered appropriate for linear material behaviour in hyperelastic media [Raayai-Ardakani et al., 2016]. We further support this by noting that the neo-Hookean and Mooney-Rivlin models show little difference from linear material behaviour, under uniaxial extension, for strains $\sim 1\%$ (cf. section 6). Thus we expect that the linear constitutive hypothesis of the Föppl-von Kármán model will be appropriate, at least for rubber-like materials. This also serves to make the comparison between the assumptions of Föppl-von Kármán and the ensuing nonlinear bending models more direct, allowing us to attribute differences in the models to purely geometrical effects.

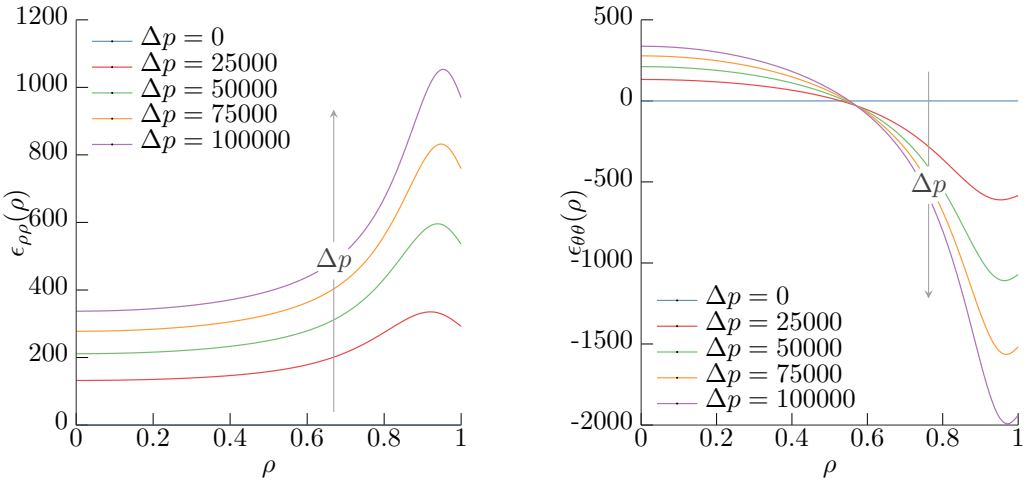

Figure 7.4: Scaled radial strain, $\bar{\epsilon}_{\rho\rho}$, (a) and scaled azimuthal strain, $\bar{\epsilon}_{\phi\phi}$, (b) as a function of the radial position, as predicted by the axisymmetric Föppl-von Kármán equations. Results are shown for increasing nondimensional pressure, with the increasing direction indicated by an arrow.

We can perform a linear stability analysis for a range of wavenumbers, to identify the nondimensional pressures at which we expect wrinkling solutions with a particular wavenumber. We show the corresponding nondimensional onset pressure versus the wavenumber in figure 7.5. Though physically wavenumbers can only take integer values, in the discretized

equation there is no such necessity: we might expect that between integer values the nondimensional onset pressure varies continuously. As can be seen in figure 7.5, this is indeed the case, which allows a continuous plot to be made. The minimum of the resulting curve is extremely shallow: nearby wavenumbers $k = 13$ and $k = 15$ wrinkle occur at nondimensional pressure values of 65622 and 66312, respectively. Thus, we might expect that the onset wavenumber would change with only a slight perturbation, as is found to be the case when applied radial stresses, $\mu \neq 0$, are considered [Coman et al., 2015].

Considering low radial forcing, we see that for the value $\mu = 2$ the onset wavenumber shifts from $k = 14$ to $k = 15$ and occurs instead at a nondimensional pressure 88825, a difference of 26%. Thus we see that for radial forcing parameter, $\mu \gtrsim 1$, the system has two important nondimensional parameters. For simplicity, however, in the remainder of this chapter we focus on the case of $\mu \ll 1$, taking $\mu = 0$. This allows us instead to explore variation in $h = h^*/R$.

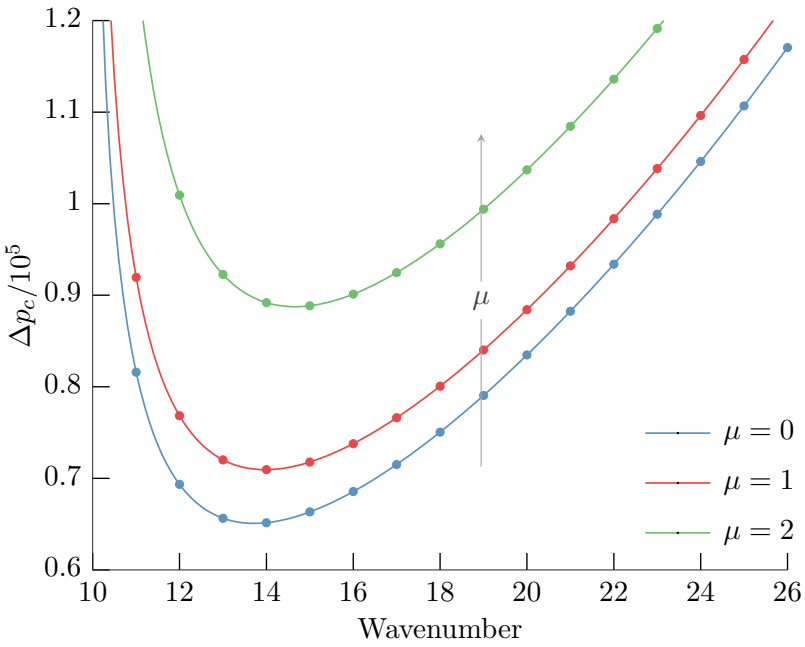

Figure 7.5: The critical nondimensional onset pressure Δp_c as a function of wavenumber, k, for the Föppl-von Kármán model at three values of radial forcing, μ. Integer values are shown with points: the first wrinkling mode to become available in this system will be the integer-valued wavenumber with the smallest nondimensional pressure: $k = 14$.

7.2.1 Estimating the Limit of Moderate Rotation

It is useful to estimate the typical deflection gradients, to provide an estimate of when we expect the nondimensional onset pressure predicted by Föppl-von Kármán to be inappropriate. Using an asymptotic result from [Coman et al., 2015], the typical size of the derivative of the nondimensional deflection in this system scales as:

$$\frac{\partial u_3}{\partial \rho} \sim (\Delta p)^{\frac{1}{2}} \tag{7.2.10}$$

modulo an order 1 function. We may expect, from the formula for the (truncated) unit normal,

$$\hat{\boldsymbol{N}} \approx -\boldsymbol{\nabla} u_3^* + (1 + \frac{1}{2}\boldsymbol{\nabla} u_3^* \cdot \boldsymbol{\nabla} u_3^*)\, \boldsymbol{k}\,, \tag{7.2.11}$$

introduced in section 3.6 that when the deflection gradient $\partial u_3^*/\partial \rho^*$ becomes order unity, the moderate rotation assumption breaks down. Thus, un-scaling the nondimensional displacements, we have: $\partial u_3^*/\partial \rho^* \sim h u_3' \sim 1$, which we can combine with equation (7.2.10) to predict that the moderate rotation assumption will break down for

$$h(\Delta p)^{\frac{1}{2}} \sim 1\,. \tag{7.2.12}$$

Using this relation, along with the critical nondimensional onset pressure $\Delta p_c = 65130$, we may predict that the assumption of moderate rotations is appropriate until $h \sim 0.004$. We can make further estimates using the numerical simulations shown in figure 7.2b. For $p = 75000$ (which is near to the nondimensional onset pressure), the scaled deflection gradient will be $\partial u_3/\partial \rho \approx 120$. We estimate that the moderate rotation assumption becomes invalid once the gradient reaches

$$\frac{\partial u_3^*}{\partial \rho^*} = \frac{h}{\sqrt{12(1-\nu^2)}} \frac{\partial u_3}{\partial \rho} \approx \frac{1}{5}\,. \tag{7.2.13}$$

Rearranging for h and introducing the numerical factors suggests that the predictions of the Föppl-von Kármán model become invalid for relative thickness $h \approx 0.005$.

7.2.2 2D Numerical Simulation

We also compute the wrinkling onset using a 2D full numerical solution, to ascertain whether to expect the $k = 14$ wavenumber to be present for nondimensional pressures past the onset. The onset can be measured by considering the non-axisymmetry measure of section 5.2.3, which is given by:

$$||\rho^{-1}\partial_\phi u_3||_2 = \left[\int_\Omega \left(\frac{1}{\rho}\frac{\partial u_3(\boldsymbol{y})}{\partial \phi}\right)^2 d\Omega\right]^{\frac{1}{2}}\,, \tag{7.2.14}$$

where u_3 is once again the nondimensional deflection and $d\Omega$ is the undeformed area element of the circular (undeformed) sheet Ω. As before, ρ and ϕ are the standard polar coordinates on the undeformed sheet.

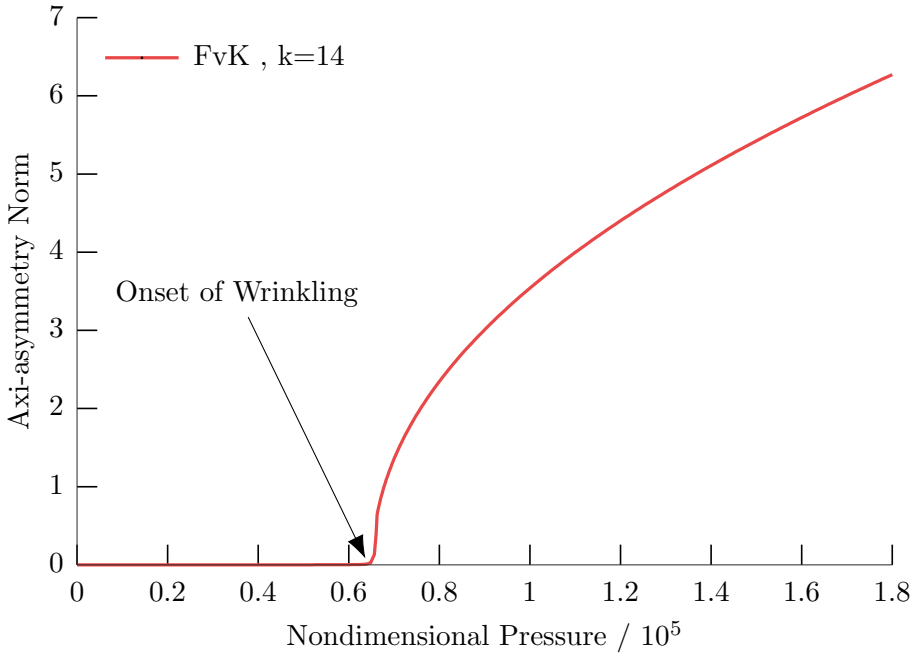

Figure 7.6: Non-axisymmetry norm (equation (7.2.14)), versus applied nondimensional pressures obtained from full numerical simulations of the inflation of a Föppl-von Kármán sheet. The Föppl-von Kármán model predict a universal onset of wrinkling, with wavenumber $k = 14$, for all values of relative sheet thickness $h = h^*/R$.

The 2D-numerical solution of the equations reveals that the sheet first wrinkles at critical nondimensional pressure[1] $\Delta p_c = 65130$ with wavenumber $k = 14$, as shown in figure 7.6. This is in agreement with the value of $\Delta p_c = 65130$ obtained from the linear stability analysis and also agrees with the value of $\Delta p_c = 65128$ obtained by Coman et al. [2015] to within 0.003%.

In principle, before the sheet wrinkles the measure should be zero, however, when solved on a discretized domain the measure will be small but nonzero. After the wrinkling instability occurs the measure should grow with an initially square-root amplitude, assuming that an appropriate asymmetry measure has been chosen, in accordance with predictions from

[1]This is calculated by fitting a straight line to the square of the non-axisymmetry measure and extrapolating the Δp-intercept. Using this method, errors in the calculated intercept are introduced both by the imperfect nature of the bifurcation and the assumption of perfect square-root type behaviour, so high resolution numerical simulation is required.

bifurcation theory [Strogatz, 2015].

The form of the solution near to the onset is:

$$u_3(r) = \bar{u}_3(\rho) + \epsilon \hat{u}_3(\rho)\sin(k\phi) \tag{7.2.15}$$

and thus, the measure we have chosen will assume the following form:

$$||\rho^{-1}\partial_\phi u_3||_2 = \epsilon \left[k^2 \int_0^{2\pi} (\sin(k\phi))^2 d\phi \int_{\rho=0}^{1} \hat{u}_3(\rho)\rho d\rho\right]^{1/2} \tag{7.2.16}$$

where $\hat{u}_3(\rho)$ is the solution to the perturbation problem. The integrals will be constant for a particular wavenumber, k and for $\epsilon \ll 1$. Thus the measure will initially grow proportionally to the amplitude of the perturbation and we therefore expect square root type behaviour in the vicinity of the bifurcation. We demonstrate the square-root-type behaviour in figure 7.7, in which we square the non-axisymmetry measure and show that it follows a straight line.

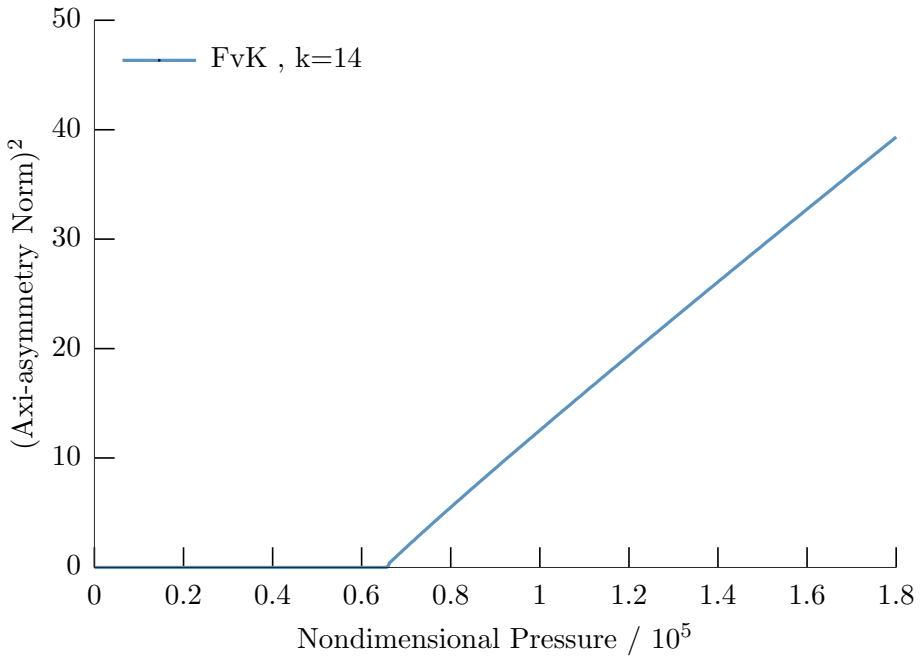

Figure 7.7: Squared non-axisymmetry norm, versus applied nondimensional pressures obtained from full numerical simulations of the inflation of a Föppl-von Kármán sheet. The apparent linear growth in this measure after onset indicates that the non-axisymmetry measure does indeed give square-root type behaviour.

No secondary bifurcations were observed past the bifurcation point, although other wavenumber solutions are expected to bifurcate from the (now unstable) axisymmetric solutions, indicating that there may be regions of multi-stability. This is to be expected, and

in very thin sheets a complicated morphology is expected in the intermediate regime before fine-scale wrinkling relaxes the stresses and leads to a far-from-threshold limit.

We now proceed to the next section, in which we assess when the moderate rotation assumption of the Föppl-von Kármán model breaks down. As discussed, this can equivalently be considered as the small relative thickness, $h = h^*/R^*$, regime at fixed nondimensional forcing, Δp^*, given that the nondimensional displacements are scaled on relative thickness. Once the displacements (or equivalently the relative thickness) get large enough, the linearised bending moment will cease to be appropriate, and nonlinear bending effects will start to become important in the ensuing morphology. We expect from the above argument that at $h \approx 0.004$ we will begin to see the effects of the nonlinear bending terms.

7.3 The Effects of Nonlinear Bending

We can use the nonlinear-bending-type plate models that we have implemented to probe the wrinkling onset at varying values of relative thickness, and investigate how the inclusion of geometrically nonlinear bending affects the system. As discussed, in this system the strain is not expected to be large, as the outer edge is stress free. Thus, it is appropriate to use a linear constitutive relation for the sheet.

Computation of the onset curve for different values of the relative thickness, h, reveals that the morphology is sensitive to the geometrical nonlinear bending, as shown in figure 7.8. This culminates in the onset of wrinkling happening at value of nondimensional pressure that increases with relative-thickness. The discrepancy between the predicted nondimensional onset-pressures of the Koiter-Steigmann and the Föppl-von Kármán model is small at 5% for sheets with relative thickness smaller than $h = 0.0075$. However, the nondimensional onset pressure predicted by the Koiter-Steigmann model is 10% larger by $h = 0.01$ and doubles for the thickness value $h = 0.0225$.

Another difference that can be observed is onset wavenumber variation: as the sheet gets thicker the onset wavenumber shifts from $k = 14$ to $k = 15$, at a thickness $h = 0.018$, and to $k = 16$ at $h = 0.0225$. Just like in the predictions of the Föppl-von Kármán model, other modes exist past the initial onset, and bifurcate instead from the (now unstable) axisymmetric branch. The change in wavenumber is thus a far less sensitive to the choice of model.

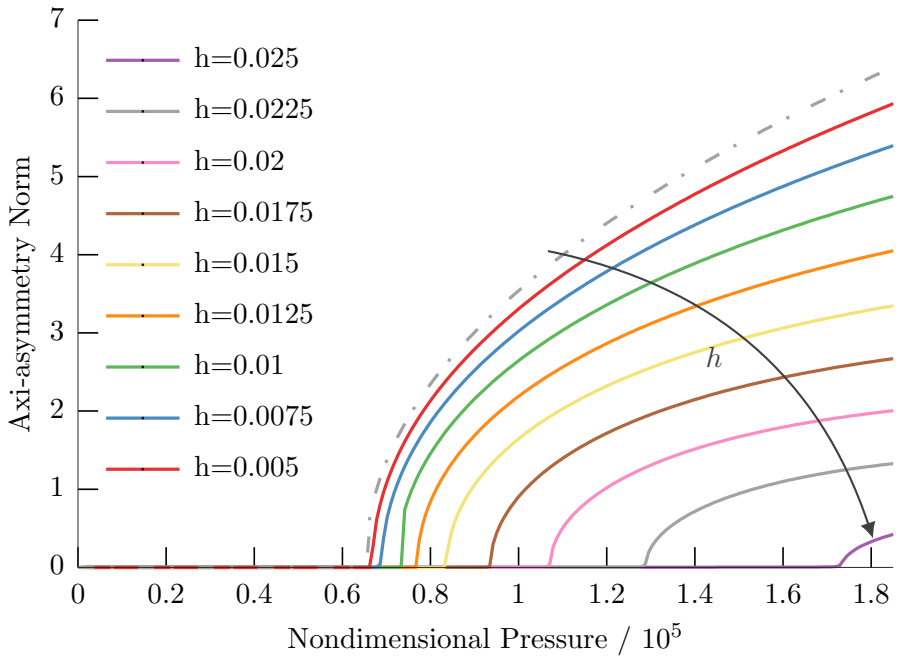

Figure 7.8: Nondimensional pressure versus non-axisymmetry norm, showing the wrinkling onset for sheets of various relative thickness, obtained from full numerical simulation of the Koiter-Steigmann model. The direction of increasing thickness is shown with an arrow. The Föppl-von Kármán curve is shown as a dashed line for comparison.

We can now test the predictions of the simplified model derived in section 3.6, which we refer to as the extended Föppl-von Kármán model, and see how well it agrees with the Koiter-Steigmann model: in figure 7.10 we compute the onsets for the same range of thickness as in figure 7.8. We find that the extended Föppl-von Kármán model behaves qualitatively the same, and agrees well quantitatively up to relative thickness of $h = 0.0175$, where the relative difference between the nondimensional onset pressure predictions of the models is only 7%. However, beyond this point the prediction diverges from that of the Koiter-Steigmann model.

A comparison of nondimensional onset pressure versus relative thickness for all three models is displayed in figure 7.11, which clearly shows the agreement of the extended Föppl-von Kármán model and the Koiter Steigmann model. It can clearly be seen that for relative thickness greater than $h = 0.0075$ the Föppl-von Kármán model begins to disagree significantly with the Koiter-Steigmann model and that it becomes increasingly necessary to use a more geometrically accurate model. Thus, the estimate of $h \approx 0.004$ made in the previous section appears to have been appropriate. We show the shape of the solutions for several

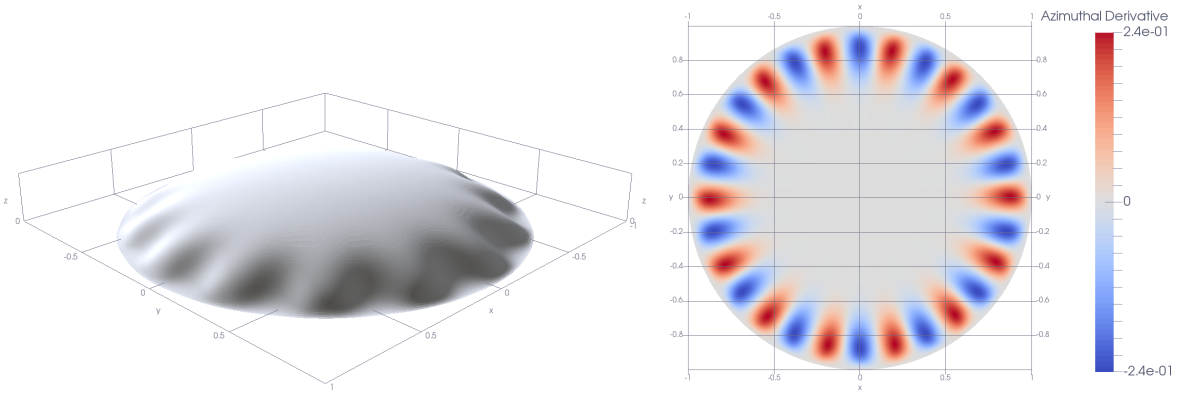

(a) $h = 0.01$

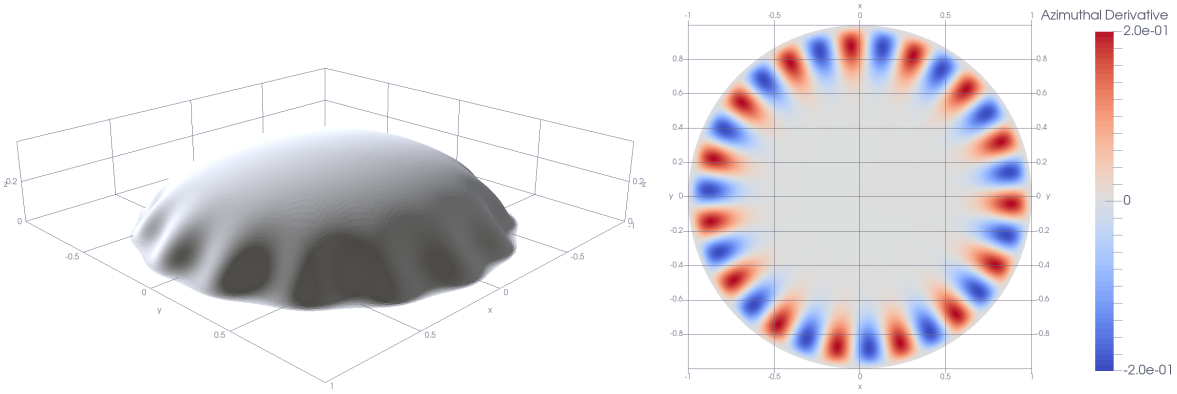

(b) $h = 0.02$

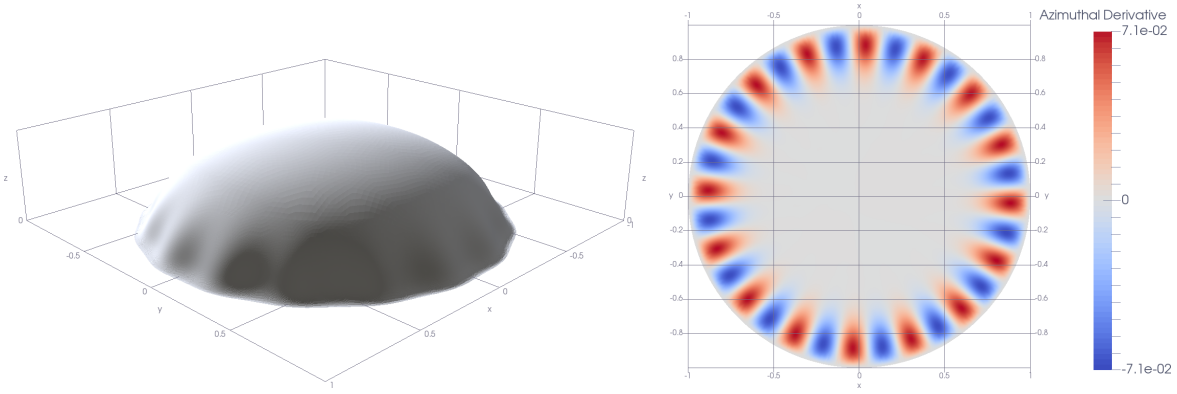

(c) $h = 0.025$

Figure 7.9: Wrinkling solutions predicted by the Koiter-Steigmann model for various values of thickness. The deformed shape of the sheet is shown in the left hand plots, with the corresponding azimuthal derivative shown on the right. These images are computed at $\Delta p = 2.0 \times 10^5$, which is far past the onset in all cases.

values of relative thickness in figure 7.9.

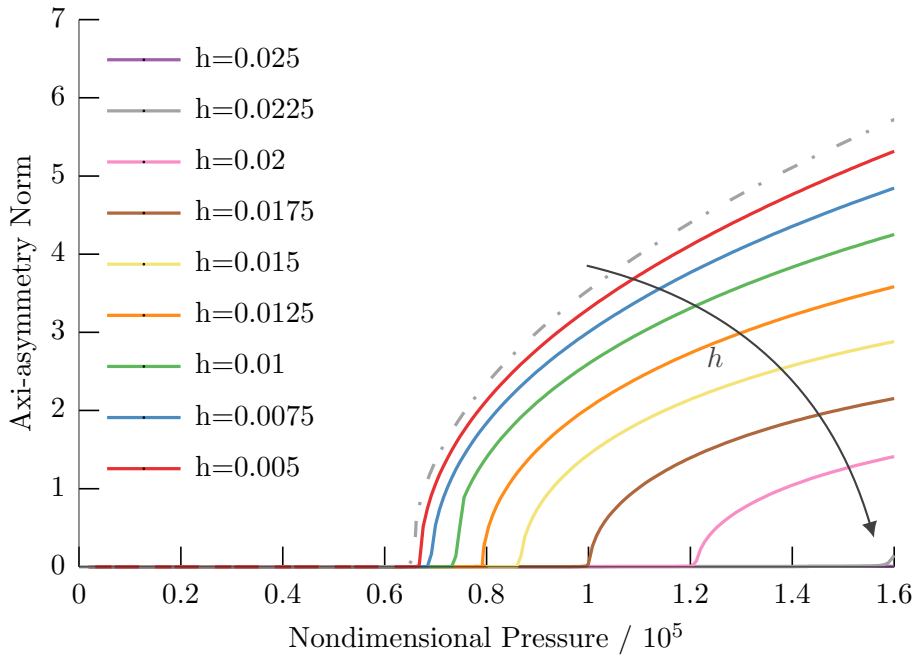

Figure 7.10: Nondimensional pressure versus non-axisymmetry norm, showing the wrinkling onset for sheets of various relative thickness, obtained from full numerical simulation of the extended Föppl-von Kármán model. The direction of increasing thickness is shown with an arrow. The Föppl-von Kármán curve is shown as a dashed line for comparison.

We obtain an excellent fit to the numerical data for the $k = 14$ mode, seen in figure 7.11, for a function of the form:

$$\Delta p_c = a\, h^4 + b\, h^2 + \Delta p_c^{FvK}\,, \tag{7.3.1}$$

with $a = 1.6 \times 10^6 \Delta p_c^{FvK}$ and $b = 9.0 \times 10^2 \Delta p_c^{FvK}$, which suggests that the nondimensional onset pressure dependence is described by power law-type behaviour. This form should be expected, as in the extended Föppl-von Kármán model only even powers of h enter: via the curvature $\hat{N}_i v_{i,\alpha\beta}$ and the loading term $\hat{N}_i\, \delta v_i$ where we recall from chapter 3.6 that displacements are assumed to scale as $v_3 \sim h$ and $v_\alpha \sim h^2$, similarly to the assumptions of the Föppl-von Kármán model. As such the small parameter is h^2 *not* h.

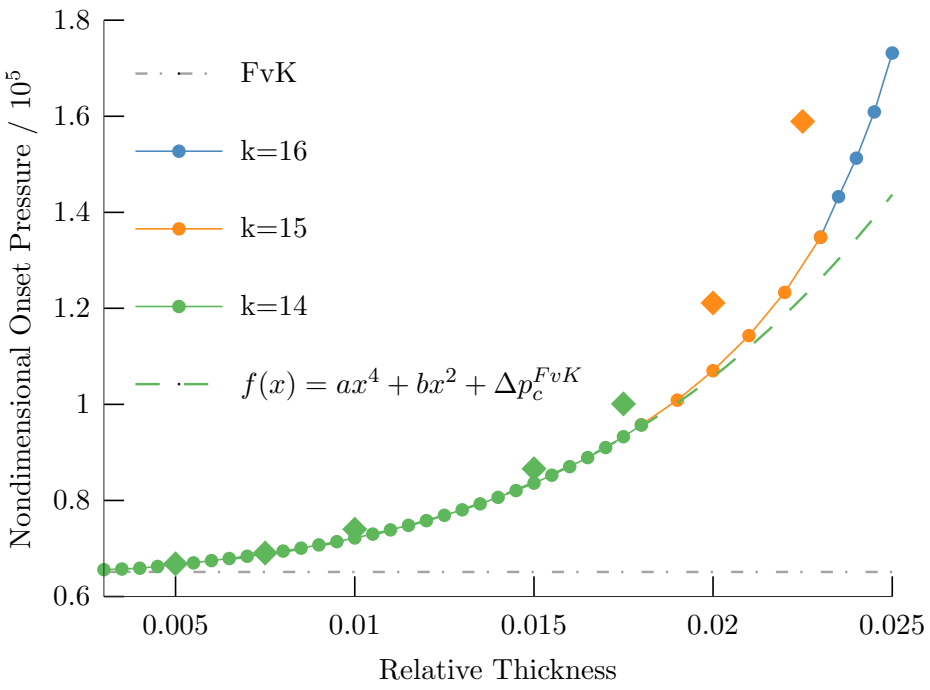

Figure 7.11: Nondimensional pressure onset, p_c, versus relative thickness, h, predicted by the Koiter-Steigmann (circles) and extended Föppl-von Kármán model (diamonds). The (constant) Föppl-von Kármán prediction is shown as a dot-dashed grey line. We also show the fit to the $k = 14$ mode, shown as a green dashed line.

For the physical problem considered here, the use of the moderate-rotation Föppl-von Kármán model results in qualitatively and quantitatively inaccurate behaviour, even for sheets of relative thickness $h \sim 0.01$: well within the thickness ranges usually considered for thin plate models. For instance, in the related indentation problem of Box et al. [2017], circular sheets up to relative thickness 0.02 are considered, though only for the axisymmetric pre-buckling problem. In the corresponding wrinkling problem sheets of up to $h = 0.00625$ are considered, for which the difference between the models in the present system would be smaller than 4%.

In the present system, the onset wavenumber and nondimensional pressure are found to vary with relative-thickness, h, therefore negating the relative-thickness scaling of the dimensional onset pressure of wrinkling predicted by the Föppl-von Kármán model. This is of interest experimentally, because if the range of thickness values used for measurement covers the region in which the Föppl-von Kármán predictions are invalid, the determination of the Young's modulus will fail. We have also demonstrated that the overall behaviour of this system can be replicated qualitatively by a simplified model, the extended Föppl-von

Kármán model, which agrees quantitatively for relative thickness up to $h \approx 0.0175$.

Finally, we highlight that it would be interesting to observe the effects material nonlinearity has on the observed wrinkling behaviour: in other wrinkling systems, such as the strip-pull wrinkling set-up, material nonlinearity has been observed to result in quite different behaviour [Li and Healey, 2016]. As this system has zero stress at the outer edge, any large stresses would need to be self-induced, so the effects of material nonlinearity would likely only be present in the wrinkling of thicker sheets.

7.4 Summary of Results

In summary, we have seen that the choice of plate model can have a large bearing on the predicted morphology of thin sheets, by considering a simple wrinkling problem in which there is a single parameter. In this system both the nondimensional onset pressure and wavenumber are predicted to be universal by the Föppl-von Kármán model and independent of the relative thickness, $h = h^*/R$. This behaviour agrees with the predictions of a geometrically accurate model up to a relative thickness of $h \approx 0.0075$ whereupon this h-independence breaks down. The extended Föppl-von Kármán model was also found to describe this breakdown, but failed to do so quantitatively at larger values of relative thickness. This example provides useful benchmark that allows us to assess for which values of thickness, and size of the corresponding rotations, the Föppl-von Kármán model is appropriate. It also serves to highlight a regime where thickness and/or Young's modulus could be measured by considering a single observation, provided that the system could be realized experimentally. If thicker sheets are considered, however, the scaling behaviour quickly breaks down. Thus, this study serves to highlight a regime in which measurements that rely on the predictions of the Föppl-von Kármán model are appropriate. Perhaps surprisingly, it only holds only for extremely thin sheets.

Chapter 8

Cantilever-Type Displacement of a Sheet

In this section we investigate the bending of a thin sheet, clamped at one end and undergoing a constant pressure load normal to the sheet. To demonstrate the flexibility of the methods outlined in this thesis we choose a sheet with a complex geometry: a fish shaped sheet, as shown in figure 8.1. The mesh for this shape is straightforward to construct using the quality mesh generator `Triangle` [Shewchuk, 1996], in-line within `oomph-lib` [Heil and Hazel, 2006].

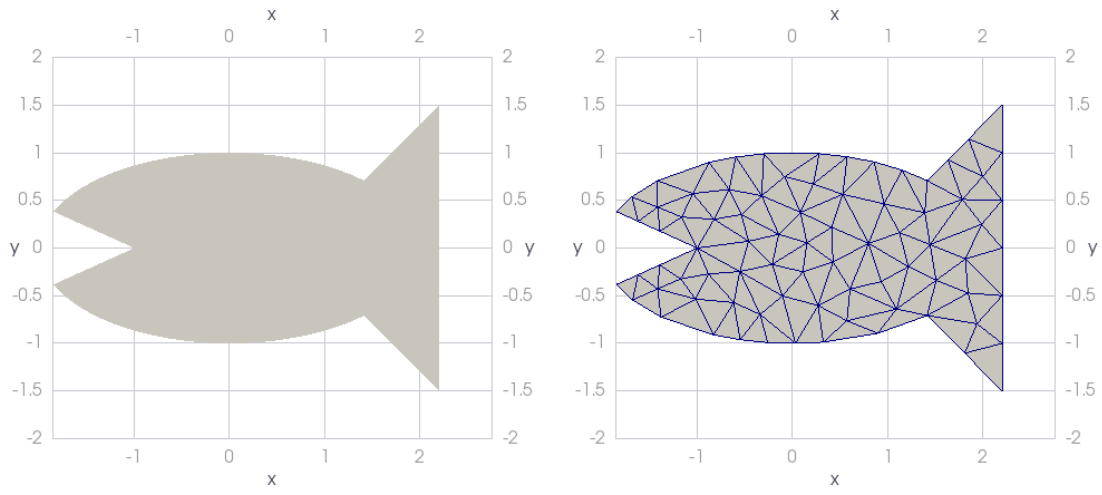

(a) (b)

Figure 8.1: The interpolated domain (a) and input triangle mesh (b).

We compare the predictions of the Föppl-von Kármán model, the new extended model presented in section 3.6, and the Koiter-Steigmann model for this system. This illustrates the effect of the assumptions made regarding rotation in the two geometrically in-exact

models, when the system undergoes large-displacement deformations. The deformation itself is bending-dominated and the sheet remains virtually un-stretched.

The sheets we examine are of relative thickness $h = h^*/L = 0.01$, in which L is the half-width of the fish's body. We first examine small displacement behaviour, over a range of nondimensional pressures $\Delta p = (12(1-\nu^2)^{3/2})\Delta p^* L^4/Eh^{*4}$ for the sheet, demonstrating that in the limit of small displacements all three models coincide.

8.1 Small Displacement Behaviour

In the limit of small displacements, seen in figure 8.2, all three models coincide exactly. This region corresponds to the linear, bending-dominated limit, in which we expect $u_3^*/L \sim \Delta p^* L^3/D$. For a vertical displacement of order unity, $u_3^*/L \sim 1$, and a sheet of thickness $h \sim 0.01$, the applied pressure is estimated to be $\Delta p \sim \Delta p^* L/Dh^* \sim 10^2$, in the bending dominated regime. This value is in good agreement with observations from the numerics (cf. figure 8.2).

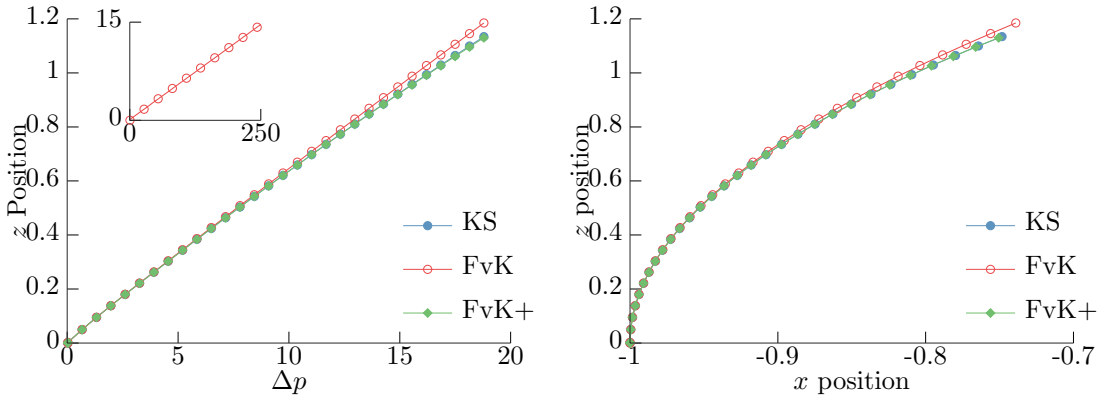

Figure 8.2: (a) The vertical position of the fish's mouth versus the applied pressure, Δp. Inset in this graph is the Föppl-von Kármán prediction over a 10× larger pressure range. (b) The position of the fish's mouth traced over the (equally-spaced) pressure values from (a). In both the predictions are shown for the Föppl-von Kármán model (FvK, red, hollow circles), the Koiter-Steigmann model (KS, blue, filled circles) and the new extended Föppl-von Kármán model (FvK+, green, diamonds).

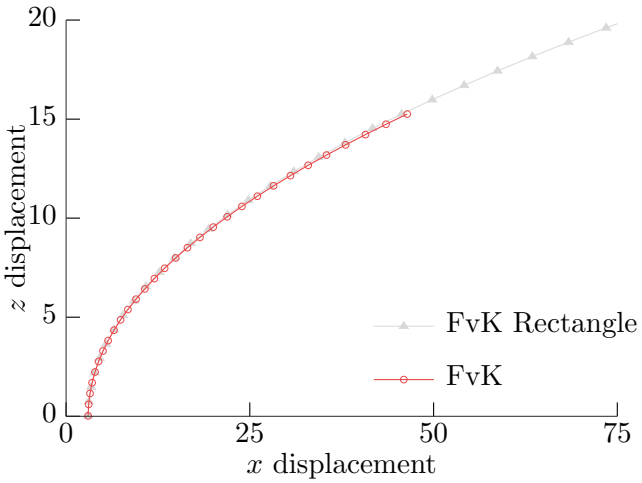

Figure 8.3: Displacement of the fish's mouth predicted by the Föppl-von Kármán model over a large range of pressure, compared to the approximate displacement of a wide, rectangular sheet of comparable length[1], at identical pressures, obtained using the solution of appendix H. The rectangular sheet can be seen to overestimate the deformation response of the sheet.

The Föppl-von Kármán model is observed to diverge from the two, nonlinear bending models as soon as their deflection response becomes nonlinear. In fact, the Föppl-von Kármán model does not predict a nonlinear response even for large deflections (up to $u_3^*/L \sim 15$). Thus, we propose that a linear bending solution for the deflection exists for all values of Δp, and that the in-plane displacements satisfy the 'approximate isometry' imposed by the Föppl-von Kármán strain tensor, effectively set via a one-way coupling with the deflection. This 'approximate isometry', however will result in erroneous stretching for large values of nondimensional displacement.

Indeed, by considering the case of a wide, rectangular sheet subject to a constant pressure load (see appendix H) we find that a zero Föppl-von Kármán-strain solution exists for all values of pressure, resulting in displacements that scale as $u_3^* \sim \Delta p^*$ and $u_x^* \sim (\Delta p^*)^2$. This further supports our supposition of the 'approximate-isometry' solution of the Föppl-von Kármán sheet. We compare the two solutions in figure 8.3 and find excellent qualitative agreement. The pressure-deflection relation is however, out by an order 1 factor, as we have not accounted for the shape of the fish in the simplified model.

[1] We have chosen the length of the rectangle to be the length from head-to-tail of the fish. We plot the displacement of a point located where the mouth of the fish would be, if overlaid on the rectangular sheet.

8.2 Moderate-to-Large Displacement Behaviour

The displacement predicted by all three models initially agree in figure 8.4, until they become approximately 150 times the sheet thickness, at pressures around $\Delta p \approx 18.9$. By this point, the relative difference in deflection at the mouth of the fish has grown to $\sim 13\%$, between the Föppl-von Kármán prediction and the predictions of the other two models. Subsequently, this difference grows rapidly and the sheet using the Föppl-von Kármán model behaves qualitatively differently to the other two models. Its deflection grows, continuing to increase linearly (cf. inset figure 8.2a) even for larger pressures whilst undergoing significant stretching, as can be seen in figure 8.5.

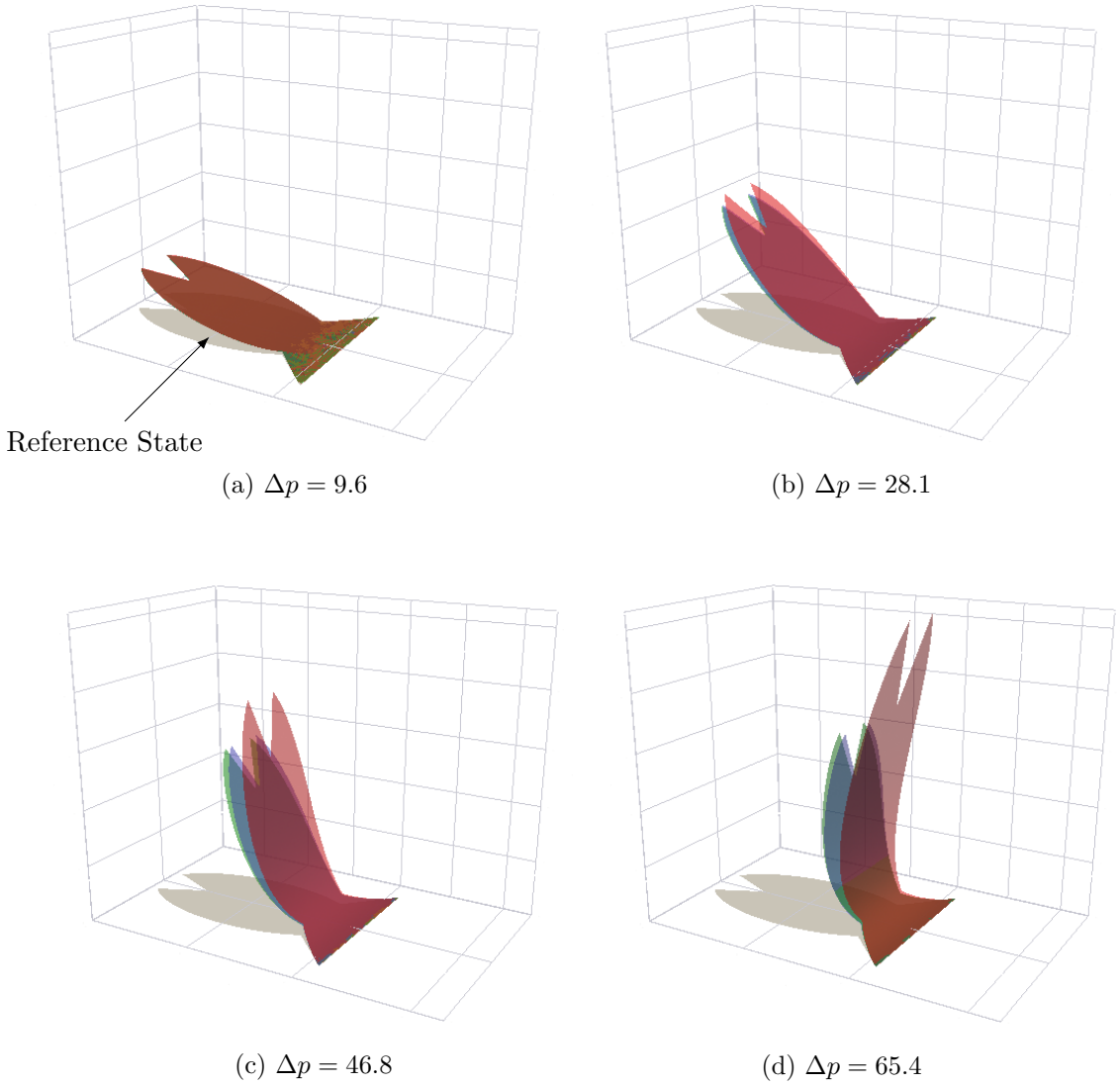

(a) $\Delta p = 9.6$ (b) $\Delta p = 28.1$

(c) $\Delta p = 46.8$ (d) $\Delta p = 65.4$

Figure 8.4: Moderate-to-large displacements of the fish at different values of pressure. The Föppl-von Kármán model (red) predicts a large erroneous stretching which is not predicted by the Koiter-Steigmann (blue) and the new extended Föppl-von Kármán model (green).

It can be seen that the Föppl-von Kármán model is inappropriate for large in-plane strains and out-of-plane rotations, as might be expected, and predicts qualitatively different behaviour from the other two models. This is catastrophic for the large-rotation bending seen in this problem, as the Föppl-von Kármán model predicts large (erroneous) strains almost immediately after it begins to diverge from the other two models.

The extended Föppl-von Kármán model and the Koiter-Steigmann model agree well in the moderate-to-large rotation regime (see figures 8.5-8.6), differing less than 10% in deflection up until the sheet reaches 90° with the horizontal plane at $\Delta p \approx 65$. This is to be expected: at very large rotations the approximate unit normal underlying the extended Föppl-von Kármán model becomes inaccurate. Indeed, based on the diagrams (figure 3.9) showing the approximate unit normal as compared to the exact shown in chapter 3.6, once the rotations reach 90° the predictions of the extended Föppl-von Kármán model start to diverge from the arbitrary-rotation Koiter-Steigmann model.

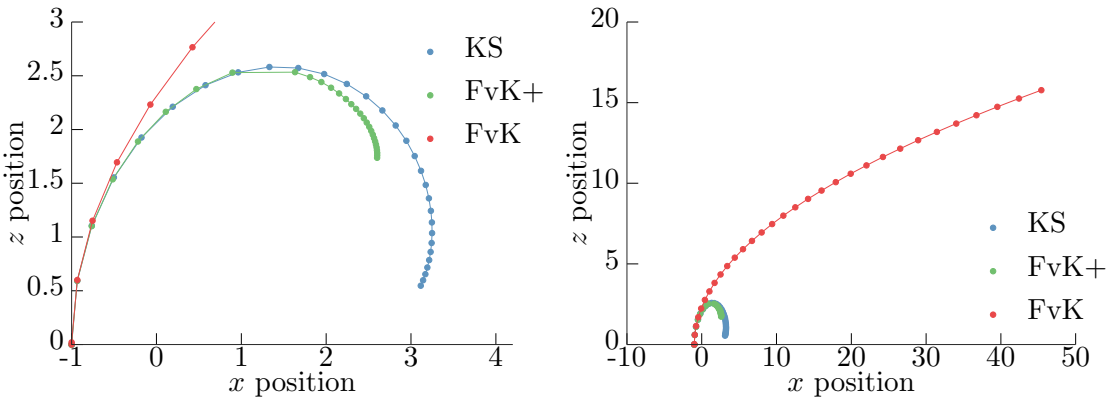

Figure 8.5: The position of the fish's mouth traced for increasing pressure predicted by the Föppl-von Kármán model (FvK, red), the Koiter-Steigmann model (KS, blue) and the new extended Föppl-von Kármán model (FvK+, green). Results are shown over a reduced deflection range (a) and the full range (b). Each point corresponds to a single pressure step. The pressure is increased in constant increments over a range $0 < \Delta p < 270$.

Qualitatively the two large rotation models behave similarly up until the point where the Koiter-Steigmann model predicts sheet angles greater than 180°: at this stage the extended Föppl-von Kármán model ceases to predict any further curling, whereas the arbitrary-rotation Koiter-Steigmann model predicts that the sheet will bend inward towards itself. This is to be expected as, due to the truncation in the forcing, the approximated normal can never

reach angles greater than 90° (cf. figure 3.9), and therefore the stage of 'curling' back can never occur. As mentioned, given that the strongest region of bending is near to the clamp, the largest error is then expected to be from the application of the truncated forcing in the extended FvK model. It should therefore expected that results would be of higher accuracy if the extended Föppl-von Kármán model was to be supplemented with the exact loading term.

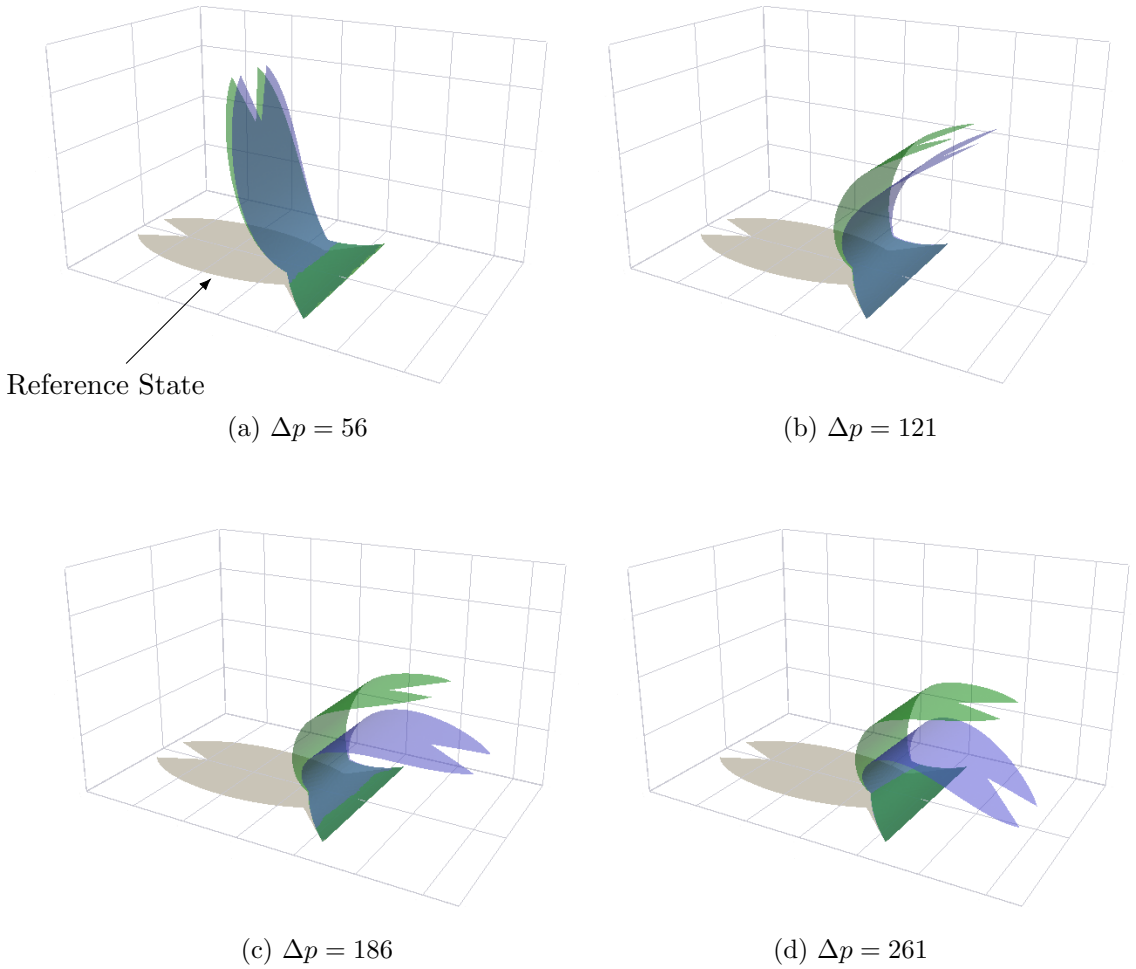

(a) $\Delta p = 56$ (b) $\Delta p = 121$

(c) $\Delta p = 186$ (d) $\Delta p = 261$

Figure 8.6: Large displacements of the fish-shaped sheet for various values of pressure calculated using the Koiter-Steigmann model (KS, blue) and the extended Föppl-von Kármán model (FvK+, green). The latter consistently under predicts the deformation.

8.3 Summary of Results

In conclusion, we have seen that, once again, the Föppl-von Kármán model gives accurate results only up to small sheet angles, $\lesssim 30°$ and at this point significant divergence of the models occurs. Interestingly the Föppl-von Kármán model predicts an apparently monotonic

increase in deflection and erroneous large strains. This is due to the truncated Föppl-von Kármán strain tensor. On the other hand, the extended Föppl-von Kármán model can be used until very large rotations occur.

We have shown in this section that model comparison can be made easily even for a relatively complicated geometry, using a unified method of discretization. This demonstrates the capabilities of the implemented code which will hopefully provide a strong basis for future research.

Chapter 9

Conclusion

In this thesis we have outlined several plate models and their descent from three-dimensional elasticity, these are:

1. The Koiter-Steigmann model, suitable for finite strains and arbitrary rotations.
2. The well-known Föppl-von Kármán model, which is suitable for small displacements and moderate rotations.
3. An apparently novel moderate-to-large rotation model which we refer to as the extended Föppl-von Kármán model.

Following this, we described a generic method for discretizing fourth-order, two-dimensional variational equations using a combination of Bell elements and boundary patches of curved elements. As the explicit construction of the curved-Bell basis is not available in the literature, we provided it along with derivation of the relevant sub-matrices needed in the construction. We proceeded by describing the implementation of these methods into the open-source finite element library, `oomph-lib`. Using this method, we discretized the three plate models and validated the results.

Finally we used the finite element plate models, in conjunction with other numerical and analytic techniques, to analyze three simple systems in order to highlight the differences between the various models discussed in this thesis.

In the study of the first system, a clamped inflated circular sheet, we used a two-parameter fitting strategy to determine both Young's modulus and pre-stretch, by comparing numerical predictions of the sheet deflection to an inflation experiment. The accuracy of this technique was assessed by comparison to a uniaxial tension experiment. We completely characterized

the system and achieved a quantitative agreement with the experiments. Importantly, non-axisymmetric pre-stretch was found to be unimportant to the maximum deflection of the sheet. We also established bounds in which fitting using the Föppl-von Kármán model was appropriate. Ultimately it was found that when the Föppl-von Kármán model became inaccurate the Koiter-Steigmann model provided a realistic alternative for the fitting procedure. Alternatively, using the appropriate (established) bounds, the Föppl-von Kármán performed appreciably but had larger associated errors. This system served to highlight the importance of choosing the appropriate plate model when determining constitutive properties of sheets, e.g. Young's modulus.

In the second study, we considered a circular sheet subject to a sliding-type clamp: this set-up is prone to a wrinkling instability at a particular inflation pressure. For this system we demonstrated that the choice of plate model greatly affects the onset of wrinkling. In particular, the Föppl-von Kármán model predicts wrinkling onset at a universal value of nondimensional pressure with a single onset wavenumber, independent of the relative thickness. The Koiter-Steigmann model, in contrast, predicted that this thickness-independent behaviour broke down for sheets of greater relative thickness than $h \approx 0.0075$. The extended Föppl-von Kármán model successfully described this breakdown and agreed quantitatively with the Koiter-Steigmann model for sheets of moderate thickness: however for relatively thicker sheets the extended Föppl-von Kármán model failed to quantitatively predict the correct onset pressures.

Finally, we demonstrated the flexibility of our implementation by considering a complicated domain shape: a fish-shaped sheet, clamped at one end. This cantilever-type displacement of a sheet further served the purpose of highlighting the differences between the various plate models, and more specifically the approximations in the underlying unit-normal. The Föppl-von Kármán equations picked up the correct, approximately isometric behaviour at small pressures, but failed to predict the onset of nonlinear pressure-deflection behaviour. This culminated in the prediction of large erroneous stretching in the moderate displacement regime. The origin of this stretching was then confirmed by considering a simplified system. The arbitrary-rotation Koiter-Steigmann model, by contrast, predicted approximately isometric behaviour throughout the whole regime. The new, extended Föppl-von Kármán model was found to perform well in this scenario and remained in quantitative agreement with the Koiter-Steigmann prediction until the sheet turned over. This further highlights

the utility of the newly derived model.

These simple systems serve to highlight differences between the various models and provide useful benchmarks for when various approximations are appropriate, particularly assumptions on the magnitude of rotations. They further serve to highlight the necessity of having a generic framework for comparing models, which we have provided in this thesis.

For future work an important further comparison would be between the predictions of the Koiter-Steigmann model and three-dimensional elasticity. In this study we have described the Koiter-Steigmann model as 'accurate' based on the minimal assumptions made in its descent from three-dimensional elasticity: however, to what extent these assumptions manifest themselves in the accuracy of the predicted deformations is still an open question. The most important result of this study is that, perhaps surprisingly, the Föppl-von Kármán model is only appropriate for the study of very thin-sheets, for which Föppl-von Kármán only described the leading order behaviour in a thickness-wise expansion.

Bibliography

E. Acerbi, G. Buttazzo, and D. Percivale. Thin inclusions in linear elasticity: a variational approach. *Journal für die reine und angewandte Mathematik*, 386(99):115, 1988.

M. S. Alnæs, J. Blechta, J. Hake, A. Johansson, B. Kehlet, A. Logg, C. Richardson, J. Ring, M. E. Rognes, and G. N. Wells. The FEniCS Project Version 1.5. *Archive of Numerical Software*, 3(100), 2015.

J. Argyris, I. Fried, and D. Scharpf. The TUBA family of plate elements for the matrix displacement method. *The Aeronautical Journal*, 72(692):701–709, 1968.

D. Arnold and F. Brezzi. Locking-free finite element methods for shells. *Mathematics of Computation of the American Mathematical Society*, 66(217):1–14, 1997.

D. N. Arnold. Mixed finite element methods for elliptic problems. *Computer Methods in Applied Mechanics and Engineering*, 82(1):281 – 300, 1990. Proceedings of the Workshop on Reliability in Computational Mechanics.

A. Arza, R. Schroll, and E. Cerda. Near and far from the threshold analysis of rectangular elastic plates. *Journal of Physics A: Mathematical and Theoretical*, 46(13), 2013.

H. Askes and E. C. Aifantis. Gradient elasticity in statics and dynamics: An overview of formulations, length scale identification procedures, finite element implementations and new results. *International Journal of Solids and Structures*, 48(13):1962 – 1990, 2011.

B. Audoly and Y. Pomeau. *Elasticity and geometry: from hair curls to the non-linear response of shells*. Oxford University Press, 2010.

J. M. Ball. Convexity conditions and existence theorems in nonlinear elasticity. *Archive for Rational Mechanics and Analysis*, 63(4):337–403, 1976.

Y. Bard. *Nonlinear Parameter Estimation*. Academic Press, New York, New York, USA, 1974.

K.-J. Bathe and E. N. Dvorkin. A four-node plate bending element based on Mindlin/Reissner plate theory and a mixed interpolation. *International Journal for Numerical Methods in Engineering*, 21(2):367–383, 1985.

K.-J. Bathe, F. Brezzi, and S. W. Cho. The MITC7 and MITC9 plate bending elements. *Computers & Structures*, 32(3):797 – 814, 1989.

Y. Bazilevs, V. Calo, J. Cottrell, J. Evans, T. Hughes, S. Lipton, M. Scott, and T. Sederberg. Isogeometric analysis using T-splines. *Computer Methods in Applied Mechanics and Engineering*, 199(5):229 – 263, 2010.

E. Becker, G. Carey, and J. Oden. *Finite elements: an introduction*. Texas finite element series. Prentice-Hall, 1981.

M. R. Begley and T. J. Mackin. Spherical indentation of freestanding circular thin films in the membrane regime. *Journal of the Mechanics and Physics of Solids*, 52(9):2005 – 2023, 2004.

K. Bell. A refined triangular plate bending finite element. *International Journal for Numerical Methods in Engineering*, 1(1):101–122, 1969.

P. Bella and R. Kohn. Wrinkling of a thin circular sheet bonded to a spherical substrate. *Philosophical Transactions of the Royal Society A: Mathematical, Physical and Engineering Sciences*, 375(2093), 2017.

C. Berger, R. Phillips, A. Centeno, A. Zurutuza, and A. Vijayaraghavan. Capacitive pressure sensing with suspended graphene-polymer heterostructure membranes. *Nanoscale*, 9: 17439–17449, 2017a.

C. Berger, R. Phillips, I. Pasternak, J. Sobieski, W. Strupinski, and A. Vijayaraghavan. Touch-mode capacitive pressure sensor with graphene-polymer heterostructure membrane. *2D Materials*, 5(1):015025, 2017b.

C. N. Berger, M. Dirschka, and A. Vijayaraghavan. Ultra-thin graphene-polymer heterostructure membranes. *Nanoscale*, 8:17928–17939, 2016.

M. Bernadou. C1-curved finite elements with numerical integration for thin plate and thin shell problems : part 1 : construction and interpolation properties of curved C1 finite elements. Research Report RR-1626, INRIA, 1992. Projet MODULEF.

M. Bernadou. C1-curved finite elements with numerical integration for thin plate and thin shell problems, part 1: construction and interpolation properties of curved C1 finite elements. *Computer Methods in Applied Mechanics and Engineering*, 102(2):255 – 289, 1993a.

M. Bernadou. C1-curved finite elements with numerical integration for thin plate and thin shell problems, part 2: Approximation of thin plate and thin shell problems. *Computer Methods in Applied Mechanics and Engineering*, 102(3):389 – 421, 1993b.

M. Bernadou. C1-curved finite elements and applications to plate and shell problems. *Journal of Computational and Applied Mathematics*, 50(1):133 – 144, 1994.

M. Bernadou and J.-M. Boisserie. Curved finite elements of class C1: implementation and numerical experiments. Research Report RR-1718, INRIA, 1992. Projet MODULEF.

M. Bernadou and J.-M. Boisserie. Curved finite elements of class C1: Implementation and numerical experiments. part 1: Construction and numerical tests of the interpolation properties. *Computer Methods in Applied Mechanics and Engineering*, 106(1):229 – 269, 1993.

M. Bernadou, P.-L. George, and A. Hassim. *MODULEF: A modular library of finite elements.* Inria, 1986.

M. Bischoff and E. Ramm. Shear deformable shell elements for large strains and rotations. *International Journal for Numerical Methods in Engineering*, 40(23):4427–4449, 1997.

J. R. Blandino, J. D. Johnston, and U. K. Dharamsi. Corner wrinkling of a square membrane due to symmetric mechanical loads. *Journal of Spacecraft and Rockets*, 39(5):717–724, 2002.

D. Boffi and C. Lovadina. Analysis of new augmented Lagrangian formulations for mixed finite element schemes. *Numerische Mathematik*, 75(4):405–419, 1997.

F. Bogner. The generation of interelement-compatible stiffness and mass matrices by the use of interpolation formulas. In *Proc. Conf. Matrix Meth. Struct. Mech.*, pages 397–443. Wright-Patterson AFB, 1965.

F. Box, D. Vella, R. W. Style, and J. A. Neufeld. Indentation of a floating elastic sheet: geometry versus applied tension. *Proceedings of the Royal Society A: Mathematical, Physical and Engineering Sciences*, 473(2206):20170335, 2017.

A. Braides. *Gamma-convergence for beginners*, volume 22 of *Oxford Lecture Series in Mathematics and its Applications*. Clarendon Press, 2002.

A. Braides and L. Truskinovsky. Asymptotic expansions by Γ-convergence. *Continuum Mechanics and Thermodynamics*, 20(1):21–62, 2008.

K. A. Brakke. The surface evolver. *Experimental Mathematics*, 1(2):141–165, 1992. URL `http://dx.doi.org/10.1080/10586458.1992.10504253`.

F. Brezzi and K.-J. Bathe. A discourse on the stability conditions for mixed finite element formulations. *Computer Methods in Applied Mechanics and Engineering*, 82(1):27 – 57, 1990. Proceedings of the Workshop on Reliability in Computational Mechanics.

F. Brezzi and M. Fortin. *Mixed and hybrid finite element methods*, volume 15 of *Springer Series in Computational Mechanics*. Springer-Verlag, 1991.

H. Brunner. Collocation methods for Volterra integral and related functional differential equations. Cambridge Monographs on Applied and Computational Mathematics. Cambridge University Press, 2004.

J. F. Caseiro, R. A. F. Valente, A. Reali, J. Kiendl, F. Auricchio, and R. J. Alves de Sousa. On the assumed natural strain method to alleviate locking in solid-shell NURBS-based finite elements. *Computational Mechanics*, 53(6):1341–1353, 2014.

A. Castellanos-Gomez, M. Poot, G. A. Steele, H. S. J. van der Zant, N. Agraït, and G. Rubio-Bollinger. Elastic properties of freely suspended MoS2 nanosheets. *Advanced Materials*, 24(6):772–775, 2012.

E. Cerda. Mechanics of scars. *Journal of Biomechanics*, 38(8):1598–1603, 2005.

E. Cerda and L. Mahadevan. Geometry and physics of wrinkling. *Physical Review Letters*, 90:074302, 2003.

E. Cerda, K. Ravi-Chandar, and L. Mahadevan. Wrinkling of an elastic sheet under tension. *Nature*, 419(6907):579–580, 2002.

C. Chinosi and C. Lovadina. Numerical analysis of some mixed finite element methods for Reissner-Mindlin plates. *Computational Mechanics*, 16(1):36–44, 1995.

J. Chopin and A. Kudrolli. Helicoids, wrinkles, and loops in twisted ribbons. *Physical Review Letters*, 111:174302, 2013.

J. Chopin, V. Démery, and B. Davidovitch. Roadmap to the morphological instabilities of a stretched twisted ribbon. *Journal of Elasticity*, 119(1):137–189, 2015.

P. Ciarlet. Basic error estimates for elliptic problems. In *Finite Element Methods (Part 1)*, volume 2 of *Handbook of Numerical Analysis*, pages 17 – 351. Elsevier, 1991.

P. G. Ciarlet. A justification of the von Kármán equations. *Archive for Rational Mechanics and Analysis*, 73(4):349–389, 1980.

P. G. Ciarlet. *Mathematical elasticity, vol. I: Three-dimensional elasticity*, volume 20 of *Studies in Mathematics and its Applications*. Elsevier, 1988.

P. G. Ciarlet. *Mathematical elasticity, vol. II: Theory of plates*, volume 27 of *Studies in Mathematics and its Applications*. 1997.

P. G. Ciarlet. An introduction to differential geometry with applications to elasticity. *Journal of Elasticity*, 78(1-3):1–215, 2005.

F. Cirak and M. Ortiz. Fully C1-conforming subdivision elements for finite deformation thin-shell analysis. *International Journal for Numerical Methods in Engineering*, 51(7): 813–833, 2001.

F. Cirak, M. Ortiz, and P. Schröder. Subdivision surfaces: a new paradigm for thin-shell finite-element analysis. *International Journal for Numerical Methods in Engineering*, 47 (12):2039–2072, 2000.

F. Cirak, M. J. Scott, E. K. Antonsson, M. Ortiz, and P. Schröder. Integrated modeling, finite-element analysis, and engineering design for thin-shell structures using subdivision. *Computer-Aided Design*, 34(2):137 – 148, 2002.

B. H. Coburn, A. Pirrera, P. M. Weaver, and S. Vidoli. Tristability of an orthotropic doubly curved shell. *Composite Structures*, 96:446 – 454, 2013.

C. D. Coman. Asymmetric bifurcations in a pressurised circular thin plate under initial tension. *Mechanics Research Communications*, 47:11 – 17, 2013.

C. D. Coman and A. P. Bassom. On the wrinkling of a pre-stressed annular thin film in tension. *Journal of the Mechanics and Physics of Solids*, 55(8):1601 – 1617, 2007.

C. D. Coman and A. P. Bassom. On the nonlinear membrane approximation and edge-wrinkling. *International Journal of Solids and Structures*, 82:85 – 94, 2016.

C. D. Coman, M. T. Matthews, and A. P. Bassom. Asymptotic phenomena in pressurized thin films. *Proceedings of the Royal Society of London A: Mathematical, Physical and Engineering Sciences*, 471(2182), 2015.

H. Dannenberg. Measurement of adhesion by a blister method. *Journal of Applied Polymer Science*, 5(14):125–134, 1961.

B. Davidovitch, R. D. Schroll, D. Vella, M. Adda-Bedia, and E. A. Cerda. Prototypical model for tensional wrinkling in thin sheets. *Proceedings of the National Academy of Sciences*, 108(45):18227–18232, 2011.

B. Davidovitch, R. D. Schroll, and E. Cerda. Nonperturbative model for wrinkling in highly bendable sheets. *Physical Review E*, 85:066115, 2012.

B. Davidovitch, Y. Sun, and G. M. Grason. Geometrically incompatible confinement of solids. *Proceedings of the National Academy of Sciences*, 116(5):1483–1488, 2019.

E. de Doncker and I. Robinson. Algorithm 612: Triex: Integration over a triangle using nonlinear extrapolation. *ACM Trans. Math. Softw.*, 10(1):17–22, 1984.

M. Delfani. Nonlinear elasticity of monolayer hexagonal crystals: Theory and application to circular bulge test. *European Journal of Mechanics - A/Solids*, 68:117 – 132, 2018.

M. A. Dias, J. A. Hanna, and C. D. Santangelo. Programmed buckling by controlled lateral swelling in a thin elastic sheet. *Physical Review E*, 84:036603, 2011.

A. Drozdov and J. deClaville Christiansen. Bending of multilayer nanomembranes. *Composite Structures*, 182:261 – 272, 2017.

E. N. Dvorkin and K.-J. Bathe. A continuum mechanics based four-node shell element for general nonlinear analysis. 1984.

J. W. Eaton, D. Bateman, S. Hauberg, and R. Wehbring. *GNU Octave version 3.8.1 manual: a high-level interactive language for numerical computations*. CreateSpace Independent Publishing Platform, 2014. URL `http://www.gnu.org/software/octave/doc/interpreter`.

E. Efrati, E. Sharon, and R. Kupferman. Elastic theory of unconstrained non-Euclidean plates. *Journal of the Mechanics and Physics of Solids*, 57(4):762 – 775, 2009.

P. Fischer. *C1 continuous methods in computational gradient elasticity*. PhD thesis, Technischen Fakultät der Universität Erlangen-Nürnberg, 2011.

P. Fischer, J. Mergheim, and P. Steinmann. On the C1 continuous discretization of non-linear gradient elasticity: A comparison of NEM and FEM based on Bernstein-Bézier patches. *International Journal for Numerical Methods in Engineering*, 82(10):1282–1307, 2010.

M. Focardi. Γ-convergence: a tool to investigate physical phenomena across scales. *Mathematical Methods in the Applied Sciences*, 35(14):1613–1658, 2012.

D. D. Fox, A. Raoult, and J. C. Simo. A justification of nonlinear properly invariant plate theories. *Archive for Rational Mechanics and Analysis*, 124(2):157–199, 1993.

G. Friesecke, D. R. James, and S. Müller. A hierarchy of plate models derived from nonlinear elasticity by gamma-convergence. *Archive for Rational Mechanics and Analysis*, 180(2): 183–236, 2006.

B. Fu, E. Sperber, and F. Eke. Solar sail technology–a state of the art review. *Progress in Aerospace Sciences*, 86:1 – 19, 2016.

J. Géminard, R. Bernal, and F. Melo. Wrinkle formations in axi-symmetrically stretched membranes. *European Physics Journal E*, 15(2):117–126, 2004.

A. N. Gent and L. H. Lewandowski. Blow-off pressures for adhering layers. *Journal of Applied Polymer Science*, 33(5):1567–1577, 1987.

J. Genzer and J. Groenewold. Soft matter with hard skin: From skin wrinkles to templating and material characterization. *Soft Matter*, 2:310, 2006.

A. E. Green. The equilibrium and elastic stability of a thin twisted strip. *Proceedings of the Royal Society of London. Series A-Mathematical and Physical Sciences*, 154(882):430–455, 1936.

A. E. Green. The elastic stability of a thin twisted strip. II. *Proceedings of the Royal Society of London. Series A, Mathematical and Physical Sciences*, 161(905):197–220, 1937.

S. Guo, K.-T. Wan, and D. A. Dillard. A bending-to-stretching analysis of the blister test in the presence of tensile residual stress. *International Journal of Solids and Structures*, 42(9):2771 – 2784, 2005.

J. S. Hale, M. Brunetti, S. P. Bordas, and C. Maurini. Simple and extensible plate and shell finite element models through automatic code generation tools. *Computers & Structures*, 209:163 – 181, 2018.

W. Hamouche, C. Maurini, S. Vidoli, and A. Vincenti. Multi-parameter actuation of a neutrally stable shell: a flexible gear-less motor. *Proceedings of the Royal Society A: Mathematical, Physical and Engineering Sciences*, 473(2204):20170364, 2017.

T. J. Healey, Q. Li, and R.-B. Cheng. Wrinkling behavior of highly stretched rectangular elastic films via parametric global bifurcation. *Journal of Nonlinear Science*, 23(5):777–805, 2013.

M. Heil and A. L. Hazel. *Fluid-Structure Interaction: Modelling, Simulation, Optimisation*, chapter oomph-lib – An Object-Oriented Multi-Physics Finite-Element Library, pages 19–49. Springer Berlin Heidelberg, Berlin, Heidelberg, 2006. URL `http://dx.doi.org/10.1007/3-540-34596-5_2`.

M. G. Hilgers and A. C. Pipkin. Elastic sheets with bending stiffness. *The Quarterly Journal of Mechanics and Applied Mathematics*, 45(1):57–75, 1992a.

M. G. Hilgers and A. C. Pipkin. Bending energy of highly elastic membranes. *Quarterly of Applied Mathematics*, 50(2):389–400, 1992b.

M. G. Hilgers and A. C. Pipkin. Bending energy of highly elastic membranes II. *Quarterly of Applied Mathematics*, LIV(2):307–316, 1996.

D. P. Holmes and A. J. Crosby. Draping films: A wrinkle to fold transition. *Physical Review Letters*, 105:038303, 2010.

J. Hřebíček. Numerical analysis of the general biharmonic problem by the finite element method. *Aplikace matematiky*, 27(5):352–374, 1982.

M.-C. Hsu and Y. Bazilevs. Fluid–structure interaction modeling of wind turbines: simulating the full machine. *Computational Mechanics*, 50(6):821–833, 2012.

J. Huang, M. Juszkiewicz, W. H. de Jeu, E. Cerda, T. Emrick, N. Menon, and T. P. Russell. Capillary wrinkling of floating thin polymer films. *Science*, 317(5838):650–653, 2007.

J. Huang, B. Davidovitch, C. D. Santangelo, T. P. Russell, and N. Menon. Smooth cascade of wrinkles at the edge of a floating elastic film. *Physical Review Letters*, 105:038302, 2010.

T. Hughes, J. Cottrell, and Y. Bazilevs. Isogeometric analysis: CAD, finite elements, NURBS, exact geometry and mesh refinement. *Computer Methods in Applied Mechanics and Engineering*, 194(39):4135 – 4195, 2005.

J. Hure, B. Roman, and J. Bico. Stamping and wrinkling of elastic plates. *Physical Review Letters*, 109:054302, 2012.

C. Jaupart and F. Lévy. Folding in regions of extension. *Geophysical Journal International*, 185(3):1120–1134, 2011.

M. Kapl, G. Sangalli, and T. Takacs. Construction of analysis-suitable G1 planar multi-patch parameterizations. *Computer-Aided Design*, 97:41 – 55, 2018.

M. Kapl, G. Sangalli, and T. Takacs. An isogeometric C1 subspace on unstructured multi-patch planar domains. *Computer Aided Geometric Design*, 69:55 – 75, 2019.

P. Kere and M. Lyly. Reissner-Mindlin-von Kármán type plate model for nonlinear analysis of laminated composite structures. *Composite Structures*, 71(3):289 – 292, 2005. Fifth International Conference on Composite Science and Technology.

E. Khestanova, F. Guinea, L. Fumagalli, A. Geim, and I. Grigorieva. Universal shape and pressure inside bubbles appearing in van der Waals heterostructures. *Nature communications*, 7:12587, 2016.

J. Kiendl. *Isogeometric analysis and shape optimal design of shell structures*. PhD thesis, Technische Universität München, 2011.

J. Kiendl, K.-U. Bletzinger, J. Linhard, and R. Wüchner. Isogeometric shell analysis with Kirchhoff-Love elements. *Computer Methods in Applied Mechanics and Engineering*, 198 (49):3902 – 3914, 2009.

J. Kiendl, Y. Bazilevs, M.-C. Hsu, R. Wüchner, and K.-U. Bletzinger. The bending strip method for isogeometric analysis of Kirchhoff-Love shell structures comprised of multiple patches. *Computer Methods in Applied Mechanics and Engineering*, 199(37):2403 – 2416, 2010.

J. Kiendl, M.-C. Hsu, M. C. Wu, and A. Reali. Isogeometric Kirchhoff-Love shell formulations for general hyperelastic materials. *Computer Methods in Applied Mechanics and Engineering*, 291:280 – 303, 2015.

J. Kierzenka and L. F. Shampine. A BVP solver based on residual control and the Matlab PSE. *ACM Transactions on Mathematical Software*, 27(3):299–316, 2001.

D.-H. Kim, J.-H. Ahn, W. M. Choi, H.-S. Kim, T.-H. Kim, J. Song, Y. Y. Huang, Z. Liu, C. Lu, and J. A. Rogers. Stretchable and foldable silicon integrated circuits. *Science*, 320 (5875):507–511, 2008.

D.-H. Kim, N. Lu, R. Ma, Y.-S. Kim, R.-H. Kim, S. Wang, J. Wu, S. M. Won, H. Tao, A. Islam, K. J. Yu, T. il Kim, R. Chowdhury, M. Ying, L. Xu, M. Li, H.-J. Chung, H. Keum, M. McCormick, P. Liu, Y.-W. Zhang, F. G. Omenetto, Y. Huang, T. Coleman, and J. A. Rogers. Epidermal electronics. *Science*, 333(6044):838–843, 2011.

H. King, R. D. Schroll, B. Davidovitch, and N. Menon. Elastic sheet on a liquid drop reveals wrinkling and crumpling as distinct symmetry-breaking instabilities. *Proceedings of the National Academy of Sciences*, 109(25):9716–9720, 2012.

S. P. Koenig, N. G. Boddeti, M. L. Dunn, and J. S. Bunch. Ultrastrong adhesion of graphene membranes. *Nature nanotechnology*, 6(9):543, 2011.

W. T. Koiter. On the nonlinear theory of thin elastic shells. *Proceedings of the Koninklijke Nederlandse Akademie van Wetenschappen Series B-Physical Sciences*, 69:1–54, 1966.

W. T. Koiter. On foundations of linear theory of thin elastic shells. 1. *Proceedings of the Koninklijke Nederlandse Akademie van Wetenschappen Series B-Physical Sciences*, 73(3): 169, 1970.

A. Kudrolli and J. Chopin. Tension-dependent transverse buckles and wrinkles in twisted elastic sheets. *Proceedings of the Royal Society A: Mathematical, Physical and Engineering Sciences*, 474(2214), 2018.

L. Landau and E. Lifshitz. *Theory of elasticity (third edition)*, volume 7 of *Course of Theoretical Physics*. Butterworth-Heinemann, Oxford, 3rd edition, 1986.

H. Le Dret and A. Raoult. The membrane shell model in nonlinear elasticity: A variational asymptotic derivation. *Journal of Nonlinear Science*, 6(1):59–84, 1996.

Y. Lecieux and R. Bouzidi. Numerical wrinkling prediction of thin hyperelastic structures by direct energy minimization. *Advances in Engineering Software*, 50(1):57–68, 2012.

Q. Li and T. J. Healey. Stability boundaries for wrinkling in highly stretched elastic sheets. *Journal of the Mechanics and Physics of Solids*, 97:260 – 274, 2016.

G. López-Polín, C. Gómez-Navarro, V. Parente, F. Guinea, M. I. Katsnelson, F. Perez-Murano, and J. Gómez-Herrero. Increasing the elastic modulus of graphene by controlled defect creation. *Nature Physics*, 11(1):26, 2015.

G. López-Polín, M. Jaafar, F. Guinea, R. Roldán, C. Gómez-Navarro, and J. Gómez-Herrero. The influence of strain on the elastic constants of graphene. *Carbon*, 124:42 – 48, 2017.

J. Los, A. Fasolino, and M. Katsnelson. Mechanics of thermally fluctuating membranes. *npj 2D Materials and Applications*, 1(1):9, 2017.

J. H. Los, A. Fasolino, and M. I. Katsnelson. Scaling behavior and strain dependence of in-plane elastic properties of graphene. *Physical Review Letters*, 116:015901, 2016.

C. Lovadina. A new class of mixed finite element methods for Reissner-Mindlin plates. *SIAM Journal on Numerical Analysis*, 33(6):2457–2467, 1996.

L. Mahadevan, R. Bendick, and H. Liang. Why subduction zones are curved. *Tectonics*, 29 (6), 2010.

E. H. Mansfield. *Tension field theory, a new approach which shows its duality with inextensional theory*, pages 305–320. Springer Berlin Heidelberg, Berlin, Heidelberg, 1969.

L. Mansfield. Approximation of the boundary in the finite element solution of fourth order problems. *SIAM Journal on Numerical Analysis*, 15(3):568–579, 1978.

G. Marckmann and E. Verron. Comparison of hyperelastic models for rubber-like materials. *Rubber Chemistry and Technology*, 79(5):835–858, 2006.

O. Masayuki. Full-explicit interpolation formulas for the Argyris triangle. *Computer Methods in Applied Mechanics and Engineering*, 106(3):381 – 394, 1993.

M. Mooney. A theory of large elastic deformation. *Journal of applied physics*, 11(9):582–592, 1940.

J. J. Moré, D. C. Sorensen, K. Hillstrom, and B. Garbow. The MINPACK project. *Sources and development of mathematical software*, 25:88–111, 1984.

I. Müller and P. Strehlow. *Rubber and rubber balloons: paradigms of thermodynamics*, volume 637. Springer Science & Business Media, 2004.

P. Naghdi. The theory of shells and plates. In C. Truesdell, editor, *Linear Theories of Elasticity and Thermoelasticity*. Berlin: Springer, 1973.

P. M. Naghdi. Foundations of elastic shell theory. Technical report, University of California, Berkeley Institute of Engineering Research, 1962.

V. Nayyar, K. Ravi-Chandar, and R. Huang. Stretch-induced stress patterns and wrinkles in hyperelastic thin sheets. *International Journal of Solids and Structures*, 48(25-26):3471 – 3483, 2011.

T. Nguyen, K. Karčiauskas, and J. Peters. C1 finite elements on non-tensor-product 2d and 3d manifolds. *Applied Mathematics and Computation*, 272:148 – 158, 2016. Subdivision, Geometric and Algebraic Methods, Isogeometric Analysis and Refinability.

V. P. Nguyen, C. Anitescu, S. P. Bordas, and T. Rabczuk. Isogeometric analysis: An overview and computer implementation aspects. *Mathematics and Computers in Simulation*, 117: 89 – 116, 2015.

W. L. Oberkampf, T. G. Trucano, and C. Hirsch. Verification, validation, and predictive capability in computational engineering and physics. *Applied Mechanics Reviews*, 57(5): 345–384, 2004.

J. T. Oden and J. N. Reddy. *An introduction to the mathematical theory of finite elements*. Wiley, 1976.

M. Okabe. Explicit interpolation formulas for the Bell triangle. *Computer Methods in Applied Mechanics and Engineering*, 117(3):411 – 421, 1994.

J. D. Paulsen, V. Démery, C. D. Santangelo, T. P. Russell, B. Davidovitch, and N. Menon. Optimal wrapping of liquid droplets with ultrathin sheets. *Nature materials*, 14(12):1206, 2015.

J. D. Paulsen, E. Hohlfeld, H. King, J. Huang, Z. Qiu, T. P. Russell, N. Menon, D. Vella, and B. Davidovitch. Curvature-induced stiffness and the spatial variation of wavelength in wrinkled sheets. *Proceedings of the National Academy of Sciences*, 113(5):1144–1149, 2016.

J. Petera and J. F. T. Pittman. Isoparametric Hermite elements. *International Journal for Numerical Methods in Engineering*, 37(20):3489–3519, 1994.

L. Piegl and W. Tiller. *The NURBS book*. Monographs in Visual Communication. Springer-Verlag, 1997.

D. Pihler-Puzović, R. Périllat, M. Russell, A. Juel, and M. Heil. Modelling the suppression of viscous fingering in elastic-walled Hele-Shaw cells. *Journal of Fluid Mechanics*, 731: 162–183, 2013.

D. Pihler-Puzović, A. Juel, G. G. Peng, J. R. Lister, and M. Heil. Displacement flows under elastic membranes. Part 1. Experiments and direct numerical simulations. *Journal of Fluid Mechanics*, 784:487–511, 2015.

A. C. Pipkin. The relaxed energy density for isotropic elastic membranes. *IMA journal of applied mathematics*, 36(1):85–99, 1986.

P. Portela, P. Camanho, P. Weaver, and I. Bond. Analysis of morphing, multi stable structures actuated by piezoelectric patches. *Computers & Structures*, 86(3):347 – 356, 2008. Smart Structures.

M. J. Powell. A hybrid method for nonlinear equations. *Numerical methods for nonlinear algebraic equations*, 1970.

H. Press, A. Teukolsky, T. Vetterling, and P. Flannery. *Numerical Recipes in C++. The Art of Computer Programming*. Cambridge University Press New York, 1988.

E. Puntel, L. Deseri, and E. Fried. Wrinkling of a stretched thin sheet. *Journal of Elasticity*, 105(1):137–170, 2010.

S. Raayai-Ardakani, J. L. Yagüe, K. K. Gleason, and M. C. Boyce. Mechanics of graded wrinkling. *Journal of Applied Mechanics*, 83(12):121011, 2016.

A. Reali and H. Gomez. An isogeometric collocation approach for Bernoulli-Euler beams and Kirchhoff plates. *Computer Methods in Applied Mechanics and Engineering*, 284:623 – 636, 2015.

J. A. Rogers, T. Someya, and Y. Huang. Materials and mechanics for stretchable electronics. *Science*, 327(5973):1603–1607, 2010.

M. Rubinstein and R. H. Colby. *Polymer physics*, volume 23. Oxford University Press New York, 2003.

H. Růžičková and A. Ženíšek. Finite elements methods for solving viscoelastic thin plates. *Aplikace matematiky*, 29(2):81–103, 1984.

T. Schiffer, F. Aurenhammer, and M. Demuth. Computing convex quadrangulations. *Discrete Applied Mathematics*, 160(4):648 – 656, 2012.

D. Schillinger. *Isogeometric Finite Element Analysis*, pages 1–19. Springer Berlin Heidelberg, Berlin, Heidelberg, 2018.

R. D. Schroll, E. Katifori, and B. Davidovitch. Elastic building blocks for confined sheets. *Physical Review Letters*, 106:074301, 2011.

R. D. Schroll, M. Adda-Bedia, E. Cerda, J. Huang, N. Menon, T. P. Russell, K. B. Toga, D. Vella, and B. Davidovitch. Capillary deformations of bendable films. *Physical Review Letters*, 111:014301, 2013.

M. Scott, R. Simpson, J. Evans, S. Lipton, S. Bordas, T. Hughes, and T. Sederberg. Isogeometric boundary element analysis using unstructured t-splines. *Computer Methods in Applied Mechanics and Engineering*, 254:197 – 221, 2013.

K. A. Seffen and C. Maurini. Growth and shape control of disks by bending and extension. *Journal of the Mechanics and Physics of Solids*, 61(1):190 – 204, 2013.

M. Sheploak and J. Dugundji. Large deflections of clamped circular plates under initial tension and transitions to membrane behavior. *Journal of Applied Mechanics*, 65(1):107–115, 1998.

J. R. Shewchuk. Triangle: Engineering a 2D Quality Mesh Generator and Delaunay Triangulator. In M. C. Lin and D. Manocha, editors, *Applied computational geometry: towards geometric engineering*, volume 1148 of *Lecture Notes in Computer Science*, pages 203–222. Springer-Verlag, 1996. From the First ACM Workshop on Applied Computational Geometry.

J. C. Simo and M. S. Rifai. A class of mixed assumed strain methods and the method of incompatible modes. *International Journal for Numerical Methods in Engineering*, 29(8): 1595–1638, 1990.

A. A. Sipos and E. Fehér. Disappearance of stretch-induced wrinkles of thin sheets: A study of orthotropic films. *International Journal of Solids and Structures*, 97-98:275 – 283, 2016.

M. K. Small and W. Nix. Analysis of the accuracy of the bulge test in determining the mechanical properties of thin films. *Journal of Materials Research*, 7(6):1553–1563, 1992.

M. Smith. *ABAQUS/Standard User's Manual, Version 6.9*. Simulia, 2009.

D. J. Steigmann. Tension-field theory. In *Proceedings of the Royal Society of London A: Mathematical, Physical and Engineering Sciences*, volume 429, pages 141–173. The Royal Society, 1990.

D. J. Steigmann. Equilibrium theory for magnetic elastomers and magnetoelastic membranes. *International Journal of Non-Linear Mechanics*, 39(7):1193 – 1216, 2004.

D. J. Steigmann. Two-dimensional models for the combined bending and stretching of plates and shells based on three-dimensional linear elasticity. *International Journal of Engineering Science*, 46(7):654–676, 2008.

D. J. Steigmann. Applications of polyconvexity and strong ellipticity to nonlinear elasticity and elastic plate theory. In *Poly-, quasi-and rank-one convexity in applied mechanics*, volume 516 of *CISM International Centre for Mechanical Sciences*, pages 265–299. Springer, 2010.

D. J. Steigmann. A well-posed finite-strain model for thin elastic sheets with bending stiffness. *Mathematics and Mechanics of Solids*, 18(1):103–112, 2013.

D. J. Steigmann and R. W. Ogden. Elastic surface—substrate interactions. *Proceedings of the Royal Society of London A: Mathematical, Physical and Engineering Sciences*, 455 (1982):437–474, 1999.

M. Stein and J. M. Hedgpeth. *Analysis of Partly Wrinkled Membranes.* NASA, 1961. (Technical Note D-813).

S. H. Strogatz. *Nonlinear Dynamics and Chaos: With Applications to Physics, Biology, Chemistry, and Engineering.* CRC Press, 2015.

K. Y. Sze. Three-dimensional continuum finite element models for plate/shell analysis. *Progress in Structural Engineering and Materials*, 4(4):400–407, 2002.

K. Y. Sze and L. Q. Yao. A hybrid stress ANS solid-shell element and its generalization for smart structure modelling. Part I—solid-shell element formulation. *International Journal for Numerical Methods in Engineering*, 48(4):545–564, 2000.

R. Szilard. *Theories and applications of plate analysis: classical, numerical and engineering methods.* John Wiley & Sons, 2004.

M. Taylor, K. Bertoldi, and D. J. Steigmann. Spatial resolution of wrinkle patterns in thin elastic sheets at finite strain. *Journal of the Mechanics and Physics of Solids*, 62:163–180, 2014.

M. Taylor, B. Davidovitch, Z. Qiu, and K. Bertoldi. A comparative analysis of numerical approaches to the mechanics of elastic sheets. *Journal of the Mechanics and Physics of Solids*, 79:92 – 107, 2015.

S. Timoshenko and J. Goodier. *Theory of elasticity*. McGraw-Hill, 1969.

S. Timoshenko and S. Woinowsky-Krieger. *Theory of plates and shells*. Engineering Society Monographs. McGraw-Hill, 2nd edition, 1959a.

S. Timoshenko and S. Woinowsky-Krieger. *Theory of plates and shells*, page 418. McGraw-Hill, 2nd edition, 1959b.

K. Trabelsi. Modeling of a membrane for nonlinearly elastic incompressible materials via gamma-convergence. *Analysis and Applications*, 04(01):31–60, 2006.

D. Vella and B. Davidovitch. Indentation metrology of clamped, ultra-thin elastic sheets. *Soft Matter*, 13(11):2264–2278, 2017.

D. Vella, M. Adda-Bedia, and E. Cerda. Capillary wrinkling of elastic membranes. *Soft Matter*, 6:5778–5782, 2010.

D. Vella, A. Ajdari, A. Vaziri, and A. Boudaoud. Wrinkling of pressurized elastic shells. *Physical Review Letters*, 107:174301, 2011.

D. Vella, J. Huang, N. Menon, T. P. Russell, and B. Davidovitch. Indentation of ultrathin elastic films and the emergence of asymptotic isometry. *Physical Review Letters*, 114: 014301, 2015.

R. Vetter, N. Stoop, F. K. Wittel, and H. J. Herrmann. Simulating thin sheets: Buckling, wrinkling, folding and growth. *Journal of Physics: Conference Series*, 487:012012, 2014.

S. Vidoli. Discrete approximations of the Föppl-Von Kármán shell model: From coarse to more refined models. *International Journal of Solids and Structures*, 50(9):1241 – 1252, 2013.

S. Vidoli and C. Maurini. Tristability of thin orthotropic shells with uniform initial curvature. *Proceedings of the Royal Society A: Mathematical, Physical and Engineering Sciences*, 464 (2099):2949–2966, 2008.

J. Voorthuyzen and P. Bergveld. The influence of tensile forces on the deflection of circular diaphragms in pressure sensors. *Sensors and Actuators*, 6(3):201 – 213, 1984.

K.-T. Wan, S. Guo, and D. A. Dillard. A theoretical and numerical study of a thin clamped circular film under an external load in the presence of a tensile residual stress. *Thin Solid Films*, 425(1):150 – 162, 2003.

C. Wang, X. Du, H. Tan, and X. He. A new computational method for wrinkling analysis of gossamer space structures. *International Journal of Solids Structures*, 46(6):1516 – 1526, 2009.

G. Wempner and D. Talaslidis. *Mechanics of solids and shells: theories and approximations*. CRC press, 2002.

J. Williams. Energy release rates for the peeling of flexible membranes and the analysis of blister tests. *International Journal of Fracture*, 87(3):265–288, 1997.

X. Xu, A. Jagota, D. R. Paretkar, and C. Y. Hui. Surface tension measurement from the indentation of clamped thin films. *Soft matter*, 12 23:5121–6, 2016.

E. Zeidler. *Nonlinear functional analysis and its applications*. Nonlinear functional analysis and its applications. Springer, 1st edition, 1986.

A. Ženíšek. Curved triangular finite C^m-elements. *Aplikace matematiky*, 23(5):346–377, 1978.

A. Ženíšek. Nonhomogeneous boundary conditions and curved triangular finite elements. *Aplikace matematiky*, 26(2):121–141, 1981a.

A. Ženíšek. Discrete forms of Friedrichs' inequalities in the finite element method. *RAIRO. Anal. numér.*, 15(3):265–286, 1981b.

D.-B. Zhang, E. Akatyeva, and T. Dumitrică. Bending ultrathin graphene at the margins of continuum mechanics. *Physical Review Letters*, 106:255503, 2011.

Appendix A

Derivation of the Koiter-Steigmann Variational Equation

A.1 Partial Derivatives of the Energy

We provide the derivation of the variational equation from a generic strain-energy function which depends on the curvature $B_{\alpha\beta}$ and the metric tensor $G_{\alpha\beta}$, following the derivation of Steigmann and Ogden [1999]. We start with the assumption of an energy:

$$W = W(G_{\alpha\beta}, B_{\alpha\beta})\,. \tag{A.1.1}$$

In this section, we continue to use the Cartesian material basis of section 3.4, such that $\boldsymbol{g}_\alpha = \hat{\boldsymbol{e}}_\alpha$ and $g = 1$.

The total derivative, written as $\dot{W}$, will thus be given by:

$$\dot{W} = \frac{\partial W}{\partial G_{\alpha\beta}}\dot{G_{\alpha\beta}} + \frac{\partial W}{\partial B_{\alpha\beta}}\dot{B_{\alpha\beta}}\,. \tag{A.1.2}$$

Noting that $\epsilon_{\alpha\beta} = \frac{1}{2}(G_{\alpha\beta} - g_{\alpha\beta})$, we can write:

$$\dot{W} = \frac{1}{2}\frac{\partial W}{\partial \epsilon_{\alpha\beta}}\dot{G_{\alpha\beta}} + \frac{\partial W}{\partial B_{\alpha\beta}}\dot{B_{\alpha\beta}} \tag{A.1.3}$$

By definition of the second Piola-Kirchhoff stress tensor we write:

$$\dot{W} = \frac{1}{2}S_{\alpha\beta}\dot{G_{\alpha\beta}} + \frac{\partial W}{\partial B_{\alpha\beta}}\dot{B_{\alpha\beta}} \tag{A.1.4}$$

where

$$S_{\alpha\beta} \equiv \frac{\partial W}{\partial \epsilon_{\alpha\beta}}. \tag{A.1.5}$$

Now computing the latter derivative we have:

$$\dot{W} = S_{\alpha\beta}(\boldsymbol{G}_\alpha \cdot \dot{\boldsymbol{G}}_\beta) + \frac{\partial W}{\partial B_{\alpha\beta}}\dot{B_{\alpha\beta}}\,. \tag{A.1.6}$$

We proceed by following the results of Steigmann and Ogden [1999] to derive the relevant partial derivative $\partial B_{\gamma\delta}/\partial Y_{i,\alpha}$.

Here we insert a factor of $\sqrt{G}$ for convenience then use the product rule:

$$\dot{B_{\gamma\delta}} = \big(B_{\gamma\delta}\sqrt{G}\frac{1}{\sqrt{G}}\dot{\big)} = -B_{\gamma\delta}\frac{\dot{\sqrt{G}}}{\sqrt{G}} + \frac{1}{\sqrt{G}}(\sqrt{G}\dot{B_{\gamma\delta}}\dot{)} \tag{A.1.7}$$

and computing $\dot{\sqrt{G}}$ we get:

$$\dot{\sqrt{G}} = \frac{1}{2}\frac{\dot{G}}{\sqrt{G}} = \frac{1}{2\sqrt{G}}\mathrm{adj}(\boldsymbol{G})_{\gamma\delta}\,\dot{G_{\gamma\delta}} \tag{A.1.8}$$

where we have used the chain rule and that the derivative of the determinant is the adjugate matrix, written as $\mathrm{adj}(\boldsymbol{G})$. The tensor $\boldsymbol{G}$, here is the *surface* metric tensor:

$$\boldsymbol{G} = G_{\alpha\beta}\hat{\boldsymbol{e}}_\alpha \otimes \hat{\boldsymbol{e}}_\beta\,, \tag{A.1.9}$$

not the 3D metric tensor, $\tilde{\boldsymbol{G}}$, evaluated at the surface, in line with our definition of the midplane stretch G. By definition of the adjugate matrix, which is simply the transpose of the matrix of cofactors, we can write:

$$\dot{\sqrt{G}} = \frac{\sqrt{G}}{2}G^{\gamma\delta}\,\dot{G_{\gamma\delta}} = \sqrt{G}\,G^{\gamma\delta}\,\boldsymbol{G}_\gamma \cdot \dot{\boldsymbol{G}}_\delta = \sqrt{G}\,\boldsymbol{G}^\delta \cdot \dot{\boldsymbol{G}}_\delta \tag{A.1.10}$$

which gives us the full expression:

$$\dot{B_{\gamma\delta}} = -B_{\gamma\delta}\boldsymbol{G}^\mu \cdot \dot{\boldsymbol{G}}_\mu + \frac{1}{\sqrt{G}}(\sqrt{G}\dot{B_{\gamma\delta}}\dot{)} \tag{A.1.11}$$

Next we compute the term: $(\sqrt{G}\,\dot{B_{\gamma\delta}}\dot{)}$. Using the product rule we write:

$$(\sqrt{G}\,\dot{B_{\gamma\delta}}\dot{)} = \dot{Y_{j,\gamma\delta}}\sqrt{G}\hat{N}_j + (\epsilon^{\mu\nu 3}\dot{\boldsymbol{G}}_\mu \times \boldsymbol{G}_\nu) \cdot \boldsymbol{G}_{\gamma,\delta} \tag{A.1.12}$$

Using the Gauss formulae, $\boldsymbol{G}_{\alpha,\beta} = B_{\alpha\beta}\hat{\boldsymbol{N}} + \Gamma^\gamma_{\alpha\beta}\boldsymbol{G}_\gamma$, we can express this as:

$$(\sqrt{G}\,\dot{B_{\gamma\delta}}\dot{)} = \dot{Y_{j,\gamma\delta}}\sqrt{G}\hat{N}_j + (\epsilon^{\mu\nu 3}\dot{\boldsymbol{G}}_\mu \times \boldsymbol{G}_\nu) \cdot (\hat{\boldsymbol{N}}\dot{B_{\gamma\delta}} + \Gamma^\gamma_{\alpha\beta}\boldsymbol{G}_\gamma)\,. \tag{A.1.13}$$

To proceed we need expressions for the last two terms in the equation. We start with the term containing the Christoffel symbol and apply the triple product formula:

$$\epsilon^{\mu\nu 3}(\dot{\boldsymbol{G}}_\mu \times \boldsymbol{G}_\nu) \cdot \boldsymbol{G}_\gamma = \epsilon^{\mu\nu 3}(\boldsymbol{G}_\gamma \times \boldsymbol{G}_\nu) \cdot \dot{\boldsymbol{G}}_\mu \tag{A.1.14}$$

we note that $\boldsymbol{G}_\alpha \times \boldsymbol{G}_\beta = \sqrt{G}\epsilon^{\alpha\beta 3}\hat{\boldsymbol{N}}$ [Wempner and Talaslidis, 2002] and that $\epsilon^{\mu\nu 3}\epsilon^{\sigma\nu 3} = \delta_{\sigma\mu}$ in order to write

$$\epsilon^{\mu\nu 3}(\dot{\boldsymbol{G}}_\mu \times \boldsymbol{G}_\nu) \cdot \boldsymbol{G}_\gamma = \sqrt{G}\,\delta_{\mu\gamma}\,\hat{\boldsymbol{N}} \cdot \dot{\boldsymbol{G}}_\mu = \sqrt{G}\,\hat{\boldsymbol{N}} \cdot \dot{\boldsymbol{G}}_\gamma\,. \tag{A.1.15}$$

We now focus on the curvature term, again applying the triple product formula

$$\epsilon^{\mu\nu 3}(\dot{\boldsymbol{G}}_\mu \times \boldsymbol{G}_\nu) \cdot \hat{\boldsymbol{N}} = \epsilon^{\mu\nu 3}(\boldsymbol{G}_\nu \times \hat{\boldsymbol{N}}) \cdot \dot{\boldsymbol{G}}_\mu \tag{A.1.16}$$

which we can write as:

$$\epsilon^{\mu\nu 3}(\dot{\boldsymbol{G}}_\mu \times \boldsymbol{G}_\nu) \cdot \hat{\boldsymbol{N}} = \sqrt{G}\epsilon^{\mu\nu 3}\epsilon^{\nu\gamma 3}\,\boldsymbol{G}^\gamma \cdot \dot{\boldsymbol{G}}_\mu \tag{A.1.17}$$

using the triple product formula and $\boldsymbol{G}_\alpha \times \hat{\boldsymbol{N}} = \sqrt{G}\,\epsilon^{\alpha\beta 3}\,\boldsymbol{G}^\beta$ [Wempner and Talaslidis, 2002]. We then use the self-inverse property of the Levi-Civita tensor to write:

$$\epsilon^{\mu\nu 3}(\dot{\boldsymbol{G}}_\mu \times \boldsymbol{G}_\nu) \cdot \hat{\boldsymbol{N}} = \sqrt{G}\,\boldsymbol{G}^\mu \cdot \dot{\boldsymbol{G}}_\mu\,. \tag{A.1.18}$$

Combining these results we get the expression for $\dot{B}_{\gamma\delta}$:

$$\dot{B_{\gamma\delta}} = -B_{\gamma\delta}\boldsymbol{G}^\mu \cdot \dot{\boldsymbol{G}}_\mu + \dot{\boldsymbol{G}}_{\gamma,\delta} \cdot \hat{\boldsymbol{N}} + B_{\gamma\delta}\boldsymbol{G}^\mu \cdot \dot{\boldsymbol{G}}_\mu + \Gamma^\gamma_{\alpha\beta}\hat{\boldsymbol{N}} \cdot \dot{\boldsymbol{G}}_\gamma \tag{A.1.19}$$

or cancelling the terms involving curvature:

$$\dot{B_{\gamma\delta}} = \dot{\boldsymbol{G}}_{\gamma,\delta} \cdot \hat{\boldsymbol{N}} + \Gamma^\gamma_{\alpha\beta}\hat{\boldsymbol{N}} \cdot \dot{\boldsymbol{G}}_\gamma\,. \tag{A.1.20}$$

So, putting all together, we have the following expression for the energy:

$$\dot{W} = S_{\alpha\beta}(\boldsymbol{G}_\alpha \cdot \dot{\boldsymbol{G}}_\beta) + \frac{\partial W}{\partial B_{\alpha\beta}}(\hat{\boldsymbol{N}} \cdot \dot{\boldsymbol{G}}_{\alpha,\beta} + \Gamma^\gamma_{\alpha\beta}\hat{\boldsymbol{N}} \cdot \dot{\boldsymbol{G}}_\gamma)\,. \tag{A.1.21}$$

We finally define the bending moment, $\boldsymbol{M}_{\alpha\beta}$, to be:

$$\boldsymbol{M}_{\alpha\beta} \equiv \frac{\partial W}{\partial B_{\alpha\beta}}\hat{\boldsymbol{N}}\,, \tag{A.1.22}$$

giving us the final expression for the energy:

$$\dot{W} = (S_{\alpha\beta}\boldsymbol{G}_\alpha + \boldsymbol{M}_{\alpha\beta}\Gamma^\gamma_{\alpha\beta})\,.\,\dot{\boldsymbol{G}}_\beta + \boldsymbol{M}_{\alpha\beta} \cdot \dot{\boldsymbol{G}}_{\alpha,\beta} \quad . \tag{A.1.23}$$

Appendix B

Expansion of the Unit Normal

For the derivation of the improvement to the Föppl-von Kármán model it is necessary to expand the expression for the unit normal.

The exact expression for curvature is given by (c.f equations 3.4.74-3.4.75)

$$\boldsymbol{B} = \hat{N}_i \boldsymbol{\nabla}\boldsymbol{\nabla} v_i \,. \tag{B.0.1}$$

However, by assumption the in-plane and out-of-plane displacements scale as $\sim h^2$ and $\sim h$ respectively. Thus, the next order correction in the expression for unit normal will be order $\mathcal{O}(h)$ for the in-plane component and order $\mathcal{O}(h^2)$ for the out-of-plane component.

We begin by considering the following expression for $\hat{\boldsymbol{N}} = \sqrt{G}$:

$$\hat{\boldsymbol{N}}\sqrt{G} = \frac{1}{2}\, \epsilon_{\alpha\beta 3}\, \boldsymbol{G}_\alpha \times \boldsymbol{G}_\beta \tag{B.0.2}$$

We rewrite the expression for the cross product as:

$$\begin{aligned} \boldsymbol{G}_\alpha \times \boldsymbol{G}_\beta = (\delta_{\gamma\alpha} + v_{\gamma,\alpha})(\delta_{\mu\beta} + v_{\mu,\beta})\hat{\boldsymbol{e}}_\gamma \times \hat{\boldsymbol{e}}_\mu \\ + [v_{3,\alpha}(\delta_{\mu\beta} + v_{\mu,\beta}) - v_{3,\beta}(\delta_{\mu\alpha} + v_{\mu,\alpha})]\hat{\boldsymbol{e}}_3 \times \hat{\boldsymbol{e}}_\mu \,. \end{aligned} \tag{B.0.3}$$

Now introducing the rescaled displacements of Section 3.5.6, and truncating to h^3, we find:

$$\begin{aligned} \boldsymbol{G}_\alpha \times \boldsymbol{G}_\beta = (\delta_{\mu\beta} + h^2\bar{v}_{\mu,\beta} + \mathcal{O}(h^4))\hat{\boldsymbol{e}}_\alpha \times \hat{\boldsymbol{e}}_\mu + (h^2\bar{v}_{\gamma,\alpha} + \mathcal{O}(h^4))\hat{\boldsymbol{e}}_\gamma \times \hat{\boldsymbol{e}}_\beta \\ + (h\,\bar{v}_{3,\alpha}\delta_{\mu\beta} - h\,\bar{v}_{3,\beta}\delta_{\mu\alpha} + \mathcal{O}(h^3))\hat{\boldsymbol{e}}_3 \times \hat{\boldsymbol{e}}_\mu \,, \end{aligned} \tag{B.0.4}$$

which we substitute into the expression for $\hat{\boldsymbol{N}}\sqrt{G}$:

$$\begin{aligned} \hat{\boldsymbol{N}}\sqrt{G} = \frac{1}{2}\, \epsilon_{\alpha\beta 3}\, [(\delta_{\mu\beta} + h^2\bar{v}_{\mu,\beta} + \mathcal{O}(h^4))\hat{\boldsymbol{e}}_\alpha \times \hat{\boldsymbol{e}}_\mu + (h^2\bar{v}_{\gamma,\alpha} + \mathcal{O}(h^4))\hat{\boldsymbol{e}}_\gamma \times \hat{\boldsymbol{e}}_\beta \\ + (h\,\bar{v}_{3,\alpha}\delta_{\mu\beta} - h\,\bar{v}_{3,\beta}\delta_{\mu\alpha} + \mathcal{O}(h^3))\hat{\boldsymbol{e}}_3 \times \hat{\boldsymbol{e}}_\mu] \,. \end{aligned} \tag{B.0.5}$$

We can simplify this to write:

$$\hat{\boldsymbol{N}}\sqrt{G} = \frac{1}{2}\,\epsilon_{\alpha\beta 3}\,\left[(\delta_{\mu\beta} + 2h^2\bar{v}_{\mu,\beta} + \mathcal{O}(h^4))\hat{\boldsymbol{e}}_\alpha \times \hat{\boldsymbol{e}}_\mu + (2h\,\bar{v}_{3,\alpha} + \mathcal{O}(h^3))\hat{\boldsymbol{e}}_3 \times \hat{\boldsymbol{e}}_\beta\right], \tag{B.0.6}$$

by noting the anti-symmetric property of $\epsilon_{\alpha\beta 3}$ under exchange of indices α and β.

Computing the summations and cross products we can now write:

$$\hat{\boldsymbol{N}}\sqrt{G} = (1 + h^2\bar{v}_{\beta,\beta} + \mathcal{O}(h^4))\hat{\boldsymbol{e}}_3 - (h\,\bar{v}_{3,\alpha} + \mathcal{O}(h^3))\hat{\boldsymbol{e}}_\alpha\,, \tag{B.0.7}$$

which is our final expression for this term.

We now focus our attention on expanding the term $1/\sqrt{G}$. The first term in Taylor expansion will be $1/\sqrt{G}|_{h=0} = 1$. Next we need the derivative of $1/\sqrt{G}$, with respect to h, which is given by:

$$\frac{\partial}{\partial h}\left(\frac{1}{\sqrt{G}}\right) = -\frac{1}{2G^{3/2}}\mathrm{adj}(G)_{\gamma\delta}\;\frac{\partial G_{\gamma\delta}}{\partial h}\,.$$

Thus the coefficient of h in the Taylor expansion is:

$$\frac{\partial}{\partial h}\left(\frac{1}{\sqrt{G}}\right)|_{h=0} = -\frac{1}{2}\mathrm{Tr}\left(\frac{\partial \boldsymbol{G}}{\partial h}\right)|_{h=0}$$

but as the surface metric-tensor $\boldsymbol{G} = \mathbb{1} + 2h^2\bar{\boldsymbol{\epsilon}}$, this term vanishes.

Finally we investigate the h^2 term in the Taylor expansion:

$$\frac{\partial^2}{\partial h^2}\left(\frac{1}{\sqrt{G}}\right)|_{h=0} = -\frac{1}{2G^{3/2}}\mathrm{adj}(G)_{\gamma\delta}\;\frac{\partial^2 G_{\gamma\delta}}{\partial h^2}|_{h=0} - \frac{\partial}{\partial h}\left(\frac{1}{2g^{3/2}}\mathrm{adj}(G)_{\gamma\delta}\right)\;\frac{\partial G_{\gamma\delta}}{\partial h}|_{h=0}\,.$$

The second term in this expression will vanish in the same way as the order $\mathcal{O}(h)$ term, so the coefficient of h^2 will be:

$$\frac{\partial^2}{\partial h^2}\left(\frac{1}{\sqrt{G}}\right)|_{h=0} = -\frac{1}{2}\mathrm{Tr}\left(\frac{\partial^2 \boldsymbol{G}}{\partial h^2}\right)|_{h=0} = -2\,\mathrm{Tr}(\bar{\boldsymbol{\epsilon}}^{vK})\,,$$

where we used the fact that $\boldsymbol{\epsilon} = h^2\bar{\boldsymbol{\epsilon}}$ under the displacement scaling assumptions.

Thus, the final expression for $1/\sqrt{G}$ will be:

$$\frac{1}{\sqrt{G}} = 1 - \mathrm{Tr}(\bar{\boldsymbol{\epsilon}}^{vK})\,h^2 + \mathcal{O}(h^4)$$

with the next order correction entering at $\mathcal{O}(h^4)$.

Combining the two parts of the expansion we get the final expression for the unit normal:

$$\hat{\boldsymbol{N}} = -(h\bar{v}_{3,\alpha} + \mathcal{O}(h^3))\hat{\boldsymbol{e}}_\alpha \;+\; (1 - \frac{1}{2}h^2\bar{v}_{3,\alpha}\bar{v}_{3,\alpha} + \mathcal{O}(h^4))\,\hat{\boldsymbol{e}}_3\,,$$

or in terms of vector operators:

$$\hat{\boldsymbol{N}} \approx -h\boldsymbol{\nabla}\bar{v}_3 \;+\; \left(1 - \frac{1}{2}h^2(\boldsymbol{\nabla}\bar{v}_3)^{\mathrm{T}}.(\boldsymbol{\nabla}\bar{v}_3)\right)\,\hat{\boldsymbol{e}}_3\,.$$

Appendix C

Hierarchy of Plate Models

Here, we summarize the hierarchy of gamma-convergent plate models described by Friesecke et al. [2006].

C.1 Clamped Boundary Conditions

For clamped boundary conditions ($\tilde{\boldsymbol{v}} = 0$ on the edge), we have the hierarchy displayed in table C.1. The models referred to by the table are the (relaxed) nonlinear membrane model, the relaxed Föppl membrane model, the Föppl-von Kármán model and finally the linear bending model, with (nondimensional) energies:

$$W^{NLM} = h \int_\Omega \mathcal{W}(\boldsymbol{F}) d\Omega \,, \tag{C.1.1}$$

$$W^{F\ddot{o}ppl} = h \int_\Omega \left(\frac{2\lambda\mu}{\lambda + 2\mu} (\mathrm{Tr}\boldsymbol{\epsilon}^{vk})^2 + 2\mu(\boldsymbol{\epsilon}^{vK} \cdot \boldsymbol{\epsilon}^{vK}) \right) d\Omega \,, \tag{C.1.2}$$

$$W^{vK} \quad = W^{F\ddot{o}ppl} + W^{LB} \,, \tag{C.1.3}$$

and

$$W^{LB} = \frac{h^3}{24} \int_\Omega \left(\frac{2\lambda\mu}{\lambda + 2\mu} (\mathrm{Tr}(\boldsymbol{\nabla}\boldsymbol{\nabla} v_3)^2 + 2\mu(\boldsymbol{\nabla}\boldsymbol{\nabla} v_3) \cdot (\boldsymbol{\nabla}\boldsymbol{\nabla} v_3) \right) d\Omega \tag{C.1.4}$$

respectively. The membrane models must be relaxed in regions of compressive stress, as outlined in Steigmann [1990].

Model	$t^{\pm}/h \sim h^{\alpha}$	$W/h \sim h^{\beta}$	$\boldsymbol{v} \sim h^{\gamma}$	$v_3 \sim h^{\delta}$
Membrane	$\alpha = 0$	$\beta = 0$	$\gamma = 0$	$\delta = 0$
Relaxed Föppl	$0 < \alpha < 3$	$\beta = (4/3)\alpha$	$\gamma = (2/3)\alpha$	$\delta = (1/3)\alpha$
Föppl-von Kármán	$\alpha = 3$	$\beta = 2\alpha - 2$	$\gamma = 2(\alpha - 2)$	$\delta = \alpha - 2$
Linear Bending	$\alpha > 3$	$\beta = 2\alpha - 2$	$\gamma = \alpha - 1$	$\delta = \alpha - 2$

Table C.1: A summary of the hierarchy of plate models for fully clamped ($\tilde{\boldsymbol{v}} = 0$ at the edge) conditions, derived by Friesecke et al. [2006]. Here $h^* = h/L$ is the relative thickness and $t^{\pm}$ are the tractions on the top and bottom faces of the plate and W/h is the energy per unit thickness.

C.2 Free Boundary Conditions

A similar hierarchy emerges for plates subject to traction free boundary conditions at the edge. However, the intermediate range energy scaling between membrane theory and the Föppl-von Kármán model admits a more varied set of behaviours. These are summarised in table C.2.

The new hierarchy includes the nonlinear bending energy:

$$W^{NLB} = \frac{h^3}{24} \int_{\Omega} \left(\frac{2\lambda\mu}{\lambda + 2\mu} (\mathrm{Tr}\boldsymbol{\kappa})^2 + 2\mu(\boldsymbol{\kappa} \cdot \boldsymbol{\kappa}) \right) d\Omega. \tag{C.2.1}$$

subject to the (exact) isometry constraint

$$(\boldsymbol{\nabla} \boldsymbol{y})^T (\boldsymbol{\nabla} \boldsymbol{y}) = \mathbb{I}_3 \,. \tag{C.2.2}$$

Mathematically, all deformations must belong to the subset of admissible displacements: in practise, one would impose this constraint via a Lagrange multiplier. The hierarchy further includes the isometric linear[1] bending model:

$$W^{LB} = \frac{h^3}{24} \int_{\Omega} \left(\frac{2\lambda\mu}{\lambda + 2\mu} (\mathrm{Tr}(\boldsymbol{\nabla}\boldsymbol{\nabla} v_3)^2 + 2\mu(\boldsymbol{\nabla}\boldsymbol{\nabla} v_3) \cdot (\boldsymbol{\nabla}\boldsymbol{\nabla} v_3) \right) d\Omega \tag{C.2.3}$$

subject to the nonlinear, small-displacement, moderate-rotation, isometry constraint

$$\det(\boldsymbol{\nabla}\boldsymbol{\nabla} v_3) = 0 \,. \tag{C.2.4}$$

The above constraint specifies that the Gaussian curvature (using the linearised curvature $\boldsymbol{\nabla}\boldsymbol{\nabla} v_3$) remains zero everywhere. It is worth stressing that contrasts with linear bending in which there is a small stretch induced by bending, that enters at lower order.

Model	$t^{\pm}/h \sim h^{\alpha}$	$W/h \sim h^{\beta}$	$\boldsymbol{v} \sim h^{\gamma}$	$v_3 \sim h^{\delta}$
Membrane	$\alpha = 0$	$\beta = 0$	$\gamma = 0$	$\delta = 0$
Nonlinear bending	$\alpha = 2$	$\beta = 0$	$\gamma = 0$	$\delta = 0$
Linear[1] isometric bending	$2 < \alpha < 3$	$\beta = 2\alpha - 2$	$\gamma = 2(\alpha - 2)$	$\delta = \alpha - 2$
Föppl-von Kármán	$2 < \alpha < 2$	$\beta = 2\alpha - 2$	$\gamma = 2(\alpha - 2)$	$\delta = \alpha - 2$
Linear Bending	$\alpha > 3$	$\beta = 2\alpha - 2$	$\gamma = \alpha - 1$	$\delta = \alpha - 2$

Table C.2: A summary of the hierarchy of plate models for traction free conditions at the edge, derived by Friesecke et al. [2006]. Here $h = h^*/L$ is the relative thickness and $t^{\pm}$ are the tractions on the top and bottom faces of the plate and W/h is the nondimensional energy per unit thickness.

[1]This is termed isometric linear bending as it uses the linear bending energy: however, deformations must satisfy the have a nonlinear isometry constraint

Appendix D

Intermediate Results for Curved-Bell Elements

We now derive some intermediate results which become useful in expressing the submatrix $\tilde{b}_{32}$, in the construction of the shape functions of the curved Bell element.

D.1 Expressing Second Derivative Degrees of Freedom on the Reference Element

In general the tangent vectors will depend on the position. For example, in general we have

$$\frac{\partial^2 \hat{w}}{\partial \hat{x}_\alpha \partial \hat{x}_\beta} = \frac{\partial}{\partial \hat{x}_\alpha}\left(\frac{\partial w}{\partial x_\gamma}\frac{\partial F_{K\gamma}}{\partial \hat{x}_\beta}\right) = \frac{\partial^2 w}{\partial x_\gamma \partial x_\delta}\frac{\partial F_{K\gamma}}{\partial \hat{x}_\beta}\frac{\partial F_{K\delta}}{\partial \hat{x}_\alpha} + \frac{\partial w}{\partial x_\gamma}\frac{\partial^2 F_{K\gamma}}{\partial \hat{x}_\alpha \partial \hat{x}_\beta}\,, \tag{D.1.1}$$

where $\boldsymbol{F}_k = \boldsymbol{x}$.

However, as the sides 1 and 2 transform to straight lines on the reference element (i.e the transformation of these edges is affine), we can straightforwardly express four of the degrees of freedom as follows

$$\boldsymbol{\nabla} w(\boldsymbol{a}_1)\cdot(\boldsymbol{A}_1 \otimes \boldsymbol{A}_1) = \tilde{\boldsymbol{\nabla}}\tilde{w}(\hat{\boldsymbol{a}}_1)\cdot(\hat{\boldsymbol{a}}_1 \otimes \hat{\boldsymbol{a}}_1)\,, \tag{D.1.2}$$

$$\boldsymbol{\nabla} w(\boldsymbol{a}_2)\cdot(\boldsymbol{B}_2 \otimes \boldsymbol{B}_2) = \tilde{\boldsymbol{\nabla}}\tilde{w}(\hat{\boldsymbol{a}}_2)\cdot(\hat{\boldsymbol{a}}_2 \otimes \hat{\boldsymbol{a}}_2)\,, \tag{D.1.3}$$

$$\boldsymbol{\nabla} w(\boldsymbol{a}_3)\cdot(\boldsymbol{A}_1 \otimes \boldsymbol{A}_1) = \tilde{\boldsymbol{\nabla}}\tilde{w}(\hat{\boldsymbol{a}}_3)\cdot(\hat{\boldsymbol{a}}_1 \otimes \hat{\boldsymbol{a}}_1)\,, \tag{D.1.4}$$

$$\boldsymbol{\nabla} w(\boldsymbol{a}_3)\cdot(\boldsymbol{B}_2 \otimes \boldsymbol{B}_2) = \tilde{\boldsymbol{\nabla}}\tilde{w}(\hat{\boldsymbol{a}}_3)\cdot(\hat{\boldsymbol{a}}_2 \otimes \hat{\boldsymbol{a}}_2)\,. \tag{D.1.5}$$

The other two tangent vectors, $\boldsymbol{A}_2$ and $\boldsymbol{B}_1$ are functions of the arc length s, and as such the reference second derivatives also depend on both the second and first local derivatives.

Noting that, by definition of the tangent vectors, we have

$$\boldsymbol{A}_1 \equiv -\boldsymbol{F}_{K,\hat{x}_1}(\boldsymbol{a}_1) = -\boldsymbol{F}_{K,\hat{x}_1}(\boldsymbol{a}_3)\,, \tag{D.1.6}$$

$$\boldsymbol{B}_2 \equiv -\boldsymbol{F}_{K,\hat{x}_2}(\boldsymbol{a}_2) = -\boldsymbol{F}_{K,\hat{x}_2}(\boldsymbol{a}_3)\,, \tag{D.1.7}$$

and

$$\boldsymbol{A}_2 \equiv -\boldsymbol{F}_{K,\hat{x}_1}(\boldsymbol{a}_1) + \boldsymbol{F}_{K,\hat{x}_2}(\boldsymbol{a}_1)\,, \tag{D.1.8}$$

$$\boldsymbol{B}_1 \equiv -\boldsymbol{F}_{K,\hat{x}_2}(\boldsymbol{a}_2) + \boldsymbol{F}_{K,\hat{x}_1}(\boldsymbol{a}_2) \tag{D.1.9}$$

which can be verified by taking the derivative of equation (4.5.7).

We also need to compute second derivatives of the mapping, which for the P_3 elements will be

$$\frac{\partial^2}{\partial\hat{x}_1\partial\hat{x}_2}\boldsymbol{F}_K(a_1) = 2(\boldsymbol{B}_2 - \boldsymbol{A}_1) + \frac{1}{2}(3\boldsymbol{A}_2 - \boldsymbol{B}_1)\,, \tag{D.1.10}$$

$$\frac{\partial^2}{\partial\hat{x}_2\partial\hat{x}_2}\boldsymbol{F}_K(a_1) = 2(\boldsymbol{A}_1 - \boldsymbol{B}_2) - (\boldsymbol{A}_2 - \boldsymbol{B}_1)\,, \tag{D.1.11}$$

$$\frac{\partial^2}{\partial\hat{x}_1\partial\hat{x}_1}\boldsymbol{F}_K(a_2) = 2(\boldsymbol{B}_2 - \boldsymbol{A}_1) + (\boldsymbol{A}_2 - \boldsymbol{B}_1)\,, \tag{D.1.12}$$

$$\frac{\partial^2}{\partial\hat{x}_1\partial\hat{x}_2}\boldsymbol{F}_K(a_2) = 2(\boldsymbol{A}_1 - \boldsymbol{B}_2) + \frac{1}{2}(3\boldsymbol{B}_1 - \boldsymbol{A}_2)\,, \tag{D.1.13}$$

$$\frac{\partial^2}{\partial\hat{x}_1\partial\hat{x}_2}\boldsymbol{F}_K(a_3) = \frac{1}{2}(\boldsymbol{B}_1 + \boldsymbol{A}_2)\,, \tag{D.1.14}$$

and

$$\frac{\partial^2}{\partial\hat{x}_1^2}\boldsymbol{F}_K(a_1) = \frac{\partial^2}{\partial\hat{x}_2^2}\boldsymbol{F}_K(a_2) = \frac{\partial^2}{\partial\hat{x}_2^2}\boldsymbol{F}_K(a_3) = \frac{\partial^2}{\partial\hat{x}_1^2}\boldsymbol{F}_K(a_3) = 0\,. \tag{D.1.15}$$

Finally we may express the second derivative degrees of freedom on the reference element

as

$$\frac{\partial^2 \hat{w}}{\partial \hat{x}_1 \partial \hat{x}_1}(\hat{\boldsymbol{a}}_1) = \boldsymbol{\nabla}\boldsymbol{\nabla} w(\boldsymbol{a}_1) \cdot (\boldsymbol{A}_1 \otimes \boldsymbol{A}_1)\,, \tag{D.1.16}$$

$$\frac{\partial^2 \hat{w}}{\partial \hat{x}_1 \partial \hat{x}_2}(\hat{\boldsymbol{a}}_1) = \boldsymbol{\nabla}\boldsymbol{\nabla} w(\boldsymbol{a}_1) \cdot (\boldsymbol{A}_1 \otimes (\boldsymbol{A}_1 - \boldsymbol{A}_2)) + \boldsymbol{\nabla} w(\boldsymbol{a}_1) \cdot \left(2(\boldsymbol{B}_2 - \boldsymbol{A}_1) + \frac{1}{2}(3\boldsymbol{A}_2 - \boldsymbol{B}_1)\right)\,, \tag{D.1.17}$$

$$\frac{\partial^2 \hat{w}}{\partial \hat{x}_2 \partial \hat{x}_2}(\hat{\boldsymbol{a}}_1) = \boldsymbol{\nabla}\boldsymbol{\nabla} w(\boldsymbol{a}_1) \cdot ((\boldsymbol{A}_1 - \boldsymbol{A}_2) \otimes (\boldsymbol{A}_1 - \boldsymbol{A}_2)) + \boldsymbol{\nabla} w(\boldsymbol{a}_1) \cdot (2(\boldsymbol{A}_1 - \boldsymbol{B}_2) - (\boldsymbol{A}_2 - \boldsymbol{B}_1))\,, \tag{D.1.18}$$

$$\frac{\partial^2 \hat{w}}{\partial \hat{x}_1 \partial \hat{x}_1}(\hat{\boldsymbol{a}}_2) = \boldsymbol{\nabla}\boldsymbol{\nabla} w(\boldsymbol{a}_2) \cdot ((\boldsymbol{B}_2 - \boldsymbol{B}_1) \otimes (\boldsymbol{B}_2 - \boldsymbol{B}_1)) + \boldsymbol{\nabla} w(\boldsymbol{a}_2) \cdot (2(\boldsymbol{B}_2 - \boldsymbol{A}_1) + (\boldsymbol{A}_2 - \boldsymbol{B}_1))\,, \tag{D.1.19}$$

$$\frac{\partial^2 \hat{w}}{\partial \hat{x}_1 \partial \hat{x}_2}(\hat{\boldsymbol{a}}_2) = \boldsymbol{\nabla}\boldsymbol{\nabla} w(\boldsymbol{a}_2) \cdot ((\boldsymbol{B}_2 - \boldsymbol{B}_1) \otimes \boldsymbol{B}_2) + \boldsymbol{\nabla} w(\boldsymbol{a}_2) \cdot \left(2(\boldsymbol{A}_1 - \boldsymbol{B}_2) + \frac{1}{2}(3\boldsymbol{B}_1 - \boldsymbol{A}_2)\right)\,, \tag{D.1.20}$$

$$\frac{\partial^2 \hat{w}}{\partial \hat{x}_2 \partial \hat{x}_2}(\hat{\boldsymbol{a}}_2) = \boldsymbol{\nabla}\boldsymbol{\nabla} w(\boldsymbol{a}_2) \cdot (\boldsymbol{B}_2 \otimes \boldsymbol{B}_2)\,, \tag{D.1.21}$$

$$\frac{\partial^2 \hat{w}}{\partial \hat{x}_1 \partial \hat{x}_2}(\hat{\boldsymbol{a}}_3) = \boldsymbol{\nabla}\boldsymbol{\nabla} w(\boldsymbol{a}_3) \cdot (\boldsymbol{A}_1 \otimes \boldsymbol{A}_1)\,, \tag{D.1.22}$$

$$\frac{\partial^2 \hat{w}}{\partial \hat{x}_1 \partial \hat{x}_2}(\hat{\boldsymbol{a}}_3) = \boldsymbol{\nabla}\boldsymbol{\nabla} w(\boldsymbol{a}_3) \cdot (\boldsymbol{A}_1 \otimes \boldsymbol{B}_2) + \boldsymbol{\nabla} w(\boldsymbol{a}_3) \cdot \frac{1}{2}(\boldsymbol{B}_1 + \boldsymbol{A}_2)\,, \tag{D.1.23}$$

$$\frac{\partial^2 \hat{w}}{\partial \hat{x}_2 \partial \hat{x}_2}(\hat{\boldsymbol{a}}_3) = \boldsymbol{\nabla}\boldsymbol{\nabla} w(\boldsymbol{a}_3) \cdot (\boldsymbol{B}_2 \otimes \boldsymbol{B}_2)\,. \tag{D.1.24}$$

In the above expression, it becomes necessary to express $\boldsymbol{\nabla}\boldsymbol{\nabla} w \cdot (\boldsymbol{A}_1, \boldsymbol{A}_2)$ in terms of the three local second degrees of freedom, $\boldsymbol{\nabla}\boldsymbol{\nabla} w \cdot \boldsymbol{A}_1 \otimes \boldsymbol{A}_1$, $\boldsymbol{\nabla}\boldsymbol{\nabla} w \cdot \boldsymbol{A}_2 \otimes \boldsymbol{A}_2$ and $\boldsymbol{\nabla}\boldsymbol{\nabla} w \cdot \boldsymbol{B}_2 \otimes \boldsymbol{B}_2$, which we do below.

We first relate the expression $\boldsymbol{B}_2 - \boldsymbol{A}_1 = \boldsymbol{a}_1 - \boldsymbol{a}_2$ to the tangent vectors at $\boldsymbol{a}_1$:

$$\boldsymbol{B}_2 - \boldsymbol{A}_1 = \tilde{a}^\alpha \boldsymbol{A}_\alpha \tag{D.1.25}$$

thus we can relate $\boldsymbol{A}_1$ to $\boldsymbol{A}_2$ and $\boldsymbol{B}_2$ by

$$\boldsymbol{A}_1 = \frac{\boldsymbol{B}_2 - \tilde{a}^2 \boldsymbol{A}_2}{1 + \tilde{a}^1}\,, \quad \boldsymbol{A}_2 = \frac{\boldsymbol{B}_2 - (1 + \tilde{a}^1)\boldsymbol{A}_1}{\tilde{a}^2} \quad \text{and} \quad \boldsymbol{B}_2 = (1 + \tilde{a}^1)\boldsymbol{A}_1 + \tilde{a}^2 \boldsymbol{A}_2\,. \tag{D.1.26}$$

Here, we have tacitly assumed that $1 + \tilde{a}_1$ and $\tilde{a}_2$ are nonzero, which corresponds to the condition that both vectors $\boldsymbol{A_1}$ and $\boldsymbol{B}_2$ and vectors $\boldsymbol{A}_2$ and $\boldsymbol{B_2}$ are linearly independent. We then use the above relations successively to gain an expression in terms of the three

tangent directions, $\boldsymbol{A}_1 \otimes \boldsymbol{A}_1$, $\boldsymbol{A}_2 \otimes \boldsymbol{A}_2$ and $\boldsymbol{B}_2 \otimes \boldsymbol{B}_2$, as follows

$$\begin{aligned}
\boldsymbol{\nabla\nabla} w \cdot (\boldsymbol{A}_1 \otimes \boldsymbol{A}_2) &= -\frac{\tilde{a}^2}{1+\tilde{a}^1} \boldsymbol{\nabla\nabla} w \cdot (\boldsymbol{A}_2 \otimes \boldsymbol{A}_2) + \frac{1}{1+\tilde{a}^1} \boldsymbol{\nabla\nabla} w \cdot (\boldsymbol{B}_2 \otimes \boldsymbol{A}_2) && \text{(D.1.27)} \\
&= -\frac{\tilde{a}^2}{1+\tilde{a}^1} \boldsymbol{\nabla\nabla} w \cdot (\boldsymbol{A}_2 \otimes \boldsymbol{A}_2) + \frac{1}{\tilde{a}^2(1+\tilde{a}^1)} \boldsymbol{\nabla\nabla} w \cdot (\boldsymbol{B}_2 \otimes \boldsymbol{B}_2) && \text{(D.1.28)} \\
&\quad - \frac{1}{\tilde{a}^2} \boldsymbol{\nabla\nabla} w \cdot (\boldsymbol{B}_2 \otimes \boldsymbol{A}_1) \\
&= -\frac{\tilde{a}^2}{1+\tilde{a}^1} \boldsymbol{\nabla\nabla} w \cdot (\boldsymbol{A}_2 \otimes \boldsymbol{A}_2) + \frac{1}{\tilde{a}^2(1+\tilde{a}^1)} \boldsymbol{\nabla\nabla} w \cdot (\boldsymbol{B}_2 \otimes \boldsymbol{B}_2) && \text{(D.1.29)} \\
&\quad - \frac{1+\tilde{a}^1}{\tilde{a}^2} \boldsymbol{\nabla\nabla} w \cdot (\boldsymbol{A}_1 \otimes \boldsymbol{A}_1) \quad - \boldsymbol{\nabla\nabla} w \cdot (\boldsymbol{A}_2 \otimes \boldsymbol{A}_1) \,.
\end{aligned}$$

Finally, rearranging terms we get

$$\begin{aligned}
\boldsymbol{\nabla\nabla} w \cdot (\boldsymbol{A}_1 \otimes \boldsymbol{A}_2) = &-\frac{1+\tilde{a}^1}{2\tilde{a}^2} \boldsymbol{\nabla\nabla} w \cdot (\boldsymbol{A}_1 \otimes \boldsymbol{A}_1) - \frac{\tilde{a}^2}{2(1+\tilde{a}^1)} \boldsymbol{\nabla\nabla} w \cdot (\boldsymbol{A}_2 \otimes \boldsymbol{A}_2) \\
&+ \frac{1}{2\tilde{a}^2(1+\tilde{a}^1)} \boldsymbol{\nabla\nabla} w \cdot (\boldsymbol{B}_2 \otimes \boldsymbol{B}_2) \,. \qquad \text{(D.1.30)}
\end{aligned}$$

Similarly, we can express $\boldsymbol{\nabla\nabla} w \cdot (\boldsymbol{B}_1 \otimes \boldsymbol{B}_2)$ in terms in terms of the three local second degrees of freedom, $\boldsymbol{\nabla\nabla} w \cdot \boldsymbol{B}_1 \otimes \boldsymbol{B}_1$, $\boldsymbol{\nabla\nabla} w \cdot \boldsymbol{B}_2 \otimes \boldsymbol{B}_2$ and $\boldsymbol{\nabla\nabla} w \cdot \boldsymbol{A}_1 \otimes \boldsymbol{A}_1$. We introduce the constants $\tilde{b}^\alpha$, such that

$$\boldsymbol{A}_1 - \boldsymbol{B}_2 = \tilde{b}^\alpha \boldsymbol{B}_\alpha \,. \qquad \text{(D.1.31)}$$

Using identical algebraic steps to the above derivation we arrive at

$$\begin{aligned}
\boldsymbol{\nabla\nabla} w \cdot (\boldsymbol{B}_1 \otimes \boldsymbol{B}_2) = &-\frac{1+\tilde{b}^2}{2\tilde{b}^1} \boldsymbol{\nabla\nabla} w \cdot (\boldsymbol{B}_2 \otimes \boldsymbol{B}_2) - \frac{\tilde{b}^1}{2(1+\tilde{b}^2)} \boldsymbol{\nabla\nabla} w \cdot (\boldsymbol{B}_1 \otimes \boldsymbol{B}_1) \\
&+ \frac{1}{2\tilde{b}^1(1+\tilde{b}^2)} \boldsymbol{\nabla\nabla} w \cdot (\boldsymbol{A}_1 \otimes \boldsymbol{A}_1) \,. \qquad \text{(D.1.32)}
\end{aligned}$$

The final second derivative term for which we need an expression is $\boldsymbol{\nabla\nabla} w \cdot (\boldsymbol{A}_1 \otimes \boldsymbol{B}_2)$. With this objective in mind, we introduce the new vectors $\boldsymbol{C}_1 = -\boldsymbol{B}_2$ and $\boldsymbol{C_2} = -\boldsymbol{A}_1$, and relate these to the tangents $\boldsymbol{A}_2$ and $\boldsymbol{B}_1$ as follows

$$\boldsymbol{A}_2 = \tilde{c}^\alpha \boldsymbol{C}^\alpha \quad \text{and} \quad \boldsymbol{B}_1 = \tilde{\tilde{c}}^\alpha \boldsymbol{C}^\alpha \qquad \text{(D.1.33)}$$

where we have introduced the constants $\tilde{c}^\alpha$ and $\tilde{\tilde{c}}^\alpha$. Using the above relations in the same manner as previously, after some algebra we can derive

$$\begin{aligned}
\boldsymbol{\nabla\nabla} w \cdot (\boldsymbol{A}_1 \otimes \boldsymbol{B}_2) = &-\frac{\tilde{c}^1 \tilde{\tilde{c}}^1}{\tilde{c}^1 \tilde{\tilde{c}}^2 + \tilde{c}^2 \tilde{\tilde{c}}^1} \boldsymbol{\nabla\nabla} w \cdot (\boldsymbol{C}_1 \otimes \boldsymbol{C}_1) - \frac{\tilde{c}^2 \tilde{\tilde{c}}^2}{\tilde{c}^1 \tilde{\tilde{c}}^2 + \tilde{c}^2 \tilde{\tilde{c}}^1} \boldsymbol{\nabla\nabla} w \cdot (\boldsymbol{C}_2 \otimes \boldsymbol{C}_2) \\
&+ \frac{1}{\tilde{c}^1 \tilde{\tilde{c}}^2 + \tilde{c}^2 \tilde{\tilde{c}}^1} \boldsymbol{\nabla\nabla} w \cdot (\boldsymbol{A}_2 \otimes \boldsymbol{B}_1) \,. \qquad \text{(D.1.34)}
\end{aligned}$$

Finally we introduce four additional constants that relate $\boldsymbol{A}_\alpha$ and $\boldsymbol{B}_\alpha$ to $\boldsymbol{B}_1$ and $\boldsymbol{A}_2$ respectively. We introduce $\tilde{\tilde{a}}^\alpha$ and $\tilde{\tilde{b}}^\alpha$ to allow us to express $\boldsymbol{B_1}$ and A_2 in terms of quantities intrinsic to the opposing curved-edge vertex using the defining relations

$$\boldsymbol{B}_1 = -\tilde{\tilde{a}}^\alpha \boldsymbol{A}_\alpha \quad \text{and} \quad \boldsymbol{A}_2 = \quad \tilde{\tilde{b}}^\alpha \boldsymbol{B}_\alpha \,. \tag{D.1.35}$$

Putting this all together we can now express equations (D.1.16–D.1.24) in terms of the local degrees of freedom and the introduced constants. The final expressions for the reference second derivative degrees of freedom are

$$\boldsymbol{RDOF2} = \boldsymbol{LDOF1} \quad \tilde{\boldsymbol{b}}_{3a} + \boldsymbol{LDOF1} \quad \tilde{\boldsymbol{b}}_{3b} \tag{D.1.36}$$

with the reference second derivative degrees of freedom vector

$$\begin{aligned} \boldsymbol{RDOF2} = \Bigg[& \frac{\partial^2 \hat{w}}{\partial \hat{x}_1^2}(\hat{\boldsymbol{a}}_1)\,;\ \frac{\partial^2 \hat{w}}{\partial \hat{x}_1 \partial \hat{x}_2}(\hat{\boldsymbol{a}}_1)\,;\ \frac{\partial^2 \hat{w}}{\partial \hat{x}_2^2}(\hat{\boldsymbol{a}}_1)\,;\ \frac{\partial^2 \hat{w}}{\partial \hat{x}_1^2}(\hat{\boldsymbol{a}}_2)\,;\ \frac{\partial^2 \hat{w}}{\partial \hat{x}_1 \partial \hat{x}_2}(\hat{\boldsymbol{a}}_2)\,;\ \frac{\partial^2 \hat{w}}{\partial \hat{x}_2^2}(\hat{\boldsymbol{a}}_2)\,; \\ & \frac{\partial^2 \hat{w}}{\partial \hat{x}_1^2}(\hat{\boldsymbol{a}}_3)\,;\ \frac{\partial^2 \hat{w}}{\partial \hat{x}_1 \partial \hat{x}_2}(\hat{\boldsymbol{a}}_3)\,;\ \frac{\partial^2 \hat{w}}{\partial \hat{x}_2^2}(\hat{\boldsymbol{a}}_3) \Bigg], \end{aligned} \tag{D.1.37}$$

the local first derivative degrees of freedom vector

$$\begin{aligned} \boldsymbol{LDOF1} = \Bigg[& (\boldsymbol{\nabla} w(\boldsymbol{a}_1)) \cdot \boldsymbol{A}_1 \ ;\ (\boldsymbol{\nabla} w(\boldsymbol{a}_1)) \cdot \boldsymbol{A}_2 \ ;\ (\boldsymbol{\nabla} w(\boldsymbol{a}_2)) \cdot \boldsymbol{B}_1 \ ;\ (\boldsymbol{\nabla} w(\boldsymbol{a}_2)) \cdot \boldsymbol{B}_2 \ ; \\ & - (\boldsymbol{\nabla} w(\boldsymbol{a}_3)) \cdot \boldsymbol{A}_1 \ ;\ -(\boldsymbol{\nabla} w(\boldsymbol{a}_3)) \cdot \boldsymbol{B}_2 \Bigg], \end{aligned} \tag{D.1.38}$$

the local second derivative degrees of freedom vector

$$\begin{aligned} \boldsymbol{LDOF2} = \Bigg[& (\boldsymbol{\nabla}\boldsymbol{\nabla} w(\boldsymbol{a}_1)) \cdot \boldsymbol{A}_1 \otimes \boldsymbol{A}_1 \ ;\ (\boldsymbol{\nabla}\boldsymbol{\nabla} w(\boldsymbol{a}_1)) \cdot \boldsymbol{A}_2 \otimes \boldsymbol{A}_2 \ ;\quad (\boldsymbol{\nabla}\boldsymbol{\nabla} w(\boldsymbol{a}_2)) \cdot \boldsymbol{B}_1 \otimes \boldsymbol{B}_1 \ ; \\ & (\boldsymbol{\nabla}\boldsymbol{\nabla} w(\boldsymbol{a}_2)) \cdot \boldsymbol{B}_2 \otimes \boldsymbol{B}_2 \ ;\ (\boldsymbol{\nabla}\boldsymbol{\nabla} w(\boldsymbol{a}_3)) \cdot \boldsymbol{A}_1 \otimes \boldsymbol{A}_1 \ ;\quad (\boldsymbol{\nabla}\boldsymbol{\nabla} w(\boldsymbol{a}_3)) \cdot \boldsymbol{B}_2 \otimes \boldsymbol{B}_2 \ ; \\ & (\boldsymbol{\nabla}\boldsymbol{\nabla} w(\boldsymbol{a}_1)) \cdot \boldsymbol{B}_2 \otimes \boldsymbol{B}_2 \ ;\ (\boldsymbol{\nabla}\boldsymbol{\nabla} w(\boldsymbol{a}_2)) \cdot \boldsymbol{A}_1 \otimes \boldsymbol{A}_1 \ ;\ -(\boldsymbol{\nabla}\boldsymbol{\nabla} w(\boldsymbol{a}_3)) \cdot \boldsymbol{A}_2 \otimes \boldsymbol{B}_1 \Bigg], \end{aligned} \tag{D.1.39}$$

and finally the submatrices $\tilde{\boldsymbol{b}}_{3a}$ and $\tilde{\boldsymbol{b}}_{3b}$. These matrices, in turn, are given by

$$\tilde{\boldsymbol{b}}_{3a} = \begin{pmatrix} 0 & (2\tilde{a}^1 + \frac{1}{2}\tilde{\tilde{a}}^1) & -(2\tilde{a}^1 + \tilde{\tilde{a}}^1) & 0 & 0 & 0\,0 & 0 & 0 \\ 0 & (\frac{3}{2} + 2\tilde{a}^2 + \frac{1}{2}\tilde{\tilde{a}}^2) & -(1 + 2\tilde{a}^2 + \tilde{\tilde{a}}^2) & 0 & 0 & 0\,0 & 0 & 0 \\ 0 & 0 & 0 & -(1 + 2\tilde{b}^1 - \tilde{\tilde{b}}^1) & (\frac{3}{2} + 2\tilde{b}^1 - \frac{1}{2}\tilde{\tilde{b}}^1) & 0\,0 & 0 & 0 \\ 0 & 0 & 0 & -(2\tilde{b}^2 - \tilde{\tilde{b}}^2) & (2\tilde{b}^2 - \frac{1}{2}\tilde{\tilde{b}}^2) & 0\,0 & 0 & 0 \\ 0 & 0 & 0 & 0 & 0 & 0\,0 & \frac{1}{2}(\tilde{c}^1 + \tilde{\tilde{c}}^1) & 0 \\ 0 & 0 & 0 & 0 & 0 & 0\,0 & \frac{1}{2}(\tilde{c}^2 + \tilde{\tilde{c}}^2) & 0 \end{pmatrix} \tag{D.1.40}$$

and

$$\tilde{\boldsymbol{b}}_{3b} = \begin{pmatrix} 1 & \left(1+\frac{1+\tilde{a}^1}{2\tilde{a}^2}\right) & \left(1+\frac{1+\tilde{a}^1}{\tilde{a}^2}\right) & 0 & 0 & 0 & 0 & 0 & 0 \\ 0 & \frac{\tilde{a}^2}{2(1+\tilde{a}^1)} & \left(1+\frac{\tilde{a}^2}{1+\tilde{a}^1}\right) & 0 & 0 & 0 & 0 & 0 & 0 \\ 0 & 0 & 0 & \left(1+\frac{\tilde{b}^1}{1+\tilde{b}^2}\right) & \frac{\tilde{b}^1}{2(1+\tilde{b}^2)} & 0 & 0 & 0 & 0 \\ 0 & 0 & 0 & \left(1+\frac{1+\tilde{b}^2}{\tilde{b}^1}\right) & \left(1+\frac{1+\tilde{b}^2}{2\tilde{b}^1}\right) & 1 & 0 & 0 & 0 \\ 0 & 0 & 0 & 0 & 0 & 0 & 0 & \frac{-\tilde{c}^1\widetilde{\tilde{c}}^1}{\tilde{c}^1\widetilde{\tilde{c}}^2+\tilde{c}^2\widetilde{\tilde{c}}^1} & 1 \\ 0 & 0 & 0 & 0 & 0 & 0 & 1 & \frac{-\tilde{c}^2\widetilde{\tilde{c}}^2}{\tilde{c}^1\widetilde{\tilde{c}}^2+\tilde{c}^2\widetilde{\tilde{c}}^1} & 0 \\ 0 & \frac{-1}{2\tilde{a}^2(1+\tilde{a}^1)} & \frac{-1}{\tilde{a}^2(1+\tilde{a}^1)} & 0 & 0 & 0 & 0 & 0 & 0 \\ 0 & 0 & 0 & \frac{-1}{\tilde{b}^1(1+\tilde{b}^2)} & \frac{-1}{2\tilde{b}^1(1+\tilde{b}^2)} & 0 & 0 & 0 & 0 \\ 0 & 0 & 0 & 0 & 0 & 0 & 0 & \frac{-1}{\tilde{c}^2\widetilde{\tilde{c}}^2+\tilde{c}^2\widetilde{\tilde{c}}^1} & 0 \end{pmatrix}. \tag{D.1.41}$$

D.2 1D Hermite Polynomials

Consider the function $F(s)$ with $s \in (0,1)$. We can interpolate this function using a basis ψ_3^{1D}, such that the interpolant $f(s) = \boldsymbol{\Sigma}_3^{1D} \cdot \boldsymbol{\psi}_3^{1D} \approx F(s)$ with the Hermite degrees of freedom

$$\boldsymbol{\Sigma}_3^{1D} = \Big[F(0)\,;\, F'(0)\,;\, F(1)\,;\, -F'(1)\Big]. \tag{D.2.1}$$

It can be shown that the basis will be given by

$$\boldsymbol{\psi}_3^{1D} = \Big[(1-s)^2(1+2s)\,;\, (1-s)^2 s\,;\, (3-2s)s^2\,;\, (1-s)s^2\Big]^T, \tag{D.2.2}$$

which again can be deduced as described in the next section.

Likewise, we can interpolate a function $G(s)$ with $s \in (0,1)$ using a basis ψ_5^{1D}, such that the interpolant $g(s) = \boldsymbol{\Sigma}_5^{1D} \cdot \boldsymbol{\psi}_5^{1D} \approx G(s)$ with the Hermite degrees of freedom

$$\boldsymbol{\Sigma}_5^{1D} = \Big[F(0)\,;\, F'(0)\,;\, F''(0)\,;\, F(1)\,;\, -F'(1)\,;\, F''(1)\Big]. \tag{D.2.3}$$

It can be shown that the basis will be given by

$$\begin{aligned} \boldsymbol{\psi}_5^{1D} = \Big[&(1-s)^3(1+3s+6s^2)\,;\, (1-s)^3 s(1+3s)\,;\, \frac{1}{2}(1-s)^3 s^2\,; \\ &s^3(10-15s+6s^2)\,;\, s^3(4-7s+3s^2)\,;\, \frac{1}{2}s^3(1-s)^2\Big], \end{aligned} \tag{D.2.4}$$

which again can be deduced as described in the next section.

D.3 Constructing a Basis

In this section we discuss how to construct a complete basis on a right-angled triangle. For a Lagrange-interpolated basis it will be possible to use this method to construct the generic basis, however the situation is complicated for Hermite basis functions which have differing degrees of freedom on reference and physical triangles.

Let $p_n(s)$ be the space of 1D polynomials of degree n on range $s \in [0,1]$ and let m_i be the set of basis monomials $m_i(s) = s^i$ with $i \in \{0,\dots,n\}$, i.e that are linearly independent and span the space such that we can express any $\bar{p} = \sum_{i=0}^{n} P_i\, s^i\,,\ \forall \bar{p} \in p_n\,,\ P_i \in \Re$.

Let us construct a new basis $\psi_i(s)$, such that

$$\bar{p} = \sum_{i=0}^{n} \Sigma_i\, \psi_i\,, \forall \bar{p} \in p_n \tag{D.3.1}$$

for $\Sigma_i = \hat{H}_i \bar{p}$ where $\hat{H}_i$ is a linear operator on the space $p_n(s)$ and $\Sigma_i \in \mathbb{R}$.

By the linear property of the operator, we have

$$\Sigma_i = \sum_{j=0}^{n} \hat{H}_i P_j s^j = \sum_{j=0}^{n} P_j \hat{H}_i s^j \equiv \sum_{j=0}^{n} P_j \hat{\Sigma}_{ij}\,, \tag{D.3.2}$$

with $\hat{\Sigma}_{ij} \equiv \hat{H}_i s^j$. Thus we can write

$$\sum_{i=0}^{n} P_i s^i = \sum_{i=0}^{n} \Sigma_i\, \psi_i = \sum_{i=0}^{n}\sum_{j=0}^{n} P_j \hat{\Sigma}_{ij}\, \psi_i \tag{D.3.3}$$

which in turn implies

$$s^j = \sum_{i=0}^{n} \hat{\Sigma}_{ij}\, \psi_i\,. \tag{D.3.4}$$

Therefore we can determine ψ_i by the following equation

$$\boldsymbol{\psi} = \hat{\boldsymbol{\Sigma}}^{-T} \boldsymbol{m}\,, \tag{D.3.5}$$

where $\hat{\Sigma}_{ij} = \hat{H}_i s^j$ and $\boldsymbol{m}$ is the vector with components $m_i(s) = s^i$ This method can be straightforwardly extended to higher-dimensional bases.

D.4 Basis Monomials

The vector of p_7 basis monomials is given by

$$\tilde{\boldsymbol{m}}_7 = \Big[\hat{x}_1^7, \hat{x}_1^6\hat{x}_2, \hat{x}_1^5\hat{x}_2^2, \hat{x}_1^4\hat{x}_2^3, \hat{x}_1^3\hat{x}_2^4, \hat{x}_1^2\hat{x}_2^5, \hat{x}_1\hat{x}_2^6, \hat{x}_2^7, \hat{x}_1^6, \hat{x}_1^5\hat{x}_2, \hat{x}_1^4\hat{x}_2^2, \hat{x}_1^3\hat{x}_2^3, \hat{x}_1^2\hat{x}_2^4, \hat{x}_1\hat{x}_2^5, \hat{x}_2^6, \hat{x}_1^5, \hat{x}_1^4\hat{x}_2,$$
$$\hat{x}_1^3\hat{x}_2^2, \hat{x}_1^2\hat{x}_2^3, \hat{x}_1\hat{x}_2^4, \hat{x}_2^5, \hat{x}_1^4, \hat{x}_1^3\hat{x}_2, \hat{x}_1^2\hat{x}_2^2, \hat{x}_1\hat{x}_2^3, \hat{x}_2^4, \hat{x}_1^3, \hat{x}_1^2\hat{x}_2, \hat{x}_1\hat{x}_2^2, \hat{x}_2^3, \hat{x}_1^2, \hat{x}_1\hat{x}_2, \hat{x}_2^2, \hat{x}_1, \hat{x}_2, 1\Big]\,. \tag{D.4.1}$$

$$
\tilde{\boldsymbol{A}} = \left(\begin{array}{cccccccccccccccccccccccccccccccccccc}
\frac{6496}{27} & 0 & \frac{55376}{27} & \frac{15296}{3} & \frac{86464}{27} & \frac{464}{3} & 0 & 0 & -\frac{6896}{9} & 0 & -\frac{136424}{27} & -\frac{187040}{27} & -\frac{27880}{27} & 0 & 0 & \frac{7750}{9} & 0 & \frac{98371}{27} & \frac{41027}{27} & 0 & 0 & -\frac{10501}{27} & 0 & -\frac{17323}{27} & 0 & 0 & \frac{490}{9} & 0 & 0 & 0 & 0 & 0 & 0 & 0 & 0 & 0 \\
0 & 0 & \frac{464}{3} & \frac{86464}{27} & \frac{15296}{3} & \frac{55376}{27} & 0 & \frac{6496}{27} & 0 & 0 & -\frac{27880}{27} & -\frac{187040}{27} & -\frac{136424}{27} & 0 & -\frac{6896}{9} & 0 & 0 & \frac{41027}{27} & \frac{98371}{27} & 0 & \frac{7750}{9} & 0 & 0 & -\frac{17323}{27} & 0 & -\frac{10501}{27} & 0 & 0 & 0 & \frac{490}{9} & 0 & 0 & 0 & 0 & 0 & 0 \\
-\frac{6496}{27} & 0 & \frac{14176}{27} & -\frac{2944}{27} & -\frac{2944}{27} & \frac{14176}{27} & 0 & -\frac{6496}{27} & \frac{24784}{27} & 0 & -\frac{5680}{27} & \frac{12736}{9} & -\frac{5680}{27} & 0 & \frac{24784}{27} & -\frac{11846}{9} & 0 & -\frac{26758}{27} & -\frac{26758}{27} & 0 & -\frac{11846}{9} & \frac{22789}{27} & 0 & \frac{18262}{27} & 0 & \frac{22789}{27} & -\frac{5566}{27} & 0 & 0 & -\frac{5566}{27} & 0 & 0 & 0 & 0 & 0 & 1 \\
-\frac{400}{9} & 0 & -\frac{3080}{9} & -816 & -\frac{4496}{9} & -\frac{232}{9} & 0 & 0 & \frac{416}{3} & 0 & \frac{7448}{9} & \frac{9872}{9} & \frac{1472}{9} & 0 & 0 & -\frac{457}{3} & 0 & -\frac{1177}{2} & -\frac{4337}{18} & 0 & 0 & \frac{607}{9} & 0 & \frac{619}{6} & 0 & 0 & -\frac{28}{3} & 0 & 0 & 0 & 0 & 0 & 0 & 0 & 0 & 0 \\
0 & -\frac{896}{9} & -\frac{392}{9} & \frac{2384}{9} & \frac{2512}{9} & \frac{232}{9} & 0 & 0 & 0 & \frac{2336}{9} & -\frac{8}{9} & -\frac{3920}{9} & -\frac{976}{9} & 0 & 0 & 0 & -\frac{2104}{9} & \frac{123}{2} & \frac{1981}{18} & 0 & 0 & 0 & \frac{766}{9} & -\frac{307}{18} & 0 & 0 & 0 & -\frac{31}{3} & 0 & 0 & 0 & 0 & 0 & 0 & 0 & 0 \\
0 & 0 & \frac{232}{9} & \frac{2512}{9} & \frac{2384}{9} & -\frac{392}{9} & -\frac{896}{9} & 0 & 0 & 0 & -\frac{976}{9} & -\frac{3920}{9} & -\frac{8}{9} & \frac{2336}{9} & 0 & 0 & 0 & \frac{1981}{18} & \frac{123}{2} & -\frac{2104}{9} & 0 & 0 & 0 & -\frac{307}{18} & \frac{766}{9} & 0 & 0 & 0 & -\frac{31}{3} & 0 & 0 & 0 & 0 & 0 & 0 & 0 \\
0 & 0 & -\frac{232}{9} & -\frac{4496}{9} & -816 & -\frac{3080}{9} & 0 & -\frac{400}{9} & 0 & 0 & \frac{1472}{9} & \frac{9872}{9} & \frac{7448}{9} & 0 & \frac{416}{3} & 0 & 0 & -\frac{4337}{18} & -\frac{1177}{2} & 0 & -\frac{457}{3} & 0 & 0 & \frac{619}{6} & 0 & \frac{607}{9} & 0 & 0 & 0 & -\frac{28}{3} & 0 & 0 & 0 & 0 & 0 & 0 \\
-\frac{400}{9} & 0 & \frac{1456}{9} & -\frac{992}{9} & -\frac{5248}{9} & -\frac{4096}{9} & -\frac{896}{9} & 0 & \frac{1552}{9} & 0 & -\frac{464}{3} & \frac{2464}{3} & \frac{3424}{3} & \frac{3040}{9} & 0 & -\frac{761}{3} & 0 & -\frac{1831}{9} & -938 & -\frac{1288}{3} & 0 & \frac{1528}{9} & 0 & \frac{2266}{9} & \frac{2210}{9} & 0 & -\frac{406}{9} & 0 & -\frac{499}{9} & 0 & 0 & 0 & 0 & 1 & 0 & 0 \\
0 & -\frac{896}{9} & -\frac{4096}{9} & -\frac{5248}{9} & -\frac{992}{9} & \frac{1456}{9} & 0 & -\frac{400}{9} & 0 & \frac{3040}{9} & \frac{3424}{3} & \frac{2464}{3} & -\frac{464}{3} & 0 & \frac{1552}{9} & 0 & -\frac{1288}{3} & -938 & -\frac{1831}{9} & 0 & -\frac{761}{3} & 0 & \frac{2210}{9} & \frac{2266}{9} & 0 & \frac{1528}{9} & 0 & -\frac{499}{9} & 0 & -\frac{406}{9} & 0 & 0 & 0 & 0 & 1 & 0 \\
\frac{8}{3} & 0 & \frac{52}{3} & 40 & 24 & \frac{4}{3} & 0 & 0 & -8 & 0 & -\frac{124}{3} & -\frac{160}{3} & -8 & 0 & 0 & \frac{17}{2} & 0 & \frac{349}{12} & \frac{47}{4} & 0 & 0 & -\frac{11}{3} & 0 & -\frac{61}{12} & 0 & 0 & \frac{1}{2} & 0 & 0 & 0 & 0 & 0 & 0 & 0 & 0 & 0 \\
0 & \frac{32}{3} & \frac{8}{3} & -\frac{80}{3} & -\frac{80}{3} & -\frac{8}{3} & 0 & 0 & 0 & -\frac{80}{3} & \frac{8}{3} & \frac{128}{3} & \frac{32}{3} & 0 & 0 & 0 & \frac{70}{3} & -\frac{43}{6} & -\frac{65}{6} & 0 & 0 & 0 & -\frac{25}{3} & \frac{11}{6} & 0 & 0 & 0 & 1 & 0 & 0 & 0 & 0 & 0 & 0 & 0 & 0 \\
0 & 0 & 4 & \frac{40}{3} & \frac{40}{3} & \frac{4}{3} & 0 & 0 & 0 & 0 & -\frac{28}{3} & -\frac{64}{3} & -\frac{16}{3} & 0 & 0 & 0 & 0 & \frac{29}{4} & \frac{65}{12} & 0 & 0 & 0 & 0 & -\frac{17}{12} & 0 & 0 & 0 & 0 & 0 & 0 & 0 & 0 & 0 & 0 & 0 & 0 \\
0 & 0 & \frac{4}{3} & \frac{40}{3} & \frac{40}{3} & 4 & 0 & 0 & 0 & 0 & -\frac{16}{3} & -\frac{64}{3} & -\frac{28}{3} & 0 & 0 & 0 & 0 & \frac{65}{12} & \frac{29}{4} & 0 & 0 & 0 & 0 & -\frac{17}{12} & 0 & 0 & 0 & 0 & 0 & 0 & 0 & 0 & 0 & 0 & 0 & 0 \\
0 & 0 & -\frac{8}{3} & -\frac{80}{3} & -\frac{80}{3} & \frac{8}{3} & \frac{32}{3} & 0 & 0 & 0 & \frac{32}{3} & \frac{128}{3} & \frac{8}{3} & -\frac{80}{3} & 0 & 0 & 0 & -\frac{65}{6} & -\frac{43}{6} & \frac{70}{3} & 0 & 0 & 0 & \frac{11}{6} & -\frac{25}{3} & 0 & 0 & 0 & 1 & 0 & 0 & 0 & 0 & 0 & 0 & 0 \\
0 & 0 & \frac{4}{3} & 24 & 40 & \frac{52}{3} & 0 & \frac{8}{3} & 0 & 0 & -8 & -\frac{160}{3} & -\frac{124}{3} & 0 & -8 & 0 & 0 & \frac{47}{4} & \frac{349}{12} & 0 & \frac{17}{2} & 0 & 0 & -\frac{61}{12} & 0 & -\frac{11}{3} & 0 & 0 & 0 & \frac{1}{2} & 0 & 0 & 0 & 0 & 0 & 0 \\
-\frac{8}{3} & 0 & \frac{56}{3} & \frac{80}{3} & \frac{32}{3} & 0 & 0 & 0 & \frac{32}{3} & 0 & -40 & -32 & -\frac{8}{3} & 0 & 0 & -\frac{33}{2} & 0 & \frac{51}{2} & \frac{19}{3} & 0 & 0 & \frac{73}{6} & 0 & -\frac{25}{6} & 0 & 0 & -\frac{25}{6} & 0 & 0 & 0 & \frac{1}{2} & 0 & 0 & 0 & 0 & 0 \\
0 & -\frac{32}{3} & -\frac{160}{3} & -\frac{320}{3} & -\frac{320}{3} & -\frac{160}{3} & -\frac{32}{3} & 0 & 0 & \frac{112}{3} & \frac{448}{3} & 224 & \frac{448}{3} & \frac{112}{3} & 0 & 0 & -50 & -150 & -150 & -50 & 0 & 0 & \frac{95}{3} & \frac{190}{3} & \frac{95}{3} & 0 & 0 & -\frac{28}{3} & -\frac{28}{3} & 0 & 0 & 1 & 0 & 0 & 0 & 0 \\
0 & 0 & 0 & \frac{32}{3} & \frac{80}{3} & \frac{56}{3} & 0 & -\frac{8}{3} & 0 & 0 & -\frac{8}{3} & -32 & -40 & 0 & \frac{32}{3} & 0 & 0 & \frac{19}{3} & \frac{51}{2} & 0 & -\frac{33}{2} & 0 & 0 & -\frac{25}{6} & 0 & \frac{73}{6} & 0 & 0 & 0 & -\frac{25}{6} & 0 & 0 & \frac{1}{2} & 0 & 0 & 0 \\
0 & 0 & 0 & 256 & 768 & 768 & 256 & 0 & 0 & 0 & -64 & -896 & -1600 & -768 & 0 & 0 & 0 & 176 & 992 & 816 & 0 & 0 & 0 & -160 & -352 & 0 & 0 & 0 & 48 & 0 & 0 & 0 & 0 & 0 & 0 & 0 \\
0 & 256 & 768 & 768 & 256 & 0 & 0 & 0 & 0 & -768 & -1600 & -896 & -64 & 0 & 0 & 0 & 816 & 992 & 176 & 0 & 0 & 0 & -352 & -160 & 0 & 0 & 0 & 48 & 0 & 0 & 0 & 0 & 0 & 0 & 0 & 0 \\
0 & 0 & 0 & 128\sqrt{2} & 128\sqrt{2} & 0 & 0 & 0 & 0 & 0 & -32\sqrt{2} & -192\sqrt{2} & -32\sqrt{2} & 0 & 0 & 0 & 0 & 40\sqrt{2} & 40\sqrt{2} & 0 & 0 & 0 & 0 & -8\sqrt{2} & 0 & 0 & 0 & 0 & 0 & 0 & 0 & 0 & 0 & 0 & 0 & 0 \\
0 & 0 & 0 & -\frac{65536}{27} & -\frac{114688}{27} & -\frac{40960}{27} & 0 & -\frac{8192}{27} & 0 & 0 & \frac{16384}{27} & \frac{53248}{9} & \frac{38912}{9} & 0 & \frac{26624}{27} & 0 & 0 & -\frac{32768}{27} & -\frac{10240}{3} & 0 & -\frac{10240}{9} & 0 & 0 & \frac{16384}{27} & 0 & \frac{14336}{27} & 0 & 0 & 0 & -\frac{2048}{27} & 0 & 0 & 0 & 0 & 0 & 0 \\
0 & 0 & \frac{53248}{27} & \frac{40960}{9} & \frac{69632}{27} & -\frac{8192}{27} & 0 & \frac{8192}{27} & 0 & 0 & -\frac{48128}{9} & -\frac{22528}{3} & -1024 & 0 & -\frac{10240}{9} & 0 & 0 & \frac{14336}{3} & \frac{8192}{3} & 0 & \frac{14336}{9} & 0 & 0 & -\frac{37888}{27} & 0 & -\frac{26624}{27} & 0 & 0 & 0 & \frac{2048}{9} & 0 & 0 & 0 & 0 & 0 & 0 \\
\frac{8192}{27} & 0 & -\frac{8192}{27} & \frac{69632}{27} & \frac{40960}{9} & \frac{53248}{27} & 0 & 0 & -\frac{10240}{9} & 0 & -1024 & -\frac{22528}{3} & -\frac{48128}{9} & 0 & 0 & \frac{14336}{9} & 0 & \frac{8192}{3} & \frac{14336}{3} & 0 & 0 & -\frac{26624}{27} & 0 & -\frac{37888}{27} & 0 & 0 & \frac{2048}{9} & 0 & 0 & 0 & 0 & 0 & 0 & 0 & 0 & 0 \\
-\frac{8192}{27} & 0 & -\frac{40960}{27} & -\frac{114688}{27} & -\frac{65536}{27} & 0 & 0 & 0 & \frac{26624}{27} & 0 & \frac{38912}{9} & \frac{53248}{9} & \frac{16384}{27} & 0 & 0 & -\frac{10240}{9} & 0 & -\frac{10240}{3} & -\frac{32768}{27} & 0 & 0 & \frac{14336}{27} & 0 & \frac{16384}{27} & 0 & 0 & -\frac{2048}{27} & 0 & 0 & 0 & 0 & 0 & 0 & 0 & 0 & 0 \\
0 & 0 & -\frac{71680}{27} & -\frac{145408}{27} & -\frac{88064}{27} & -\frac{2048}{9} & 0 & 0 & 0 & 0 & \frac{150016}{27} & \frac{183296}{27} & \frac{31232}{27} & 0 & 0 & 0 & 0 & -\frac{94208}{27} & -\frac{40960}{27} & 0 & 0 & 0 & 0 & \frac{15872}{27} & 0 & 0 & 0 & 0 & 0 & 0 & 0 & 0 & 0 & 0 & 0 & 0 \\
0 & 0 & -\frac{2048}{9} & -\frac{88064}{27} & -\frac{145408}{27} & -\frac{71680}{27} & 0 & 0 & 0 & 0 & \frac{31232}{27} & \frac{183296}{27} & \frac{150016}{27} & 0 & 0 & 0 & 0 & -\frac{40960}{27} & -\frac{94208}{27} & 0 & 0 & 0 & 0 & \frac{15872}{27} & 0 & 0 & 0 & 0 & 0 & 0 & 0 & 0 & 0 & 0 & 0 & 0 \\
0 & 0 & 0 & 0 & -\frac{2048}{9} & -\frac{4096}{9} & -\frac{2048}{9} & 0 & 0 & 0 & 0 & \frac{512}{3} & \frac{7168}{9} & \frac{5632}{9} & 0 & 0 & 0 & -\frac{256}{9} & -\frac{3584}{9} & -\frac{1792}{3} & 0 & 0 & 0 & \frac{512}{9} & \frac{2048}{9} & 0 & 0 & 0 & -\frac{256}{9} & 0 & 0 & 0 & 0 & 0 & 0 & 0 \\
0 & 0 & -\frac{2048}{9} & -\frac{8192}{9} & -\frac{4096}{3} & -\frac{8192}{9} & -\frac{2048}{9} & 0 & 0 & 0 & \frac{6656}{9} & \frac{6656}{3} & \frac{6656}{3} & \frac{6656}{9} & 0 & 0 & 0 & -\frac{7936}{9} & -\frac{15872}{9} & -\frac{7936}{9} & 0 & 0 & 0 & \frac{4096}{9} & \frac{4096}{9} & 0 & 0 & 0 & -\frac{256}{3} & 0 & 0 & 0 & 0 & 0 & 0 & 0 \\
0 & -\frac{2048}{9} & -\frac{8192}{9} & -\frac{4096}{3} & -\frac{8192}{9} & -\frac{2048}{9} & 0 & 0 & 0 & \frac{6656}{9} & \frac{6656}{3} & \frac{6656}{3} & \frac{6656}{9} & 0 & 0 & 0 & -\frac{7936}{9} & -\frac{15872}{9} & -\frac{7936}{9} & 0 & 0 & 0 & \frac{4096}{9} & \frac{4096}{9} & 0 & 0 & 0 & -\frac{256}{3} & 0 & 0 & 0 & 0 & 0 & 0 & 0 & 0 \\
0 & -\frac{2048}{9} & -\frac{4096}{9} & -\frac{2048}{9} & 0 & 0 & 0 & 0 & 0 & \frac{5632}{9} & \frac{7168}{9} & \frac{512}{3} & 0 & 0 & 0 & 0 & -\frac{1792}{3} & -\frac{3584}{9} & -\frac{256}{9} & 0 & 0 & 0 & \frac{2048}{9} & \frac{512}{9} & 0 & 0 & 0 & -\frac{256}{9} & 0 & 0 & 0 & 0 & 0 & 0 & 0 & 0 \\
0 & 0 & \frac{1024\sqrt{2}}{9} & \frac{1024\sqrt{2}}{9} & 0 & 0 & 0 & 0 & 0 & 0 & -\frac{1}{9}\left(1792\sqrt{2}\right) & -\frac{1}{3}\left(256\sqrt{2}\right) & 0 & 0 & 0 & 0 & 0 & \frac{896\sqrt{2}}{9} & \frac{128\sqrt{2}}{9} & 0 & 0 & 0 & 0 & -\frac{1}{9}\left(128\sqrt{2}\right) & 0 & 0 & 0 & 0 & 0 & 0 & 0 & 0 & 0 & 0 & 0 & 0 \\
0 & 0 & 0 & 0 & \frac{1024\sqrt{2}}{9} & \frac{1024\sqrt{2}}{9} & 0 & 0 & 0 & 0 & 0 & -\frac{1}{3}\left(256\sqrt{2}\right) & -\frac{1}{9}\left(1792\sqrt{2}\right) & 0 & 0 & 0 & 0 & \frac{128\sqrt{2}}{9} & \frac{896\sqrt{2}}{9} & 0 & 0 & 0 & 0 & -\frac{1}{9}\left(128\sqrt{2}\right) & 0 & 0 & 0 & 0 & 0 & 0 & 0 & 0 & 0 & 0 & 0 & 0 \\
0 & 0 & 4096 & 8192 & 4096 & 0 & 0 & 0 & 0 & 0 & -9216 & -10240 & -1024 & 0 & 0 & 0 & 0 & 6144 & 2048 & 0 & 0 & 0 & 0 & -1024 & 0 & 0 & 0 & 0 & 0 & 0 & 0 & 0 & 0 & 0 & 0 & 0 \\
0 & 0 & 0 & 4096 & 8192 & 4096 & 0 & 0 & 0 & 0 & -1024 & -10240 & -9216 & 0 & 0 & 0 & 0 & 2048 & 6144 & 0 & 0 & 0 & 0 & -1024 & 0 & 0 & 0 & 0 & 0 & 0 & 0 & 0 & 0 & 0 & 0 & 0 \\
0 & 0 & -4096 & -12288 & -12288 & -4096 & 0 & 0 & 0 & 0 & 11264 & 22528 & 11264 & 0 & 0 & 0 & 0 & -10240 & -10240 & 0 & 0 & 0 & 0 & 3072 & 0 & 0 & 0 & 0 & 0 & 0 & 0 & 0 & 0 & 0 & 0 & 0
\end{array}\right)
$$

D.5 Computing the Inverse Hessian

For the computation of the second derivatives, we must compute the value of the second $\boldsymbol{x}$ derivative of $\hat{x}$, which we refer to as the inverse Hessian. Since the inverse mapping is a priori unknown, it is inconvenient to invert a 5×5 matrix each time second derivatives are required. Instead, we perform some matrix algebra to determine a more accessible expression for the inverse hessian. The quantity we are interested in is:

$$(\boldsymbol{\nabla} \boldsymbol{J}^{-1})_{\alpha\beta\gamma} = (\boldsymbol{\nabla}\boldsymbol{\nabla}\hat{\boldsymbol{x}})_{\alpha\beta\gamma} = \frac{\partial^2 \hat{x}_\alpha}{\partial x_\alpha \partial x_\beta} \,. \tag{D.5.1}$$

We start by using the chain rule to express this as:

$$(\boldsymbol{\nabla} \boldsymbol{J}^{-1})_{\alpha\beta\gamma} = (\hat{\boldsymbol{\nabla}} \boldsymbol{J}^{-1})_{\alpha\beta\delta} (\boldsymbol{J}^{-1})_{\delta\gamma} \,. \tag{D.5.2}$$

Now, by considering the derivative of an identity matrix we can express the derivative of an inverse as:

$$(\boldsymbol{J}^{-1})' = -\boldsymbol{J}^{-1}\boldsymbol{J}'\boldsymbol{J}^{-1} \,, \tag{D.5.3}$$

and therefore we have:

$$(\boldsymbol{\nabla} \boldsymbol{J}^{-1})_{\alpha\beta\gamma} = -(\boldsymbol{J}^{-1})_{\alpha\nu} \, (\hat{\boldsymbol{\nabla}} J^{-1})_{\mu\nu\delta} \, (\boldsymbol{J}^{-1})_{\nu\beta} \, (\boldsymbol{J}^{-1})_{\delta\gamma} \,, \tag{D.5.4}$$

as our final expression. We recognise the rank three tensor as the Hessian defined as:

$$\boldsymbol{H} \equiv \hat{\boldsymbol{\nabla}} \boldsymbol{J} = \hat{\boldsymbol{\nabla}}\hat{\boldsymbol{\nabla}} \boldsymbol{x}(\hat{x}) \,, \tag{D.5.5}$$

which can be easily computed from the mapping. Thus our final expression for the second $\hat{x}$ derivative of the local coordinate, $\hat{\boldsymbol{x}}$, is:

$$(\boldsymbol{\nabla} \boldsymbol{J}^{-1})_{\alpha\beta\gamma} = -(\boldsymbol{J}^{-1})_{\alpha\delta} \, (\boldsymbol{H})_{\delta\mu\nu} \, (\boldsymbol{J}^{-1})_{\mu\beta} \, (\boldsymbol{J}^{-1})_{\nu\gamma} \,. \tag{D.5.6}$$

Appendix E

Lagrange Shape Functions

E.1 The Cubic Lagrange Basis

For completeness we record the cubic Lagrange basis below. The basis is given by:

$$\boldsymbol{\psi}_L^C = \begin{pmatrix} \frac{1}{2}\hat{x}_0\left(9\left(\hat{x}_0-1\right)\hat{x}_0+2\right) \\ \frac{1}{2}\hat{x}_1\left(9\left(\hat{x}_1-1\right)\hat{x}_1+2\right) \\ -\frac{1}{2}\left(\hat{x}_0+\hat{x}_1-1\right)\left(3\hat{x}_0+3\hat{x}_1-2\right)\left(3\hat{x}_0+3\hat{x}_1-1\right) \\ \frac{9}{2}\hat{x}_0\left(\hat{x}_0+\hat{x}_1-1\right)\left(3\hat{x}_0+3\hat{x}_1-2\right) \\ \frac{1}{2}(-9)\hat{x}_0\left(3\hat{x}_0-1\right)\left(\hat{x}_0+\hat{x}_1-1\right) \\ \frac{9}{2}\hat{x}_0\left(3\hat{x}_0-1\right)\hat{x}_1 \\ \frac{9}{2}\hat{x}_0\hat{x}_1\left(3\hat{x}_1-1\right) \\ \frac{1}{2}(-9)\hat{x}_1\left(\hat{x}_0+\hat{x}_1-1\right)\left(3\hat{x}_1-1\right) \\ \frac{9}{2}\hat{x}_1\left(\hat{x}_0+\hat{x}_1-1\right)\left(3\hat{x}_0+3\hat{x}_1-2\right) \\ -27\hat{x}_0\hat{x}_1\left(\hat{x}_0+\hat{x}_1-1\right) \end{pmatrix}. \tag{E.1.1}$$

Appendix F

Approximate Solution to the Clamped Inflation Problem

F.1 The Föppl-von Kármán Equations

In this appendix we describe an approximate solution for the clamped, circular geometry of the inflation experiments described in chapter 6. Assuming and axisymmetric solution, the system is described by the following nondimensional equations

$$\Delta^2 u_3 - \left(S_{\rho\rho} u_\rho'' + \frac{1}{\rho} S_{\phi\phi} u_\rho' \right) = \Delta p \,, \tag{F.1.1}$$

$$S_{\rho\rho}' + \frac{1}{\rho} \left(S_{\rho\rho} - S_{\phi\phi} \right) = 0 \,. \tag{F.1.2}$$

subject to the boundary conditions

$$u_\rho(\rho = 1) = e_\rho \, \frac{12(1-\nu^2)}{h^2} \,, \quad u_3(\rho = 1) = 0 \,, \quad u_3'(\rho = 1) = 0 \,, \tag{F.1.3}$$

in which $e_\rho > 0$ is the pre-stretch parameter and the shorthand $f'(x) = df(x)/dx$ is used for the derivatives. Finally, at the centre, we have the following regularity conditions

$$u_\rho(\rho = 0) = 0 \,, \quad u_3'(\rho = 0) = 0 \quad u_3'''(\rho = 0) = 0 \,, \tag{F.1.4}$$

which ensure that the stress and displacements are continuous. Here the (nondimensional) radial, azimuthal and vertical displacements are given by u_ρ, u_ϕ[1] and u_3. ρ and ϕ correspond to the radial and azimuthal coordinates of a plane polar coordinate system. Once again, we use the nondimensionalization introduced in chapter 6.

[1] The azimuthal displacement does not enter the equations, due to the assumed axisymmetry.

F.2 Reductions

We make several assumptions to make the problem more tractable. The first assumption we make is that we may neglect bending: instead solving the Föppl membrane equations. Thus we assume that $S_{\rho\rho} \gg 1$, $S_{\phi\phi} \gg 1$. Following this assumption, the equations become

$$\left(S_{\rho\rho}u''_\rho + \frac{1}{\rho}S_{\phi\phi}u'_\rho\right) = \Delta p\,, \tag{F.2.1}$$

$$S'_{\rho\rho} + \frac{1}{\rho}\left(S_{\rho\rho} - S_{\phi\phi}\right) = 0\,. \tag{F.2.2}$$

The equations are now second order and subject to the boundary conditions

$$u_\rho(\rho = 1) = U_\rho\,, \quad u_3(\rho = 1) = 0\,, \tag{F.2.3}$$

and the following regularity conditions at the centre

$$u_\rho(\rho = 0) = 0\,, \quad u'_3(\rho = 0) = 0 \tag{F.2.4}$$

which ensure that the stress and displacements are continuous.

F.3 Approximate Solution Space

To further reduce the problem, we assume that the solutions are low order polynomials of the radial coordinate: $u_\rho(\rho) \in P_3(\rho)$ and $u_3(\rho) \in P_2(\rho)$. Thus we have

$$u_\rho(\rho) = U_\rho^{[0]} + U_\rho^{[1]}\rho + U_\rho^{[2]}\rho^2 - U_\rho^{[3]}\rho^3 \tag{F.3.1}$$

$$u_3(\rho) = U_3^{[0]} + U_3^{[1]}\rho + U_3^{[2]}\rho^2\,. \tag{F.3.2}$$

In order to satisfy the boundary conditions (equations (F.2.3)-(F.2.4)) the polynomials must assume following form

$$u_\rho(\rho) = U_\rho\,\rho + U_\rho^{[3]}\rho\,(1 - \rho^2)\,, \tag{F.3.3}$$

$$u_3(\rho) = U_3(1 - \rho^2)\,. \tag{F.3.4}$$

where U_3 and $U_\rho^{[3]}$ are constants to be determined.

This results in the following stress components

$$S_{\rho\rho} = \frac{1}{1-\nu^2}\left(U_\rho(1+\nu) + U_\rho^{[3]}((1+\nu) - (3+\nu)\rho^2) + 2{U_3}^2\,\rho^2\right)\,, \tag{F.3.5}$$

$$S_{\phi\phi} = \frac{1}{1-\nu^2}\left(U_\rho(1+\nu) + U_\rho^{[3]}((1+\nu) - (3\nu+1)\rho^2) + 2\nu{U_3}^2\,\rho^2\right)\,. \tag{F.3.6}$$

F.4 In-Plane Stress Balance

Substituting this into the in-plane stress balance results in the following equation

$$\left(-8U_\rho^{[3]} + (6-2\nu){U_3}^2\right)\rho = 0\,, \tag{F.4.1}$$

allowing us to express $U_\rho^{[3]}$ as a function of U_3:

$$U_\rho^{[3]} = \frac{1}{4}(3-\nu){U_3}^2\,. \tag{F.4.2}$$

Thus, we see that the polynomial ansatz exactly satisfies the in-plane stress balance, if the above equation holds.

F.5 Out of Plane Force Balance

It remains to relate the pressure to the deflection, by solving the out-of-plane force balance. The ansatz we have made does not satisfy the equations exactly. However, it can be seen that in the limit $U_\rho \gg {U_3}^2$, the stress components will be approximately constant. Thus, we make the approximation that both stress components are constant and given by the maximum values of the stress obtained from the in-plane force balance:

$$S_{\rho\rho}(\rho) \approx S_{\rho\rho}(\rho=0) = \frac{1}{1-\nu}\left(U_\rho + \frac{1}{4}(3-\nu){U_3}^2\right)\,, \tag{F.5.1}$$

and $S_{\phi\phi} \approx S_{\phi\phi}(\rho=0) = S_{\rho\rho}(\rho=0)$. Substituting the constant stress into the solution we find

$$\Delta p = 4\,S_{\rho\rho}\,U_3\,. \tag{F.5.2}$$

Finally, introducing the expression for the approximate stress (equation (F.5.1)) allows us to write the pressure as the following function of U_3 and U_ρ

$$\Delta p = \frac{1}{1-\nu}\left(4U_3\,U_\rho + (3-\nu){U_3}^3\right)\,, \tag{F.5.3}$$

or in terms of dimensional quantities

$$\Delta p^* = \frac{Eh^*}{R(1-\nu)}\left(4\frac{U_3^*\,U_\rho^*}{R^2} + (3-\nu)\left(\frac{U_3^*}{R}\right)^3\right)\,, \tag{F.5.4}$$

where R is the radius of the clamp. It transpires that this method is in fact equivalent to a collocation method, with a single collocation point at $\rho = 0$, choosing the $P_3(\rho)$ solution space for both unknowns.

Whilst this result is strictly speaking only appropriate for $U_\rho \gg {U_3}^2$, numerical experiments reveal that even in the case $U_\rho = 0$, the error does not exceeds 5% in the membrane limit of the equations. However, this approximation is not appropriate when bending is not negligible, as per our assumptions. In the limit $U_3/U_\rho \to 0$, we may neglect $U_\rho^{[3]}$ in the strain and the resulting solution will exactly satisfy the membrane equations. We refer to this limit as the strong pre-stretch regime, in which $\Delta p \sim U_\rho U_3$.

Interestingly, for membrane-type deformations, a spherical-cap out-of-plane solution (i.e $u_3 \sim (1 - \rho^2)$) approximately holds in both the in-plane stretch dominated (linear) regime, and the self-induced tension dominated (cubic) regime. Thus, when bending is negligible there is *no* way to distinguish which regime a system is using the shape of the membrane at a particular forcing alone: multiple measurements over a range of forcing must be made. This mirrors similar observations made of indentation-type systems made by Vella and Davidovitch [2017].

Appendix G

Linear Stability Analysis of the Föppl-von Kármán Equations

G.1 Linear Stability Analysis

To compute the onset of the symmetry breaking bifurcation we use the method of linear stability analysis. For wrinkling problems, in a circular geometry, with polar coordinates (ρ, ϕ), this entails assuming an initially axi-symmetric solution, that buckles at some critical threshold in parameter space, giving rise to a wrinkling solution.

To explain the concepts of linear stability analysis, we begin with a general example, proceeding to discuss the Föppl-von Kármán equations in depth. We begin by considering a set of nonlinear partial-differential equations

$$\boldsymbol{F}\left(\rho, \phi, \boldsymbol{u}(\rho, \phi)\,;\, P\right) = \boldsymbol{0}\,, \tag{G.1.1}$$

with unknown variables, $\boldsymbol{u}$, and independent variables ρ and ϕ and parameter P.

We assume an initially axisymmetric solution which at some point, as we vary the parameter P, undergoes a symmetry breaking bifurcation that corresponds to the plate wrinkling. Thus, we make the following ansatz for the unwrinkled state

$$\boldsymbol{u}(\rho, \phi) = \bar{\boldsymbol{u}}(\rho)\,. \tag{G.1.2}$$

The set of partial differential equations in (G.1.1) become the axisymmetric equations,

$$\bar{\boldsymbol{F}}\left(\rho, \bar{\boldsymbol{u}}(\rho)\,;\, P\right) = \boldsymbol{0}\,, \tag{G.1.3}$$

which will in general represent a set of nonlinear, ordinary differential equations. These equations can then be solved to provide the base-state for the bifurcation analysis.

To find the wrinkling onset and the wrinkling pattern (i.e. the number of wrinkles observed at the onset), the axisymmetric solution is then assumed to be perturbed by a sinusoidal wrinkling state with infinitesimal amplitude, ϵ:

$$\boldsymbol{u}(\rho,\phi) = \bar{\boldsymbol{u}}(\rho) + \epsilon\,\tilde{\boldsymbol{u}}(\rho)\,e^{ik\phi}\,, \tag{G.1.4}$$

where only the k^{th} term of the Fourier expansion of the solution is considered. Here, we use complex coefficients so that any phase difference between unknown variables can be absorbed into the coefficients.

This ansatz, equation (G.1.4), is substituted into the governing equation, (G.1.1),

$$\boldsymbol{F}\left(\rho,\phi,\bar{\boldsymbol{u}}(\rho) + \epsilon\,e^{ik\phi}\,\tilde{\boldsymbol{u}}(\rho)\,;\,P\right) = \boldsymbol{0}\,, \tag{G.1.5}$$

and terms up to linear order in ϵ are retained.

The $\mathcal{O}(1)$ terms in this equation will constitute the axisymmetric equations, which the base-state will satisfy. The $\mathcal{O}(\epsilon)$ (perturbation) terms must be linear in the perturbed solution, $\tilde{\boldsymbol{u}}$, as the equations are linear in the amplitude ϵ. Thus the equation (G.1.5) becomes

$$\bar{\boldsymbol{F}}\left(\rho,\phi,\bar{\boldsymbol{u}}(\rho)\,;\,P\right) + \epsilon\,e^{ik\phi}\,\tilde{\boldsymbol{F}}\left(\rho,\tilde{\boldsymbol{u}}(\rho)\,;\,\bar{\boldsymbol{u}}(\rho),k\right) = \boldsymbol{0}\,, \tag{G.1.6}$$

where the perturbed equation, $\tilde{\boldsymbol{F}}$, is a linear, ordinary differential equation. As any boundary conditions and loading conditions are satisfied at leading order by the axisymmetric equation, the perturbation equation,

$$\tilde{\boldsymbol{F}}\left(\rho,\tilde{\boldsymbol{u}}(\rho)\,;\,\bar{\boldsymbol{u}}(\rho),k\right) = \boldsymbol{0}\,, \tag{G.1.7}$$

is homogeneous. Thus, we can reformulate the perturbation equation (G.1.7) in terms of a 3×3 differential operator, $\hat{\boldsymbol{J}}$, to write the equation as

$$\hat{\boldsymbol{J}}\left(\rho\,;\,\bar{\boldsymbol{u}}(\rho),k\right)\;\tilde{\boldsymbol{u}}(\rho) = \boldsymbol{0}\,. \tag{G.1.8}$$

The perturbation equations, (G.1.8), will depend on the base-state as a functional parameter, as well as the assumed wavenumber of the perturbation, k. Examining equation (G.1.8), it is clear that the trivial solution $\tilde{\boldsymbol{u}} = \boldsymbol{0}$ will always be a solution to these equations; thus, wrinkling solutions exist at isolated points in parameter space, (P,k), at which multiple solutions exist. The non-trivial solutions, in turn, exist when the Jacobian operator has a

zero eigenvalue: the corresponding eigenvector will be the solution. By searching for these non-trivial solutions, we can find both the bifurcation point, (P_c, k_c), and the corresponding solution, $\tilde{\boldsymbol{u}}(\rho)\exp(ik\phi)$.

We proceed to outline the base-state and bifurcation equations for the displacement-based Föppl-von Kármán equations for the wrinkling problem outlined in chapter 7, applying the above methodology.

G.2 Axisymmetric Base State

To compute the onset of wrinkling, we may perform a linear stability analysis about an initially axisymmetric state. Making the following ansatz

$$\begin{aligned} u_\rho(\rho,\phi) &= \bar{u}_\rho(\rho) + \epsilon\,\tilde{u}_\rho(\rho)\cos(k\phi) \\ u_\phi(\rho,\phi) &= \epsilon\,\tilde{u}_\phi(\rho)\sin(k\phi) \\ u_3(\rho,\phi) &= \bar{u}_3(\rho) + \epsilon\,\tilde{u}_3(\rho)\cos(k\phi) \end{aligned} \tag{G.2.1}$$

we are left with the base-state axisymmetric equations at leading order:

$$\left(\frac{d^2}{d\rho^2} + \frac{1}{\rho}\frac{d}{d\rho}\right)^2 \bar{u}_3 - \left(S_{\rho\rho}\bar{u}_\rho'' + \frac{1}{\rho}S_{\phi\phi}\bar{u}_\rho'\right) = \Delta p\,, \tag{G.2.2}$$

$$S_{\rho\rho}' + \frac{1}{\rho}\left(S_{\rho\rho} - S_{\phi\phi}\right) = 0\,. \tag{G.2.3}$$

Here the stress tensor, $\bar{\boldsymbol{S}}$, is related to the Föppl-von Kármán strain tensor, $\bar{\boldsymbol{S}}^{vK}$, by

$$\bar{\boldsymbol{S}}(\rho) = \frac{1}{1-\nu^2}\left((1-\nu)\bar{\boldsymbol{E}}^{vK} + \nu\mathbb{I}_2\mathrm{Tr}\bar{\boldsymbol{E}}^{vK}\right), \tag{G.2.4}$$

with the components of the axisymmetric Föppl-von Kármán strain tensor given by

$$\bar{E}^{vK}_{\rho\rho} = \tilde{u}_\rho{}' + \frac{1}{2}\left(\tilde{u}_3{}'\right)^2\,, \quad \bar{E}^{vK}_{\rho\phi} = 0 \quad \text{and} \quad \bar{E}^{vK}_{\phi\phi} = \frac{1}{\rho}\bar{u}_\rho\,. \tag{G.2.5}$$

These equations are subject to the boundary conditions

$$\bar{u}_3(\rho=1) = 0\,, \quad \bar{u}_3{}'(\rho=1) = 0 \quad \text{and} \quad \bar{S}_{\rho\rho}(\rho=1) = 0\,, \tag{G.2.6}$$

and the regularity conditions at the centre

$$\bar{u}_\rho(\rho=0) = 0\,, \quad \bar{u}_3'(\rho=0) = 0 \quad \text{and} \quad \bar{u}_3'''(\rho=0) = 0\,. \tag{G.2.7}$$

Thus we have reduced a set of fourth-order, nonlinear, partial-differential equations, into a set of fourth-order, nonlinear, ordinary differential equations.

These equations are identical to the system outlined in section 6, save for the replacement of the stress free boundary condition with an imposed radial displacement condition. As such, both sets of equations are discretized in the same manner, as outlined in the next section.

G.3 Discretization of the Axisymmetric Equations

Before perturbing the system, we solve equations (G.2.2–G.2.3) to determine the axisymmetric base-state. This can be achieved readily numerically, by discretizing the system using the finite difference method with a uniform 1D grid of N nodes, at positions R_n, for $n = \{1, \dots, N\}$. Two discrete unknowns, $\bar{U}_{\rho n}$ and $\bar{U}_{3 n}$, are associated with each point, resulting in a system of $2N$ unknowns.

In the discrete equations, derivatives are computed in terms of combinations of these unknowns, as second-order, central, finite difference derivatives. For boundary conditions, derivatives are computed in terms of second-order, forward and backward finite difference derivatives, at $\rho = 0$ and $\rho = 1$, respectively. Thus, the continuous equations are replaced with a set of $2N$ nonlinear algebraic equations (residuals), $\bar{\boldsymbol{F}}$, in terms of the $2N$ unknowns:

$$\bar{\boldsymbol{F}}(\boldsymbol{R}, \bar{\boldsymbol{U}}_\rho, \bar{\boldsymbol{U}}_3 \,;\, \Delta p) = \boldsymbol{0}\,. \tag{G.3.1}$$

Thus we have reduced the nonlinear ordinary differential equations (G.2.2–G.2.3), to a set of nonlinear algebraic equations. These can be readily solved using the octave function `fsolve`, which uses the `MINPACK` implementation of Powell's hybrid method to find the local minima [Powell, 1970; Moré et al., 1984; Eaton et al., 2014]. This method is a hybrid algorithm, that combines the Newton method with steepest descent methods and relies upon a so-called trust-region, inside which steps are contained. This extension makes Powell's algorithm significantly more stable than a standard newton algorithm [Powell, 1970].

Newton-type methods work more efficiently with an analytic Jacobian, which we can readily determine from the discrete residuals

$$\boldsymbol{J}(\boldsymbol{R}, \bar{\boldsymbol{U}}_\rho, \bar{\boldsymbol{U}}_3) = \frac{\partial}{\partial \bar{\boldsymbol{U}}}\, \bar{\boldsymbol{F}}(\boldsymbol{R}, \bar{\boldsymbol{U}}_\rho, \bar{\boldsymbol{U}}_3 \,;\, \Delta p)\,. \tag{G.3.2}$$

In this case, the Jacobian will depend on the unknowns, due to the nonlinearity of the equations. Here $\bar{\boldsymbol{U}} = \bar{\boldsymbol{U}}_\rho \frown \bar{\boldsymbol{U}}_3$ is the concatenation of the two length N vectors of the (unknown) discrete displacements.

G.4 Perturbation Equations

To compute the wrinkling solution at the onset we must solve the perturbation equations. Substitution of the ansatz, equation (G.2.1), into the Föppl-von Kármán equations (see chapter 7) yields the following perturbation equations

$$\left(\frac{d^2}{d\rho^2}+\frac{1}{\rho}\frac{d}{d\rho}+\frac{k^2}{\rho^2}\right)^2\tilde{u}_3-\left(\bar{S}_{\rho\rho}\tilde{u}_\rho''+\bar{S}_{\phi\phi}\left(\frac{1}{\rho}\tilde{u}_\rho'+\frac{k^2}{\rho^2}\tilde{u}_\phi\right)+\tilde{S}_{\rho\rho}\bar{u}_\rho''+\frac{1}{\rho}\tilde{S}_{\phi\phi}\bar{u}_\rho'\right)=0\,, \quad \text{(G.4.1)}$$

$$\tilde{S}_{\rho\rho}'+\frac{1}{\rho}\left(\ \tilde{S}_{\rho\rho}-\ \tilde{S}_{\phi\phi}\right)=0\,, \quad \text{(G.4.2)}$$

$$\tilde{S}_{\rho\phi}'-\frac{1}{\rho}\left(k\tilde{S}_{\rho\rho}-2\tilde{S}_{\rho\phi}\right)=0\,. \quad \text{(G.4.3)}$$

The components of the perturbed stress tensor are related to the perturbed strain tensor by

$$\tilde{\boldsymbol{S}}(\rho)=\frac{1}{1-\nu^2}\left((1-\nu)\tilde{\boldsymbol{E}}^{vK}+\nu\mathbb{I}_2\mathrm{Tr}\tilde{\boldsymbol{E}}^{vK}\right), \quad \text{(G.4.4)}$$

whose components, in turn, are given by

$$\tilde{E}_{\rho\rho}^{vK}=\tilde{u}_\rho{}'+\bar{u}_3{}'\tilde{u}_3{}'\,,\quad \tilde{E}_{\phi\phi}^{vK}=\frac{1}{\rho}\left(\tilde{u}_\rho+k\tilde{u}_\phi\right)\,, \quad \text{(G.4.5)}$$

and

$$\tilde{E}_{\rho\phi}^{vK}=\frac{1}{2\rho}\left(r\tilde{u}_\phi{}'-\tilde{u}_\phi+k(\tilde{u}_\rho+\bar{u}_3'\,\tilde{u}_3)\right)\,. \quad \text{(G.4.6)}$$

Finally, the boundary conditions for the perturbation equations will be

$$\tilde{u}_3(\rho=1)=0\,,\quad \tilde{u}_3{}'(\rho=1)=0\,,\quad \tilde{S}_{\rho\phi}(\rho=1)=0\quad\text{and}\quad \tilde{S}_{\rho\phi}(\rho=1)=0\,, \quad \text{(G.4.7)}$$

with the regularity conditions at the centre

$$\tilde{u}_\rho(\rho=0)=0\,,\quad \tilde{u}_\phi(\rho=0)=0\,,\quad \tilde{u}_3'(\rho=0)=0\quad\text{and}\quad \tilde{u}_3'''(\rho=0)=0\,. \quad \text{(G.4.8)}$$

These equations are now linear in the unknown displacements and homogeneous.

G.5 Discretization of the Perturbation Equations

We discretize this system, using the same mesh as for the axisymmetric equations, and using the axisymmetric solution as a functional parameter. Thus the continuous equations are replaced by the $3N$ discrete, linear equations:

$$\tilde{\boldsymbol{F}}(\boldsymbol{R},\tilde{\boldsymbol{U}}_\rho,\tilde{\boldsymbol{U}}_\phi,\tilde{\boldsymbol{U}}_3\,;\,k,\bar{\boldsymbol{U}})=\boldsymbol{0}\,. \quad \text{(G.5.1)}$$

The corresponding Jacobian will be

$$\tilde{\boldsymbol{J}}(\boldsymbol{R}; k, \bar{\boldsymbol{U}}) = \frac{\partial}{\partial \tilde{\boldsymbol{U}}} \tilde{\boldsymbol{F}}(\boldsymbol{R}, \tilde{\boldsymbol{U}}_\rho, \tilde{\boldsymbol{U}}_\phi, \tilde{\boldsymbol{U}}_3; k, \bar{\boldsymbol{U}}) = \boldsymbol{0}\,. \tag{G.5.2}$$

This equation does *not* depend on the unknowns, as the discrete equations are linear.

To find symmetry breaking bifurcations, we search for isolated points at which multiple solutions occur: these will occur when the Jacobian determinant is zero. Thus, we can find the wrinkling onset for a particular wavenumber, k, by searching for the first instance when the Jacobian determinant changes sign. Once the parameter values are determined, the form of the wrinkling solution can be found by solving the eigenproblem for the minimum eigenvalue, which will be exactly zero at the numerical onset.

Appendix H

Approximate Solution for a Sheet Clamped at One End

We may make a prediction by for the displacement of the fish-shaped domain, by considering rectangular domain of (nondimensional) length $\ell = \ell^*/L$ and width $w = w^*/L$, where L is a dimensional length scale associated with the sheet. Firstly, we assume that the bending dominates at leading order. We use a nondimensional Cartesian coordinate system $x_2 \in [-w, w]$ and $x_1 \in [0, \ell]$. Thus we have the following in-plane force balance

$$\nabla^4 u_3^*(x_1, x_2) = \Delta p^* L^4/D \tag{H.0.1}$$

where u_3^* is the dimensional deflection, Δp^* is the (constant) applied pressure and D is the bending moment. This equation is subject to clamped boundary conditions at $x_1 = 0$ and free boundary conditions on all other sides. Assuming the domain is wide $w \gg \ell$, such that $u_3(x_1, x_2) \approx u_3(x_1)$, we may write this as

$$\nabla^4 u_3^*(x_1) = \Delta p^* L^4/D \tag{H.0.2}$$

subject to $u_3^*(0) = u_3^{*\prime}(0) = 0$ and $u^{*\prime\prime}{}_3^*(\ell) = u^{*\prime\prime\prime}{}_3^*(\ell) = 0$ with the nondimensional length ℓ. Determination of the solution to this equation is trivial, and the deflection is given by

$$u_3^*/L = \frac{1}{24} F x_1^2 \left(6\ell^2 - 4\ell x_1 + x_1^2\right) , \tag{H.0.3}$$

with F given by $F = \Delta p^* L^3/D$.

This will be an exact solution if the Föppl-von Kármán strain component $\epsilon_{x_1 x_1}^{vK} = 0$. Thus, assuming this to be the case implies that the in-plane displacement will be

$$u_1^*/L = -\frac{1}{2} \int_0^{x_1} u_3'(\bar{x_1}) d\bar{x_1} \, . \tag{H.0.4}$$

Computing this, we find that the solution is given by

$$u_1^*/L = -\frac{F^2 x_1^3 \left(42\ell^4 - 63\ell^3 x_1 + 42\ell^2 x_1^2 - 14\ell x_1^3 + 2x_1^4\right)}{1008}\,. \tag{H.0.5}$$

This result will be exact for an infinitely wide sheet, but is only an approximation for sheets of finite width. Thus, choosing $x = 16/5$ and $\ell = 11/5 - 2\cos(\pi/8)$, as the position of the fishes mouth and length of strip, respectively, we may estimate the displacement of the fish-shaped sheet.